IntechOpen

Noble and Precious Metals

Properties, Nanoscale Effects and Applications

Edited by Mohindar Singh Seehra and Alan D. Bristow

NOBLE AND PRECIOUS METALS - PROPERTIES, NANOSCALE EFFECTS AND APPLICATIONS

Edited by **Mohindar Singh Seehra**
and **Alan D. Bristow**

Noble and Precious Metals - Properties, Nanoscale Effects and Applications
http://dx.doi.org/10.5772/intechopen.69142
Edited by Mohindar Singh Seehra and Alan D. Bristow

Contributors

Jiro Kitagawa, Masami Tsubota, Shouju Wang, Guangming Lu, Jakub Siegel, Marketa Polivkova, Marek Staszek, Michaela Valova, Pavla Sulakova, Vaclav Svorcik, Salem Marhaba, Marga Lensen, Zhenfang Zhang, Gonzalo De Vicente, Fang Ren, Cigdem Yesildag, Lingwen Zeng, Zhiyuan Fang, Pankaj Kashyap, Rajni Yadav, Anil Kumar Sahu, Koushlesh Mishra, Sarawati Prasad Mishra, Deepak Kumar Dash, Lyudmila Moskaleva, Sandra Hoppe, Alena Reznickova, Ondrej Kvitek, Dominik Fajstavr, Nikola Slavikova, Piotr Piszczek, Aleksandra Radtke, Tanujjal Bora, Keith Stine, Jay Bhattarai, Dharmendra Neupane, Vasily Mikhalov, Alexei Demchenko, Joseph Adekoya, Kehinde Ogunniran, Tolutope Siyanbola, Enock Olugbenga Dare, Neerish Revaprasadu, Yi-Lung Cheng, Abhinav Malasi, Ritesh Sachan, Hiroaki Matsui, Bongephiwe Thethwayo, Iva Paterova, Jan Patera, Jiri Krupka, Kveta Jiratova, Mohindar Singh Seehra, Alan Bristow

First published in London, United Kingdom, 2018 by IntechOpen
eBook (PDF) Published by IntechOpen, 2019
IntechOpen is the global imprint of INTECHOPEN LIMITED, registered in England and Wales, registration number: 11086078, The Shard, 25th floor, 32 London Bridge Street
London, SE19SG – United Kingdom
Printed in Croatia

British Library Cataloguing-in-Publication Data
A catalogue record for this book is available from the British Library

Additional hard and PDF copies can be obtained from orders@intechopen.com

Noble and Precious Metals - Properties, Nanoscale Effects and Applications
Edited by Mohindar Singh Seehra and Alan D. Bristow

p. cm.

Print ISBN 978-1-78923-292-9

Online ISBN 978-1-78923-293-6

eBook (PDF) ISBN 978-1-83881-377-2

Meet the editors

Following an early education in India and a PhD degree study from the University of Rochester (USA) in 1969, Mohindar Seehra joined the West Virginia University as an assistant professor of Physics. He became an associate professor in 1973, a professor in 1977, and an Eberly Distinguished Professor in 1992. His honors include the Sloan Foundation Research Fellow (1974–1976); the Fellow of the American Physical Society (1984–present); the Fellow of the Institute of Physics, UK (2001–present); and the Outstanding Referee Award from the American Physical Society in 2010. He supervised the research of 65 graduate and postdoctoral students. He has published over 300 publications on the magnetic, dielectric, optical, and catalytic properties of materials and nanoparticles and authored edited books on magnetic spinels and nanostructured materials. In 2016, he became an Eberly Professor Emeritus.

Alan Bristow was educated in the United Kingdom and received his PhD degree in Physics from the University of Sheffield in 2004. Previously, he was a postdoctoral fellow at the University of Toronto, a research associate at JILA (a division of the National Institute of Standards and Technology at the University of Colorado), an adjunct instructor at the Colorado School of Mines in 2009, and an assistant professor at the West Virginia University from 2010 to 2016, and currently, he is an associate professor at WVU. He leads the Ultrafast Nanophotonics Group in the study of light-matter interaction relevant to quantum and energy technology. He is a member of the American Physical Society, a senior member of the Optical Society of America, and an associate editor of the *Optical Materials Express*.

Contents

Preface

This book was conceived and designed to address the properties and applications of noble and precious metals, which include copper (Cu), silver (Ag), gold (Au), platinum (Pt), palladium (Pd), iridium (Ir), osmium (Os), rhodium (Rh), ruthenium (Ru), and rhenium (Re). The book begins with an introductory chapter written by the editors providing an overview of the properties and applications of these metals. The remaining 18 chapters are written by international authors, and these chapters provide more details about the properties and applications of specific metals including their compounds and nanostructures. The chapters written by international authors were solicited through a proposal and review process. Although the editors reviewed these submitted chapters and made editorial and other substantial changes that were largely accepted by the authors, the style and contents of each chapter reflect primarily the scientific talent and contributions of these authors.

Elements such as copper, silver, and gold are materials with a long-standing link to human wealth and prosperity through their various applications and adornments. Discovery of each of the broader list of noble and precious elements has been followed by the applications ranging from high-tech engineering to developing areas in nanotechnology at the intersection of physical and life sciences. As with many metals, the conduction properties and high-"free" electron concentration are at the heart of their applications. The noble aspect of these metals is their stability at high temperatures and in corrosive chemical environments making them very useful in extreme engineering and chemical applications. Many of these metals and their nanostructures are also finding extensive applications in the biomedical fields as presented by various authors in these chapters.

The 18 chapters following the introductory chapter are arranged into the following sections: (i) "Theoretical Aspects, Modeling, and SERS (Surface-Enhanced Raman Scattering)" containing five chapters; (ii) "Synthesis and Properties of Nanostructures" containing six chapters; (iii) "Biomedical and Other Applications" consisting of five chapters; and (iv) "Metallurgy and Recovery" containing two chapters. The last section on "Metallurgy and Recovery" contains a chapter on the extraction of platinum-group metals and a chapter on the extraction of rare earths from used magnets. Although rare earths are not traditionally included in *Noble and Precious Metals - Properties, Nanoscale Effects, and Applications*, the editors decided to include this chapter in this book because of the importance of the rare earths in modern technology.

The editors would like to thank all the authors contributing to this book, and to Ms. Kristina Kardum at IntechOpen for her valuable assistance in bringing this book to conclusion. Alan D. Bristow also wishes to acknowledge the support from the Technische Universität Dortmund in Germany, where he was on sabbatical during the writing of this book.

Mohindar Singh Seehra and Alan D. Bristow
Department of Physics and Astronomy
West Virginia University
Morgantown, WV, USA

General

Chapter 1

Introductory Chapter: Overview of the Properties and Applications of Noble and Precious Metals

Mohindar S. Seehra and Alan D. Bristow

Additional information is available at the end of the chapter

http://dx.doi.org/10.5772/intechopen.75503

1. Introduction

The noble and precious metals correspond to a selection of the transition-metal group of the periodic table (see **Figure 1**), including copper (Cu), silver (Ag), gold (Au), platinum (Pt), palladium (Pd), iridium (Ir), osmium (Os), ruthenium (Ru), rhodium (Rh), and rhenium (Re). Pt also gives its name to a distinct subset of these elements, known as the platinum group, which include Ru, Rh, Pd, Os, Ir, and of course Pt. Additionally, Ru, Rh, Re, Os, and Ir are considered refractory metals—defined by melting points exceeding about 2000°C—along with several more abundant and commonly used transition metals, such as titanium (Ti), chromium (Cr), molybdenum (Mo), and tungsten (W). The noble and precious metals generally crystallize in the face-centered cubic (fcc) structure except for Ru, Re, and Os, which have the hexagonal close-packed (hcp) structure. The use of Cu, Ag, Au, and Pt in jewelry and coinage has been known throughout human history. The chapters presented in this book deal with other applications of some of these metals along with their fundamental properties.

This introductory chapter presents a survey of important properties and applications of noble and precious metals. These include properties at the nanoscale and their applications, particularly in the areas of catalysis and biomedicine. Only a brief mention of these properties is made, giving references to recent papers and reviews, which the readers can utilize to gain access to more comprehensive literature on the subject. The chapter is organized in sections with each section devoted to a single noble and precious metal.

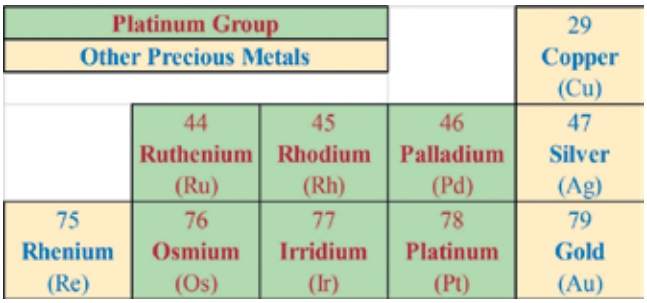

Figure 1. Section of the periodic table corresponding to precious and noble metals, depicting atomic number chemical name and symbol.

2. Copper (Cu)

Being the most abundant and least expensive of the noble and precious metals, with excellent electrical and thermal conductivity, copper is used extensively in electrical power transmission, plumbing, cookware, etc. However, because of the reactivity of Cu toward oxygen, water, and other chemicals, synthesis of Cu nanoparticles (NPs) requires special procedures [1]. The synthesis and applications of Cu and Cu-based nanoparticles (NPs) to catalysis including gas-phase catalysis, electro-catalysis, and photocatalysis are reviewed by Gawande et al. [1]. The review paper by Din et al. [2] has described various methods for the synthesis of Cu NPs including chemical, physical, and biological methods. Medical applications of Cu NPs include their use as antibiotic, antifungal, and antimicrobial agents.

3. Silver (Ag)

The important properties of silver include its good electrical conductivity and its chemical stability. Bulk Ag is a common material for high-quality reflectors of electromagnetic radiation in the visible regime, superseding cheaper non-noble metals such as aluminum. On the nanoscale, Ag-NP applications include their catalytic activity and antimicrobial properties such as improving the microbial quality of drinking water [3]. Various methods for synthesizing Ag-NPs are described in the recent paper of Alaqad and Saleh [3]. Synthesis of metallic nanoparticles of Ag, Au, Pt, and Pd employing plant extracts is reviewed in the recent paper by Akhtar et al. [4]. Other review papers on the synthesis, applications, and toxicology of Ag-NPs are those by Iravani et al. [5] and Tran et al. [6]. Finally, Jo et al. [7] have reported ferromagnetism in Ag-NPs and associated it with the surface atoms on the Ag-NPs whose percentage concentration increases with decrease in particle size. In addition to extensive NP fabrication, nanoscale films of Ag have been grown using molecular beam epitaxy to improve the underdeveloped area of plasmonics [8], where optical excitation leads to a collective oscillation of electronic plasma in the metal.

4. Gold (Au)

Historically, accumulation of gold by people and nations has marked their economic wealth. Because of exceptional chemical stability and good electrical conductivity, gold is a good scientific material for contacts. Au is one of the best optical reflectors throughout the infrared region of the electromagnetic spectrum. Like many of the noble metals discussed here, its optical and dielectric constants can be found in both Johnson and Christy [9] and Palik [10].

Au-NPs exhibit a strong size-dependent position of a localized plasmon resonance and attracted considerable attention in recent years in technologies such as biomedicine (diagnosis, imaging, sensing), catalysis, and electronics. The review paper by Daniel and Astruc [11] and follow-up papers by Jain et al. [12], Huang et al. [13], and Piella et al. [14] are good sources for accessing literature on Au-NPs and their many applications. Another interesting aspect of Au-NPs is their size-dependent magnetic properties which are believed to originate from electron transfer between surface atoms of Au and capping agent (thiols) [15, 16]. The strength of ferromagnetic moment originating from this electron exchange at the surface varies as 1/D where D is the size of the particles. Furthermore, Au-NPs can be readily coated with dielectric materials to protect the metal from erosion due to photocatalyzing chemical reactions and provide a wider range of absorption energies for solar light harvesting [17].

5. Platinum (Pt)

Platinum is less abundant than Cu, Au, or Ag but has a similar place in history as the latter two as a material of value. Like the other metals, it is ductile and malleable but denser and harder to work. Pt is remarkably chemical unreactive, but as the electronic structure calculations of Andersen for Pt, Pd, Ir, and Rh show [18], Pt has a large free electron density, making it a good chemical catalyst. Pt is widely used in catalytic converters to oxidize carbon monoxide produced in internal combustion engines [19]. Pt is also used as contacts in situations that exploit the chemical stability, for example, at extreme temperatures or in salt water conditions [20]. It is also a versatile electrode in electrochemical experiments [21].

At the nanoscale, Pt NPs have also been engineered, primarily for catalytic applications [22]. Other potential applications of Pt NPs reported in literature are in cancer therapy [23, 24]. For size <5 nm of Pt NPs, observations of superparamagnetism [25] and ferromagnetism [26] have been reported.

6. Palladium (Pd)

Pd is a silvery white metal, and it is often found in deposits along with Pt as well as deposits of Ni and Cu. Pd is resistant to corrosion, and its alloys are used in jewelry as “white gold.”

One of the distinguishing properties of Pd is its enormous capacity to absorb hydrogen in the ratio of about 900:1 by volume, making it an excellent catalyst for hydrogenation and dehydrogenation reaction [27]. The absorption of H_2 leads to the reversible formation of PdH_x.

Several groups have reported the synthesis of Pd NPs by different techniques [28, 29] and their various applications such as antimicrobial agents [30, 31] and for surface-enhanced Raman scattering [32, 33]. Regarding its magnetic properties, development of a ferromagnetic moment with decrease in particle size of Pd to nanoscale sizes has been reported by several groups and interpreted on a core-shell model [34–37]. In this model, atoms in the core retain the properties of bulk Pd, whereas atoms in the shell develop a ferromagnetic feature due to reduced symmetry of the surface atoms and electron exchange with the capping agents.

7. Iridium (Ir)

Iridium is a silvery white metal with high resistance to corrosion, and it is very dense (density = 22.55 gm/cm^3). In Earth's crust, it is quite rare, about two parts per billion (ppb), and often found with other noble metals. As a metal, it is unworkable but finds use in space components and specialty spark plugs when alloyed with Pt. In recent years, nanoparticles of Ir have been synthesized using various chemical techniques [38, 39] and tested as catalysts [40–42] and as sensors [43–45]. Examples of catalytic activity are the use of Ir NPs for the degradation of dyes [38] and for hydrogenation reactions [41, 42]. As biosensors, Ir NPs have been tested for the detection of glucose [43, 44].

8. Osmium (Os)

Osmium is a member of platinum (Pt) group, and it is often found in ores of Pt. Like Ir, it is also very rare in Earth's crust (~1 ppb) and has very high density (22.58 gm/cm^3) and high melting point (~ 3000°C). Although Os is an unworkable metal, Os-Pt alloys are harder than Pt and are often used in specialty equipment. Its oxide, OsO_4, is quite toxic to the respiratory system.

In recent years, there have been several reports on the synthesis of nanoparticles of Os [46–47] and Os alloys for potential applications. Applications reported so far include the following: use of Ni-Ir and Ni-Os bimetallic NP alloys for hydrogenation reactions [48], Os NPs for CO oxidation [49, 50], and Os NP electro-catalysts for PEM fuel cells [51] and direct methanol fuel cells [52].

9. Ruthenium (Ru)

Ruthenium is normally found as a minor component of Pt ores, is chemically inert, and has a silvery color. Ru has the electron configuration of a $5s^1$ outer shell, making it more like Rh, Au, and Pt than the rest of its own group [iron (Fe), Os, and hassium (Hs)] which have an s^2

outer shell. In many respects Ru differs from Fe, except in the aqueous cations it can form. It marks a point in the periodic table that distinguishes the second and third rows, as well as the left and right sides of the block of transition metals.

At the level of less than 1% concentration, Ru can increase the hardness of Pt and Pd alloys, can markedly increase the corrosion resistance of titanium (Ti), [53] and is found in superalloys that operate in extreme high temperatures, such as in jet engine turbines [54]. Of course, like most noble and precious metals, Ru is a contact material that has comparable properties to Rh alloys achieved at a lower cost [54]. In particular, Ru can be found in dimensionally stable anodes and optode sensors operating in corrosive environments. Moreover, ReO_2 and $MReO_3$ (where M is a metal) compounds appear in electronics as thick-film resistors [55]. Other ruthenates appear in explorations of superconductivity, magnetism, and multiferroic prototypes. Although bulk Ru is a paramagnet at room temperature and when alloyed with molybdenum, it becomes a superconductor below 10.6 K [56]. Organometallic NPs and carbon-supported NPs containing Ru have been synthesized for application related to solar cells [57] and catalysis [58, 59]. There is a wide range of work on Ru in both homogeneous and heterogeneous catalyses and the synthesis of Ru NPs [47, 49, 50].

10. Rhodium (Rh)

Rhodium is hard, silvery-white transition metal that is both corrosion resistant and chemically inert. Rh is one of the rarest elements to be found on Earth, which slowed its uptake as anything other than a precious metal used for decoration in white-gold jewelry. Rh is now in common use, since the invention and legal requirement for three-way catalytic converters to reduce NO_x produced in the exhaust of combustion engines [54]. Hence, the predominant use of Rh is in the automotive industry. There have been other applications, such as early-generation Rh-based neutron flux detectors and electrical contacts where economics meet the small electrical resistance requirements. Current alternative uses include coatings for optical instruments [60] and catalysis in biological applications [61–63]. Heterogeneous catalysis has also been advanced by the fabrication and use of bimetallic Rh-based core-shell nanoparticles [64]. Ferromagnetism in Rh NPs has been reported in Ref. [35].

Depending on how the automotive and other industries progress in the next few decades, new or recycled sources of Rh may be required. Recycling from electronic and catalytic industries seems promising. Alternatively, because Rh is a by-product of uranium-235 fission, reclamation from nuclear fuel waste may become commercially viable.

11. Rhenium (Re)

Rhenium has a melting point that is exceeded only by W and carbon (C). It is dense metal with a white-silver hue. Unlike many of the other noble metals, Re is more commonly extracted along with Mo than with Pt; hence, it is not part of the platinum group. Nonetheless, it has similar

corrosion-resistant, high-temperature alloying advantages of much of that group. Once again, major applications are in extreme conditions Examples include Pt-Re alloys used for refining lead-free high-octane fuels where its inert properties avoid chemical degradation [65, 66] or W-Re and nickel-Re superalloys that withstand high temperatures as jet engine coatings [67]. W-Re alloys are more ductile at low temperature and more stable at high temperature, properties which also allow them to withstand electron impacts during the generation of X-rays and acting at thermocouples for extreme temperatures. In more recent years, metal–organic NPs containing Re has been explored for use in biological application [61] and to enhance catalysts [68]. The synthesis of Re NPs has been reported by Ayvali et al. [69] and Kundu et al. [70], the latter authors also reporting the applications of Re NPs in catalysis and surface-enhanced Raman scattering. Also, Re dichalcogenide films have been grown to study their electronic, optronic, and spintronic properties [71], extending the family of van der Waals-bonded transition-metal dichalcogenide which offer layer-by-layer tailoring of device properties.

12. Concluding remarks

As described above, noble and precious metals play essential roles in a wide range of technologies. Development of new coating materials, contacts, emitters, and catalysts is essential to better performances in engines, synfuels, and electrical components alike. Not only is material fabrication, especially at the nanoscale, an ongoing and vital area of research and development, so is the extraction, refining, and reclamation. One such example is the growing industry of metal recovery from the vast output of old products produced by the consumer electronic market. Similarly, transition-metal compounds are routinely at the center of new breakthroughs in fundamental physics that may one day lead to unthought of technologies. Regardless of the direction, the investigations into the properties and applications of these metals remains active, with more developments expected in the future.

Author details

Mohindar S. Seehra* and Alan D. Bristow

*Address all correspondence to: mohindar.seehra@mail.wvu.edu

Department of Physics and Astronomy, West Virginia University, Morgantown, WV, USA

References

[1] Gawande MB, Goswani A, Felpin F, Asefa T, Huang X, Silva R, Zou X, Zboril R, Verma RS. Chemical Reviews. 2016;**116**:3722-3811

[2] Din MI, Rihan R. Analytical Letters. 2017;**50**:50-62

[3] Alaqad K, Saleh TA. Journal of Environmental & Analytical Toxicology. 2016;**6**:384 (10 pages)

[4] Akhtar MS, Panwar J, Yun Y-S. ACS Sustainable Chemical Engineer. 2013;**1**:591-602

[5] Iravani S, Korbekandi H, Mirmohammadi SV, Zolfaghari B. Research in Pharmaceutical Sciences. 2014;**9**:385-406

[6] Tran QH, Nguyen VQ, Le A-T. Advances in Natural Sciences: Nanoscience and Nanotechnology. 2013;**4**:033001 (20 pages)

[7] Jo Y, Jung MH, Kyum MC, Park KH, Kim YN. Journal of Magnetics. 2006;**11**:160-163

[8] Sun L, Zhang C, Wang C-Y, Su P-H, Zhang M, Gwo S, Shih C-K, Li X, Wu Y. Scientific Reports. 2017;**7**:8917 (6 pages)

[9] Johnson PB, Christy RW. Physical Review B. 1972;**6**:4370-4379

[10] Palik ED. Handbook of optical constant of solids. Elsevier. 2012

[11] Daniel M-C, Astruc D. Chemical Reviews. 2004;**104**:293-346

[12] Jain PK, Lee KS, El-Sayed IH, El-Sayed MA. The Journal of Physical Chemistry. B. 2006;**110**:7238-7248

[13] Huang X, El-Sayed MA. Journal of Advanced Research. 2010;**1**:13-28

[14] Piella J, Bastus NG, Puntes V. Chemistry of Materials. 2016;**28**:1066-1075

[15] Crespo P et al. Physical Review Letters. 2004;**93**:087204 (4 pages)

[16] Dutta P, Pal S, Seehra MS, Anand M, Roberts CB. Applied Physics Letters. 2007;**90**:213102 (3 pages)

[17] Li J, Cushing SK, Meng F, Senty TR, Bristow AD, Wu N. Nature Photonics. 2015;**9**:601-608

[18] Krogh Andersen O. Physical Review B. 1970;**2**:883-906

[19] Gerhard E. Angewandte Chemie. 2008;**47**:3524-3535

[20] Lide DR. Handbook of Chemistry and Physics. Vol. 4. New York: CRC Press; 2007-2008. p. 26

[21] Seehra MS, Bollineni S. International Journal of Hydrogen Energy. 2009;**34**:6078-6084

[22] Long NV, Chien ND, Hayakawa T, Hirata H, Lakshminarayana G, Nogami M. Nanotechnology. 2009;**21**:035605

[23] Porcel E et al. Nanotechnology. 2010;**21**:085103

[24] Yamada M, Foote M, Prow TW. WIREs Nanomedicine and Nanobiotechnology. 2015;**7**: 428-445

[25] Litran R et al. Physics Review. 2006;**B73**:054404

[26] Garcia MA et al. Chemistry of Materials. 2007;**19**:889-893

[27] Bacik DB, Zhang M, Zhao D, Roberts CB, Seehra MS, Singh V, Shah N. Nanotechnology. 2012;**23**:294004 (13 pages)

[28] Nadagouda MN, Verma RS. Green Chemistry. 2008;**10**:859-862

[29] Sharada S, Suryawanshi PL, Kumar R, Gumfekar SP, Narsaiah TB, Sonawane SH. Colloids and Surfaces A: Physicochemical and Engineering Aspects. 2016;**498**:297-304

[30] Hazarika M, Borah D, Bora P, Silva AR, Das P. PLoS One. 2017;**12**(9):e0184936

[31] Saldan I, Semenyuk Y, Marchuk I, Reshetnyak O. Journal of Materials Science. 2015;**50**: 2337-2354

[32] Chen H, Wei G, Ispas A, Hickey SG, Eychmuller A. Journal of Physical Chemistry C. 2010;**114**:21976-21981

[33] Xu D, Yan X, Diao P, Yin P, Phys J. Journal of Physical Chemistry C. 2014;**118**:9758-9768

[34] Oba Y, Okamoto H, Sato T, Shinohara T, Suzuki J, Nakamura T, Muro T, Osawa H. Journal of Physics D: Applied Physics. 2008;**41**:134024 (5 pages)

[35] Jeon YT, Lee GH. Journal of Applied Physics. 2008;**103**. DOI: 094313

[36] Seehra MS, Rall JD, Liu JC, Roberts CB. Materials Letters. 2012;**68**:347-349

[37] Shinohara T, Sato T, Taniyama T. Physical Review Letters. 2003;**91**:197201

[38] Yee CK, Jordan R, Ulman A, White H, King A, Rafailovich M, Sokolov J. Langmuir. 1999;**15**:3486-3491

[39] Rueping M, Koenigs RM, Borrmann R, Zoller J, Weirich TE, Mayer J. Chemistry of Materials. 2011;**23**:2008-2010

[40] Goel A, Lasyal R. Water. Science and Technology. 2016;**74**:2551-2559

[41] Liu D et al. Scientific Reports. 2016;**6**:21365

[42] Redel E, Kramer J, Thomann R, Janiak C. Journal of Organometallic Chemistry. 2009;**694**: 1069-1075

[43] Zhou C, Shi Y, Ding X, Li M, Luo J, Lu Z, Xiao D. Analytical Chemistry. 2013;**85**:1171-1176

[44] Shen J, Dudik L, Liu C-C. Sensors and Actuators B: Chemical. 2007;**125**:106-113

[45] da Silva CP, Franzoi AC, Fernandes SC, Dupont J, Vieira IC. Enzyme and Microbial Technology. 2013;**52**:296-301

[46] Pitto-Barry A, Perdigao LM, Walker M, Lawrence J, Costantini G, Sadler PJ, Barry NP. Dalton Transactions. 2015;**44**:20308-20311

[47] Kramer J, Redel E, Thomann R, Janiak C. Organometallics. 2008;**27**:1976-1978

[48] Egeberg A, Dietrich C, Kind C, Popescu R, Gerthsen D, Behrens S, Feldmann C. Chem CatChem. 2017;**9**:3534-3543

[49] Liu C, Leong WK, Zhong Z. Journal of Organometallic Chemistry. 2009;**694**:2315-2318

[50] Dimakis N, Navarro NE, Smotkin ES. The Journal of Chemical Physics. 2013;**138**:174704

[51] Lam VWS, Gyenge EL. Journal of the Electrochemical Society. 2008;**155**:B1155-B1160

[52] Borja-Arco E, Jimenez-Sandoval O, Escalante-Garcia J, Magallon-Cacho L, Sebastian PJ. International Journal of Electrochemistry. 2011:830541 (8 pages)

[53] Schutz RW. Platinum Metals Review. 1996;**40**:54-61

[54] Loferski PJ. 2014 Minerals Yearbook: Platinum-Group Metals. US Geological Survey; 2014 URL: https://minerals.usgs.gov/minerals/pubs/commodity/platinum/

[55] Rane S, Prudenziati M, Morten B. Materials Letters. 2007;**61**:595-599

[56] Rammakrishnan TV, Rao CNR. Superconductivity Today. University Press; 1999

[57] Kuang D, Ito S, Wenger B, Klein C, Moser J-E, Humphry-Baker R, Zakeeruddin SM, Grätzel M. Journal of the American Chemical Society. 2006;**128**:4146-4154

[58] Lara P, Philipott K, Chaudret B. ChemCatChem. 2013;**5**:28-45

[59] Ohyama J, Sato T, Yamamoto Y, Arai S, Satsuma A. Journal of the American Chemical Society. 2013;**135**:8016-8021

[60] Smith WJ. "Reflectors" in Modern Optical Engineering: The Design of Optical Systems. McGraw-Hill; 2007. pp. 247-248

[61] Portenkirchner E, Oppelt K, Egbe DAM, Knör G, Sariçiftçi NS. Nanomaterials Engineering. 2013;**2**:134-147

[62] Öhrström L. Nature Chemistry. 2016;**8**:90 (1-page)

[63] Chen W-W, M-H Xu. Organic & Biomolecular Chemistry. 2017;**15**:1029-1050

[64] Tao F, Grass ME, Zhang YW, Butcher DR, Renzas JR, Liu Z, Chung JY, Mun BS, Salmeron M, Samorjai GA. Science. 2008;**322**:932-934

[65] Polyak DE. Minerals Yearbook: Rhenium. US Geological Survey; 2015, 2015 URL: https://minerals.usgs.gov/minerals/pubs/commodity/rhenium/myb1-2015-rheni.pdf

[66] Kunkes EL et al. Journal of Catalysis. 2008;**260**:164-177

[67] Naumov AV. Russian Journal of Non-Ferrous Metals. 2007;**48**:418-423

[68] Martin-Aranda RM, Čejka J. Journal of Catalysis. 2010;**53**:141-153

[69] Ayvali T et al. Chemical Communications. 2014;**50**:10809

[70] Kundu S, Ma L, Dai W, Chen Y, Sinyukov AM, Liang H. ACS Sustainable Chemistry & Engineering. 2017;**5**:10186-10198

[71] Hafeez M, Gan L, Bhatti AS, Zhai T. Materials Chemistry Frontiers. 2017;**1**:1917-1932

Section 2

Theoretical Aspects, Modeling and SERS

Chapter 2

Band Structure, Morphology, Functionality, and Size-Dependent Properties of Metal Nanoparticles

Joseph Adeyemi Adekoya,
Kehinde Olurotimi Ogunniran,
Tolutope Oluwasegun Siyanbola,
Enock Olugbenga Dare and Neerish Revaprasadu

Additional information is available at the end of the chapter

http://dx.doi.org/10.5772/intechopen.72761

Abstract

Metallic nanoparticles are gradually emerging as important materials because of their novel shape and size-dependent chemical and physical properties that differ drastically from their bulk counterparts. The main challenges in the field of nano-chemistry are the rational control and manipulation of synthesis to derive materials with one of their dimensions in nanometer regime, and upscale production of nanomaterials for device fabrication. This chapter reviews the fundamentals of the quantum properties of metals and quantum mechanical size effects with special focus on clusters of Pd, Pt, Au and Ag. Effects of reduction in size of metal nanoparticles to nanoscale on their various properties (structural, thermal, mechanical, chemical, electronic, magnetic and optical) are reviewed. The chapter concludes with a review of select medical applications of metal nanoparticles.

Keywords: metal nanoparticles, quantum theory, density functional theory, finite size effects, vacancies and dislocations, medical applications

1. Introduction

The discovery and development of novel materials has led to rapid industrial and technological use of these materials [1]. It has produced synergistic effect between scientific discovery and astronomical technology growth. More recently, the ability to 'synthesise-up' nanoscale architectures and components has given rise to the field of 'nanochemistry' the preparation and manipulation of molecular structures on a length-scale of 0.1–100 nm [2]. This phenomenal breakthrough has been achieved by exploiting the properties of materials at the nanoscale

dimension. As a result, nanoscience is producing in-depth knowledge of the properties of matter as it transforms from bulk to nano-phase, in which state, most of the properties differ from the conventional atomic or bulk phase. Meanwhile, it is imperative to understand the properties of matter as atom, molecule, or crystal in the bulk phase in order to gain an appreciation of the quantum properties of nanomaterials.

The diversity of the physical and chemical properties of inorganic nanoparticles can be attributed to phase transformation which has significantly affected the arrangement of the constituent atoms in a way that leads to quantization of energy levels. An understanding of this can be obtained from the chemistry of atomic structure which is discussed in details in many textbooks on Quantum Mechanics and Quantum Chemistry [3–6].

The ability to synthesise and process nanomaterials or nanostructures is an essential aspect of nanotechnology. The study of new physical properties and applications of nanomaterials or nanostructures are possible only when nanostructured materials are made available with the desired size, morphology and chemical composition. However, nanoparticles of noble metals have a history of fundamental synthetic strategies known for some decades. A number of synthetic routes have been developed for metal nanoparticles which emanate from the knowledge of small particulate as earlier mentioned. The main objective of which is to obtain monodisperse metal particles with high degree size, structure and composition functionalities, diameters ranging from 1 to 100 nm, consistent crystal or amorphous structure, large surface area to volume ration and a high degree of mono-dispersity. Moreover, one of the challenges encountered in this process is the need to control the size of nanoparticles. Among the synthetic methods developed, gas-phase technique would have been one of the best with respect to size and mono-dispersity but for the high reaction temperature which often leads to uncontrolled particle size during anisotropic nucleation and nanoparticle growth. Rigorous control over reduction, nucleation-condensation and growth, as well as effective purification and isolation methods ensure monodispersed nanoparticles with tunable morphological properties. The homogeneity of metal nanoparticles and their ability to resist agglomeration, sintering, and flocculation can be enhanced by re-dispersing the nanoparticles in solution. However, polar solvents and surfactants have been used to stabilize semiconductors and metallic nanoparticles respectively in most syntheses aimed at producing monodispersed nanoparticles. In the preparation of nanomaterials, organic compounds are known to play similar role as surfactants in the processing of mesoporous materials. In this chapter, some fundamental principles are first considered in order to rationalise the concept of quantum size effect in the evolution of properties of materials at the nanoscale level.

2. Crystalline solids and their periodicity

In the above, it has been stated that properties of materials change as the materials transform from bulk to nano-phase. Let us consider a crystalline solid having a three-dimensional system, in which the electronic properties of bulk crystalline solids can be rationalized based on existing principle of the eigen wave-functions, φ. For a perfectly ordered three-dimensional

http://dx.doi.org/10.5772/intechopen.72761

crystal, the periodic repetition of atoms (molecules) along the one dimension is replaced by three-dimensional repeating unit cell. The unit cell is made up of atoms arranged in the characteristic crystal structure, such that repeating unit cells in all the space are enough to form the entire crystal structure. Consequently, the crystal has translational symmetry because the structure of the crystal can be generated by translation of the unit cell in all three dimensions. Translational symmetry in a periodic structure is also referred to as discrete symmetry because only certain translations that correspond to integer multiples of the lattice translation vectors derived from the unit cell lead to symmetry equivalent points. Invariably, the weak discrete translation symmetry in crystals leads to a weaker quasi conservation law for quasi or crystal momentum. This discrete translation symmetry can be used to give an account of the electronic properties of crystals which is described by Bloch's theorem [7].

A brief rationalization of the Bloch's theorem is hereby considered. In a crystalline solid, the three-dimensional periodicity of the atomic arrangement gives rise to a corresponding periodicity in the internal electric potential due to the ionic cores. When this periodic potential is incorporated into the Schrodinger equation, the outcomes are certain allowed wave functions that are modulated by the lattice periodicity. Bloch's theorem therefore states that these wave functions appear in form of a plane wave. Such wave functions are known as Bloch functions and represent travelling waves passing through the crystal but with a form modified periodically by the crystal potential due to each atomic site.

The two important inferences drawn from Bloch theorem are (i) the volume of k-space occupied by each wave-vector state in one-dimension (1D) is $2\pi/L$; for a three- dimension (3D) crystal, a k-space volume is $8\pi^3/L^3$ and (ii) the number of wave-vector states contained within each energy band. The lattice periodicity also gives rise to diffraction effects which is a key characterization tool in solid state materials. It is well known that electrons possess wave-like properties, therefore, the free electrons in the crystal would experience diffraction effect which invariably affects the spectrum of apparent electron energies.

We imagine an electron travelling along a one-dimension chain of atoms of spacing a, where each atom would generate a reflection of the wave. These reflections can be reproduced if $m\lambda = 2a$, for a given m, λ is de Broglie wavelength for the electron. Given this condition, both the forth and backward traveling waves coexist and can be superimposed over each other creating standing waves. The standing waves give rise to electron density distributions of the order $|\varphi(x)|^2$ having either nodes or antinodes at the lattice sites x = a, 2a, 3a,…. These solutions may have the same wave-vector value but they definitely have different energies domains as a result of different interaction between the energy level of electron and the positively charged ions. As a result, a band gap appears in the electron dispersion curve corresponding to certain values of wave-vector [3].

3. Morphological properties of metals

As mentioned earlier, understanding the structure and mechanical properties of nanostructured materials is important for the manipulation and modification at the atomic level.

Increasing the number of atoms from a single one via a cluster to the bulk, one finds 'magic number' which corresponds to crystalline structures of high stability. These are reflected, for example by peaks representing different clusters of various sizes. In the case of rare gas clusters with an isotropic atom interaction potential, the stable configurations correspond to a dense packing of atoms, for instance, icosaeders around a central atom with increasing particle numbers ('magic numbers' of 13, 55, 147…). With increasing size, these five-fold symmetries show more and more defects. In the case of argon one observes at about 1000 atoms the crystalline structure of the bulk solid.

For more complex atoms such as metals, with anisotropic interaction potentials or open shells the morphologic rules become more complicated. For large clusters magic numbers exist, but for smaller clusters electronic effects dominate. In this range of smaller clusters the closed electronic shells (N = 8, 18, 20…) result in most stable clusters [8]. As it were, it would be interesting to observe simple morphologic rules since crystal structures are affected by small changes in the long range interaction potentials. For aggregates with dimensions of the order of several atom distances, a strong influence of these 'surface' effects is expected and stability of such an aggregate cannot be easily predicted. Moreover, it is possible to calculate or measure the resulting structures for a given number of atoms or better still deduce the structure of a nanoscaled aggregate of given dimensions and determine whether such a structure is stable or not. In this context the most important structures are these connecting elements between specific aggregates, for example, simple wire. An important question is how thin could this wire be?

The mechanical properties of a wire of individual gold atoms have recently been investigated by a combination of scanning tunnelling microscopy (STM) and an atomic force (AFM) sensor [9]. The gold wire was connected between the force microscope tip and the golden tip of an STM. The force necessary to stretch the wire was then determined with the help of a second STM which detected the extension of the AFM tip. The surprising result was that the bond strength between the atoms in the nanowire was twice that of the bond strength in the bulk. Apparently, the effective stiffness of a nanostructure depends on the exact configuration of the atoms at the base.

4. Electronic structure and optical properties of metals

Quantum mechanical size effects occur if the size of a crystal or particle approaches the characteristic length scale which determines the coherence of its wavefunction. At or below this size the electronic, optical and magnetic properties become size-and shape-dependent. In particular, the optical behaviour is very sensitive to quantum effects otherwise called 'quantum confinement'. The significance of the effects depends on the temperature and the distance between neighbouring energy levels or bands which has to be large compared to thermal energy, $k_B T$, in order to avoid a smear-out of the effect by thermal fluctuations.

The absorption of a photon results in an electron–hole pair in the material, precisely a quantized state called exciton. In semiconductors, due to the small effective masses of electrons, m_e, and hole, m_h, (effective meaning the masses in the presence of the lattice) and the large

dielectric constant ϵ, the exciton is large on the atom scale, with Bohr radii a_0 between 5 and 50 nm. The Bohr radius of an exciton is given by

$$a_0 = \frac{h^2 \in}{e^2}\left[\frac{1}{m_e} + \frac{1}{m_h}\right] \quad (1)$$

If the semiconducting aggregate reaches one (quantum gas), two (quantum wire) or three dimensions (quantum dot engineered by self-assembly on a substrate) [10] a size that is comparable with a_0 or the de Broglie wavelength $\lambda_{dB,}$ substantial changes in the optical properties are observed. In metals however, such effects are observed only for very small aggregate of a few nano-meters on account of the missing band gap and the corresponding small distances between relevant energy levels [11, 12].

4.1. Electronic conduction as it relates to different geometry in crystal systems

In three-dimensional crystal, the location of energy band gaps in the electron dispersion is still determined from electron diffraction by the lattice planes, but the Brillouin zones (which is the region of k-space which lies between any two diffraction conditions, where k = −π/a and +π/a in one dimension) don't exist as simple variables of k, as in 1D but, they exist as more diverse surfaces in 3D k-space, which geometry depends on the unit cell and atomic structure. The energy-wave-vector relationship for this crystal which extends over multiple Brillouin zones when mapped completely into the first Brillouin zones, results into a large number of energy bands and consequently the density of energy states (DOS) is strongly modified (**Figure 1**).

An example of the multiple energy bands and corresponding density of states in a real crystal is shown for Ag_2ZnGeO_4 crystal in **Figure 2a**.

The series of allowed k values extend up to the edge of the Brillouin zone, at k = ±π/a since one of these endpoints may be mapped onto the other by a reciprocal lattice vector translation. The total number of allowed k values is precisely N, where N is a positive integer. Meanwhile, each k state may be taken up by both (+) spin or (−) spin electron, where the total number of states to be occupied is 2N per energy band. In three dimensional states, this result is translated to $2N_u$ states per band where N_u represents the number of unit cells in the crystal.

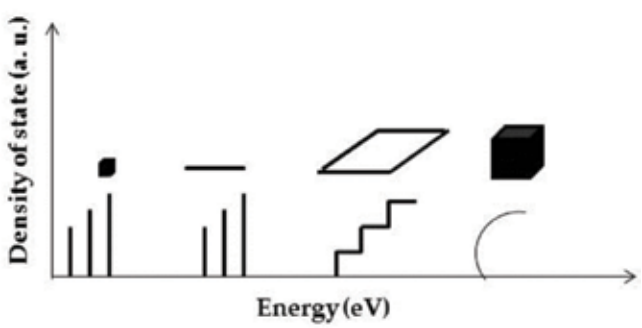

Figure 1. Electronic densities of state for nanostructures of various dimensions (reproduced with permission from Ref. [13]).

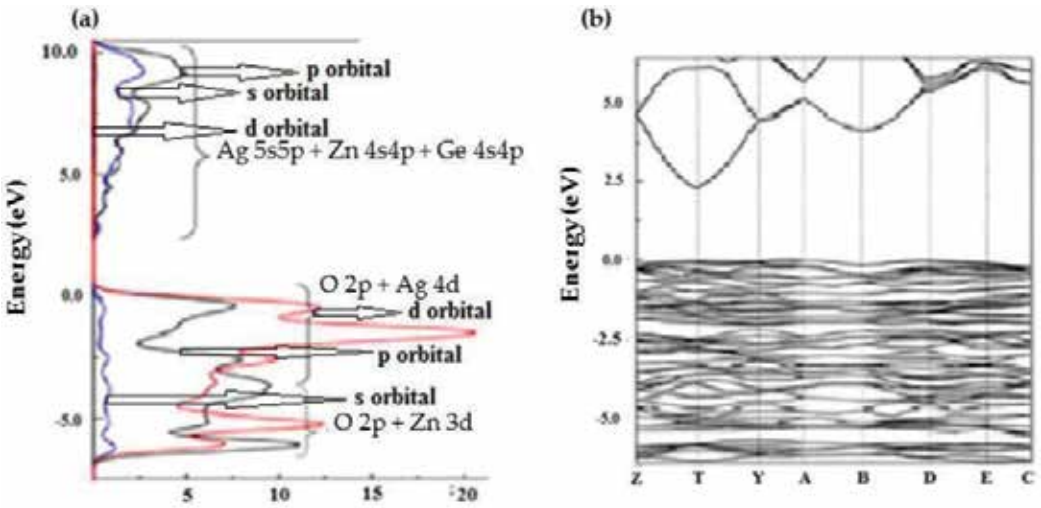

Figure 2. (a) Density of states for crystalline Ag_2ZnGeO_4 showing the symmetry along the Brillouin zone boundary (b) diagram of electron energy band gap structure (reproduced with permission from Ref. [14]).

Therefore, the sum of valence electrons in the crystal is zN_u, where z is given as the valence electron per unit cell, leading to two different electronic configurations in a crystalline solid.

For an even integer of z, one energy band will be fully filled, while the next band will be completely empty (**Figure 2b**). Apparently, the valence band is the highest densely filled band while the conduction band is the next unoccupied band. It is impossible for electrical conduction to occur in the valence band because there are no unoccupied states equivalent to the small increase in energy due to externally applied voltage. This phenomenon results in an insulator, but if the band gap is considerably small, a semiconductor is formed. Conversely, if z is an odd integer, the highest occupied energy band will be half filled and there will be many unoccupied states with comparable energy to the highest occupied states. This invariably results in vigorous electrical conduction typical of a metal material.

There is one further special case which gives rise to metallic behaviour, namely, when the valence band is completely full (z is even), but the valence and conduction bands overlap in energy, such that there are vacant states immediately adjacent to the top of the valence band, just as in the case of a half-filled band. Such a material is called a semi-metal or metalloid. Moreover, in amorphous solid DOS is primarily determined by the short-range order in the material, that is, the nearest neighbours. Another approach is to represent the amorphous solid by a very large unit cell with a large number of slightly different atomic environments [15, 16].

4.2. Properties of metal clusters

Over the past decades, researchers have been interested in studying nanoparticles and/or small clusters of noble metal materials in which the system sizes under investigation have been experimentally synthesized, which enables direct theory-experiment comparison. More often, the size-dependence of the properties of these materials such as their HOMO-LUMO gap (**Figure 3**), magnetic properties and optical properties are of immense interest.

http://dx.doi.org/10.5772/intechopen.72761

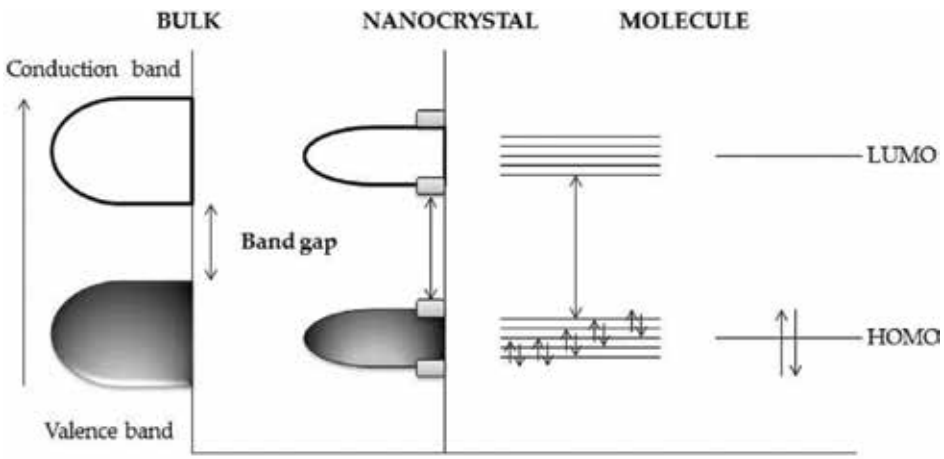

Figure 3. Band structures of bulk and nanoparticles.

Therefore, computational methods employ time-dependent density functional theory (TDDFT) using either the linear response (LR) formalism of Casida or a real-time (RT) approach to calculate the excited-state in solid crystals. The TDDFT calculations usually employ the adiabatic local density approximation (ALDA) which is sometimes referred to as the time-dependent local density approximation (TDLDA). Recent model potentials used in TDDFT calculations include the asymptotically correct exchange functional (LB94) [17]. Like all DFT calculations, the results depend on the type of system and the particular exchange-correlation functional employed. We shall briefly consider some model noble metal systems and the implications of DFT studies on their structure and DOS or band gap energy.

4.2.1. Pd clusters

Palladium is of immense interest due to its many uses in applications such as fuel cells and catalytic converters. The properties of palladium clusters and nanoparticles have been studied by many researchers, who investigated 13-atom Pd metal clusters [18]. They used the linear combination of atomic orbitals method for their calculations within the density functional formalism, at the same time, the von Barth-Hedin form was also used to include the exchange correlation effects in their calculations. In concluding, it was discovered that the icosahedral geometry is more stable for Pd_{13} than the face-centred cubic (fcc) octahedron, and it has a nonzero magnetic moment unlike the bulk, which is diamagnetic. In addition, the binding energy per atom of the 13-atom Pd cluster was calculated and compared to the bulk cohesive energy. Other researchers also reported the icosahedron structure as the most stable isomer for Pd_{13} [19] but, the final structure was found to be a distorted icosahedron with D5d symmetry with a zero spin only magnetic moment. Furthermore, the mutual dependence between electronic structure and geometric characteristics of small Pd clusters was equally measured using the self-consistent-field/configuration interaction (SCF/CI) level of theory.

By extension, the cuboctahedral and icosahedral symmetries of Pd_{13} were studied to explore its atomic and electronic structures by means of the linear combination of norm-conserving

pseudopotential atomic orbitals (LCPSAO) method with both PZ and PBE exchange correlation functionals. It was found that the cuboctahedral Pd^{13} is more stable with a small spin polarization, S = 3. The accuracy of the numerical calculation and the treatment of the core electrons were attributed to account for the difference observed in contrast with previous studies [20].

A low symmetry structure with relatively close packing has been identified as the lowest energy isomer using the DFT-PW91 level of theory for the Pd_{13} cluster. It was discovered that the structural orientation of Pd closely resembles that of noble metals rather than transition metals due to the complete filling of the d orbitals. Therefore, Pd_{13} exhibited a distorted icosahedron [21], while in a subsequent study the authors reported that two different density functionals can lead to two global minimum structures that are very close in energy and have the same spin states. The PBE functional has favoured the icosahedrons, whereas a structure that is similar to the one proposed by Wang and Johnson [22] has been preferred by the B3LYP functional.

Other theoretical studies using DFT-PBE calculations to study the electronic structure of Pd_{13} resulted in a bilayer structure which can be considered as a relaxed bulk fragment [23]. The icosahedral cluster was found to be slightly above the ground state, while stabilization by the p- or d-like cluster orbitals caused the near degeneracy of the bilayer or icosahedral clusters, respectively. The low-lying spin states were found to be important in controlling the electronic property of the cluster. Reveles and co-workers [24] used the linear combination of atomic orbitals-molecular orbital approach at the PBE/DZVP level of theory to learn the structural changes of bilayer C_S ground state and the octahedron of Pd_{13} upon charging and oxidation or reduction. It was observed that the bare Pd_{13} has C_S geometry, whereas $Pd_{13}O_2$ has an icosahedral Pd_{13} core (**Figure 4**), indicating an interesting structural change during an oxidation/reduction reaction. The location of 1P, 1D, and 2P cluster orbitals and the amount of hybridization between the atomic p orbitals and the cluster 1D orbitals determine the order of stability of the isomers.

DFT theory calculations within the spin-polarized generalized gradient approximation (GGA) were performed by Kumar and Kawazoe [25] to study the evolution of the atomic and electronic structure of Pd clusters having 2–23, 55, and 147 atoms. They observed that the binding

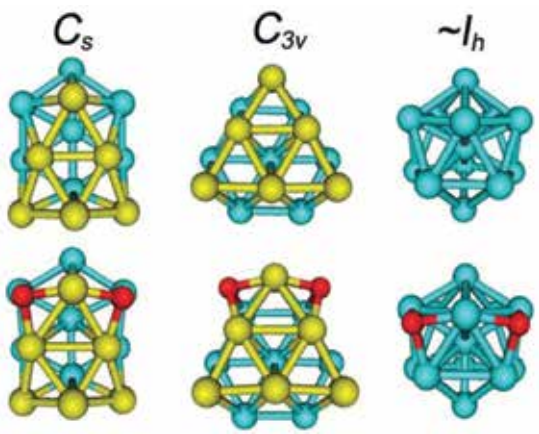

Figure 4. Topology of optimized Pd_{13} isomers (reproduced with permission from Ref. [24]).

energy increases monotonically toward the bulk value with the increasing cluster size. The 10-, 13-, 15-, 18-, 21-, and 22-atom clusters magic numbers were shown by the second-order energy differences. All of these arrangements show that numerous isomeric structures that are very close in energy were found for small Pd_n clusters $n \leq 15$, which prefer high spin states with small HOMO − LUMO gaps. Pd clusters having more than 100 atoms in the fcc arrangement showed higher cohesive energies than icosahedra and decahedra, suggesting a strong preference for the bulk packing.

4.2.2. Pt clusters

Platinum clusters have also been of keen interest due to their applications in catalysis. In most of the earliest investigations, semi-empirical methods were used and very small clusters such as dimers or trimers were studied due to limited computational resources. The self-consistent-field-Xα scattered wave (SCF-Xα-SW) approach to molecular orbital (MO) theory was used to study the electronic structure of Pt_{13} cluster with the cuboctahedral geometry [26]. The overlap of d-band by the s, p band and the sharp peak in the density of states around the Fermi level of Pt_{13} exhibited the main features of the Pt-bulk band structure. They also reported that the ionization potential of the Pt_{13} cluster is about 2 eV greater than the average bulk work function.

The PW91 level of theory along with a plane wave basis set has been used to study Pt clusters up to 55 atoms, and these systems have been compared for their stabilities and HOMO-LUMO gaps. Xiao and Wang [27] found that while the binding energy increases, the relative stability of the Pt clusters is not affected by the consideration of spin-orbit coupling. It was also discovered that out of several different isomers of 10-atom Pt clusters, the tetrahedral Pt_{10} is the most stable, while Pt_{55} is most stable in the icosahedral geometry.

However, a combined molecular dynamics simulations and DFT calculations study carried out to investigate the amorphization mechanism of icosahedral Pt nanoclusters was done by Apra et al. [28] using the Becke functional to describe exchange and Perdew-Wang functional for correlation with a Gaussian-type orbital (GTO) basis set. The authors proposed an amorphization mechanism of icosahedral (Ih) clusters, where the rosette-like structural excitations at the five-fold vertices take place. In the icosahedral 55-atom cluster, a vertex atom is inserted between the five neighbours on the surface, to form a six-fold ring centred on the original position of the vertex. The bond directionality effects due to d-d interactions increase the favourability of the rosette-like structure for Pt clusters.

4.2.3. Gold clusters

The study of gold has been of interest to researchers for many decades due to its wide variety of applications in catalysis, sensing and bio-tagging. The properties of gold nanoparticles and clusters are known to vary widely as the size of the system decreases so that the structures and properties of gold clusters are examined as a function of size.

The structures of pure gold clusters, especially the two-dimensional to three-dimensional structural transition have been the subject of many studies. The small clusters with fewer than 20 atoms were thoroughly investigated by several research groups [29, 30]. Some of the earliest work on large systems focused on symmetrical structures. Haberlen et al. [29]

examined octahedral and icosahedral Au_{55} using the Vosko, Wilks and Nusair (VWN) functional and found that the Kohn-Sham orbitals and their energy orderings agreed well with a jellium model once energy level splittings due to symmetry reduction were considered. Furthermore, it was found that relativistic calculations lowered the energy levels arising from s orbitals toward the d-band. Lately, examination of Oh-symmetric Au_{38}, Au_{44}, and Au_{55}, as well as Ih symmetric Au_{55} and Au_{147} showed that the VWN functional correlation predicts average gold–gold distances whose extrapolated values are in better agreement with experiment than BP86 [30]. However, the cohesive energies per atom were found to be better for BP86, while the energy differences between the two Au_{55} structures were found to be small, although the icosahedral structure was preferred by a factor less than 0.1 eV. Tetrahedral Au_{20} was also computed to have a HOMO-LUMO gap of 1.818 eV, which was in very good agreement with experimental estimates. Au_{40}, using a PBE-based basin-hopping search had that the lowest energy isomer with C_1 symmetry and a HOMO-LUMO gap of 0.69 eV [31, 32].

4.2.4. Silver clusters

Silver nanoparticles and clusters have many uses, some of which include optical sensing and surface enhanced Raman scattering (SERS). As a result, their structures, optical properties, and adsorbate binding have been studied by many researchers. Jennison et al. [33] examined Ag_{55}, Ag_{135}, and Ag_{140} with icosahedral and/or cuboctahedral structures using the Perdew-Zunger LDA parametrization. It was discovered that the icosahedral structures were energetically preferred. The central atoms in icosahedral structures were computed to have compressions in atomic distances of up to 6% as compared to bulk, but small surface compressions of ~1%, whereas the cuboctahedral structures were found to have core compressions of 1% and surface compressions of 2–3%.

The investigation of Ag_{55}^- using combined theory-experiment showed that the photoelectron spectrum of Ag_{55}^- was well-reproduced by an icosahedral structure, which was also found to be the lowest energy isomer for this cluster size [34]. But the structures of Ag_{55}^- and Ag_{55}^+ were later established using both DFT (BP86 with a SVP basis set) and trapped ion electron diffraction (TIED). Their reduced molecular scattering functions were found to be in excellent agreement with those predicted for icosahedral structures. The lowest energy isomer for Ag_{55}^- was predicted to be a slightly Jahn-Teller distorted singlet icosahedral structure; although a triplet state with D_{5h} symmetry was found to be almost isoenergetic [35].

A combination of TIED with DFT calculations was also employed using the PBE functional to examine Ag_n^+ (n = 36–46, 55). It was found that although clusters with fewer than 55 atoms exhibited local 5-fold symmetry in the absence of an icosahedral structure. In Ag_{38}^+, their ground-state structure had truncated octahedral symmetry, while their isomer that best fits the experimental data had 5-fold symmetry. The combined DFT and TIED study was expanded to investigate the structures of Ag_{19}^+, Ag_{38}^+, Ag_{55}^+, Ag_{59}^+, Ag_{75}^+, and Ag_{79}^+. The result was a truncated decahedral structure estimated to be 0.26 eV lower in energy than the truncated octahedral structure at the TPSS/TZVP level of theory [36].

The optical absorption spectrum of silver chains up to 18 atoms long was computed using real-time TDLDA calculations. It was found that the longitudinal excitation of the silver chains

http://dx.doi.org/10.5772/intechopen.72761

was not strongly affected by the presence of d electrons in the system, whereas the transverse plasmon modes were suppressed and mixed by the d electrons [37]. But studies conducted by means of statistical average of orbital potentials (SAOP) and XC functional of Van Leeuwen and Baerends (LB94) calculations showed that excitation of atomic wires in Ag_{20} and Ag_{40} demonstrated longitudinal peak arising primarily from a HOMO → LUMO transition, whereas the transverse excitation originates from a mixture of occupied-unoccupied orbital transitions [38].

5. The effects of the nanometer length scale

Once again, we recall the principle of quantum size effect as it directly influences the energy band structure which can lead indirectly to a number of changes in the associated atomic or crystal structure. These effects are generally termed quantum confinement, and they give rise to different observable changes in material properties.

The free electron model describes the energies of the electronic states as a function of $1/L^2$, where L is defined as the dimension of the system in a definite direction. The distance between successive energy levels is directly proportional to $1/L^2$. This property suitably describes a solid as a giant molecule. Therefore, the rate of increase in the number of atoms in the molecule results in decrease in molecular orbitals spacing. Therefore, if the number of atoms in a system, that is, the length scale, is considerably different from that in a bulk material, the energies and the energy spacing of the individual electronic states will be very different. Although the Fermi level (the upper most occupied level according to molecular orbital theory) would not be subject to change because the free electron density N/V would remain constant although there may be resultant modification in structure which will change this quantity. Invariably, decrease in the size of the system, causes the allowed energy bands to be considerably narrower than in an infinite solid. As a result, the delocalized electronic properties of a solid are remotely affected and the electrons in a reduced-dimensional system tend to behave more like the 'particle in a box' which is the phenomenon of 'quantum confinement'. The electronic states in such circumstances are more like those found in localized molecular bonds rather than those in a macroscopic solid [39].

Consequently, the total energy and thermodynamic stability of the reduced length scale system change relative to that of a normal bulk crystal, as a result of alterations to the bulk electronic structure provided that entropy consideration is negligible. Usually, this behaviour has important implications in the sense that it may change the most energetically stable form of a particular material, for example small nanoparticles and nano dimensional systems may adopt different crystal structures from that of the bulk material. Instances have shown that some metals which normally adopt a hexagonal close-packed atomic arrangement have been reported to adopt a face-centred cubic structure in confined systems such as metallic multilayers [40, 41]. If a different crystallographic structure is adopted below certain critical length scale, which is as a result of corresponding change in electronic density of states, it often results in a reduced total energy for the system.

The decrease in length scale may as well result in change in chemical reactivity, physical properties such as electrical, thermal, optical and magnetic characteristics, which depend on the structure and occupation of the outermost electronic energy levels. For instance, in a metallic system

there is a transition between metallic and insulation properties as the system size decreases, giving rise to the formation of a forbidden energy band gap. Other properties such as mechanical strength and transport properties which depend on change in the electronic structure and exhibition of a quantized behaviour respectively may also change in the length scale system [42].

5.1. Changes in the system structure

To understand the changes observed in systems of reduced dimension, let us consider the proportion of atoms which are in contact with either a free surface, for example an isolated nanoparticle, or an internal interface, such as a grain boundary in nanocrystallites. Therefore, the surface to volume ratio (S/V) and the specific surface area ($m^2\ g^{-1}$) of a typical system are indirectly proportional to particle size and they increase progressively for particles below 100 nm in diameter. The surface area per unit mass of material for isolated spherical particles of radius r and density ρ, is equal to

$$\frac{SA}{mass} = 4\pi r^2 \Big/ \left(\frac{4}{3\pi r^3 \rho}\right) = 3/r\rho \tag{2}$$

Therefore, the specific surface area (SSA) for 2 nm diameter spherical particles of typical densities can be approximately 500 $m^2\ g^{-1}$, but for particles forming crystals, the value will be reduced by half. The large surface area will definitely change the total energy of the system, leading to formation of metastable structures in nanosized systems that are different from the bulk structure and may induce a simple contraction or expansion of the normal crystalline lattice which could in turn change other material properties. For example, volume specific surface areas of 5 and 10 nm diameter spherical gold nanoparticles measured by the BET method were 342 and 316 m^2/cm^3 respectively [43], underscoring the quantum size effect.

For an atom that is near the surface, the number of nearest neighbouring atoms will be reduced thereby affecting bonding. Consequently, the surface tension or surface energy and electronic structure of the system will be affected. In a 2.5 nm particle only about 35–55% of the atoms are surface bound in contrast with a fewer percent for a 100 nm particle. This phenomenon applies mainly to nanocrystallites, most of their atoms either appear at or close to the grain boundaries and as a result, they exhibit structural properties different from the bulk [44].

5.2. Occurrence of vacancies in nanocrystals

This is another specific property that may control many physical properties such as conductivity and reactivity in materials. Vacancies are point defects in the crystalline structure of a solid, which exist in thermal equilibrium. In microcrystalline solids at temperatures above 0 K, vacancies invariably exist in thermal equilibrium. In the simple case of metals with one type of vacancies in a crystal having N atom sites is given by the Arrhenius equation

$$n_v = Nexp(-Q/RT) \tag{3}$$

where R is the gas molar constant, T is the absolute temperature and Q_f is the energy needed to form one mole of vacancies. Thus Q_f is given as

$$Q_f = N_A q_f \tag{4}$$

where N_A is the Avogadro number and q_f is the activation energy for the formation of one vacancy. q_f is an estimation of the energy required to remove an atom from the interior of a crystal to its surface. Since a surface atom is considered to be bonded to half the number of atoms compared to an interior atom, therefore, q_f is approximately half the bonding energy per atom. q_f is expected to have a near linear function with the melting temperature T_m since T_m of a metal is a function of the bond energy, so alternatively, Q_f may be calculated from the surface energy per unit area if one atom occupies an area of b^2, then the number of atoms per unit area is equal to $1/b^2$ and the surface energy, σ is given as

$$\sigma = {}^{q}/_{b^2} \tag{5}$$

Surface energy is also a function of T_m and varies within the range 1.1 Jm^{-2} (for aluminium) to 2.8 Jm^{-2} (for tungsten). Assuming a mean value σ = 2.2 Jm^{-2} and b = 2.5 × 10^{-10} m, then

$$Q_f = N_A \sigma b^2 = 83\ x\ 10^3\ J\ mol^{-1} \tag{6}$$

This agrees with the acceptable value of 90 $KJmol^{-1}$. However, the contribution of internal pressure, P to the surface energy term σ may be employed to modify the value of Q_f for nanoparticles in the following expression: $P = 4\sigma/d$, where d is the diameter of the nanoparticle. The effect of P introduces another energy term, q_n, for the formation of a vacancy and is given as Pb^3. Again taking σ as 2.2 Jm^{-2}, the additional energy per mole $Q_n = N_A q_n$ which is equal to 8.3 × 10^3 $Jmol^{-1}$ for a 10 nm diameter nanoparticle. This term is only approximately 10% of Q_f and rapidly decreases for large particle sizes. Thus, the effect of surface energy and internal pressure on the concentration of vacancy will be minimal (**Table 1**). In addition, the internal pressure, P causes an elastic compressive volume strain which results in linear strain ε, given by

$$\varepsilon = P/3E = 4\sigma/3dE \tag{7}$$

Thus, E is the Young's modulus. This equation shows that linear strain is inversely proportional to particle size hence; there will be a decrease in lattice parameter or interatomic spacing for nanoscale dimensional particles.

Finally, substituting a value of $Q = 90 \times 10^3$ $Jmol^{-1}$ into the Arrhenius expression for the vacancy gives the ratio n_v/N of 2.4 × 10^{-16} at 300 K, 6.5 × 10^{-7} at 600 K, 4.8 × 10^{-4} at 1000 K, depicting an exponential increase in vacancy concentration with temperature. In the case of a spherical

Metal	Surface energy, σ (eV) [45]	Specific surface area per atom, b^2 (m^2/cm^3)[a] [46]	T_m (°C)
Cu	1.29 ± 0.02	138.06	480
Ag	1.16 ± 0.02	124.15	480
Pt	1.62	312.62	480
Au	0.97 ± 0.01	104.89	480

[a]Calculated based on $\varepsilon = P/3E = 4\sigma/3dE$, assumption of d = 10 nm.

Table 1. Values of vacancy formation energy determined for copper, silver, platinum and gold (reproduced with permission from refs. [45, 46] As indicated).

nanoparticle of about 50 nm in diameter, if each atom occupies a volume of b^3, assuming $b = 0.25$ nm, there will be a total of 4.2×10^6 atoms in the particle. This implies that the number of vacancies, n_v very much less than 1 (except at very high temperature). Hence, nanocrystals are predictably vacancy free; their small size prevents any vacancy. This phenomenon has far reaching consequence for all thermo mechanical properties and chemical processes involving precipitation because they are based on the presence and migration of vacancies in the crystal lattice [47]. For instance gold nanowires having a diameter as small as 40 nm have a plastic deformation mechanism which is dominated by the motion of dislocations, a behaviour commonly observed in macro crystalline materials. As a result, the deformation mechanism of nanocrystalline gold films depends on its grain size [48].

5.3. Dislocation in nanocrystals

The mechanical properties of materials can be explained in terms of planar defects caused by dislocations in the crystalline structure of a solid. Dislocations plays less dominant role in the description of the properties of nanocrystals compared to microcrystals, due to the dominance of crystal surfaces and interfaces. The free energy of dislocation can be defined in terms of the following: (i) the core energy that is within a radius of about three lattice planes from the dislocation core; (ii) the elastic strain energy outside the core and extending to the boundaries of the crystal; and (iii) the free energy as a result of entropy contributions. It follows that, in microcrystals, the first and second terms which are the most dominant terms increase the free energy. Therefore, dislocations do not exist in thermal equilibrium making it different from vacancies. The core energy approximately 1 eV per lattice plane which, for an inter-planar spacing b of 0.25 nm, is equivalent to 6.5×10^{-10} Jm^{-1} is expected to be independent of grain size. The elastic strain energy per unit length for an edge dislocation is given by

$$E = \frac{G\,b^2}{4\pi(1-\nu)}\, x\, ln\left(\frac{r_1}{r_0}\right) \tag{8}$$

In this expression, G is the bulk modulus, r_0 is the core radius, r_1 is the crystal radius and ν is Poison's ratio, ν is usually around 1/3 for a crystalline sample. For a screw dislocation $(1-\nu)$ term is usually omitted, resulting in an energy approximately 2/3 that of an edge dislocation. If $G = 40 \times 10^9$ Pa, then the constant term $Gb^2/4\pi(1-\nu) = 3 \times 10^{-10}$ Jm^{-1}. The grain size dependence is the $ln(r_1/r_0)$ term, which for grain size $(2r_1)$ values of 10, 50, 1000 and 10,000 nm increases as 3, 4.6, 7.6 and 9.9 respectively. This suggests that, the elastic strain energy of dislocations in nanoparticles is almost one-third of that in microcrystals. For a 10 nm grain size, the core energy and elastic strain energy are not significantly different. In comparison, the core energy for a microcrystal is about one-tenth of the elastic strain energy.

The decrease in the elastic strain energy of dislocation in nanocrystals will invariably affect the forces of dislocations due to externally applied stresses; the interactive forces between dislocations will be reduced by a factor of about 10. Therefore, the rates of recovery and annealing out of dislocations to free surfaces are expected to be reduced. If there is a dislocation near the surface of a semi-infinite solid, the stress towards the surface will be defined as the interaction of the stress field of an image dislocation at an equal distance on the opposite side. Since nanocrystals do not approximate to semi-infinite solids, such image stresses will result in dislocations that are relatively immobile.

Further evaluation of the contributions of entropy to the free energy can be considered under the following conditions: (i) configurational entropy (that is, arrangement of the dislocation in different ways); (ii) entropy factor for a perfectly elastic dislocation by assumption; and (iii) the associated effect of dislocation on thermal vibrations of crystal. Interestingly, out of these three factors only (ii) and (iii) are not affected by crystal size and their values have been given as $2k_BT$ and $3k_BT$, respectively, per atomic plane. These values correspond to about 3×10^{-11} Jm^{-1}, considerably less than the core and elastic strain energy terms at a temperature of 300 K.

The configurational entropy contribution to the energy term is given as

$$E = \frac{b\,k_B\,T}{L}\,ln\left(\frac{L^2}{b^2}\right) \tag{9}$$

per atomic plane, where L is the length of the dislocation. At 300 K this gives values of 3.0×10^{-12}, 5.7×10^{-14} and 7.6×10^{-15} Jm^{-1} for L = 10, 1000 and 10,000 nm, respectively. In conclusion, unlike microcrystals, dislocations do not exist in nanocrystals as thermodynamically stable lattice defects [7, 49].

5.4. Effect of nanoscale dimensions on the properties of nanomaterials

Many properties of nanomaterials can be modified based on the length scale property (size). More often, extrinsic properties for example resistance, which depends on the actual size of the particle, may be affected. Whereas, other properties such as yield strength, τ solely depends on the microstructure of a material as expressed by the Hall–Petch equation for the material which is a function of average grain size (d)

$$\tau = k\,(d)^{-\frac{1}{2}} + \tau_0 \tag{10}$$

where k and τ_0 are constants. Resistivity which is an intrinsic material property is presumed to be independent of particle size, although this is usually not predictable for many intrinsic properties of matter at nanoscale compared to bulk phase due to the emergence of quantum size confinement resulting in the presence of wave-like transport processes, changes in electronic structure and the predominance of interfacial effects [50].

5.4.1. Effect on structural properties

The increase in surface area and surface free energy, with decreasing particle size leads to changes in interatomic spacing. This effect can be explained by the compressive strain induced by the internal pressure arising from the small radius of curvature in the nanoparticle. Furthermore, another effect previously mentioned is the apparent stability of metastable structures in small nanoparticles and clusters, such that all traces of the usual bulk atomic arrangement become lost. Metallic nanoparticles such as silver (**Figure 5a**, **b**, **d**), platinium (**Figure 5h**, **i**), palladium (**Figure 5e**, **f**), Co (**Figure 5g**), Ni (**Figure 5c**), ruthenium, gold (**Figure 6**) and some noble metals are known to adopt polyhedral shapes such as face centred cubic structure, cube-octahedra, multiply twinned icosahedra and multiply twinned decahedra.

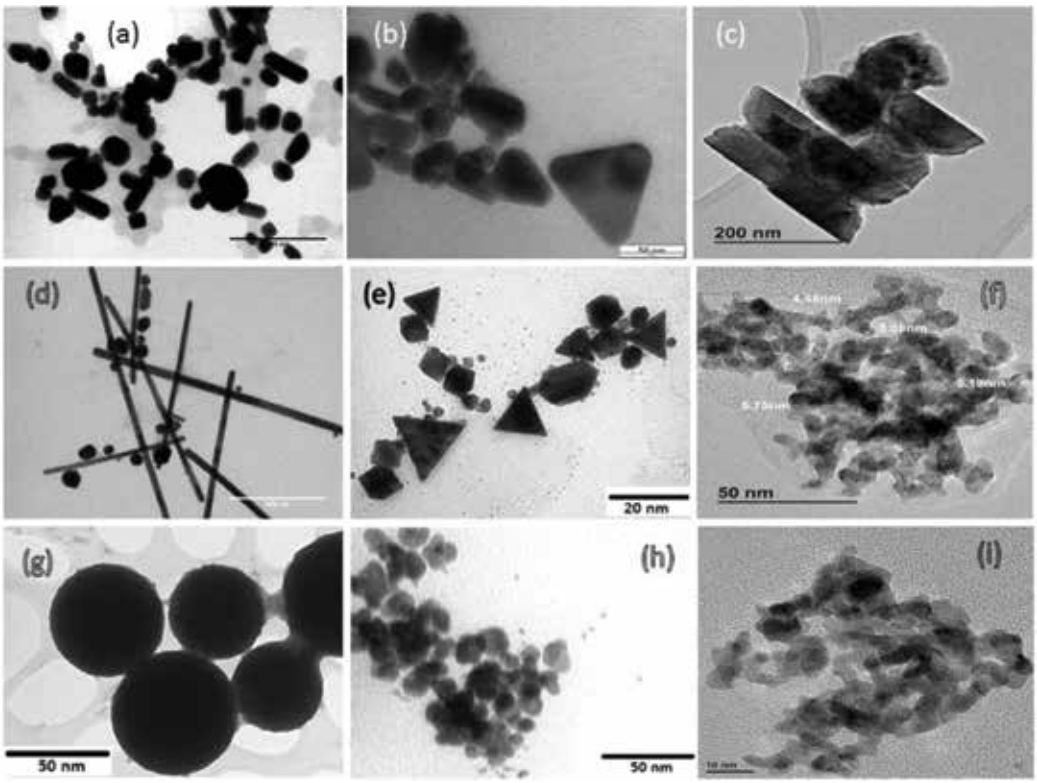

Figure 5. Transmission electron microscope (TEM) images of metal NCs: (a) face centered cubic and cube-octahedra Ag NCs; (b) multiple twinned Ag NCs; (c) disc-like Ni NCs; (d) Ag nanorods; (e) face centered hexoctahedral Pd NCs; (f) a dendritic Pd NC; (g) Co nanosphere; (h) hexoctahedral Pt NCs (i) Pt nanorods [51, 52].

Some of the nanoparticles are referred to as multiplied twinned crystalline particles (MTPs). Their shapes are considered based on the surface energies of various diffraction planes from x-ray diffraction (XRD) pattern, the growth rates of the crystals and the energy required to form defects such as twin boundaries. Moreover, evidence has shown that such particles are not true crystals but are referred to as quasiperiodic crystals or crystalloids. Some of these quasi nanostructures, icosahedral and decahedral quasicrystals (**Figure 5**) usually become seed for further growth of the nanocluster; until more regular crystalline packing arrangements are formed.

There is enormous difference between crystalline and amorphous solids in sense that the former possess long-range periodic order, their patterns and symmetries correspond to those of the 230 space groups. But quasiperiodic crystals do not exhibit such property; they possess fivefold-symmetry, which is not allowed in the 230 space groups. Some metals exhibit the cubic close-packed and hexagonal close-packed structures in which, each atom is coordinated by 12 neighbouring atoms. Although, other configurations exist in which each coordinating atom is situated at the vertices of an icosahedron while in contact with the central atom. Relaxing this rigid atomic model by allowing the central atom to reduce in diameter by ten percent (10%), the coordinating atoms shift position and the shape and symmetry of a regular icosahedron forms with point group symmetry 235, indicating the presence of 30 twofold, 20 threefold and 12 fivefold axes of

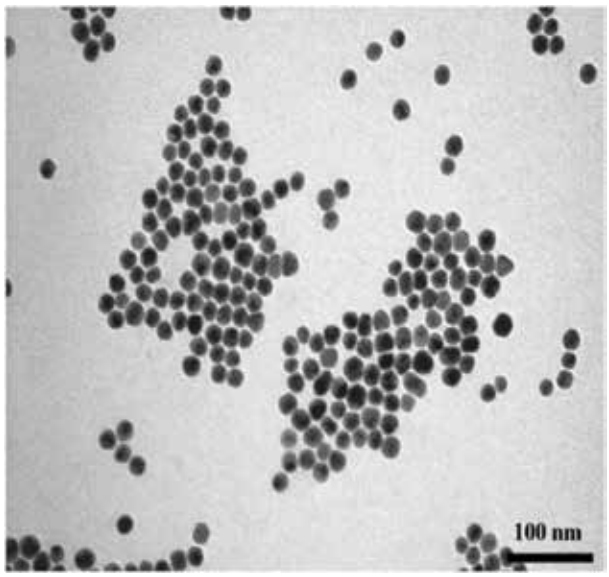

Figure 6. Face centered cubic structure au NCs (reproduced with permission from Ref. [53]).

symmetry. This kind of geometry of a quasiperiodic crystal nucleus may grow to form icosahedra or pentagonal dodecahedra. In these two solids having identical symmetry; the apices of one are replaced by the faces of the other, but the understanding of their size-related instability characteristics and mechanism still remains unclear. More often, electron diffraction pattern is employed to distinguish between multiple twinned crystals and quasiperiodic crystals [54].

5.4.2. Effect on thermal properties

The perceived large increase in surface area and the change in interatomic spacing as a function of nanoparticle size as mentioned earlier, have a marked effect on material properties. For metallic nanoparticles, the smaller the size the higher the melting point. But there is a correlation between the size functionality of metal nanoparticles, their plasmon resonance behaviour arising from electron–electron/electron phonon couplings and conductivity which is related to thermal dissipation or release of heat energy to the environment.

Specifically, the relationship between the size, temperature and the surface plasmon energy of silver nanoparticles (size range 11–30 nm) embedded in a silica host matrix has been studied for the temperature interval 293–650 K. This study confirmed the dependence surface plasmon energy on the size and temperature of silver nanoparticles [55]. An increase in temperature and size of nanoparticle, shifts the surface plasmon resonance band to the red side of the spectrum. A decrease in the size of nanoparticles invariably results in increase in the rate of scattering of surface conduction electrons and leading to a nonlinear red shift of the surface plasmon resonance. This temperature dependence of SPR energy and its red shift is linear for larger nanoparticles but is nonlinear for smaller ones. Therefore, the volume thermal expansion of nanoparticles leads to a red shift of the surface plasmon resonance at higher temperature. It also reveals that the thermal volume expansion coefficient depends on size and temperature.

5.4.3. Effect on chemical properties

There is a relationship between change in structure as a function of particle size and electronic properties. Ionization energy of small atomic clusters is higher than the corresponding bulk material. In addition, ionization energy remarkably varies with cluster size, which is also related to chemical reactivity.

It has been established that nanoscale structures have very high surface area to volume ratio and possess varying crystallographic structures which has implication for chemical reactivity. Therefore, catalysts consisting of finely divided nanoscale system can increase the rate, selectivity and efficiency of chemical reactions while simultaneously significantly reducing waste and pollution in the sense that only a few quantity of the material as catalyst is required to be deposited on a support inside a reactor and it can be used repeatedly. Once the cycle of usage or lifetime is spent, it can be recharged and reused again. Similarly, the ease of transport to and from internal reaction sites can be enhanced by employing nanoscale catalytic support with nanoporous structure which selects the reactants and product of chemical reactions based on size. In addition, the solubility property of nanoparticles often differs from their bulk counterparts, for example, while some new drugs in micron-sized particle form may be insoluble in water, but when nanostructured, they easily dissolve because of improved permeability occasioned by increased surface to volume ratio. Also, the reduced particle size renders the possibility of intravenous administration of poorly soluble drugs without any blockade of the blood capillaries. The suspensions can also be lyophilized into a solid matrix [56–59].

5.4.4. Effect on mechanical properties

It well known that toughness as a mechanical property is inversely proportional to ease of formation or defects within a material. Therefore, as particle size decreases, the ability to sustain defects becomes increasingly more difficult which will alter mechanical properties. So it expected that new nanostructures that are different from their bulk materials in terms of morphology and structure will definitely show different mechanical properties. As the structural scale reduces to the nanometer range, for example in nanolayered composites, based on the Hall-Petch relationship, yield strength apparent increases. Furthermore, the high surface to volume ratio of nanostructured materials may also promote interface-driven processes such as plasticity, ductility and strain to failure. Several nano metals and ceramics are known to be superplastic, because they are capable of undergoing extensive deformation process without necking or fracture as a result of grain boundary diffusion and sliding, which is very significant in nanosized materials. Therefore, these effects offer an advantage in the sense that the strength-ductility limit of novel nanomaterials is extended over that of the conventional materials [60].

5.4.5. Effect on magnetic properties

The large surface area to volume ratio effect also results in a substantial proportion of atoms having a different magnetic coupling with neighbouring atoms leading to a variation in magnetic properties. Some important applications of magnetic nanoparticles include bioprocessing, colour imaging, ferrofluids, refrigeration and high storage density magnetic memory media. **Figure 4** shows average magnetic moments per atom of metal clusters such as Fe (**Figure 7a**),

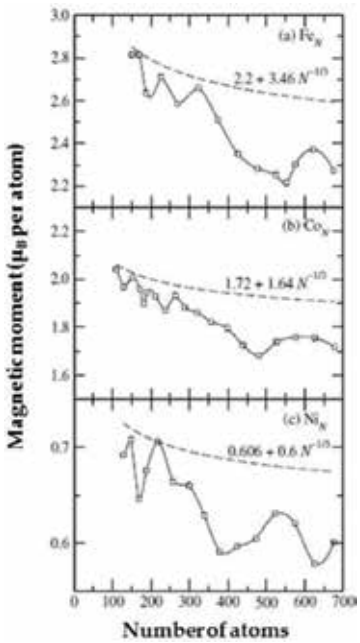

Figure 7. Average magnetic moment per atom for (a) Fe clusters at 120 K, (b) co clusters at 78 K, and (c) Ni clusters at 78 K, as a function of the number of atoms (reproduced with permission from Ref. [61]).

Co (**Figure 7b**) and Ni (**Figure 7c**) at different temperature. Bulk ferromagnetic materials often form characteristic multiple magnetic domains, while small magnetic nanoparticles usually exhibit only one domain and possess superparamagnetism [62].

Other related effect in this regard is giant magnetoresistance (GMR) which is observed in nanoscale multilayers consisting of a strong ferromagnet, such as Fe and Co and a weaker magnetic or nonmagnetic buffer (Cr and Cu). It is used in data storage and sensing. Another unique feature of GMR is the ability to produce different spin alignments with or without a magnetic field which result in antiferromagnetic coupling leading to maximum scattering from the interlayer interface and hence a high resistance parallel to the layers. The reverse occurs for co-aligned spins which results in decreased resistance of the device [63].

5.4.6. Effect on optical properties

The resultant effect of reduced dimensionality in nanocluster on electronic structure is profound in semiconductors as a result of the interaction between the highest occupied molecular orbital (HOMO) also called the valence band, and the lowest unoccupied molecular orbital (LUMO), known as the conduction band. Optical absorption and emission depend on transition between these states leading to changes their optical properties, such as colour which is as a function of particle size. A very good example of variation of colour with particle size is colloidal silver nanoparticles. It has a light yellow colour which progressively becomes more yellowish with increase in particle size. Since the seventeenth century silver colloids have been

used as a pigment for stained glass. Most metallic nanoparticles show similar size-dependent behaviour in terms of frequency and intensity of light emission and modified non-linear optical properties. Reduced dimensionality also has effect on photoemission, photoconductivity, photocatalysis and electro-luminescence [64, 65].

5.4.7. Effect on electronic properties

The effect of reduced dimensionality on the electronic properties of the system is related mainly to the increasing influence of the wave-like property of the electrons and the paucity of scattering centres. The discrete nature of the energy states become apparent in systems that are confined in all three dimensions due to quantum mechanical effect based on de Broglie wavelength theory. In addition, owing to their intrinsic wave-like nature, electrons can form tunnel by quantum mechanical effect between two closely adjacent nanostructures. If a voltage is applied between these two nanostructures which align the discrete energy levels in the DOS, resonant tunnelling occurs, leading to abrupt increase in tunnelling current (this phenomenon is different from simple dipolar coupling which results from each electron spin generating a magnetic field that is oriented parallel to the nuclear spin vector).

As a result, below a critical length scale, conducting materials may become insulators, as the energy bands cease to overlap. Whereas in bulk materials, electronic transport is mainly determined by scattering caused by phonons, impurities or rough interfaces. At nanoscale dimension electron motion can be diffusive and become purely ballistic if the electron free path can travel through the system without randomization of the phase of their wavefunction. This principle operates in superconductors. Conduction in highly confined structures like quantum dots is very sensitive to the presence of charge carriers. These Coulomb blockade effects result in conduction processes involving single electron which only requires a small amount of energy to operate a transistor, switch or memory device. These devices can be utilized to produce state of the art components for electronic, optoelectronic and information processing applications, such as resonant tunnelling transistors and single-electron transistors [16, 42, 66]. We provide an illustration of this phenomenal critical length scale considering the work of Yao et al. [67] in which X-ray absorption fine structure, XAFS, was employed to look at the bonding between gold atoms. The ideal theoretical calculated gold bond length was within the range of 2.55–2.70 Å for gold nanoparticles which is much shorter than the bulk bond length of 2.87 Å [68].

6. Application of metallic nanoparticles

Metal nanoparticles have host of applications ranging from electronic, optical, magnetic imaging, biomedical therapy, catalysis and many more. The ultimate goal of their application is to explore the intrinsic physical and chemical properties of the colloidal nanoparticle whether in isolated or combined form to fabricate devices with specific functionality. In view of this, different strategies such as solvent evaporation, electrostatic attraction, hydrogen bonding, DNA-driven assembly, and cross-linking induced by bio-specific interaction like antigen–antibody and so on have been developed to form NP assemblies and utilize them in the fabrication of nanostructured devices. The utilization of quantum dots as functional materials

due to their extremely small size and extra high fluorescence quantum yield, [69] is however hampered as a result of their toxicity potential in biomedical applications. Meanwhile, metallic NPs have enjoyed increased application in this regard [70].

6.1. Therapeutic in-vivo applications

The use of metallic nanoparticles in biomedical can be classified based on their mode of application inside (in-vivo) or outside (in-vitro) the body. The in-vivo application can be further characterized as therapeutic (hyperthermia and drug-targeting) and diagnostic (nuclear magnetic resonance, NMR imaging). The main divisions of the in- vitro application involve magneto relaxometry and diagnostic separation or selection.

6.1.1. Hyperthermia therapeutic method

This is a therapeutic procedure administered to raise the temperature of part of the body infected by a malignant tumour or cancerous growths. Hyperthermia therapy is usually applied together with other cancer treatments, and the technique is known as multimodal oncological strategies. Clinical examination has shown that at temperatures above 41–42°C, target cells can be mortified. Recent development in clinical hyperthermia trials now seeks to optimize thermal homogeneity at controlled temperatures between 42 and 43°C in the target volume. Among other methods, finely divided iron cobalt magnetic nanoparticles have used to deliver the temperature increase required for hyperthermia. In theory, magnetic hyperthermia, which is the controlled heating of a cell by a magnetic material under the influence of an external alternating magnetic field, occurs as a result of the loss processes associated with reorientation of the magnetization of magnetic materials with low electrical conductivity. This procedure functions by restricting the heating to the tumour area, which serves as a useful advantage in medical therapy. In recent times, the use of subdomain magnetic particles (nanosized) is preferred over multi domain (micronsized) particles, because the former absorb much more AC magnetic fields. Therefore, morphological properties such as particle size and shape are strong determinants of the heating potential of magnetic nanoparticles; that is why synthetic routes must be defined to produce uniform particles with particle size within the length scale regime [71, 72].

6.1.2. Drug delivery

The application of magnetic nanoparticles for the delivery of drugs or antibodies to organs or tissues infected by diseases is an interesting field of research with challenging opportunities. The process of drug transport to target site using magnetic delivery systems depends on the competition between forces exerted by blood compartment on the particles and magnetic forces generated from the applied magnet field. For magnetic particles to be retained at the target site, the magnetic forces must exceed the linear blood flow rates in arteries (10 cms^{-1}) or capillaries (0.05 cms^{-1}). Therefore, the pioneering concept proposed by Freeman and coworkers [73] which suggests that fine magnetic carrier particles could be transported through the vascular system and be concentrated at a particular point in the body with the aid of a magnetic field (**Figure 8a**) has be validated. The main advantage of this procedure is that the transport of nanoparticles through capillary systems, organs and tissues is favoured, so that vessel embolism could be prevented [75].

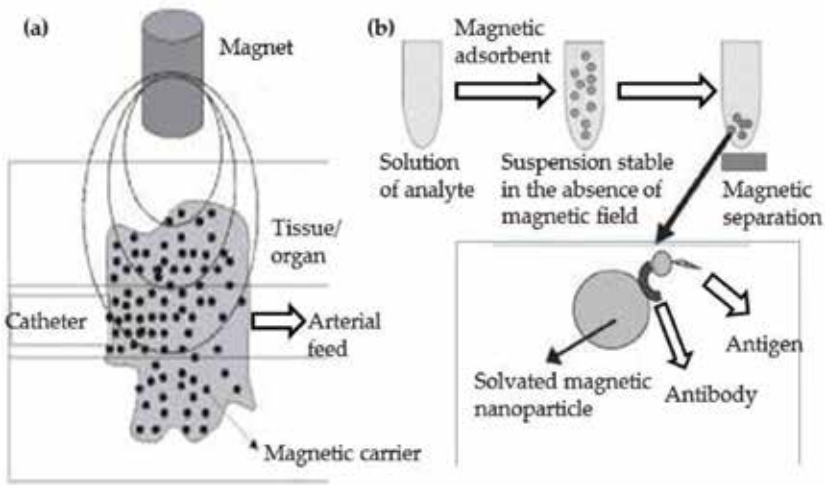

Figure 8. (a) Schematic diagram of magnetically driven transport of drug to a specific target and (b) representation of a magnetically assisted separation of substances. Magnetic nanosphere to which an antibody has been anchored is dispersed into a liquid medium containing antigen (reproduced with permission from Ref. [74]).

6.2. Diagnostic in-vitro applications

6.2.1. Separation and selection

Solid phase extraction (SPE) is a viable alternative to the conventional sample separation or concentration methods, for example, liquid–liquid extraction. At present, considerable attention is being paid to SPE as a means of isolating and pre-concentrating desired components from a sample matrix. The separation and pre-concentration of the substance from large volumes of solution is highly time consuming when using standard SPE column, but with the advent of magnetic adsorbents in magnetic solid-phase extraction (MSPE) this task can be made relatively easier. Using this procedure, the magnetic adsorbent is added to a suspension or solution containing the target material, which is adsorbed onto the magnetic adsorbent and then desorbed or recovered from the suspension by using an appropriate magnetic separator (**Figure 8b**). The use of magnetic nanoparticles instead of micronsized magnetic particles in this procedure is of advantage because suspensions that are resistant to sedimentation can be prepared in the absence of an applied magnetic field [76].

6.2.2. Magnetorelaxometry

Magnetorelaxometry is a procedure that measures the magnetic viscosity or the relaxation of the net magnetic moment of a system of magnetic nanoparticles after withdrawal of a magnetic field. This method was recently introduced for the evaluation of immunoassays. It uses two different relaxation mechanisms: (i) Néel relaxation occurs if the internal magnetization vector of a nanoparticle relaxes in the direction of the easy axis inside the core: and (ii) Brownian relaxation occurs if the particles accomplish rotational diffusion in a carrier liquid. Both Néel and Brownian relaxations can be identified by their individual relaxation times. Other distinguishing properties include, Brownian relaxation only takes place in liquids, while Neel

relaxation does not depend on dispersion medium. Since magneto-relaxometry is a function of particle core size, hydrodynamic size and particle anisotropy, the technique can effectively distinguish between free and bound conjugates by their unique magnetic behaviour. As a result, it can be used as an analytical tool for the evaluation of immunoassays [77, 78].

6.2.3. Future applications of magnetic nanoparticles

Tremendous effort has been made to contribute to research in the field of magnetic therapeutic medicine. Magnetically directed microspheres containing radionuclides are currently used for internal radiotherapy. There is a need to improve dose localization when administering drugs and metabolites which have been labelled with radioactive isotopes in a quantity sufficient to deactivate tumour cells. Therefore, the use of capped magnetic nanoparticles could have tremendous impact in improving the efficiency cancer treatments. Sufficient advance in magnetic nanoparticles research could evolve into their use in human body repair called prosthetics or artificial replacement [79].

7. Conclusions

In this review, the periodic properties of both crystalline and amorphous solids have been discussed as well as their unique physical and chemical properties at nanoscale level with their corresponding applications. Metallic nanoparticles and nano-layers have very high surface area to volume ratio and potentially different crystallographic structures which result in their unique physical and chemical reactivity both as solids and as colloidal dispersions.

Author details

Joseph Adeyemi Adekoya[1,3]*, Kehinde Olurotimi Ogunniran[1],
Tolutope Oluwasegun Siyanbola[1], Enock Olugbenga Dare[2] and Neerish Revaprasadu[3]

*Address all correspondence to: yemidunni20022001@gmail.com

1 Department of Chemistry, Covenant University, Ota, Ogun, Nigeria

2 Department of Chemistry, Federal University of Agriculture, Abeokuta, Nigeria

3 Department of Chemistry, University of Zululand, KwaDlangezwa, South Africa

References

[1] Brian LC, Vladimir LK, Charles JO. Recent advances in the liquid-phase syntheses of inorganic nanoparticles. Chemical Reviews. 2004;**104**:3893-3946

[2] Jonathan WS, David RT, Karl JW. Core Concepts of Supramolecular Chemistry and Nanochemistry. England: John Wiley and Sons Limited; 2007

[3] John PL. Quantum Chemistry. Student ed. London: Academic Press Incorporated; 1978

[4] Gary LM, Donald AT. Inorganic Chemistry. 3rd ed. London: Pearson Education International; 1998. pp. 337-520

[5] Roco MC, Williams RS, Alivisatos P. Nanotechnology Research Directions. 2nd ed. Dordecht: Kluwer Press; 2000. pp. 71-111

[6] Robert GM. Physical Chemistry. 3rd ed. Burlington: Elsevier Academic Press; 2008. pp. 108-240

[7] Robert WK, Lan WH, Mark G, editors. Nanoscale Science and Technology. 1st ed. England: John Wiley and Sons Limited; 2005. pp. 15-220

[8] Gohlich H, Lange T, Bergmann T, Martin TP. Electronic shell structure in large metallic clusters. Physical Review Letters. 1990;**65**(6):748-751

[9] Rubio-Bollinger G, Balm SR, Agrait N, Jacebsen KW, Vieira S. Mechanical properties and formation mechanism of a wire of single gold atoms. Physics Review Letters. 2001; **87**(02):6101

[10] Plain J, Sonnefraud Y, Viste P, Lérondel G, Huant S, Royer P. Self assembly drives quantum dot photoluminescence. Journal of Fluorescence. 2009;**19**(2):311-316

[11] Levy B. Photochemistry of nanostructured materials for energy applications. Journal of Electroceramics. 1997;**1**(3):239-272

[12] Törmä P, Barnes WL. Strong coupling between surface plasmon polaritons and emitters: A review. Reports on Progress in Physics. 2015;**78**:013901 (34 pp)

[13] Horst-Gunter R. Basics of Nanotechnology. 3rd revised ed. London: Wiley-VCH; 2008. pp. 10-13

[14] Xiukai L, Shuxin O, Naoki K, Jinhua Y. Novel Ag_2ZnGeO_4 photo catalyst for dye degradation under visible light irradiation. Applied Catalysis A: General. 2008;**334**:51-58

[15] Hammond C. The Basics of Crystallography and Diffraction. London: Oxford University Press; 1997. pp. 119-254

[16] Kolasinkin KW. Surface Science: Foundation of Catalysis and Nanoscience. Chichester: Wiley-VCH; 2002. pp. 43-65

[17] van Leeuwen R, Baerends EJ. Exchange-correlation potential with correct asymptotic behavior. Physical Review A. 1994;**49**:2421-2431

[18] Reddy BV, Khanna SN, Dunlap BI. Giant magnetic moments in 4d clusters. Physical Review Letters. 1993;**70**:3323-3326

[19] Estiu GL, Zener MCJ. Interplay between geometric and electronic structure and the magnetism of small Pd clusters. The Journal of Physical Chemistry. 1994;**98**(18):4793-4799

[20] Watari N, Ohnishi S. Atomic and electronic structures of Pd_{13} and Pt_{13} clusters. Physical Review B. 1998;**58**:1665-1677

[21] Sun Y, Zhang M, Fournier R. Periodic trends in the geometric structures of 13-atom metal clusters. Physical Review B. 2008;**77**:075435-075438

[22] Wang LL, Johnson DD. Density functional study of structural trends for late-transition-metal 13-atom clusters. Physical Review B. 2007;**75**:235405-235410

[23] Köster AM, Calaminici P, Orgaz E, Roy DR, Reveles JU, Khanna SN. On the ground state of Pd_{13}. Journal of the American Chemical Society. 2011;**133**:12192-12196

[24] Reveles JU, Köster AM, Calaminici P, Khanna SN. Structural changes of Pd_{13} upon charging and oxidation/reduction. The Journal of Chemical Physics. 2012;**136**:114505-114506

[25] Kumar V, Kawazoe Y. Evolution of atomic and electronic structure of Pt clusters: Planar, layered, pyramidal, cage, cubic, and octahedral growth. Physical Review B. 2008;**77**:205418-205410

[26] Messmer RP, Knudson SK, Johnson KH, Diamond JB, Yang CY. Molecular-orbital studies of transition- and noble-metal clusters by the self-consistent-field-Xα scattered-wave method. Physical Review B. 1976;**13**(4):1396-1415

[27] Xiao L, Wang L. Structures of platinum clusters: Planar or spherical? Journal of Physical Chemistry A. 2004;**108**:8605-8614

[28] Apra E, Baletto F, Ferrando R, Fortunelli A. Amorphization mechanism of icosahedral metal nanoclusters. Physical Review Letters. 2004;**93**(6):065502-065504

[29] Haberlen OD, Chung SC, Rösch N, Rösch N. Relativistic density-functional studies of naked and ligated gold clusters. International Journal of Quantum Chemistry. 1994;**52** (28 S):595-610

[30] Haberlen OD, Chung S-C, Stener M, Rösch N. From clusters to bulk: A relativistic density functional investigation on a series of gold clusters Au_n n = 6,…,147. The Journal of Chemical Physics. 1997;**106**(12):5189-5201

[31] Hakkinen H. Atomic and electronic structure of gold clusters: Understanding flakes, cages and superatoms from simple concepts. Chemical Society Reviews. 2008;**37**:1847-1859

[32] Garzón IL, Beltrán MR, Posada-Amarillas A, Ordejón P, Artacho E, Sánchez-Portal D, Soler JM. Lowest energy structures of gold nanoclusters. Physical Review Letters. 1998;**81**(8):1600-1603

[33] Jennison DR, Schultz PA, Sears MP. Ab initio calculations of Ru, Pd, and Ag cluster structure with 55, 135, and 140 atoms. The Journal of Chemical Physics. 1997;**106**(5):1856-1862

[34] Hakkinen H, Moseler M, Kostko O, Morgner N, Hoffmann MA, von Issendorff B. Symmetry and electronic structure of Noble-metal nanoparticles and the role of relativity. Physical Review Letters. 2004;**93**(9):093401-093404

[35] Schooss D, Blom MN, Parks JH, Issendorff BV, Haberland H, Kappes MM. The structures of Ag55+ and Ag55−: Trapped ion electron diffraction and density functional theory. Nano Letters. 2005;**5**(10):1972-1977

[36] Blom MN, Schooss D, Stairs J, Kappes MM. Experimental structure determination of silver cluster ions ($Ag_{(n)}$+, 19 < or = n < or = 79). The Journal of Chemical Physics. 2006;**124**(24):244308-244310

[37] Yan J, Gao S. Plasmon resonances in linear atomic chains: Free-electron behavior and anisotropic screening of *d* electrons. Physical Review B. 2008;**78**:235413-235410

[38] Guidez EB, Aikens CM. Theoretical analysis of the optical excitation spectra of silver and gold nanowires. Nanoscale. 2012;**4**:4190-4198

[39] Wenxin N, Guobao Y. Review: Crystallographic control of Noble metal nanocrystals. Nano Today. 2011;**6**:265-285

[40] Zheng J, Nicovich PR, Dickson RM. Highly fluorescent Noble metal quantum dots. Annual Review of Physical Chemistry. 2007;**58**:409-431

[41] Melnikov G, Emelyanov S, Ignatenko N, Ignatenko G. The quantization of the radii of coordination spheres cubic crystals and cluster systems. IOP Conference Series: Materials Science and Engineering. 2016;**110**:012065

[42] Rao CNR, Muller A, Cheetham AK. The Chemistry of Nanomaterials; Properties and Applications. Weinheim: Wiley-VCH Verlag GmbH and Co.; 2004. pp. 12-49

[43] EAF VD, PRH DT, MAD F, Mast J. Determination of the volume-specific surface area by using transmission electron tomography for characterization and definition of nanomaterials. Journal of Nanobiotechnology. 2011;**9**(17):8

[44] Feynman R. There's plenty of room at the bottom. Engineering Science. 1992;**23**:22

[45] Triftshiiuser W, McGervey JD. Monovacancy formation energy in copper, silver, and gold by positron annihilation. Applied Physics. 1975;**6**:177-180

[46] Gao P, Wu Q, Li X, Ma H, Zhang H, Volinsky AA, Qiao L, Su Y. Size-dependent concentrations of thermal vacancies in solid films. Physical Chemistry Chemical Physics. 2016;**18**:22661-22667

[47] Goldstein AN. Handbook of Nanophase Materials. Vol. 3. New York: Marcel Dekker; 1997. pp. 105-301

[48] Korkin A, Rosei F, Lockwood DJ, editors. Nanoelectronics and Photonics: From Atoms to Materials, Devices, and Architectures. New York: Springer Science & Business Media; 2008

[49] Suryanarayana C, Singh J, Froes FH, editors. Processing and Properties of Nanocrystalline Materials. Warrendale: TMS; 1996

[50] Poole CP, Owens FJ. Introduction to Nanotechnology. New Jersey: Wiley-VCH; 2003. pp. 1-23

[51] Adekoya JA, Dare EO, Ogunniran KO, Siyanbola TO, Akinsiku AA, Ehi-Eromosele CO, et al. Facile route to synthesize organically capped size controlled silver nanoparticles. International Journal of Scientific & Engineering Research. 2014;**5**(3):1220-1226

[52] Adekoya JA, Dare EO, Ogunniran KO, Siyanbola TO, Ajani OO, Ehi-Eromosele CO, et al. Tandem synthesis of some low and high indexed monometallic nanoparticles in polyols, poly(vinylpyrrolidone), trisodium citrate and dodecanethiol matrices. Digest Journal of Nanomaterials and Biostructures. 2015;**10**(4):1311-1327

[53] Sosibo NM, Keter FK, Skepu A, Tshikhudo RT, Revaprasadu N. Facile attachment of TAT peptide on gold monolayer protected clusters: Synthesis and characterization. Nanomaterials. 2015;**5**(3):1211-1222

[54] Jurgen O, Rainer G, Rolf EJ, Marc A, Frank G, Kirill K, et al. Palladium-gallium intermetallic compounds for the selective hydrogenation of acetylene. Part 1: Preparation and structural investigation under reaction conditions. Journal of Catalysis. 2008;**258**:210-218

[55] Yeshchenko OA, Dmitruk IM, Alexeenko AA, Kotko AV, Verdal J, Pinchuk AO. Size and temperature dependence of the surface plasmon resonance in silver nanoparticles. Ukrainian Journal of Physics. 2012;**57**(2):266-277

[56] Tan N, Zhou ZY, Sun SG, Ding Y, Wang ZL. Synthesis of tetrahedral platinum nanocrystals with high index facets and high electro-oxidation activity. Science. 2007;**316**:732-735

[57] Tan N, Zhou ZY, Sun GS. Electrochemical preparation of Pd nanorods with high-index facets. Chemical Communication. 2009;**45**:1502-1504

[58] Tan N, Zhou ZY, Yu NF, Wang LY, Sun GS. Direct electrodeposition of tetrahedral Pd nanocrystals with high-index facets and high catalytic activity for ethanol electro-oxidation. Journal of America Chemical Society. 2010;**132**:7580-7581

[59] Patel VR, Agrawal YK. Nanosuspension: An approach to enhance solubility of drugs. Journal of Advanced Pharmaceutical Technology and Research. 2011;**2**(2):81-87

[60] Edelstein AS, Cammarata RC. Nanomaterials: Synthesis, Properties and Applications. 2nd ed. London: CRC Press, Taylor and Francis Group; 1998

[61] Xie Y, Blackman JA. On the oscillation of the magnetic moment of free transition metal clusters. Journal of Physics: Condensed Matter. 2003;**15**:L615-L622

[62] Carcia PF, Shah SI, Zeper WB. Effect of energetic bombardment on the magnetic coercivity of sputtered Pt/co thin-film multilayers. Applied Physics Letters. 1990;**56**(23):2345-2347

[63] Marickam M. Electronic magneto-thermal properties of ferromagnetic clusters. Journal of Physics and Chemistry of Solids. 2005;**66**:977-983

[64] Janos HF, editor. Nanoparticles and Nanostructured Films-Preparation, Characterization and Applications. New York: Wiley-VCH; 1998

[65] Moffit M, McMahon L, Pessel V, Eisenberg A. Size control of nanoparticles in semiconductor-polymer composites, 2: Control via sizes of spherical ionic microdomains in styrene based diblock ionomers. Chemistry of Materials. 1995;**7**:1185-1192

[66] Wells AF. Structural Inorganic Chemistry. 4th ed. London: Oxford University Press; 1975. pp. 74-120

[67] Yao T, Sun Z, Li Y, Pan Z, Wei H, Xie Y, Nomura M, Niwa Y, Yan W, Wu Z, Jiang Y, Liu Q, Wei S. Insights into initial kinetic nucleation of gold nanocrystals. Journal of the American Chemical Society. 2010;**132**(22):7696-7701

[68] Thanh NTK, Maclean N, Mahiddine S. Mechanisms of nucleation and growth of nanoparticles in solution. Chemical Reviews. 2014;**114**:7610-7630

[69] Biju V, Itoh T, Anas A, Sujith A, Ishikawa M. Semiconductor quantum dots and metal nanoparticles: Syntheses, optical properties, and biological applications. Analytical and Bioanalytical Chemistry. 2008;**391**:2469-2495

[70] Nikolai GK, Lev AD. Optical properties and biomedical applications of plasmonic nanoparticles. Journal of Quantitative Spectroscopy and Radiative Transfer. 2010;**111**:1-35

[71] Charles SW, Popplewell J. Properties and applications of magnetic liquids. In: Buschow KHJ, editor. Hand Book of Magnetic Materials. Vol. 2. UK: Wiley Publisher; 1986. p. 153

[72] Rosensweig RE. Heating magnetic fluid with alternating magnetic field. Journal of Magnetism and Magnetizable Materials. 2002;**252**:370-374

[73] Freeman MW, Arrot A, Watson HHL. Structure in vitreous silicate fibers as shown by small–angle scattering of x-rays. Journal of Applied Physics. 1960;**31**:404

[74] Tartaj P, del Puerto Morales M, Veintemillas-Verdaguer S, Gonzalez-Carreno T, Serna CJ. The preparation of magnetic nanoparticles for applications in biomedicine. Journal of Physics D: Applied Physics. 2003;**36**:R182-R197

[75] Goodwin S, Peterson C, Hoh C, Bittner C. Targeting and retention of magnetic targeted carriers (MTCs) enhancing intra-arterial chemotherapy. Journal of Magnetism and Magnetizable Material. 1999;**194**:132-139

[76] Safarikova M, Safarik I. Magnetic solid phase extraction. Journal of Magnetism and Magnetizable Materials. 1999;**194**:108-112

[77] Rheinlander T, Kotitz R, Weitschies W, Semmler W. Magnetic fractionation of magnetic fluids. Journal of Magnetism and Magnetizable Materials. 2000;**219**:219-228

[78] Coombs RRH, Robinson DW, editors. Nanotechnology in Medicine and Bioscience. Vol. 3. New York: Gordon and Breach; 1996

[79] Dailey JP, Phillips JP, Li C, Riffle JS. Synthesis of silicone magnetic fluid for use in eye surgery. Journal of Magnetism and Magnetizable Material. 1999;**194**:140-280

Chapter 3

Effect of Size, Shape and Environment on the Optical Response of Metallic Nanoparticles

Salem Marhaba

Additional information is available at the end of the chapter

http://dx.doi.org/10.5772/intechopen.71574

Abstract

The aim of this chapter is to investigate the effect of size, shape and environment on the optical properties of metallic nanoparticles in a large spectral range (λ = 300–900 nm) using quasi-static approximation for nanoparticles of sizes (D = 10–40 nm) and Mie theory for nanoparticles of sizes (D = 40–100 nm). Extinction (scattering and absorption) cross-sectional spectrum of nanoparticles is obtained for different diameters embedded in different matrices. Collective oscillation of electrons in conduction band in metallic nanoparticles is known as surface plasmon resonance (SPR) phenomena. SPR of metallic nanoparticles has significant applications in optics, communications and biosensors. We present in this chapter the effects of the interparticle distance on the optical response of gold dimer nanoparticles of 100 nm diameter. The extinction spectra of dimer nanoparticles are calculated by using generalized Mie theory.

Keywords: metallic nanoparticles, noble metals, optical properties, surface plasmon resonance, extinction cross section, morphology, dimer of nanoparticles

1. Introduction

Nanomaterials are macroscopic systems but constructed and organized from elementary bricks of nanometric dimensions known as nanoparticles. They have many fields of application, in the fields of optics [1, 2], magnetism [3, 4], electronics [5, 6], telecommunications [7, 8], superconductors [9, 10], chemical catalysis [11] or biological marking [12].

The phenomena of absorption, scattering and reemission of an electromagnetic wave by particles of micrometric or even nanometric size are numerous and varied. For example, sunlight incident on the Earth's atmosphere is dispersed by gas molecules and suspended particles (aerosols), giving rise to a blue sky, white clouds and various optical phenomena such as the rainbows or the halos. Another example that concerns us more closely is that of the

variety of colors of stained-glass windows whose origin is based on the very specific scattering properties of light by very fine metallic grains trapped in transparent glasses [13].

The metallic clusters of nanometric size, well below the optical wavelength, have been known and exploited for centuries for their spectacular optical properties (stained glass, ceramics) [14]. Take, for example, the case of gold nanoparticles, which can be obtained in colloidal form by chemical synthesis. When diluted in solution, they exhibit varying colors, ranging from red to violet as their size decreases. Other colors like green and blue can be obtained by also playing on their shape. These optical properties are a consequence of the dielectric confinement in these objects whose size is less than the wavelength of the excitatory light and which is at the origin of the well-known phenomenon of surface plasmon resonance (SPR), which dominates the extinction spectrum in the visible domain. This oscillation is analogous to that of an electron gas in a massive system (plasmon mode) but modified by the presence of interfaces.

Among the nanoscale systems that possess very interesting optical properties, metals and especially noble metals (gold, silver and copper) have been the most widely studied in this way [15–17]. Noble metals and gold in particular lend themselves well to the synthesis of such materials, thanks to their resistance to aging (oxidation), even in a divided form. Great progress has been made in understanding the optical properties of composite materials based on nanoparticle well as in their methods of synthesis. These range from techniques of precipitation of metal salts in glasses or gels, to the assembly of preformed particles, chemically (colloid) or physically (sources of clusters).

In this chapter, we recall the theoretical results concerning the optical properties of bulk and confined metal systems. Particular emphasis is placed on the remarkable origin and properties of surface plasmon resonance (SPR) and its dependence on the size, shape and dielectric environment of nanoparticles. We study the basic formalisms for the calculation of the different cross sections of nanoparticle interaction with light (extinction, scattering and absorption) in the framework of:

i. Quasi-static approximation for spherical and spheroidal particles

ii. Mie theory for homogeneous spherical particles.

Finally, we briefly discuss the effects of the interparticle distance on the optical response of dimer nanoparticles based on the generalized Mie theory.

2. Drude model and plasma frequency

The first situation envisaged, since it is the simplest, is that of a metal whose optical properties are essentially due to the behavior of the conduction electrons (as for the alkali metals). The Drude model [18] is then quite appropriate to describe the behavior of these quasi-free electrons. In this model, the conduction electrons of solid metal, considered as independent, move almost freely. These electrons undergo random collisions with other particles (other electrons, phonons, defects, etc.), with a probability per unit of time given by the electronic collision

(or relaxation) rate $\gamma_0 = \tau^{-1}$. The corresponding time τ is connected to the mean free path of the electrons by $l = v_F\tau$ where v_F is the Fermi velocity of conduction electrons. For example, in the case of bulk sodium, $l \cong 35$ nm at 273 K [4] and v_F =1.07 $nm.fs^{-1}$ [19], resulting an average collision time $\tau \cong 32$ fs (estimated from electrical resistivity measurements [20]). Each collision is an instantaneous event with a sudden change in the speed of the electron, without memory of its initial velocity. The average effect of these collisions, which the Drude model does not claim to describe the mechanism, can then be modeled by a friction force whose damping coefficient is γ_0. In the presence of an external field $\vec{E} = \vec{E}_0 e^{-i\omega t}$, the fundamental principle of the dynamics applied to a conduction electron of effective mass m_{eff} and of charge $-e$ is written as:

$$m_{eff}\frac{d^2\vec{r}}{dt^2} = -\frac{m_{eff}}{\tau}\frac{d\vec{r}}{dt} - e\vec{E} \tag{1}$$

In this equation, $\vec{r}$ is the displacement of the electron around an average position, and the second term is a damping term related to the different collision processes cited above. An oscillating solution of this equation is as follows:

$$\vec{r} = \frac{e\vec{E}}{m_e\omega(\omega + i\gamma_0)} \tag{2}$$

The displacement of Drude's electrons induces a dipole moment $\vec{p} = -e\vec{r}$, and the electron gas polarization, defined as the dipolar moment per unit volume, is thus written as:

$$\vec{\mathrm{P}} = -ne\vec{r} = \frac{-\varepsilon_0\omega_p^2}{\omega^2 + i\gamma_0\omega}\vec{E} \tag{3}$$

where n is the number of free electrons per unit volume and $\omega_p = \sqrt{\frac{ne^2}{m_e\varepsilon_0}}$ is called plasma frequency of bulk metal. The Drude model allows us to introduce simply the notion of dielectric constant, a characteristic magnitude of the optical response of a solid.

3. Dielectric constant and dielectric susceptibility

In a material, the two macroscopic vector quantities, which are the electric field $\vec{\mathrm{E}}$ and the electric displacement $\vec{\mathrm{D}}$, are connected together by the relation

$$\vec{\mathrm{D}} = \varepsilon_0\vec{\mathrm{E}} + \vec{\mathrm{P}} \tag{4}$$

where ε_0 is the vacuum permittivity and $\vec{\mathrm{P}}$ is the induced electrical polarization. Since the intensity of the applied field is not too high, the polarization $\vec{\mathrm{P}}$ is connected linearly with $\vec{\mathrm{E}}$ through the dielectric susceptibility χ of the medium according to the relation:

$$\vec{P} = \varepsilon_0 \chi \vec{E} \tag{5}$$

which allows us to establish a relation between the electric displacement and the electric field by defining the dielectric constant ε such that:

$$\vec{D} = \varepsilon_0 \varepsilon \vec{E} \text{ with } \varepsilon = 1 + \chi \tag{6}$$

By combining the three equations: Eqs. (3), (4) and (6), the dielectric constant ε is obtained in the form:

$$\varepsilon(\omega) = 1 - \frac{\omega_p^2}{\omega(\omega + i\gamma_0)} \tag{7}$$

The dielectric constant $\varepsilon(\omega)$ is generally written in complex form:

$$\varepsilon(\omega) = \varepsilon_1(\omega) + i\varepsilon_2(\omega) \tag{8}$$

The real and imaginary parts of $\varepsilon(\omega)$ are written as:

$$\begin{cases} \varepsilon_1(\omega) = 1 - \dfrac{\omega_p^2}{\omega^2 + {\gamma_0}^2} \\ \varepsilon_2(\omega) = \dfrac{\omega_p^2 \gamma}{\omega(\omega^2 + {\gamma_0}^2)} \end{cases} \tag{9}$$

In the optical domain where the frequencies are such that $\omega >> \gamma_0$, these expressions are simplified in the form:

$$\begin{cases} \varepsilon_1(\omega) = 1 - \dfrac{\omega_p^2}{\omega^2} \\ \varepsilon_2(\omega) = \dfrac{\omega_p^2}{\omega^3}\gamma_0 \end{cases} \tag{10}$$

We then see, in a classical approach, how the core electrons are introduced in the study of the optical properties of noble metals.

4. Interband absorption: contribution of d electrons

The optical response of bulk noble metals cannot be completely described by the Drude model. To take into account the contribution of core electrons (d band electrons) in the optical response of noble metals, a term must be added to the dielectric constant as calculated from the Drude model (Eq. 9). The dielectric constant can be written in the following way:

$$\varepsilon = 1 + \chi^D + \chi^{IB} \text{ or } \varepsilon = \varepsilon^D + \varepsilon^{IB} - 1; \tag{11}$$

ε^D and ε^{IB} are complex ($\varepsilon^D = 1 + \chi^D$ and $\varepsilon^{IB} = 1 + \chi^{IB}$).

The first term ε^D represents the intraband component of the dielectric constant. It is connected to the optical transitions of a free electron of the conduction band to a higher energy level of the same band. This term is well described by the Drude model, hence the index *D*. The second term ε^{IB} corresponds to the interband component of the dielectric constant, linked to the optical transitions between the valence band (essentially from the d band) and the conduction band sp. There is, therefore, a threshold energy E^{IB} for interband transitions (located in the visible (for gold) or near UV (for silver)). This component may be neglected in the infrared domain, where the optical response is dominated by intraband absorption. The real and imaginary parts of the experimental dielectric constants of gold and silver, as given in Johnson and Christy [21] and Palik [22], represented in **Figures 1** and **2**, reproduce well the predictions of the Drude model (Eq. 9) in the sense that they diverge very similarly for low energies (E < 1.5 eV approximately).

The role of the core electrons d is manifested by the deviation from the Drude function. It is mainly observed in the imaginary parts of ε. The strong growth of the imaginary component ε_2, observed around 620 *nm* for gold and 310 *nm* for silver, marks the beginning of interband transitions. It should be noted that the dielectric constants tabulated in the literature may differ according to the sources since they are extracted from experimental measurements obtained with techniques and under conditions which may be different. For example, some discrepancies between the values of Palik and those of Johnson and Christy may have important implications for the predictions of theoretical models when injected into calculations.

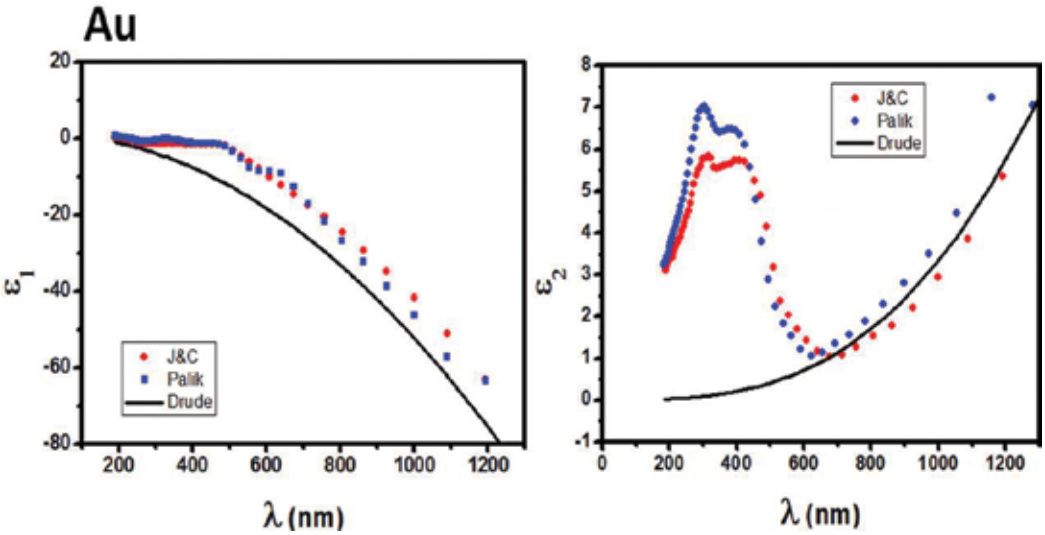

Figure 1. Real and imaginary parts of the dielectric constant of bulk gold. The experimental results of Johnson and Christy (red •) and Palik (blue ▪) are compared to the Drude model (solid lines).

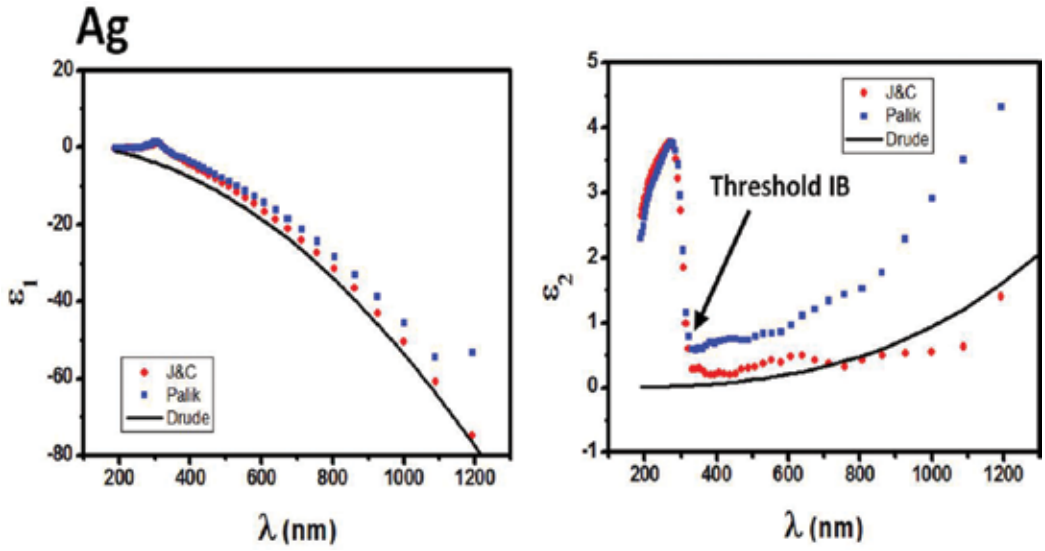

Figure 2. Real and imaginary parts of the dielectric constant of bulk silver. The experimental results of Johnson and Christy (red •) and Palik (blue ▪) are compared to the Drude model (solid lines).

5. Extinction, scattering and absorption of wave by a sphere in the quasi-static approximation

We study the optical response of a metal sphere in the quasi-static approximation, that is to say when the wavelength λ of the incident radiation (plane wave) is much greater than the diameter D of the sphere. In this case, it is possible to consider that the applied electromagnetic field is uniform at each instant and at any point of the object volume (no delay effect). The sphere of radius R is characterized by a complex dielectric constant. The dielectric constant ε_m of the environment is real since this dielectric medium is transparent in our frequency domain ($n_m = \sqrt{\varepsilon_m}$). In the quasi-static approximation and if the temporal variation of the applied field is set aside, the problem returns to that of a sphere subjected to a uniform field $\vec{E}_o$. The electric potentials take the form [23]:

$$\begin{cases} V_1(r,\theta) = -\dfrac{3\varepsilon_m}{\varepsilon_1 + 2\varepsilon_m} E_o r\cos\theta \\ V_m(r,\theta) = -E_o r\cos\theta + R^3 E_o \dfrac{\varepsilon_1 - \varepsilon_m}{\varepsilon_1 + 2\varepsilon_m}\dfrac{\cos\theta}{r^2} = V_i(r,\theta) + V_s((r,\theta) \end{cases} \tag{12}$$

V_i is the electric potential due to the incident electric field E_0, and V_s is the electric potential due to the scattered electric field E_s.

Given the symmetry of the problem, the azimuthal angular dependence ϕ does not intervene, and then the system is reduced to a two-dimensional problem: r and θ. The internal field is uniform $\vec{E}_1 = -\vec{\nabla}V_1 = \frac{3\varepsilon_m}{\varepsilon_1+2\varepsilon_m}\vec{E}_o$, and from the expression of V_m above, we see that the total

external field is the sum of the incident field derived from V_i and an additional field $\vec{E}_s$ derived from V_s. Note that V_s has the structure of the potential generated by a dipole:

$$V_s(r,\theta) = R^3 E_o \frac{\varepsilon_1 - \varepsilon_m}{\varepsilon_1 + 2\varepsilon_m} \frac{\cos\theta}{r^2} = \frac{\vec{p}.\vec{r}}{4\pi\varepsilon_m r^3} \tag{13}$$

where $\vec{p}$ is written as

$$\vec{p} = 4\pi\varepsilon_m R^3 \frac{\varepsilon_1 - \varepsilon_m}{\varepsilon_1 + 2\varepsilon_m} \vec{E}_o \tag{14}$$

The application of the electric field $\vec{E}_o$ induces a polarization of the sphere (**Figure 3**) and the appearance of a charge surface distribution:

$$\sigma(\theta) = 3\frac{\varepsilon_1 - \varepsilon_m}{\varepsilon_1 + 2\varepsilon_m} E_o \cos\theta \tag{15}$$

One can write: $\vec{p} = 3\varepsilon_m \alpha \vec{E}_o$

where

$$\alpha = V \frac{\varepsilon_1 - \varepsilon_m}{\varepsilon_1 + 2\varepsilon_m} \tag{16}$$

α is defined as the polarizability of the sphere, and $V = 4/3\pi R^3$ is the volume of the particle. The extinction and scattering cross sections in general form are

$$C_{ext} = 3k\,\mathrm{Im}\{\alpha\} = 3kV\,\mathrm{Im}\left\{\frac{\varepsilon_1 - \varepsilon_m}{\varepsilon_1 + 2\varepsilon_m}\right\} \tag{17}$$

$$C_{diff} = \frac{3k^4}{2\pi}|\alpha|^2 = \frac{3}{2}k^4V^2\left|\frac{\varepsilon_1 - \varepsilon_m}{\varepsilon_1 + 2\varepsilon_m}\right|^2 \tag{18}$$

$$C_{abs} = C_{ext} - C_{diff} \tag{19}$$

The essential point here is that the polarization and consequently the different cross sections can become very important if the common term to their denominator vanishes or takes very low values. Knowing that the dielectric constant ε_1 of the metal (Eq. 5) depends on the frequency of the excitation wave, a resonance phenomenon is observed when

$$|\varepsilon_1 + 2\varepsilon_m|^2 = [\mathrm{Re}\{\varepsilon_1(\omega)\} + 2\varepsilon_m]^2 + \mathrm{Im}\{\varepsilon_1(\omega)\}_2^2 \tag{20}$$

will be minimum.

If the imaginary component $\mathrm{Im}\{\varepsilon_1(\omega)\} << 1$ or its variation $\partial\,\mathrm{Im}\{\varepsilon_1(\omega)\}/\partial\omega$ is minimal, then the expression (Eq. 20) can cancel out for a pulsation $\omega = \omega_{RPS}$ such as $\mathrm{Reel}\{\varepsilon_1(\omega_{RPS})\} = -2\varepsilon_m$. By writing the dielectric constant of the determined metal in the case of noble metals (Eq. 8)

and using the Drude model to explain the contribution of free electrons (Eq. 7), we deduce the expression of resonance pulsation ω_{RPS}:

$$\omega_{RPS} = \frac{\omega_p}{\sqrt{\mathrm{Re}\{\varepsilon^{(IB)}(\omega_{RPS})\} + 2\varepsilon_m}} \tag{21}$$

In the dipolar approximation, the pulsation ω_{RPS} is conventionally interpreted as the oscillation pulsation of the electronic cloud with respect to the ions of the nanoparticle. Such a phenomenon is associated with a collective excitation of electrons within the metallic nanoparticles and known as surface plasmon resonance due to the fact that the restoring force which intervenes in the oscillatory motion is mainly due to the charges located at the surface as this is illustrated in **Figure 3** [24]. By explicating the real and imaginary parts of the dielectric constant of the metal and the wave vector k, the extinction and scattering cross sections (Eqs. 17 and 18) can be written as:

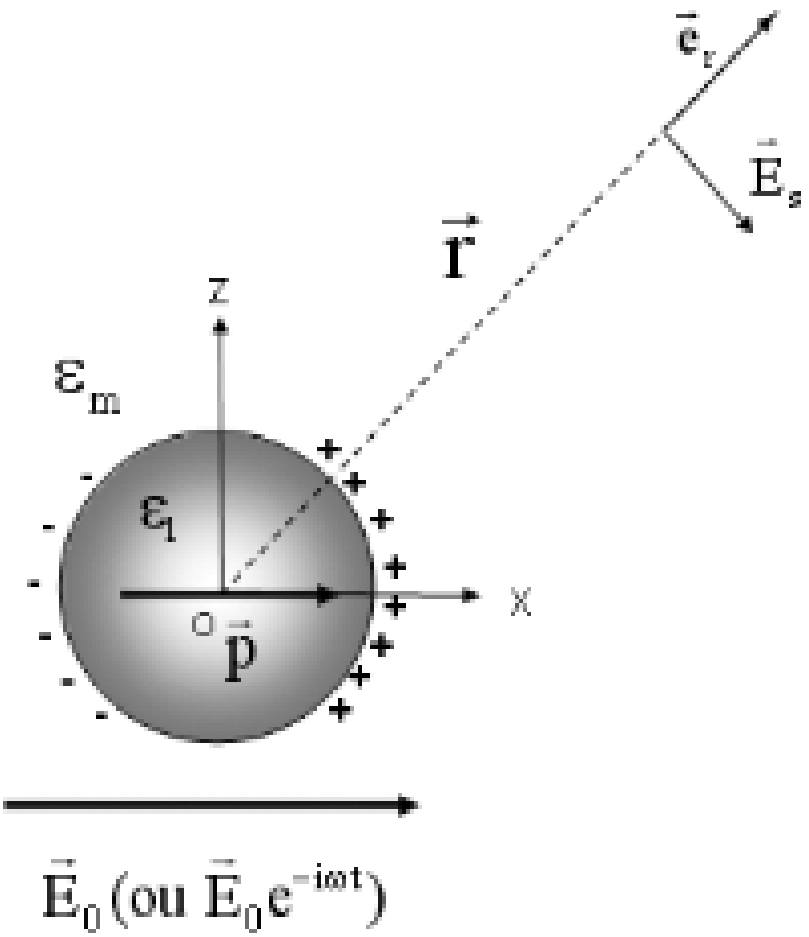

Figure 3. Polarization of a sphere metal subjected to a uniform field E_0. The dipole radiates a field E_s.

$$\sigma_{ext}(\lambda) = 18\pi\varepsilon_m^{3/2}\frac{V}{\lambda}\frac{\varepsilon_I(\lambda)}{(\varepsilon_R(\lambda)+2\varepsilon_m)^2+(\varepsilon_I(\lambda))^2} \tag{22}$$

$$\sigma_{diff}(\lambda) = 144\pi^4\varepsilon_m^2\left(\frac{V^2}{\lambda^4}\right)\frac{(\varepsilon_R(\lambda)-\varepsilon_m)^2+(\varepsilon_I(\lambda))^2}{(\varepsilon_R(\lambda)+2\varepsilon_m)^2+(\varepsilon_I(\lambda))^2} \tag{23}$$

Here, $\varepsilon_R = \mathrm{Re}\{\varepsilon\}$ and $\varepsilon_I = \mathrm{Im}\{\varepsilon\}$ and we note C_{ext} and C_{scat} in the more usual form σ_{ext} and σ_{scat}. It is chosen to express the spectral dependence of these quantities as a function of the wavelength. We find the dependence in $1/\lambda^4$ of σ_{scat}, characteristic of Rayleigh scattering of nanometric particles. For the same nanoparticle, the ratio of the scattering and extinction cross sections is proportional to the volume V:

$$\frac{\sigma_{diff}}{\sigma_{ext}} \propto \frac{V}{\lambda^3} \propto \left(\frac{R}{\lambda}\right)^3 \tag{24}$$

Thus, for nanoparticles such as $R << \lambda$, that is, in the quasi-static approximation considered so far, extinction is largely dominated by absorption and we have:

$$\sigma_{abs} \cong \sigma_{ext} \tag{25}$$

6. Dielectric constant of a confined system

In the previous description, the dielectric constant of the particles was taken as that of solid bulks. This explains, for example, the absence of size effects on the value of the SPR in the quasi-static approximation. Strictly speaking, it is expected that the effective dielectric constant of the particles will be different from that of the solid bulk, essentially due to the fact that the confinement and the presence of an interface with the external environment must introduce significant modifications. The confinement can be taken into account in the Drude model by introducing phenomenologically a collision effective term for free electrons with surfaces. When the particle size is smaller than the mean free path of electrons, the collision frequency with the surfaces of a sphere of radius R is proportional to v/R, where v is the velocity of the electron. Only the electrons close to the Fermi level can contribute to these collisions (because of Pauli's exclusion principle). The speed v can therefore be taken equal to the Fermi speed v_F:

$$v_F = \sqrt{\frac{2E_F}{m_{eff}}} \tag{26}$$

The total collision rate is written as [25]

$$\gamma(R) = \gamma_0 + g\frac{v_F}{R} \tag{27}$$

where γ_0 is the rate of intrinsic electronic collisions (electron/electron and electron/phonon) of the infinite solid, and the parameter g is a dimensionless corrective factor called a surface scattering coefficient. Its value can be estimated according to the simple quantum-box model.

It is of the order of one [25]. Typically, the collision characteristic times $\frac{1}{\gamma_0}$ are of the order of a few tens of femtoseconds (40 fs for Ag and 30 fs for Au from [20]). It is then assumed that the intraband contribution is given by an expression of Drude model with a collision rate given by Eq. (27). The Drude contribution (Eq. 9) damped is thus written as:

$$\begin{cases} \varepsilon_1^D(\omega, R) = 1 - \dfrac{\omega_p^2}{\omega^2 + \gamma^2(R)} \\ \varepsilon_2^D(\omega, R) = \dfrac{\omega_p^2 \gamma(R)}{\omega(\omega^2 + \gamma^2(R))} \end{cases} \tag{28}$$

The dielectric constant of the bulk solid is written as:

$$\varepsilon(\omega, \infty) = \underbrace{\varepsilon^D(\omega, \infty)}_{\text{Drude Massif}} + \varepsilon^{IB}(\omega, \infty) - 1 \tag{29}$$

and the dielectric constant of a confined metal:

$$\varepsilon(\omega, R) = \underbrace{\varepsilon^D(\omega, R)}_{\text{Drude Amortie}} + \varepsilon^{IB}(\omega, R) - 1 \tag{30}$$

The interband transitions are little modified for sizes up to 3 nm [26] and then $\varepsilon^{IB}(\omega, R) \approx \varepsilon^{IB}(\omega, \infty)$; it is therefore possible to obtain the expression of the dielectric constant of a confined metal from Eq. (28) and a knowledge of $\varepsilon^{IB}(\omega, \infty)$. $\varepsilon^{IB}(\omega, R)$ can be estimated by subtracting from the experimental dielectric constant (table) [21, 22] the Drude bulk part (Eq. 9):

$$\varepsilon(\omega, R) \cong \varepsilon^D(\omega, R) + \left(\varepsilon_{\exp}(\omega, \infty) - \varepsilon^D(\omega, \infty)\right) \tag{31}$$

$$\varepsilon(\omega, R) \cong \varepsilon_{\exp}(\omega, \infty) + \omega_p^2 \left(\frac{1}{\omega^2 + \gamma_0^2} - \frac{1}{\omega^2 + \gamma^2(R)}\right) + i \frac{\omega_p^2}{\omega} \left(\frac{\gamma(R)}{\omega^2 + \gamma^2(R)} - \frac{\gamma_0}{\omega^2 + \gamma_0^2}\right) \tag{32}$$

In the optical domain, the frequencies are such that $\omega >> \gamma(R)$ and γ_0; the expression of the dielectric constant of confined metal is reduced to:

$$\varepsilon(\omega, R) \approx \varepsilon_{\exp}(\omega, \infty) + i \frac{(\omega_p)^2}{(\omega)^3} \left(g \frac{v_F}{R}\right) \tag{33}$$

The constant g is of the order of unity. Its value and its dependence in R are one of the stakes of the optical studies on the nanoparticles. The reducing size is therefore the main effect of widening and attenuating the surface plasmon resonance band. **Figures 4** and **5** show the calculations of the extinction cross section for 20 nm gold and silver spheres immersed in vacuum by using a modified dielectric constant to take account of confinement effect.

It should be noted that the profile of the spectra is given by Eq. (22) in which the modified value of the dielectric constant of the particle (Eq. 31) is introduced. In the case where the

http://dx.doi.org/10.5772/intechopen.71574

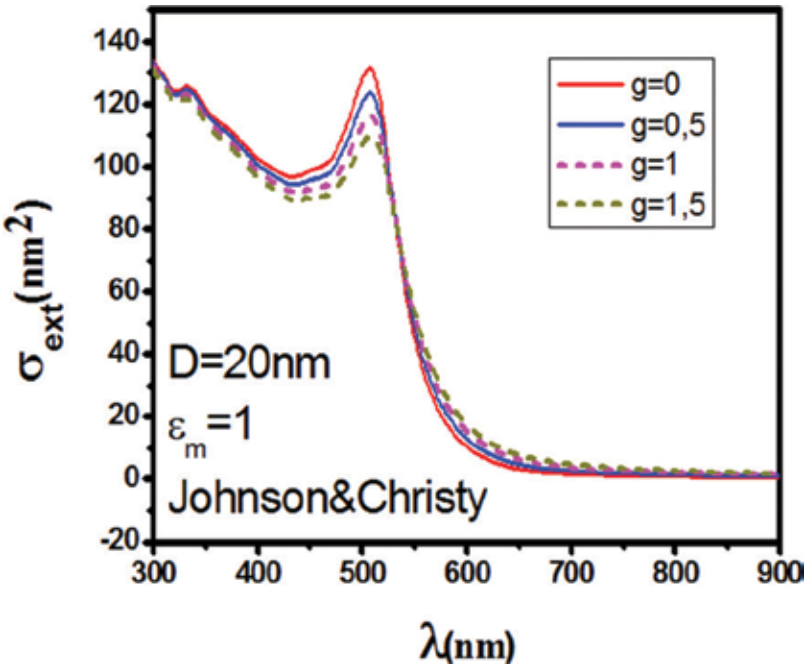

Figure 4. Calculations of the extinction cross sections in the dipolar approximation for a gold nanoparticle with a diameter of 20 nm in a dielectric matrix $\varepsilon_m = 1$ for four values of the surface scattering coefficient g = 0, 0.5, 1 and 1.5.

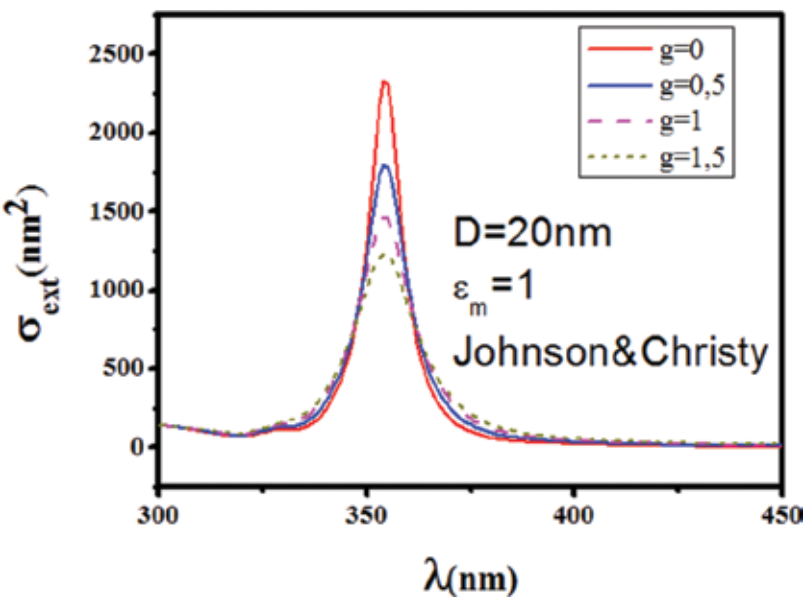

Figure 5. Calculations of the extinction cross sections in the dipolar approximation for a silver nanoparticle with a diameter of 20 nm in a dielectric matrix $\varepsilon_m = 1$ for four values of the surface scattering coefficient g = 0, 0.5, 1 and 1.5.

surface plasmon resonance is far from the interband threshold (like silver), it is possible to show that the spectrum adopts a quasi-Lorentzian profile. The full width at half maximum (FWHM) can be expressed approximately in the form [27, 28]:

$$\Gamma \cong \gamma_0 + g\frac{v_F}{R} + \left(\frac{\omega_{RPS}^3}{\omega_p^2}\right)\varepsilon_I^{IB}(\omega_{RPS}) = \gamma(R) + \left(\frac{\omega_{RPS}^3}{\omega_p^2}\right)\varepsilon_I^{IB}(\omega_{RPS}) \tag{34}$$

The width of the resonance spectrum depends not only on the modified electronic collision rate but also on the imaginary part of the interband dielectric constant in the vicinity of the plasmon resonance. For silver with $g = 1$ and $R = 10$ nm, it is estimated that $\gamma_0 \cong 2.5 \times 10^{13}\ s^{-1}$ ($\tau = 40$ fs) and $g\frac{v_F}{R} \cong 1.4 \times 10^{14}\ s^{-1}$. These two terms contribute to a spectral width $\Delta\lambda \cong 7$ nm around 400 nm. This is consistent with **Figure 5** and indicates that the third term of Eq. (34) contributes little for silver as expected. In this case, an increase in g is sensitive to the width of the spectrum. In the case of gold (**Figure 4**), assuming that Eq. (34) remains fairly valid, one could show that the proximity of the interband transitions with plasmon resonance contributes strongly to the width, which also explains why it is less sensitive to the value of g than in the case of silver.

7. Environment effect on the surface plasmon resonance

From the expression (Eq. 22), it is clear that the extinction cross-sectional spectrum is very sensitive to the value of ε_m. For a given metal, the SPR profile can be modified by its environment by means of its dielectric constant ε_m. The spectral position will move to red by increasing ε_m (Eq. 21). The

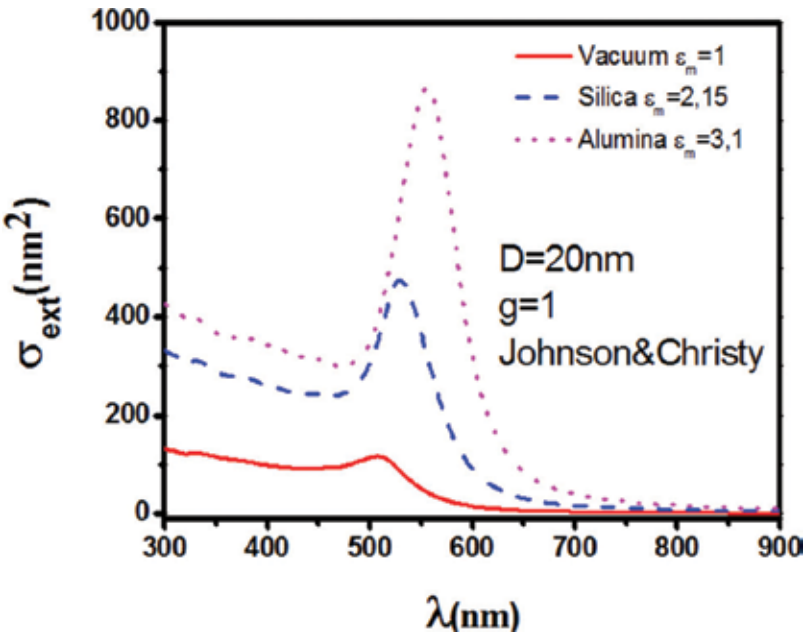

Figure 6. Extinction cross sections for a gold nanoparticle with a diameter of 20 nm calculated by the quasi-static approximation in different environments: Vacuum ($\varepsilon_m = 1$), silica ($\varepsilon_m = 2, 15$) and alumina ($\varepsilon_m = 3, 1$).

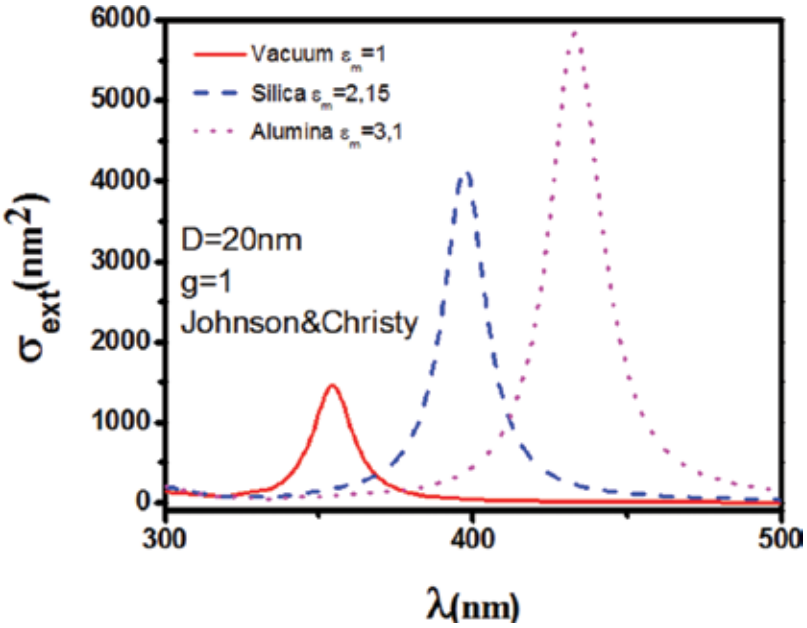

Figure 7. Extinction cross sections for a silver nanoparticle with a diameter of 20 nm calculated by the quasi-static approximation in different environments: Vacuum ($\varepsilon_m = 1$), silica ($\varepsilon_m = 2, 15$) and alumina ($\varepsilon_m = 3, 1$).

extinction cross section of silver and gold nanoparticles in different environments was calculated (**Figures 6** and **7**). The dielectric constant used for the metallic nanoparticle was deduced from bulk metal by adding a surface contribution with $g = 1$ (Eq. 32). The redshift of the resonances is correlated to the increase of the dielectric constant of the external environment. It should be noted that this effect is more visible in the case of silver than in that of gold. For the latter, the immediate proximity of the threshold of interband transitions has the effect of attenuating and widening the surface plasmon resonance band when the spectral position is shifted toward the small wavelengths. Hence, an increase of ε_m has a less noticeable effect on gold than on silver.

8. Shape effect

So far, we have considered spherical nanoparticles. Experimentally, we are often led to study deformed particles which adopt ellipsoidal forms. On the basis of the notion of polarizability of particles, we establish here the general formulas of extinction cross sections for ellipsoids (semiaxes: a, b and c) in the quasi-static approximation (a, b and c < <λ) and discuss the shape effect on the optical response.

By analogy with the case of the sphere, it is possible to show that the polarizability of an ellipsoid when an electric field is applied to it in one of the x, y or z directions is equal to [29]:

$$\alpha_{x,y,z} = \frac{4\pi}{3} abc \frac{\varepsilon_1 - \varepsilon_m}{3\varepsilon_m + 3L_{x,y,z}(\varepsilon_1 - \varepsilon_m)} \tag{35}$$

To obtain this result, the Maxwell equations are solved in a system of ellipsoidal coordinates. The establishment of the boundary conditions at the interface between the particle and the external environment makes it possible to express the electrical potentials in each region and to identify the dipole responsible of the scattered field. The geometric factors $L_{x,y,z}$ are defined by:

$$\begin{cases} L_x = \dfrac{abc}{2}\displaystyle\int_o^\infty \dfrac{dt}{(t+a^2)^{3/2}\left(t+b^2\right)^{1/2}(t+c^2)^{1/2}} \\ L_y = \dfrac{abc}{2}\displaystyle\int_o^\infty \dfrac{dt}{\left(t+b^2\right)^{3/2}(t+a^2)^{1/2}(t+c^2)^{1/2}} \\ L_z = \dfrac{abc}{2}\displaystyle\int_o^\infty \dfrac{dt}{(t+c^2)^{3/2}(t+a^2)^{1/2}\left(t+b^2\right)^{1/2}} \end{cases} \tag{36}$$

$$\mathrm{L_x + L_y + L_z = 1} \tag{37}$$

By analogy with the problem of the sphere treated above, the cross sections can be expressed in the form:

$$\sigma_{ext} = 3k\,\mathrm{Im}\left\{\alpha_x\left(\vec{e}_z{}'.\vec{e}_x\right)^2 + \alpha_y\left(\vec{e}_z{}'.\vec{e}_y\right)^2 + \alpha_z\left(\vec{e}_z{}'.\vec{e}_z\right)^2)\right\} \tag{38}$$

$$\sigma_{diff} = \frac{3k^4}{2\pi}\left\{|\alpha_x|^2\left(\vec{e}_z{}'.\vec{e}_x\right)^2 + |\alpha_y|^2\left(\vec{e}_z{}'.\vec{e}_y\right)^2 + |\alpha_z|^2\left(\vec{e}_z{}'.\vec{e}_z\right)^2)\right\} \tag{39}$$

$$\sigma_{abs} = \sigma_{\mathrm{ext}} - \sigma_{diff} \cong \sigma_{ext} \tag{40}$$

An important case is that of an excitation by an electric field polarized collinearly with one of the principal axes of the ellipsoid. We can write:

$$\sigma_{ext}^{x,y,z} = \frac{2\pi\varepsilon_m^{3/2}}{L_{x,y,z}^2}\frac{V}{\lambda}\frac{\varepsilon_I}{\left(\varepsilon_R + \frac{1-L_{x,y,z}}{L_{x,y,z}}\varepsilon_m\right)^2 + (\varepsilon_I)^2} \tag{41}$$

with $V = \frac{4}{3}\pi\,abc$ the volume of the ellipsoid. Depending on the direction of polarization $i = x, y$ or z, the resonance wavelength λ_{RPS}^i is determined by the relation:

$$L_i\varepsilon_R\left(\lambda_{RPS}^i\right) + (1 - L_i)\varepsilon_m \cong 0 \tag{42}$$

The surface plasmon frequency for an ellipsoid:

$$\omega^{x,y,z}{}_{RPS} = \frac{\omega_p}{\sqrt{\mathrm{Re}\{\varepsilon^{(IB)}(\omega_{RPS})\} + \frac{\left(1-L_{x,y,z}\right)}{L_{x,y,z}}\varepsilon_m}} \tag{43}$$

If the case of prolate ellipsoid (a = c > b), then $\mathrm{L_x = L_z}$ and $\mathrm{L_y}$ depend only on its aspect ratio $\eta = \frac{a}{b}$. L_z is written as a function of the ellipticity e of the spheroids defined by: $e^2 = 1 - \eta^2$

$$L_y = \frac{(1-e^2)}{e^2}\left[-1+\frac{1}{2e}\ln\left(\frac{1+e}{1-e}\right)\right] \text{ and } L_{x,z} = \frac{1-L_y}{2} \tag{44}$$

Figures 8 and **9** illustrate the evolution of SPR as a function of the shape of the ellipsoid in the case of gold and silver nanoparticles, respectively. The cross sections are calculated according to Eq. (41) for a prolate ellipsoid whose volume is equivalent to that of a 20-nm nanoparticle embedded in vacuum with $g = 1$. First, due to the anisotropy of the nanoparticle, there are two distinct modes for SPR on either side of SPR position of a sphere of the same volume. The difference between the two cases is more marked by decreasing the aspect ratio, as seen in

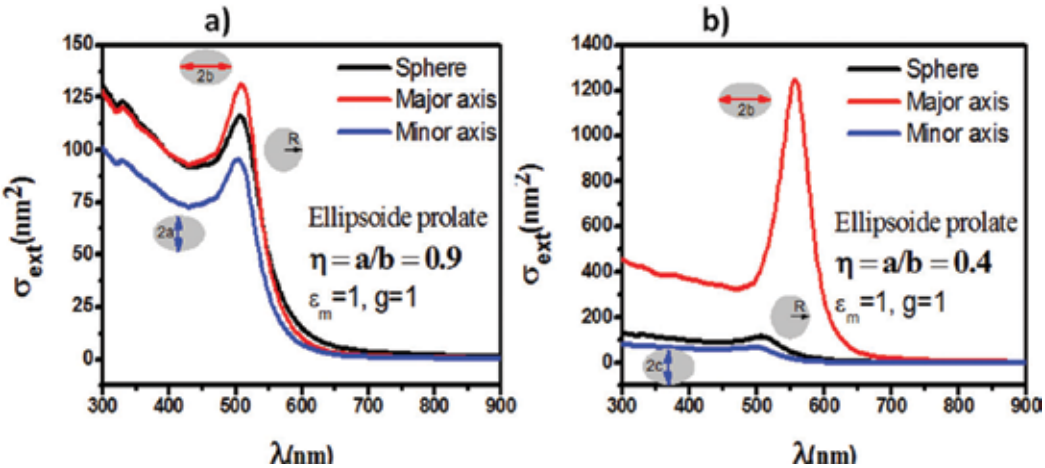

Figure 8. Extinction spectra calculated for a prolate gold nanoparticle for two aspect ratio values: (a) η = 0.9, (b) η = 0.4. The nanoparticle is placed in vacuum. The coefficient g of the surface term is taken to be equal to 1.

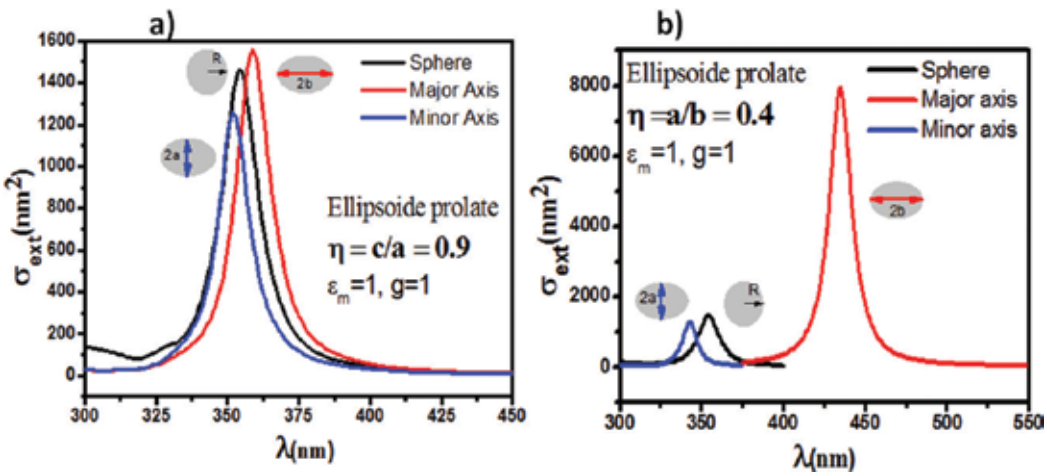

Figure 9. Extinction spectra calculated for a prolate silver nanoparticle for two aspect ratio values: (a) η = 0.9, (b) η = 0.4. The nanoparticle is placed in a vacuum. The coefficient g of the surface term is taken to be equal to 1.

Figures 8 and **9** for η = 0.9 and 0.4. Indeed, the mode along the major axis gives a larger cross section because it is equivalent to a larger volume of material probed with respect to the sphere. In the case of gold and with the aspect ratio $\eta = 0.4$, it is found that the mode along the minor axis is wider than that along the major axis because the coupling with the interband transitions becomes stronger.

9. Mie theory

The quasi-static description developed previously is strictly valid only in the limit where $k \cong 0$. It gives a good approximation when $kR << 1$. For example, when $R \cong \lambda$, the applied electric field varies spatially on the volume of the particle. The distribution of surface charges does not necessarily have the dipole structure obtained for a uniform field, and multipolar contributions of higher orders are to be taken into account. We briefly present the formalism of the Mie theory which gives an exact general calculation of the optical response of a spherical particle of any diameter in a range of sizes where kR is no longer limited and may be greater than unit. In 1908, Gustav Mie developed a theory of the interaction of an electromagnetic wave with a homogeneous spherical metal nanoparticle based on a multipolar development of the electromagnetic field. This model describes the absorption spectrum of colloidal suspensions of gold particles in water [30]. We introduce the ratio M of the refractive indices of the nanoparticle and of the external dielectric medium and x the dimensionless size parameter:

$$M^2 = \frac{\varepsilon}{\varepsilon_m} = \left(\frac{n}{n_m}\right)^2 \text{ and } x = kR = \frac{2\pi n_m R}{\lambda} \tag{45}$$

The important final result is that the extinction, scattering and absorption cross sections for a nanoparticle of diameter D are simply expressed as series [31, 32]:

$$\sigma_{ext} = \frac{2\pi}{k^2}\sum_{n=1}^{\infty}(2n+1)\mathrm{Re}\{a_n + b_n\} \tag{46}$$

$$\sigma_{diff} = \frac{2\pi}{k^2}\sum_{n=1}^{\infty}(2n+1)\left(|a_n|^2 + |b_n|^2\right) \tag{47}$$

$$\sigma_{abs} = \sigma_{ext} - \sigma_{diff} \tag{48}$$

The coefficients a_n and b_n are defined by

$$\begin{cases} a_n = \dfrac{M\varphi_n(Mx)\varphi_n'(x) - \varphi_n(x)\varphi_n'(Mx)}{M\varphi_n(Mx)\zeta_n'(x) - \xi_n(x)\varphi_n'(Mx)} \\ b_n = \dfrac{\varphi_n(Mx)\varphi_n'(x) - M\varphi_n(x)\varphi_n'(Mx)}{\varphi_n(Mx)\zeta_n'(x) - M\xi_n(x)\varphi_n'(Mx)} \end{cases} \tag{49}$$

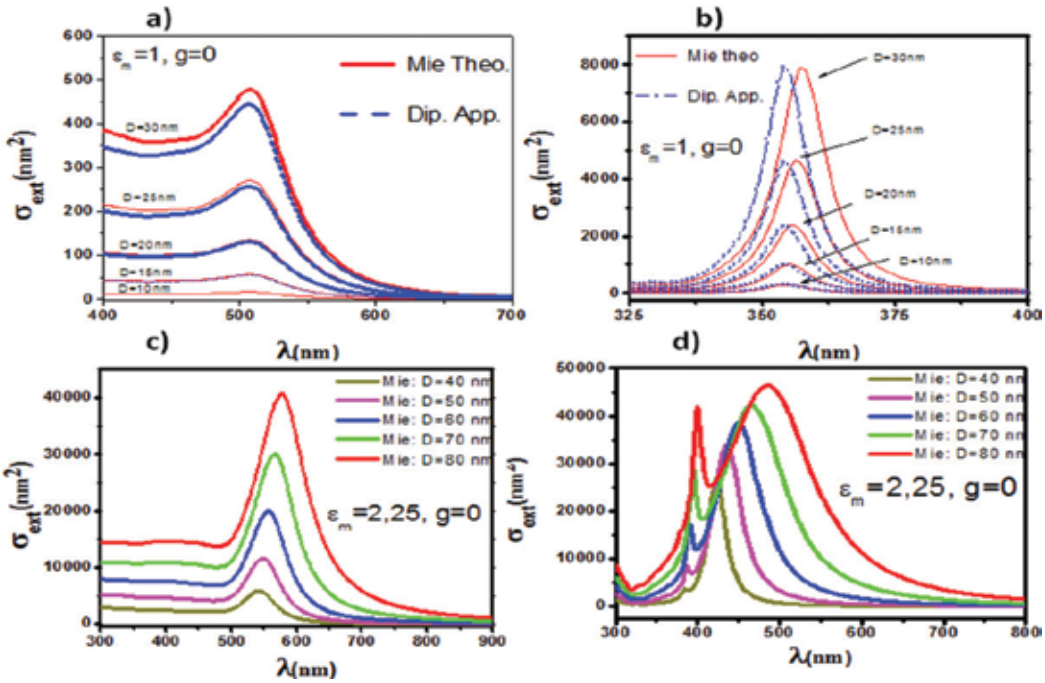

Figure 10. Extinction spectra calculated in the context of the Mie theory as a function of the size of nanoparticles in the case of gold (a) and (c) and silver (b) and (d). The spectra are compared with the calculations of the dipole approximation for sizes ranging from 10 to 30 nm in the case of gold (a) and silver (b).

where $\varphi_n(x)$ and $\xi_n(x)$ are the Riccati-Bessel functions of order n. The index n is the order of the multipole expansion. The quasi-static approximation is valid for diameters less than about 20 nm. In the case of gold, the resulting spectra show a dipolar peak which corresponds to the surface plasmon resonance at about 530–560 nm. Moreover, these spectra have a plateau below 500 nm which corresponds to the interband transitions. Finally, the signal falls to 0 and is practically zero from 750 nm (**Figure 10a** and **c**). In the case of silver, it can be seen that the increase of the size induces a widening and a redshift of the resonance due to the increasing influence of the multipolar terms (**Figure 10b** and **d**). This effect also exists for gold but is less clear due to the coupling of SPR with the interband transitions. The main peak in **Figure 10d** is attributed to the dipole character of the surface plasmon resonance, and the present appearance of second peak at higher energy is due to the quadrupolar contribution. The proximity of the interband transitions in gold (**Figure 10c**) explains that this contribution is not visible for a comparable nanoparticle size.

10. Optical response of several spherical particles: generalized Mie theory

Finally, we study a situation that can be encountered experimentally: the optical response of a group of close particles. This situation is illustrated in **Figure 11**. The incident field on a particle i is the sum of the applied field and the set of scattered fields by the other particles.

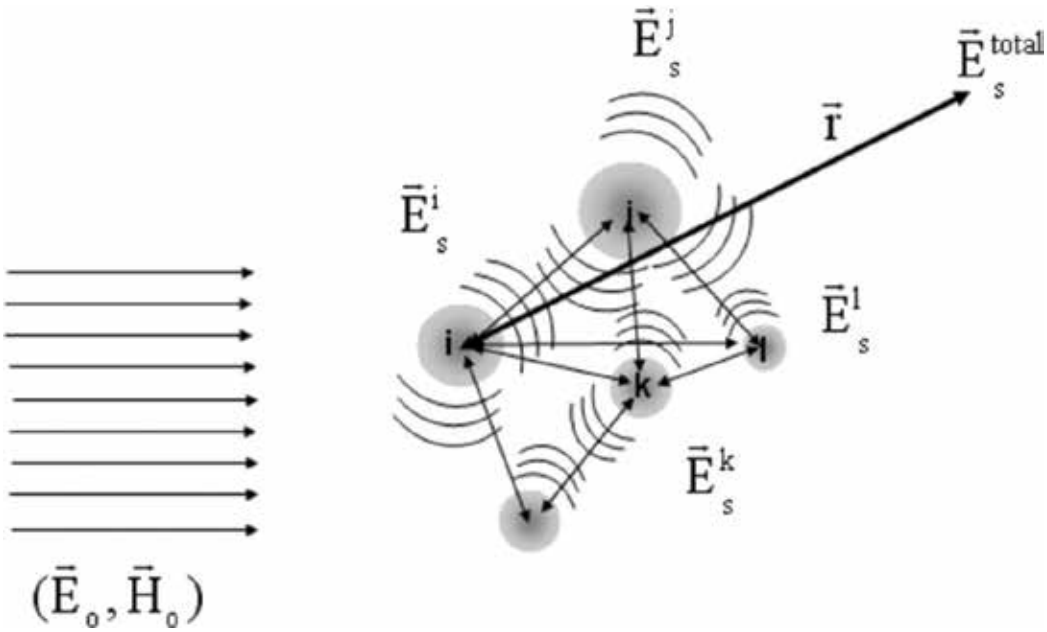

Figure 11. A scheme for exciting a group of spheres by an incident electromagnetic wave. The fields scattered by each particle can in turn excite neighboring particles.

$$\vec{E}_{inc}^{\,i} = \vec{E}_o + \sum_{j=1,\, j\neq i}^{N} \vec{E}_s^{\,j} \tag{50}$$

The scattered field by a particle j depends on $\vec{E}_o$ and $\vec{E}_{inc}^{\,j}$. The optical response of the set will be obtained by solving this problem in a self-consistent way (coupled equations):

$$\vec{E}_{inc}^{\,i} = \vec{E}_o + \sum_{j=1,\, j\neq i}^{N} f\left(\vec{E}_o, \vec{E}_{inc}^{\,j}\right) \tag{51}$$

In the case of spherical particles, this problem can be solved accurately but at the cost of a large numerical effort. The idea is to apply the results of the Mie theory developed previously since it allows to express the field scattered by a particle as a function of the incident field on this same particle. Nevertheless, for each of the particles considered, the theory requires to define a reference whose origin (center of the particle) and the orientation are fixed and linked to this particle [33–35]. **Figure 12** shows the extinction spectra of gold dimer nanoparticles as a function of the interparticle distance d calculated from the generalized Mie theory. The nanoparticles are supposed to be spherical, with a diameter D = 100 nm, and trapped in a medium with an effective index n_m = 1.15. The dielectric constant of gold is given by Johnson and Christy. For a distance d = 10 nm, the extinction spectra are presented for two orthogonal polarizations (**Figure 12**). When light is polarized perpendicular to the axis of the dimer (dotted spectrum in **Figure 12**), the extinction spectrum is similar to that of a single gold nanoparticle but twice more intense. The calculation shows that this extinction spectrum is in

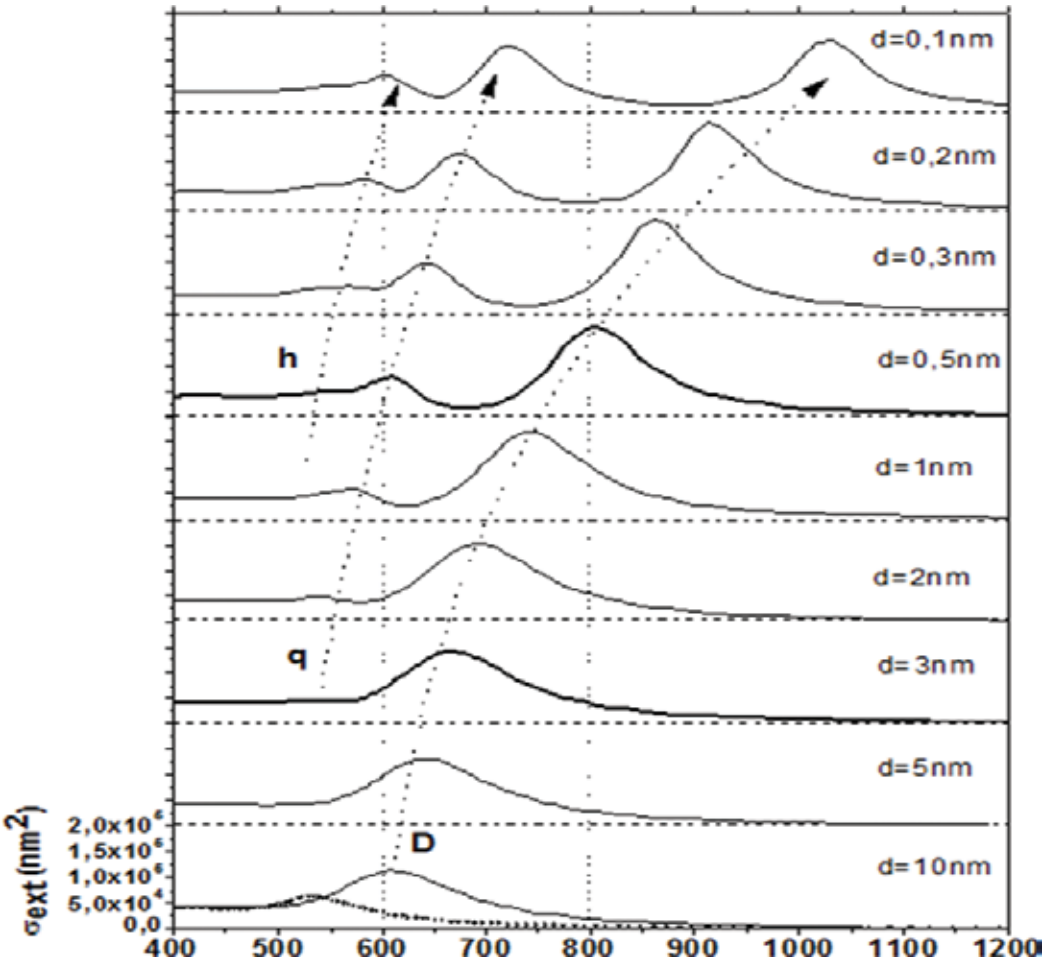

Figure 12. Extinction spectra (longitudinal excitation) of gold dimers (R = 50 nm, n_m = 1.15) calculated by the generalized Mie theory as a function of the interparticle distance d. The dotted spectrum (for d = 10 nm) is obtained for transverse excitation. To guide the eye, dotted arrows indicate the redshift of the dipolar (D), quadrupolar (q) and hexapolar (h) resonance. The spectra for d = 0.5 nm and d = 3 nm are highlighted.

fact independent of the distance *d*. For a direction of polarization of light along the axis of the dimer, it is found that the main resonance (peak *D*) shifts to red when d decreases. As the particles approach, peaks can be seen in the blue part of the spectrum (q and h). These peaks appear sequentially (q then h), grow and move toward red.

11. Conclusion

In this chapter, we demonstrated the capabilities of the Mie theory and quasi-static approximation to calculate the optical response of metallic nanoparticles. The quasi-static approximation is typically valid for nanoparticle diameter $D \leq \lambda/10$ (λ is the wavelength of the incident light). For other dimensions of size, we calculated the optical response in the framework of Mie

theory. We recalled the differences between extinction, absorption and scattering cross section of metallic nanoparticles. The spectrum of the extinction cross section present a resonance attributed to the collective oscillation of electrons in the conduction band: surface plasmon resonance (SPR). SPR spectral profile is very sensitive to the size, morphology and environment of the metallic nanoparticles. It is concluded that as the size of the spherical nanoparticle increases, the extinction magnitude increases whereas the spectral position of the surface plasmon resonance (SPR) is redshifted by using Mie theory. However, the peak position of SPR in quasi-static approximation is independent of size. We used the parameter g for confined nanoparticles to introduce the collision between electrons and the surface of nanoparticles. As the g factor increases, then there are more damping of oscillations. We concluded that the extinction cross-sectional magnitude is decreased and the width at half peak of SPR is increased. We investigated the effect of shape using dipolar approximation. We found that the surface plasmon resonance depends strongly on the polarization of the electromagnetic incident wave on the nanoparticle. As the aspect ratio decreases, the spectral position is shifted toward higher wavelength (when the light is polarized along major axis) and shifted toward smaller wavelength (when the light is polarized along minor axis). The mode along the long axis gives a larger extinction cross section because it is equivalent to a larger volume of material probed in relative to the sphere. We studied the extinction cross section of metallic nanoparticle embedded in different matrices. We remarked that the SPR is redshifted and accompanied by a large enhancement of its absorption cross section with increasing dielectric constant of the matrix. In the case of interacting systems, we have seen that the distance between nanoparticles is a crucial parameter. In the case of gold dimer nanoparticles, the smaller the interparticle distance, the more the dipolar resonance is redshifted with the appearance of higher order resonances.

Author details

Salem Marhaba

Address all correspondence to: s.marhaba@bau.edu.lb

Physics Department, Faculty of Science, Beirut Arab University, Lebanon

References

[1] So DWC, Seshadri SR. Metal-island-film polarizer. Journal of the Optical Society of America B. 1997;**14**:2831

[2] Lal U, Link S, Halas NJ. Nano-optics from sensing to waveguiding. Nature Photonics. 2007;**1**:641

[3] Sharrouf M, Awad R, Marhaba S, Bakeer DE. Structural, optical and room temperature magnetic study of Mn-doped ZnO nanoparticles. Nano. 2016;**11**:1650042

[4] Sharrouf M, Awad R, Roumié M, Marhaba S. Structural, optical and room temperature magnetic study of Mn_2O_3 nanoparticles. Materials Sciences and Applications. 2015;**5**:850

[5] Stuart HR, Hall DG. Island size effects in nanoparticle-enhanced photodetector. Applied Physics Letters. 1998;**73**:3815

[6] Akella A, Honda T, Liu AY, Hesselink L. Two photon holographic recording in aluminosilicate glass containing silver particles. Optics Letters. 1997;**22**:967

[7] Ricard D, Roussignol P, Flytzanis C. Surface-mediated enhancement of optical phase conjugation in metal colloids. Optics Letters. 1985;**10**;511

[8] Elvira D, Braive R, Beaudoin G, Sagnes I, Hugonin JP, Abram I, Philip IR, Lalanne P, Beveratos A. Broadband enhancement and inhibition of single quantum dot emission in plasmonic nano-cavities operating at telecommunications wavelengths. Applied Physics Letters. 2013;**103**:061113

[9] Roumié M, Marhaba S, Awad R, Kork M, Hassan I, Mawassi R. Effect of Fe_2O_3 nano-oxide addition on the superconducting properties of the (Bi,Pb)-2223 phase. Journal of Superconductivity and Novel Magnetism. 2014;**27**:143

[10] Basma H, Awad R, Roumie M, Isber S, Marhaba S, Abou Aly AI. Study of the irreversibility line of $GdBa_2Cu_3O_{7-\delta}$ added with nanosized ferrite $CoFe_2O_4$. Journal of Superconductivity and Novel Magnetism. 2016;**29**:179

[11] Henry CR. Catalytic activity of supported nanometer-sized metal clusters. Applied Surface Science. 2000;**164**:252

[12] Burchez M, Moronne M, Gin P, Weiss S, Alivisatos AP. Semi-conductors nanocrystals as fluorescent biological labels. Science.1998;**281**:2013

[13] Faraday M. Experimental relations of gold (and other metals) to light. Royal Society of London. 1857;**147**:145-181

[14] Maxwell Garnett JC. Colours in metal glasses and in metallic films. Philosophical transactions of the Royal Society of London, Serie B. 1904;**203**:385

[15] Marhaba S. Gold nanoparticle arrays spectroscopy: Observation of electrostatic and radiative dipole interactions. S. Nano. 2015;**10**:1550007

[16] Baida H, Billaud P, Marhaba S, Christofilos D, Cottancin E, Crut A, Lermé J, Maioli P, Pellarin M, Broyer M, Del Fatti N, Vallée F, Sánchez-Iglesias A, Pastoriza-Santos I, Liz-Marzán LM. Quantitative size dependence of the surface plasmon resonance damping in single $Ag@SiO_2$ nanoparticles. Nano-Letters. 2009;**9**:3463–3469

[17] Billaud P, Marhaba S, Cottancin E, Arnaud L, Bachelier G, Bonnet C, Del Fatti N, Lermé J, Vallée F, Vialle JL, Broyer M, Pellarin M. Correlation between the extinction spectrum of a single metal nanoparticle and its electron microscopy image. Journal of Physical Chemistry C. 2008;**112**:978-982

[18] Pines D. A collective description of electron interactions. IV.Electron interactions in metals. Physical Review. 1953;**92**(3):626

[19] Kittel C. Physique de l'état solide, 7ème édition. Dunod, Paris; 1998

[20] Ashcroft NW, ND Mermin. Solid State Physics. International Edition, Saunders College, Philadelphia; 1976

[21] Johnson PB, Christy RW. Optical constants of the noble metals. Physical Review B. 1972; **6**(12):4370

[22] Palik ED. Handbook of optical constants of solids. London: Academic Press Inc; 1985

[23] Berthier S. Optique des milieux composites. Paris: Polytechnica; 1993

[24] Kreibig U, Vollmer M. Optical properties of Metal Clusters. Berlin: Springer Verlag; 1995

[25] Kreibig U, Genzel L. Optical absorption of small metallic particles. Surface Science. 1985;**156**:678

[26] Billaud P. Propriétés optiques de nanoparticules uniques de métaux nobles. Thèse de Doctorat, Université Lyon 1; 2006

[27] Del Fatti N. Dynamique électronique femtoseconde dans les systèmes métalliques massifs et confinés. Thèse de Doctorat, Université Bordeaux 1; 1999

[28] Muskens OL, Bachelier G, Del Fatti N, Vallée F, Brioude A, Jiang X, Pileni MP. Quantitative absorption spectroscopy of a single gold nanorod. Journal of Physical Chemistry C. 2008;**112**(24):8917

[29] Bohren CF, Huffman DP. Absorption and scattering of light by small particles. New York: Wiley; 1983

[30] Mie GG. Beiträge zur Optik trüber Medien, speziell kolloidaler Metallösungen. Annals of Physics. 1908;**25**(3):377

[31] Lermé J, Bonnet C, Broyer M, Cottancin E, Marhaba S, Pellarin M. Optical response of metal or dielectric nano-objects in strongly convergent light beams. Physical Review B. 2008;**77**:245406

[32] Lermé J, Bachelier G, Billaud P, Bonnet C, Broyer M, Cottancin E, Marhaba S, Pellarin M. Optical response of a single spherical particle in a tightly focused light beam: Application to the spatial modulation spectroscopy technique. Journal of the Optical Society of America A. 2008;**25**:493-514

[33] Gérardy JM, Ausloos M. Absorption spectrum of clusters of spheres from the general solution of Maxwell's equations. The long-wavelength limit. Physical Review B. 1980;**22**(10):4950

[34] Gérardy JM, Ausloos M. Absorption spectrum of clusters of spheres from the general solution of Maxwell's equations. II. Optical properties of aggregated metal spheres. Physical Review B. 2004;**25**(6):4950

[35] Marhaba S, Bachelier G, Bonnet C, Broyer M, Cottancin E, Grillet N, Lermé J, Vialle JL, Pellarin M. Surface plasmon resonance of single gold nanoparticle pairs near the conductive contact limit. Journal of Physical Chemistry C. 2009;**113**:4349-4356

Chapter 4

Origins of the High Reactivity of Au Nanostructures Deduced from the Structure and Properties of Model Surfaces

Sandra Hoppe and Lyudmila V. Moskaleva

Additional information is available at the end of the chapter

http://dx.doi.org/10.5772/intechopen.74006

Abstract

In this chapter, experimental and theoretical studies on surface segregation in Ag-Au systems, including our own thermodynamic studies and molecular dynamics simulations of surface restructuring, on the basis of density functional theory are reviewed. The restructuring processes are triggered by adsorbed atomic O, which is supplied and consumed during catalysis. Experimental evidence points to the essential role of Ag impurities in nanoporous gold for activating O_2. At the same time, increasing Ag concentration may be detrimental for the selectivity of partial oxidation. Understanding the role of silver requires a knowledge on its chemical state and distribution in the material. Recent studies using electron microscopy and photoelectron spectroscopy shed new light on this issue revealing a non-uniform distribution of residual Ag and co-existence of different chemical forms of Ag. We conclude by presenting an outlook on electromechanical coupling at Ag-Au surfaces, which shows a way to systematically tune the catalytic activity of bimetallic surfaces.

Keywords: nanoporous gold, Au-Ag alloy, surface, segregation, atomistic simulations, cluster expansion, density functional theory, electromechanical coupling, ab initio

1. Introduction

For centuries, the use of gold has been restricted mainly to jewelry and coinage. Being considered unreactive, gold did not represent an attractive material for catalytic applications [1]. This image began to change in the 1970s, when the first studies hinted at the potential reactivity of small gold particles [2–5]. In 1985, Hutchings reported that cationic gold was the best catalyst

for hydrochlorination of acetylene to vinyl chloride [6]. At about the same time, Haruta et al. [7, 8] discovered the high reactivity of ultra-fine Au particles supported on 3*d* transition metals as a catalyst for aerobic CO oxidation at temperatures below 0°C. Not only gold's reactivity caught the attention of the catalytic community, but also its selectivity, as it has been found that gold does not attack C–C or C–H bonds in organic compounds [9]. These characteristics make gold a promising candidate for "green chemical industry," especially for developing processes operating at ambient pressure and temperature with the benefit of avoiding toxic materials [10]. More recent studies focused on bimetallic Ag-Au nanoparticles supported on aluminosilicate [11–14] or titania [15] for low temperature CO oxidation. Compared to monometallic Au nanoparticle catalysts, they showed higher catalytic activity [11–14, 16, 17].

Through electrochemical corrosion and selective leaching of the second metal (typically silver) from a bimetallic Au-M (M = Ag, Cu, Al, Si) alloy, the sponge-like nanoporous gold (npAu) can be obtained [18–20]. The microstructure and ligament dimensions of this unsupported catalyst can be adjusted in its synthesis as desired for the respective application. Its open porosity makes it permeable for liquids as well as gases. Furthermore, it possesses a strongly curved surface with a very high surface-to-volume ratio [18, 19]. Research on npAu has mainly focused on aerobic CO oxidation [19, 21–26] and oxidative coupling/cross-coupling of alcohols [8, 22, 26]. The partial oxidation products, esters, are valuable bulk chemicals in chemical industry. In particular, methyl formate is formed in the oxidative coupling of methanol and provides an important precursor for the production of formic acid, formamide, and dimethylformamide [27]. Other organic transformations have also been explored as covered in recent reviews [26, 28–30].

The literature reports two possible origins for the high reactivity of npAu, for example, towards CO oxidation. First, the curved surface of the npAu ligaments shows high density of low-coordinated Au atoms at steps and kinks [31], which may serve as reactive sites. However, several studies dealing with oxygen adsorption on Au surfaces indicated that roughening the Au surfaces by sputtering did not make them active towards CO oxidation, unless atomic oxygen was pre-adsorbed at the surface, even though many low-coordinated Au atoms were present [32–35]. Second, the residual silver which is left in the npAu after the dealloying process was suggested to promote reactivity [21, 36, 37]. This has been proposed by Bäumer and associates [21, 37], who investigated the morphology, surface composition, and catalytic activity of npAu towards CO oxidation. Even for npAu samples with almost no Ag left in the bulk, Ag surface concentrations of up to 10% were measured. Importantly, all samples had to be activated for a certain time before catalytic activity was detected. While the morphology of the activated samples did not undergo any notable change during the activation, *in situ* X-ray photoelectron spectroscopy (XPS) characterization revealed a change in the chemical state of the Ag atoms at the surface. However, the chemical state of Ag was not clearly assigned. It could not be attributed to chemisorbed O on Ag or to Ag_2O or to AgO species. It was suggested [21, 37] that Ag impurities play a decisive role for the activation of molecular oxygen and that npAu should actually be considered a bimetallic catalyst.

The favorable role of Ag impurities for CO oxidation was corroborated in further experimental studies [25, 38], which demonstrated a clearly positive correlation between the Ag content in

the npAu samples and the catalytic activity. With the help of density functional theory (DFT) calculations and using the stepped and kinked Au (321) model surface to mimic the structural motifs of npAu, Moskaleva et al. [39] found an increase in the adsorption strength of O_2 and a reduction of the O_2 dissociation barrier with the increasing size of Ag ensembles at the reaction site located at the step edge. These Ag ensembles were identified as sites capable to dissociate O_2 and to supply atomic O to surrounding Au sites, where it may then react with chemisorbed CO to form CO_2. Consequently, a high density of atomic steps at the ligament surface as well as the presence of surface Ag impurities is believed important for achieving high catalytic activity.

Fujita et al. [31] established a connection between the rough npAu surface and the residual Ag content via *in situ* high-resolution TEM of npAu catalyzing CO oxidation. They reported that a higher residual Ag content suppressed {111} faceting at the surface and thereby stabilized steps and kinks containing many low-coordinated Au atoms. Hence, the role played by Ag for the high catalytic activity of npAu appears to be twofold and consists of the supply of reactive sites on the one hand and of the preservation of the rough morphology on the other hand.

Within our studies reviewed in this chapter, we shed new light on the distribution of Ag in Ag-Au surfaces and on the role of Ag for the reactivity of npAu. To this end, we first analyzed the segregation behavior at the flat Ag-Au (111) surface to better understand the underlying phenomenology. Furthermore, we considered the effect of adsorbed oxygen on the surface composition. Apart from flat surfaces, we also studied silver segregation at the stepped Au (321) surface induced by adsorbed O atoms, the formation of –(Au-O)– oxide chains, and how such chains affect Ag segregation [40, 41]. In the following, we give an overview of experimental and theoretical studies on segregation in the Ag-Au system, followed by our theoretical results, directed at understanding segregation phenomena in npAu. Next, we reflect on the role of Ag impurities and Ag distribution at the catalyst surface for the catalytic activity. Finally, we give an outlook on ongoing investigations about electromechanical coupling at Ag-Au surfaces.

2. Surface segregation and restructuring

The term surface segregation refers to the concentration gradient at the surface of a material consisting of at least two elements resulting from diffusion of one component to the surface. This process is driven by a difference in chemical potential between the bulk and the surface and it may lead to a completely different atomic ordering and composition in the surface region compared to the bulk structure. Understanding segregation and surface reconstruction is important for many technologies involving heterogeneous catalysis, corrosion resistance, adsorption, or magnetic, electronic, and optical materials [42, 43], since these effects alter the physical and chemical properties at the surface. Consequently, various theoretical models to predict surface segregation based on different parameters have been developed over the last decades [44–48].

When a surface is created, bonds between atoms are locally broken, which is accompanied by a cost in energy. Within the framework of the so-called bond-breaking models, the total energy of the crystal is represented as the sum of pair-bond energies. Either an ideal (no enthalpy of mixing) or a regular (non-zero mixing enthalpy allowed) solution model can be adapted and depending on the choice of parameters, the resulting segregation may be limited to the surface layer only or include multiple layers. According to this theory, the element with the lowest bond strength will preferably be located at the surface to keep the energy cost as low as possible. To link this prediction to an experimentally measurable surface parameter, a correlation between the free energy of segregation and the surface energy has been established, yielding the surface segregation of the element with the lower surface energy [46]. Apart from different bond strengths, a potential atomic size mismatch may also affect the segregation behavior. If the element with the larger atomic radius is located at the surface, fewer atoms are needed to populate the surface layer and the number of broken bonds there is thus minimized. This approach consequently predicts segregation of the larger atomic species to the surface. An atomic size mismatch between two elements also leads to elastic strain contributions to the free energy of a material, because a solute atom residing in a significantly smaller or larger host lattice is surrounded by an elastic strain field. Within this model of continuum elastic theory, segregation of this solute atom to the surface would result in a relief of lattice strain in the bulk and is thus energetically favorable [46, 47, 49–51].

These two concepts involving broken bonds at the surface and elastic strain in the bulk may lead to contradicting results when applied separately [49], which is why they have been combined to achieve a more realistic prediction of surface segregation. Using pair-potential approximation models, for example, the total energy of a material is calculated as the sum of pairwise interactions. In contrast to the bond-breaking theory, however, relaxation of the atoms to their equilibrium positions is included, thereby also considering strain energy.

When applied to the Ag-Au system, which is of interest in this study, the theories described above result in a clear tendency: The strain contributions due to atomic mismatch should be negligible, since Ag and Au have almost the same lattice constant, with Au being slightly smaller [52]. If there was any size effect, it would cause Ag to sit in the surface layer to reduce the number of broken bonds. Additionally, Ag possesses a smaller surface energy than Au [53], which should also stabilize it in the topmost layer. Despite the seemingly clear answer coming from phenomenological theories, various experimental studies on surface segregation in the Ag-Au system from the past report conflicting results. Even if there is qualitative agreement between several papers, a quantitative agreement is hardly found in the literature. These conflicting results from the past may have their origin in either the choice of the experimental method, the calibration of instruments, or the sample preparation.

Thorough surface preparation represents a crucial procedure and also a major challenge for experiments targeting surface segregation. The desired surface orientation must be carefully cut and cleaned from contaminants, such as oxygen, carbon monoxide, and other gases, which may severely influence the segregation profile. In their review on the surface segregation in gold-containing alloys, Dowben et al. [51] stated that gold alloys are usually more easily characterized and yield more reliable results than other materials. They attribute this to a

simple cleaning procedure and a low contamination level on gold alloy surfaces due to low sticking coefficients of typical contaminants. Typical contaminants for the Ag-Au surface have been identified as S, Cl, O and N [54, 55]. They are commonly removed by successive Ar^+ sputtering and annealing procedures [51]. Regarding gold alloy surfaces, Dowben et al. [51] emphasize that preferential sputtering represents a usual problem and lengthy and thorough annealing steps are crucial to obtain surfaces in thermodynamic equilibrium.

Not only the way the samples are prepared but also the measurement techniques and even their respective calibration methods may influence the obtained results. This has been pointed out by Bouwman et al. [56], who conducted Auger Electron Spectroscopy (AES) measurements on annealed polycrystalline Ag-Au bulk samples with varying Ag content. In contrast to calculations employing the regular solution model, which predicts Ag enrichment in the surface layer, they observed a bulk-like surface composition, independent of temperature. While their results are in good agreement with an earlier AES study by Fain and McDavid [57] on epitaxially grown Ag-Au thin films, they stand in contrast to yet another AES study by Somorjai and Overbury [58], who reported Ag surface enrichment in polycrystalline Ag-Au foils. Bouwman et al. report that they applied a so-called "internal calibration," meaning they recorded AES spectra of the freshly cut, homogeneous Ag-Au surface as a reference. Somorjai and Overbury, however, recorded spectra from the respective elements, which is referred to as "external calibration." This example already illustrates possible difficulties in measuring surface segregation. Other possible source of incorrect data interpretation could be neglecting the effect of different backscattering factors of Ag and Au as pointed out by Overbury and Somorjai [54]. These authors reported slight Ag enrichment, which is, however, within the experimental error. They furthermore observed that cleaning the surface with Ag^+ led to Au surface enrichment. Similar observations were reported by Yabumoto et al. [55] for polycrystalline Ag-Au surfaces.

In experiments targeting surface segregation, it is of course desired to measure the composition of the very topmost layer and not only an averaged value over a certain number of atomic surface layers. Nelson [59] hinted at potential drawbacks of AES, including the uncertainty about backscattering contributions and as well the necessity to know the exact escape depth of the Auger electrons to evaluate the surface sensitivity of this method. He argued that ion scattering spectroscopy (ISS) represented a more suitable method to investigate surface segregation, as it offered monolayer sensitivity as well as the possibility to clean and anneal the sample *in situ*. His results for thoroughly polished polycrystalline Ag-Au samples indicated Ag surface enrichment, though slightly less pronounced than predicted by the regular solution model. Shortly afterwards, his findings were corroborated by an ISS study by Kelley et al. [60], who also reported Ag surface segregation in the Ag-Au system.

The AES and ISS studies summarized above have been carried out with polycrystalline samples, so that no conclusions could be drawn from them regarding the effect of crystallographic orientation for the segregation. King and Dononelly [61] addressed this issue by identifying (111), (110) and (100) planes on some surface domains or grains on their polycrystalline samples, applying low energy electron diffraction (LEED) and selected area channeling pattern (SACP). They used AES to obtain the composition of the first two surface layers for varying

crystallographic orientation, temperature, and Ag bulk concentration. In agreement with Monte Carlo simulations also conducted in their work, King and Dononelly found strong Ag surface segregation for the Ag-Au (100) domains, while it is less pronounced for the (110) domains and relatively weak for the (111) planes. Shortly afterwards, Meinel et al. [62] investigated epitaxially grown Ag-Au films with (111) orientation via AES. Even though they also found Ag surface enrichment, their results did not agree quantitively with those from King and Dononelly, but rather with the ISS results from Nelson [59] and Kelley [60].

The first surface structural measurement on a Ag-Au surface was conducted by Derry and Wan [63], who performed a LEED structure analysis of the Ag-Au (100) surface of an alloy containing 50% Ag. Derry and Wan predicted Ag enrichment in the surface layer and slight Ag depletion in the subsurface layer, but no quantitative agreement with earlier studies was reached.

In summary, experimental results on surface segregation in the Ag-Au system reach from no observed segregation to very pronounced Ag surface enrichment, but there is no quantitative consistency. As mentioned before, this may arise due to different measurement techniques, choice of parameters and calibration methods, and different sample characteristics.

A wide variety of simulation methods available today represents a promising way to verify or explain the experimental outcomes of segregation studies. However, theoretical studies on the surface segregation at Ag-Au extended surfaces are relatively scarce. Bozzolo et al. [64] studied segregation behavior in Ag-Au. In their quantum approximate approach, the energy of a certain atomic configuration is calculated as the sum of strain energy and chemical atomic contributions. The parameters required for their simulations were determined from first principles LAPW calculations. While their simulations yielded Ag enrichment in the surface layer and Ag depletion in the subsurface layer in all cases, they found a strong dependence of the amount of segregation on temperature and Ag bulk concentration. Interestingly, for the $Ag_{30}Au_{70}$ (100) surface, they obtained a perfectly ordered surface layer and a pure Au subsurface layer for temperatures approaching 0 K. At about 100 K, a drastic change in segregation behavior occurred and the surface plane was pure Ag. From there on, the Ag surface layer concentration decreased monotonically until reaching an approximately constant value around 600 K. The authors attribute this phenomenon to two competing effects: the favorable Ag–Au bonds lead to ordering at low temperatures and the lower surface energy of Ag causes it to segregate to the surface at higher temperatures.

Since nanoparticles are highly interesting for the catalytic community, many studies focusing on the structure and composition of Ag-Au clusters of various sizes can be found in the literature. Conflicting results emerged from these theoretical works, depending on the simulation method and choice of input parameters. In a Monte Carlo study on the segregation in trimetallic Ag-Cu-Au clusters, Cheng et al. [65] predicted Ag segregation to the surface of the particles, while Cu was located at the center and Au mainly in the middle shell. As Cu possesses the highest surface energy, followed by Au and then Ag, their results are in good agreement with simple bond-breaking models.

Curley et al. [66] simulated bimetallic Ag-Au clusters containing 38 atoms with an empirical potential, the so-called "Gupta potential," based on tight-binding theory and combined it with

a genetic-algorithm search technique to identify energetically favorable compositions. In these favorable structures, they found a clear Ag enrichment in the particle surface and explained their findings by the lower surface energy of Ag and the strong Au–Au metal bonds, stabilizing Au in the core of the particle. In their discussions, they argue that an electron transfer from the less electronegative Ag to Au should promote heterometallic Ag–Au bonds. However, according to them, the fact that Ag-Au is a random alloy without order may speak for a negligible effect of charge transfer.

In Monte Carlo simulations based on the modified analytic embedded atom method (MAEAM), Deng et al. [67] predicted segregation in Ag-Au nanoparticles and analyzed the effect of composition, particle size, and temperature. A more pronounced Ag surface enrichment was obtained for a higher Ag bulk concentration, larger particles, and lower temperature. They furthermore mention a possible influence of a charge transfer from Ag to Au, but state that this influence was small for large particles and bulk materials. Indeed, numerous studies found this charge transfer to promote heterometallic Ag–Au bonds and to stabilize Au in the shell of small Ag-Au particles containing less than eight until up to 20 atoms [68–72]. It is worth noting that almost all these studies employed density functional theory (DFT) calculations, while most of the investigations of larger particles were carried out with empirical potentials [67, 73].

In this context, Paz-Borbon et al. [73] made an interesting observation when they studied the segregation behavior of 38-atom binary clusters composed of transition metals. They used an empirical Gupta potential combined with a genetic algorithm to identify energetically favorable structures, which were then investigated further via DFT calculations. To analyze the correct chemical order, they also inverted the positions of the respective elements in clusters containing 19 atoms of each species. Like in previous studies employing empirical potentials, the Gupta potential yielded Ag segregation to the surface of the particle, while Au was located at the core. Surprisingly, DFT optimization and calculation of the inverted particle resulted in the contrary, namely that a particle with a Au shell and Ag core was energetically most favorable. While models considering surface energies and bonding interactions would not predict Au surface segregation, Paz-Borbon et al. [73] explained this discrepancy with a charging effect from Ag to the more electronegative Au, which is not captured by standard empirical potentials. As their calculations were limited to 38 atom nanoparticles, it is, of course, questionable, whether their findings can be transferred to clean Ag-Au surfaces. There exists, however, a DFT study by Dianat et al. [74] revealing the influence of charge transfer on the segregation at the adsorbate-free and oxygen-covered Pt-Pd surface. Their work was motivated by a discrepancy between experimental results observing a Pt-enriched surface and simulations using the embedded atom model or empirical potentials, which indicated Pd surface segregation. The segregation behavior they obtained for the Pt-Pd (111) surface modeled in a 1×1 cell depended on the underlying bulk composition. For a Pd-rich bulk, Pd was preferably located at the surface, as the element with the lower surface energy. For a Pt-rich bulk, however, the energetically most favorable configuration had a Pt surface and a Pd subsurface layer. With the help of a Bader analysis [75–78], they showed that for all surface structures, a charge transfer from Pd to the more electronegative Pt takes place. Thereby, the *d*-band filling of the surface Pt atoms is increased, while the *d*-bands of the subsurface Pd atoms

are depleted. Dianat et al. [74] argued that according to a model proposed by Friedel et al. [79], the surface energy of metals with more than half-filled *d*-bands decreased upon increasing *d*-band filling. Therefore, the calculated charge transfer stabilizes Pt at the surface, even though it has the higher surface energy. Upon oxygen adsorption, the strong affinity of Pd towards O caused Pd segregation to the surface layer in all calculated structures.

Thus, the charge transfer caused by the difference in electronegativity between Pt and Pd is a decisive factor for segregation. The electronegativity values on the Pauling scale amount to 2.28 and 2.20 for Pt and Pd, respectively, and to 2.54 and 1.93 for Au and Ag, respectively. This larger difference theoretically implies an even larger charge transfer between Ag and Au. In our investigations on surface segregation at Ag-Au surfaces [39, 79] reviewed below, we aimed at shedding light on the subtle mechanisms leading to the energetically most favorable surface configurations. As those mechanisms may be captured by accurate quantum mechanical modeling, we employed DFT calculations in combination with statistical physics to scan the whole configuration space. An overview of the methods we applied will be given in the next section.

3. Methodology

In this section, we will give an overview of the methods applied in our study on segregation, dynamic restructuring, and electromechanical coupling at Ag-Au surfaces. A more detailed report of important calculation parameters and information on the surface models is given in Refs. [40, 41, 80].

3.1. Density functional theory calculations

The modeling studies reviewed in the following have been performed on the basis of density functional theory (DFT) [81]. In the past two to three decades, DFT has developed into a powerful methodology. Thanks to the computational power available nowadays, electronic structure calculations of systems containing hundreds of atoms can be handled, making DFT-based approaches attractive for material science, computational physics, and chemistry.

Static DFT calculations reported below were carried out with the program code Vienna ab initio simulation package (VASP) [82–85], employing plane-wave basis sets to expand the electron density. Ab initio molecular dynamics (AIMD) simulations of surface restructuring were carried out with the CP2K software [86], which uses mixed plane-wave and Gaussian basis sets. Concerning the choice of an appropriate exchange-correlation functional, we had several prerequisites. As already mentioned in Section 2, two critical quantities, which may influence the segregation behavior, are the surface energy and the equilibrium lattice parameter. To ensure as realistic predictions of the segregation behavior at Ag-Au surfaces as possible, we aimed at fulfilling two conditions observed experimentally: First, the two lattice constants of the pure elements should be almost identical and second, silver should have a smaller surface energy than gold. We found reasonable agreement with experimental values for the

http://dx.doi.org/10.5772/intechopen.74006

GGA Perdew-Burke-Ernzerhof functional (PBE) [87, 88] with additional dispersion corrections (DFT-D3) as proposed by Grimme et al. [89]. In this approach, the total energy equals the sum of the energy resulting from electronic convergence with PBE plus a van der Waals correction term which is added subsequently. This functional was thus employed in all DFT calculations to investigate surface segregation. The AIMD simulations were carried out using PBE functional, without including dispersion corrections, because the qualitative trends were not affected by including D3 correction, as test calculations have revealed. Our computational approach was based on periodic DFT and employed slab models. As one of our goals was to study the influence of Ag bulk concentration on the segregation profile, we considered three different clean (i.e. adsorbate-free) surfaces: cut from: pure Au bulk, pure Ag bulk, and from a $L1_2$ ordered bulk structure with 25% Ag, respectively. The latter was chosen as it represents a ground state in the Ag-Au phase diagram at very low temperatures. Additionally, an oxygen-covered surface slab cut from $L1_2$ bulk with O atoms occupying fcc hollow sites was built. In the (2×2) unit cell, this corresponds to O coverage of 0.25 monolayer (ML). Side and top views of the adsorbate-free and oxygen-covered surface slabs are shown in **Figure 1**.

Additionally, we modeled the stepped Au (321) surface with an infinite oxide chain. Such chains of alternating Au and O atoms were previously identified as a common feature of thermodynamically stable surface configurations of the Au (111) [90, 91], the Au (110) [92, 93] as well as the Au (321) [94] surfaces. The latter surface features steps and terraces with both high- and low-coordinated Au atoms and therefore provides an ideal model for the rough npAu surface morphology [31, 94, 95]. As this oxide chain structure was apparently stabilized by the presence of Ag with respect to the adsorbate-free surface [94], we aimed at finding the preferred atomic positions of Ag impurities within the oxygen-covered Au (321) surface. The asymmetric (2×1) surface slab contained 28 Au atoms and two O atoms (see **Figure 2**). This corresponds to an O coverage of 0.2 ML, which is the minimum possible coverage allowing for chain formation for the chosen unit cell size [94]. The lower 14 Au atoms were considered as

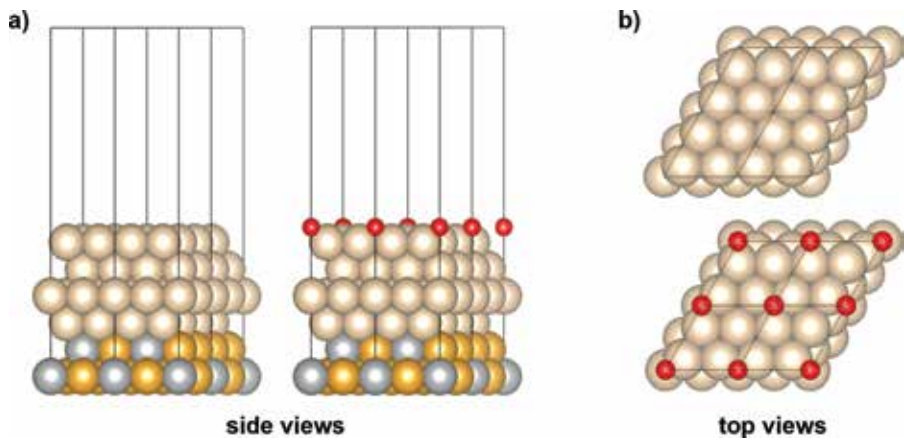

Figure 1. Side (a) and top (b) views of the adsorbate-free and oxygen-covered Ag-Au (111) surface slab with $L1_2$ bulk ordering. Au atoms are shown in yellow, Ag in gray, and O in red. The top four surface layers were allowed to be replaced by Au or Ag in the CE calculations and are depicted in beige. The (2×2) unit cell is indicated. Reproduced from Ref. [149] with the permission of AIP Publishing.

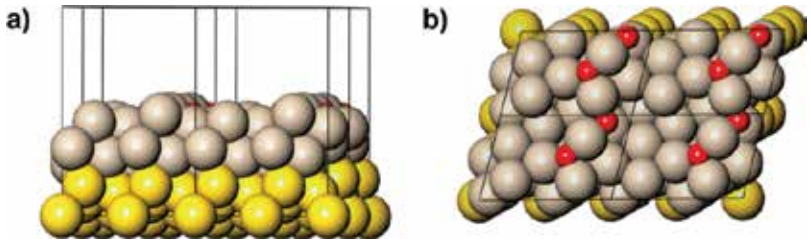

Figure 2. Side view (a) and top view (b) of the Au (321) surface slab with an infinite oxide chain. Atoms which were subsequently substituted by Ag are depicted in beige, while the O atoms are shown in red. The (2 × 1) unit cell is indicated. Reproduced from Ref. [40] with permission from the PCCP owner societies.

bulk atoms and kept fixed during the calculations, while the upper 14 Au atoms were allowed to relax. Since the DFT calculations served as input for the cluster expansion, the Ag content within the beige atoms in **Figures 1** and **2** was varied from 0 to 100%, with 0% corresponding to pure gold and 100% corresponding to all beige atoms occupied by silver.

3.2. Ab initio MD simulations

AIMD simulations based on DFT (at the GGA-PBE level) were performed at 700 K using the CP2K code [86]. We employed a (3 × 2) unit cell of the Au (321) surface. All initial geometries that served as input for AIMD simulations were fully optimized to a local minimum by means of electronic structure computations performed with CP2K. In the simulations, we used Nose-Hoover thermostat (NVT) to sample from the canonical ensemble [96, 97]. See Refs. [40, 41] for further details.

3.3. Cluster expansion and Monte Carlo simulations

Because calculating all possible surface configurations by means of DFT would represent a tedious, very time-consuming task, we tackled this problem by performing a cluster expansion (CE) [98], providing us access to the whole configuration space. Within the cluster expansion approach, the many-body interactions of a crystal structure are decomposed into a sum over bonds, also called figures or clusters. Any observable, which is a functional of the atomic configuration of all lattice points, can then be represented as a linear combination of characteristic interactions J_F of those clusters. Hence, the surface formation enthalpy $\Delta H_{\mathrm{f}}^{\mathrm{surf}}(\sigma)$ of structure σ with the two constituents A and B can be calculated as follows:

$$\Delta H_{\mathrm{f}}^{\mathrm{surf}}(\sigma) = \sum_{F} J_F \Pi_F(\sigma) - x_{\mathrm{A}}^{\mathrm{surf}}(\sigma) E_{\mathrm{A}}^{\mathrm{slab}} - x_{\mathrm{B}}^{\mathrm{surf}}(\sigma) E_{\mathrm{B}}^{\mathrm{slab}}, \tag{1}$$

where $\Pi_F(\sigma)$ is a correlation functional for each class of symmetry-equivalent clusters F, where equivalence is determined by the symmetry of the underlying grid of atomic sites. $x_{\mathrm{A}}^{\mathrm{surf}}$ and $x_{\mathrm{B}}^{\mathrm{surf}}$ are the respective concentration of the elements A and B within the atoms depicted in beige in **Figures 1** and **2**. The reference energies of surfaces with only Au or Ag at these positions are given by $E_{\mathrm{A}}^{\mathrm{slab}}$ and $E_{\mathrm{B}}^{\mathrm{slab}}$, respectively. Throughout our work, we used the program

package UNCLE [99] to perform the surface cluster expansions. Starting from a random set of DFT input structures, each of which contained the unrelaxed atomic coordinates with the corresponding total energy of the fully relaxed geometry, the values of J_F were determined via a genetic algorithm [100, 101]. In a next step, energetically favorable surface configurations were identified on the basis of the obtained Hamiltonian and employing an exhaustive enumeration algorithm [101–103]. These structures were then calculated at the DFT level and added to the input database, thereby iteratively improving the fit quality regarding configurations close to the convex hull of the energetically most favorable structures, the so-called "ground-state line." When the predicted and the input ground state lines finally coincide, the cluster expansion is considered converged. The Hamiltonian resulting from the CE fit was subsequently employed in Monte Carlo simulations to account for the influence of configuration entropy on the surface segregation profile at higher temperatures. We thereby modeled a simulated annealing process for the clean as well as the partially oxygen-covered Ag-Au (111) surface cut from an $L1_2$-ordered bulk structure.

4. Computational studies of segregation on clean and O-covered Au-Ag surfaces

4.1. Segregation at the Ag-Au (111) surface

In a recent publication [80], we have analyzed the segregation behavior at the Ag-Au (111) surface. From the cluster expansion, we obtained surface formation enthalpies for all possible Ag concentrations and configurations within the four surface layers depicted in **Figure 1**. This allowed us to identify the energetically most favorable structures, the ground states, and to construct the convex hull curve [80]. Three exemplary ground states for the (111) surface with $L1_2$-ordered bulk are shown in **Figure 3** in top and side views, along with their corresponding Ag surface concentration $x_{\mathrm{Ag}}^{\mathrm{surf}}$. Interestingly, the CE predicts Au enrichment within the topmost surface layer, while the second topmost layer is enriched in Ag. For only one Ag atom

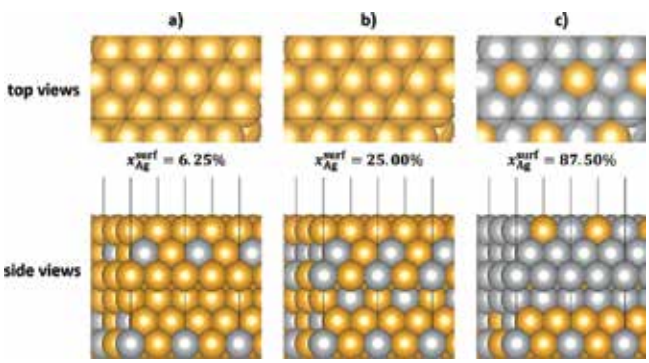

Figure 3. (a)–(c) Top and side views of three selected ground state surface configurations for the Ag-Au (111) surface with $L1_2$-ordered bulk. The respective Ag surface concentration x_{Ag}^{surf} is given below the top view.

replacing an Au atom within the four surface layers, the energetically preferred position is in the second topmost layer (see **Figure 3a**). With rising Ag surface concentration, the third and fourth layers adapt the $L1_2$ bulk structure, which agrees well with the tendency of Ag and Au to mix and form ordered structures close to 0 K and a solid solution at finite temperatures. Up to Ag surface concentrations of $x_{\mathrm{Ag}}^{\mathrm{surf}} = 31.25$ at.%, the topmost layer contains only Au atoms. Even for only one Au atom left within the four surface layers, that Au atom is located in the topmost layer for the energetically most favorable structure.

Our investigation showed that this segregation behavior is almost independent of the Ag bulk content, as the ground state surface configurations were nearly identical for pure Au bulk, pure Ag bulk, and the $L1_2$ bulk structure. To ensure that the obtained segregation profiles did not result from our choice of exchange-correlation functional, we repeated the CE with DFT input calculations employing different functionals: LDA, PBE, PBEsol, and opt86B-vdW. However, all functionals led to Au enrichment in the topmost layer. Even though the calculated surface formation enthalpies are fairly small, with values up to and around 35 meV, some driving force apparently causes Au to segregate to the topmost layer against predictions based on the surface energy hierarchies or lattice constants. As reported in Section 2, so far, no Au surface segregation has been observed experimentally for the Ag-Au system.

Comparing our results to those obtained for Pd-Pt by Dianat et al. [74], we believe that an electron transfer from Ag to Au caused by their large difference in electronegativity (1.93 and 2.54, respectively) stabilizes Au within the topmost surface layer. According to a model proposed by Friedel [79], further filling the *d* shell of a transition metal with an originally more than half-filled *d* shell leads to a decrease in surface energy. While this argument is plausible for Pd-Pt, both Ag and Au have filled 5*d* orbitals. Nevertheless, Au shows strong *s*-*d* hybridization, which decreases the energy gap between the 5*d* states and the 6*s* states and causes a depletion of the 5*d* states population. Hence, a charge transfer from Ag into the destabilized Au 5*d* orbital becomes possible. Our calculations comprising Bader analyses corroborate our assumption and show that a pure Au topmost layer followed by a pure Ag layer leads to a negative excess charge within the Au layer of -0.10 e (where e corresponds to the elementary charge). All ground states found for the CE for the (111) surface with $L1_2$ bulk have nearly the same excess charge within their topmost layer of about -0.04 e. Their configurations appear to be the result of the counteracting effects of charge transfer, the lower surface energy of Ag, and the general tendency of Ag and Au to mix and form heterometallic bonds.

The presence of adsorbed oxygen on an fcc hollow site, however, revokes this fine balance of interacting effects. The strong affinity of Ag towards oxygen causes the segregation behavior to reverse and draws Ag to the topmost surface layer. Our CE for the oxygen-covered (111) surface predicts that already for a Ag surface concentration of $x_{\mathrm{Ag}}^{\mathrm{surf}} = 68.75$ at.%, the surface is purely Ag-terminated.

Finally, we analyzed the influence of configuration entropy by performing canonical Monte Carlo simulations for the Ag-Au (111). **Figure 4** shows the four layers of the simulation cell containing 40×40 atoms in the lateral directions at room temperature for the adsorbate-free surface (a) and the oxygen-covered surface (b). Clearly, the same tendencies as obtained in the

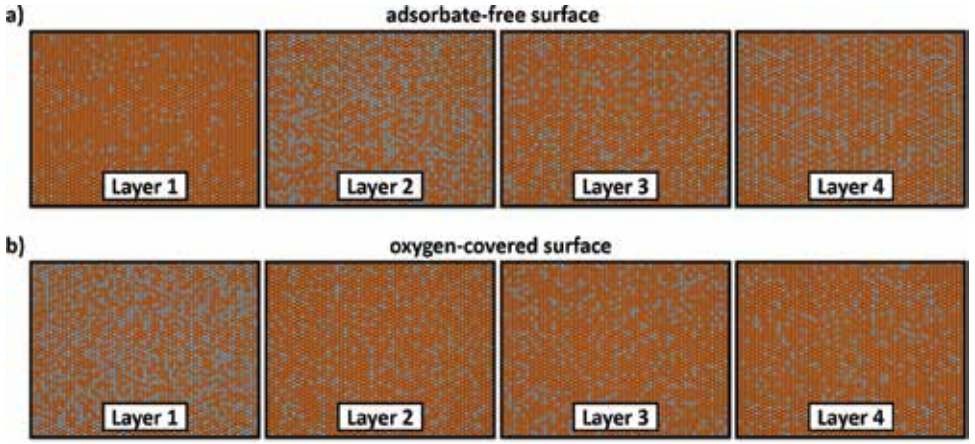

Figure 4. Monte Carlo simulation results at $T = 300$ K for the Ag-Au (111) surface free from adsorbates (a) and with atomic O at an fcc hollow site (b). The first four surface layers of the unit cell containing $40 \times 40 \times 6$ atoms are shown, where layer 1 corresponds to the topmost surface layer.

cluster expansion for $T = 0$ K are still valid at room temperature, even though the long-range order is lost. Without taking into consideration the contribution of phonons, Au enrichment in the topmost layer should be possible to observe in experiments, presuming a thoroughly prepared surface free from adsorbates.

4.2. How silver segregation stabilizes 1D surface gold oxide on the Au (321) surface

Our results for the Ag-Au (111) surface show that the presence of adsorbed oxygen draws Ag to the top surface layer [80]. Ag binds more strongly to O, as it is less noble than Au, and is therefore expected to occupy positions close to the O-adsorbates. Our recently published results [40] on the basis of the CE performed for the stepped Au (321) surface with an infinite oxide chain and Ag impurities resulted in a surprising observation: up to very high Ag surface concentrations of $x_{\mathrm{Ag}}^{\mathrm{surf}} = 87.5$ at.%, the energetically most favorable positions for Ag are located adjacent to the oxide chain, but never within the chain. At Ag surface concentrations lower than that value, atomic positions in the topmost layer next to the chain are first occupied by Ag, followed by positions underneath the chain. When no more direct Ag–O contacts can be created without Ag being located inside the chain, positions at and beneath the edges of the (111) terraces are occupied by Ag. This unexpected behavior can be explained with gold's special electronic structure, namely, the pronounced *s-d* hybridization. The latter leads to a partly covalent bonding character for Au, stabilizing it within the oxide chain. We have characterized the strong, partly covalent Au–O bonds within the chain by analyzing the electronic structure of selected surface configurations.

First, the partial density of states (DOS) reveals strongly overlapping peaks between the Au 5*d* states and the O 2*p* states close to the Au–O bonding and antibonding states in the absence of Ag impurities (see **Figure 5c**). A Ag atom residing next to the infinite oxide chain further increases this overlap, thereby stabilizing Au within the chain (see **Figure 5d**). If Ag occupies

one or both positions inside the chain, the overlap and the covalent bonding character become less pronounced (see **Figure 5a** and **b**). Second, we showed the different nature of the bonding character of an –(O–Au)– chain and an –(O–Ag)– chain by calculating their electron localization functionals (ELF) (see **Figure 6**). The more covalent Au–O bonds manifest themselves in high ELF values around the O atoms as well as the Au atoms and also in the bonding regions. The –(O–Ag)– chain, in contrast, exhibits a small probability for electrons to be located around

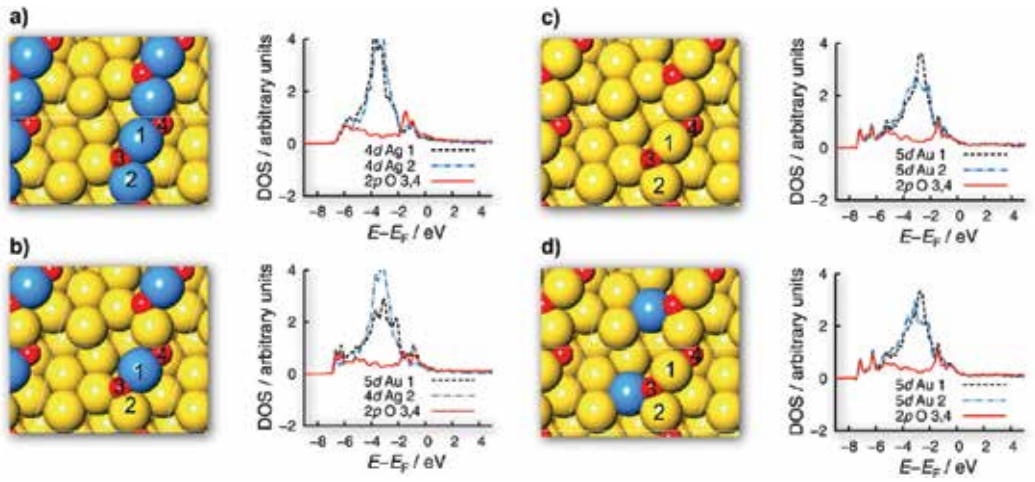

Figure 5. Partial density of states (DOS) of four surface configurations featuring an –(O–Ag)– chain (a), a mixed oxide chain with alternating Ag and Au atoms (b), an –(O–Au)– chain (c), and an –(O–Au)– chain with Ag atoms adjacent to the chain (d). The corresponding top views of the surface are shown near each diagram. Color code for the top views: Au in yellow, Ag in blue, and O in red. Reproduced from Ref. [40] with permission from the PCCP Owner Societies.

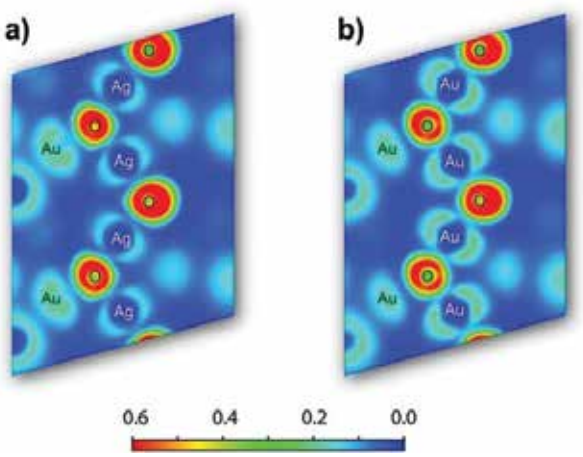

Figure 6. Two-dimensional view of the electron localization function (ELF) for two surface configurations: with an –(O–Ag)– chain (a) and an –(O–Au)– chain (b). Low ELF values are shown in blue, while red areas indicate high ELF values. Reproduced from Ref. [40] with permission from the PCCP Owner Societies.

the Ag atoms and sharp boundaries of the ELF in the bonding regions, indicating a more ionic bonding character. Third, an analysis of the bond lengths within the oxide chain revealed slightly longer bond lengths for Ag–O bonds than for Au–O bonds in the chain, which also suggests a more covalent Au–O bonding character.

Our detailed analysis of the electronic structure of the Au (321) surface with an infinite oxide chain and Ag impurities yields two effects responsible for the obtained ground state configurations: on the one hand, Au is stabilized within the chain by strong, partially covalent Au–O bonds. On the other hand, Ag binds strongly to O and is therefore preferably located close to the O atom. We complemented the cluster expansion study by ab initio molecular dynamics (AIMD) simulations, which support the thermodynamic and electronic structure analyses above.

5. Ab initio MD simulations reveal dynamic surface restructuring

As revealed by our earlier work [94] and incorporated in the analysis above, −(O–Au)– chains are thermodynamically favored over individually adsorbed O atoms on gold. In a recent work [41], we studied the formation of –(O–Au)– chains from adsorbed O atoms by conventional (static) DFT and by DFT-based AIMD simulations. **Figure 7** illustrates an AIMD simulation from a starting structure (0 ps) with several individually adsorbed O atoms placed at their most favorable threefold fcc positions close to step edges of Au (321). After 20 picoseconds of a simulation, a chain consisting of four O atoms linked together was formed. Our simulations were run at an elevated temperature of 700 K to speed up the diffusion and make structural rearrangements as well as the following relaxation happen within the computationally accessible simulation time. AIMD simulations often help us to identify new reaction pathways, such as complex surface rearrangements involving multiple atoms. Approximate transition states and minima identified in a simulation can then be refined by static DFT. The activation barriers for the formation of the first link were calculated to be <0.5 eV, suggesting that this process would take place already at ambient temperature. We have also shown that Ag impurities at low concentration reduce the activation barrier for the –(Au–O)– chain formation, whereas formation of –O–Ag–O– links is energetically slightly unfavorable, especially at high Ag concentration. Interestingly, no chain formation was found on the flat Au (111) surface covered by O atoms at a similar coverage. Hence, the presence of surface steps seems to be crucial for facile –(Au–O)– chain formation.

Once the chains are formed on the surface, they can induce further global restructuring processes, driven by the affinity of Ag atoms to oxygen. The thermodynamic analysis of Refs. [40, 80] summarized in the preceding section revealed two driving forces acting in bimetallic surfaces with adsorbed oxygen. On the one hand, −(Au–O)– chains are thermodynamically preferred over individually adsorbed O on Au, and on the other hand, Ag has a higher affinity to O than Au and Ag–O bonds are more favorable than Au–O bonds.

To study the surface restructuring, which occurs because of these thermodynamic driving forces acting in our bimetallic system with O adsorbate, we carried out AIMD simulations.

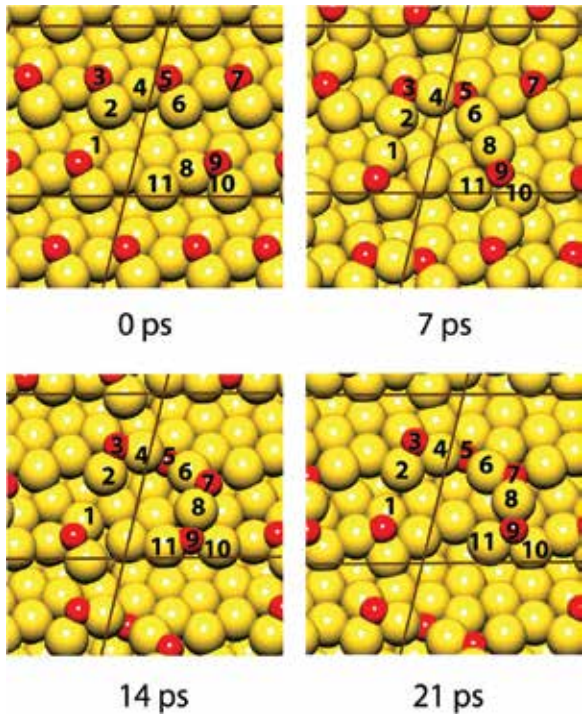

Figure 7. Snapshots of an AIMD simulation showing –(Au–O)– chain formation from individually adsorbed O atoms on Au (321) without Ag impurities. (3 × 2) Unit cell and O coverage of 0.17 ML. Color coding: Au, yellow; O, red. Reproduced with permission from Ref. [39]. Copyright 2017 American Chemical Society.

Two key observations were made in these simulations: first, Ag atoms diffuse towards oxygen of an –(O–Au)– chain and stay in an adjacent position, which shows that the Au–O bonds within the chain are stronger than external Au–O bonds. Second, also the –(O–Au)– chains are able to move towards Ag atoms to maximize the number of external Ag–O contacts, without breaking the internal chain structure [40, 41].

In the simulation illustrated in **Figure 8** [41], we were able to monitor Ag diffusion from subsurface layers to the surface driven by the attractive interaction with two short O–Au–O chains. From **Figure 8**, it can be seen that already after 8 ps a silver atom labeled Ag(**1**) initially located in the subsurface layer directly under the step migrates to the surface and links the two short chains into a longer one. Subsequently, a deeper lying Ag(**2**), initially more than 4 Å away from the surface finds its way to the surface and occupies a position next to one of the O–Au–O fragments. In a reference simulation with a starting structure containing no adsorbed O, no Ag or Au diffusion occurred on the time scale of the simulation. This example illustrated that Ag segregation onto the surface is induced by adsorbed O. Experiments under UHV conditions employing Ag covered stepped Au (332) surface provided evidence in support of our theoretical prediction, showing that oxygen is able to induce surface segregation of Ag already at 200 K [41].

http://dx.doi.org/10.5772/intechopen.74006

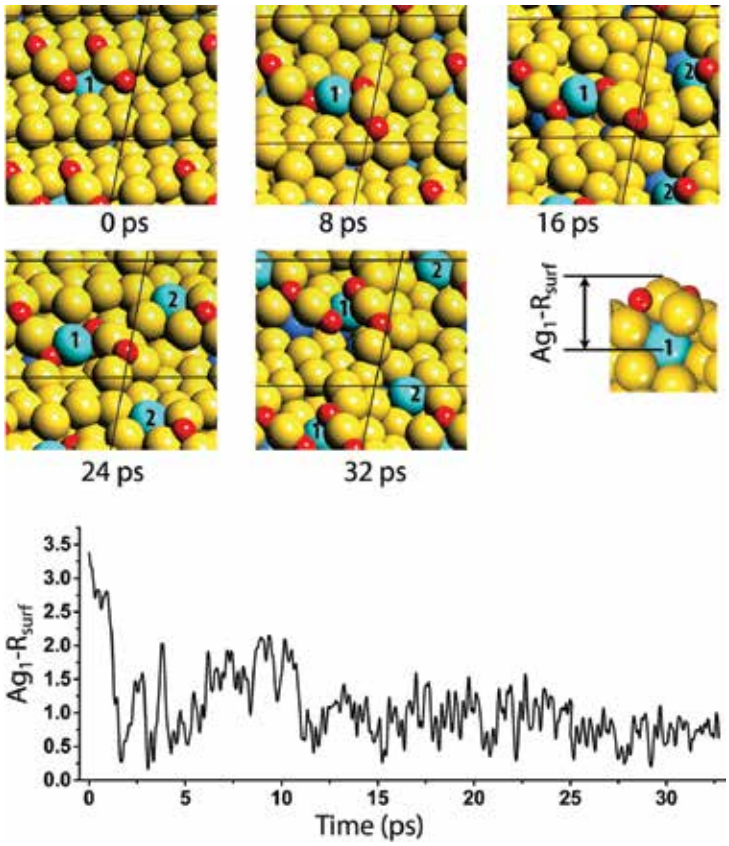

Figure 8. An AIMD simulation showing vertical Ag diffusion from a subsurface layer to the surface. Ag_1-R_{surf} represents the distance of Ag(1) atom initially located near the step edge to a reference surface. The reference surface is chosen as a Z coordinate slightly above the Au atom of the O–Au–O fragment at 0 ps and is kept fixed during the simulation. Reproduced with permission from Ref. [39]. Copyright 2017 American Chemical Society.

6. Role of surface silver for the catalytic activity of nanoporous gold

Nanostructured gold-based catalysts show unique behavior, being active at sub-ambient temperature and exceptionally selective for partial oxidation and partial hydrogenation reactions [104–106]. These characteristics are also held by npAu, which has been demonstrated to catalyze preferential CO oxidation (PROX) in hydrogen stream [107], oxidative coupling of alcohols to esters [10, 28], cross-coupling reactions of alcohols [108, 109], alcohols and aldehydes [110, 111], and alcohols and amines [112] at mild conditions. Selective hydrogenation has been little explored on npAu because of generally poor ability of gold to catalyze H_2 dissociation. However, Yamamoto et al. [113] found a way to generate atomic H on npAu by oxidizing organosilanes with water. Using this method of *in situ* hydrogen generation and amine additives, they reached high selectivity and high yields in the selective hydrogenation of

alkynes to alkenes [114] and quinones to 1,2,3,4-hydroquinones [115]. Yamamoto group also reported several C–C coupling reactions catalyzed by npAu [114]. Nevertheless, oxidation reactions remain the main area where npAu is currently being studied as a catalyst. The ability of nanostructured gold to catalyze aerobic oxidation with O_2 as oxidant makes it attractive from the standpoint of "green" chemistry.

However, the question of how npAu catalyzes O_2 activation and, in particular, whether silver residuals are crucial for the catalytic activity, has been much debated in the literature. Until now, direct experimental evidence justifying a particular mechanism is lacking, although theoretical studies provided valuable insights into possible mechanistic scenarios. In most studies, a dissociative mechanism of O_2 activation has been postulated on npAu, in which O_2 molecule adsorbs dissociatively forming atomic O, which oxidizes adsorbed molecules on the surface in further reaction steps. However, it was difficult to explain, why O_2 can dissociate on npAu, while it does not adsorb or dissociate on extended gold surfaces. Bäumer and co-workers [21] suggested that silver impurities in npAu should assist in the activation of molecular oxygen. Theoretical studies by Moskaleva et al. [39] and Fajín et al. [116] have shown that (i) steps and kinks are crucial for O_2 adsorption and dissociation and (ii) O_2 adsorbs stronger at Ag-rich sites and the activation barrier for O_2 dissociation is reduced at such sites. However, significant lowering of the activation barrier was computationally predicted only for rather large ensembles of >4 Ag atoms, which raised a question of how high is the probability to find such large ensembles, taking into account that the total concentration of residual silver is typically <1 at.% in the bulk. Very recent studies using high-resolution scanning transmission electron microscopy (STEM) combined with elemental mapping using energy-dispersive X-ray spectroscopy (EDXS) shed new light on this question [117, 118]. These two groups independently discovered that Ag is not evenly distributed in npAu but can be concentrated in Ag-rich regions that are probably the fragments of the original Ag-rich master alloy, which evaded corrosion [117]. X-ray photoelectron spectroscopy revealed at least three types of Ag in np-Au samples with different oxidation states or chemical environment, whereas the measured surface content of each type before and after catalytic cycling depended on the sample preparation [119]. Furthermore, theoretical DFT-based studies [41] and experimental studies using Auger and X-ray photoelectron spectroscopies [41, 120] showed that adsorbed surface O should trigger Ag diffusion and enrichment in the surface region. These results indicated that not only Ag impurities, but also atomic O (which is generated in the course of O_2 activation or even already contained in as-prepared samples), may affect the reaction mechanisms on npAu. Recent theoretical studies [41, 94, 121] showed that adsorbed O on gold may be present not only as individual O atoms but also as 1D or 2D chains containing alternating Au and O atoms. Furthermore, theoretical studies demonstrated that the barrier for O_2 dissociation may be lowered significantly as a result of O co-adsorption [94] or due to the formation of Ag-rich regions near –(Au-O)– chains [121]. Therefore, the adsorption energy of O_2 and the activation energy of its dissociation are expected to be very sensitive to the surface composition in terms of Ag and O content as well as the type of phases they form.

Theoretical work [122–124] also suggested a possibility of another mechanism, an associative one, in which O_2 does not dissociate first but reacts directly with CO, water, or methanol, with significantly lower activation energy than required for O_2 dissociation on pure gold and even

on Ag-substituted surfaces. The adsorption of O_2 on extended gold surfaces could be stabilized not only by Ag impurities but also by another admetal, such as Cu [25, 123], as well as through favorable co-adsorption with water or methanol [122, 125]. An especially interesting case is the reaction of O_2 with water, in which water acts as a co-catalyst and helps to dissociate O_2 according to the following reaction sequence:

$$O_2 + H_2O \rightarrow OOH + OH \tag{2}$$

$$OOH \rightarrow O + OH \tag{3}$$

$$2OH \rightarrow O + H_2O \tag{4}$$

The combination of reactions (2)–(4) gives (5):

$$O_2 \rightarrow O + O \tag{5}$$

Hence, water is not consumed in the overall reaction. Because traces of water are often present in the reaction feed, water may be one of the important ingredients, making npAu an active catalyst. In agreement with theoretical predictions, a favorable effect of water co-feed on the activity of CO oxidation on Au nanoparticles and on npAu was observed in catalytic experiments [38, 126].

Several experimental and theoretical studies to date revealed the essential role of Ag impurities for CO oxidation on npAu [21, 37, 39, 116, 121, 127, 128]. For CO oxidation, changing Ag concentration from 1 to 10 at.% increased the activity by more than a factor of 2 at 40°C. However, the presence of Ag may not always be beneficial for the selectivity or perhaps only up to certain Ag concentrations. For instance, increasing Ag content in npAu was shown to reduce the selectivity of gas-phase methanol oxidation towards partial oxidation product methyl formate [10]. Whereas increasing Ag content from <1 to 2.5 at.% worsens the selectivity as the temperature increases [97% (20°C) → 67% (80°C)], further increase of Ag content makes the reaction completely unselective (only CO_2 and H_2O are formed). The drop of the selectivity on npAu with relatively high residual Ag content was attributed to a stronger binding of intermediates on Ag-rich sites, which leads to their fast reaction to total oxidation products (CO, CO_2, and H_2O), whereas low adsorption energy on Au sites allows for a fast desorption of partial oxidation products [10]. Also, for the liquid-phase methanol oxidation at 60°C, the formation of the coupling product was found to be reduced by half when the average Ag content in the whole sample was increased from around 1 to 15 at.%, confirming the above trend. Therefore, optimal concentration of Ag in npAu has to be identified for a particular application to achieve a trade-off between activity and selectivity.

Beyond applications in gas-phase and liquid-phase catalysis, npAu shows good prerequisites (high surface area, high electrical conductivity, good permeability for gas or liquid molecules, ability to host other compounds) for usage in electrocatalysis. In a recent study [119], npAu was investigated in electrocatalysis of methanol. A clear correlation between the content of residual silver and the product distribution, e.g. on the selectivity, was also found in these studies. Samples with higher Ag content favored deeper oxidation product, formate, rather

than formaldehyde. However, the authors also explain that this correlation with Ag content is rather indirect, because samples with high Ag content also had finer ligament and pore size, which, in their opinion, was the decisive property favoring deeper oxidation. Decreasing pore size increased transport limitations, which more strongly affected the two-electron oxidation to HCHO than the four-electron oxidation to $HCOO^-$. This example illustrates that not only the surface composition but also the ligament size affects the observed catalytic behavior. Because these two factors are likely related [129], determining the role of Ag independent from other sample properties from experimental studies alone appears to be a tricky task.

7. Outlook on electromechanical coupling at Ag-Au surfaces

In heterogeneous catalysis, the reaction rate typically depends on the dissociative adsorption enthalpy H_{ads} of the key reactant and exhibits a pronounced maximum at a certain H_{ads} value (volcano curve [130, 131]). In 2005, Kibler et al. [132] conducted electrochemical experiments and thereby established a relation between H_{ads} and the electrode lattice spacing. For this purpose, they deposited pseudo-morphic palladium monolayers on seven single-crystal substrates with different lattice constants. As the Pd adapted the substrate lattice constant, strain was induced in the monolayers. From voltammetric peak electrode potentials arising from hydrogen desorption, they directly derived the adsorption enthalpy H. Furthermore, they found a linear relation between these peak potentials and a shift of the *d*-band center, which can be related to strain according to a model by Hammer and Nørskov [133, 134]. In 2011, Weissmüller et al. [135] derived a linear dependence between the peak electrode potential and strain from the data of Kibler et al. and defined a strain response parameter ς_E from the slope:

$$\varsigma_E = \left.\frac{\partial E}{\partial e}\right|_q, \tag{6}$$

where e is the strain and q is the charge density. This response parameter is characteristic for the electrode material and independent of a potential adsorbate used to determine it. The phenomenon described here had already been investigated by Gokhshtein [136, 137], but he did not identify a value for the strain response parameter ς_E at that point.

Due to strain relaxation and the lack of reliable and precise strain measurements, it is usually easier to measure the response ς_f of the surface stress f to the charge density q at the electrode surface [135]. The two response parameters are identical for a surface at equilibrium, as they are connected via a Maxwell relation [138, 139]:

$$\left.\frac{\partial f}{\partial q}\right|_e = \left.\frac{\partial E}{\partial e}\right|_q. \tag{7}$$

Several electrochemical experiments from the past aimed at determining response parameters ς_f for different electrode materials under varying conditions [135, 140–142]. Haiss et al. [140]

conducted voltammetry and surface stress measurements of anions adsorption on the Au (111) surface and obtained a linear correlation between surface stress and interfacial charge at the metal/electrolyte interface. However, the choice of electrolyte influenced the response parameter ς_f and therefore they did not provide a measured value of ς_f. By cantilever bending through electrochemical charging of a (111)-textured gold electrode in solutions of fluoride and perchlorate anions, Smetanin et al. [142] measured a surface stress-charge response parameter of −2 V, which agrees very well with the theoretical value of −1.98 V determined by earlier ab initio calculations [138]. In 2009, Smetanin et al. [143] also determined the strain response parameter ς_E directly via cyclic deformation of a thin gold film on a polymer substrate and by measuring the potential variation. They obtained a value of −1.83 V, which is close to the surface stress-charge response parameter ς_f of −2 V determined in their earlier work [142]. This represents an experimental confirmation of the Maxwell relation in Eq. (7).

Instead of measuring the response of the electrode potential, it is also possible to determine that of the electronic work functional ϕ [138]. The latter describes the work needed to remove an electron from a solid to a point right outside its surface, which is the difference between the vacuum potential and the Fermi level. It has been found that the potential of zero charge of an electrode surface in an electrolyte is closely related to the work functional of a neutral surface in vacuum [144, 145]. The response parameter ς can therefore be calculated from the work functional strain response of a neutral surface without considering an electrolyte in the model system [138]:

$$\varsigma = q_0^{-1} \left. \frac{\partial \phi}{\partial e} \right|_{q=0}, \tag{8}$$

where q_0 is the elementary charge $1.6022 \cdot 10^{-19}$ C. In this way, ς can be easily obtained from DFT calculations, as the determination of the work functional is relatively straightforward.

Recently, Albina et al. [146] calculated response parameters for various transition and also noble metals by means of DFT. For the Ag (111) and (100) surfaces, they report values of −2.31 and −0.81 V, respectively. Comparing their results to values for the Au (111) and (100) surfaces (−1.86 and −0.90 V, respectively [138]), the response of the close-packed (111) surface is more pronounced for Ag, while the coefficient for the loosely packed (100) surface has a slightly smaller magnitude for Ag.

While for pure metals, especially gold, the electromechanical coupling phenomenon has been thoroughly studied experimentally as well as in theory, the effect of alloying and more specifically surface segregation remains an open question. The strongly curved npAu surface probably contains numerous strained areas, where the catalytic reactivity may be different from the unstrained surface. Furthermore, systematically straining the material to tune the reactivity may be an attractive option. Therefore, it is crucial to understand the influence of the presence of a second metal on the electromechanical coupling behavior.

We have performed cluster expansions for different Ag-Au surfaces as well as for a varying Ag bulk concentration to determine energetically favorable configurations. Since the electromechanical

coupling coefficient is a quantity that depends on the surface configuration, it can also be expanded by means of the cluster expansion. We can then combine the two expansions and find out how surface formation enthalpy and electromechanical coupling are related. For this purpose, we will apply small strain values to our surface slabs and additionally account for contraction in the direction of the surface normal. The corresponding equilibrium interlayer spacings for the bulk layers emerge from Murnaghan fits [147] for strained bulk cells. The work functional ϕ is subsequently determined for different strain values by calculating the difference between the vacuum potential outside the surface V_{vac} and the Fermi level E_{F}. Our goal is to analyze the influence of a varying Ag bulk concentration, Ag surface concentration, and the surface configuration on the electromechanical coupling parameter. We expect the values of ς to lie between those of pure Ag and Au, i.e. between -2.31 and -1.86 V for the (111) surface. We are currently in the process of finalizing this study, which will be fully covered in a forthcoming publication [148].

8. Conclusions

Nanoporous gold (npAu) is a fascinating material with intriguing properties and an immense potential for controlled modification and design of smart materials. At first glance, this porous noble metal seems to be astonishingly simple, but a closer look at it reveals a rather complex surface composition and rich surface chemistry. The knowledge gained over the past decades regarding the structure, composition, and reactivity of npAu brought us further in our understanding of this material but at the same time posed new questions to be answered in future studies.

Twelve years after the discovery of its catalytic activity, npAu is now widely regarded as a bimetallic catalyst, since the role of a residual less noble metal for its activity has been recognized as essential. In this chapter, we discussed silver as the second (minor) metal component and commented on its role for oxidation catalysis. However, the focus of this review has been on the theoretical and experimental studies of Ag segregation in npAu and in Ag-Au model surfaces. Particularly, we were interested in segregation induced by the presence of O adsorbates. Therefore, a detailed overview of experimental and theoretical studies on surface segregation in Ag-Au systems has been presented here. While most previous investigations report either no segregation or a slight Ag enrichment in the surface, our own theoretical analysis predicted thermodynamically favorable Au termination for Au-Ag (111) surfaces in the absence of surface O. We also demonstrated that chemisorbed atomic oxygen draws Ag to the surface. The diffusion and restructuring processes were predicted to be facilitated by a stepped surface structure. For such stepped surfaces, Ag diffusion is fast enough to happen on the time scale of catalytic experiments, as demonstrated by Auger spectroscopy already at 200 K. Because in oxidation catalysis, the surface of a catalyst is expected to be covered by oxygen atoms, oxygen-driven Ag segregation would result in a silver enriched surface.

Our theoretical work discussed here revealed that O atoms at Au-rich Au-Ag surfaces may dynamically form –(O–Au)– chain structures, which are thermodynamically preferred over individually adsorbed O and that Ag atoms tend to occupy positions next to –(O–Au)– chains.

Such small assemblages of Ag impurities near the oxide chains may serve as reactive sites, e.g. for the dissociation of O_2.

Experimental evidence from catalytic studies on np-Au shows that these catalysts are exceptionally selective towards partial oxidation, which is a unique property of Au catalysts; however, increasing Ag concentration favors deep oxidation and hence deteriorates the selectivity towards partial oxidation products. At the same time, increasing Ag content was found beneficial for enhancing the overall activity and was suggested to improve the stability against catalysis-induced ligament coarsening.

Finally, we presented an outlook on electromechanical coupling at Ag-Au surfaces, which may provide a possibility to systematically tune the catalytic activity of bimetallic surfaces. We are currently investigating the effect of Ag admetal on the electromechanical coupling parameter.

Acknowledgements

We acknowledge the financial support from the German Research Foundation (DFG) within framework of research unit 2213 "NAGOCAT" Project No. MO 1863/4-1 and MU 1648/7-1. We thank the North-German Supercomputing Alliance (HLRN) for providing computational resources.

Author details

Sandra Hoppe[1] and Lyudmila V. Moskaleva[2]*

*Address all correspondence to: moskaleva@uni-bremen.de

1 Institute of Advanced Ceramics, Hamburg University of Technology, Hamburg, Germany

2 Institute of Applied Physical Chemistry and Center for Environmental Research, University of Bremen, Bremen, Germany

References

[1] Bond GC, Louis C, Thompson DT. Catalysis by Gold. London, Singapore: Imperial College Press; 2006

[2] Cha DY, Parravano G. Surface reactivity of supported gold: I. Oxygen transfer between CO and CO_2. Journal of Catalysis. 1970;**18**(2):200-211. DOI: 10.1016/0021-9517(70)90178-8

[3] Bond GC, Sermon PA. Gold catalysts for olefin hydrogenation. Gold Bulletin. 1973;**6**(4): 102-105. DOI: 10.1007/BF03215018

[4] Bond GC, Sermon PA, Webb G, Buchanan DA, Wells PB. Hydrogenation over supported gold catalysts. Journal of the Chemical Society, Chemical Communications. 1973;(13): 444-445. DOI: 10.1039/C3973000444B

[5] Galvagno S, Parravano G. Chemical reactivity of supported gold: IV. Reduction of NO by H_2. Journal of Catalysis. 1978;**55**(2):178-190. DOI: 10.1016/0021-9517(78)90204-X

[6] Hutchings GJ. Vapor phase hydrochlorination of acetylene: Correlation of catalytic activity of supported metal chloride catalysts. Journal of Catalysis. 1985;**96**(1):292-295. DOI: 10.1016/0021-9517(85)90383-5

[7] Haruta M, Kobayashi T, Sano H, Yamada N. Novel gold catalysts for the oxidation of carbon monoxide at a temperature far below 0°C. Chemistry Letters. 1987;**16**(2):405-408. DOI: 10.1246/cl.1987.405

[8] Haruta M. When gold is not noble: Catalysis by nanoparticles. Chemical Record. 2003; **3**(2):75-87. DOI: 10.1002/tcr.10053

[9] Freyschlag CG, Madix RJ. Precious metal magic: Catalytic wizardry. Materials Today. 2011;**14**(4):134-142. DOI: 10.1016/S1369-7021(11)70085-2

[10] Wittstock A, Zielasek V, Biener J, Friend CM, Bäumer M. Nanoporous gold catalysts for selective gas-phase oxidative coupling of methanol at low temperature. Science. 2010; **327**(5963):319-322. DOI: 10.1126/science.1183591

[11] Liu J-H, Wang A-Q, Chi Y-S, Lin H-P, Mou C-Y. Synergistic effect in an Au-Ag alloy nanocatalyst: CO oxidation. The Journal of Physical Chemistry. B. 2005;**109**(1):40-43. DOI: 10.1021/jp044938g

[12] Wang A-Q, Liu J-H, Lin SD, Lin T-S, Mou C-Y. A novel efficient Au-Ag alloy catalyst system: Preparation, activity, and characterization. Journal of Catalysis. 2005;**233**(1):186-197. DOI: 10.1016/j.jcat.2005.04.028

[13] Liu X, Wang A, Yang X, et al. Synthesis of thermally stable and highly active bimetallic Au-Ag nanoparticles on inert supports. Chemistry of Materials. 2009;**21**(2):410-418. DOI: 10.1021/cm8027725

[14] Yen C-W, Lin M-L, Wang A, Chen S-A, Chen J-M, Mou C-Y. CO oxidation catalyzed by Au-Ag bimetallic nanoparticles supported in *Mesoporous silica*. Journal of Physical Chemistry C. 2009;**113**(41):17831-17839. DOI: 10.1021/jp9037683

[15] Sandoval A, Aguilar A, Louis C, Traverse A, Zanella R. Bimetallic Au-Ag/TiO_2 catalyst prepared by deposition-precipitation: High activity and stability in CO oxidation. Journal of Catalysis. 2011;**281**(1):40-49. DOI: 10.1016/j.jcat.2011.04.003

[16] Iizuka Y, Kawamoto A, Akita K, et al. Effect of impurity and pretreatment conditions on the catalytic activity of Au powder for CO oxidation. Catalysis Letters. 2004;**97**(3/4):203-208. DOI: 10.1023/B:CATL.0000038585.12878.9a

[17] Hutchings GJ. Catalysis by gold. Catalysis Today. 2005;**100**(1–2):55-61. DOI: 10.1016/j.cattod.2004.12.016

[18] Ding Y, Kim Y-J, Erlebacher J. Nanoporous gold leaf: "Ancient technology"/advanced material. Advanced Materials. 2004;**16**(21):1897-1900. DOI: 10.1002/adma.200400792

[19] Seker E, Reed ML, Begley MR. Nanoporous gold: Fabrication, characterization, and applications. Materials. 2009;**2**(4):2188-2215. DOI: 10.3390/ma2042188

[20] Scaglione F, Rizzi P, Celegato F, Battezzati L. Synthesis of nanoporous gold by free corrosion of an amorphous precursor. Journal of Alloys and Compounds. 2014;**615**: S142-S147. DOI: 10.1016/j.jallcom.2014.01.239

[21] Zielasek V, Jürgens B, Schulz C, et al. Gold catalysts: Nanoporous gold foams. Angewandte Chemie, International Edition. 2006;**45**(48):8241-8244. DOI: 10.1002/anie.200602484

[22] Jürgens B, Kübel C, Schulz C, et al. New gold and silver-gold catalysts in the shape of sponges and sieves. Gold Bulletin. 2007;**40**(2):142-149. DOI: 10.1007/BF03215571

[23] Xu C, Su J, Xu X, et al. Low temperature CO oxidation over unsupported nanoporous gold. Journal of the American Chemical Society. 2007;**129**(1):42-43. DOI: 10.1021/ja0675503

[24] Wittstock A, Wichmann A, Bäumer M. Nanoporous gold as a platform for a building block catalyst. ACS Catalysis. 2012;**2**(10):2199-2215. DOI: 10.1021/cs300231u

[25] Wang L-C, Zhong Y, Jin H, Widmann D, Weissmüller J, Behm RJ. Catalytic activity of nanostructured Au: Scale effects versus bimetallic/bifunctional effects in low-temperature CO oxidation on nanoporous Au. Beilstein Journal of Nanotechnology. 2013;**4**:111-128. DOI: 10.3762/bjnano.4.13

[26] Wittstock A, Bäumer M. Catalysis by unsupported skeletal gold catalysts. Accounts of Chemical Research. 2014;**47**(3):731-739. DOI: 10.1021/ar400202p

[27] Bipp H, Kieczka H. Formamides. In: Ullmann's Encyclopedia of Industrial Chemistry, Electronic Release. Weinheim: Wiley-VCH; 2000

[28] Personick ML, Zugic B, Biener MM, Biener J, Madix RJ, Friend CM. Ozone-activated nanoporous gold: A stable and storable material for catalytic oxidation. ACS Catalysis. 2015;**5**(7):4237-4241. DOI: 10.1021/acscatal.5b00330

[29] Yamamoto Y. Perspectives on organic synthesis using nanoporous metal skeleton catalysts. Tetrahedron. 2014;**70**(14):2305-2317. DOI: 10.1016/j.tet.2013.09.065

[30] Kim SH. Nanoporous gold films as catalyst. In: Mishra NK, editor. Catalytic Application of Nano-Gold Catalysts. Rijeka: InTech; 2016. Ch. 01

[31] Fujita T, Guan P, McKenna K, et al. Atomic origins of the high catalytic activity of nanoporous gold. Nature Materials. 2012;**11**(9):775-780. DOI: 10.1038/nmat3391

[32] Pireaux JJ, Chtaïb M, Delrue JP, Thiry PA, Liehr M, Caudano R. Electron spectroscopic characterization of oxygen adsorption on gold surfaces. Surface Science. 1984;**141**(1):211-220. DOI: 10.1016/0039-6028(84)90206-1

[33] Saliba N, Parker D, Koel B. Adsorption of oxygen on Au(111) by exposure to ozone. Surface Science. 1998;**410**(2):270-282. DOI: 10.1016/S0039-6028(98)00309-4

[34] Kim J, Samano E, Koel BE. Oxygen adsorption and oxidation reactions on Au(211) surfaces: Exposures using O_2 at high pressures and ozone (O_3) in UHV. Surface Science. 2006;**600**(19):4622-4632. DOI: 10.1016/j.susc.2006.07.057

[35] Gong J, Flaherty DW, Ojifinni RA, White JM, Mullins CB. Surface chemistry of methanol on clean and atomic oxygen pre-covered Au(111). Journal of Physical Chemistry C. 2008; **112**(14):5501-5509. DOI: 10.1021/jp0763735

[36] Haruta M. New generation of gold catalysts: Nanoporous foams and tubes – Is unsupported gold catalytically active? ChemPhysChem. 2007;**8**(13):1911-1913. DOI: 10.1002/cphc.200700325

[37] Wittstock A, Neumann B, Schaefer A, et al. Nanoporous Au: An unsupported pure gold catalyst? Journal of Physical Chemistry C. 2009;**113**(14):5593-5600. DOI: 10.1021/jp808185v

[38] Wittstock A, Biener J, Baumer M. Nanoporous gold: A new material for catalytic and sensor applications. Physical Chemistry Chemical Physics. 2010;**12**(40):12919-12930. DOI: 10.1039/C0CP00757A

[39] Moskaleva LV, Röhe S, Wittstock A, et al. Silver residues as a possible key to a remarkable oxidative catalytic activity of nanoporous gold. Physical Chemistry Chemical Physics. 2011;**13**(10):4529-4539. DOI: 10.1039/c0cp02372h

[40] Hoppe S, Li Y, Moskaleva LV, Müller S. How silver segregation stabilizes 1D surface gold oxide: A cluster expansion study combined with ab initio MD simulations. Physical Chemistry Chemical Physics. 2017;**19**(22):14845-14853. DOI: 10.1039/c7cp02221b

[41] Li Y, Dononelli W, Moreira R, et al. Oxygen-driven surface evolution of nanoporous gold: Insights from Ab initio molecular dynamics and Auger electron spectroscopy. Journal of Physical Chemistry C. 2017. DOI: 10.1021/acs.jpcc.7b08873

[42] Dowben PA, Miller A, editors. Surface Segregation Phenomena. Boca Raton, FL.: CRC Press; 1990

[43] Polak M. Surface segregation. Journal of Physics: Condensed Matter. 2016;**28**(6):60301

[44] van Santen RA, Sachtler W. A theory of surface enrichment in ordered alloys. Journal of Catalysis. 1974;**33**(2):202-209. DOI: 10.1016/0021-9517(74)90264-4

[45] Burton JJ, Hyman E, Fedak DG. Surface segregation in alloys. Journal of Catalysis. 1975; **37**(1):106-113. DOI: 10.1016/0021-9517(75)90138-4

[46] Overbury SH, Bertrand PA, Somorjai GA. Surface composition of binary systems. Prediction of surface phase diagrams of solid solutions. Chemical Reviews. 1975;**75**(5):547-560. DOI: 10.1021/cr60297a001

[47] Williams FL, Nason D. Binary alloy surface compositions from bulk alloy thermodynamic data. Surface Science. 1974;**45**(2):377-408. DOI: 10.1016/0039-6028(74)90177-0

[48] Balseiro CA, Morán-López JL. Electronic theory for surface segregation: Noble-metal alloys. Physical Review B. 1980;**21**(2):349-354. DOI: 10.1103/PhysRevB.21.349

[49] Wynblatt P, Ku RC. Surface energy and solute strain energy effects in surface segregation. Surface Science. 1977;**65**(2):511-531. DOI: 10.1016/0039-6028(77)90462-9

[50] Abraham FF, Nan-Hsiung T, Pound GM. Bond and strain energy effects in surface segregation: An atomic calculation. Surface Science. 1979;**83**(2):406-422. DOI: 10.1016/0039-6028(79)90053-0

[51] Dowben PA, Miller AH, Vook RW. Surface segregation from gold alloys. Gold Bulletin. 1987;**20**(3):54-65. DOI: 10.1007/BF03214658

[52] Suh I-K, Ohta H, Waseda Y. High-temperature thermal expansion of six metallic elements measured by dilatation method and X-ray diffraction. Journal of Materials Science. 1988;**23**(2):757-760. DOI: 10.1007/BF01174717

[53] Kittel C. Introduction to Solid State Physics. 8th ed. Hoboken, NJ: Wiley; 2005

[54] Overbury S, Somorjai G. The surface composition of the silver-gold system by Auger electron spectroscopy. Surface Science. 1976;**55**(1):209-226. DOI: 10.1016/0039-6028(76)90385-X

[55] Yabumoto M, Watanabe K, Yamashina T. An AES study of surface segregation of Ag-Au alloys with ion bombardment and annealing. Surface Science. 1978;**77**(3):615-625. DOI: 10.1016/0039-6028(78)90145-0

[56] Bouwman R, Toneman L, Boersma M, van Santen R. Surface enrichment in Ag-Au alloys. Surface Science. 1976;**59**(1):72-82. DOI: 10.1016/0039-6028(76)90292-2

[57] Fain SC, McDavid JM. Work-function variation with alloy composition: Ag-Au. Physical Review B. 1974;**9**(12):5099-5107. DOI: 10.1103/PhysRevB.9.5099

[58] Somorjai GA, Overbury SH. Auger electron spectroscopy of alloy surfaces. Faraday Discussions of the Chemical Society. 1975;**60**:279. DOI: 10.1039/dc9756000279

[59] Nelson G. Determination of the surface versus bulk composition of silver-gold alloys by low energy ion scattering spectroscopy. Surface Science. 1976;**59**(1):310-314. DOI: 10.1016/0039-6028(76)90310-1

[60] Kelley MJ, Swartzfager DG, Sundaram VS. Surface segregation in the Ag-Au and Pt-Cu systems. Journal of Vacuum Science and Technology. 1979;**16**(2):664-667. DOI: 10.1116/1.570052

[61] King TS, Donnelly RG. Surface compositions and composition profiles of Ag-Au (100), (110), and (111) surfaces determined quantitatively by Auger electron spectroscopy. Surface Science. 1985;**151**(2):374-399. DOI: 10.1016/0039-6028(85)90382-6

[62] Meinel K, Klaua M, Bethge H. Segregation and sputter effects on perfectly smooth (111) and (100) surfaces of Au-Ag alloys studied by AES. Physica Status Solidi A. 1988;**106**(1):133-144. DOI: 10.1002/pssa.2211060117

[63] Derry GN, Wan R. Comparison of surface structure and segregation in AgAu and NiPd alloys. Surface Science. 2004;**566–568**:862-868. DOI: 10.1016/j.susc.2004.06.022

[64] Bozzolo G, Garcés JE, Derry GN. Atomistic modeling of segregation and bulk ordering in Ag-Au alloys. Surface Science. 2007;**601**(9):2038-2046. DOI: 10.1016/j.susc.2007.02.035

[65] Cheng D, Liu X, Cao D, Wang W, Huang S. Surface segregation of Ag-Cu-Au trimetallic clusters. Nanotechnology. 2007;**18**(47):475702. DOI: 10.1088/0957-4484/18/47/475702

[66] Curley BC, Rossi G, Ferrando R, Johnston RL. Theoretical study of structure and segregation in 38-atom Ag-Au nanoalloys. European Physical Journal D: Atomic, Molecular, Optical and Plasma Physics. 2007;**43**(1–3):53-56. DOI: 10.1140/epjd/e2007-00091-y

[67] Deng L, Hu W, Deng H, Xiao S, Tang J. Au-Ag bimetallic nanoparticles: Surface segregation and atomic-scale structure. Journal of Physical Chemistry C. 2011;**115**(23):11355-11363. DOI: 10.1021/jp200642d

[68] Bonačić-Koutecký V, Burda J, Mitrić R, Ge M, Zampella G, Fantucci P. Density functional study of structural and electronic properties of bimetallic silver-gold clusters: Comparison with pure gold and silver clusters. The Journal of Chemical Physics. 2002;**117**(7):3120-3131. DOI: 10.1063/1.1492800

[69] Mitrić R, Bürgel C, Burda J, Bonačić-Koutecký V, Fantucci P. Structural properties and reactivity of bimetallic silver-gold clusters. European Physical Journal D: Atomic, Molecular, Optical and Plasma Physics. 2003;**24**(1):41-44. DOI: 10.1140/epjd/e2003-00124-7

[70] Weis P, Welz O, Vollmer E, Kappes MM. Structures of mixed gold-silver cluster cations $(Ag(m)Au(n)^+$, $m + n < 6)$: Ion mobility measurements and density-functional calculations. The Journal of Chemical Physics. 2004;**120**(2):677-684. DOI: 10.1063/1.1630568

[71] Zhang M, Fournier R. Structure of 55-atom bimetallic clusters. THEOCHEM. 2006;**762**(1):49-56. DOI: 10.1016/j.theochem.2005.08.042

[72] Chen F, Johnston RL. Charge transfer driven surface segregation of gold atoms in 13-atom Au-Ag nanoalloys and its relevance to their structural, optical and electronic properties. Acta Materialia. 2008;**56**(10):2374-2380. DOI: 10.1016/j.actamat.2008.01.048

[73] Paz-Borbón LO, Johnston RL, Barcaro G, Fortunelli A. Structural motifs, mixing, and segregation effects in 38-atom binary clusters. The Journal of Chemical Physics. 2008;**128**(13):134517. DOI: 10.1063/1.2897435

[74] Dianat A, Zimmermann J, Seriani N, Bobeth M, Pompe W, Ciacchi LC. Ab initio study of element segregation and oxygen adsorption on PtPd and CoCr binary alloy surfaces. Surface Science. 2008;**602**(4):876-884. DOI: 10.1016/j.susc.2007.12.016

[75] Bader RFW. Atoms in Molecules: A Quantum Theory. Reprinted. Oxford [England]: Clarendon Press; 2003. cop. 1990

[76] Henkelman G, Arnaldsson A, Jónsson H. A fast and robust algorithm for Bader decomposition of charge density. Computational Materials Science. 2006;**36**(3):354-360. DOI: 10.1016/j.commatsci.2005.04.010

[77] Sanville E, Kenny SD, Smith R, Henkelman G. Improved grid-based algorithm for Bader charge allocation. Journal of Computational Chemistry. 2007;**28**(5):899-908. DOI: 10.1002/jcc.20575

[78] Tang W, Sanville E, Henkelman G. A grid-based Bader analysis algorithm without lattice bias. Journal of Physics: Condensed Matter. 2009;**21**(8):84204. DOI: 10.1088/0953-8984/21/8/084204

[79] Friedel J. The physics of clean metal surfaces. Annals of Physics. 1976;**1**:257-307. DOI: 10.1051/anphys/197601060257

[80] Hoppe S, Müller S. A first principles study on the electronic origins of silver segregation at the Ag-Au (111) surface. Journal of Applied Physics. 2017;**122**:235303. DOI: 10.1063/1.5017959

[81] Sholl DS, Steckel JA. Density Functional Theory. Hoboken, NJ, USA: John Wiley & Sons, Inc.; 2009

[82] Kresse G, Hafner J. Ab initio molecular dynamics for liquid metals. Physical Review B. 1993;**47**(1):558-561. DOI: 10.1103/PhysRevB.47.558

[83] Kresse G, Hafner J. Norm-conserving and ultrasoft pseudopotentials for first-row and transition elements. Journal of Physics: Condensed Matter. 1994;**6**(40):8245

[84] Kresse G, Furthmüller J. Efficient iterative schemes for ab initio total-energy calculations using a plane-wave basis set. Physical Review B. 1996;**54**(16):11169-11186. DOI: 10.1103/PhysRevB.54.11169

[85] Kresse G, Joubert D. From ultrasoft pseudopotentials to the projector augmented-wave method. Physical Review B. 1999;**59**(3):1758-1775. DOI: 10.1103/PhysRevB.59.1758

[86] VandeVondele J, Krack M, Mohamed F, Parrinello M, Chassaing T, Hutter J. Quickstep: Fast and accurate density functional calculations using a mixed Gaussian and plane waves approach. Computer Physics Communications. 2005;**167**(2):103-128. DOI: 10.1016/j.cpc.2004.12.014

[87] Perdew JP. Density-functional approximation for the correlation energy of the inhomogeneous electron gas. Physical Review B. 1986;**33**(12):8822-8824. DOI: 10.1103/PhysRevB.33.8822

[88] Perdew JP, Burke K, Wang Y. Generalized gradient approximation for the exchange-correlation hole of a many-electron system. Physical Review B. 1996;**54**(23):16533-16539. DOI: 10.1103/PhysRevB.54.16533

[89] Grimme S, Antony J, Ehrlich S, Krieg H. A consistent and accurate ab initio parametrization of density functional dispersion correction (DFT-D) for the 94 elements H-Pu. The Journal of Chemical Physics. 2010;**132**(15):154104. DOI: 10.1063/1.3382344

[90] Shi H, Stampfl C. First-principles investigations of the structure and stability of oxygen adsorption and surface oxide formation at Au(111). Physical Review B. 2007;**76**(7):27. DOI: 10.1103/PhysRevB.76.075327

[91] Baker TA, Xu B, Liu X, Kaxiras E, Friend CM. Nature of oxidation of the Au(111) surface: Experimental and theoretical investigation. Journal of Physical Chemistry C. 2009; **113**(38):16561-16564. DOI: 10.1021/jp9052192

[92] Landmann M, Rauls E, Schmidt WG. Chainlike Au-O structures on Au(110) − (1 × r) surfaces calculated from first principles. Journal of Physical Chemistry C. 2009;**113**(14): 5690-5699. DOI: 10.1021/jp810581s

[93] Hiebel F, Montemore MM, Kaxiras E, Friend CM. Direct visualization of quasi-ordered oxygen chain structures on Au(110) − (1 × 2). Surface Science 2016;**650**:5-10. DOI: 10.1016/j.susc.2015.09.018

[94] Moskaleva LV, Weiss T, Klüner T, Bäumer M. Chemisorbed oxygen on the Au(321) surface alloyed with silver: A first-principles investigation. Journal of Physical Chemistry C. 2015;**119**(17):9215-9226. DOI: 10.1021/jp511884k

[95] Moskaleva LV, Zielasek V, Klüner T, Neyman KM, Bäumer M. CO oxidation by co-adsorbed atomic O on the Au(321) surface with Ag impurities: A mechanistic study from first-principles calculations. Chemical Physics Letters. 2012;**525-526**:87-91. DOI: 10.1016/j.cplett.2011.12.050

[96] Nosé S. A unified formulation of the constant temperature molecular dynamics methods. The Journal of Chemical Physics. 1984;**81**(1):511-519. DOI: 10.1063/1.447334

[97] Hoover WG. Canonical dynamics: Equilibrium phase-space distributions. Physical Review A. 1985;**31**(3):1695-1697

[98] Sanchez JM, Ducastelle F, Gratias D. Generalized cluster description of multicomponent systems. Physica A: Statistical Mechanics and its Applications. 1984;**128**(1–2):334-350. DOI: 10.1016/0378-4371(84)90096-7

[99] Lerch D, Wieckhorst O, Hart GLW, Forcade RW, Müller S. UNCLE: A code for constructing cluster expansions for arbitrary lattices with minimal user-input. Modelling and Simulation in Materials Science and Engineering. 2009;**17**(5):55003

[100] Blum V, Hart GLW, Walorski MJ, Zunger A. Using genetic algorithms to map first-principles results to model Hamiltonians: Application to the generalized Ising model for alloys. Physical Review B. 2005;**72**(16):165113

[101] Hart GLW, Blum V, Walorski MJ, Zunger A. Evolutionary approach for determining first-principles hamiltonians. Nature Materials. 2005;**4**(5):391-394. DOI: 10.1038/nmat1374

[102] Hart GLW, Forcade RW. Generating derivative structures from multilattices: Algorithm and application to hcp alloys. Physical Review B. 2009;**80**(1):14120

[103] Hart GL, Nelson LJ, Forcade RW. Generating derivative structures at a fixed concentration. Computational Materials Scienc. 2012;**59**(Supplement C):101-107. DOI: 10.1016/j.commatsci.2012.02.015

[104] Corma A, Garcia H. Supported gold nanoparticles as catalysts for organic reactions. Chemical Society Reviews. 2008;**37**(9):2096-2126. DOI: 10.1039/B707314N

[105] Sharma AS, Kaur H, Shah D. Selective oxidation of alcohols by supported gold nanoparticles: Recent advances. RSC Advances. 2016;**6**(34):28688-28727. DOI: 10.1039/C5RA25646A

[106] Mallat T, Baiker A. Potential of gold nanoparticles for oxidation in fine chemical synthesis. Annual Review of Chemical and Biomolecular Engineering. 2012;**3**(1):11-28. DOI: 10.1146/annurev-chembioeng-062011-081046

[107] Li D, Zhu Y, Wang H, Ding Y. Nanoporous gold as an active low temperature catalyst toward CO oxidation in hydrogen-rich stream. Scientific Reports. 2013;**3**:3015 EP. DOI: 10.1038/srep03015

[108] Wang L-C, Stowers KJ, Zugic B, et al. Exploiting basic principles to control the selectivity of the vapor phase catalytic oxidative cross-coupling of primary alcohols over nanoporous gold catalysts. Journal of Catalysis. 2015;**329**(Supplement C):78-86. DOI: 10.1016/j.jcat.2015.04.022

[109] Stowers KJ, Madix RJ, Biener MM, Biener J, Friend CM. Facile ester synthesis on Ag-modified nanoporous Au: Oxidative coupling of ethanol and 1-Butanol under UHV conditions. Catalysis Letters. 2015;**145**(6):1217-1223. DOI: 10.1007/s10562-015-1525-4

[110] Wang L-C, Stowers KJ, Zugic B, et al. Methyl ester synthesis catalyzed by nanoporous gold: From 10-9 Torr to 1 atm. Catalysis Science & Technology. 2015;**5**(2):1299-1306. DOI: 10.1039/C4CY01169D

[111] Lackmann A, Mahr C, Schowalter M, et al. A comparative study of alcohol oxidation over nanoporous gold in gas and liquid phase. Journal of Catalysis. 2017;**353**(Supplement C):99-106. DOI: 10.1016/j.jcat.2017.07.008

[112] Wichmann A, Bäumer M, Wittstock A. Oxidative coupling of alcohols and amines over bimetallic unsupported nanoporous gold: Tailored activity through mechanistic predictability. ChemCatChem. 2015;**7**(1):70-74. DOI: 10.1002/cctc.201402843

[113] Asao N, Ishikawa Y, Hatakeyama N, et al. Nanostructured materials as catalysts: Nanoporous-gold-catalyzed oxidation of organosilanes with water. Angewandte Chemie, International Edition. 2010;**49**(52):10093-10095. DOI: 10.1002/anie.201005138

[114] Yan M, Jin T, Ishikawa Y, et al. Nanoporous gold catalyst for highly selective Semihydrogenation of alkynes: Remarkable effect of amine additives. Journal of the American Chemical Society. 2012;**134**(42):17536-17542. DOI: 10.1021/ja3087592

[115] Yan M, Jin T, Chen Q, et al. Unsupported nanoporous gold catalyst for highly selective hydrogenation of quinolines. Organic Letters. 2013;**15**(7):1484-1487. DOI: 10.1021/ol400229z

[116] Fajín JLC, Cordeiro MNDS, Gomes JRB. On the theoretical understanding of the unexpected O_2 activation by nanoporous gold. Chemical Communications. 2011;**47**(29):8403-8405. DOI: 10.1039/C1CC12166A

[117] Krekeler T, Straßer AV, Graf M, et al. Silver-rich clusters in nanoporous gold. Materials Research Letters. 2017;**5**(5):314-321. DOI: 10.1080/21663831.2016.1276485

[118] Mahr C, Kundu P, Lackmann A, et al. Quantitative determination of residual silver distribution in nanoporous gold and its influence on structure and catalytic performance. Journal of Catalysis. 2017;**352**:52-58. DOI: 10.1016/j.jcat.2017.05.002

[119] Graf M, Haensch M, Carstens J, Wittstock G, Weissmuller J. Electrocatalytic methanol oxidation with nanoporous gold: Microstructure and selectivity. Nanoscale. 2017;**9**(45): 17839-17848. DOI: 10.1039/C7NR05124G

[120] Schaefer A, Ragazzon D, Wittstock A, et al. Toward controlled modification of nanoporous gold. A detailed surface science study on cleaning and oxidation. Journal of Physical Chemistry C. 2012;**116**(7):4564-4571. DOI: 10.1021/jp207638t

[121] Montemore MM, Madix RJ, Kaxiras E. How does nanoporous gold dissociate molecular oxygen? Journal of Physical Chemistry C. 2016;**120**(30):16636-16640. DOI: 10.1021/acs.jpcc.6b03371

[122] Dononelli W, Klüner T, Moskaleva L. Understanding the oxygen activation on nanoporous gold (in preparation)

[123] Dononelli W, Klüner T. CO oxidation over unsupported group 11 metal catalysts: New mechanistic insight from first principles. Faraday Discussions. 2018, accepted. DOI: 10.1039/C7FD00225D

[124] Tomaschun G, Dononelli W, Li Y, Bäumer M, Klüner T, Moskaleva L. Oxidative dehydrogenation of methanol on the Au(310) surface: The role of surface morphology from a DFT modeling study (submitted)

[125] Chang C-R, Yang X-F, Long B, Li J. A water-promoted mechanism of alcohol oxidation on a Au(111) surface: Understanding the catalytic behavior of bulk gold. ACS Catalysis. 2013;**3**(8):1693-1699. DOI: 10.1021/cs400344r

[126] Ojeda M, Zhan B-Z, Iglesia E. Mechanistic interpretation of CO oxidation turnover rates on supported Au clusters. Journal of Catalysis. 2012;**285**(1):92-102. DOI: 10.1016/j.jcat.2011.09.015

[127] Déronzier T, Morfin F, Massin L, Lomello M, Rousset J-L. Pure nanoporous gold powder: Synthesis and catalytic properties. Chemistry of Materials. 2011;**23**(24):5287-5289. DOI: 10.1021/cm202105k

[128] Déronzier T, Morfin F, Lomello M, Rousset J-L. Catalysis on nanoporous gold-silver systems: Synergistic effects toward oxidation reactions and influence of the surface composition. Journal of Catalysis. 2014;**311**:221-229. DOI: 10.1016/j.jcat.2013.12.001

[129] Graf M, Roschning B, Weissmüller J. Nanoporous gold by alloy corrosion: Method-structure-property relationships. Journal of the Electrochemical Society. 2017;**164**(4): C194-C200. DOI: 10.1149/2.1681704jes

[130] Nørskov JK, Bligaard T, Logadottir A, et al. Trends in the exchange current for hydrogen evolution. Journal of the Electrochemical Society. 2005;**152**(3):J23. DOI: 10.1149/1.1856988

[131] Parsons R. Volcano curves in electrochemistry. In: Catalysis in Electrochemistry. Hoboken, New Jersey, United States of America: John Wiley & Sons, Inc.; 2011. pp. 1-15

[132] Kibler LA, El-Aziz AM, Hoyer R, Kolb DM. Tuning reaction rates by lateral strain in a palladium monolayer. Angewandte Chemie, International Edition. 2005;**44**(14):2080-2084. DOI: 10.1002/anie.200462127

[133] Hammer B, Nørskov JK. Electronic factors determining the reactivity of metal surfaces. Surface Science. 1995;**343**(3):211-220. DOI: 10.1016/0039-6028(96)80007-0

[134] Ruban A, Hammer B, Stoltze P, Skriver H, Nørskov J. Surface electronic structure and reactivity of transition and noble metals1Communication presented at the First Francqui Colloquium, Brussels, 19–20 February 1996.1. Journal of Molecular Catalysis A: Chemical. 1997;**115**(3):421-429. DOI: 10.1016/S1381-1169(96)00348-2

[135] Weissmüller J, Viswanath RN, Kibler LA, Kolb DM. Impact of surface mechanics on the reactivity of electrodes. Physical Chemistry Chemical Physics. 2011;**13**(6):2114-2117. DOI: 10.1039/c0cp01742f

[136] Gokhshtein AY. Investigation of surface tension of solid electrodes at several frequencies simultaneously. Electrochimica Acta. 1970;**15**(1):219-223. DOI: 10.1016/0013-4686(70)90023-X

[137] Gokhshtein AY. The estance method. Russian Chemical Reviews. 1975;**44**(11):921

[138] Umeno Y, Elsässer C, Meyer B, et al. Ab initio study of surface stress response to charging. Europhysics Letters. 2007;**78**(1):13001. DOI: 10.1209/0295-5075/78/13001

[139] Smetanin M. Mechanics of electrified interfaces in diluted electrolytes. Saarländische Universitäts- und Landesbibliothek. 2010. https://publikationen.sulb.uni-saarland.de/handle/20.500.11880/25689

[140] Haiss W, Nichols RJ, Sass JK, Charle KP. Linear correlation between surface stress and surface charge in anion adsorption on Au(111). Journal of Electroanalytical Chemistry. 1998;**452**(2):199-202. DOI: 10.1016/S0022-0728(98)00137-5

[141] Viswanath RN, Kramer D, Weissmüller J. Variation of the surface stress−charge coefficient of platinum with electrolyte concentration. Langmuir. 2005;**21**(10):4604-4609. DOI: 10.1021/la0473759

[142] Smetanin M, Viswanath RN, Kramer D, et al. Surface stress-charge response of a (111)-textured gold electrode under conditions of weak ion adsorption. Langmuir. 2008;**24**(16): 8561-8567. DOI: 10.1021/la704067z

[143] Smetanin M, Kramer D, Mohanan S, Herr U, Weissmüller J. Response of the potential of a gold electrode to elastic strain. Physical Chemistry Chemical Physics. 2009;**11**(40):9008-9012. DOI: 10.1039/b913448d

[144] Trasatti S. Work function, electronegativity, and electrochemical behaviour of metals: II. Potentials of zero charge and "electrochemical" work functions. Journal of Electroanalytical Chemistry and Interfacial Electrochemistry. 1971;**33**(2):351-378. DOI: 10.1016/S0022-0728(71)80123-7

[145] Rath DL, Kolb DM. Continuous work function monitoring for electrode emersion. Surface Science. 1981;**109**(3):641-647. DOI: 10.1016/0039-6028(81)90432-5

[146] Albina J-M, Elsässer C, Weissmüller J, Gumbsch P, Umeno Y. Ab initio investigation of surface stress response to charging of transition and noble metals. Physical Review B. 2012;**85**(12):959. DOI: 10.1103/PhysRevB.85.125118

[147] Murnaghan FD.The compressibility of media under extreme pressures. Proceedings of the National Academy of Sciences of the United States. 1944;**30**(9):244-247

[148] Hoppe S, Müller S. Electromechanical coupling at Ag-Au surfaces via first principles: Influence of alloy composition and surface segregation (in preparation)

[149] Hoppe S, Müller S. Journal of Applied Physics. 2017;**122**:235-303

Chapter 5

Exciton-Plasmon Interactions in Quantum Well Structures Near Silver Nanoparticles

Hiroaki Matsui

Additional information is available at the end of the chapter

http://dx.doi.org/10.5772/intechopen.71466

Abstract

The chapter reports photoluminescence (PL) and an energy transfer dynamic in a hybrid heterostructure consisting of an Ag nanoparticle (NP) layer and $Cd_{0.08}Zn_{0.92}O$/ZnO quantum well (QW). The observed PL quenching was closely related to electronic states of excitons confined in the QW. The PL quenching of the QW emission was only observed at low temperatures which excited carriers were radiatively recombined due to excitonic localization derived from fluctuated energy potentials in the QW. In contrast, delocalization of excitons from the QW with increasing temperature resulted in disappearance of the PL quenching. Time-resolved PL measurements revealed a decay rate of PL from the QW emission through the presence of energy transfer from the QW to Ag NP layer. The temperature-dependent energy-transfer rate was similar to that of the radiative recombination rate. The Ag NP layer surface showed a visible light absorption caused by localized surface plasmons (LSPs), which was very close to the PL peak energy of the QW. These results indicated that the excitonic recombination energy in the QW was nonradiatively transferred to Ag NP layer owing to energy resonance between the LSP and the QW. These phenomena could be explained by a surface energy transfer mechanism.

Keywords: silver, plasmon, energy transfer, exciton, quantum well

1. Introduction

Semiconductor-based quantum wells (QWs) with metallic nanostructures, such as nanodots, nanoparticles and nanogratings, have received much attention as promising hybrid structures towards fabrications of plasmon-coupled emitting devices. In particular, the energy interactions between surface plasmons (SPs) and QW emitters have been investigated in relation to exciton-plasmon coupling [1–5]. SPs can effectively capture dipole oscillator energy in QWs. As a result, spontaneous decay rates of light emissions from QWs are remarkably modified in

close proximity to metallic nanostructures [6]. These phenomena usually lead to enhancing or quenching processes. Enhanced luminescence is promoted by localized electromagnetic fields (near-fields) induced by SPs on metallic nanostructured surfaces. On the other hand, quenching of luminescence is attributed to various energy dissipation mechanisms based on plasmon damping in metals, such as plasmonic absorptions, excitonic diffusions, and electron-hole pair excitations [7–9]. Dissipation processes related to these mechanisms are more significant than the nonradiative recombination in QWs, which results in remarkable decrease of quantum efficiency of QWs. An elucidation of luminescent quenching is a key issue for the fabrications of the plasmon-based emitting devices on QWs.

Detailed investigations concerning photoluminescent (PL) quenching have been demonstrated hybrid structures of metallic nanoparticles and semiconductor quantum dots (QDs) [10–14]. The quenching effect has been utilized to bio-photonic applications such as chips for the detections of DNA, protein molecules, and energy transfer assays [15]. In the cases of Au nanoparticles (NPs)–CdSe QDs, the efficient PL quenching has been closely related to the spectral overlap of plasmon absorptions of Au NPs and light emissions from the QDs, as well as the separation length between Au nanoparticles and the QDs. The recombination energy of confined excitons in the QDs has been nonradiatively transferred to the Au NPs, leading to shortening lifetimes of light emissions from the QDs, which could be explained by both mechanisms of Förster energy transfer (FRET) [16] and surface energy transfer (SET) processes [17]. A FRET process induced between Au NPs and QDs is based on a dipole-dipole interaction between Au NPs and QDs. A dipole-dipole interaction is known as short-range coupling with d^{-6} order, where d represents separation distance between Au NPs and QDs. On the other hand, a SET process has been known as a dipole-surface energy transfer, which has long-range coupling with d^{-4} order. Therefore, difference in mechanism between FRET and SET processes is closely related to spatial distance of a field interaction.

Recently, energy coupling between QWs and SPs has been studied on $In_xGa_{1-x}N$-based and $Cd_xZn_{1-x}O$-based QWs with Ag nanostructures. Some studies demonstrated PL enhancement [18], while others reported quenched PL [19, 20]. For $In_xGa_{1-x}N$ and $Cd_xZn_{1-x}O$ alloys, it is known that electronic states in QWs are present either in the form of bound electron–hole pairs (localized excitons) or free electrons and holes (free excitons), as realized by carrier localization or delocalization, respectively. These electronic states give an influence to the quantum efficiency of $In_xGa_{1-x}N$ and $Cd_xZn_{1-x}O$ QWs, which is further dependent on temperature [21–23]. High quantum efficiency is based on excitonic localization at defect sites such as interface disorders and atom fluctuations. In the concrete cases of $In_xGa_{1-x}N$ QWs with Ag nanostructures, it was reported that the plasmon-coupled PL properties at room temperature were suppressed at low temperatures [24]. Furthermore, it was confirmed that the PL quenching became strong with increasing quantum efficiency of $In_xG_{a1-x}N$ QWs [25]. These results resulted in the conjecture that the PL quenching is closely attributed to the electronic states of $In_xGa_{1-x}N$ QWs in the presence of Ag nanostructures. However, the influence of plasmonic fields on PL quenching has, for the most part, remained undocumented at present. Accordingly, the origin of nonradiative energy transfer contributing to PL quenching is not fully understood.

In this study, I focus on $Cd_xZn_{1-x}O$ QWs with visible PL for studies of plasmon-exciton coupling. To date, we have investigated band-edge luminescence of $Cd_xZn_{1-x}O$ QWs in order to understand optical properties of excitonic recombination in the QWs [26–28].

$Cd_xZn_{1-x}O$ QWs along the polar axis produce internal fields due to piezoelectric and spontaneous polarizations between well and barrier layers. In the case, we must consider two kinds of radiative processes. One process involves excitonic localization because of spatial cadmium fluctuations. The cadmium-rich regions have functions of radiative recombination centers of localized excitons at potential minima formed in $Cd_xZn_{1-x}O$ wells. The other process is related to the quantum-confinement Stark effect (QCSE) generated by an internal field induced in wells [29]. For a well whose width is greater than the excitonic Bohr diameter of the free exciton (R_{ex} = 3.6 Å in ZnO), excitonic localization is weakened by the QCSE. As a consequence, excitonic localization is enhanced by interfacial fluctuations such as interface defects and well-width variations because the excitonic wave function confined in a well penetrates into a barrier. This behavior is well observed for narrow well widths less than R_{ex}, which leads to efficient PL due to a strong radiative recombination.

This chapter reports the temperature-dependent optical dynamics of PL quenching in a $Cd_xZn_{1-x}O$ QW placed in the vicinity of Ag NP layer. The samples in this work do not exhibit PL enhancement at any temperature, which is convenient for optical studies of quenching behaviors. In our case, pulsed optical excitations are used to evaluate the dynamics of energy transfer and other competing processes concerning carrier recombination in the QW. To an effort to understand the exciton-plasmon coupling, two kinds of relaxation steps in the QW were considered, namely, radiative or nonradiative recombination of excited carriers (electrons and holes). These physical states can be alternatively realized by changing the temperature. In addition, a ZnO spacer of variable thickness spatially separated the QW from the Ag nanostructures on top of the QW structure, which was capable of revealing subsequent energy transfer processes.

2. Fabrications and evaluations of $Cd_xZn_{1-x}O$ QWs

Single $Cd_{0.08}Zn_{0.92}O$/ZnO quantum wells (QWs) were deposited on O-polar ZnO (000-1) substrates using a pulsed laser deposition method [30]. ArF excimer laser pulses (193 nm, 3 Hz and 1 J/cm²) were focused on Cd-rich $Cd_{0.50}Zn_{0.50}O$ ceramic targets in an oxygen flow of 10^{-5} mbar. The Cd content in the well was precisely confirmed by a Rutherford backscattering technique. A $Cd_{0.08}Zn_{0.92}O$ well layer was embedded between a 100-nm thick ZnO buffer layer and a 5-nm thick ZnO capping layer. The ZnO buffer and capping layers were deposited at 650 and 270°C, respectively. The low growth temperature of the capping ZnO layer avoids any annealing effects that may occur at high temperature.

The cross-sectional images of scanning transmittance electron microscopy (STEM) revealed the local structure of a QW with a well width (L_W) of 3.2 nm (**Figure 1(a)**). According to the *Z*-contrast image of STEM, the layer with a brighter contrast indicated a $Cd_{0.08}Zn_{0.92}O$ well, whereas the darker layers presented ZnO barrier layers. The heterointerface between the well and buffer layers in the QW was found to be smooth. However, *ex situ* atomic force microscopy (AFM) observations exhibited that the ZnO buffer layer consisted of hexagonal island structures composed of regular terraces and equal width (**Figure 1(c)**), whereas the surface of the well layer possessed small island structures with a roughness height of 1.5 nm (**Figure 1(b)**). The capping/well and well/buffer heterointerfaces were not smooth at the atomic scale.

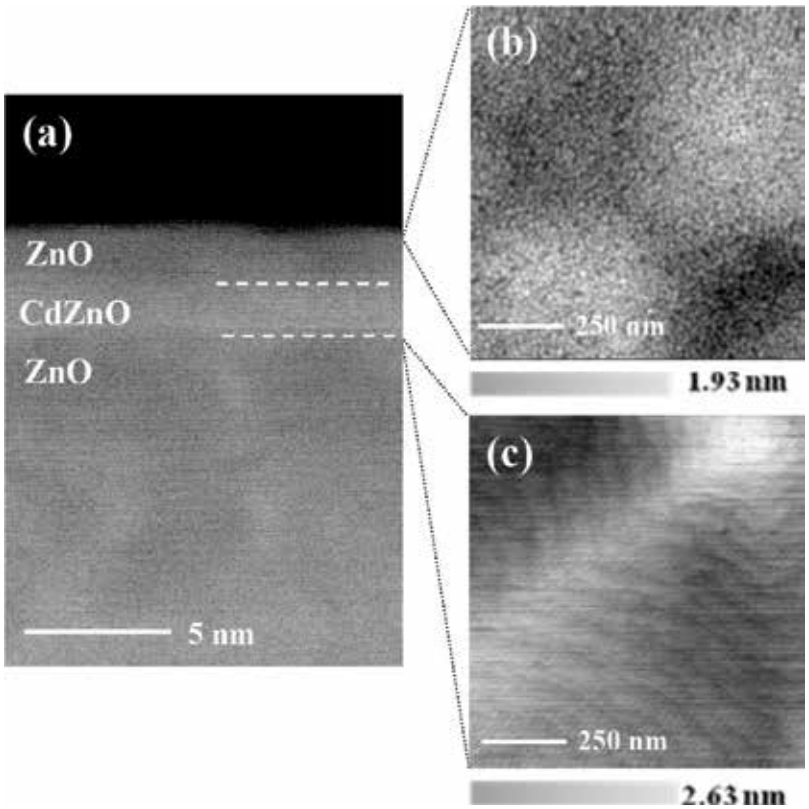

Figure 1. (a) Cross-section STEM image of the QW with a L_W of 3.2 nm. Surface AFM images of the QW with a L_W of 3.2 nm (b) and the ZnO buffer layer grown at T_g of 650°C (c). (**Figure 3** of [23]). Copyright 2011 by the American Institute of Physics.

3. Optical and structural properties of assembled Ag nanoparticles

Figure 2(a) shows a surface AFM image for the Ag structure fabricated on the QW. Ag layer consisted of small nanoparticles. The homogeneity of assembled Ag NPs was identified from a fast Fourier transform pattern (inset of **Figure 2(a)**). The extinction spectrum of the Ag NP layer showed a peak top at 2.60 eV, relating to a LSP resonance (**Figure 2(b)**) [31]. The photon energy of the LSP overlapped with that of the QW emission. This can produce an efficient energy interaction between the LSP and the QW. In addition, the reflection spectra in **Figure 2(c)** revealed that the Ag NP layer exhibited weak reflection intensity at 2.60 eV, i.e., the extinction of the Ag NP layer was almost dominated not by light scattering but by absorption. These optical properties were derived from a LSP field generated on the Ag NP layer surface [32]. Therefore, an increase of light absorption in the QW due to light extraction by reflection from the metal "mirror" is very small.

Figure 3(a) shows the cross-section TEM image of local structure of the $Cd_{0.08}Zn_{0.92}O$ QW and the Ag NP layer at atomic scale. No threading dislocation was seen at the interface between the buffer layer and the substrate. A detailed structure of the Ag NP layer was clearly obtained.

http://dx.doi.org/10.5772/intechopen.71466

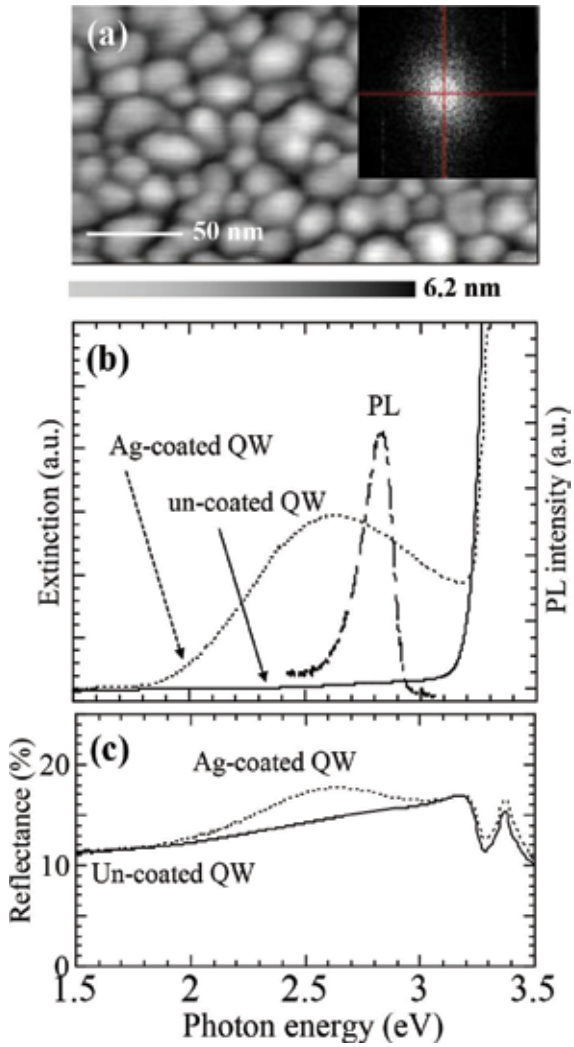

Figure 2. (a) An AFM image of an Ag-coated QW surfaces. The inset image indicates a fast Fourier transform (FFT) pattern. (b) Extinction spectra of uncoated (straight line) and Ag-coated QW (dot line) at room temperature (RT). The dot-straight line represents a PL spectrum of uncoated QW. (c) Reflectance spectra of uncoated (straight line) and Ag-coated QWs (dot line) taken at RT.

Figure 3(b) shows a cross-section TEM image focused on a heterointerface between Ag NP and ZnO layers. The Ag NP layer was composed of homogeneous alignment structure of Ag NPs with lateral and vertical sizes of 20 nm. Each Ag NP was directly located on the ZnO capping layer with a very flat surface. No thin-layered Ag nanostructure was found at the interface. In an effort to measure the local structure of the QW, a STEM was used to observe a Z-contrast image. Spatial separation between the QW and the Ag NP layer was clearly identified. The interface of the well and capping layers was found to be smooth. This also indicated that excited carriers generated in the QW were spatially separated from the Ag NP layer at nanoscale.

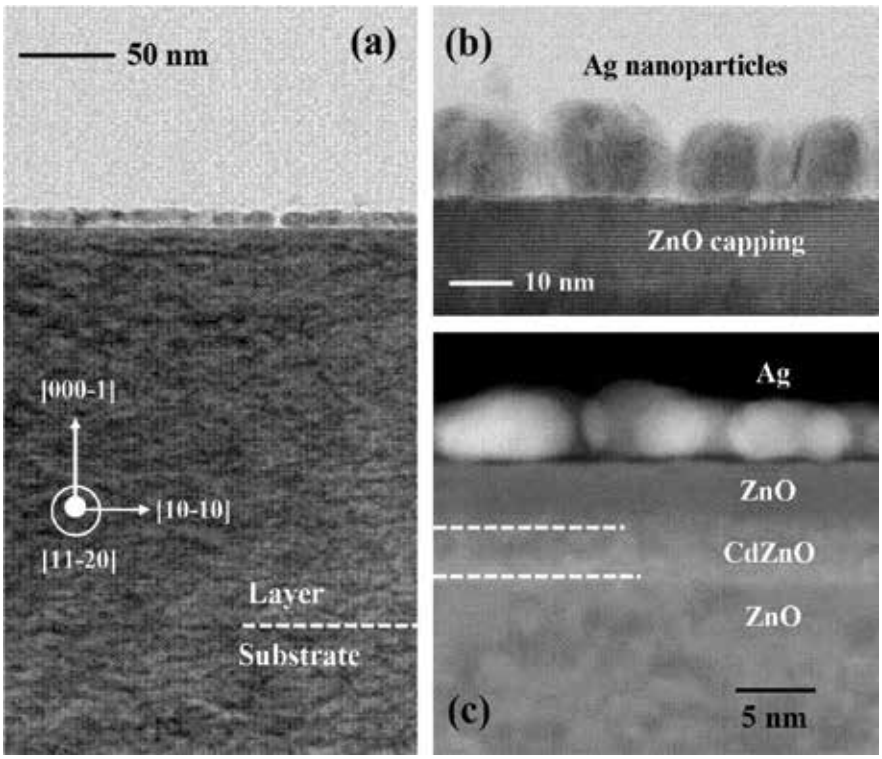

Figure 3. (a) Cross-section TEM image of the QW with Ag NP layer. (b) Cross-section TEM image at an Ag-ZnO heterointerface. (c) High-resolution STEM image focused on the QW region (**Figure 1** of [33]). Copyright [2011] the Optical Society of America.

4. PL modulation and excitonic localization

Figure 4(a) shows the steady-state PL spectra of uncoated and Ag-coated $Cd_{0.08}Zn_{0.92}O$ QW as a function of temperature. A cw InGaN laser (403 nm) was selected as excitation source to perform steady-state PL of light emission from the QW. The luminescence is dispersed by a single monochromator glazed at 500 nm. The PL intensity was dependent on the presence of Ag NP layer. At a temperature of 10 K with the Ag-coated QW, the intensity of the PL emission from the QW (hv = 2.678 eV) markedly decreased by over one order of magnitude. The quenching effect became smaller with increasing temperature and then completely vanished at 300 K (**Figure 4(b)**). **Figure 4(c)** shows the PL intensity ratio (I_{PL}^{*}/I_{PL}) of uncoated (I_{PL}) and Ag-coated (I_{PL}^{*}) QWs at different temperatures. I_{PL}^{*}/I_{PL} ratio increased quickly in low temperatures below 80 K and then reached as high as 92% at 10 K. This result correlated with recombination processes of excited carriers in the QW. The PL peak energy from the uncoated QW showed an *S*-shaped temperature dependence indicated localizations of excitons in the QW, which were derived from spatial Cd fluctuations and interface roughnesses (black dots in **Figure 4(c)**). If a Gaussian-like distribution of the density of state (DOS) for the conduction

http://dx.doi.org/10.5772/intechopen.71466

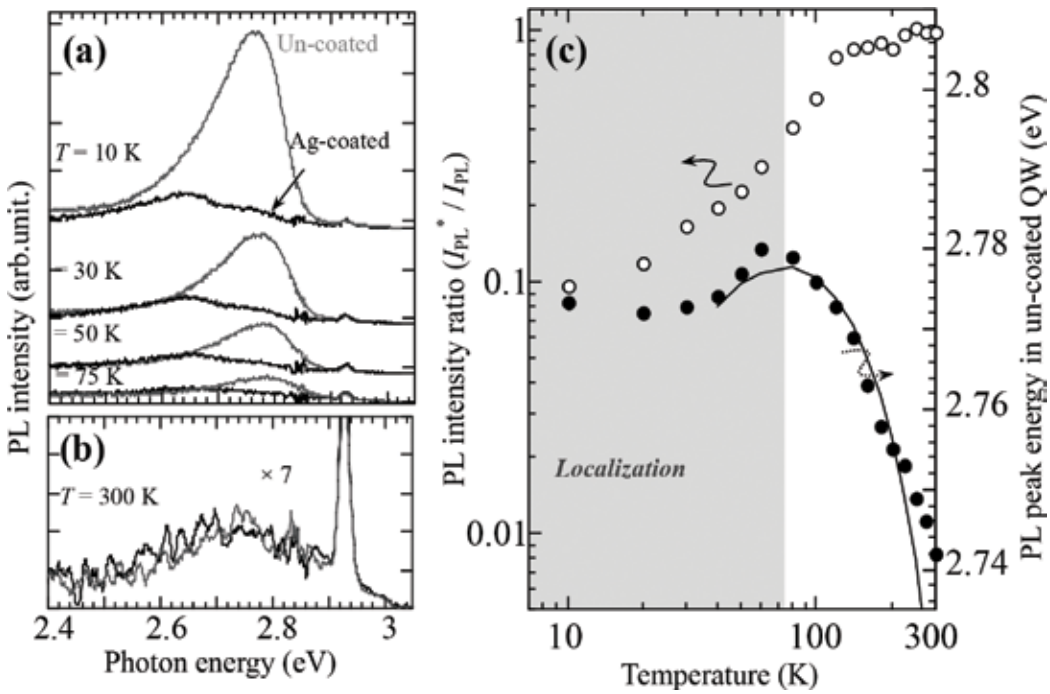

Figure 4. (a) and (b) PL spectra of uncoated (gray) and Ag-coated (black) QWs at different temperatures. (c) Open circles indicate the temperature dependence of the PL intensity ratio (I_{PL}^{*}/I_{PL}). Closed circles show the temperature dependence of the PL energy of the uncoated QW. The straight line indicates the Varshni equation: $E_g(T) = E_g(0) - \alpha T^2/(\beta + T)$, where T is the temperature in kelvin, $E_g(0)$ is the band gap at 0 K, and α and β are constants. Values of $E_g(0)$, α, and β were estimated as 2.793 eV, 7.6 meV, and 750 K, respectively. (**Figure 2** of [33]). Copyright [2011] the Optical Society of America.

and valence band is assumed, the *S*-shaped shift was parameter fitted by the following relation with the local amplitude of the potential fluctuations (σ) of 8 meV [34];

$$E(T) = E - \frac{\alpha T^2}{T+\beta} - \frac{\sigma^2}{k_B T} \quad (1)$$

where E represents the energy band gap at 10 K. α and β are Varshni parameters. When $k_B T$ is smaller than the local amplitude of a potential fluctuation at low temperatures, the excitons are trapped in local potential minima. Excited carriers were trapped in localized states at low temperatures below 80 K in order to form localized excitons for radiative recombination. On the other hand, excited carriers are free to escape from the localized states at high temperatures above 80 K. An electron-hole pair is not sufficiently strong to form a localized exciton. Therefore, a nonradiative recombination process dominates carrier relaxation. The starting temperature of PL quenching was close to the temperature at which excitonic localization occurred. To study optical dynamics, we monitored the temporal evolution of PL in the QW by a time-correlated single-photon counting system that provides a time resolution of 80 ps. The sample was excited at 400 nm by 2 ps pulses of the frequency-doublet output of an amplified Ti:sapphire laser. The light emission from the QW was selected by a

monochromator. The pump excitation energy was chosen to be below the band gap of ZnO, so that electrons and holes were generated only in the well. PL excitation and emission collection were carried out from the substrate side at various temperatures.

Figure 5(a) shows the time-resolved PL (TRPL) signals at 10 K taken at the PL peak energy of the uncoated and Ag-coated QWs. The TRPL signals obeyed bi-exponential decays

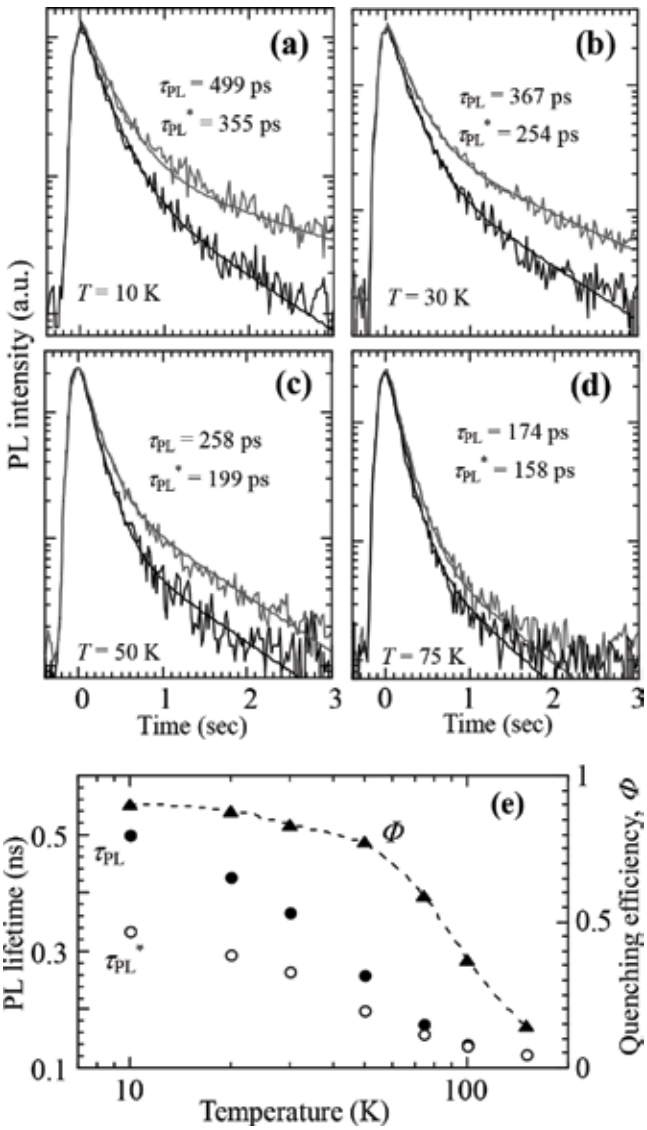

Figure 5. TRPL signals of uncoated and Ag-coated QWs at 10 K (a), 30 K (b), 50 K (c), and 75 K (d). Solid lines are fitted with bi-exponential decays represented by $I(t) = \Sigma_{i=1,2} I_i \exp.(-t/\tau_i)$, where τ_i^{-1} and I_i are the lifetime and amplitude, respectively. (e) Temperature dependence of PL lifetime for uncoated (τ_{PL}: Closed dots) and Ag-coated (τ_{PL}^*: Open dots) QWs. Closed squares indicate the quenching efficiency ($Q = 1 - I_{PL}^*/I_{PL}$).

represented by $I(t) = \Sigma_{i=1,2} I_i \exp.(-t/\tau_i)$, where τ_i^{-1} and I_i are the lifetime and amplitude, respectively. From the fitting results of the uncoated QW (gray lines), the fast decay component τ_1 (266 ps) represents a PL lifetime of the QW, whereas the slow decay component τ_2 (2.09 ns) is related to trapping and de-trapping of carriers. In contrast, the τ_1 and τ_2 values of the Ag-coated QW were similarly determined as 242 ps and 1.75 ns, respectively. The PL lifetime obtained by $(I_1\tau_1 + I_2\tau_2)/(I_1 + I_2)$ showed that τ_{PL}^* (335 ps) of the Ag-coated QW was shorter than τ_{PL} (499 ps) of the uncoated QW (black lines). The TRPL signals at 30 and 50 K were described by the bi-exponential decays (**Figure 5(b)** and **5(c)**). However, the difference in TRPL signals became small at 75 K (**Figure 5(b)**). All values of τ_{PL} and τ_{PL}^* as a function of temperature are given in **Figure 5(e)**. The difference between τ_{PL}^* and τ_{PL} became small with increasing temperature and then vanished at 100 K, which was correlated with the quenching efficiency of PL ($\Phi = 1 - I_{PL}^*/I_{PL}$) (**Figure 5(e)**). The difference between τ_{PL} and τ_{PL}^* was found for the temperature ranges in which excitonic localization occurred. However, both PL lifetimes gave the same values at the high temperatures, at which delocalization of excitons was started. The difference in the PL intensity and lifetime between uncoated and Ag-coated QWs was simultaneously observed, which indicates that energy coupling between the QW and LSP should be more effective at low temperatures.

5. Nonradiative energy transfer

For the uncoated QW, excited carriers undergo by radiative (k_R) or nonradiative (k_{NR}) decay rates. Quantum efficiency (Φ_{int}) is determined by the ratio of these two decay rates as $\eta_{int} = k_R/(k_R + k_{NR})$. In the Ag-coated QW, in contrast, new relaxation process becomes possible due to the presence of the additional electronic system of the Ag NP layer. It is for this reason that the PL decay rate of the Ag-coated QW is faster than the uncoated QW. This situation could involve a nonradiative energy transfer. The added electronic states of a metallic nanosystem offer new relaxation pathways. This relaxation should be quite effective in PL quenching as the recombination energy of excitons in the QW overlapped with the LSP absorption [35]. In this case, exciton-plasmon coupling leads to a rapid annihilation of the exciton and creation of the plasmon. Such a process gives rise to the nonradiative decay rate (k_{ET}) in carrier relaxation processes of the QW [35]. The τ_{PL}^* for the Ag-coated QW is described by the following relation:

$$\tau_{PL}^* = \frac{1}{k_{PL}^*} = \frac{1}{k_R + k_{NR} + k_{ET}} \tag{2}$$

The k_{ET} parameter is estimated from the difference in PL decay rates of the QW in the presence and absence of the Ag layer: $k_{ET} = k_{PL}^* - k_{PL}$. In **Figure 6(a)**, the temperature dependence of k_R, k_{NR}, and k_{ET} is plotted for the uncoated QW. k_R and k_{NR} rates are calculated from the relationships $k_R = k_{PL}/\Phi_{int}$ and $k_{NR} = k_{PL}(1 - \Phi_{int})$ with the quantum yield (Φ_{int}) of the uncoated QW. Φ_{int} is defined as the PL intensity at a particular temperature divided by that at 8 K (Φ_{int}: 1.3% at

300 K). At 10 K, the value of k_{PL} (2.01 ns^{-1}) was matched by that of k_R (1.90 ns^{-1}), indicating that excitons radiatively recombined at 10 K, because the value of k_R was higher than that of k_{NR}. However, the value of k_{NR} gradually became larger than that of k_R with increasing temperature, attributing to nonradiative recombination activated by delocalization of excitons. On the other hand, the values of k_{ET} were in the order of 1.0 ns^{-1} in temperature ranges from 10 to 50 K (**Figure 6(b)**). The temperature dependence of k_{ET} was similar to that of k_R, which indicated that k_{ET} was associated with k_R. At above 75 K, k_{ET} quickly decreased with an increase of k_{NR}. The carrier relaxation processes of the QW are either radiative or nonradiative, or it may experience energy transfer. At 10 K, the energy transfer rate is fast enough to compete with the radiative decay rate of the QW, so that the radiative recombination in the QW would be partially consumed by the energy transfer to the Ag nanostructures, leading to a quenched PL. The energy transfer efficiency (η_{ET}) between the QW and Ag nanostructures was calculated using the following relation:

$$\eta_{ET} = \frac{k_{ET}}{k_{ET} + k_R} \tag{3}$$

The calculated transfer efficiency achieved was as high as 34% at 10 K and then decreased quickly at high temperatures above 75 K (**Figure 6(b)**). Thus, the long PL lifetime of the QW emission at the low temperatures can make QW-LSP coupling highly probable. However, a short PL lifetime could not provide a sufficient energy transfer rate, resulting in no change in PL intensity of the QW emission.

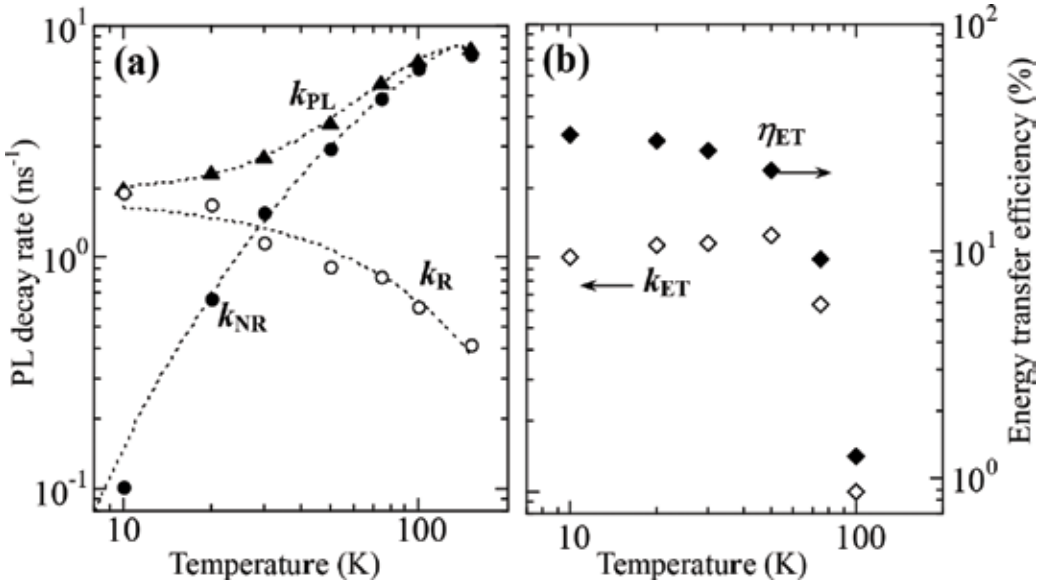

Figure 6. PL decay rate (k_{PL}: Black triangles) of the uncoated QW as a function of temperature. The open and closed circles indicate the radiative decay rate (k_R) and nonradiative decay rate (k_{NR}), respectively. Dotted lines are drawn as a visual guide. (b) Temperature dependence of the energy transfer rate (k_{ET}: Open diamonds) and efficiency of energy transfer (η_{ET}: Black diamonds). (**Figure 4** of [33]). Copyright [2011] the Optical Society of America).

6. Spatial length of quenching efficiency

The relationship between a separation length (d) of the QW from the Ag NP layer and the quenching efficiency was also studied. For the Ag-coated QW, the plot of the quenching efficiency (Q) at 10 K as a function of d is shown in **Figure 7**. This length is controlled by the layer thickness of the ZnO capping layer. The narrow length of 5 nm yielded a high Q value of 92%. The dependence of Q on length was observable up to a distance of 400 Å. The energy transfer from the QW to the proximal Ag NP layer caused efficient PL quenching of the QW even at large lengths. We now consider the use of FRET and SET mechanisms applied to transfer processes of the hybrid structure of metal NPs and semiconductor QDs [13]. A FRET process that occurs between two proximity molecules (donor and acceptor) is commonly employed to explain the quenching process in regard to the quencher as the acceptor. Like dipole-dipole interactions in a FRET process, a dipole-surface energy transfer (SET) is known as metal-induced quenching. The quenching efficiency of FRET and SET processes is dependent on the spectral overlap of acceptor's absorption with the donor's emission and also affects the separation distance of between the donor and acceptor molecules. Quenching efficiency $Q(d)$ can be described by the following equations [13]:

$$Q(d) = 1 - \frac{1}{1 + \left(\frac{d}{d_0}\right)^n} \tag{4}$$

where $n = 4$ and $n = 6$ represent SET and FRET mechanisms, respectively; d_0 is the length at which the QW displays equal probabilities for energy transfer and PL emission, representing a 50% PL intensity. The experimental data (black circles) were well fitted to Eq. (1) with $n = 4$ and $d_0 = 133$ Å (straight line in **Figure 7(a)**), which was close to the theoretical value for d_0 of 103 Å, as follows [13]:

$$d_0 = \left(0.225 \frac{cn^2}{(2\pi)^2 \omega_f k_f} \Phi_{em} \lambda_{QW}^2\right)^{1/4} \tag{5}$$

where c is the speed of light in a vacuum, n is the index of refraction of the medium (1.95 in ZnO), Φ_{em} is the quantum yield of the uncoated QW (0.96 at 10 K), λ_{QW} is the QW emission wavelength (4.47×10^{-5} cm), and ω_f and k_f are the angular frequency (8.40×10^{15} cm^{-1}) and Fermi wave vector (1.20×10^{8} cm^{-1}) for Ag, respectively. The PL quenching due to energy transfer from the QW to Ag NP layer obeyed a SET process with d^{-4} dependence.

Previous studies on quenching related to metallic-induced luminescence have suggested two different models. One is the contact model proposed by Choosing *et al.* [36], in which the luminescent quench was associated with the diffusion of excitons in the organic film to the metal/organic interface. The other is the noncontact model of Chance *et al.* [37] based on interactions between organic dipoles (excited organic molecules) and electron gas (electron-hole pairs) in metal, which would induce energy transfer from the organic to the metal surface. Electron-hole pairs in metal are generated through relaxation processes

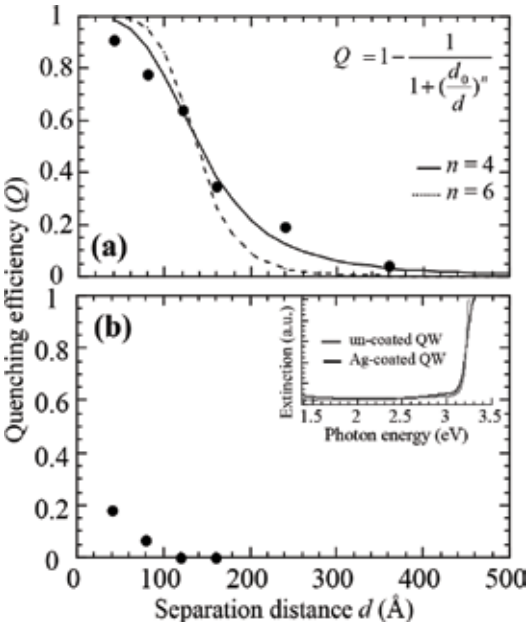

Figure 7. (a) Quenching efficiency (Q) at 10 K as a function of the separation length (d) between the QW and Ag NP layer (black dots). The straight and dot lines are theoretically fitted with n = 4 and 6 using Eq. (4), respectively. (b) the values of Q at 10 K a function of d between the QW and flat Ag layer fabricated by a RF sputtering technique (black triangles). The inset figures indicate extinction spectra taken at RT of uncoated (gray) and Ag-coated QWs (black) fabricated using the flat Ag layer.

of plasmon resonances, which operate as quenchers of luminescence. In our case, excitonic emissions from the QWs could be considered as dipole emitters, which were energetically suppressed by electron-hole pairs related to the LSPs on the Ag NP layers. That is, the Ag-coated QWs did not obey a FRET process with a dipole-dipole interaction but a SET process with a dipole-surface interaction. This represents the fact that the oscillating dipoles in the QW are coupled directly with the free carriers (electron and holes) on the layer surface of Ag NPs. From AFM and TEM images, the Ag NP layer showed a large surface area, producing high surface energy. It was thought that the LSP resonance induced on the surface of the Ag NP layer enhanced the quenching efficiency of PL. Slight difference between experimental (closed dots) and theoretical data (straight line) is related to structural imperfections. As shown in **Figure 3**, inhomogeneity of spatial distance between the QW and Ag NP layer was observed, which affects quenching efficiency as a function of separation distance.

As another aspect, participation of the LSP involving the PL quenching was explored using a flat Ag layer. The RD-sputtered Ag layer showed a very flat surface with a roughness of 1 nm and had no LSP absorption (inset of **Figure 7(b)**). In this case, the value of Q was as small as 18% at a short length of 5 nm and then quickly decreased down to zero at a distance of 12 nm (**Figure 7(b)**). The comparative study revealed that the LSP absorption played a determinant role in increasing quenching efficiency of PL.

http://dx.doi.org/10.5772/intechopen.71466

7. Discussion

The PL enhancement of $In_xGa_{1-x}N$/GaN QWs with Ag nanostructures has been observed near room temperature (RT), relating to the electronic states in the QWs. Lu *et al*. reported that transfer probability to a SP mode of a pair of trapped carriers "localized excitons" is significantly lower than that of a pair of free carriers [25]. They insisted that localization of carriers with decreasing temperature suppressed the QW-SP coupling rate. In addition, Okamoto *et al.* showed that the temperature dependence of the QW-SP coupling rate was similar to that of nonradiative decay rate [24]. Their prior reports imply that the QW-SP coupling is enhanced, when the QW has electronic states consisting of free electrons and holes, which gives effective energy transfer for PL enhancement. Energy of free carriers excited in the QW is directly coupled to an SP mode. This concept can be also applicable to an energy transfer process from a semiconductor QW to a proximal monolayer of a semiconductor QD (or an organic dye) based on $In_xGa_{1-x}N$ QWs [38, 39]. This transfer efficiency enhances with increasing temperature, relating to a change of electronic states in a QW from trapped carriers to free carriers. The above precedent indicates that the energy of free carriers excited in a QW is indispensable for being resonant with an SP mode or a QD.

In contrast, PL quenching of the $Cd_xZn_{1-x}O$ QW with Ag NP layer in this work showed the opposite tendency. The transfer efficiency enhanced with decreasing temperature. The temperature dependence of the energy transfer rate was similar to that of the radiative decay rate (**Figure 6(a)** and **6(b)**). Therefore, the recombination energy of localized excitons in the QW is partially consumed by nonradiative energy transfer to the Ag NP layer, resulting in quenching PL. This originates from an overlap of photon energy between the QW emission and the LSP absorption. This situation has been also observed on Au NP–CdSe QDs [40]. The difference in energy transfer processes between PL enhancement and quenching is attributed to electronic states in a QW placed in vicinity of metallic nanostructures, that is, localization or delocalization of excited carriers. It is suggested that radiative QW emission due to excitonic localization contributes to PL quenching, which supported the past reports that PL suppression became strong with decreasing temperature as well as with increasing quantum efficiency on $In_xGa_{1-x}N$ QWs. The prevention of localized excitons in the QW would be desired to reduce PL quenching phenomenon if possible toward efficient plasmon-coupled emitting devices.

8. Conclusion

The remarkable PL quenching in the hybrid structure of $Cd_xZn_{1-x}O$ QW with Ag NP layer was observed at low temperatures, which was strongly dependent on the electronic states in the QW. The quenching effect was found in the temperature region in which excited carriers radiatively recombined owing to excitonic localization. On the other hand, delocalization of excitons with increasing temperature led to a decreased quenching efficiency. Energy transfer for the PL quenching was generated when the photon energy of the QW emission overlapped with that of LSP absorption. In addition, the spatial separation of the QW from the Ag NP layer revealed that the PL quenching showed a long-range length obeyed almost, which could be explained by a SET process. The comparative study used the Ag NP layers with different character clarified that the

origin of PL quenching was attributed to the local LSP field induced on Ag NP layer. As a consequence, it was indicated that QW-LSP coupling played an important role in quenching PL. This coupling required existence of a pair of trapped carriers "localized excitons" as an electronic state in the QW. On the other hand, the quenching effect was not observed at the high temperatures at which excited carriers exist as free electrons and holes in the QW. Then, QW emission was dominated by a decay rate that was exhibited in the PL as a nonradiative contribution. It was identified that the electronic states of a QW played an important role in quenching PL.

Acknowledgements

This research was supported by a grant-in-Aid for Exploratory Research (No. 15 K13331) and Scientific Research (B) (No. 25289084).

Author details

Hiroaki Matsui[1,2]*

*Address all correspondence to: hiroaki@ee.t.u-tokyo.ac.jp

1 Department of Bioengineering, University of Tokyo, Tokyo, Japan

2 Department of Electric Engineering and Information Systems, University of Tokyo, Tokyo, Japan

References

[1] Wing WJ, Sadeghi SM, Gutha RR, Campbell Q, Mao C. Metallic nanoparticle shape and size effects on aluminum oxide-induced enhancement of exciton-plasmon coupling and quantum dot emission. Journal of Applied Physics. 2015;**118**:124302(1-5). DOI: 10.1063/1.4931378

[2] Gao H, Teng J, Chua SJ. Simultaneous coupling of surface plasmon resonance and photonic band gap to InGaAs quantum well emission. Journal of Applied Physics. 2016;**119**:013104(1-6). DOI: 10.1063/1.4939502

[3] Li Y, Liu B, Zhang R, Xie Z, Zhuang Z. Investigation of surface-plasmon coupled red light emitting InGaN/GaN multi-quantum well with Ag nanostructures coated on GaN surface. Journal of Applied Physics. 2015;**117**:153103(1-5). DOI: 10.1063/1.4918555

[4] Bellessa J, Symonds C, Meynaud C, Plenet JC, Cambril E, Miard A, Ferlazzo L. Exciton/plasmon polaritons in GaAs/Al0.93Ga0.07As heterostructures near a metallic layer. Physical Review B. 2008;**78**:205326(1-4). DOI: 10.1103/PhysRevB78.205326

[5] Okamoto K, Niki I, Shvartser A, Narukawa Y, Mukai T. Surface-plasmon-enhanced light emitters based on InGaN quantum wells. Nature Materials. 2004;**3**:601-605. DOI: 10.1038/namt1198

[6] Neogi A, Morkoç H, Kuroda T, Takeuchi A. Coupling of spontaneous emission from GaN-AlN quantum dots into silver surface Plasmons. Optics Letters. 2005;**30**:93-95. DOI: 10.1364/OL.30.000093

[7] Chance RP, Prock A, Sibey R. Molecular florescence and energy transfer near interfaces. Advances in Chemical Physics. 2007;**37**:1-65. DOI: 10.1002/9780470142561.ch1

[8] Gebauer W, Langner A, Schneider M, Sokolowski M, Umbach E. Luminescence quenching of ordered π-conjugated molecules near a metal surface: Quaterthiophene and PTCDA on Ag (111). Physical Review B. 2004;**69**:155432(1-8). DOI: 10.1103/PhysRevB.69.155431

[9] Li X, Qian J, Jang L, He S. Florescence quenching of quantum dots by gold Nanorods and its application to DNA detection. Applied Physics Letters. 2009;**94**:063111(1)-(3). DOI: 10.1063/1.3080662

[10] Hoshen EC, Bryant GW, Pinkas I, Sperling J, Bar-Joseph I. Exciton-plasmon interactions in quantum dot-gold nanoparticle structures. Nano Letters. 2012;**12**:4260-4264. DOI: 10.1021/nl301917d

[11] Akselrod GM, Weidman MC, Li Y, Argyropoulos C, Tisdale WA, Mikkelsen MH. Efficient nanosecond photoluminescence from infrared PbS quantum dots coupled to plasmonic nanoantennas. ACS Photonics. 2016;**3**:1741-1746. DOI: 10.1021/acsphotonics.6b00357

[12] Matsumoto Y, Tamitake R, Nakanishi S, Ishikawa M, Biju V. Photoluminescence quenching and intensity fluctuations of CdSe-ZnS quantum dots on an Ag nanoparticle film. Journal of Physical Chemistry C. 2008;**112**:1345-1350. DOI: 10.1021/jp076659+

[13] Pons T, Medintz IL, Sapsford KE, Higashiya S, Grimes AF, English DS, Mattoussi H. On the quenching of semiconductor quantum dot photoluminescence by proximal gold nanoparticles. Nano Letters. 2007;**7**:3157-3164. DOI: 10.1021/nl071729+

[14] Viste P, Plain J, Jaffiol R, Vial A, Adam PM, Royer P. Enhancement and quenching regimes in metal-semiconductor hybrid optical nanosources. ACS Nano. 2010;**4**:759-764. DOI: 10.1021/nn901294d

[15] Gueroui Z, Libchaber A. Single-molecule measurements of gold-quenched quantum dots. Physical Review Letters. 2004;**93**:166108(1-4). DOI: 10.1103/PhysRevLett93.166108

[16] Förster T. 10th Spiers memorial lecture. Transfer mechanisms of electronic excitation. Discuss Faraday Society. 1959;**27**:7-17. DOI: 10.1039/DF9592700007

[17] Jennings TL, Singh MP, Strouse GF. Fluorescent lifetime quenching near d = 1.5 nm gold nanoparticles: Probing NSET validity. Journal of the American Society. 2006;**128**:5462-5467. DOI: 10.1021/ja0583665

[18] Henson J, Heckel JC, Dimakis E, Abell J, Bhattacharyya A. Plasmon enhanced light emission from InGaN quantum wells via coupling to chemically synthesized silver nanoparticles. Applied Physics Letters. 2009;**95**:151109(1-3). DOI: 10.1063/1.3249579

[19] Liu B, Cheng CW, Chen R, Ekahana A, Yang WF. Surface plasmon induced exciton redistribution in ZnCdO/ZnO coaxial multi-quantum-well nanowires. Applied Physics Letters. 2010;**97**:081107(1-3). DOI: 10.1063/1.3480414

[20] Chen CY, Yeh DM, Lu YC, Yang CC. Dependence of resonant coupling between surface plasmons and InGaN quantum wells on metallic structure. Applied Physics Letters. 2006;**89**:203113(1-3). DOI: 10.1063/1.2390639

[21] Estrin Y, Rich DH, Keller S, DenBaars SP. Temperature dependence of exciton-surface plasmon polariton coupling in Ag, au and au films on $In_xInGa_{1-x}N$/GaN quantum wells studied with time-resolved cathodoluminescence. Journal of Applied Physics. 2015;**117**:043105(1-14). DOI: 10.1063/1.4906850

[22] Chichibu SF, Onuma T, Aoyama T, Nakajima K, Ahmet P, Chikyow T, Sota T, DenBaars SP, Nakamura S, Kitamura T, Ishida Y, Okuyama H. Recombination dynamics of localized excitons in cubic $In_xGa_{1-x}N$/GaN multiple quantum wells grown by radio frequency molecular beam epitaxy on 3C-SiC substrate. Journal of Vacuum Science and Technology B. 2003;**21**:1856-1862. DOI: 10.1116/1.1593645

[23] Matsui H, Osone T, Tabata H. Band alignment and excitonic localization of ZnO/Cd0.08Zn0.92O quantum wells. Journal of Applied Physics. 2010;**107**:093523(1-7). DOI: 10.1063/1.3359720

[24] Okamoto K, Niki I, Scherer A, Narukawa Y, Mukai T, Kawakami Y. Surface plasmon enhanced spontaneous emission rate of InGaN/GaN quantum wells probed by time-resolved photoluminescence spectroscopy. Applied Physics Letters. 2005;**87**:071102(1-3). DOI: 10.1063/1.2010602

[25] Lu YC, Chen CY, Yeh DM, Huang CF, Tang TY. Temperature dependence of surface plasmon coupling with an InGaN/GaN quantum well. Applied Physics Letters. 2007;**90**:193103(1-3). DOI: 10.1063/1.2738194

[26] Matsui H, Tabata H. The contribution of quantum confinement to optical anisotropy of A-plane $Cd_{0.06}Zn_{0.94}O$/ZnO quantum wells. Applied Physics Letters. 2012;**100**:171910(1-3) 10.1063/1.4707384

[27] Matsui H, Tabata H. In-plane light polarization in nonpolar M-plane $Cd_xZn_{1-x}O$/ZnO quantum wells. Applied Physics Letters. 2011;**98**:261902(1-3). DOI: 10.1063/1.3603931

[28] Matsui H, Tabata H. In-plane anisotropy of polarized photoluminescence in M-plane (10-10) ZnO and MgZnO/ZnO multiple quantum wells. Applied Physics Letters. 2009;**94**: 161907(1-3). DOI: 10.1063/1.3124243

[29] Matsui H, Tabata H. Critical thickness and lattice relaxation of mg-rich strained $Mg_{0.37}Zn_{0.63}O$ (0001) layers towards multi-quantum wells. Journal of Applied Physics. 2006;**99**:024902(1)-(6). DOI: 10.1063/1.2161422

[30] Matsui H, Saeki H, Kawai T, Sasaki A, Yoshimoto M, Tsubaki M, Tabata H. Characteristics of polarity-controlled ZnO films fabricated using the homoepitaxy technique. Journal of Vacuum Science and Technology. 2004;**22**:2454-2460. DOI: 10.1116/1.792237

[31] Donnelly T, Doggett B, Lunney JG. Pulsed laser deposition of nanostructured Ag films. Applied Surface Science. 2006;**252**:4445-4448. DOI: 10.1016/apsusc.2005.048

[32] Matsuda K, Ito Y, Kanemitsu Y. Photoluminescence enhancement and quenching of single CdSe/ZnS nanocrystals on metal surfaces dominated by Plasmon resonant energy transfer. Applied Physics Letters. 2008;**92**:211911(1-3). DOI: 10.1063/1.2937142

[33] Matsui H, Nomura W, Yatsui T, Ohtsu M, Tabata H. Optical dynamics of energy-transfer from a CdZnO quantum well to a proximal Ag nanostructure. Optics Letters. 2011;**36**:3735-3737. DOI: 10.1364/OL.36.003735

[34] Bai J, Wang T, Sakai S. Influence of the quantum –well thickness on the radiative recombination of InGaN/GaN quantum well structures. Journal of Applied Physics. 2000;**88**:4729-4734. DOI: 10.1063/1.311831

[35] Neretina S, Qian W, Dreaden E, El-Sayed MA, Hughes RA, Preston JS, Mascher P. Nano Letters. Plasmon Field Effects on the Nonradiative Relaxation of Hot Electrons in an Electronically Quantized System: CdTe-Au Core-Shell Nanowires. 2008;**8**:2410

[36] Choong V, Park Y, Gao Y, Wehrmmeister T, Müllen K, Hsieh BR, Tang CW. Dramatic photoluminescence quenching of phenylene vinylene oligomer thin films upon submonolayer Ca deposition. Applied Physics Letters. 1996;**71**:1492-1494. DOI: 10.1063/1.116918

[37] Neretina S, Qian W, Dreden E, El-Sayed MA, Hughes RA, Preston JS, Mascher P. Plasmon field effects on the nonradiative relaxation of hot electrons in an electronically quantized system: CdTe-au core-shell nanowires. Nano Letters. 2008;**8**:2410-2418. DOI: 10.1021/nl801303g

[38] Kos Š, Achermann M, Klimov VI, Smith DL. Different regimes of Förster-type energy transfer between an epitaxial quantum well and a proximal monolayer of semiconductor nanocrystals. Physical Review B. 2005;**71**:205309(1-8). DOI: 10.1103/PhysRevB71.205309

[39] Blumstengel S, Sadofev S, Xu C, Puls J, Henneberger F. Converting Wannier into Frenkel excitons in an inorganic/organic hybrid semiconductor nanostructure. Physical Review Letters. 2006;**97**:237401(1-4). DOI: 10.1103/PhysRevLett97.237401

[40] Haridas M, Tripathi LN, Basua JK. Photoluminescence enhancement and quenching in metal-semiconductor quantum dot hybrid arrays. Applied Physics Letters. 2011;**98**:063305(1-3). DOI: 10.1063/1.3553766

Chapter 6

Recent Developments on Metal Nanoparticles for SERS Applications

Tanujjal Bora

Additional information is available at the end of the chapter

http://dx.doi.org/10.5772/intechopen.71573

Abstract

Surface-enhanced Raman spectroscopy (SERS) is a popular and potential area of investigation in many applications because of its high sensitivity even at mono-molecular level. SERS substrates that typically composed of metal nanostructures can enhance the Raman signal level up to several orders of magnitude, making it a powerful analytical tool in chemical and biomedical applications. The present book chapter is aimed to provide insight about design and latest developments on metal nanoparticles and their application in the field of SERS. The chapter starts with the discussion of basic concept and theories of Raman scattering and SERS based on examples from recent research. It then primarily reviews various potential metallic nanostructures and their geometry as SERS substrates, followed by recent reports and theories on application of bimetallic nanostructures for the purpose. Toward the end, we briefly discuss the research progress in designing hybrid SERS substrates using emerging materials like photonic crystals and graphene.

Keywords: SERS, Raman spectroscopy, plasmonic materials, vibrational spectroscopy, metal nanostructures, electromagnetic enhancement

1. Introduction

Raman spectroscopy is a type of vibrational spectroscopy which is based on inelastic scattering of photons from a chemical or biological molecule, causing changes in the scattered photon frequency that is proportional to the difference in the vibrational energy levels in the molecule. It can therefore give us various information about the target molecule, like chemical composition and structure of the molecule, its surface information including surface or interfacial reactions, impurity identification and so on [1, 2]. The phenomenon of Raman scattering was discovered in 1928 by Sir Chandrasekhara Venkata Raman, for which he received Nobel prize in physics in 1930. In his discovery, he observed that certain molecules scatter a small portion

of incident light at a different frequency, where the scattering is therefore inelastic type and the energy difference between the incident and scattered light is proportional to the vibrational frequency of the molecule [3]. Although he used sunlight to explain his discovery, modern day Raman spectroscopy uses high energy monochromatic laser light to excite samples.

Figure 1 illustrates the Raman effect in terms of an incident laser light and the vibrational energy levels of a sample. Once the incident light hit the sample, the energy can be absorbed, transmitted or scattered by the sample. The major portion of the scattered light from the sample carry same frequency (ω_{inc}), representing the Rayleigh scattering effect. However, about one in every million photons scatter inelastically from the sample with an energy different from the incident energy, representing the Raman scattering effect. This energy difference (ω_{vib}) is associated with the molecular vibrations of the sample and is unique for every molecule resulting in exclusive Raman spectrum for each sample providing precise spectral fingerprint of the samples [2]. Inelastically scattered photons typically carries lower frequencies ($\omega_{inc} - \omega_{vib}$) which are called as '*Stokes scattering*'. However, if the molecular vibrational states are significantly excited with high energy, then the inelastic scattering can occur at higher frequencies ($\omega_{inc} + \omega_{vib}$) than the incident frequency. In that case, the vibrational frequency gets added to the incident frequency and is called as '*anti-Stokes scattering*'.

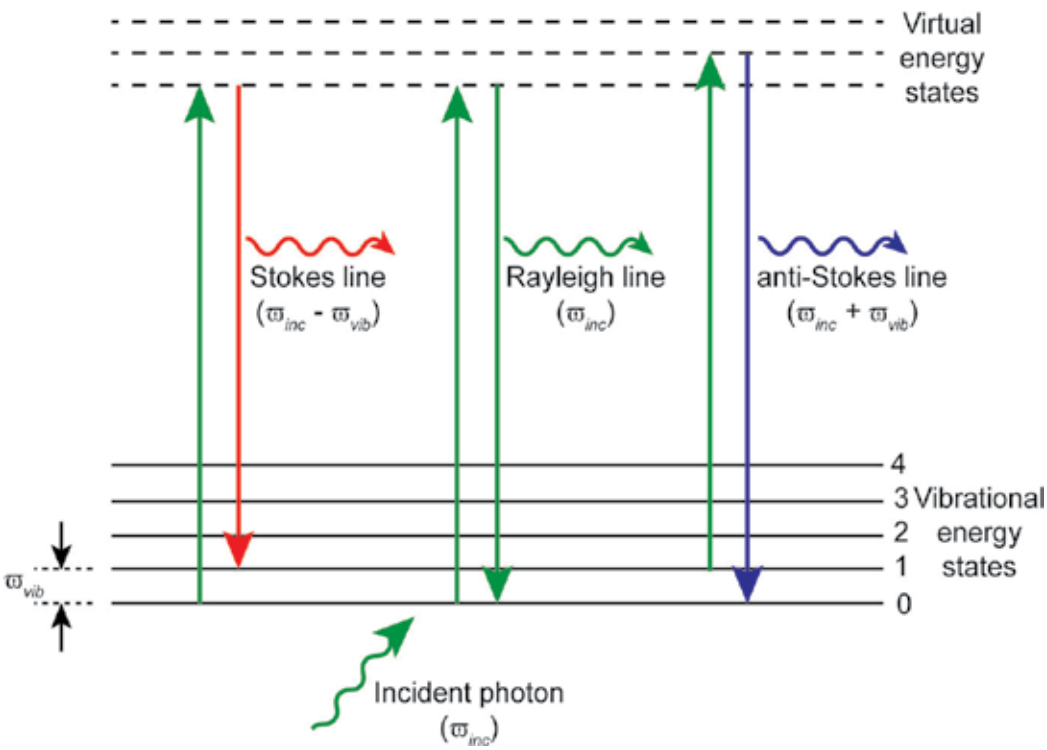

Figure 1. Schematic representation of the concept of Rayleigh, Stokes and anti-Stokes scattering when an incident photon with frequency ω_{inc} interacts with a sample molecule with vibrational frequency ω_{vib}. In the case of Stokes scattering, the molecule absorbs energy resulting in the reduction in the scattered energy, while for anti-Stokes scattering, the molecule loses energy resulting in an increased in the scattered energy.

Since only a small fraction of incident photons show inelastic scattering, the Raman signal is therefore a very weak signal which sometimes can be very difficult to detect even by using latest detector technologies available till date. Therefore, a new technique was developed in 1973 by Martin Fleischmann, Patrick J. Hendra and A. James McQuillan at the University of Southampton, UK to enhance the Raman signal of a molecule by adsorbing it onto a rough metallic surface. Since the technique is surface sensitive, it was termed as '*surface-enhanced Raman scattering*' or '*surface-enhanced Raman spectroscopy*' (SERS). However, the mechanism behind SERS was explained independently by two research groups later in 1977. Van Duyne and coworkers linked the Raman signal enhancement to an electromagnetic effect, while Creighton and coworkers proposed a charge transfer mechanism for the enhancement [4].

At the beginning, this chapter will briefly discuss the SERS mechanism based on both the proposed routes, followed by discussions on some recent developments in applications of noble metal nanostructures in terms of SERS signal enhancement. Toward the end, the chapter will also briefly touch upon some emerging nonmetallic materials which have potential SERS applications.

2. Principle of SERS

The mechanism behind SERS enhancement is always an area of interest for several researchers to understand and explain the phenomena. There are two commonly accepted theories which were proposed and demonstrated by various groups [4, 5]. The first one is the electromagnetic (EM) enhancement and the second one is chemical enhancement. In any cases, samples are typically placed on or at a proximity of a nanostructured metallic substrate, known as SERS substrate, where the enhancement occurs as a result of the interaction among the incoming light, the target sample molecule and the metallic surface. Nanostructures of noble metals, such as silver and gold, are common examples for SERS substrates since they do not have any Raman active modes for themselves.

The EM enhancement occurs when excitation of localized surface plasmon resonance (LSPR) modes of the metallic nanostructures occur at the resonance frequency of the incoming light, which can be considered as an EM wave [6]. At this condition, localized dipoles are created resulting in an enhancement in the localized electric field around the metal nanostructure (**Figure 2a**). The magnitude of such induced dipoles is dependent on the incident electric field strength (E_{inc}) and the polarizability of the metal structure (α_{metal}) [7]. The enhanced localized electric field around the metal nanostructure then interacts with the sample molecule placed near the metallic surface and results in another induced dipole in the target molecule. The induced dipole in the target molecule has three possible dipole components: a dipole with similar angular frequency (ω_{inc}) as the incident EM radiation, a second component with slightly lower angular frequency ($\omega_{inc} - \omega_{vib}$) than the incident EM radiation, and a third component with slightly higher angular frequency ($\omega_{inc} + \omega_{vib}$) than the incident EM radiation, where the difference in the angular frequencies in the last two components are proportional to the vibrational energy of the molecule. These three components therefore correspond to the Rayleigh, Stokes, and anti-Stokes scattering, respectively.

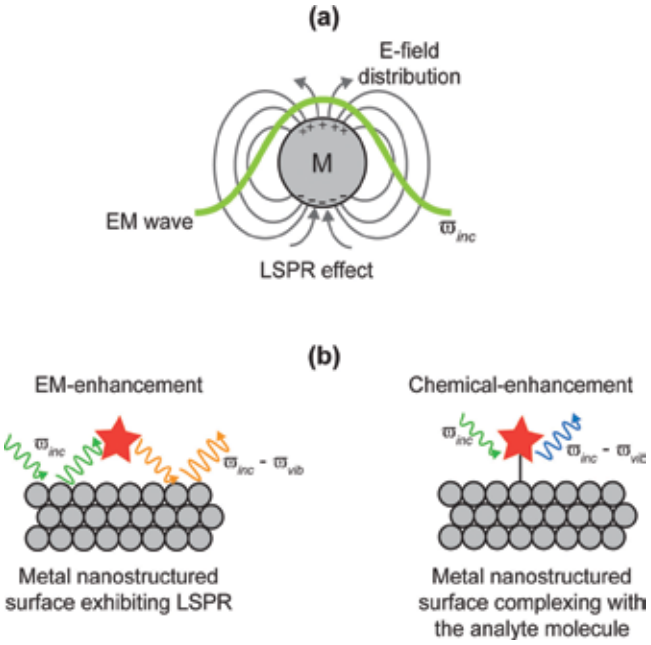

Figure 2. (a) Localized surface plasmon resonance (LSPR) effect exhibited by a metal nanoparticle (M) in the presence of an electromagnetic wave (EM wave) with frequency ω_{inc} resonating with the plasmon frequency. (b) SERS enhancement mechanism showing both electromagnetic (left) and chemical (right) enhancement of the scattering signal. In chemical enhancement, formation of substrate-analyte complex takes place leading to a change in the polarizability of the analyte molecule.

The chemical enhancement, on the other hand, involves enhancement through charge transfer mechanism between the substrate and the target molecule (**Figure 2b**) [8, 9]. Upon chemisorption of target molecules on the metallic substrate, new electronic states are formed having possible intermediate energies resonating with the resonance frequency of the metal. Under resonance, exchange of charges occurs between the substrate and the molecule resulting an enhancement in the Raman signal. However, chemical enhancement mechanism is molecule specific and typically shows lower enhancement factor (in the order of 10^3–10^5) compared to the EM enhancement, where the enhancement can be in the order of 10^8–10^{12} [10].

The SERS enhancement factor (EF_{SERS}) is therefore one of the major aspect to characterize SERS effect or a SERS substrate. The total enhancement factor is normally contributed by both the EM and chemical enhancements. The most widely used mathematical form for EF_{SERS} is given as:

$$EF_{SERS} = \frac{I_{SERS}/N_s}{I_{RS}/N_V} \tag{1}$$

In Eq. (1), I_{SERS} denotes the intensity of the specific Raman band of the target molecule adsorbed on a SERS substrate, I_{RS} is the intensity of the same Raman band of the target molecule without any SERS effect, and N_S and N_V represents the average number of molecules in the scattering volume for the SERS and non-SERS Raman measurements, respectively. An

in-depth comprehensive study about the SERS enhancement factors considering several overlooked issues was reported by Ru et al. [10].

3. Preparation of SERS substrates

It is now clear that SERS enhancement is dependent on the interaction between the target molecule and SERS substrate. Therefore, preparation of the SERS substrate is crucial for the success of the SERS enhancement. The SERS enhancement is mainly contributed by EM enhancement, which is highly dependent on the size, shape and structure of the material used to prepare the substrate. Typically, nanostructured plasmonic materials, like gold (Au), silver (Ag) and copper (Cu), are used for the preparation of SERS substrates. However, application of Cu is limited since the material show oxidation problem in air. Gold and silver are, on the other hand, most widely used due to their high stability compared to copper and most importantly they have LSPR frequencies in the visible to NIR range where most of the Raman scattering occurs. In this part, we will therefore briefly describe the application of some of the promising plasmonic noble metals for SERS substrates.

3.1. Nanoparticles of plasmonic metals

Nanoparticles of noble metals are most commonly used materials for the preparation of SERS substrates, because of their LSPR properties. These properties are useful only when the materials are in nanoscale, that is, less than 100 nm in dimensions. Several papers are now available reporting the synthesis and development of noble metal nanostructures focusing on their tailored shapes and sizes for SERS applications. Colloidal monodisperse metal nanoparticles show high SERS enhancement due to the controlled size and shape of the nanoparticles. A systematic study on colloidal Ag nanostructures with sizes ranging from 60 to 100 nm showed dependency of the SERS enhancement on the shape and size of the nanoparticles [11]. It was found that EF_{SERS} improves with the increasing size of the nanoparticles from 60 to 100 nm, while cubical nanoparticles with sharp edges produced EF_{SERS} in the order of 10^5 when compared to the EF_{SERS} of almost spherical Ag nanoparticle (in the order of 10^4). The shape dependency of the EF_{SERS} is mainly due to the concentrated nonuniform electric field density (hot spots) near the sharp edges of the cubical Ag nanoparticle, whereas in case of the spherical nanoparticles the field spreads over the surface uniformly. For example, it has been shown that the strength of the hot spots can be altered by varying the shape of the colloidal nanoparticles from spherical to anisotropic shapes [12]. It was found that a spherical nanoparticle exhibits weak hot spot compared to an anisotropic particle resulting in improved EF_{SERS} from 10^4 to 10^7 making the anisotropic particles suitable for single molecule detection. The authors have also demonstrated that more anisotropy or higher aspect ratio of such colloidal metal nanoparticles can further improve the EF_{SERS} [13]. An enhancement factor as high as 10^{14} was also reported by using aggregated colloidal Ag nanoclusters [14, 15]. SERS application of colloidal gold (Au) nanoparticles was also explored by many researchers. The cost of gold is on the higher side compared to Ag, and gold typically results in moderate EF_{SERS} compared to Ag nanoparticles. However, Au has excellent biocompatible properties, which makes it a

suitable SERS candidate for biological samples. SERS properties of Au nanoparticles with different sizes (10–200 nm) and shapes (spherical, triangles, hexagons and pentagons) has been studied by Quester et al. [16]. Similarly, Liu et al. [17] has reported a laser irradiation rapid synthesis route of various shaped colloidal gold nanoparticles for SERS applications (**Figure 3**). Using the nanospheres of Au nanoparticles, they have successfully demonstrated detection of Rhodamine 6G (R6G) dyes at concentration levels as low as 10^{-11} M.

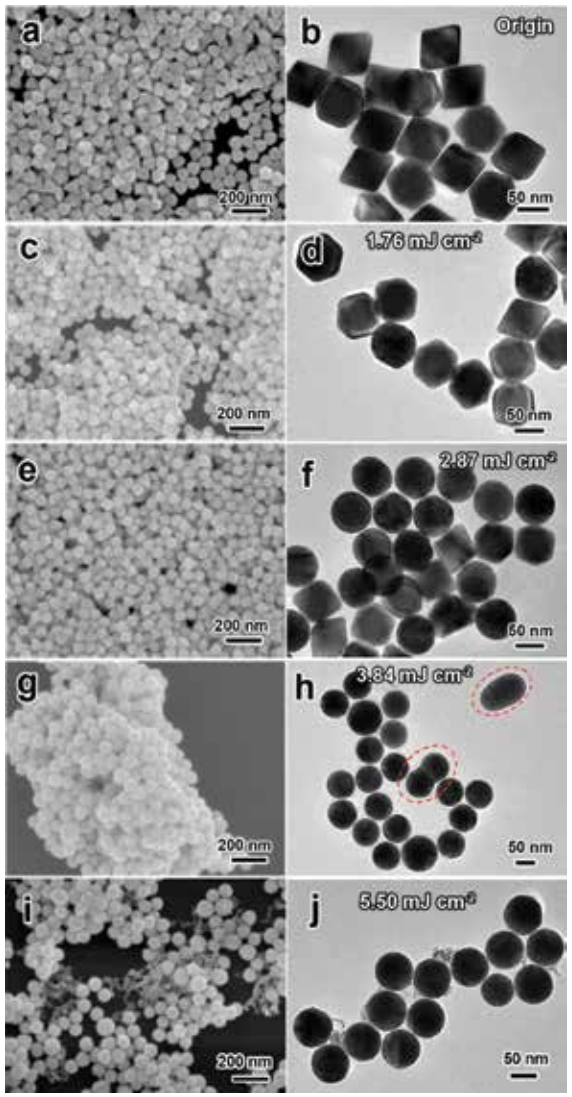

Figure 3. SEM and TEM micrographs of laser irradiated various shaped colloidal SERS Au nanoparticles. Au nanoparticles were prepared by a polyol route at 195 °C. (a, b) original octahedral nanoparticles and nanoparticles in (c, d), (e, f), (g, h) and (i, j) were irradiated with a Nd: YAG laser (532 nm, pulse duration: 10 s) operated at 20 Hz with laser fluences equal to 1.76, 2.87, 3.84 and 5.50 mJ.cm^{-2} respectively. Reprinted by permission from Macmillan Publishers Ltd.: Scientific Reports [17], copyright 2015.

The size of the metal nanoparticles also is another crucial factor contributing to the SERS enhancement. It is well known that for LSPR effect, the size of the metal nanoparticles should be comparable to or smaller than the wavelength of the incident light. However, at very small size the nanoparticles start to show poor polarization resulting in loss of LSPR properties, making them inoperable for SERS applications [18]. A recent study on the size effect of Ag nanoparticles on SERS showed reduction (in the order of 10^2) in the signal EF_{SERS} when particle size was reduced from about 65 to 35 nm [19]. Earlier, similar observations were reported for gold nanoparticles as well [20].

3.2. Bimetallic nanoparticles

As the name suggests, the bimetallic nanoparticles are composed of two types of metals atoms in various configurations. These bimetallic nanoparticles are not only interesting for SERS point of view, but also for their other tunable properties like catalytic, optical, and magnetic properties. There are two common configurations of bimetallic nanoparticles used for SERS applications, namely alloyed and core-shell nanoparticles. In the alloyed configuration, the two types of metals are mixed homogeneously at their atomic level and hence the surface of the nanoparticle contains both the metal atoms. The EF_{SERS}, in case of bimetallic nanoparticles, is dependent on both the composition and ratio of the bimetallic nanoparticle [21–24]. Alloyed Ag-Au hollow nanocubes have been reported by Li et al. [25] for SERS applications with EF_{SERS} in the order of 10^7, which was found to vary with varying configuration of the alloyed nanostructure (**Figure 4**). Sun et al. [26] has reported significant enhancement in the SERS signal for Au-Pd bimetallic flower shaped nanoparticles compared to the similar sized spherical Au-Pd nanoparticles. Application of Au-Pd alloyed nanoparticles for SERS with high EF_{SERS} was also reported. Lee et al. [27] has reported synthesis of hexagonal shaped Au-Pd alloyed nanoparticles with {110} facets exposed at the surface and demonstrated SERS enhancement at least twice than the regular spherical Au-Pd alloyed nanoparticles. It was proposed that the {110} facets of the hexagonal Au-Pd nanoparticles provide higher SERS activity through preferential adsorption of certain molecules at the {110} facets. On the other hand, Liu et al. [28] has reported nanoporous Au-Pd nanoparticles with enhanced SERS activity compared to the traditional Au based SERS substrates.

The core-shell bimetallic nanoparticles, on the other hand, have inhomogeneous distribution of the two metals, where one metal termed as *core* is completely surrounded by another metal termed as *shell*. Hence, only the shell metal is exposed at the surface of the core-shell nanoparticle. Both single and bimetallic core-shell nanoparticles have been reported for SERS applications [29]. In case of the single metallic core-shell nanoparticles, the core is primarily a plasmonic metal nanoparticle, such as Ag or Au, coated with a thin shell layer of non-plasmonic materials, such as silica. In such configuration, the plasmonic core is protected from degradation by the non-plasmonic shell which normally exhibits high chemical stability. Although the single metallic core-shell nanoparticles are not bimetallic system, they are still core-shell type nanoparticles exhibiting excellent SERS properties. An ultrathin silica or alumina shell coating on Au nanoparticles were reported to show significant improvement in the Raman signal [30]. Authors have demonstrated both contact and non-contact SERS modes for these core-shell nanoparticles, and showed that the thin shell layer isolates the plasmonic metal nanoparticle from the probed molecules preventing any unwanted

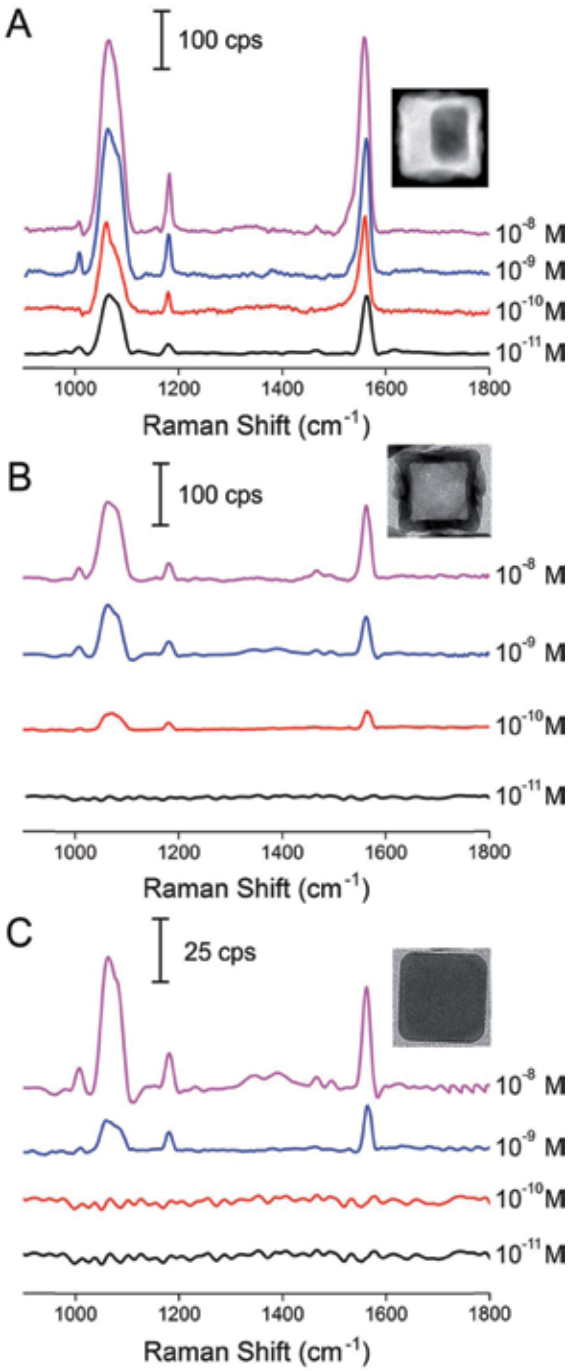

Figure 4. SERS spectra of 1,4-benzenedithiol in ethanol at various concentrations. (A) Hollow nanobox, (B) hollow nanocubes and (C) solid nanocubes of alloyed Ag-Au bimetallic nanoparticles are used as SERS substrate where hollow alloyed nanostructures exhibited improved EF_{SERS} compared to the solid alloyed particles. Reproduced and adapted from Ref. [25] with permission of The Royal Society of Chemistry.

interaction between the molecules and the nanoparticles. The mechanism of these shell-isolated nanoparticle-enhanced Raman spectroscopy (SHINERS) modes is shown in **Figure 5**. They have also shown successful detection of pesticides on fruits by using these SHINERS core-shell nanoparticles. Bimetallic Au-Ag core-shell nanoparticles are also widely studied for SERS applications. Non-spherical nanoparticles, such as core-shell Au-Ag cuboids and dumbbells were reported by Khlebtsov et al. [31] with EF_{SERS} in the order of 10^6. SERS application of Au-Ag core-shell nanoparticles for DNA and RNA detection was also reported by Cao et al. [32] with detection limit as low as 20 fM. Au-SiO_2 core-shell nanoparticles were used by Zavaleta et al. [33] as SERS tags for bioimaging applications. Transition metal coated Au cores (Au@TM; TM = Pt, Pd, Rh, Ru, Co, Ni) are reported for determining the structure of interfacial water adsorbed on transition metal surface [34]. The use of Au-SiO_2, Ag-C, Au-Ag type core-shell nanoparticles as SERS substrates for food safety applications have been reported as well [35–37].

3.3. Anisotropic plasmonic nanostructures

As described in Section 3.1, anisotropic metal nanostructures enhance the localized electric field resulting in improved SERS signal enhancement. Especially, nanorods or nanowire-shaped metal nanostructures are mostly preferred since they also exhibit surface plasmon polariton (SPP) propagation along the metal-surrounding interface. Template assisted bundled Ag nanowires were reported for SERS detection by Lee et al. [38] and demonstrated ~50-fold increase in the signal intensity for benzenethiol (BT) used as a Raman probe. The enhancement was attributed to the hot spots created at the tips of the Ag nanowires, where most of the probe

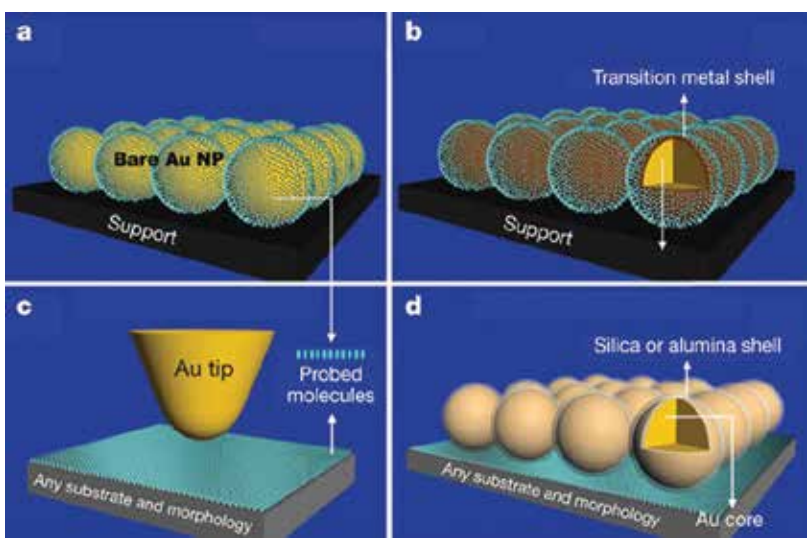

Figure 5. Working mechanism of four types of SERS substrates where small dots represent the probed molecules. (a) Bare Au nanoparticles with probed molecules directly adsorbed to their surfaces, (b) Au core and transition metal shell nanoparticles with probed molecules directly adsorbed to the shell surface, (c) Au tip enhanced Raman probe in non-contact mode and (d) SHINERS: shell-isolated mode preventing the direct contact of the plasmonic core with the probed molecules. Reprinted by permission from Macmillan Publishers Ltd.: Nature Letters [30], copyright 2010.

molecules were adsorbed. Another strategy for preparing monolayers of Ag nanowires using Langmuir-Blodgett (L-B) technique was reported by Tao et al. [39]. In both the cases, the goal was to obtain closely packed Ag nanowires and form hot spots in the region of close contact. The template-assisted method resulted in almost vertically standing Ag nanowires, while L-B method, which is a relatively less complex method, provided a bed of horizontally aligned monolayer of Ag nanowires. The EF_{SERS} for these robust solid substrates was in the order of 10^9 against R6G as probe molecules, which was mainly due to the strong coupling of EM fields among the monolayered Ag nanowires. Another well-ordered assembly of Ag nanowires was reported by Liu et al. [40] by flowing the nanowires through a glass capillary tube, which then demonstrated as a robust, portable and reusable SERS substrate with significant signal enhancement (**Figure 6**). Au nanorods with various aspect ratio were also reported for SERS applications, mostly in the biosensing areas, such as SERS imaging of tumor cells and photothermal heating therapy [41].

Other types of anisotropic nanostructures, such as nanoprism, nanostar, nanosheets of plasmonic metals have also been investigated as SERS substrate by several researchers [42–45]. Due to the presence of corners, edges or branches, such nanostructures always exhibit strong EM enhancement. Highly branched concave nanostructures of bimetallic Au-Pd were reported for their improved catalytic and SERS properties [46]. SERS application of Ag nanoprism and factors affecting its enhancement factors were investigated by Ciou et al. [47]. They presented three possibilities that contribute to the total SERS enhancement in case of the Ag nanorpism. They were namely higher target molecule adsorption, improved SPR resonance in the nanoprism with the excitation laser compared to the regular spherical Ag nanoparticles and presence of Ag nanoclusters along with the nanoprisms.

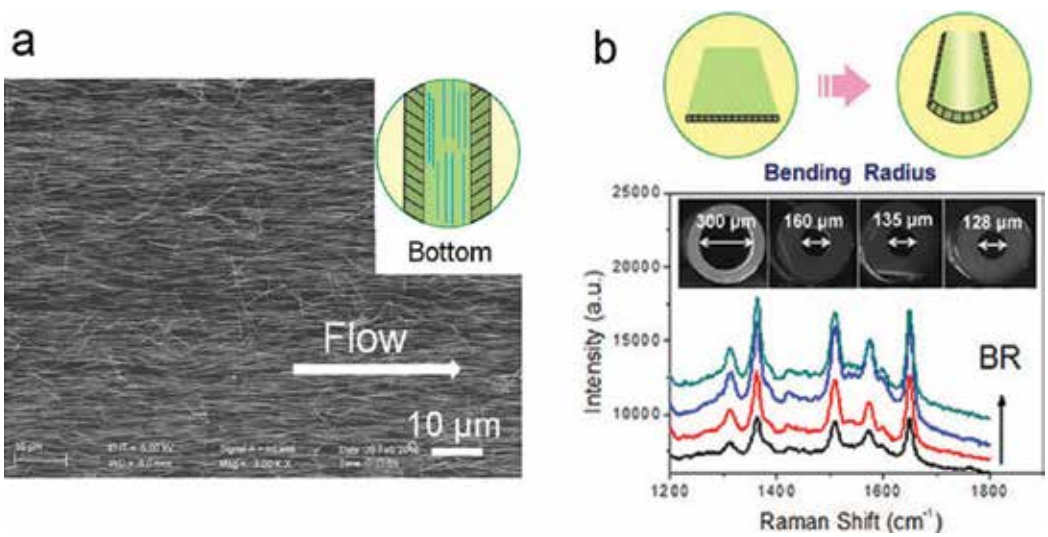

Figure 6. (a) SEM micrographs of highly ordered Ag nanowires assembly in a capillary tube and (b) SERS enhancement of Rhodamine 6G as probed molecule and the ordered Ag nanowires as substrates with respect to the bending radius of the capillary tube. The EF_{SERS} was observed to improve with increasing bending radius of the tubes. Reprinted by permission from Macmillan Publishers Ltd.: Scientific Reports [40], copyright 2012.

3.4. Patterned SERS substrates

While a significant development is taking place in the areas of solution processed SERS substrate preparations, reports on preparation of SERS substrates using non-solution processed techniques to directly transfer patterns on a surface are also surfacing. For example, lithographic techniques are widely used these days to produce highly sensitive, stable and reproducible SERS substrates [48–50]. One of the major advantages for lithographic techniques is the precise control over the geometry and arrangement of the nanostructured substrates, which is crucial for enhanced SERS signal. In this regard, electron beam (E-beam) lithography was employed to produce Au nanostructures showing the highly dependency of the SERS enhancement factors on the geometry and arrangement of the nanostructures [51]. Van Duyne and coworkers [52–54] have invented a novel nanosphere lithography (NSL) technique to produce metallic nanotriangle patterns (**Figure 7**). In their technique, a self-assembled monolayer of similar sized metal nanospheres on a substrate was used a mask and then a thin layer of metal film (such as Au or Ag) was deposited in the gaps using evaporation or vapor phase techniques. The mask layer was then removed by simply applying ultrasonic vibration resulting in regularly spaced triangular shaped metallic patterns which showed EF_{SERS} up to single molecule detection level. In a separate study, Dinish and coworkers [55] compared the performance of SERS substrates fabricated by NSL and deep UV lithography techniques and reported superior SERS enhancement for the NSL fabricated SERS substrates. Combining electroless plating with island lithography technique, Green and Liu [56] has fabricated nanopillars of silver on Si substrate with EF_{SERS} in 10^7 orders. They have also observed dependency of the SERS signal on the surface coverage of the nanopillars, and concluded that the SERS sites must be larger than the area occupied by the adsorbed molecules. Nanolithography was also employed to fabricate silver-based SERS substrates for single molecule detection applications [57].

Periodic metallic structures and plasmonic gratings are also reported to exhibit SERS enhancement. A two-dimensional finite array of Au nanopatches was investigated by Grande et al. [58] reporting EF_{SERS} near 10^5. A narrow groove (sub 15 nm) plasmonic nano-grating was also proposed for SERS applications [59]. However, application of such SERS substrate is limited due to their low EF_{SERS} which is in the range of 10^4–10^5.

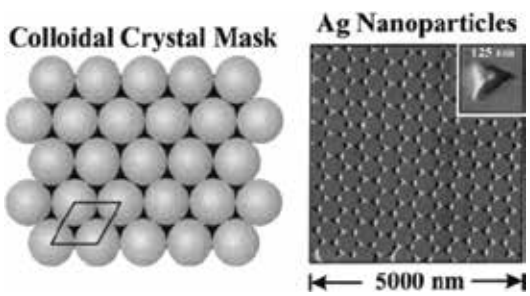

Figure 7. Schematic representation (left) and real AFM image (right) of highly ordered Ag nanotriangles as SERS substrates fabricated by using nanosphere lithography (NSL) technique. Reprinted and adapted with permission from Ref. [52]. Copyright (2001) American Chemical Society.

4. Nontraditional SERS substrates

When traditional plasmonic materials are widely used for SERS substrates, few researchers also started to explore other possible nontraditional materials to prepare SERS substrates. Photonic crystal fibers with embedded metal nanoparticles as a potential SERS substrate were reported [60, 61]. The coverage density of the plasmonic metal nanoparticle in these fibers is the key for the successful SERS applications of such configurations. Zhao et al. [62] has reported significant increasing of the electromagnetic field in amorphous Si photonic crystals embedded in multiple metallo-dielectric units. Sensitivity level of such systems is found to be up to picomolar concentration levels of probe molecules. Another photonic crystal SERS substrate composed of plasmonic SiO_2 nanotubes deposited on silicon nitride substrates was demonstrated by Xu et al. [63], exhibiting almost 10 times higher Raman signal intensities (see **Figure 8**).

Single sheet of carbon atoms, known as graphene was also explored as a potential SERS substrate [64, 65]. For graphene no evidence of EM enhancement is reported, and SERS enhancement is

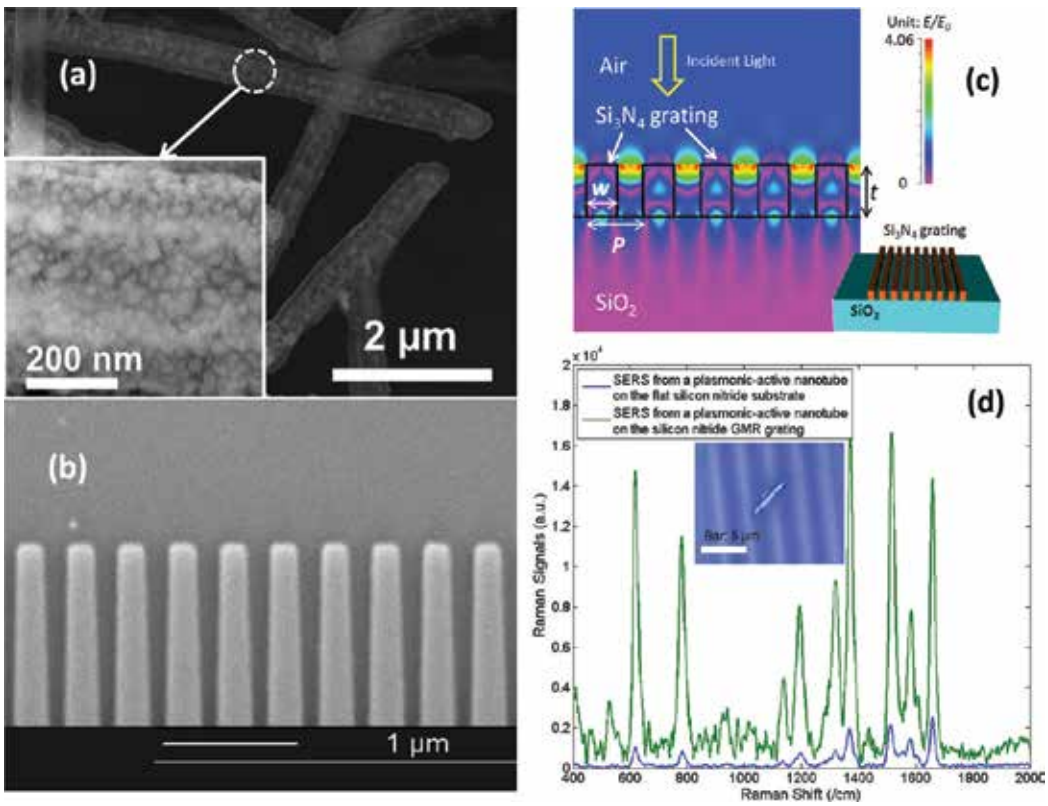

Figure 8. SEM micrographs of (a) plasmonic SiO_2 nanotubes and (b) Si_3N_4 GMR grating used to fabricate the hybrid photonic crystal-based SERS substrates with high sensitivity. (c) TM mode E-field distribution in the GMR grating showing the hot spots at 532 nm excitation and (d) Raman signal from Rhodamine 6G with (high intensity signal) and without (low intensity signal) the Si_3N_4 GMR gratings. Reprinted and adapted from Ref. [63], with the permission of AIP Publishing.

therefore mainly contributed by the chemical enhancement route exhibiting EF_{SERS} in the order of 10^3. To further improve the EF_{SERS}, Wang et al. [66] prepared a composite of Au and graphene by depositing Au nanoparticles on graphene sheets. A strong resonance energy transfer from gold to graphene was evidenced suggesting their potential use for SERS at low concentrations of probed molecules.

Chemically enhanced SERS using semiconductor TiO_2 nanoparticles was also explored by Musumeci et al. [67] reporting an EF_{SERS} in 10^3 range. A slightly improved EF_{SERS} (in the range of 10^4–10^5) was reported for CdSe/ZnBeSe semiconductor quantum dots [68]. InAs/GaAs based SERS substrates were first reported by Quagliano [69] with an EF_{SERS} of 10^3. EF_{SERS} in the order of 10^4 was also reported for 3 nm CdTe nanoparticles [70]. However, in all these cases the overall EF_{SERS} was low due to the lack of EM enhancement in the SERS substrates, and contribution only from the chemical enhancement mechanism. Further work is therefore underway to improve the EF_{SERS} of these nontraditional SERS materials mainly due to advantage of their low preparation cost.

5. Conclusions

Without any doubt, SERS is a very powerful technique in various fields such as biomedical, material science, pharmaceutical, and even sensor application. With the emergence of nanotechnology as an enabling technology, applications of noble metal nanostructures with remarkable optoelectrical properties for SERS applications becomes a major area of R&D, which is not only limited to the synthesis of plasmonic nanostructures for SERS substrates, but also includes patterning of surfaces at nanoscale to enhance the effect. Challenges are there in terms of producing highly sensitive, large area robust and reusable SERS substrates with low-cost fabrication techniques. This chapter highlighted some of the numerous developments happening in this area, exhibiting wide range of SERS substrates available to date.

Author details

Tanujjal Bora

Address all correspondence to: tbora@ait.asia

Nanotechnology, School of Engineering and Technology, Asian Institute of Technology, Klong Luang, Pathumthani, Thailand

References

[1] Dieing T, Hollricher O, Toporski J. Confocal Raman Microscopy. 1st ed. Berlin: Springer; 2010. 292 p. DOI: 10.1007/978-3-642-12522-5

[2] Ferraro JR, Nakamoto K, Brown CW. Introductory Raman Spectroscopy. 2nd ed. Amsterdam: Academic Press; 2003. 434 p. DOI: 10.1016/B978-0-12-254105-6.50020-2

[3] Gardiner DJ, Graves PR. Practical Raman Spectroscopy. 1st ed. Berlin: Springer; 1989. 157 p. DOI: 10.1007/978-3-642-74040-4

[4] Stiles PL, Dieringer JA, Shah NC, Van Duyne RP. Surface-enhanced Raman spectroscopy. Annual Review of Analytical Chemistry. 2008;**1**:601-626. DOI: 10.1146/annurev.anchem.1.031207.112814

[5] Jensen L, Aikens CM, Schatz GC. Electronic structure methods for studying surface-enhanced Raman scattering. Chemical Society Reviews. 2008;**37**:1061-1073. DOI: 10.1039/b706023h

[6] Brown RJC, Wang J, Milton MJT. Electromagnetic modelling of Raman enhancement from nanoscale structures as a means to predict the efficacy of SERS substrates. Journal of Nanomaterials. 2007;**2007**:12086. DOI: 10.1155/2007/12086

[7] Schlücker S. Surface-enhanced Raman spectroscopy: Concepts and chemical applications. Angewandte Chemie International Edition. 2014;**53**:4756-4795. DOI: 10.1002/anie.201205748

[8] Campion A, Ivanecky JE, Child CM, Foster M. On the mechanism of chemical enhancement in surface-enhanced Raman scattering. Journal of the American Chemical Society. 1995;**117**:11807-11808. DOI: 10.1021/ja00152a024

[9] Campion A, Kambhampati P. Surface-enhanced Raman scattering. Chemical Society Reviews. 1998;**27**:241-250. DOI: 10.1039/a827241z

[10] Le Ru EC, Blackie E, Meyer M, Etchegoin PG. Surface enhanced Raman scattering enhancement factors: A comprehensive study. The Journal of Physical Chemistry C. 2007;**111**:13794-13803. DOI: 10.1021/jp0687908

[11] McLellan JM, Siekkinen A, Chen J, Xia Y. Comparison of the surface-enhanced Raman scattering on sharp and truncated silver nanocubes. Chemical Physics Letters. 2006;**427**:122-126. DOI: 10.1016/j.cplett.2006.05.111

[12] ECL R, Etchegoin PG. Single-molecule surface-enhanced Raman spectroscopy. Annual Review of Physical Chemistry. 2012;**63**:65-87. DOI: 10.1146/annurev-physchem-032511-143757

[13] Boyack R, Le Ru EC. Investigation of particle shape and size effects in SERS using T-matrix calculations. Physical Chemistry Chemical Physics. 2009;**11**:7398-7405. DOI: 10.1039/b905645a

[14] Kneipp K, Wang Y, Kneipp H, Perelman LT, Itzkan I, Dasari RR, Feld MS. Single molecule detection using surface-enhanced Raman scattering (SERS). Physical Review Letters. 1997;**78**:1667-1670. DOI: 10.1103/PhysRevLett.78.1667

[15] Nie S, Emory SR. Probing single molecules and single nanoparticles by surface-enhanced Raman scattering. Science. 1997;**275**:1102-1106. DOI: 10.1126/science.275.5303.1102

[16] Quester K, Avalos-Borja M, Vilchis-Nestor AR, Camacho-López MA, Castro-Longoria E. SERS properties of different sized and shaped gold nanoparticles biosynthesized under different environmental conditions by *Neurospora crassa* extract. PLoS One. 2013;**8**:e77486. DOI: 10.1371/journal.pone.0077486

[17] Liu D, Li C, Zhou F, Zhang T, Zhang H, Li X, Duan G, Cai W, Li Y. Rapid synthesis of monodisperse Au nanospheres through a laser irradiation-induced shape conversion, self-assembly and their electromagnetic coupling SERS enhancement. Scientific Reports. 2015;**5**:7686. DOI: 10.1038/srep07686

[18] Ko H, Singamaneni S, Tsukruk VV. Nanostructured surfaces and assemblies as SERS media. Small. 2008;**4**:1576-1599. DOI: 10.1002/smll.200800337

[19] He RX, Liang R, Peng P, Norman Zhou Y. Effect of the size of silver nanoparticles on SERS signal enhancement. Journal of Nanoparticle Research. 2017;**19**:267. DOI: 10.1007/s11051-017-3953-0

[20] Krpetić Ž, Guerrini L, Larmour IA, Reglinski J, Faulds K, Graham D. Importance of nanoparticle size in colorimetric and SERS-based multimodal trace detection of Ni(II) ions with functional gold nanoparticles. Small. 2012;**8**:707-714. DOI: 10.1002/smll.201101980

[21] Kim K, Kim KL, Choi J-Y, Lee HB, Shin KS. Surface enrichment of Ag atoms in Au/Ag alloy nanoparticles revealed by surface-enhanced Raman scattering of 2,6-dimethylphenyl isocyanide. The Journal of Physical Chemistry C. 2010;**114**:3448-3453. DOI: 10.1021/jp9112624

[22] Jiang Z, Zhang Q, Zong C, Liu B-J, Ren B, Xie Z, Zheng L. Cu-Au alloy nanotubes with five-fold twinned structure and their application in surface-enhanced Raman scattering. Journal of Materials Chemistry. 2012;**22**:18192-18197. DOI: 10.1039/c2jm33863g

[23] Amendola V, Scaramuzza S, Litti L, Meneghetti M, Zuccolotto G, Rosato A, Nicolato E, Marzola P, Fracasso G, Anselmi C, Pinto M, Colombatti M. Magneto-plasmonic Au-Fe alloy nanoparticles designed for multimodal SERS-MRI-CT imaging. Small. 2014;**10**:2476-2486. DOI: 10.1002/smll.201303372

[24] Amendola V, Scaramuzza S, Agnoli S, Polizzi S, Meneghetti M. Strong dependence of surface plasmon resonance and surface enhanced Raman scattering on the composition of Au-Fe nanoalloys. Nanoscale. 2014;**6**:1423-1433. DOI: 10.1039/c3nr04995g

[25] Li J-M, Yang Y, Qin D. Hollow nanocubes made of Ag-Au alloys for SERS detection with sensitivity of 10^{-8} M for melamine. Journal of Materials Chemistry C. 2014;**2**:9934-9940. DOI: 10.1039/c4tc02004a

[26] Sun D, Zhang G, Jiang X, Huang J, Jing X, Zheng Y, He J, Li Q. Biogenic flower-shaped Au-Pd nanoparticles: Synthesis, SERS detection and catalysis towards benzyl alcohol oxidation. Journal of Materials Chemistry A. 2014;**2**:1767-1773. DOI: 10.1039/c3ta13922k

[27] Lee YW, Kim M, Kang SW, Han SW. Polyhedral bimetallic alloy Nanocrystals exclusively bound by {110} facets: Au–Pd rhombic dodecahedra. Angewandte Chemie International Edition. 2011;**50**:3466-3470. DOI: 10.1002/anie.201007220

[28] Liu H, Yang Q. Facile fabrication of nanoporous Au-Pd bimetallic foams with high catalytic activity for 2-nitrophenol reduction and SERS property. Journal of Materials Chemistry. 2011;**21**:11961-11967. DOI: 10.1039/c1jm10109a

[29] Li J-F, Zhang Y-J, Ding S-Y, Panneerselvam R, Tian Z-Q. Core–shell nanoparticle-enhanced Raman spectroscopy. Chemical Reviews. 2017;**117**:5002-5069. DOI: 10.1021/acs.chemrev.6b00596

[30] Li JF, Huang YF, Ding Y, Yang ZL, Li SB, Zhou XS, Fan FR, Zhang W, Zhou ZY, WuDe Y, Ren B, Wang ZL, Tian ZQ. Shell-isolated nanoparticle-enhanced Raman spectroscopy. Nature. 2010;**464**:392-395. DOI: 10.1038/nature08907

[31] Khlebtsov BN, Liu Z, Ye J, Khlebtsov NG. Au@Ag core/shell cuboids and dumbbells: Optical properties and SERS response. Journal of Quantitative Spectroscopy and Radiative Transfer. 2015;**167**:64-75. DOI: 10.1016/j.jqsrt.2015.07.024

[32] Cao YC, Jin R, Mirkin CA. Nanoparticles with Raman spectroscopic fingerprints for DNA and RNA detection. Science. 2002;**297**:1536-1540. DOI: 10.1126/science.297.5586.1536

[33] Zavaleta CL, Smith BR, Walton I, Doering W, Davis G, Shojaei B, Natan MJ, Gambhir SS. Multiplexed imaging of surface enhanced Raman scattering nanotags in living mice using noninvasive Raman spectroscopy. In: Proceedings of the National Academy of Sciences; 11 August 2009. USA: PNAS; 2009. p. 13511-13516

[34] Jiang Y-X, Li J-F, D-Y W, Yang Z-L, Ren B, J-W H, Chow YL, Tian Z-Q. Characterization of surface water on Au core Pt-group metal shell nanoparticles coated electrodes by surface-enhanced Raman spectroscopy. Chemical Communications. 2007;**0**:4608-4610. DOI: 10.1039/b711218a

[35] Li J-F, Anema JR, Wandlowski T, Tian Z-Q. Dielectric shell isolated and graphene shell isolated nanoparticle enhanced Raman spectroscopies and their applications. Chemical Society Reviews. 2015;**44**:8399-8409. DOI: 10.1039/c5cs00501a

[36] Chen L-M, Liu Y-N. Surface-enhanced Raman detection of melamine on silver-nanoparticle-decorated silver/carbon nanospheres: Effect of metal ions. ACS Applied Materials & Interfaces. 2011;**3**:3091-3096. DOI: 10.1021/am200603y

[37] Yang D, Zhou H, Ying Y, Niessner R, Haisch C. Surface-enhanced Raman scattering for quantitative detection of ethyl carbamate in alcoholic beverages. Analytical and Bioanalytical Chemistry. 2013;**405**:9419-9425. DOI: 10.1007/s00216-013-7396-x

[38] Lee SJ, Morrill AR, Moskovits M. Hot spots in silver nanowire bundles for surface-enhanced Raman spectroscopy. Journal of the American Chemical Society. 2006;**128**:2200-2201. DOI: 10.1021/ja0578350

[39] Tao A, Kim F, Hess C, Goldberger J, He R, Sun Y, Xia Y, Yang P. Langmuir−Blodgett silver nanowire monolayers for molecular sensing using surface-enhanced Raman spectroscopy. Nano Letters. 2003;**3**:1229-1233. DOI: 10.1021/nl0344209

[40] Liu J-W, Wang J-L, Huang W-R, Yu L, Ren X-F, Wen W-C, Ordering Ag YS-H. Nanowire arrays by a glass capillary: A portable, reusable and durable SERS substrate. Scientific Reports. 2012;**2**:987. DOI: 10.1038/srep00987

[41] Wang Y, Yan B, Chen L. SERS tags: Novel optical Nanoprobes for bioanalysis. Chemical Reviews. 2013;**113**:1391-1428. DOI: 10.1021/cr300120g

[42] Yang Y, Zhong X-L, Zhang Q, Blackstad LG, Z-W F, Li Z-Y, Qin D. The role of etching in the formation of Ag nanoplates with straight, curved and wavy edges and comparison of their SERS properties. Small. 2014;**10**:1430-1437. DOI: 10.1002/smll.201302877

[43] Sun Y, Xia Y. Shape-controlled synthesis of gold and silver nanoparticles. Science. 2002;**298**:2176-2179. DOI: 10.1126/science.1077229

[44] Yuan H, Liu Y, Fales AM, Li YL, Liu J, Vo-Dinh T. Quantitative surface-enhanced resonant Raman scattering multiplexing of biocompatible gold nanostars for in vitro and ex vivo detection. Analytical Chemistry. 2013;**85**:208-212. DOI: 10.1021/ac302510g

[45] Yan J, Han X, He J, Kang L, Zhang B, Du Y, Zhao H, Dong C, Wang H-L, Xu P. Highly sensitive surface-enhanced Raman spectroscopy (SERS) platforms based on silver nanostructures fabricated on polyaniline membrane surfaces. ACS Applied Materials & Interfaces. 2012;**4**:2752-2756. DOI: 10.1021/am300381v

[46] Zhang L-F, Zhong S-L, Xu A-W. Highly branched concave Au/Pd bimetallic nanocrystals with superior electrocatalytic activity and highly efficient SERS enhancement. Angewandte Chemie International Edition. 2013;**52**:645-649. DOI: 10.1002/anie.201205279

[47] Ciou S-H, Cao Y-W, Huang H-C, Su D-Y, Huang C-L. SERS enhancement factors studies of silver nanoprism and spherical nanoparticle colloids in the presence of bromide ions. The Journal of Physical Chemistry C. 2009;**113**:9520-9525. DOI: 10.1021/jp809687v

[48] Qin L, Zou S, Xue C, Atkinson A, Schatz GC, Mirkin CA. Designing, fabricating, and imaging Raman hot spots. In: Proceedings of the National Academy of Sciences; 5 September 2006; USA. USA: PNAS; 2006. p. 13300-13303. DOI: 10.1073/pnas.0605889103

[49] Taminiau TH, Stefani FD, Segerink FB, van Hulst NF. Optical antennas direct single-molecule emission. Nature Photonics. 2008;**2**:234-237. DOI: 10.1038/nphoton.2008.32

[50] Mühlschlegel P, Eisler HJ, Martin OJF, Hecht B, Pohl DW. Resonant optical antennas. Science. 2005;**308**:1607-1609. DOI: 10.1126/science.1111886

[51] Weisheng Y, Zhihong W, Yang Y, Longqing C, Ahad S, Kimchong W, Xianbin W. Electron-beam lithography of gold nanostructures for surface-enhanced Raman scattering. Journal of Micromechanics and Microengineering. 2012;**22**:125007. DOI: 10.1088/0960-1317/22/12/125007

[52] Haynes CL, Van Duyne RP. Nanosphere lithography: A versatile nanofabrication tool for studies of size-dependent nanoparticle optics. The Journal of Physical Chemistry B. 2001;**105**:5599-5611. DOI: 10.1021/jp010657m

[53] Hulteen JC, Treichel DA, Smith MT, Duval ML, Jensen TR, Van Duyne RP. Nanosphere lithography: Size-tunable silver nanoparticle and surface cluster arrays. The Journal of Physical Chemistry B. 1999;**103**:3854-3863. DOI: 10.1021/jp9904771

[54] Zhang X, Yonzon CR, Van Duyne RP. Nanosphere lithography fabricated plasmonic materials and their applications. Journal of Materials Research. 2006;**21**:1083-1092. DOI: 10.1557/jmr.2006.0136

[55] Dinish US, Agarwal A, Yaw FC, Olivo M. Comparison of the performance of SERS substrates fabricated by deep UV lithography and nanosphere lithography. In: XXII International Conference on Raman Spectroscopy; 8-13 August 2010; Boston. AIP Conference Proceedings; 2010. p. 956-956. DOI: 10.1063/1.3482911

[56] Green M, Liu FM. SERS substrates fabricated by island lithography: The silver/pyridine system. The Journal of Physical Chemistry B. 2003;**107**:13015-13021. DOI: 10.1021/jp030751y

[57] Coluccio ML, Das G, Mecarini F, Gentile F, Pujia A, Bava L, Tallerico R, Candeloro P, Liberale C, De Angelis F, Di Fabrizio E. Silver-based surface enhanced Raman scattering (SERS) substrate fabrication using nanolithography and site selective electroless deposition. Microelectronic Engineering. 2009;**86**:1085-1088. DOI: 10.1016/j.mee.2008.12.061

[58] Grande M, Bianco GV, Vincenti MA, Stomeo T, Dd C, Vittorio MD, Petruzzelli V, Scalora M, Bruno G, D'Orazio A. Experimental surface-enhanced Raman scattering response of two-dimensional finite arrays of gold nanopatches. Applied Physics Letters. 2012;**101**:111606. DOI: 10.1063/1.4752719

[59] Dhawan A, Canva M, Vo-Dinh T. Narrow groove plasmonic nano-gratings for surface plasmon resonance sensing. Optics Express. 2011;**19**:787-813. DOI: 10.1364/oe.19.000787

[60] Han Y, Tan S, Oo MKK, Pristinski D, Sukhishvili S, Du H. Towards full-length accumulative surface-enhanced Raman scattering-active photonic crystal fibers. Advanced Materials. 2010;**22**:2647-2651. DOI: 10.1002/adma.200904192

[61] Yan H, Gu C, Yang C, Liu J, Jin G, Zhang J, Hou L, Yao Y. Hollow core photonic crystal fiber surface-enhanced Raman probe. Applied Physics Letters. 2006;**89**:204101. DOI: 10.1063/1.2388937

[62] Zhao Y, Zhang X-J, Ye J, Chen L-M, Lau S-P, Zhang W-J, Lee S-T. Metallo-dielectric photonic crystals for surface-enhanced Raman scattering. ACS Nano. 2011;**5**:3027-3033. DOI: 10.1021/nn2001068

[63] Xu X, Hasan D, Wang L, Chakravarty S, Chen RT, Fan DL, Wang AX. Guided-mode--resonance-coupled plasmonic-active SiO_2 nanotubes for surface enhanced Raman spectroscopy. Applied Physics Letters. 2012;**100**:191114. DOI: 10.1063/1.4714710

[64] Xu W, Mao N, Zhang J. Graphene: A platform for surface-enhanced Raman spectroscopy. Small. 2013;**9**:1206-1224. DOI: 10.1002/smll.201203097

[65] Ling X, Xie L, Fang Y, Xu H, Zhang H, Kong J, Dresselhaus MS, Zhang J, Liu Z. Can graphene be used as a substrate for Raman enhancement? Nano Letters. 2012;**10**:553-561. DOI: 10.1021/nl903414x

[66] Wang Y, Ni Z, Hu H, Hao Y, Wong CP, Yu T, Thong JTL, Shen ZX. Gold on graphene as a substrate for surface enhanced Raman scattering study. Applied Physics Letters. 2010;**97**: 163111. DOI: 10.1063/1.3505335

[67] Musumeci A, Gosztola D, Schiller T, Dimitrijevic NM, Mujica V, Martin D, Rajh T. SERS of semiconducting nanoparticles (TiO_2 hybrid composites). Journal of the American Chemical Society. 2009;**131**:6040-6041. DOI: 10.1021/ja808277u

[68] Livingstone R, Zhou X, Tamargo MC, Lombardi JR, Quagliano LG, Jean-Mary F. Surface enhanced Raman spectroscopy of pyridine on CdSe/ZnBeSe quantum dots grown by molecular beam epitaxy. The Journal of Physical Chemistry C. 2010;**114**:17460-17464. DOI: 10.1021/jp105619m

[69] Quagliano LG. Observation of molecules adsorbed on III-V semiconductor quantum dots by surface-enhanced Raman scattering. Journal of the American Chemical Society. 2004;**126**: 7393-7398. DOI: 10.1021/ja031640f

[70] Gu J, Fahrenkrug E, Maldonado S. Analysis of the electrodeposition and surface chemistry of CdTe, CdSe, and CdS thin films through substrate-overlayer surface-enhanced Raman spectroscopy. Langmuir. 2014;**30**:10344-10353. DOI: 10.1021/la502403q

Section 3

Synthesis and Properties of Nanoscale Structures

Chapter 7

Nano- and Micro-Patterning of Gold Nanoparticles on PEG-Based Hydrogels for Controlling Cell Adhesion

Cigdem Yesildag, Zhenfang Zhang, Fang Ren,
Gonzalo de Vicente and Marga C. Lensen

Additional information is available at the end of the chapter

http://dx.doi.org/10.5772/intechopen.71548

Abstract

Gold nanoparticles (Au NPs) have unique and tunable size- and shape-dependent optical and chemical properties and little toxicity. In this chapter, we describe results on Au NPs employed as cell-binding entities at biomaterials' interfaces. Hereby, Au NPs with different sizes and shapes were nano- or micro-patterned on the surface of poly(ethylene glycol) (PEG)-based hydrogels by using our recently developed patterning strategies based on soft lithography. These hybrid biomaterials can be applied in various biological or biomedical applications, such as for fundamental cell studies considering adhesion and migration, tissue engineering, drug delivery, or as biosensors by using surface plasmon resonance (SPR) or surface-enhanced Raman spectroscopy (SERS).

Keywords: gold nanoparticles, poly(ethylene glycol) hydrogels, biomaterials, nano- and micro-patterning, (wet) deprinting, cell adhesion

1. Introduction

In this chapter, an introduction to gold nanoparticles (Au NPs) and the applicability of them in biomaterials research as nanocomposites in combination with poly(ethylene glycol) (PEG)-based hydrogels, particularly for cell adhesion studies, will be introduced. First, Au NPs are described, with emphasis on their unique size- and shape-dependent properties; next, insight into the world of biomaterials is provided; lastly, our unique nano- and micro-patterning strategies of Au NPs on PEG-hydrogel surfaces will be explained, with the aim of controlling specific bio-interactions, for example, cell adhesion.

1.1. Gold nanoparticles

Colloidal gold particles have already been used in the seventeenth century because of their fascinating, different colors ranging from purple, green, blue to golden-yellow. They were mostly applied for decoration purposes of glass-ware or church windows. The first scientific literature on the field of gold colloids was published by Michael Faraday in June 1852, while he was studying light effects on thin gold films; he discovered nanometer-sized particles suspended in a solvent [1].

Since that time, a vast amount of research about colloidal and nanometer-sized gold nanoparticles (Au NPs) has been undertaken. Gold, as a noble metal, has great characteristics, such as chemical inertness, high stability, non-corrosive nature, and conductivity, which makes it a highly desired material in engineering, materials science, and catalysis. On top of that, Au NPs have unique size- and shape-dependent properties, which make this material even more interesting for nanoscience and nanotechnology, for example, in sensors, biomedical applications, catalysis, and optical technologies. While gold particles are chemically inert, they do have high binding affinity toward thiol groups or other sulfur-based entities, and also toward phosphoric or amino groups with less binding energy [2–4]. These properties allow the Au NPs to be easily functionalized with different desired molecules, which have the mentioned functional groups. In that way, Au NPs can be easily tuned for their specific application.

The size- and shape-dependent optical characteristics of Au NPs originate from localized surface plasmons [2, 3]. The surface plasmons are excited by the interaction of light (electromagnetic wave) with the electron clouds of the metallic particles (see **Figure 1**).

Au NPs exhibit localized surface plasmons, which are in the visible range of the electromagnetic spectrum. Different sizes or shapes of Au NPs make them appear in different colors to human eyes. The UV–Vis absorption wavelengths range from around 515 nm for the smallest Au NPs to higher wavelength with increasing sizes. Other shapes of Au NPs have different absorption bands in a UV–Vis spectrum. For example, rod-like Au NPs (Au nanorods) exhibit

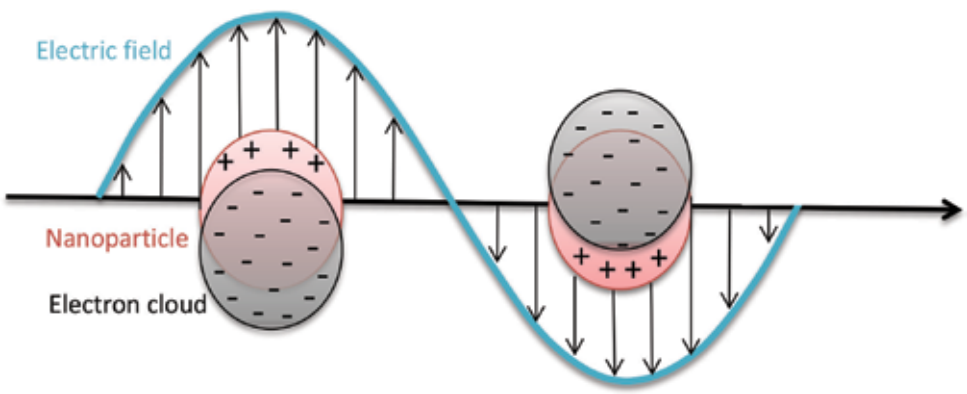

Figure 1. Surface plasmon effect of nanoparticles.

two absorption maxima. This occurs because of the correlation of the light or electromagnetic wave with the longitudinal part (longer part) of the particles and also with the transversal part (shorter part) of the Au nanorods, which appears as two different maxima in the same spectrum [5, 6]. Other shapes of Au NPs such as cubic, trihedral, decahedral, tetragonal, and so on, correlate according to the shape differently with the light, so each shape shows characteristic plasmon peaks in the UV–Vis spectra. In Section 2.1 (*vide infra*), a number of absorption spectra are depicted, corresponding to Au NPs that we synthesized with different sizes and shapes.

Au NPs have also the advantage that they are less toxic in comparison to other metallic particles. That is also why they can be applied in biological or biomedical applications [4]. We did discover recently, however, that some Au NPs with small sizes (e.g., 4.5 nm Au NPs spheres) or specific stabilizing agents, for example, cetyl trimethyl ammonium bromide (CTAB), do cause cytotoxic effects. Nevertheless, this makes them still applicable, for example, for selective killing of cancer cells [7, 8].

For biological systems, particles that exhibit surface plasmons in the IR range (around >700 nm) of the electromagnetic spectrum are highly desired, because in that region the biological tissues are transparent for this light and the light can go into deeper regions without hindrance, which is known as the optical biological window [9]. In this respect, rather large spherical Au NPs, for example, larger than 100 nm, or other shapes are interesting. Especially, Au nanorods are highly promising in this field because as mentioned before, they exhibit two localized plasmon stages: one in the wavelength at around 520 nm and the other one in the IR range depending on the length or aspect ratio of the particles. In that way, the Au NPs can be, for example, locally heated even above around 100°C by irradiation of the particles with IR-light source. This property of the Au NPs is used for photothermal therapy for killing unhealthy tissues and cancer cells. This is an alternative and less invasive cancer-healing method in comparison with the commonly used radiotherapy or chemotherapy [9]. Not only for photothermal therapy but also due to the high electron density of Au NPs, they are as useful as contrast agents for X-rays, magnetic resonance imaging (MRI), or other diagnostic devices. The optical properties of the Au NPs make them also useful for spectroscopic devices, especially for surface plasmon resonance spectroscopy (SPR) or surface-enhanced Raman spectroscopy (SERS). Based on these spectroscopic devices, many biosensor applications are conceivable [2].

Another promising application of Au NPs discussed in this chapter is in the area of fundamental cell adhesion studies. In our research, the respective Au NPs are patterned on bio-inert surfaces, namely on poly(ethylene glycol) (PEG)-based hydrogels (which will be further specified in the next section), and cell adhesion behavior of murine fibroblasts on the as-prepared nanocomposite biomaterial is investigated. The idea is that the specifically patterned Au NPs acted as anchor points for cell adhesion, and the particular micro- and nanoscale dimensions are investigated for their effectiveness to control cell behavior [10–12]. This goal is schematically depicted in **Figure 2**.

Such *in vitro* studies of fibroblast cell adhesion offer the possibility to get more insight into integration of implants or wound-healing processes and lead to develop novel biomaterials for applications in tissue engineering and regeneration. More information about biomaterials and an introduction into the basic phenomena at the bio-interfaces are given subsequently.

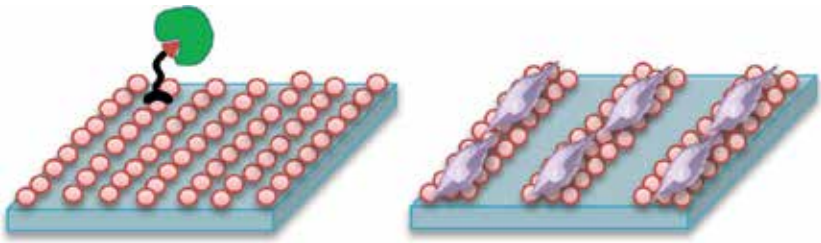

Figure 2. Nano- and micro-patterning of Au NPs on PEG-hydrogels for controlled binding of biomolecules and whole cells.

1.2. Biomaterials

In 1987, Williams defined biomaterials as "A biomaterial is a nonviable material used in a (medical) device, intended to interact with biological systems" [13]. Biomaterials are mainly used for implants [14, 15], prostheses [15], wound healing or tissue regeneration [16, 17], repairing or supporting materials [15, 18], and in biochips [19–21], which interact with biological fluids and can be used, for example, as biosensors [19, 21–24]. Biomaterials can be organic or inorganic in nature, for example, consisting of natural or synthetic polymers, metals, or ceramics, and may be composed of more than one type of nanomaterial or nanocomposite. Examples for polymeric biomaterials are hydrogels: hydrophilic polymeric networks which can adsorb huge amounts of water, without being dissolved and are similar to natural tissue scaffolds. That is why they are favorably used for biological tissue engineering, drug delivery, or cell biological research [25, 26]. In addition, combined hybrid or nanocomposite biomaterials, where the polymeric biomaterials are enriched with natural or inorganic nanoparticles, also offer novel, unique, and multifunctional properties for various biological applications.

Biomaterials contact and interact with biological systems at what is called the bio-interface [15, 27, 28]. Hence, there are several requirements for biomaterials not to elicit unwanted foreign body responses, such as inflammation reactions. The cyto-compatibility of biomaterials can be tested by several, standardized cytotoxicity tests. Also, the long-term stability or biodegradability may be important factors to consider. Before designing and fabricating new and improved biomaterials, the fundamental interactions at the bio-interface need to be understood. Therefore, it is important to realize that cell-substrate interactions are usually preceded by protein adsorption, which may be nonspecific, but could be predicted. Thus, controlling the initial protein adsorption is key to control specific bio-interaction, for example, cell adhesion.

Depending on the application, the interaction of cells with a biomaterial needs to be adherent or non-adherent. For example, biomaterials which are intended to be applied to interact with blood vessels, such as stents or artificial heart valves, should not be adhesive in order to avoid thrombosis effects [29]. Other biomaterials, which are designed for tissue regeneration, should enable specific cellular adhesion, guide constructive cellular migration, and

promote the proliferation and biosynthesis [30]. Protein adsorption and cell adhesion depend on (and thus can be controlled by) the chemical, physical, and mechanical properties of the bio-interface. These properties are the hydrophilicity, surface charges, anchored specific chemical functional groups or nanoparticles, surface roughness and porosity, nano- or micro-topography, and elasticity.

In order to enable the desired, specific bio-interaction, the nonspecific protein adsorption (NSPA) and unwanted cell adhesion should be suppressed. We have employed poly(ethylene glycol) (PEG)-based hydrogels as inert backgrounds onto which bioactive or adhesive cues (e.g., chemical, physical, or mechanical patterns), both at the micrometer and at the nanometer scale, are fabricated. PEG is a very popular biomaterial, due to its non-toxicity, non-fouling characteristics, and non-immunogenicity and has been widely used for drug delivery in medicine, in pharmacy, cell biological research, and in industry mainly as care products [31]. Nevertheless, even though PEG hydrogels are renowned for their intrinsically anti-adhesive properties toward proteins or cells, surface modifications such as nano- or micro-sized topography, gradient or patterned elasticity or chemical alterations do allow cell adhesion, as we and others have found [32–40].

The strategy to immobilize bio-functionalized Au NPs onto an inert PEG background to enable specific cell adhesion and prevent unwanted bio-interaction has proven to be very feasible and successful, as Spatz has demonstrated in several inspiring publications in the last two decades [41–45]. In his case, the Au NPs with controlled nanometer-sized distances were immobilized on PEG surfaces, bio-functionalized with cyclic RGD (a cell-adhesive peptide), and provided in that way integrin-mediated-binding sides for cell adhesion.

Notwithstanding the elegance and effectiveness of this strategy, we have discovered that the Au NPs do not even need to be specifically bio-functionalized in order to induce cell adhesion; we have observed unprecedented cell adhesion on nanocomposite bio-interfaces of PEG-based hydrogels with (citrate-stabilized) Au NPs [7, 10, 46]. The amount of cell adhesion was found to depend rationally on the density of the Au NPs at the bio-interface, indicating that the Au NPs are effective in enabling cell adhesion. Quite astonishingly, the number of adherent cells was observed to be even higher than on the positive control, tissue culture polystyrene (TCPS) surfaces [10]. We assume that the cell adhesion is promoted by the adsorption of adhesion-mediating proteins from the serum onto the Au NPs at the bio-interface. Besides tuning the density (and thus the average distance between Au NPs), we have strived to make controlled micro- and nano-patterns of Au NPs in order to elucidate which dimensions are critical in controlling cell adhesion and viability. For that, we have recently developed and reported about several novel patterning methodologies based on soft lithographic procedures. Both unpublished and published results will be discussed in the "Results and discussion" section.

1.3. Micro- and nano-patterning methods

Mimicking the characteristics of biological structures, especially micro- or nano-sized patterns of topography, elasticity or chemistry on biomaterials are highly desired in order to

first understand and then control the interaction of proteins, enzymes, or whole cells with bio-interfaces. There are several techniques to create patterned structures on surfaces which mostly rely on lithographic methods using irradiation or soft lithography. With some lithographic methods such as X-ray lithography or electron beam lithography, really small feature sizes of around 10 nm are accessible; if the irradiation energy is further increased, even sub-10-nm sizes can be achieved [47–49]. The drawback of these processes is that they require high-energy sources to modify very small areas during a long time period. By contrast, photolithography can be carried out using less expensive irradiation sources, but the resolution is inherently limited and the feature sizes are typically in the micrometer range. Scanning-probe-based-patterning techniques such as dip-pen lithography are promising methods to get sub-50-nm-sized structures without any irradiation source, but again this process is highly time consuming [50, 51].

Soft lithographic methods are versatile and attractive because of the following advantages: they are relatively cheap as they do not utilize high-energy irradiation sources, it is feasible to pattern large areas in a short period of time, and the processing is quite easy to handle. Micro-contact printing (μ-CP) is a widely used soft lithographic procedure, developed by Whitesides et al., where through stamping procedures with polydimethylsiloxane (PDMS) molecules or particles are transferred from the elastomeric stamp onto flat substrates [52, 53]. With this method, patterns of micrometer dimensions down to 250-nm sizes can be achieved.

In our lab, we have developed a very versatile soft lithographic method employing PEG-based hydrogel molds, which are filled by capillary action with another PEG-hydrogel precursor. With this method, called fill-molding in capillaries (FIMIC), we have successfully fabricated micro-patterns of elasticity and chemistry on PEG-based hydrogels, while the surface is topographically smooth [35, 54]. Those unique bio-interfaces are great platforms to control and study cellular behavior.

As far as nano-patterning is concerned, we have exploited Au NPs, which we either created on a hard substrate (e.g., glass or silicon wafer) by the so-called block copolymer micelle nanolithography method as developed by Glass et al. [41], or synthesized by wet chemistry and then immobilized on hard and soft surfaces (*vide infra*). In the former case, the characteristic, regular spacing between the Au NPs is determined by the length of the block copolymer chains. On top of that, Spatz et al. fabricated aperiodic micrometer-sized patterns by electron beam lithography, which is costly and slow.

We have taken a different approach to make micro-patterns of Au NPs, in that we have developed a micro-contact deprinting method (μ-CdP) where the Au NP-loaded block copolymer micelles were selectively peeled off from the hard substrate by a polystyrene (PS) stamp that was softened after annealing above its glass transition temperature [55]. With this soft lithographic approach, we were able to pattern large areas and even curved ones. Such hierarchical patterns can be transferred to soft hydrogel surfaces, for instance by nanomolding, using the Au NPs as templates to create nano-sized indents on PEG hydrogels [56]. By serendipity, we discovered that we could also transfer the whole pattern of Au NPs from the hard substrate to the soft hydrogel, namely by swelling the hydrogel replica before separating it from the mold. We observed selective cell adhesion to the micro-patterns of Au NPs, which we reasoned

could not be due to the tiny nano-topography. Atomic force microscopy (AFM) revealed that indeed the Au NPs had been transferred. Those yet unpublished results were the incentive of developing our wet micro-contact deprinting (wet μ-CdP) method, among others, which will be described in more detail in this chapter [12].

In addition, we have fabricated unique, hybrid hierarchical patterns, in which we "glued" micrometer-sized bars of PEG hydrogels onto the micro-patterns of Au NPs [57]. This was achieved by what we call "adhesive embossing," which is basically similar to the MIMIC method as developed by Whitesides [58, 59]. Starting from block copolymer micelles is, however, not always practical, since hard substrates are required. That is why, in the most recent years, we have synthesized Au NPs in solution, which can then be deposited on any substrate, including PDMS stamps and soft hydrogels. This advantage has enabled us to develop our own nano-contact printing (n-CP) strategies, for example, using wrinkled PDMS stamps that exhibit nanometer-sized grooves in which the Au NPs can be accumulated prior to the transfer to hydrogels [60, 61]. These results will also be highlighted in this chapter.

Another progress that we explain in the following is the use of multifunctional, reactive hydrogels that facilitate the transfer of Au NPs from hard substrate or stamps. We are currently perfecting such reactive μ-CP strategies and will report on the results soon. Very recently, we have already reported on the nano-contact transfer (n-CT) of Au NPs from silicon to multifunctional PEG hydrogels, in which the hydrogel films were functionalized with thiol-groups to bind strongly to the Au NPs [7, 10].

2. Experimental procedures

2.1. Preparation of Au NPs with different sizes and shapes

Differently sized spherical Au NPs ranging from around 20 nm to around 135 nm were achieved via the kinetically controlled seeding growth procedure according to Puntes et al. [62]. In the SEM images in **Figure 3(a)** and **(b)**, the sizes and structures of the synthesized smaller (20 nm) and larger (50 nm) spherical Au NPs are shown as representative examples. Below the SEM images in **Figure 3**, the respective UV–Vis spectra with the plasmon peaks at around 520–540 nm are shown. Hollow urchin-like particles (Au nanostars) were synthesized using the galvanic reduction effect of gold ions on the surface of sacrificial silver nanoparticles (Ag NPs seeds) [63]. The sizes of the Au nanostars varied between 50 and 150 nm (see **Figure 3(c)**. In some cases longer, rodlike Au nanostar shapes could also be observed, which might be caused by the agglomeration of Ag NP seeds before the addition of gold ions and which might be also the reason for larger-sized spherical particles. In the UV–Vis spectrum in **Figure 3(c)**, the plasmon peak is at 750 nm and also a shoulder peak at 600 nm is observed, which is probably due to the polydispersity of the particle sizes.

Au NPs with different shapes were synthesized by the polyol process [64]. Following this procedure, among others, cubic, tetrahedral, decahedral, icosahedral, trihedral, and platelet Au NPs shapes could be achieved. In **Figure 3(d)**, the SEM image and the UV–Vis spectrum

of decahedral Au NPs are shown as example. The sizes of the particles varied between 70 and 180 nm, and the absorption maximum is found around 590 nm. Au nanorods were synthesized using cetyl trimethyl ammonium bromide (CTAB) as stabilizing agent and 5-brome salicylic acid as structure-directing agent using the seed-mediated growth process [65]. In the SEM image in **Figure 3(e)**, the structure and the UV–Vis spectrum of the Au nanorods are shown: The lengths of the Au nanorods were around 50 nm and the widths were around 15 nm. Expectedly, there were two plasmon peaks which appeared due to the longitudinal and transversal interaction of the light with the Au nanorods.

2.2. Preparation of functional PEG hydrogels

In this study, PEG hydrogels were synthesized from different precursors, for example, linear or star-shaped PEG macromonomers, bearing specific chemical end groups. More specifically, linear PEG macromonomers with a molecular weight of 575 g/mol and eight-arm star-shaped PEG precursors (8PEG) with a molecular weight of ca. 15 kDa were used. PEG macromonomers with acrylate end groups were crosslinked via the UV-photo-crosslinking procedure with 1% of photo-initiator (Irgacure 2959), while 8PEG macromonomers with acrylate or vinyl sulfone end groups could be crosslinked with the addition of ammonia via Michael-type addition reactions as well [66]. Depending on the precursor type (molecular structure, weight, and crosslinking procedure), PEG hydrogels with different network structures and corresponding elastic properties were obtained. Hydrogels from linear PEG precursors with shorter chain length were quite stiff, exhibiting Young's elastic moduli of around 20 MPa in the swollen state, whereas hydrogels from 8PEG precursors were much softer with elasticity values of 0.27 MPa for swollen hydrogels [54, 67].

The great advantage of using 8PEG hydrogels is the fact that for crosslinking, only minimally two out of eight arms are required, and the other (up to six) arms can remain available for

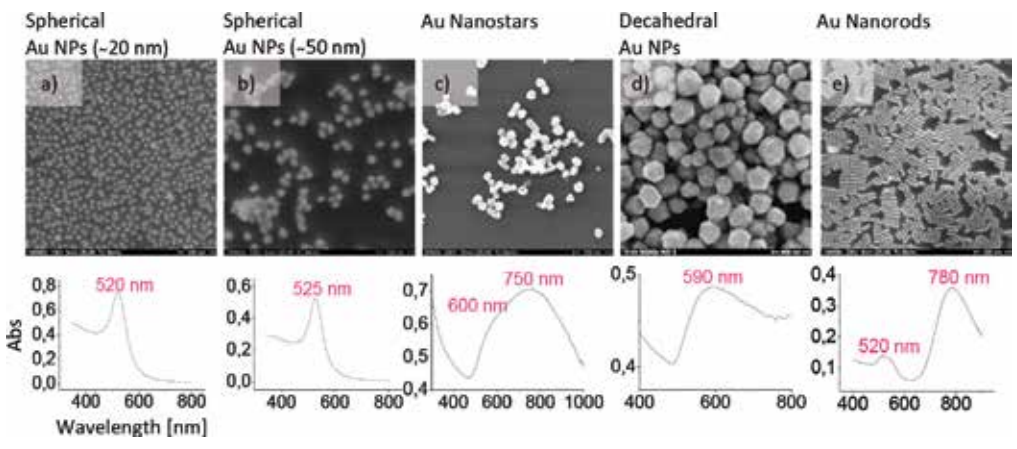

Figure 3. SEM images (top) and respective UV–Vis spectra (below) of Au NPs with different sizes and shapes: (a) smaller spheres ⟨ 20 nm); (b) larger spheres ⟨ 50 nm); (c) Au nanostars; (d) decahedral Au NPs; (e) Au nanorods. Scale bars: (a) 200 nm; (b) 200 nm; (c) 700 nm; (d) 400 nm; (e) 200 nm.

further chemical (multi-)functionalization with various end groups by clever tuning of the reaction conditions [10]. In this work, the incorporation of Au NPs was desired, so the functionalization of the hydrogels surfaces with thiol (SH)-molecules (dithiothreitol (DTT)) has been effectively employed in order to ensure strong chemical interactions between the Au NPs and the PEG hydrogels [10, 11].

2.3. Transfer of Au NPs onto PEG hydrogels

For the aim of obtaining soft, PEG-based hydrogel biomaterials with specific cell adhesion sites, Au NPs can be immobilized on PEG surfaces. Intuitively, one would expect that a covalent binding of the Au NPs with the gel is required, since the Au NPs might otherwise come loose in cell culture. Thus, it is sensible to functionalize the Au NPs with acrylate groups that will covalently link the Au NPs to the acrylate-functionalized PEG-hydrogel precursors, an approach that for instance Spatz' group has reported on. Nevertheless, as was already pointed out in Section 1.3., we have greatly simplified the mechanisms of transferring (patterned) Au NPs from hard substrates to soft, biomimetic hydrogels. For example, by virtue of swelling, no linker molecules are needed at all to transfer Au NPs from solid supports, for example, silicon wafers or glass, onto PEG-based hydrogels [12]. Interestingly, we have observed that the Au NPs are effectively embedded in the PEG hydrogel and do not escape from the bio-interface during cell culture.

Taking advantage of this simple and effective transfer mechanism, we have been able to transfer synthesized (citrate-stabilized) Au NPs from several, different substrates onto PEG hydrogels. Of particular interest is naturally the transfer of micro- or nano-patterns of Au NPs, which can be fabricated on hard substrates or stamps by the various patterning techniques that were introduced, that is, μ-CP and wet μ-CdP, and will be discussed in more detail in the next section.

In the simplest case, the surface of the solid support (glass, silicon wafer, or PDMS stamp) can be functionalized with amino-silane molecules, in order to have some, relatively weak binding of the negatively charged, citrate-stabilized Au NPs. On this Au NPs-coated layer, the acrylated PEG precursor with photo-initiator is added and the UV-photo-crosslinking procedure performed. Thereafter the hydrogel, which is still on the surface of the template with the Au NPs coating, is wetted by some drops of water. After the hydrogel has been fully hydrated, it is separated from the surface while peeling off the Au NPs from the solid support (see **Figure 4**).

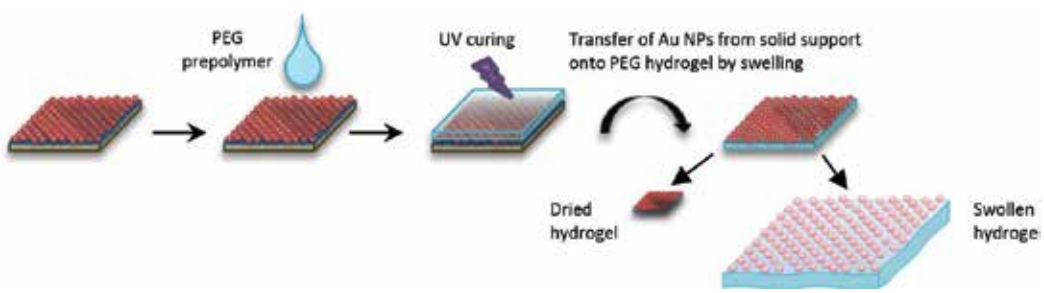

Figure 4. Scheme of transferring Au NPs from solid supports (e.g., silicon wafer or PDMS mold) onto PEG hydrogels by swelling of the hydrogel; size differences of the hydrogels in dry or swollen state. Image adapted from Yesildag et al. [12].

As an alternative to transferring Au NPs by virtue of the hydrogel's swelling property, we can employ (multi)functional or reactive PEG hydrogels to transfer whole (patterns of) Au NPs from a solid support or an elastomeric stamp. This strategy, which is schematically depicted in **Figure 5(a)**, also results in effective immobilization of Au NPs at the bio-interface, which has enabled us to study the effect of the Au NPs density on cell adhesion [10].

In this case, the physical and chemical properties of the hydrogel are of crucial importance for the transfer efficiency [10]. Non-functionalized and rigid hydrogels from linear PEG precursors need to be pressed onto the template in order to transfer maximally around 50–60% of Au NPs onto its surface [61], whereas multifunctional 8PEG hydrogels with thiol-surface functions are able to transfer the Au NPs quantitatively by mere conformal contact of the stand-alone hydrogel with the Au NPs-coated surface (see **Figure 5**).

2.4. Transferring patterns of Au NPs

After having introduced the basic transfer possibilities of the Au NPs from solid supports such as silicon wafers or PDMS molds onto PEG-based hydrogels, in the following, the transfer of micro- or nano-patterns of Au NPs will be discussed. In increasing order of complexity, these are (i) μ-CP of silane agents, (ii) wet micro-contact deprinting [12], and (iii) nano-contact transfer via wrinkled PDMS stamps [61].

2.4.1. Patterning of silane agents

In our experience, amino-silanization of silica-based substrates has proven to be effective in guiding the immobilization of citrate-stabilized Au NPs in a good, homogeneous fashion.

[12, 61]. This knowledge has been applied in fabricating micro-patterns of Au NPs on such substrates, for instance by applying μ-CP of different silanes (adhesive vs. repellent to our Au NPs). This procedure is schematically depicted in **Figure 6**.

In detail, first of all amino-silane molecules were printed on the surface of the silicon wafers using micro-relief-molded PDMS stamps [68]. The remaining, non-stamped areas were kept either non-functionalized or were backfilled with another type of silane, which has less attractive interactions with the Au NPs. While coating of a surface with amino-silanes causes highly

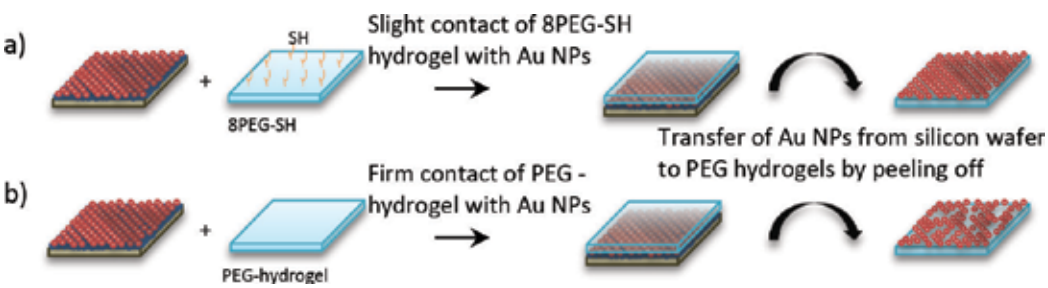

Figure 5. Scheme of transferring Au NPs from solid supports onto PEG hydrogels by contacting the hydrogel; (a) transfer to SH-functionalized 8PEG by slight contact; (b) transfer to non-functionalized linear PEG by firm contact.

http://dx.doi.org/10.5772/intechopen.71548

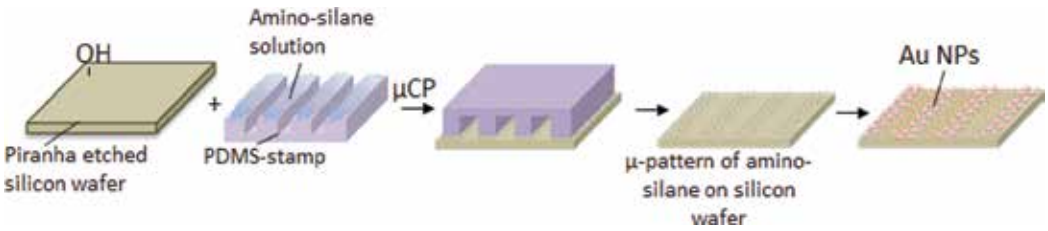

Figure 6. Schematic view of micro-patterning of silanes.

densely packed citrate-capped Au NPs [10, 11, 61] due to electrostatic interactions, backfilling of the remaining area with other silanes (e.g., with end groups: –OH, $–CH_3$, $–CF_3$) minimizes the adhesion of citrate-capped Au NPs. These Au NPs patterns were finally transferred onto PEG-hydrogel surfaces, for instance by virtue of swelling the UV-cured film before peeling it off (**Figure 7**).

As seen in the representative SEM image of the hydrogel after transfer (**Figure 8**), the Au NPs were more densely packed on amino-silane layers and more loosely packed on the other areas. While this procedure is somehow effective, the resolution and contrast of the pattern is not quite satisfactory. For achieving better-defined micro-patterns of Au NPs, we have developed novel patterning strategies, one of which is our recently invented wet μ-CdP method.

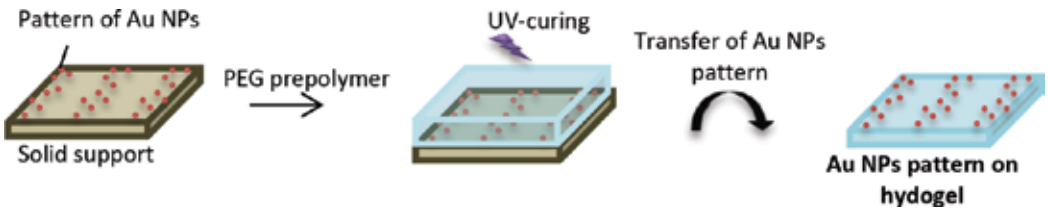

Figure 7. Schematic view of Au NPs pattern transfer from solid supports onto PEG hydrogels.

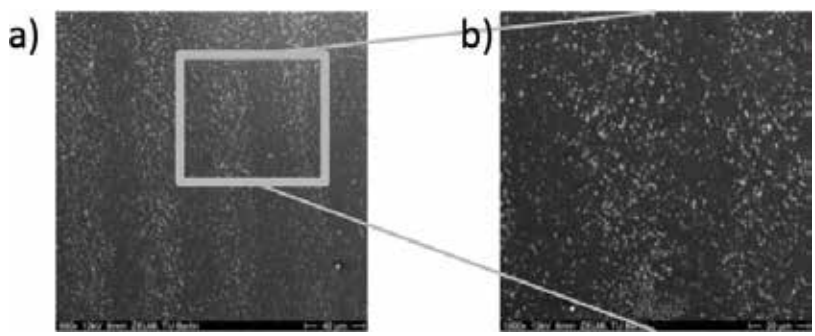

Figure 8. SEM image of Au NPs on PEG hydrogel via μ-CP of different silanes. Scale bars: (a) 40 μm; (b) 20 μm.

2.4.2. Wet micro-contact deprinting

The strategy for the wet micro-contact deprinting (wet μ-CdP) consists of removing Au NPs from defined regions of the silicon wafer by virtue of the swelling effect of the hydrogel. Using this method, well-defined micro-patterns of Au NPs lines (**Figure 9**) and rectangles (**Figure 10**) on solid supports such as silicon wafers can be created, as we recently reported [12]. Again, these resulting patterns could then be transferred from the hard substrate to the soft surface of PEG hydrogels.

In the wet μ-CdP procedure, the first challenge is to create a homogeneous monolayer of Au NPs on silicon wafers. As described earlier, the amino-silanization of silicon wafers has demonstrated to be effective to achieve a good surface coating on which the Au NPs are nicely immobilized. Next, in order to make patterns of the Au NPs, a PDMS mold with micro-sized relief line structures on its surface was placed on the Au NPs-decorated silicon wafer, creating line channels. Subsequently, by capillary action, the thus created channels were filled with the liquid PEG prepolymer and cured under UV light. After UV curing, the PDMS mold was removed, leaving an ordered pattern of PEG micro-stripes on the Au NPs-layered silicon wafer. This step, which we previously denoted "adhesive embossing" [57], is basically what Whitesides et al. coined MIMIC [58].

The novel aspect of the wet μ-CdP procedure is the last step, in which the cured PEG micro-stripes are removed by swelling in water. During the swelling, the Au NPs are taken away by the PEG hydrogel on the area where the stripes had been in contact with the Au NPs surface, while the non-contacted Au NPs are left as well-ordered micro-patterns of Au NPs on the surface of the silicon wafer [12].

In **Figure 11**, SEM images of resulting line patterns of Au NPs on silicon wafers are shown; here, the brighter lines are the Au NPs lines and the darker lines are empty areas on the silicon wafer, where the former Au NPs were deprinted by the PEG-hydrogel micro-stripes. The uptake of the Au NPs by the PEG hydrogel through swelling is so effective that no Au NPs were found on these areas. This method works with different types of Au NPs, for example, in **Figure 11(a)** spherical Au NPs and in (b) Au nanostars had been micro-patterned. Furthermore, using the wet μ-CdP process, rectangular patterns of Au NPs could be achieved as well via repeating the process with the PDMS mold oriented perpendicularly to the first pattern of micro-lines, which is shown in the SEM image in **Figure 11(c)**. In a further step,

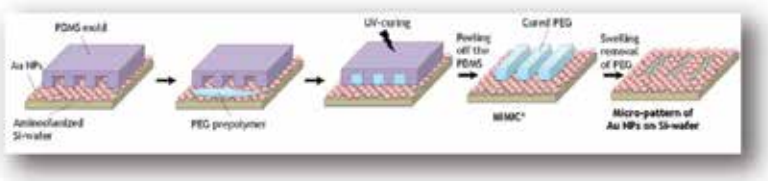

Figure 9. Schematic view of the wet micro-contact deprinting (wet μ-CdP) process for fabricating micrometer-sized line patterns [12].

http://dx.doi.org/10.5772/intechopen.71548

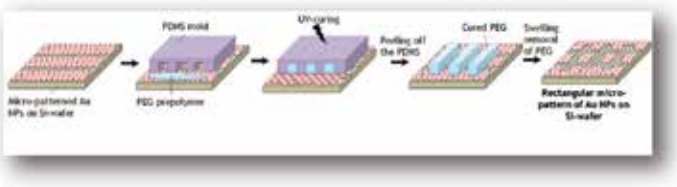

Figure 10. Schematic view of the wet micro-contact deprinting (wet μ-CdP) process for fabricating rectangular patterns [12].

again, the successful micro-patterns of Au NPs could be effectively transferred as a whole from the silicon wafer onto PEG hydrogels, for example, via the wet deprinting method, as illustrated in **Figure 7** (*vide supra*).

On the resulting micro-patterned PEG hydrogels, cell adhesion of murine fibroblasts (L929) was investigated. As can be seen in the optical images in **Figure 12**, fibroblast cells were clearly adhering and aligning only on the darker lines, which in this case correspond to the Au NPs patterns due to the optical contrast, while the non-functionalized PEG hydrogel appears as the brighter lines (see **Figure 12(a)**). Interestingly, in **Figure 12(b)**, the edge of the pattern lines, that is, where the original PDSM mold was not filled, and Au NPs were not removed in the wet μ-CdP process, can be recognized. Even more intriguingly, on this area, where the original, non-patterned layer of Au NPs has been transferred by wet deprinting, the cells were adhering and spreading in apparently random directions, whereas on the patterned lines, the cells were observed to align and elongate along the lines.

Cell adhesion of fibroblasts was also studied on the rectangular patterns of Au NPs on PEG hydrogel as fabricated by the wet μ-CdP method. The results are depicted in **Figure 13**. Similar to the case of the line patterns, it is evident that the fibroblasts preferentially adhere on the Au NPs-patterned areas, while the pure PEG areas are free of cells.

The pattern of the Au NPs rectangles in **Figure 13** had widths of 20 μm and lengths of 25 μm, which is comparable to usual fibroblast sizes of around 10–20 μm for round or little spread cells, so that on some rectangles, one or two cells were sitting next to each other. In a few cases,

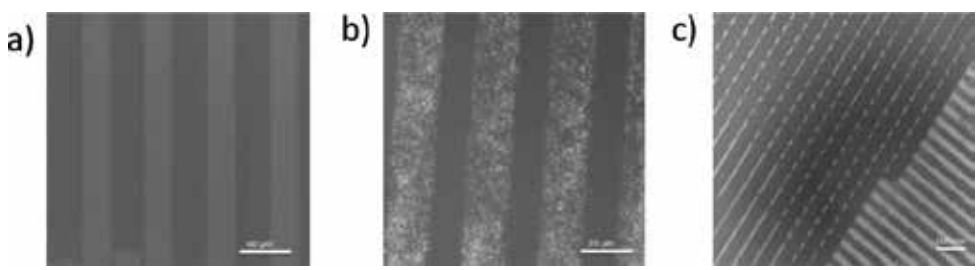

Figure 11. SEM images of Au NP (a–b) lines and (c) rectangular patterns of (a) spherical Au NPs (b) Au nanostars and (c) spherical Au NPs. Scale bars: (a) 40 μm; (b) 20 μm; (c) 100 nm. Image (c) modified from Yesildag et al. [12].

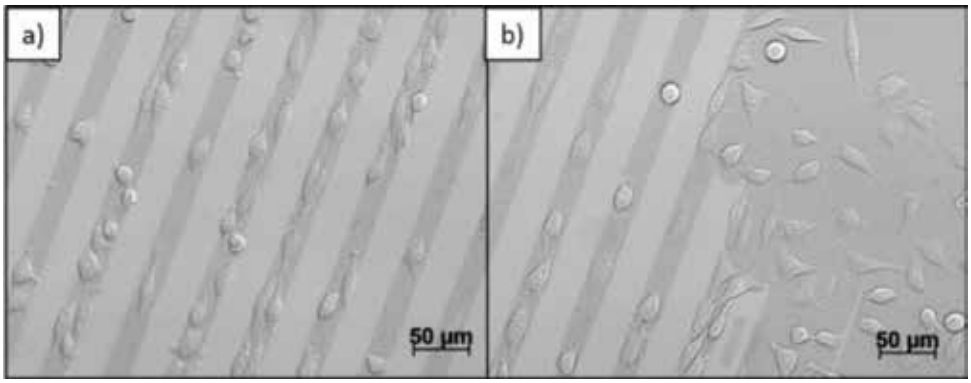

Figure 12. Optical image of fibroblast adhesion on Au NPs-patterned PEG hydrogel. The darker lines correspond to the patterns of Au NPs. Scale bars: 50 µm [12].

even three cells were accommodated in one rectangle of Au NPs. The distances among the rectangles were 10 µm on one side and 25 µm on the other side; on the area with a distance of 25 µm no cells were observable, whereas a separation of the rectangles of 10 µm allowed cells to have contacts with two parallel rectangles at the same time, so that the PEG area in the middle was bridged over by the cells, which can be observed in a few cases in **Figure 13**.

To round up this discussion of the wet µ-CdP results, by using this patterning method, very well-defined Au NPs patterns with line or rectangular shapes on PEG hydrogels could be clearly achieved, so that the cell adhesion could be specifically and precisely controlled. The sizes and distances of the line or rectangular patterns could be further specifically varied for any kinds of applications by tuning of the stamp sizes during the wet µ-CdP process, underlining the versatility of this technique. It is important to note again that no bio-functionalization was required for the effective cell adhesion. Probably, cell adhesion-mediating molecules,

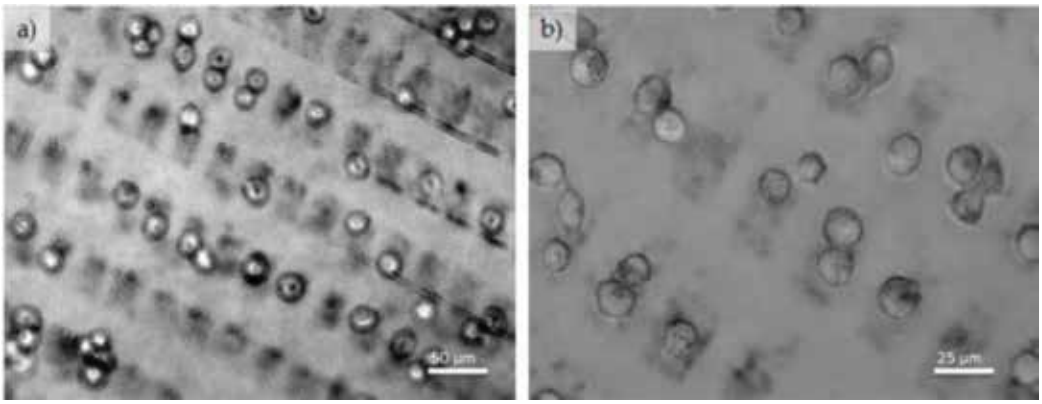

Figure 13. (a–b) Optical images of fibroblast adhesion on an Au NPs-patterned PEG hydrogel exhibiting rectangular patterns of Au NPs. Scale bars: (a) 50 µm; (b) 25 µm [12].

for example, proteins such as fibronectin and vinculin, bind (non-specifically) to the surface of the Au NPs, thereby replacing the citrate molecules. Our observation that without proteins in the medium (serum-free medium), no cell adhesion could be observed supports this assumption. While these well-defined μ-patterns of Au NPs have proven to be very useful to control cell adhesion at predefined areas, for other applications of Au NPs patterns such as in nano-plasmonics and -photonics, nanoscale pattern dimensions are also highly desirable.

2.4.3. Nano-contact transfer via wrinkled PDMS stamps

A simple, yet very effective method to make nano-patterns of Au NPs was invented by Whitesides and perfected by Fery [60, 69]. It takes advantage of the wrinkling that occurs at the surface of an elastomer exhibiting a thin, hard skin, which can be created by plasma treatment of a slab of the elastomer in a stretched conformation, upon relaxation to the original size [60]. We made use of this great invention and modified the PDMS stamp's surface and employed the nano-sized wrinkles for nano-sized patterning of Au NPs on PEG hydrogels by stamping [61].

First of all, wrinkled PDMS stamps were prepared via plasma oxidation of smooth PDMS molds in a stretched configuration and subsequent relaxation of the stamp to the original macroscopic dimensions (see **Figure 14**) [60]. By this wrinkling process, periodic and regular nano-line topographies were achieved on the surface of the PDMS stamps. The characteristic lateral and vertical dimensions appeared to depend in a predictable way on the plasma treatment time and energy. In this case, the distances of the nano-lines (from hill to hill) varied from around 0.3 μm up to around 0.6 μm by choosing a plasma oxidation time of 2 up to 15 min, respectively. Generally, it can be said that the longer the plasma oxidation time, the wider the distances of the line spaces and the deeper the grooves were [61].

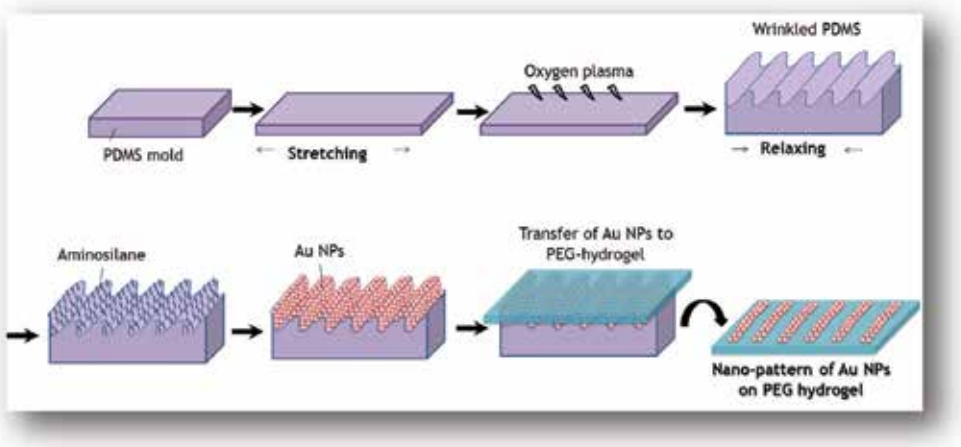

Figure 14. Schematic view of the nano-patterning of Au NPs on PEG hydrogel using wrinkled PDMS stamps [60].

In the next step, the surfaces of the wrinkled PDMS stamps were silanized with amino-silanes. The amino-silanized surfaces were subsequently coated with Au NPs. Coating of the PDMS stamp with amino-silane layer was crucial for having a good coverage of Au NPs interacting with the surface via electrostatic interactions, and which could be easily transferred to the desired end surfaces. Without amino-silane layer, no Au NPs could be seen on the PDMS stamp.

After an Au NPs-coated PDMS stamp was obtained, the Au NPs were transferred via stamping onto PEG hydrogels and cell adhesion on the nano-patterned Au NPs on PEG hydrogels were investigated. As seen in **Figure 15(a)**, the cells were adhering effectively on the nano-patterned surface containing Au NPs adhesion sites. The nano-pattern, which was transferred on PEG hydrogel, is shown in **Figure 15(b)** and **(c)** via AFM 2D and 3D height images and a cross-sectional profile.

As is already obvious from the optical micrograph in **Figure 15(a)** and is further recognized in **Figure 16(a)**, the fibroblasts do adhere quite clearly, but protrude and spread in random directions.

Part labels (b) and (c) of **Figure 16** are the enlarged images of (a) where the focal adhesions and protrusions were more clearly visible. This can be easily understood when realizing that the dimensions of the adhesive nano-patterns and the micrometer-sized cells differ by at least one order of magnitude. In other words, the adherent cells are likely spanning over a large number of nano-lines, and any elongation or alignment is not translated to the overall cell morphology.

Besides being able to direct specific cell adhesion on these nano-patterns of Au NPs on PEG-based hydrogels, these nano-patterned hydrogels can also serve as a very useful platform to immobilize certain bio-functional molecules, such as proteins, enzymes, antibodies, or supramolecular building blocks with great precision. Consequently, advanced applications

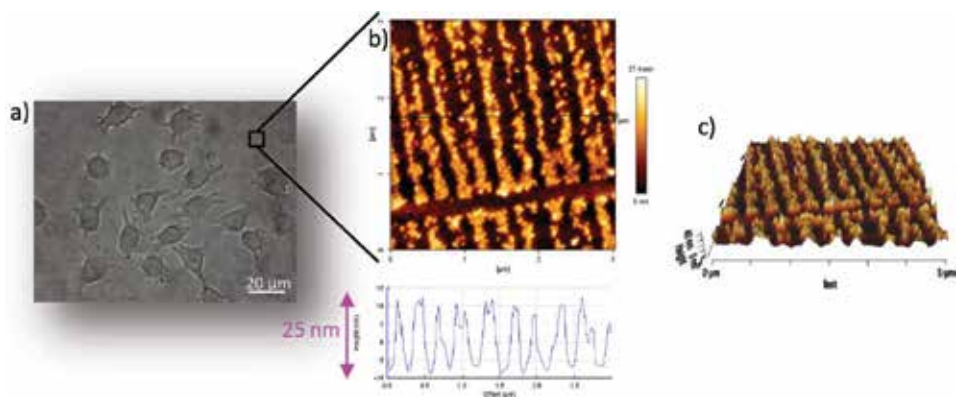

Figure 15. (a) Optical micrographs of cell adhesion on nano-patterned PEG hydrogel, fixed via formaldehyde; (b) AFM 2D height images and cross-sectional profile and (c) AFM 3D height images of Au NPs nano-lines on the surface of PEG hydrogel done with wrinkled PDMS Stamps. Scale bars: (a) 20 µm; (b) 500 nm. Images modified from Bowden et al. [60].

http://dx.doi.org/10.5772/intechopen.71548

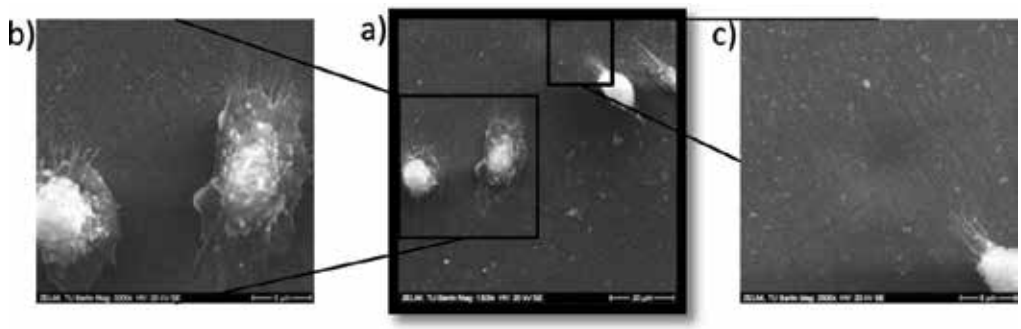

Figure 16. (a–c) SEM images of cell adhesion on Au NPs nano-patterns on PEG hydrogel. Scale bars: (a) 20 μm; (b) 8 μm; (c) 9 μm.

in biosensors and diagnostics are conceivable. Of particular interest are the modern readout methods that exploit surface plasmon resonance and surface-enhanced Raman effects, relying on relatively small probe molecules or possibly even whole cells.

3. Conclusions

Gold nanoparticles (Au NPs) with different sizes and shapes were synthesized and patterned on PEG-based hydrogels using different novel patterning strategies. Hereby, PEG hydrogels with different elastic or chemical properties could be synthesized depending on (i) the molecular structure of the macromonomer precursors (i.e., linear PEG or eight-arm star-shaped PEG), (ii) the crosslinking mechanism (e.g., UV-photopolymerization or Michael-type addition reactions), and by exploiting creating chemically modified hydrogel films with reactive end groups. The pattern sizes of Au NPs on the PEG hydrogels could be varied from the nanoscale to the microscale and with lines or rectangular pattern shapes.

On these Au NPs, cell culture studies were carried out and the results show that the cells only and effectively adhered on those areas where Au NPs were present, while the areas of pure, non-functional PEG hydrogels were free of cells. It is interesting to note that, using our presented unique nano- and micro-patterning strategies, neither for the transfer process of the Au NPs onto PEG hydrogels nor for the cell adhesion, any specific linkers or specific biofunctionalization with cell adhesion molecules were required for achieving the clearly selective eventual cell adhesion.

Besides their demonstrated applicability to control selective, localized adhesion of tissue cells, which was the focus of this chapter, and the Au NPs, which were synthesized with different sizes and shapes, exhibit different specific plasmon absorptions in the visible- or even near-infrared (NIR) range. This offers the possibility of employing these nanocomposite biomaterials (i.e., tailor-made Au NPs on tunable PEG hydrogels) to be applied in biosensor devices, for example, using SERS or (L)SPR phenomena as well. Finally, they are

promising nanomaterials for various other biomedical applications, for example, photothermal therapy, which can, for example, be used for cancer treatments or for controlled drug delivery and release.

Author details

Cigdem Yesildag, Zhenfang Zhang, Fang Ren, Gonzalo de Vicente and Marga C. Lensen*

*Address all correspondence to: lensen@chem.tu-berlin.de

Technische Universität Berlin, Nanopatterned Biomaterials, Berlin, Germany

References

[1] Faraday M. The Bakerian lecture: Experimental relations of gold (and other metals) to light. Philosophical Transactions of the Royal Society of London. 1857;**147**(January): 145-181

[2] Saha K, Agasti SS, Kim C, Li X, Rotello VM. Gold nanoparticles in chemical and biological sensing. Chemical Reviews. 2012;**112**(5):2739-2779

[3] Daniel MC, Astruc D. Gold nanoparticles: Assembly, supramolecular chemistry, quantum-size-related properties, and applications toward biology, catalysis, and nanotechnology. Chemical Reviews. 2004;**104**:293-346

[4] Giljohann DA, Seferos DS, Daniel WL, Massich MD, Patel PC, Mirkin CA. Gold nanoparticles for biology and medicine. Angewandte Chemie (International Ed. in English). Apr 2010;**49**(19):3280-3294

[5] Yu Y, Chang S, Lee C, Wang CRC. Gold Nanorods: Electrochemical synthesis and optical properties. Journal of Physical Chemistry B. 1997;**101**(34):6661-6664

[6] Alkilany AM, Thompson LB, Boulos SP, Sisco PN, Murphy CJ. Gold nanorods: Their potential for photothermal therapeutics and drug delivery, tempered by the complexity of their biological interactions. Advanced Drug Delivery Reviews. 2012;**64**:190-199

[7] Ren F. Synthesis of Gold Nanoparticle-Hydrogel Nanocomposites with Controlled Cytotoxicity and Unique Cell-Adhesive Properties. Doctoral Thesis (Dissertatation). Berlin, Germany: Technische Universität Berlin in Berlin; 2016. http://dx.doi.org/10.14279/depositonce-5575

[8] Alkilany AM, Murphy CJ. Toxicity and cellular uptake of gold nanoparticles: What we have learned so far? Journal of Nanoparticle Research. Sep 2010;**12**(7):2313-2333

[9] Riley RS, Day ES. Gold nanoparticle-mediated photothermal therapy: Applications and opportunities for multimodal cancer treatment. WIREs Nanomed Nanobiotechnol. 2017;**9**:1-16

[10] Ren F, Yesildag C, Zhang Z, Lensen MC. Functional PEG-hydrogels convey gold nanoparticles from silicon and aid cell adhesion onto the nanocomposites. Chemistry of Materials. 2017;**29**:2008-2015

[11] Ren F, Yesildag C, Zhang Z, Lensen M. Surface patterning of gold nanoparticles on PEG-based hydrogels to control cell adhesion. Polymers (Basel). Apr 2017;**9**(5):154

[12] Yesildag C, Bartsch C, de Vicente G, Lensen M. Novel wet micro-contact deprinting method for patterning gold nanoparticles on PEG-hydrogels and thereby controlling cell adhesion. Polymers (Basel). May 2017;**9**(5):176

[13] Williams DF. Definitions in biomaterials. In: Proceedings of a Consensus Conference of the European Society for Biomaterials. Vol. 4. New York: Elsevier; 1987

[14] Saini M, Singh Y, Arora P, Jain K. Implant biomaterials: A comprehensive review. World Journal of Clinical Cases. 2015;**3**(1):52-57

[15] Davis JR. Overview of biomaterials and their use in medical devices. In: Davis JR, editor. Handbook of Materials for Medical Devices. Ohio: ASM International; 2003. pp. 1-12

[16] Lee KY, Mooney DJ. Hydrogels for tissue engineering. Chemical Reviews. 2001;**101**(7): 1869-1880

[17] El-Sherbiny IM, Yacoub MH. Hydrogel scaffolds for tissue engineering: Progress and challenges. Global Cardiology Science and Practice. 2013;**2013**(3):316-342. DOI: 10.5339/gcsp.2013.38

[18] Seal BL, Otero TC, Panitch A. Polymeric biomaterials for tissue and organ regeneration. Materials Science and Engineering R. 2001;**34**:147-230

[19] Vo-Dinh T, Cullum B. Biosensors and biochips: Advances in biological and medical diagnostics. Fresenius Journal of Analytical Chemistry. 2008;**366**(6):540-551

[20] Veitinger M, Oehler R, Umlauf E, Baumgartner R, Schmidt G, Gerner C, Babeluk R, Attems J, Mitulovic G, Rappold E, Lamont J, Zellner M. A platelet protein biochip rapidly detects an Alzheimer ' s disease – specific phenotype. Acta Neuropathologica. 2014;**128**(5): 665-677

[21] Ferrari M, Bashir R, Wereley S. Volume IV: Biomolecular sensing, processing and analysis. In: Ferrari M, Bashir R, Wereley S, editors. BioMEMS and Biomedical Nanotechnology. 410. US: Springer; 2007. p. XXII

[22] Shruthi GS, Amitha CV, Mathew BB. Biosensors: A modern day achievement, Journal of Instumentation Technology. 2014;**2**(1):26-39

[23] Lee TM. Over-the-counter biosensors: Past, present, and future. Sensors. 2008;**8**:5535-5559

[24] Sabr AK. Biosensors. American Journal of Biomedical Engineering. 2016;**6**(6):170-179

[25] Wichterle O, Lim D. Hydrophilic gels for biological use. Nature. 1960;**185**(4706):117-118

[26] Jen AC, Wake MC, Mikos AG. Review: Hydrogels for cell immobilization. Biotechnology and Bioengineering. 1996;**50**:357-364

[27] Park JB, Lakes RS. Biomaterials: An Introduction. 3rd ed. New York: Springer; 2007

[28] Patel NR, Gohil PP. A review on biomaterials: Scope, applications & human anatomy significance. International Journal of Emerging Technology and Advanced Engineering. 2012;**2**(4):91-101

[29] Gorbet MB, Sefton MV. Biomaterial-associated thrombosis: Roles of coagulation factors, complement, platelets and leukocytes. Biomaterials. 2004;**25**:5681-5703

[30] Brien FJO. Biomaterials & scaffolds for tissue engineering. Materials Today. 2011;**14**(3):88-95

[31] Zalipsky S, Harris JM. Poly(ethylene glycol) Chemistry and Biological Applications. ACS Symposium Series. 1997;**680**(2):1-13. ISBN13: 9780841235373e, ISBN: 9780841216440. DOI: 10.1021/bk-1997-0680.ch001

[32] Lensen MC, Schulte VA, Diez M. Cell adhesion and spreading on an intrinsically anti-adhesive PEG biomaterial. In: Pignatello PR, editor. Biomaterials – Physics and Chemistry. Rijeka, Croatia: InTech; 2011. pp. 397-414

[33] Schulte VA, Diez M, Möller M, Lensen MC. Surface topography induces fibroblast adhesion on intrinsically nonadhesive poly (ethylene glycol) substrates. Biomacromolecules. 2009;**10**:2795-2801

[34] Diez M, Schulte VA, Stefanoni F, Natale CF, Mollica F, Cesa CM, Chen J, Möller M, Netti PA, Ventre M, Lensen MC. Molding micropatterns of elasticity on PEG-based hydrogels to control cell adhesion and migration. Advanced Engineering Materials. Oct 2011;**13**(XX):16-18

[35] Kelleher SM, Zhang Z, Löbus A, Strehmel C, Lensen MC. Blending PEG-based polymers and their use in surface micro-patterning by the FIMIC method to obtain topographically smooth patterns of elasticity. Biomaterials Science. 2014;**2**(3):410-418

[36] de Vicente G, Lensen MC. Topographically and elastically micropatterned PEG-based hydrogels to control cell adhesion and migration. European Polymer Journal. 2016;**78**:290-301

[37] Strehmel C, Perez-Hernandez H, Zhang Z, Löbus A, Lasagni AF, Lensen MC. Geometric control of cell alignment and spreading within the confinement of Antiadhesive poly(ethylene glycol) microstructures on laser-patterned surfaces. ACS Biomaterials Science & Engineering. 2015;**1**(9):747-752

[38] Chen CS, Mrksich M, Huang S, Whitesides GM, Ingber DE. Geometric control of cell life and death. Science (80–). 1997;**276**(5317):1425-1428

[39] Chen CS, Mrksich M, Huang S, Whitesides GM, Ingber DE. Micropatterned surfaces for control of cell shape, position, and function. Biotechnology Progress. 1998;**7938**(98): 356-363

[40] Wang X, Li S, Yan C, Liu P, Ding J. Fabrication of RGD micro/nanopattern and corresponding study of stem cell differentiation. Nano Letters. 2015;**15**(3):1457-1467

[41] Glass R, Möller M, Spatz JP. Block copolymer micelle nanolithography. Nanotechnology. 2003;**14**(10):1153-1160

[42] Arnold M, Cavalcanti-Adam EA, Glass R, Blümmel J, Eck W, Kantlehner M, Kessler H, Spatz JP. Activation of integrin function by nanopatterned adhesive interfaces. Chemphyschem. Mar 2004;**5**(3):383-388

[43] Graeter SV, Huang J, Perschmann N, López-García M, Kessler H, Ding J, Spatz JP. Mimicking cellular environments by nanostructured soft interfaces. Nano Letters. May 2007;**7**(5):1413-1418

[44] Young JL, Holle AW, Spatz JP. Nanoscale and mechanical properties of the physiological cell-ECM microenvironment. Experimental Cell Research. 2016;**343**(1):3-6

[45] Guasch J, Diemer J, Riahinezhad H, Neubauer S, Kessler H, Spatz JP. Synthesis of binary nanopatterns on hydrogels for initiating cellular responses. Chemistry of Materials. 2016; **28**(6):1806-1815

[46] de Vicente G. Controlled Migration of Cells on Mechanically, Physically and Chemically Patterned Biomaterials. Doctoral Thesis (Dissertatation). Berlin, Germany: Technische Universität Berlin; 2015. urn:nbn:de:kobv:83-opus4-64976, http://dx.doi.org/10.14279/depositonce-4404

[47] Heuberger A. X-ray lithography. Journal of Vacuum Science & Technology B: Microelectronics and Nanometer Structures Processing, Measurement, and Phenomena. Jan 1988;**6**(1):107

[48] Pease RFW. Electron beam lithography. Contemporary Physics. 1981;**22**(3):265-290

[49] Vieu C, Carcenac F, Pépin A, Chen Y, Mejias M, Lebib A, Manin-Ferlazzo L, Couraud L, Launois H. Electron beam lithography: Resolution limits and applications. Applied Surface Science. 2000;**164**(1):111-117. DOI: 10.1016/S0169-4332(00)00352-4

[50] Wouters D, Schubert US. Nanolithography and nanochemistry: Probe-related patterning techniques and chemical modification for nanometer-sized devices. Angewandte Chemie (International Ed. in English). 2004;**43**(19):2480-2495

[51] Piner RD, Zhu J, Xu F, Hong S, Mirkin CA. 'Dip-pen' nanolithography. Science (80–). 1999;**283**(5402):661-663

[52] Kumar A, Whitesides GM. Features of gold having micrometer to centimeter dimensions can be formed through a combination of stamping with an elastomeric stamp and an alkanethiol 'ink' followed by chemical etching. Applied Physics Letters. 1993; **63**(14):2002-2004

[53] Tien J, Xia Y, Whitesides GM. Microcontact printing of SAMs. Thin Film. 1998;**24**: 227-250

[54] Kelleher S, Jongerius A, Loebus A, Strehmel C, Zhang Z, Lensen MC. AFM Characterization of elastically micropatterned surfaces fabricated by fill-molding in capillaries (FIMIC) and investigation of the topographical influence on cell adhesion to the patterns. Advanced Engineering Materials. Mar. 2012;**14**(3):56-66

[55] Chen J, Mela P, Möller M, Lensen MC. Microcontact deprinting: A technique to pattern gold nanoparticles. ACS Nano. 2009;**3**(6):1451-1456

[56] Díez M, Mela P, Seshan V, Möller M, Lensen MC. Nanomolding of PEG-based hydrogels with sub-10-nm resolution. Small. 2009;**5**(23):2756-2760

[57] Chen J, Arafeh M, Guiet A, Felkel D, Loebus A, Kelleher SM, Fischer A, Lensen MC. Hybrid hierarchical patterns of gold nanoparticles and poly(ethylene glycol) microstructures. Journal of Materials Chemistry C. 2013;**1**(46):7709-7715

[58] Kim E, Xia Y, Whitesides GM. Micromolding in capillaries: Applications in materials science. Journal of the American Chemical Society. Jan 1996;**118**(24):5722-5731

[59] Xia Y, Kim E, Whitesides GM. Micromolding of polymers in capillaries: Applications in microfabrication. Chemistry of Materials. Jan 1996;**8**(7):1558-1567

[60] Bowden N, Huck WTS, Paul KE, Whitesides GM. The controlled formation of ordered, sinusoidal structures by plasma oxidation of an elastomeric polymer. Applied Physics Letters. 1999;**75**(17):2557

[61] Yesildag C, Tyushina A, Lensen M. Nano-contact transfer with gold nanoparticles on PEG Hydrogels and using wrinkled PDMS-stamps. Polymers. 2017;**9**(6):199

[62] Bastús NG, Comenge J, Puntes V. Kinetically controlled seeded growth synthesis of citrate-stabilized gold nanoparticles of up to 200 nm: Size focusing versus Ostwald ripening. Langmuir. Sep 2011;**27**(17):11098-11105

[63] Wang W, Pang Y, Yan J, Wang G, Suo H, Zhao C, Xing S. Facile synthesis of hollow urchin-like gold nanoparticles and their catalytic activity. Gold Bulletin. Jun 2012;**45**(2):91-98

[64] Fiévet F, Lagier JP, Figlarz M. Preparing monodisperse metal powders in micrometer and submicrometer sizes by the polyol process. Materials Research Society Bulletin. 1989;**14**:29-32

[65] Ye X, Jin L, Caglayan H, Chen J, Xing G, Zheng C, Doan-Nguyen V, Kang Y, Engheta N, Kagan CR, Murray CB. Improved size-tunable synthesis of monodisperse gold nanorods through the use of aromatic additives. ACS Nano. Mar 2012;**6**(3):2804-2817

[66] Zhang Z, Loebus A, de Vicente G, Ren F, Arafeh M, Ouyang Z, Lensen MC. Synthesis of poly(ethylene glycol)-based hydrogels via amine-Michael type addition with tunable stiffness and postgelation chemical functionality. Chemistry of Materials. Jun 2014; **26**(12):3624-3630

[67] Strehmel C. Zelluläre Reaktionen Muriner Fibroblasten Auf Planaren Und Strukturierten Polyethylenglykol-Basierten Biomaterialien. Doctoral Thesis (Dissertatation). Berlin, Germany: Technische Universität Berlin; 2013. https://depositonce.tu-berlin.de/bistream/11303/5636/1/c3bm60055f.pdf

[68] Li H, Zhang J, Zhou X, Lu G, Yin Z, Li G, Wu T, Boey F, Venkatraman SS, Zhang H. Aminosilane micropatterns on hydroxyl-terminated substrates: Fabrication and applications. Langmuir. Apr 2010;**26**(8):5603-5609

[69] Pazos-Pérez N, Ni W, Schweikart A, Alvarez-Puebla RA, Fery A, Liz-Marzán LM. Highly uniform SERS substrates formed by wrinkle-confined drying of gold colloids. Chemical Science. 2010;**1**(2):174

Chapter 8

Substrate Effects of Noble Metal Nanostructures Prepared by Sputtering

Alena Reznickova, Ondrej Kvitek, Dominik Fajstavr, Nikola Slavikova and Vaclav Svorcik

Additional information is available at the end of the chapter

http://dx.doi.org/10.5772/intechopen.71340

Abstract

Cathode sputtering is a well-established technique for preparation of metal nanostructures. However, the substrate properties are very important in this process. On glass substrates, there is a difficulty with poor adhesion of the metal layers, but thanks to this, metal nanostructures can be produced using solid state dewetting process. Thin metal films on polymer substrates are strongly influenced by the surface properties of the polymers, which originate in the method of their preparation. A recent focus is direct sputtering of metal nanoparticles (NPs) into liquid substrates and their characterizations and applications. Polyethylene glycol (PEG) is one of the most commonly used liquid, which provides "stealth" character to nanostructures. Recent results in this area are reviewed in this chapter. PEGylated NPs could find application in drug delivery systems, therapy, imaging, biosensing, and tissue regeneration.

Keywords: sputtering, noble metal, polymer, glass, adhesion, dewetting, thin film, polyethylene glycol, glycerol, nanoparticles, colloidal stability

1. Introduction

Cathode sputtering as a method of thin noble metal film preparation has been recently extended to a much wider variety of applications not only in electronics industry, but also in, for example, medicine or biotechnology. It has become an important technology for material processing for technologies such as multifunctional materials or nanoelectromechanical systems. A special attention in the process must be paid to the underlying substrate, which is the key factor in determining properties of the material. The material types used for substrates can be basically divided into metals, glass and ceramics, and polymers. While

metals as substrates for noble metal films possess some advantageous properties (such as good adhesion), the real potential of thin film structures on substrates stems from the different properties of each component of the material. In many cases, an insulating material is needed for the material to be functional. Of the insulating substrates, the most significant are glass and polymer substrates, which will be discussed further in this chapter.

Completely new possibilities have opened up with sputtering of noble metals onto liquid substrates. Under appropriate conditions, the use of liquid capture media leads to direct preparation of metal nanoparticles, which show some unique possibilities compared to those prepared by other methods. Ionic liquids (ILs) are one of the most commonly used capturing media for direct metal sputtering. Their significantly less toxic alternatives are vegetable oils. The main condition for selecting a suitable liquid substrate is sufficiently low vapor pressure in vacuum. Polyethylene glycol is one of the most used NP stabilizing polymers. Therefore, the use of liquid substrates for sputtering deposition has recently become a highly studied topic.

2. Cathode sputtering

When high-energy ions impact on a solid surface, the atoms of the surface material are ejected from the surface and spread into the vicinity. The phenomenon is called sputtering and is a widespread method used for deposition of thin films and ion etching.

Three main types of sputtering systems in practical use are: direct current (DC) sputtering, radio-frequency (RF) sputtering, and magnetron sputtering. Among these, the simplest is the DC sputtering system. It consists of two planar electrodes placed in a vacuum chamber. A sheet of the material to be deposited (target) is placed on one of the electrodes (cathode). Substrates to be covered with the target material are positioned on the anode. After a sufficient vacuum is established, an inert work gas (usually Ar at pressure of about 1–5 Pa) is introduced and high voltage is brought to the electrodes. The working gas is then ionized due to collisions with electrons and plasma is formed in the chamber. The generated Ar ions then collide with the cathode resulting in deposition of the target material on the substrates.

Two major drawbacks of the basic direct current are slow deposition rate and overheating and structural damage of the substrate due to extensive electron bombardment. Therefore, magnetic field is often introduced in magnetron sputtering systems in such a way it forces electrons to follow spiral trajectories, which lead to more ionizing collisions. This allows use of lower sputtering pressure and leads to higher sputtering yield. Furthermore, only electrically conductive materials can be deposited by DC sputtering. For deposition of insulating materials, the RF sputtering technique was introduced.

To control the sputtering rate, energy of the sputtered atoms and, in turn, the characteristics of the prepared films, discharge voltage, current, distance between the target and the substrate, and the work gas pressure can be manipulated. Another important parameter is the vacuum and work gas purity. Residual oxygen remaining in the sputtering chamber leads to oxidation

of the deposited material. Noble metals—great electrical conductors resistant to oxidation and other chemical reactions—are ideal materials to be used for thin film preparation by the DC diode sputtering method. More in-depth studies on the topic of cathode sputtering can be found in the literature [1–5].

3. Sputtering of noble metals onto solid insulating substrates

3.1. Glass substrates

Glass is an often-used substrate for preparation of thin metal films for electronics and optics. Its surface can be prepared with a very low roughness, is therefore able to support films with thickness as low as several nanometers and enables preparation of very delicate nanostructures. A downside of a glass substrate for sputtering of Au films is a poor adhesion of the films to the substrate. Due to surface morphology and chemical properties of the glass, the surface free energy between Au, and the glass is too high. The as-sputtered continuous films are therefore metastable. A lot of effort is therefore made to improve the adhesion between the substrates and the metal films, but the metastable nature of the films also enables advantageous preparation of isolated island nanostructure. While continuous Au films are necessary for preparation of reliable and durable metallization in electronics, the nanostructures can be used in construction of sensor devices due to their specific optical properties.

3.1.1. Adhesion of Au layers

The adhesion is defined as the energy required to create free surfaces from the bonded materials. In a practical arrangement, the interfacial toughness involves prevention of initiation and propagation of cracks, plastic deformation, and friction in the thin film-substrate system [6]. To achieve good adhesion, a strong bond between the film and the substrate must be established and parameters such as crystal orientation, contact area and, chemical affinity play very important roles. Typical methods to improve adhesion between noble metal film and glass substrate include preparation of interlayers of more reactive metals (e.g., Cr or Ti) [7–10], irradiation by energetic ion beams [11–13], thermal conditioning [14], or chemical modification of the substrate surface [15, 16], though each method has certain limitations. The metal interlayers create alloys with the thin film, changing its optical properties [17]. Ion irradiation leads to contamination of the substrate with material of the vacuum chamber and implantation of the ions in the substrate. Thermal processes lead to compromising homogeneity of very thin films. The chemical modifications of the substrate lead to introduction of more substances in the system worsening reproducibility of the production of the material.

The most common approaches to measure adhesion of a film to the substrate involve peeling of the films with adhesive tapes and various arrangements of a solid point penetrating the thin film [6]. The solid point methods include indentation measurements, which can be used to evaluate adhesion of brittle and weakly bonded layers, and scratch. The adhesion of the thin film is determined by critical loads at which some type of failure of the film-substrate

system begins. The adhesion is usually evaluated in optical microscope or by acoustic emission or friction force [18]. Quantitative evaluation of the interfacial toughness from the scratch test is difficult though, but it is still very useful when comparing adhesion of films deposited under different conditions [19, 20].

3.1.2. Solid state dewetting

Thin metal films on glass substrates undergo a morphology transformation upon annealing. The sputtering deposition is accomplished at relatively low substrate temperatures and the films grow too fast for the atoms to occupy spots with the lowest energy. Therefore, the as-deposited metal layers are in a metastable state. Annealing then leads to transformation of thin film structure from continuous layers to island-like structure. This process is called solid state dewetting. The cleavage of the metal layer then often manifests in the absorption spectrum of the material, where bands connected to localized surface plasmon resonance arise. This phenomenon can be observed as a change of color of the metal film (**Figure 1**).

The dewetting is then realized at elevated temperature by diffusion of the metal atoms over the substrate in solid state, without actual phase transformation. The driving force of the process is reaching the equilibrium state with the minimum surface free energy of the metal-glass interface. The equilibrium state is defined by the interfacial energies between the metal, substrate, and the surrounding atmosphere, and it is described by the Young equation (**Figure 2**). If the surface energy of the gas-substrate interface is higher than the sum of the surface energies of substrate-metal and metal-gas interfaces, then the equilibrium state is a planar film of metal over the substrate. In most cases, however, when the substrate is of a very different nature from the film, the surface energy of the gas-substrate interface is lower than the sum and the dewetting takes place during the annealing [21–23].

On glass substrates, the dewetting of Au thin films occurs at temperatures as low as about 300°C, well below the melting temperature. Evolution of island-like structure was observed after annealing for 1 h duration, with optical and electrical properties of the material dramatically changing due to the alteration of the nanostructure [24, 25]. Later, it was found that the process is gradual and longer annealing times lead to further evolution of the structure at the

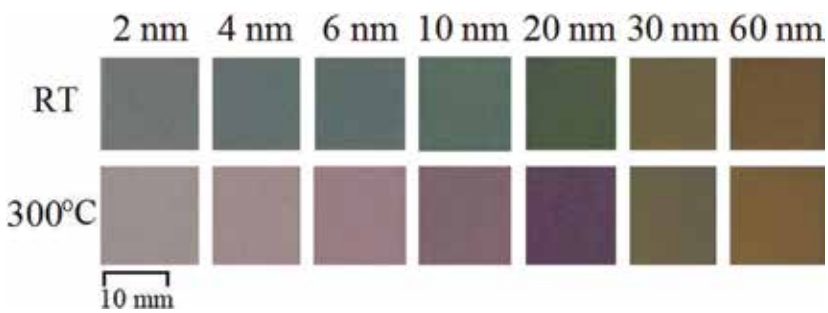

Figure 1. Photographs of 2–60 nm thin Au films sputtered on glass substrates at room temperature (RT) and after annealing at 300°C for 1 h. The distinctive color change illustrates formation of the island-like structure and the manifestation of localized surface plasmon resonance.

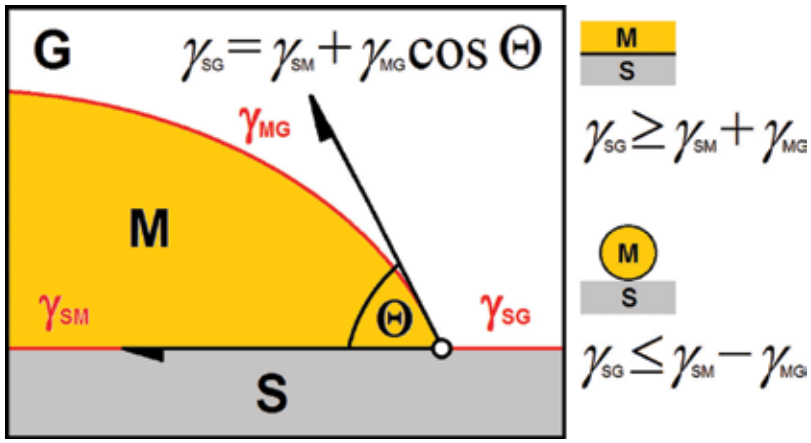

Figure 2. Illustration of the solid state dewetting in substrate (S), metal film (M), and surrounding atmosphere (G) system. The contact angle Θ between the substrate and the metal in the equilibrium state is governed by the energies of the interfaces according to the Young law. The conditions for continuous layer and total dewetting are on the right.

same temperature [26]. The dependence of the process on the surrounding atmosphere was proven by annealing of the layers in vacuum. The vacuum annealed layers tend to be more stable and the surface diffusion of the Au is somewhat slower [27]. The forming Au nanostructures were used as sensitive material for detection of vapors of organic solvents due to their specific optical properties. This is possible due to the isolated island nanostructure supporting localized surface plasmon resonance, which is strongly dependent on the refractive index of the surrounding atmosphere [28].

3.2. Polymer substrates

Due to the demand for elastic electronics for displays [29], flexible solar cells, [30] and electronic textiles [31], materials consisting of thin metal films on polymer substrates have become a highly studied subject recently. In a practical application, it is necessary to assemble stable components so the devices have the required endurance.

Compared to glass, the surface of polymers has usually higher roughness, but depending on the specific polymer, the roughness can vary a lot. Due to this fact, the morphology of film sputtered on polymers is very dependent on the surface structure of the polymer. Surface structure of substrates is formed during the preparation of the polymer foil (e.g., extrusion, casting of a solution or melted polymer, rolling, and blowing). Chemical and physical properties often govern the method that can be used to prepare a sheet the polymer—for example, sheets of polytetrafluoroethylene are prepared by cutting a block of the polymer, because it cannot be mechanically formed after its polymerization [32]. The character of functional groups on the polymer chain can also have a significant impact on the surface morphology, since it determines the polymer crystallinity [33]. This effect can be observed during annealing of the polymer. When exceeding temperatures of secondary phase transitions of the surface morphology can be significantly altered—at temperatures over the glass transition point

(T_g), polymer chain segments are enabled to shift which leads to surface recrystallization. With exceeding the melting temperature (T_m), the strain in the bulk of the polymer relaxes and a completely new surface morphology are formed [32]. The surface structure of different polymers therefore varies significantly and cannot be manipulated as precisely as the surface structure of crystalline materials.

An example of polymer substrates with very different surface morphologies are polyimide (PI) and polyetheretherketone (PEEK). The polymers were used as substrates for thin Au layer deposition and subsequently annealed. In the case of the PEEK substrate, the T_g was exceeded during annealing and the structure of the substrate surface was significantly disrupted leading to cleavage of the overlaying Au layer and changes of its optical properties (**Figure 3**).

The PI substrate is more thermally stable and preserves its surface structure during annealing at 300°C (**Figure 4**). Compared to the abovementioned case of glass substrate, the solid state dewetting was not observed on the polymer substrate, probably due to much better adhesion of the Au film [34]. Another thermally stable polymer substrate is polytetrafluoroethylene, which has a very rough surface structure. However, its surface structure can be manipulated, for example, by ion exposition in plasma discharge [35]. An intriguing substrate to support Au layers is poly-L-lactic acid. Samples with thin films show evolution of an interesting lamellar nanostructure during annealing at 60°C, which is caused by exposing of the polymer crystallites [36].

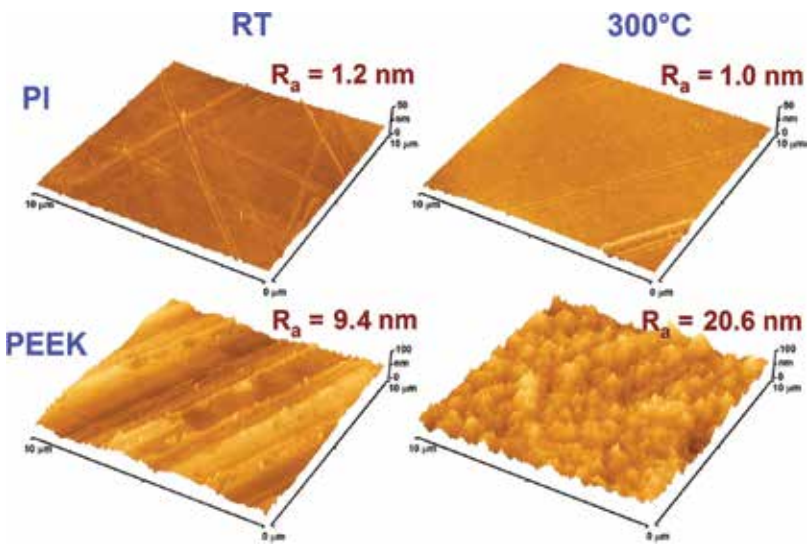

Figure 3. AFM images of the PI and PEEK substrates show significant differences of the surface structure of the polymers. While annealing of PI leads to no visible surface structure transformation, the surface of PEEK changes dramatically after annealing due to the recrystallization process. Values of surface roughness (R_a) are stated for each sample [34].

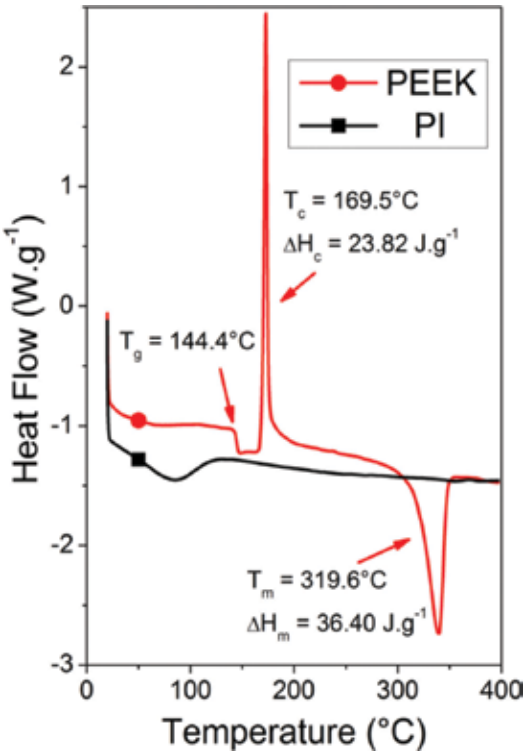

Figure 4. The DSC curves of the PI and PEEK substrates show PI is stable up to 400°C, where PEEK undergoes glass transition at ca. 144°C, then recrystallization takes place at around 170°C and it melts at about 320°C [34].

4. Sputtering of noble metals onto liquid substrates

In this part of the chapter, synthesis, properties, stability, and applications of noble metals sputtered directly into liquid substrates will be discussed. Metal nanoparticles (MNPs) have broad spectrum of applications, from electronics and catalysis to drug carriers and bio-imaging. Gold NPs (Au NPs), in particular, are widely used because of their unique properties such as size, shape, optical properties, and low toxicity [37]. NPs can be prepared by either chemical (Mie, Turkevich, Brust-Schiffrin, etc., methods) [38–40] or physical route (physical vapor deposition, laser ablation, and γ irradiation) [3, 41, 42]. The size, shape, and geometry of the NPs are strongly dependent on the employed method. Chemical synthesis offers advantages in simplicity of NP size and shape control, which enables preparation of NPs with required properties for specific application. Downside of this method is generation of harmful products and NPs with limited purity. On the other hand, the physical methods are very clean and the purity of the NPs synthesized is the same as the bulk material. In 1996 radiofrequency, sputtering of Ag NPs into a liquid substrate (silicone oil) was performed for the first time [3, 43]. However, silicone oil proved to be a suboptimal capping agent and

thus the synthesized NPs were not sufficiently stable. After 10 years of experiments, in 2006, researchers started to use ionic liquids (ILs) as liquid substrates for preparation of noble metal nanoparticles. Apart from the ILs, there are other liquid substrates, which are suitable for preparation of NPs by physical vapor deposition (i.e., sputtering). The main condition for selecting a suitable liquid substrate is sufficiently low vapor pressure in vacuum [44]. Vegetable oils [45], liquid polyethylene glycol [46, 47], molten 6-mercaptohexyltrimethylammonium bromide [48], and glycerol were used for preparation of MNPs [49]. For example, Siegel et al. demonstrated that by sputtering of various noble metals spherical NPs of different sizes can be prepared: 6.1 ± 1.0 nm for Au, 4.2 ± 0.9 nm for Ag, 2.5 ± 0.6 nm for Pd, and 1.8 ± 0.4 nm for Pt [50]. Polyethylene glycol (PEG) is one of the most commonly used stabilizing agents. It is a neutral amphiphilic polymer that gives "stealth" character to nanostructures. PEGylation of NPs is a process that introduces PEG ligands onto NPs surface. This method was introduced by Ballou et al. for the first time [51]. PEGylation generally increases circulation of NPs in blood, decreases immunity response, and slows the cleansing by the reticuloendothelial system [52]. PEG is versatile, inexpensive, and it has been approved by Food and Drug Administration (FDA) [53]. Properties of PEGylated MNPs also depend on molecular weight of the liquid PEG. Slepicka et al. prepared Au and Ag NPs by sputtering into PEG with molecular weight of 200, 400, and 600 g mol^{-1}. Since PEG-200 and PEG-600 showed lower stability during aging, only PEG-400 was used for further experiments. The prepared Au and Ag NPs were spherical with size of 7.97 ± 2.92 nm and 30–50 nm, respectively. Localized surface plasmon resonance absorption bands lied between 513 and 560 nm for Au NPs and 401–421 nm for Ag NPs [46].

4.1. Synthesis and properties of PEGylated gold nanoparticles

In this segment, results of our research for the preparation, properties, and examination of temperature and aging stability of gold nanoparticles (Au NPs) are presented. In many research papers, NPs synthesis is a multistep process consisting of many purification processes. In the first step, NPs are synthesized using a surfactant (e.g., citrate) as a stabilizing agent and, in the next step, the capping agent is exchanged with PEG molecules [54–56]. We present a simple, reproducible, environmentally friendly, low cost, and easily applicable approach of Au NPs preparation by direct sputtering of Au into a mixture of polyethylene glycol (PEG) and thiolated PEG (see **Figure 5A**). NPs consist of two components: the core and the corona, which interacts with the surrounding media (**Figure 5B**). The ─OH groups of PEG create hydrogen bridges with water, which leads to formation of a solvation shell and stabilization of the NPs, preventing aggregation during dissolution. A stronger stabilization is achieved with thiol groups that have good affinity to Au. In the case of thiolated PEGs, the bond between Au and the thiol group is very strong (197.4 kJ/mol) and minimizes desorption of PEG from NP surface (**Figure 5C**) [57].

Our research group prepared Au NPs by direct sputtering for 300, 900, and 1800 s into PEG (300 s—A; 900 s—B), PEG: PEG-SH (1800 s—C), PEG: PEG-S_2H_2 (900 s—D; 300 s—E), PEG admixed with PEG-SH (300 s—F; 900 s—G) and PEG admixed with PEG-S_2H_2 (300 s—H; 900 s—I). Immediately after sputtering, the PEG with Au NPs was mixed with distilled water in the volume ratio of 1:9 (PEG: water). Molecular weights of selected polyethylene glycols

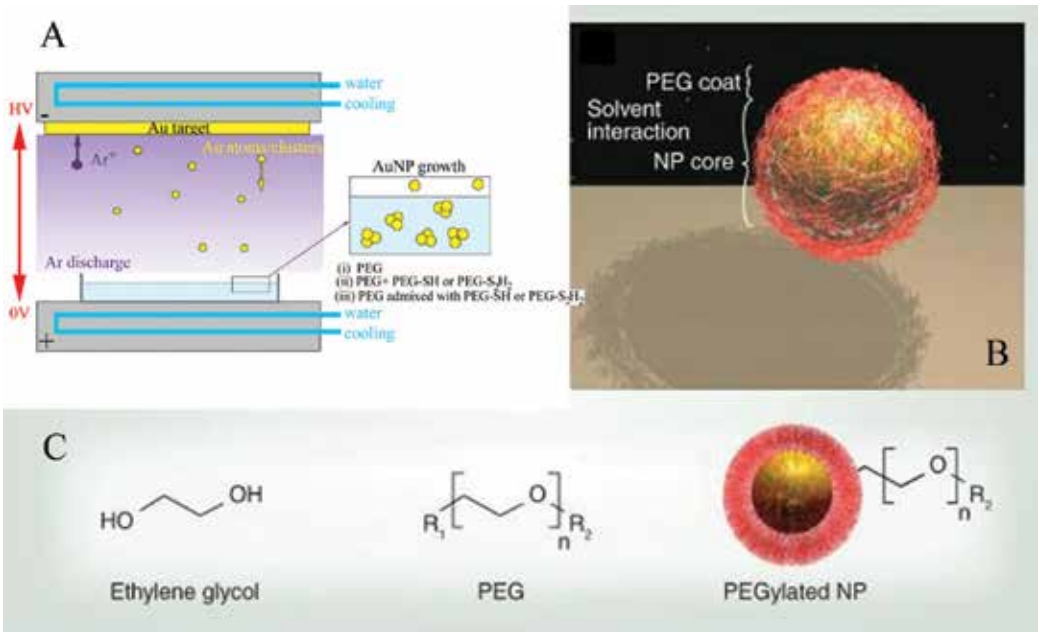

Figure 5. Schema of (A) preparation of PEGylated Au NPs by direct sputtering into liquid media of (i) PEG; (ii) PEG + PEG-SH or PEG + PEG-S_2H_2, and (iii) PEG and subsequent mixing with either PEG: PEG-SH or PEG: PEG-S_2H_2, respectively; (B) stabilization of Au NP by PEG, indicating metal core with immobilized PEG chains; (C) monomers of ethylene glycol are polymerized into PEG. PEG contains two end groups R1 linkage group and R2 terminus group, which reacts with the surrounding solvent [47].

were: 400 g mol^{-1} for PEG, 800 g mol^{-1} for PEG-SH, and 1500 g mol^{-1} for PEG-S_2H_2, respectively. The TEM images in **Figure 6** show that Au NPs were successfully prepared in all types of the capturing media. Despite the fact that the shape of Au NPs was spherical in all cases, an apparent difference in size, distribution, and concentration was detected.

The size and size distribution of individual PEGylated Au NP solutions are summarized in **Table 1** and in insets in **Figure 6**. The direct sputtering of Au atoms into pure PEG for 300 s and 900 s led to spherical NPs with an average diameter of 5.6 and 5.9 nm. TEM images show that the nanoparticles prepared under such conditions have the worst size distribution with inclination to create agglomerates (see **Figure 6A** and **B**). The Au NPs prepared in the solution of PEG-SH had average diameter of 2.9 nm. The small size of the nanoparticles can be caused by low interfacial tension of PEG-SH and high nucleation rates or by PEG-SH slowing down the growth of the Au NPs (**Figure 6C**) due to high stabilization effect of thiolated PEG [3, 58]. On top of that, these NPs have a narrower size distribution and a lower tendency to aggregate. During the stabilization of Au NPs in PEG-S_2H_2 solution, disulfide bridges are created. Due to interaction of thiol groups, the nanoparticles have higher tendency to agglomerate (**Figure 6D**). In the case of Au sputtering into PEG-S_2H_2 for 300 s, the tendency to aggregate was less apparent and the size distribution was narrower (i.e., 3.6 ± 0.6 nm, **Figure 6E**). Post-deposition addition of PEG-SH improves the homogeneity of the nanoparticles in terms of size, shape, and aggregation (**Figure 6F** and **G**) and leads

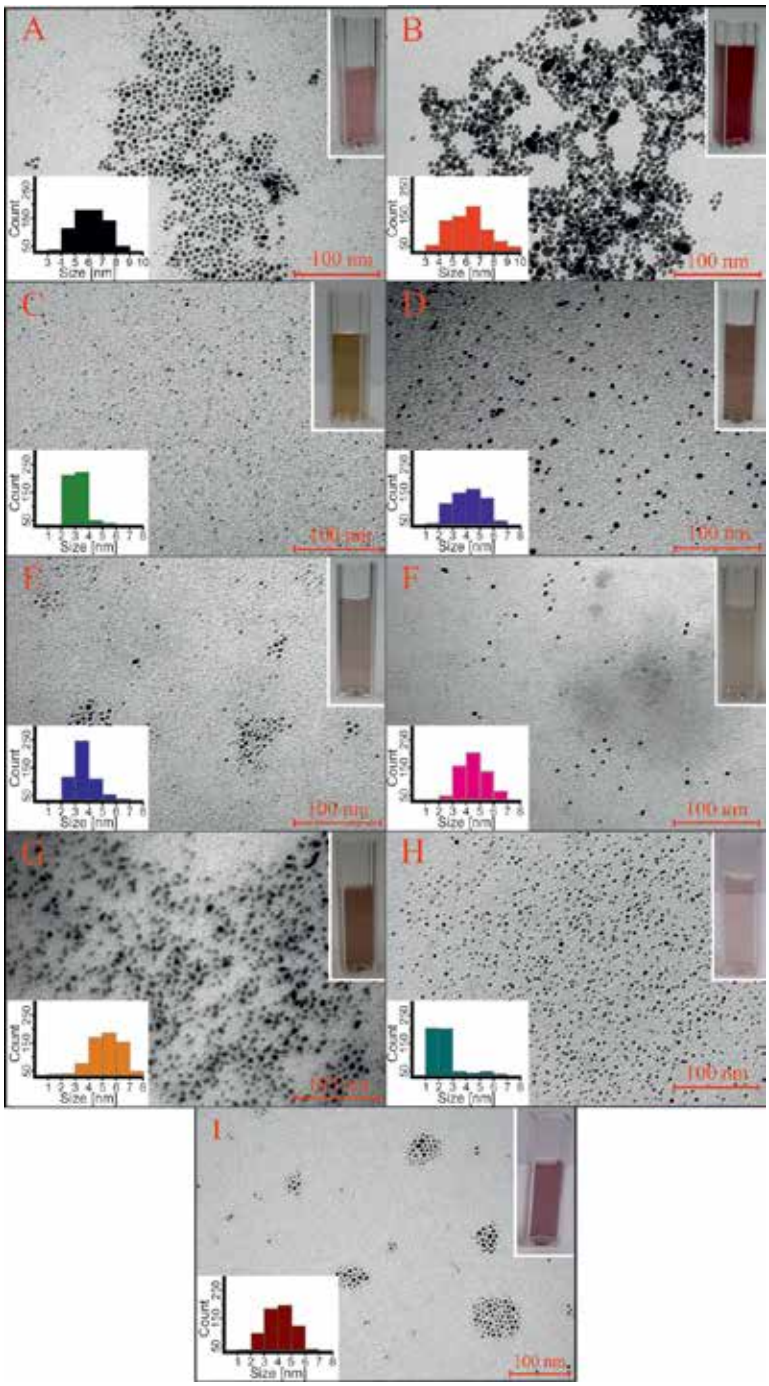

Figure 6. TEM images of Au NPs prepared by direct sputtering into PEG (300 s—A; 900 s—B), PEG: PEG-SH (1800 s—C), PEG: PEG-S_2H_2 (900 s—D; 300 s—E), PEG admixed with PEG-SH (300 s—F; 900 s—G) and PEG admixed with PEG-S_2H_2 (300 s—H; 900 s—I). Histograms of Au NPs size distribution (from TEM analysis) are shown in the inset on the left. Color of prepared PEGylated Au NPs is represented by cuvette images in insets on the right of each image [47].

to a small decrease of average NP size too (see **Table 1**). In the case of the post-deposition PEG-S_2H_2 addition (**Figure 6H**, **I** and **Table 1**) the AuNPs size decreased as well, but the agglomeration was more noticable (**Figure 6I**). This behavior might be connected to the decrease of energy of the system after post-deposition addition of PEG-S_2H_2 compared to the energy of the system after addition of PEG-SH, and thus, the growth slowdown is more pronounced [59]. Another reason could be the different molecule weights of the used PEG-S_2H_2 and PEG-SH. Sputtering of Au into thiolated PEG or its addition leads to change of the color of the solution from dark/light red to dark/light brown (depending on concentration of the Au NPs in the solution) [47].

To confirm measured dimensions of NPs obtained from TEM, dynamic light scattering (DLS) analysis was conducted. The values of nanoparticle sizes together with polydispersity index (quantifying the degree of the size dispersion) are listed in **Table 1**. In the case of DLS, the statistical significance of designated values of particle size is much higher because all particles in a particular sample are used for the calculation (determination). The prepared colloidal solutions have mono-nodal distribution of sizes (see **Table 1**), that means, they do not contain nanoparticle aggregates, which are in good agreement with TEM results (**Figure 6**). We believe that this discrepancy is caused by the coalescence of NPs during preparation of TEM sample for the analysis. The phenomenon probably occurs during evaporation of solution on the copper grid. To assess the monodispersity of the prepared PEGylated Au NPs, we present the results of DLS analysis in the form of intensity-esteemed distribution curve of the sizes. This curve is most sensitive to presence of agglomerates, which would not be visible in the case of transformation to other types of distribution curve (volume-esteemed or number-esteemed). Another reason for discrepancy between the DLS and the TEM results is that the DLS method is not based only on hydrodynamic average of the particles themselves, but also includes the solvation shel.l [60]. Since the nanoparticles are stabilized with relatively long macromolecular chains, the detected NP sizes may be influenced by PEG corona. This is the

Sample	Au NP size (nm)		PDI
	TEM	DLS	
A	5.6 ± 1.8	9.2 ± 1.5	0.429
B	5.9 ± 0.8	8.8 ± 2.2	0.201
C	2.9 ± 0.4	3.0 ± 0.6	0.026
D	4.0 ± 1.2	4.9 ± 1.0	0.066
E	3.6 ± 0.6	4.3 ± 1.2	0.107
F	4.2 ± 0.8	5.2 ± 1.5	0.517
G	5.7 ± 1.3	7.0 ± 1.9	0.311
H	2.1 ± 0.7	4.3 ± 1.1	0.112
I	4.1 ± 1.3	6.5 ± 1.3	0.214

Table 1. Size of PEGylated Au NPs (in nm; with relative error) determined by TEM and DLS methods. Polydispersity index (PDI) of colloidal systems was determined by DLS analysis [47].

reason for not using number-esteemed averages for DLS, because the calculation for this type of results may alter the output significantly. Despite some weaknesses mentioned above, the results presented on the basis of DLS correspond well with published studies [61].

Figure 7 shows UV-Vis spectra of Au NPs sputtered into solutions of different polyethylene glycols. Comparing absorbance of each sample, significant differences in the spectra of the PEGylated Au NPs are observed. The occurrence of a singular SPR absorption peak confirms that spherical NPs are present in all colloidal PEG solutions with size ranging between 4 and 50 nm. PEGylated Au NPs prepared by sputtering for 300 s into pure PEG exhibit a narrow SPR band (at 519 nm) with the highest UV-Vis absorption. With increasing sputtering time, the SPR band tends to get wider, which is caused by the poor size distribution of NPs. The absorption also decreases, which suggests formation of sedimentation aggregates (see **Figure 6B**). In contrast, SPR bands are not observed in the spectra of Au NPs sputtered for 1800 s into PEG-SH (**Figure 7**—line C). According to literature, the peak position and absorption of the plasmon band depend on Au NPs' size and shape [59]. When the diameter of spherical Au NPs is lower than 3 nm, the plasmon band disappears [62]. Weak and broad SPR band observed for NPs stabilized with PEG-S_2H_2 (**Figure 7**—line D) might be connected to the creation of disulfide bridges, aggregation of the nanoparticles, their sedimentation and the subsequent decrease of metal concentration in the colloidal solution. The disappearance

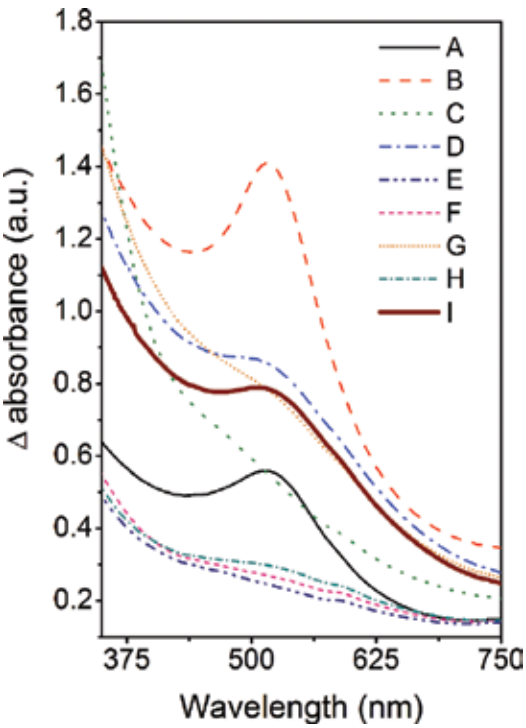

Figure 7. UV-Vis spectra of Au NPs prepared by different time of sputtering of Au into: PEG (300 s—A; 900 s—B), PEG: PEG-SH (1800 s—C), PEG: PEG-S_2H_2 (900 s—D; 300 s—E), PEG admixed with PEG-SH (300 s—F; 900 s—G) and PEG admixed with PEG-S_2H_2 (300 s—H; 900 s—I) [47].

of SPR band was noticed for Au NPs obtained by sputtering for 300 s into PEG-S_2H_2 as well as for sample C, because their size was close to 3 nm (see **Table 1**). Admixing thiolated PEG in both cases of 300 s and 900 s sputtering time leads to the disappearance of SPR bands. In the literature, the SPR absorption decrease is associated with binding of stabilizing agents containing thiol groups onto NP surface [54, 63]. Higher UV-Vis absorption of sample G is caused by the higher concentration of metal in the colloid solution. If the gold is sputtered for 300 s into PEG and the PEG-S_2H_2 is added subsequently, the prepared nanoparticles are 2.1 nm in diameter which induce the loss of the SPR band. Another possible cause is the connection of thiol groups to the Au NPs surface [54]. In the case of the gold sputtered for 900 s into pure PEG and subsequently mixed with PEG-S_2H_2, bigger nanoparticles were observed. Sputtering time of 900 s seems to be sufficient for the growth of bigger nanoparticles and, thus, the SPR band is visible in the spectrum.

Table 2 summarizes Au concentration in the solution measured by atomic absorption spectroscopy (AAS). Obtained data are in good agreement with results published by Slepicka et al.; in that, Au concentration linearly increases with the increasing sputtering time [46]. AAS confirmed results (see above) that dithiol-stabilized Au NPs are less stable aggregates and thus lower Au concentration is observed. Since these results were examined in the case of post-deposition addition of dithiols as well, we can infer that the lower concentration of Au is not connected to different liquid substrates used in the Au sputtering. With this knowledge, we are able to prepare colloids of desired NPs' size and concentration by managing the preparation conditions. Gold concentration in colloid solutions influences optical properties of the solutions such as color and UV-Vis absorption (see **Figures 6** and **7**).

4.2. Aging and temperature stability of PEGylated gold nanoparticles

For aging and temperature stability study, we have chosen samples C and D as representatives of direct Au sputtering into PEG-SH and PEG-S_2H_2, respectively. Aging and temperature stability of Au colloids was studied by UV-Vis spectroscopy (see **Figures 8** and **9**). Aging stability

Sample	c_{Au} (mg l^{-1})
A	30.0
B	84.2
C	163.0
D	77.2
E	25.5
F	22.0
G	80.9
H	24.8
I	65.6

Table 2. Concentration of Au (c_{Au}, mg l^{-1}) in water-PEG solutions (by volume 1:9) determined by AAS spectroscopy [47].

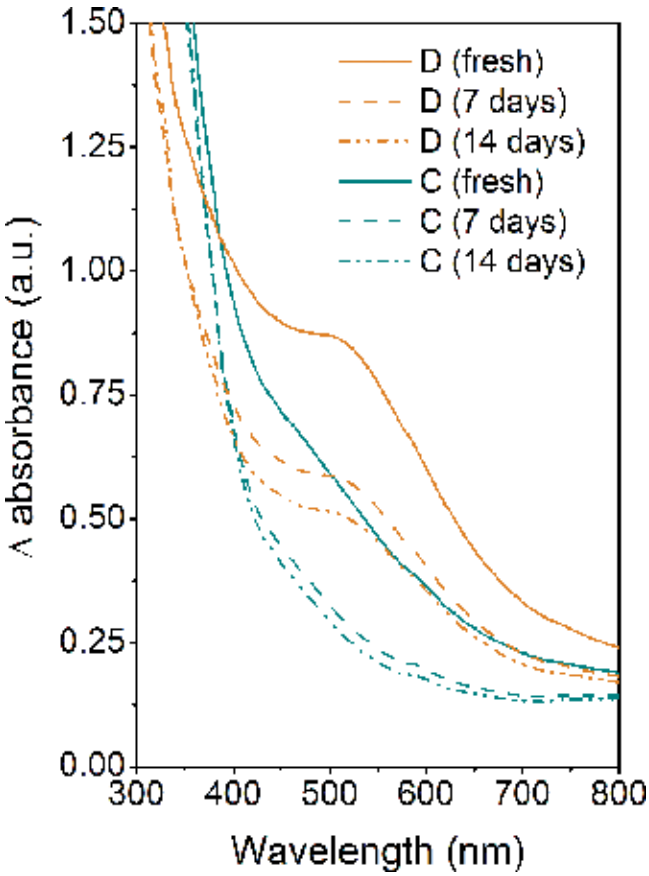

Figure 8. Aging stability (from 0 to 14 days) of Au NPs prepared by sputtering into PEG: PEG-SH (sample C) and PEG: PEG-S_2H_2 (sample D) examined by UV-Vis spectroscopy [47].

was examined in the period of 0–14 days (see **Figure 8**). **Figure 8** shows a decrease of UV-Vis absorption, which means the PEGylated Au NPs tend to slightly aggregate with aging time. Au NPs protected by PEG-SH appear to be more stable than the NPs protected by PEG-S_2H_2, since there are no significant changes in the UV-Vis absorption spectrum of those after 14 days of aging.

The progress in temperature stability of samples C and D is well documented by spectra in **Figure 9**. Immediately after the preparation of Au NPs, the samples were heated for one hour at 35, 60, 75–100°C, respectively. UV-Vis spectra measured at room temperature (RT) were used as reference. **Figure 9** shows that the post-deposition heating of colloidal solution C (Au NPs stabilized by PEG-SH) at temperature 35°C induces only a mild decrease of UV-Vis absorption, which did not change with further temperature increase. The post-sputtering heating of sample D (Au NPs protected by PEG-S_2H_2) caused a gradual decrease of UV-Vis absorption with increasing temperature. The sample D turns out to have lower temperature stability with the tendency for aggregation compared to the sample C. The results of aging and temperature stability of Au NPs with core shielded by PEG-SH molecules (sample C) are in good agreement with data published by Hatakeyama et al. [41].

http://dx.doi.org/10.5772/intechopen.71340

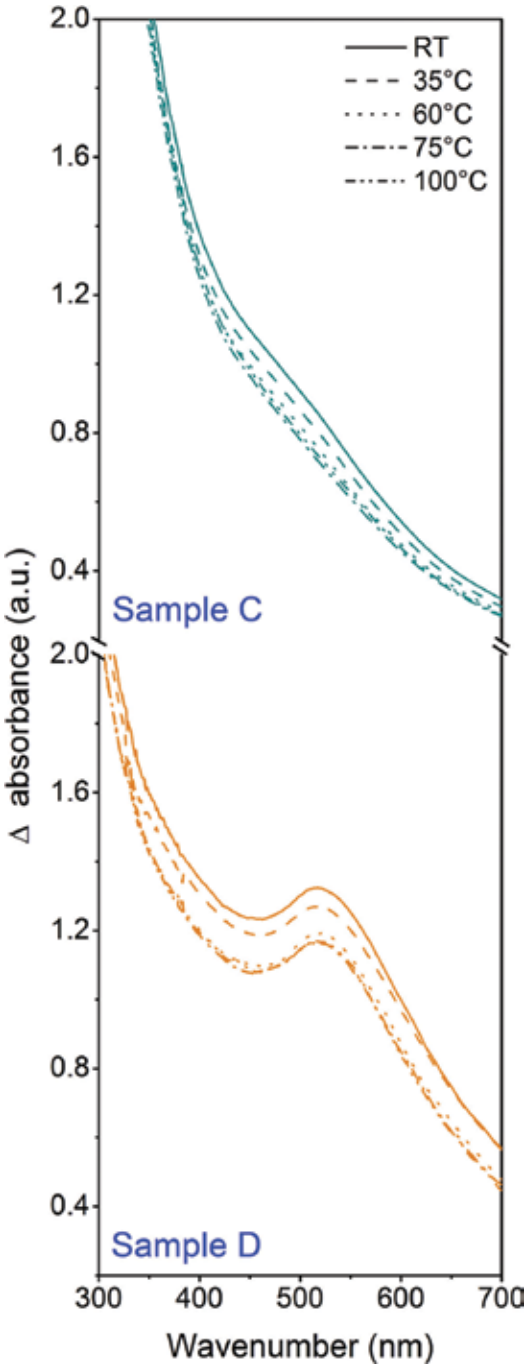

Figure 9. Temperature stability (from RT to 100°C) of Au NPs prepared by sputtering into PEG: PEG-SH (Sample C) and PEG: PEG-S_2H_2 (Sample D) examined by UV-Vis spectroscopy [47].

Hatakeyama et al. investigated the effect of temperature on the structure and growth of Au NPs prepared by sputtering method by small-angle X-ray scattering. Ionic liquid 1-buthyl-3-methylimidazolium tetrafluoroborate was used as the liquid substrate. The

liquid was heated from 20 to 80°C before sputtering. It was found that the Au NP sizes (i) are uniform at constant temperature, (ii) increase as the temperature rises, and (iii) values of W_{FWHM} (full width at half maxima of distribution curves) increase with the rising temperature. At lower temperatures (20 and 30°C), W_{FWHM} values were almost the same as d_{peak} (diameter at the peak-top of distribution curves) values. The values gradually increase and reach 40–70°C, and then increases dramatically with temperature [64].

4.3. Applications of PEGylated nanoparticles

Polyethylene glycol is one of the most used NP stabilizing polymer and the gold standard for "stealth" polymers in the emerging area of polymer-based drug carriers, gene vectors, imaging, therapeutic agents, bio-sensing, and tissue regeneration [65, 66].

Localized surface plasmon resonance (LSPR) is specific property of Au NPs that depends on particle size and distance between the particles. In the case of Au NPs, the absorption maximum connected to LSPR is between 500 and 550 nm. LSPR phenomenon is associated with oscillation of the electron gas due to excitation by incident light beam. This property puts the Au NPs to the forefront of interest in the area of biosensors technology. Creation of Au NPs aggregates invokes interparticle surface plasmon coupling, which leads to a dramatic change of color of the colloidal solution from red to blue. It also causes broadening of the surface plasmon resonance peak. Significant color change of colloids can be easily seen by the naked eye, without usage of any analytical method. Aggregation of Au NPs is extensively used in colorimetric detection of DNA, metal ions, proteins, toxins, and enzyme activity too [67, 68]. Kim et al. have found a simple procedure that can identify differences between normal and increased calcium ion (Ca^{2+}) levels in serum using calsequestrin (CSQ)-immobilized Au NPs [69, 70]. Zhang et al. successfully grafted PEG-SH onto CTAB shielded gold nanorods (Au NR) and prepared uniform monolayer of Au NRs on silicon by gradual evaporation of the residual water. This approach brings a new opportunity to prepare uniform plasmonic sensing platforms due to stability of PEGylated Au NRs in the serum [71].

Molecular imaging is associated with processes ongoing in living organisms at cellular and molecular levels. Diseases in early stage can be identified and monitored by specific molecular-imaging agents, which are very powerful method enabling a rapid and targeted treatment. Nowadays, MRI, CT, ultrasound, optical imaging, single-photon emission computed tomography (SPECT), and positron-emission tomography (PET) are the most commonly used imaging methods [72]. In contrast to other imaging agents, Au NPs offer better optical imaging properties because: (i) their light scattering effect is very strong, (ii) they are much brighter than chemical fluorophores, (iii) they resist photo-bleaching, and (iv) they can be easily spotted at low concentrations (10^{-16} M). For Au NPs-based contrast agents, the most promising imaging technique is Raman spectroscopy. Au NPs immobilized with thiolated PEG and conjugated with antibody specifically bind to the epidermal growth factor. These SERS nanoparticles for active targeting of both cancer cells and tumor xenografts were more than 200 times brighter than near-infrared-emitting quantum dots, and allowed spectroscopic detection of small tumors at a penetration depth of 1–2 cm [70]. Silvestri et al. have synthesized Au NPs

stabilized by PEG-SH and used them as CT contrast agents for *in vivo* experiments on mice. They have reported that the surface immobilization together with the small hydrodynamic diameters (3.8 nm) of the custom tailored Au NPs allowed their efficient renal cleansing, prolonged blood circulation, and stealth capability [73].

LSPR band of Au NPs leads to strong light absorption and efficient conversion of the energy into localized heat, which can be used for selective ablation of cancer cells [74]. This procedure is called plasmonic photothermal therapy (PPT). Liu et al. have shown that the multidentate PEG ligand functionalized Au NRs can be used as an effective NIR photothermal agent for tumor ablation *in vivo*. PEGylated Au NRs showed that low cytotoxicity on most mice organs *in vivo* had high efficacy of cancer cells ablation *in vitro*, accumulated in tumors preferentially and showed good stability in serum [75]. Li et al. prepared PEGylated Cu nanowires (Cu NWs) with efficient photothermal conversion (12.5%) by NIR irradiation at 808 nm and studied selective killing of cancer cells *in vitro* and effective photothermal ablation of cancer *in vivo*. The authors showed the intratumoral injection of PEGylated Cu-NWs into colon tumor-bearing mice and ensuing NIR irradiation (808 nm, 1.5 W/cm^2) for 6 min significantly raised the local temperature to >50°C, induced necrosis, and suppressed tumor growth [76]. Ruff et al. studied the effect of multivalency on the stability of NIR-absorbing Au NRs (CTAB stabilized) immobilized with mono-, bi- and tridentate PEG thiol ligands. Their PEGylation approach leads to Au NPs and Au NRs with CTAB concentration below the detection limit. Furthermore, high biocompatibility after PEGylation of both Au NPs and Au NRs was found and no significant difference in cytotoxicity against human cervical cancer cells comparing the mono-, bi- and tridentate PEGylated species was observed, which makes them suitable as biocompatible contrast agents [77].

Besides the PPT, PEGylated gold nanoparticles are very promising material for photodynamic therapy (PDT) drug delivery [78, 79]. NPs can be stabilized by steric repulsion to inhibit colloid aggregation in physiological conditions by using water-soluble PEG [80]. PEGylated Au NPs show remarkable resistance in protein adsorption due to the high degree of hydration of the randomly coiled PEG molecules [81]. According to this property, drugs carried by NPs could be shielded from being cleared/removed by the reticuloendothelial system (RES) [82]. Therefore, the blood circulation time of NPs can be prolonged. Drug distribution *in vivo* can be regulated too. Such drug carriers can preferentially accumulate in tumor sites through the leaky tumor neovasculature and do not re-enter the blood stream, which is called "enhanced permeability and retention" (EPR) effect [82]. Cheng et al. prepared PEGylated Au NPs conjugated with silicone phthalocyanine with a reversible PDT drug adsorption. It was found that the delivery mode of this system greatly improves the transport of the drug to the tumor compared to conventional drug administration [83]. Li et al. demonstrated that the 75 nm latex particles remained in rat circulation 40 times longer (from 20 min to 13 h) when immobilized with PEG larger than 5000 kDa [84]. Klibanov and Huang found that PEGylation leads to advantageous results in other drug delivery systems as well. PEGylation of liposomes improved their circulation half-life from 30 min to 5 h without increasing leakage of the liposome interior [85]. In the mid-1990s, Doxil® (liposomal delivery vehicle for doxorubicin) and Oncospar (PEG-L-asparaginase) became the first FDA approved NP therapeutics [86, 87].

5. Conclusions

Cathode sputtering is a well-established technique for the preparation of metal nanostructures. The manipulation of the deposition parameters enable formation of precisely controlled material. For the properties of the resulting material, the proper selection of substrate is necessary. For the traditional application of the thin metal films in electronics, insulating substrates are usually necessary, of which the glass and polymer substrates are the most important. In this chapter, we have discussed the problems of glass substrates in adhesion of the metal layers and possibilities of dewetting. The polymer substrates on the other hand provide better adhesion to the metals, but surface morphology effects are more pronounced. A new and perspective branch of substrates for sputtering deposition are liquids. Therefore, this chapter provides a deeper insight into the problems of direct sputtering of noble metals into liquid substrate, i.e., preparation of NPs. Basic characteristics, technology of preparation, and applications of those materials are explained. The results of the authors' team support the general overview. Direct sputtering of Au atoms onto PEG and thiol terminated PEG has led to successful formation of spherical NPs. The diameters of the prepared Au NPs ranged from 2.1 to 5.9 nm depending on the capturing medium. NPs smaller than 3 nm in diameter exhibited loss of SPR band because of the small NP size and/or attachment of thiolated PEG on the Au NPs' surface. Solution of Au NPs stabilized by PEG-SH (sample C) exhibited higher time and temperature stability compared to the solution where Au NPs were stabilized by PEG-S_2H_2 (sample D). This colloidal solution showed the best time and temperature stability with the size of Au NPs of 2.9 nm, which can have a positive effect in biomedical use and for catalysis of chemical reactions. PEGylated NPs have huge potential in biomedical applications (drug delivery, therapy, imaging, and biosensing).

Acknowledgements

Financial support of this work under the GACR projects 17-00939S and P108/12/G108 is gratefully acknowledged.

Author details

Alena Reznickova*, Ondrej Kvitek, Dominik Fajstavr, Nikola Slavikova and Vaclav Svorcik

*Address all correspondence to: reznicka@vscht.cz

Department of Solid State Engineering, University of Chemistry and Technology Prague, Prague, Czech Republic

References

[1] Wasa K, Kanno I, Kotera H, editors. Handbook of Sputter Deposition Technology: Fundamentals and Applications for Functional Thin Films, Nano-Materials and MEMS. 2nd ed. Oxford: Elsevier; 2012 660 p

[2] Frey H, Khan HR, editors. Handbook of Thin Film Technology. Berlin: Springer Verlag; 2015. 380 p. DOI: 10.1007/978-3-642-05430-3

[3] Wender H, Migowski P, Feil AF, Teixeira SR, Dupont J. Sputtering deposition of nanoparticles onto liquid substrates: Recent advances. Coordination Chemistry Reviews. 2013;**257**:2468-2483. DOI: 10.1016/j.ccr.2013.01.013

[4] Maissel I, Glang R, editors. Handbook of Thin Film Technology. 1st ed. New York: McGraw-Hill; 1970 800 p

[5] McClanahan ED, Laegreid N. Production of thin films by controlled deposition of sputtered material. In: Behrisch R, Wittmaack K, editors. Sputtering by Particle Bombardment III. Berlin: Springer Verlag; 1991. p. 339-377. DOI: 10.1007/3540534288_21

[6] Volinsky AA, Moody NR, Gerberich WW. Interfacial toughness measurements for thin films on substrates. Acta Materialia. 2002;**50**:441-466. DOI: 10.1016/S1359-6454(01)00354-8

[7] Haq KE, Behrndt KH, Kobin I. Adhesion mechanism of gold-underlayer film combinations to oxide substrates. Journal of Vacuum Science and Technology. 1969;**6**:148-152. DOI: 10.1116/1.1492648

[8] Sexton BA, Feltis BN, Davis TJ. Characterisation of gold surface plasmon resonance sensor substrates. Sensors and Actuators A. 2008;**141**:471-475. DOI: 10.1016/j.sna.2007.10.020

[9] Kim WM, Kim SH, Lee KS, Lee TS, Kim IH. Titanium nitride thin film as an adhesion layer for surface plasmon resonance sensor chips. Applied Surface Science. 2012;**261**:749-752. DOI: 10.1016/j.apsusc.2012.08.093

[10] Ito Y, Kushida K, Takeuchi H. Role of chromium sublayers in the growth of highly crystalline (111)-oriented gold-films on sapphire. Journal of Crystal Growth. 1991;**112**:427-436. DOI: 10.1016/0022-0248(91)90319-Z

[11] Jang HG, Kim KH, Han S, Choi WK, Jung HJ, Koh SK, Kim HB. Adhesion improvement between Au films and glass by 1 keV Ar+ ion irradiation. Journal of Vacuum Science and Technology A. 1997;**15**:2233-2239. DOI: 10.1116/1.580539

[12] Svorcik V, Kotal V, Blahova O, Spirkova M, Sajdl P, Hnatowicz V. Modification of surface properties of polyethylene by Ar plasma discharge. Nuclear Instruments and Methods in Physics Research Section B. 2006;**244**:365-372. DOI: 10.1016/j.nimb.2005.10.003

[13] Park JW, Pedraza AJ, Allen WR. The interface between sputter-deposited gold thin films and ion-bombarded sapphire substrates. Applied Surface Science. 1996;**103**:39-48. DOI: 10.1016/0169-4332(96)00097-9

[14] Nguyen TP, Ip J, le Rendu P, Lahmar A. Improved adhesion of gold coatings on ceramic substrates by thermal treatment. Surface and Coating Technology. 2001;**141**:108-114. DOI: 10.1016/S0257-8972(01)01165-3

[15] Mosier-Boss PA, Lieberman SH. Comparison of three methods to improve adherence of thin gold films to glass substrates and their effect on the SERS response. Applied Spectroscopy. 1999;**53**:862-873. DOI: 10.1366/0003702991947469

[16] Lahiri B, Dylewicz R, de la Rue RM, Johnson NP. Impact of titanium adhesion layers on the response of arrays of metallic split-ring resonators (SRRs). Optics Express. 2010;**18**:11202-11207. DOI: 10.1364/OE.18.011202

[17] Li X, Huang F, Curry M, Street SC, Weaver ML. Improved adhesion of Au thin films to SiOx/Si substrates by dendrimer mediation. Thin Solid Films. 2005;**473**:164-168. DOI: 10.1016/j.tsf.2004.07.080

[18] Yoshida S, Adhikari S, Gomi K, Shrestha R, Huggett D, Miyasaka C, Park I. Opto-acoustic technique to evaluate adhesion strength of thin-film systems. AIP Advances. 2012;**2**:022126. DOI: 10.1063/1.4719698

[19] Tsukamoto Y, Kuroda H, Sato A, Yamaguchi H. Microindentation adhesion tester and its application to thin-films. Thin Solid Films. 1992;**213**:220-225. DOI: 10.1016/0040-6090(92)90285-J

[20] Gerberich WW, Jungk JM, Li M, Volinsky AA, Hoehn JW, Yoder K. Length scales for the fracture of nanostructures. International Journal of Fracture. 2003;**119**:387-405. DOI: 10.1023/A:1024927812734

[21] Thompson CV. Solid-state dewetting of thin films. In: Clarke DR, editor. Annual Review of Materials Research. El Camino Way: Annual Reviews. 2012. p. 399-434. DOI: 10.1146/annurev-matsci-070511-155048

[22] Leroy F, Borowik L, Cheynis F, Almadori Y, Curiotto S, Trautmann M, Barbe JC, Muller P. How to control solid state dewetting: A short review. Surface Science Reports. 2016;**71**:391-409. DOI: 10.1016/j.surfrep.2016.03.002

[23] Kosinova A, Kovalenko O, Klinger L, Rabkin E. Mechanisms of solid-state dewetting of thin Au films in different annealing atmospheres. Acta Materialia. 2015;**83**:91-101. DOI: 10.1016/j.actamat.2014.09.049

[24] Svorcik V, Kvitek O, Lyutakov O, Siegel J, Kolska Z. Annealing of sputtered gold nanostructures. Applied Physics A: Materials Science & Processing. 2011;**102**:747-751. DOI: 10.1007/s00339-010-5977-5

[25] Svorcik V, Siegel J, Sutta P, Mistrik J, Janicek P, Worsch P, Kolska Z. Annealing of gold nanostructures sputtered on glass substrate. Applied Physics A: Materials Science & Processing. 2011;**102**:605-610. DOI: 10.1007/s00339-010-6167-1

[26] Kvitek O, Konrad P, Svorcik V. Time dependence and mechanism of Au nanostructure transformation during annealing. Functional Materials Letters. 2014;**7**:1450022. DOI: 10.1142/S1793604714500222

[27] Siegel J, Kvitek O, Lyutakov O, Reznickova A, Svorcik V. Low pressure annealing of gold nanostructures. Vacuum. 2013;**98**:100-105. DOI: 10.1016/j.vacuum.2013.03.019

[28] Tesler AB, Karakouz T, Bendikov TA, Haran G, Vaskevich A, Rubinstein I. Tunable localized plasmon transducers prepared by thermal dewetting of percolated evaporated gold films. Journal of Physical Chemistry C. 2011;**115**:24642-24652. DOI: 10.1021/jp209114j

[29] Forrest SR. The path to ubiquitous and low-cost organic electronic appliances on plastic. Nature. 2004;**428**:911-918. DOI: 10.1038/nature02498

[30] Bonderover E, Wagner S. A woven inverter circuit for e-textile applications. IEEE Electron Device Letters. 2004;**25**:295-297. DOI: 10.1109/LED.2004.826537

[31] Brabec CJ. Organic photovoltaics: Technology and market. Solar Energy Materials & Solar Cells. 2004;**83**:273-292. DOI: 10.1016/j.solmat.2004.02.030

[32] Robledo-Ortíz JR, Ramírez-Arreola DE, Rodrigue D, González-Núñez R. Blown films and ribbons extrusion. In: Saldívar-Guerra E, Vivaldo-Lima E, editors. Handbook of Polymer Synthesis, Characterization, and Processing. 1st ed. Chichester: Wiley; 2013. p. 463-472

[33] Mehmet-Alkan AA, Hay JN. The crystallinity of poly(ether ether ketone). Polymer. 1992;**33**:3527-3530. DOI: 10.1016/0032-3861(92)91116-J

[34] Kvitek O, Fajstavr D, Reznickova A, Kolska Z, Slepicka P, Svorcik V. Annealing of gold nanolayers sputtered on polyimide and polyetheretherketone. Thin Solid Films. 2016;**616**:188-196. DOI: 10.1016/j.tsf.2016.08.025

[35] Svorcik V, Siegel J, Slepicka P, Kotal V, Svorcikova J, Spirkova M. Au nanolayers deposited on polyethyleneterephtalate and polytetrafluorethylene degraded by plasma discharge. Surface and Interface Analysis. 2007;**39**:79-85. DOI: 10.1002/sia.2512

[36] Slepicka P, Fidler T, Vasina A, Svorcik V. Ripple-like structure on PLLA induced by gold deposition and thermal treatment. Materials Letters. 2012;**79**:4-6. DOI: 10.1016/j.matlet.2012.03.070

[37] Doane TL, Cheng Y, Babar A, Hill RJ, Burda C. Electrophoretic mobilities of PEGylated gold NPs. Journal of the American Chemical Society. 2010;**132**:15624-15631. DOI: 10.1021/ja1049093

[38] Mie G. Beiträge zur optik trüber medien, speziell colloidaler metallösungem. Annals of Physics. 1908;**25**:377-445. DOI: 10.1002/andp.19083300302

[39] Turkevich J, Stevenson PC, Hillier J. A study of the nucleation and growth processes in the synthesis of colloidal gold. Discussions of the Faraday Society. 1951;**11**:55-75. DOI: 10.1039/df9511100055

[40] Brust M, Walker M, Bethell D, Schiffrin DJ, Whyman R. Synthesis of thiol-derivatized gold nanoparticles in a 2-phase liquid-liquid system. Journal of the Chemical Society, Chemical Communications. 1994:801-802. DOI: 10.1039/c39940000801

[41] Hatakeyama Y, Kato J, Mukai T, Judai K, Nishikawa K. Effect of adding a thiol stabilizer on synthesis of Au nanoparticles by sputter deposition onto poly(ethylene glycol). Bulletin of the Chemical Society of Japan. 2014;**87**:773-779. DOI: 10.1246/bcsj.20140023

[42] Hori T, Nagata K, Iwase A, Hori F. Synthesis of Cu nanoparticles using gamma-ray irradiation reduction method. Japanese Journal of Applied Physics. 2014;**53**:05FC05. DOI: 10.7567/jjap.53.05fc05

[43] Ye GX, Zhang QR, Feng CM, Ge HL, Jiao ZK. Structural and electrical properties of a metallic rough-thin-film system deposited on liquid substrates. Physical Review B. 1996;**54**:14754-14757. DOI: 10.1103/PhysRevB.54.14754

[44] Wender H, Gonçalves RV, Feil AF, Migowski P, Poletto FS, Pohlmann AR, Dupont J, Teixeira SR. Sputtering onto liquids: From thin films to nanoparticles. Journal of Physical Chemistry C. 2011;**115**:16362-16367. DOI: 10.1021/jp205390d

[45] Wender H, de Oliveira LF, Feil AF, Lissner E, Migowski P, Meneghetti MR, Teixeira SR, Dupont J. Synthesis of gold nanoparticles in a biocompatible fluid from sputtering deposition onto castor oil. Chemical Communications. 2010;**46**:7019-7021. DOI: 10.1039/c0cc01353f

[46] Slepička P, Elashnikov R, Ulbrich P, Staszek M, Kolská Z, Švorčík V. Stabilization of sputtered gold and silver nanoparticles in PEG colloid solutions. Journal of Nanoparticle Research. 2015;**17**:11. DOI: 10.1007/s11051-014-2850-z

[47] Reznickova A, Slepicka P, Slavikova N, Staszek M, Svorcik V. Preparation, aging and temperature stability of PEGylated gold nanoparticles. Colloids and Surfaces A. 2017;**523**:91-97. DOI: 10.1016/j.colsurfa.2017.04.005

[48] Shishino Y, Yonezawa T, Kawai K, Nishihara H. Molten matrix sputtering synthesis of water-soluble luminescent Au nanoparticles with a large Stokes shift. Chemical Communications. 2010;**46**:7211-7213. DOI: 10.1039/c0cc01702g

[49] Siegel J, Kvítek O, Ulbrich P, Kolská Z, Slepička P, Švorčík V. Progressive approach for metal nanoparticle synthesis. Materials Letters. 2012;**89**:47-50. DOI: 10.1016/j.matlet.2012.08.048

[50] Staszek M, Siegel J, Rimpelova S, Lyutakov O, Svorcik V. Cytotoxicity of noble metal nanoparticles sputtered into glycerol. Materials Letters. 2015;**158**:351-354. DOI: 10.1016/j.matlet.2015.06.021

[51] Ballou B, Lagerholm BC, Ernst LA, Bruchez MP, Waggoner AS. Noninvasive imaging of quantum dots in mice. Bioconjugate Chemistry. 2004;**15**:79-86. DOI: 10.1021/bc034153y

[52] Liu HY, Doane TL, Cheng Y, Lu F, Srinivasan S, Zhu JJ, Burda C. Control of surface ligand density on PEGylated gold nanoparticles for optimized cancer cell uptake. Particle and Particle Systems Characterization. 2015;**32**:197-204. DOI: 10.1002/ppsc.201400067

[53] Liu GY, Luo QQ, Wang HB, Zhuang WH, Wang YB. In situ synthesis of multidentate PEGylated chitosan modified gold nanoparticles with good stability and biocompatibility. RSC Advances. 2015;**5**:70109-70116. DOI: 10.1039/c5ra11600g

[54] Abd-Elaal AA, Tawfik SM, Shaban SM. Simple one step synthesis of nonionic dithiol surfactants and their self-assembling with silver nanoparticles: Characterization, surface properties, biological activity. Applied Surface Science. 2015;**342**:144-153. DOI: 10.1016/j.apsusc.2015.03.038

[55] Gao J, Huang XY, Liu H, Zan F, Ren JC. Colloidal stability of gold nanoparticles modified with thiol compounds: Bioconjugation and application in cancer cell imaging. Langmuir. 2012;**28**:4464-4471. DOI: 10.1021/la204289k

[56] Alkilany AM, Yaseen AIB, Park J, Eller JR, Murphy CJ. Facile phase transfer of gold nanoparticles from aqueous solution to organic solvents with thiolated poly(ethylene glycol). RSC Advances. 2014;**4**:52676-52679. DOI: 10.1039/c4ra11928b

[57] Di Felice R, Selloni A. Adsorption modes of cysteine on Au (111): Thiolate, amino-thiolate, disulfide. The Journal of Chemical Physics. 2004;**120**:4906-4914. DOI: 10.1063/1.1645789

[58] Wuelfing WP, Gross SM, Miles DT, Murray RW. Nanometer gold clusters protected by surface-bound monolayers of thiolated poly(ethylene glycol) polymer electrolyte. Journal of the American Chemical Society. 1998;**120**:12696-12697. DOI: 10.1021/ja983183m

[59] Murphy CJ, Sau TK, Gole AM, Orendorff CJ, Gao J, Gou L, Hunyadi SE, Li T. Anisotropic metal nanoparticles: Synthesis, assembly, and optical applications. The Journal of Physical Chemistry. B. 2005;**109**:13857-13870. DOI: 10.1021/jp0516846

[60] Uskokovic V. Dynamic light scattering based microelectrophoresis: Main prospects and limitations. Journal of Dispersion Science and Technology. 2012;**33**:1762-1786. DOI: 10.1080/01932691.2011.625523

[61] Souza TGF, Ciminelli VST, Mohallem NDS. A comparison of TEM and DLS methods to characterize size distribution of ceramic nanoparticles. Journal of Physics: Conference Series. 2016;**733**:012039. DOI: 10.1088/1742-6596/733/1/012039

[62] Daniel MC, Astruc D. Gold nanoparticles: Assembly, supramolecular chemistry, quantum-size-related properties, and applications toward biology, catalysis, and nanotechnology. Chemical Reviews. 2004;**104**:293-346. DOI: 10.1021/cr030698+

[63] Lica GC, Zelakiewicz BS, Constantinescu M, Tong YY. Charge dependence of surface plasma resonance on 2 nm octanethiol-protected Au nanoparticles: Evidence of a free-electron system. The Journal of Physical Chemistry. B. 2004;**108**:19896-19900. DOI: 10.1021/jp045302s

[64] Hatakeyama Y, Takahashi S, Nishikawa K. Can temperature control the size of Au nanoparticles prepared in ionic liquids by the sputter deposition technique? Journal of Physical Chemistry C. 2010;**114**:11098-11102. DOI: 10.1021/jp102763n

[65] Knop K, Hoogenboom R, Fischer D, Schubert US. Poly(ethylene glycol) in drug delivery: Pros and cons as well as potential alternatives. Angewandte Chemie (International Ed. in English). 2006;**49**:6288-6308. DOI: 10.1002/anie.200902672

[66] Encabo-Berzosa MD, Sancho-Albero M, Crespo A, Andreu V, Sebastian V, Irusta S, Arruebo M, Martín-Duque P, Santamaria S. The effect of PEGylated hollow gold nanoparticles on stem cell migration: Potential application in tissue regeneration. Nanoscale. 2017;**9**:9848-9858. DOI: 10.1039/c7nr01853c

[67] Slocik JM, Zabinski JS, Phillips DM, Naik RR. Colorimetric response of peptide-functionalized gold nanoparticles to metal ions. Small. 2008;**4**:548-551. DOI: 10.1002/smll.200700920

[68] Zhao WA, Chiuman W, Lam JCF, Brook MA, Li YF. Simple and rapid colorimetric enzyme sensing assays using non-crosslinking gold nanoparticle aggregation. Chemical Communications. 2007;**36**:3279-3231. DOI: 10.1039/b705335e

[69] Kim S, Park JW, Kim D, Kim D, Lee IH, Jon S. Bioinspired colorimetric detection of calcium(II) ions in serum using calsequestrin-functionalized gold nanoparticles. Angewandte Chemie International Edition. 2009;**48**:4138-4141. DOI: 10.1002/anie.200900071

[70] Kim D, Jon S. Gold nanoparticles in image-guided cancer therapy. Inorganica Chimica Acta. 2012;**393**:154-164. DOI: 10.1016/j.ica.2012.07.001

[71] Zhang Z, Lin MS. Fast loading of PEG–SH on CTAB-protected gold nanorods. RSC Advances. 2014;**4**:17760-17767. DOI: 10.1039/c3ra48061e

[72] Sharma P, Brown S, Walter G, Santra S, Moudgil B. Nanoparticles for bioimaging. Advances in Colloid and Interface Science. 2006;**123**:471-485. DOI: 10.1016/j.cis.2006.05.026

[73] Silvestri A, Polito L, Bellani G, Zambelli V, Jumde RP, Psaro R, Evangelisti C. Gold nanoparticles obtained by aqueous digestive ripening: Their application as X-ray contrast agents. Journal of Colloid and Interface Science. 2015;**439**:28-33. DOI: 10.1016/j.jcis.2014.10.025

[74] Huang XH, Jain PK, El-Sayed IH, El-Sayed MA. Plasmonic photothermal therapy (PPTT) using gold nanoparticles. Lasers in Medical Science. 2008;**23**:217-228. DOI: 10.1007/s10103-007-0470-x

[75] Liu X, Huang N, Li H, Wang H, Jing Q, Ji J. Multidentate polyethylene glycol modified gold Nanorods for in vivo near-infrared photothermal cancer therapy. ACS Applied Materials & Interfaces. 2014;**6**:5657-5668. DOI: 10.1021/am5001823

[76] Li KC, Chu HC, Lin Y, Tuan HY, Hu YC. PEGylated copper nanowires as a novel photothermal therapy agent. ACS Applied Materials & Interfaces. 2016;**8**:12082-12090. DOI: 10.1021/acsami.6b04579

[77] Ruff J, Steitz J, Buchkremer A, Noyong M, Hartmann H, Besmehn A, Simon U. Multivalency of PEG-thiol ligands affects the stability of NIR-absorbing hollow gold nanospheres and gold nanorods. Journal of Materials Chemistry B. 2016;**4**:2828-2841. DOI: 10.1039/c6tb00674d

[78] Hone DC, Walker PI, Evans-Gowing R, FitzGerald S, Beeby A, Chambrier I, Cook MJ, Russell DA. Generation of cytotoxic singlet oxygen via phthalocyanine-stabilized gold nanoparticles: A potential delivery vehicle for photodynamic therapy. Langmuir. 2002;**18**:2985-2987. DOI: 10.1021/la0256230

[79] Connor EE, Mwamuka J, Gole A, Murphy CJ, Wyatt MD. Gold nanoparticles are taken up by human cells but do not cause acute cytotoxicity. Small. 2005;**1**:325-327. DOI: 10.1002/smll.200400093

[80] Liu YL, Shipton MK, Ryan J, Kaufman ED, Franzen S, Feldheim DL. Synthesis, stability, and cellular internalization of gold nanoparticles containing mixed peptide-poly(ethylene glycol) monolayers. Analytical Chemistry. 2007;**79**:2221-2229. DOI: 10.1021/ac061578f

[81] Blättler TM, Pasche S, Textor M, Griesser HJ. High salt stability and protein resistance of poly(L-lysine)-g-poly(ethylene glycol) copolymers covalently immobilized via aldehyde plasma polymer interlayers on inorganic and polymeric substrates. Langmuir. 2006;**22**:5760-5769. DOI: 10.1021/la0602766

[82] Paciotti GF, Kingston DGI, Tamarkin L. Colloidal gold nanoparticles: A novel nanoparticle platform for developing multifunctional tumor-targeted drug delivery vectors. Drug Development Research. 2006;**67**:47-54. DOI: 10.1002/ddr.20066

[83] Cheng Y, Samia AC, Meyers JD, Panagopoulos I, Fei B, Burda C. Highly efficient drug delivery with gold nanoparticle vectors for *in vivo* photodynamic therapy of cancer. Journal of the American Chemical Society. 2008;**130**:10643-10647. DOI: 10.1021/ja801631c

[84] Tan JS, Butterfield DE, Voycheck CL, Caldwell KD, Li JT. Surface modification of nanoparticles by PEO/PPO block copolymers to minimize interactions with blood components and prolong blood circulation in rats. Biomaterials. 1993;**14**:823-833. DOI: 10.1016/0142-9612(93)90004-L

[85] Klibanov AL, Maruyama K, Torchilin VP, Huang L. Amphipathic polyethyleneglycols effectively prolong the circulation time of liposomes. FEBS Letters. 1990;**268**:235-237. DOI: 10.1016/0014-5793(90)81016-H

[86] Petros RA, DeSimone JM. Strategies in the design of nanoparticles for therapeutic applications. Nature Reviews. Drug Discovery. 1999;**9**:615-627. DOI: 10.1038/nrd2591

[87] Jokerst JV, Lobovkina T, Zare RN, Gambhir SS. Nanoparticle PEGylation for imaging and therapy. Nanomedicine. 2011;**6**:715-728. DOI: 10.2217/nnm.11.19

Chapter 9

Silver Nanoparticles Fabricated Using Chemical Vapor Deposition and Atomic Layer Deposition Techniques: Properties, Applications and Perspectives: Review

Piotr Piszczek and Aleksandra Radtke

Additional information is available at the end of the chapter

http://dx.doi.org/10.5772/intechopen.71571

Abstract

Silver nanoparticles with unique physicochemical properties and high biocide activity attract great interest in the design and in the manufacture of the new generation materials intended for biomedical technologies. This review aims to provide assessment of the bioactivity and usefulness of Ag-based materials in biomedical technologies, which are produced with the use of chemical vapor deposition (CVD) and atomic layer deposition (ALD) methods. The use of CVD and ALD technologies in the fabrication of silver layers, nanoparticles, and nanocomposites are discussed in the first part of this chapter. The second half of this review deals with the topics associated with the release of silver ions from nanoparticles or nanolayers and discusses the antimicrobial activity, bio-integration properties and toxicity of these materials.

Keywords: silver, silver-based materials, CVD, ALD, bioactivity, biomedical materials

1. Introduction

The rapid development of nanotechnologies is a result of the numerous applications of nanomaterials in various fields of our life. The metallic nanograins or metallic nanolayers, of either simple or composite nature, are important materials in the improvement of such traditional areas as electronics, optics, and catalysis. However, in last few years we have observed a great interest in the application of these nanomaterials in biological, biomedical, pharmaceutical, cosmetic, food, and textile technologies [1–5]. The use of different methods offers the possibility of the fabrication of nano-sized materials (materials in which at least one dimension is less than 100 nm) of different structure, surface morphology,

physicochemical properties, and bioactivity [6–9]. From the medical point of view, it is interesting that silver as an antimicrobial agent has accompanied human civilization since ancient times. The use of silver vessels or putting a silver coin/spoon into tanks in order to preserve drinking water from spoilage by bacteria and algae, was practiced by ancient Egyptians and Greeks, as well as by sailors in times of great geographic discoveries [10]. In modern times, silver (usually used as colloidal silver) is applied to treatment water and its disinfection. The system working on the board of International Space Station is a good example [9, 11]. Moreover, the fabrication of this metal coating on the surface of medical devices or pieces of furniture, and also incorporation of Ag nanoparticles to the building and textile materials, influences the reduction of the hospital-related infections [12–14]. Silver nanoparticles (AgNPs) are also component of many health and cosmetic products due to their antimicrobial activity and deodorizing properties [15, 16]. Based on previous results, it is noted that the above-mentioned nanoparticles exhibit antimicrobial activity against 650 strains of pathogenic microorganisms such as bacteria, fungi, viruses, molds, and yeasts [17, 18]. A number of mechanisms have been proposed to explain the antimicrobial activity of AgNPs: (1) blocking the active respiratory chains of organisms; (2) disrupting the cellular membrane leading to leakage of cellular contents; (3) binding to the functional groups of microbial proteins that lead to protein denaturation and DNA malfunctions; and (4) blocking of nutrient transportation enzymes across the cell membrane [18]. The above-mentioned biological properties of the Ag nanoparticles and nanolayers depend strongly on their structure, shape, size, surface morphology, and the substrate used in the synthesis.

Silver may form continuous nanolayers and/or dispersed nanoparticles on the substrate surface or it can be incorporated within the matrix (ceramic, glass, and polymer). Generally, two strategies based on wet chemistry and vapor phase deposition are used for the preparation of Ag-containing nanomaterials. Analysis of the literature reports showed that the reduction processes of $AgNO_3$ are the main methods, which are used in the fabrication of AgNPs both on the substrate surface as well as in the form of the dispersed particles in colloidal systems, glasses, or polymers [12, 15]. According to these reports, the wet chemical techniques are mainly used for the fabrication of silver nanoparticles [9]. In these methods, the colloidal silver is obtained by the use of three components: (a) silver precursor, predominantly $AgNO_3$; (b) reducing agent – for example, $NaBH_4$, citric acid or its sodium salt, gallic acid, ascorbic acid [9, 19–22]; and (c) stabilizing agents—for example, polyvinyl alcohol, polyvinyl pyrrolidone, polyethylene glycol, ethylene diamine tetra-acetic acid [23, 24]. The nucleation of nanoparticles and their growth in defined conditions (temperature, pH, reduction agents, and stabilizing agents) leads to the formation of similar size and shape particles [9, 23]. Dried Ag nanopowders, which can be added to, for example, polymeric, glass, or ceramic matrix, were obtained by freeze-drying of the colloidal solution [20]. Biosynthesis of AgNPs is a promising technique which has been intensively studied recently [25–27]. It involves the reduction of silver salt (e.g. silver nitrate) by such reducing agents as plants, bacteria, and fungi [27, 28]. The great interest of the above-mentioned method is due to its potential use in medicine (especially in cancer therapy and diagnostic)

as the procedure allowing for obtaining nontoxic antimicrobial agent [26, 28]. The need to the fabrication of silver coatings, both continuous as well as composed of dispersed metallic grains on the surface of metallic, ceramic, or polymeric substrates, requires the use of other methods. Often used photochemical synthesis of AgNPs on the surface of titania nanotube (TNT) coatings is a good example [29–31]. In this method, TNT substrate is soaked in $AgNO_3$ solutions of different concentration, and after cleaning with deionized water and drying, is irradiated using UV light at room temperature. Silver particles with diameters 10–70 nm were deposited on the top edges and walls of ca. 50–180 nm TiO_2 tubes [30, 31]. AgNPs on the surface of different titania substrates may be also prepared using electrodeposition and electrochemical methods [32–34]. Above-mentioned techniques enabled the deposition of dispersed Ag particles of diameters ca. 2–12 nm on the surface of titania particles or nanotubes.

Chemical vapor deposition (CVD) and atomic layer deposition (ALD) belong to the strategy based on the fabrication of materials from vapor phase. Analysis of literature reports revealed that both methods are not widely used in the production of biomaterials, although both methods allow exact control of the nucleation and growth of metallic single grains or layers. It may be associated with necessity for the use of vacuum and high temperatures as in the case of CVD processes, which in turn translates into high price of the final product. However, the rapid development of both above-mentioned methods, related to the introduction of new precursors, improvement of the equipment, and optimization of the deposition conditions, has led to increased interest of their application in the production of materials, with strictly defined structure, morphology, physicochemical and biological properties, and also characterized by high purity. Therefore, in this chapter we have focused on a more detailed discussion on the use of CVD and ALD methods for the production of silver-based materials, their properties and biological activity.

2. Chemical vapor deposition

Chemical vapor deposition (CVD) is a technique which allows the synthesis of nanometric layers of inorganic materials on the surface of 3D substrates. The deposition process occurs in three successive stages: (i) introduction of the volatile precursor by carrier gas to the reactor chamber; (ii) adsorption of precursor vapors on the substrate surface and the formation of intermediate products; and (iii) decomposition of these products on the heated substrate followed by nucleation and growth of the solid layer/grains, and the formation of volatile by-products and their removal from the chamber by the carrier gas [35]. Among the main factors that influence the deposition process and the quality of produced nanomaterials, the following ones can be highlighted: the precursor delivery method, total pressure in the reactor chamber (p), carrier gas and its chemical properties, substrate temperature (T_D), substrate properties, flow rate of precursor vapors, deposition time (t), and deposition rate. Among these factors, precursors as a source of formed material, seem to be the most important factor. The CVD precursor

should be characterized by: (a) the appropriate volatility to achieve the highest possible concentration of the precursor in vapors; (b) the thermal stability of the compound which avoids its premature degradation during the transportation of vapors by carrier gas; (c) its ability for thermal decomposition on the substrate surface leading to the deposition of desirable materials; (d) inexpensive and simple synthesis; and (e) low toxicity. Considering these reports, we find that for CVD, two types of compounds are usually used as silver precursors, namely inorganic silver salts and volatile silver (I) complexes. Silver nitrate ($AgNO_3$) is the widely used precursor in such techniques as the flame-assisted CVD (FACVD) and the atmospheric pressure CVD (APCVD) [36–38]. The first of these method enables the deposition of metallic silver layers of thickness 60–90 nm [36] or 60–250 nm [37] on the substrate surface heated to the temperature T_D = 573 K at atmospheric pressure. The advantage of this method is the ability to the formation of Ag-metal oxide nanocomposite coatings (e.g. TiO_2 [36], SiO_2 [39]) in one deposition process on large substrate areas. The nanocomposite coatings on the textile surface, composed of silicon dioxide with in situ incorporated Ag nanoparticles were produced by APCVD technique [38]. In the classical CVD techniques (metal-organic CVD (MOCVD), aerosol-assistant CVD (AACVD), plasma-enhanced CVD (PECVD)), a variety of volatile silver(I) compounds are used as precursors [35, 40]. This group includes the silver(I) compounds with β-diketonates and carboxylates (mainly perfluorinated carboxylates), as well as their complexes [Ag(A)(L)] (A = carboxylate or β-diketonate groups, L = trimethyl phosphine (PMe_3), trimethyl phosphine (PEt_3), vinyltriethylsilane (VTES), bis(trimethylsilyl)acetylene (BTMSA), bis(trimethylsilyl)ethyne (BTMSE)) [35, 40, 41]. The detailed data concerning silver(I) complexes, which are mainly used as CVD precursors are listed in **Table 1**. Liquid Ag(I) β-diketonates and their complexes are precursors usually used in the fabrication of metallic nanofilms of appropriate electrical conductivity [35]. Results from our investigations showed that silver(I) carboxylates (solids) and their complexes with tertiary phosphines (oils) are the group of precursors, which may be applied to the deposition of coatings composed of dispersed metallic nanoparticles. Because of the weak volatility of Ag(I) acetate and Ag(I) tri-fluoro-acetate, these compounds cannot be used in conventional CVD methods, although pure silver continuous films were deposited from these compounds using laser-inducted CVD (LICVD) technique [35, 42]. The low volatile Ag(I) carboxylates and their complexes with tri-phenyl-phosphines were also introduced into the CVD reactor chamber as a solution or a suspension in AACVD method [43]. This enabled the deposition of metallic silver layers at temperatures below 573 K, but resulting materials were contaminated with carbon, oxygen, and phosphorus.

Considering results of these investigations, it is noted that silver(I) penta-fluoro-propionate ($Ag(OOCC_2F_5)$) exhibits particularly good properties as Ag CVD precursor [44, 45] since layers consisting of dispersed AgNPs of diameters d_{Ag} = 20–60 nm were obtained after 5 min of CVD process at 563 K on the surface of Si(111) substrate. After 10 min, particles already began to coalescence and after 30 min, the continuous metallic films, of thickness ca. 2.50 μm, were formed [44]. Under the same conditions, with titanium or Ti6Al4V alloy substrates, the layer composed of dispersed Ag grains of d_{Ag} = 35–40 nm were deposited (**Figure 1**). Using titania

Precursor	Deposition temperature T_D (K)	Reactor pressure (hPa)	Carrier gas
[Ag(acac)]	473–523	—	H_2
[Ag(fod)(PMe_3)]	503–573	0.13	H_2
[Ag(fod)(PEt_3)]	503–533	0.13	H_2
[Ag(hfac)(PMe_3)]	523–723	0.07	—
[Ag(hfac)(PEt_3)]	523–623	0.07	—
[Ag(hfac)(VTES)]	433–553	0.13	—
[Ag(hfac)(BTMSA)]	423–523	0.13–13.0	—
[Ag(hfac)(BTMSE)]	373–473	13.0	—
$[Ag(tfpz)]_3$	523–623	0.67	Ar, H_2
[Ag($OOCCF_3$)]	873	No data	—
[Ag($OOCC_2F_5$)]	543–563	4	Ar
[Ag($OOCC_2F_5$)(PMe_3)]	483–563	4	Ar
[Ag($OOCC_2F_5$)(PEt_3)]	463–513	4	Ar
[Ag($OOCCF_3$)(P^nBu_3)$_2$]	573–623	1–50	N_2
[Ag($OOCC_2F_5$)(P^nBu_3)]	573–623	1–50	N_2
[Ag(OOC^tBu)(PMe_3)]	583	2–3	N_2
[Ag(OOC^tBu)(PEt_3)]	453–493	1.5–3	Ar, N_2
[Ag($OOCCH_2{}^tBu$)(PEt_3)$_2$]	453–553	2	Ar, N_2
[Ag($OOCCMe_2Et$)(PEt_3)$_2$]	473–553	2	Ar, N_2

acac:acetylacetonato;fod:2,2-dimethyl-6,67,78,8,8-heptafluoro-3,5-octanedionato;hfac:1,1,1,5,5,5-hexafluoroacetylacetonato; tfpz: trifluoroacetylacetonate; VTES: vinyltriethylsilane; BTMSA: bis(trimethylsilyl)acetylene; BTMSE: bis(trimethylsilyl) ethyne.

Table 1. The selected CVD metal-organic precursors used in the deposition of silver-based nanomaterials (the presented data are based on Ref. [35, 40–49]).

nanotube (TNT) coatings as a substrate, our studies show clear correlations between the tube diameters and the grain size, their dispersion and the position on the substrate surface (**Figure 1**). The silver particles of d_{Ag} = 35–45 nm were deposited on the surface of layers composed of dense packed tubes of diameter d_{TNT} = 20–30 nm. The increase of tube diameter to 30–60 nm caused metallic grains to be mostly located in their insides and thus it determines the direction of their growth. The rapid decrease of Ag grains diameter below 15 nm and their location on the tubes top edges and walls surfaces was observed for TNT coatings composed of separated tubes of d_{TNT} = 80–150 nm (**Figure 1**) [46]. The use of complexes [Ag(OOCR′)(L)] (R′ = C_2F_5, ^nBu, ^tBu, $CH_2{}^tBu$, CMe_2Et, L = PMe_3, PEt_3) revealed that the type of carboxylate group decided the morphology of deposited metallic layers as well as the way of the grain packing on the substrate surface (**Figure 2**) [47–49].

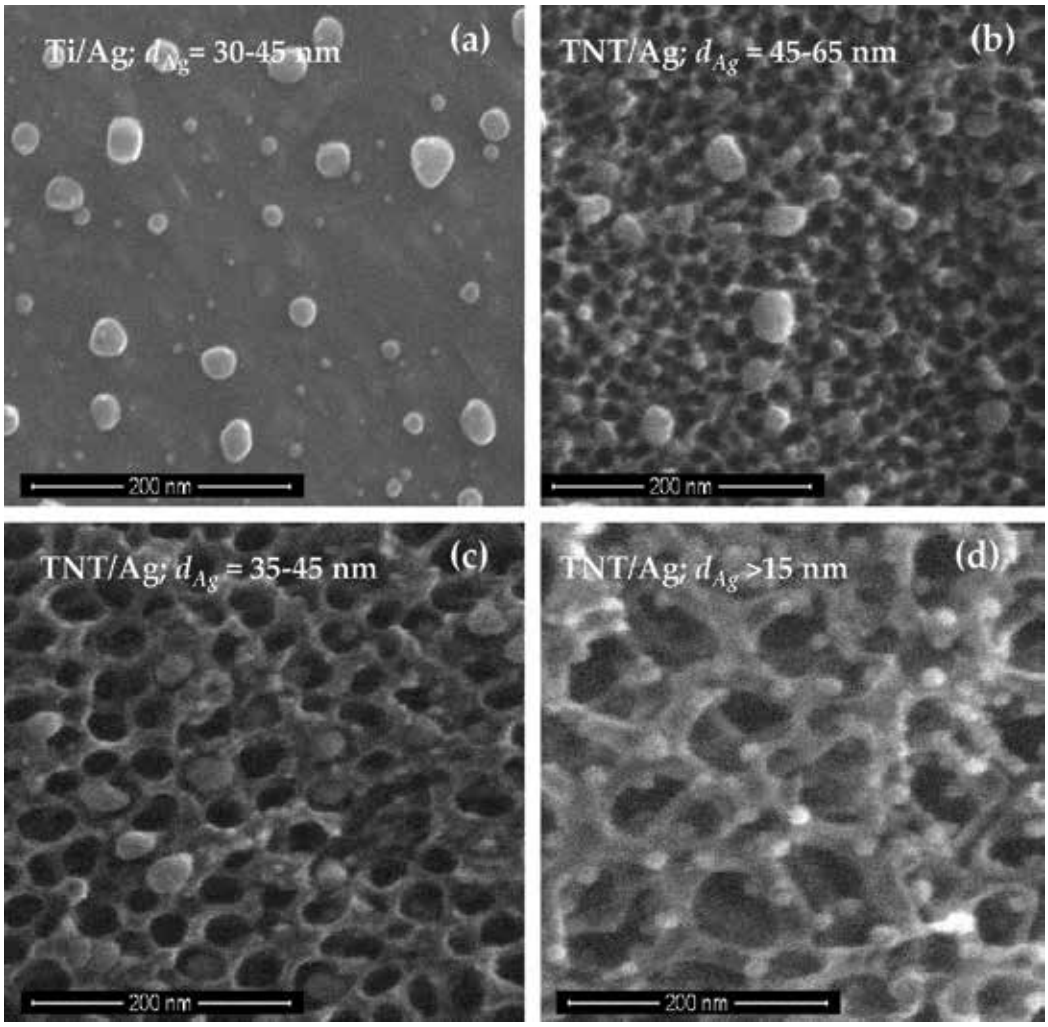

Figure 1. Scanning electron microscopy (SEM) images of titania nanotube coatings enriches with silver particles deposited by CVD method ((a) reference sample, (b) d_{TNT} = 23–30 nm, (c) d_{TNT} = 30–45 nm, (d) d_{TNT} = 80–150 nm) [46].

Summarizing this section, it can be stated that the CVD methods offer wide range of possibilities for the fabrication of silver-based materials with different morphology and structure. Moreover, the CVD method allows the formation of nanocomposite materials, in which the organic or inorganic matrix is enriched with silver nanoparticles. In this regard, the flame assistant technique, that is, FACVD, is especially useful [50]. However, TiO_2/Ag nanocomposities may also be fabricated in a one-step process, that is, direct-liquid injection metal-organic CVD (DLI-MOCVD) [51]. TiO_2/Ag materials may be also synthesized in the two-step classical CVD technique in which the titania nanocrystalline matrix is enriched with silver nanograins [52]. The above-mentioned methods allow the control of structure as well as the morphology of the TiO_2 matrix and the size of the synthesized silver particles.

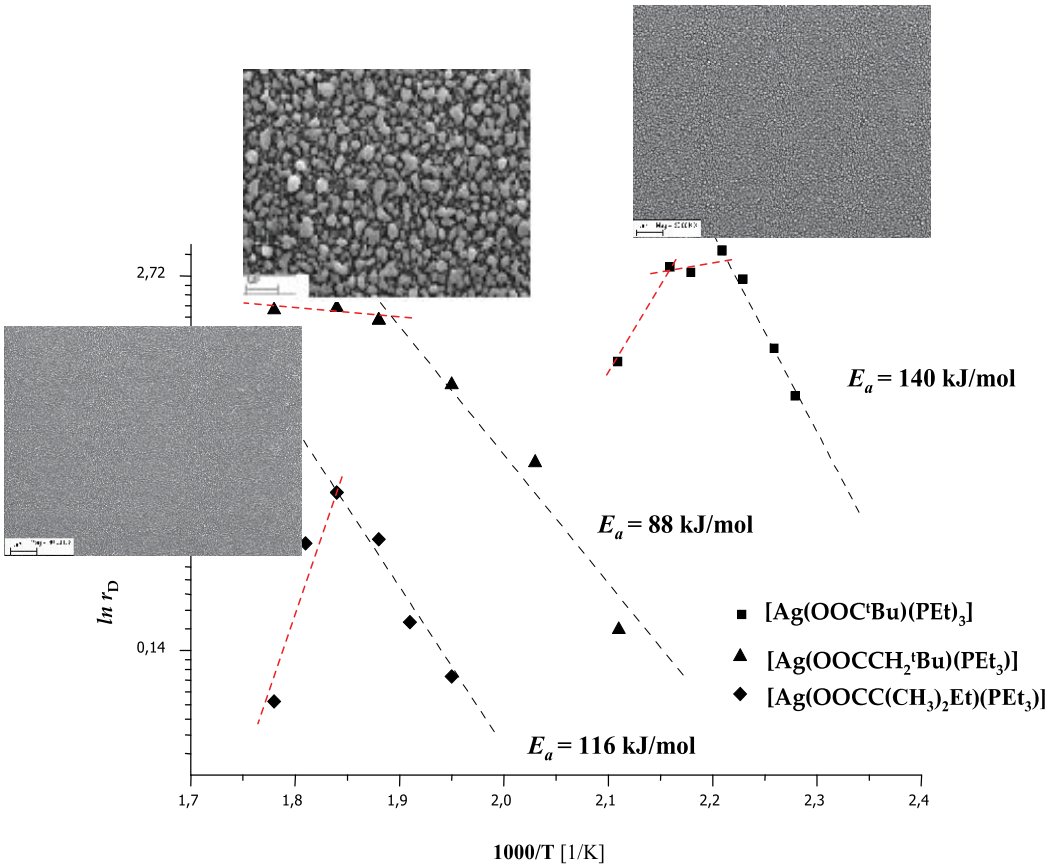

Figure 2. Influence of the carboxyl are groups on the morphology of silver layers, the deposition rate, and the value of activation energies (CVD technique, precursor [Ag(OOCR')(PEt$_3$)]; R' = –^{t}Bu (a), –CH$_2$^{t}Bu (b), and –C(Me$_2$)et (c)).

3. Atomic layer deposition

Generally, the atomic layer deposition (ALD) may be defined as a technique for the deposition of uniform conformal nanolayers by alternating exposures of a substrate surface to vapors of two precursors interacting in self-limiting reactions [53, 54]. Such reactions allow the same amount of material to be deposited on the whole surface. It provides excellent film uniformity even on large substrates. ALD technique enables controlling the film thickness at the atomic level and the layer-by-layer film deposition.

The interest in the use of ALD methods to obtain metallic silver materials (e.g. monolayers) is motivated in part by their use as catalysts in the oxidation of methanol to formaldehyde and in the epoxidation of ethylene [55]. The application of silver as an effective and relatively cheap antimicrobial agent in medical, cosmetic, and environmental technologies also led to the use of ALD techniques in these areas. According to previous reports, the following ALD techniques are used: (a) thermal ALD [56, 57], (b) plasma-enhanced ALD (PEALD [58–60]),

and (c) direct-liquid injection ALD (DLI ALD [61–63]). As in the CVD method, precursors are also the most important factor possessing a direct impact on the type of the produced material and the choice of deposition method. Considering the specificity of the discussed method, it should be noted that beside the chemical compound, being the source of the produced material (silver in this case), reducing agent must also be used. Such nature of ALD processes requires that precursors used in ALD techniques must exhibit greater chemical reactivity and lower deposition rate in comparison to CVD precursors. The silver precursors which are commonly used in ALD techniques are listed in **Table 2**.

Survey of literature reports shows that most of noble metals tend towards nucleation and grow as islands (Volmer-Weber growth mode) and many ALD cycles are required to obtain a continuous coating [64, 65]. This likely occurs because of the stronger interactions between metal atoms as compared to metal-substrate interactions leading to the formation of islands of metal nanoparticles on the substrate surface [66]. The good example is the deposition of silver film on the surface of the titania nanotubes (TNT) coating of tube diameters ca. d_{TNT} 30–65 nm (**Figure 3**) [58]. The dispersed AgNPs were deposited on the top edges of titania tubes after 25 ALD cycles. With increasing ALD cycles, the growth and the coalescence of particles were observed up to the formation of continuous metallic silver layer (after 150 ALD cycles). Moreover, results of our works revealed that the size of deposited AgNPs and their location on the surface of TNT layers significantly depend on tubes diameters [58]. The dependency between the sizes of silver particles deposited on the TNT layers of different tubes diameter confirms it (**Figure 4**). Obtained results revealed that the size of AgNPs, which were deposited on the surface of TNT coatings composed of dense packed tubes of the diameter d_{TNT} > 15–30 nm (d_{Ag} = 8–13 nm), was clearly larger in comparison to particles located on the surface of larger tubs (d_{TNT} = 30–80 nm, d_{Ag} = 6–10 nm). A similar effect has been observed for AgNPs deposited on TNT substrates using CVD technique [46]. The exchange of the substrate from titania nanotubes to titania nano-needles led to the necessity of increasing ALD cycles number from 25 up to 50, in order to obtain a layer composed of dispersed AgNPs [58]. It showed that the substrate-type also has an impact on the nucleation and the growth of nanoparticles.

Considering the results noted above, it can be stated that atomic layer deposition (ALD) is an excellent technique for the fabrication of both uniform silver nanolayers as well as dispersed

Precursor	ALD co-reactant	Deposition temperature T_D (K)	Technique	Refs.
[Ag(fod)(PEt_3)]	H_2; N_2-H_2	373–393	PEALD	[58–60]
[Ag(fod)(PEt_3)]	$BH_3(NHMe_2)$	383	ALD	[56]
[Ag(hfac)(1,5-COD)]	Propan-1-ol	383–423	DLI ALD	[61–63]
[Ag($OOCBu^t$)(PEt_3)]	H_2	413	ALD	[57]

fod: 2,2-dimethyl-6,67,78,8,8-heptafluoro-3,5-octanedionato; hfac: 1,1,1,5,5,5-hexafluoroacetylacetonato; 1,5-COD: 1,5-cyclooktadiene.

Table 2. Metallic silver precursors, which are commonly used in ALD techniques.

http://dx.doi.org/10.5772/intechopen.71571

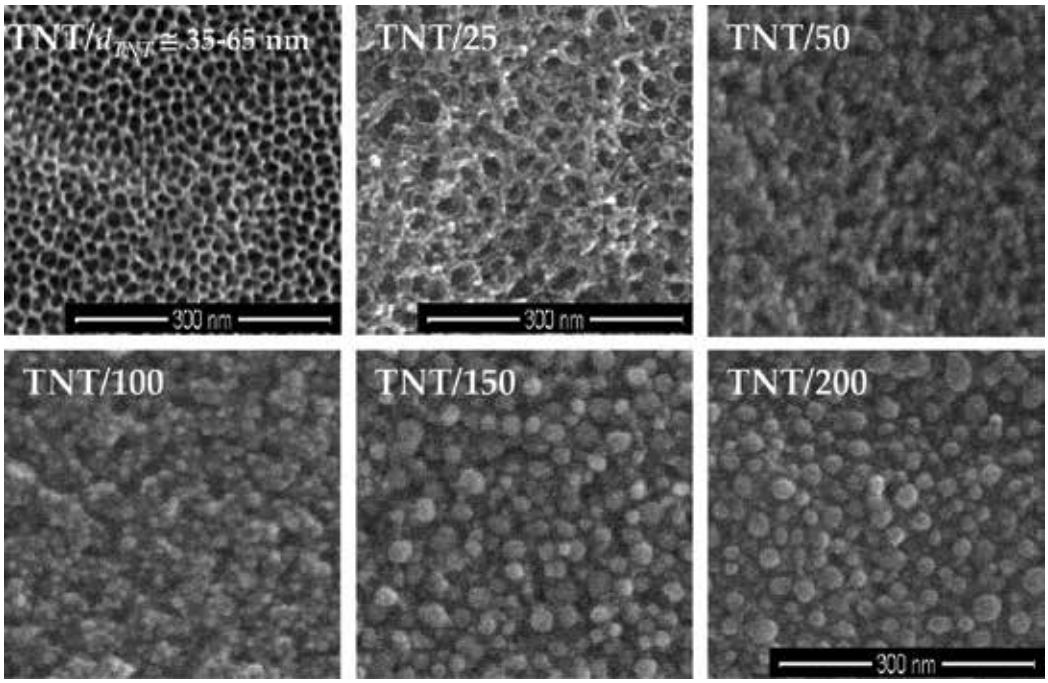

Figure 3. Silver nanoparticles deposited on the surface of TNT coatings after 25, 50, 100, 150, and 200 ALD cycles (PEALD; [Ag(fod)(PEt3)], H2; TD = 393 K; substrate Ti6Al4V/TNT; d_{TNT} = 30–65 nm).

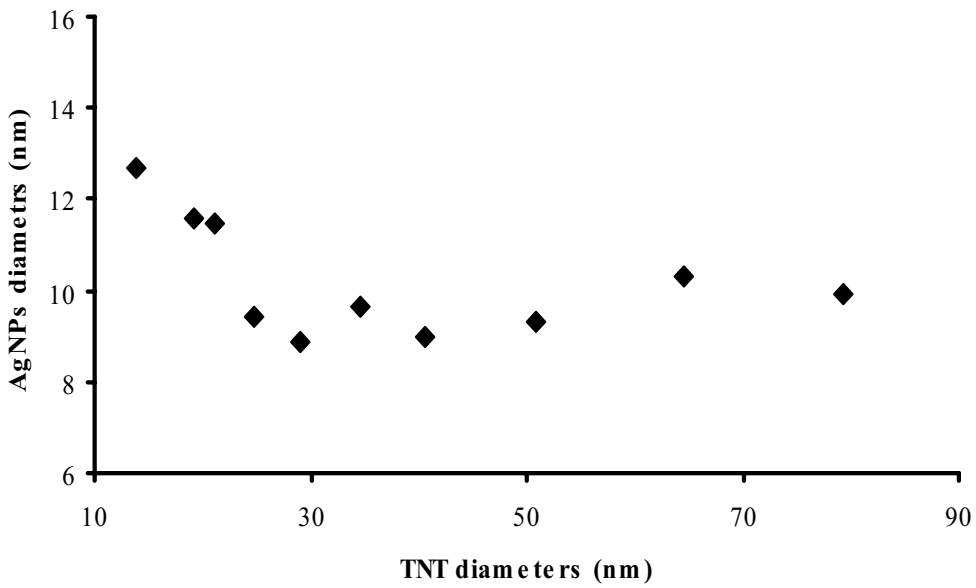

Figure 4. Effect of TNT surface morphology on the diameter of AgNPs after 100 ALD cycles on the surface of Ti6Al4V/TNT substrates.

silver nanoparticles on the surface of different substrates. The type of the precursor and the number of ALD cycles significantly affect the type of produced nanomaterial. The number of cycles allows controlling the nucleation and growth processes of nanoparticles on the substrate surface, which are important for the production of coatings composed of dispersed particles of the similar shape and size.

4. The silver ion release from the nanocomposite materials containing AgNPs

Silver is a widely used antimicrobial agent due to its effective biocide properties against a broad range of the bacteria, viruses, and fungus. This biocide activity of Ag-based materials depends on the release of silver ions (Ag^+) which is usually strongly bonded to biological molecules containing the electron donor groups, such as sulfur, oxygen, and nitrogen. The release of silver ions from the metallic layers of AgNPs and nanocomposite materials is due to the oxidation of metallic particles through their interaction with water molecules or body fluids. The release of Ag ions in a concentration level (0.1 ppb) capable of antimicrobial efficiency [67] and also their concentration below toxic level to human cells (10 mg/L) [31] should be taken into account during the design and the fabrication of silver-based materials intended for biomedical use. In studies concerning the strength of the antimicrobial activity of Ag-based materials, the amounts of the released Ag^+ from the material samples are mainly monitored in the phosphate buffered saline (PBS) solution at human body temperature (310 K) [30, 31, 67, 68]. The PBS solutions containing released Ag ions were analyzed by inductively coupled plasma atomic emission spectrometry (ICP-AES [68]), inductively coupled plasma mass spectrometry (ICP-MS [46, 58, 69]), inductively coupled plasma optical emission spectrometry (ICP OES [70]), or atomic absorption spectrometry (AAS [30]). Another method involves dissolving silver nanoparticles in nitric acid (e.g. 0.1 M), and then measuring the Ag^+ concentrations using atomic absorption spectrometry (AAS [71]) or anodic stripping voltammetry (ASV [72]).

Results of Zaho et al. [30] revealed that for the TNT/Ag system immersed in PBS solution, the concentration of silver ions after 5 h was close to 0.2 ppm and after 3 days increased up to 0.28 ppm and then remaining at this level for the next 4 days. Similar trends of the Ag^+ release were observed by Mei et al. [73] and Radtke et al. [58]; however concentration levels were different (1.4 and 0.015 ppm, respectively, after 30 days). By studying the release of AgNPs from wound dressings, Spange et al. [70] noticed the clear influence of the substrate type on this effect (AgNPs were deposited on bacteria cellulose, lyocell, and polyester/viscose textiles using atmospheric pressure plasma CVD method). The main reasons for the differences in silver release in this case were uneven swelling properties of each textile and differences in their surface areas. Holbrook et al. [74] suggest that different mechanisms are responsible for release of Ag^+ and AgNPs from wound dressings. The dissolution processes promote the release of silver ions, while AgNPs release can be caused by shear stress introduced by deformations of the solid-liquid-vapor triple line. This can be applied, for example, for better control of silver release from dressing and optimize its antimicrobial activity.

For TNT/Ag coatings, in which silver grains were localized inside of TiO_2 tubes, we observed an interesting effect. For these materials after the first week, the concentration of the released Ag^+ in PBS solutions was 0.005–0.008 ppm, independent of silver amount deposited on the surface of TNT layer [46]. This concentration level decreased below 0.005 ppm after 21 days, and rapidly increased up to 0.020–0.022 ppm after 28 days. This effect may be explained by the location of the majority of AgNPs being inside of titania tubes and the oxidation difficulty related to particles' location. The concentration decrease of silver ions, which are released from the surface of TiO_2/Ag nanocomposite, is not an exception. Studies of Zhang et al. [69] of TNT/Ag and TNT/Ag-S nanocomposites revealed that after first 3 days, the concentration of silver ion release decreased from 0.25–0.35 pm to 0.05–0.03 pm and remains at this level for another 11 days. This effect was also noticed for Ag-DOPA-Ti materials (DOPA-Ti, dopamine-functionalized titanium surface) immersed in the PBS solution. Ag^+ concentration after 20 days of releasing was lower than 0.01 ppm [75]. Similarly for Ag ion-implanted titania nanolayers, the discussed effect was observed [33]. The studies of silver ion release from Ag-TiO_2(a) (a = anatase) revealed that concentration of Ag^+ increased in the first 8 days and after this time release rate decreased [72]. Explaining the mechanism of silver ion release, Akhavan et al. [72] assumed that the initial release process of Ag ions was generally controlled by water diffusion on the surface of the TiO_2 matrix. The easy water diffusion to the surface of silver nanoparticles, which were deposited on the titania nanolayer surface, resulted in the rapid release of the Ag^+ at initial stages. The later decrease in the release rate of silver ions can be explained by the ion release through the pores of the titania layer and the change of the release mechanism. This change in the behavior of the Ag ion released from the Ag-TiO_2(a) nanocomposite thin films is completely different from that in the bulk silver-based materials exhibiting a sharp increase in the ion release process [72]. The effect of the initial decline and subsequent rapid growth of the silver ions release rate from the polyamide/silver (PA/Ag) composites was explained by Kumar et al. [67] as a result both the rate of water diffusion and the physical changes in PA/Ag system. According to this report, it can be stated that the initial high release rate of silver ions is related to the oxidation processes of the silver particles located on the surface of the layer. For the Ag particles oxidation and the Ag + ions release from the interior part of the layer, water has to cross the diffusion barrier, which likely contains many crystalline lamellae. The diffusion of water molecules to the inter-lamellar regions can change the structural state, and in the consequence oxidize silver particles and lead to the migration of Ag ions from the interior part of the layer.

In summary, analysis of literature data shows that antimicrobial properties of silver-based materials are significantly connected with the release process of silver ions. This is important both for antimicrobial activity of these materials for a longer time and also for a safe dose of silver for human [30, 76].

5. Antimicrobial activity of silver films and silver-based nanocomposite coatings produced by vapor deposition technologies

Bacterial infections associated with the introduction of implants or other medical devices into the human body are one of the important problems of medicine. These infections

are the result of bacterial adhesion and contamination of implant/devices surfaces, which can cause serious complications in short and long term after the introduction/use. Antimicrobial activity of materials used in medicine is associated with the incorporation of components that locally can kill bacteria, fungus, and viruses or which can inhibit their growth without being toxic to the surrounding tissue at the same time. Silver is the component that is distinguished by the high activity against wide spectra of microorganisms in combination with low toxicity to human cells. Therefore, the modification of, for example, the surface of the implant by enrichment with AgNPs meets the above requirements. It is therefore understandable that extensive studies on applications of AgNPs in a number of areas are still ongoing although antimicrobial properties of silver have been known for a long time.

Experiments by Khalipour et al. [77] on animals revealed excellent *in vitro* antimicrobial activity of the Ag/SiO_xC_y coatings against *Staphylococcus aureus* (ATCC 6538), *Staphylococcus epidermidis* (ATCC 35983), and *Staphylococcus epidermidis* (DSM 18857) strains for at least 28 days. Moreover, results of ISO 10993-5 biocompatibility assay showed high biocompatibility of these materials and did not reveal any indications of cytotoxic effects. The antimicrobial property studies of AgNPs and CuNPs deposited on the surface of such biomedical materials as titanium, TiAlNb alloy, and steel (317 L), confirmed the high antibacterial activity of modified materials versus unmodified ones [78]. Moreover, the biocidal activity of both metallic particles increased with the increase of their amount on the substrate surface, independently of the substrate type. Results of these studies proved the better antibacterial properties of silver-modified materials in comparison to copper-modified ones. Yoon et al. [79] confirmed the good antimicrobial activity of AgNPs and CuNPs versus *Esterichia coli* and *Bacillus subtilis* strains. Simultaneously, they noticed that activity of both systems was associated with the particles size. The results of our works, concerning CVD of silver nanolayers on the surface of titanium implants used in maxillofacial surgery (**Figure 5**, **Table 3**) showed that bacterial sensitivity to AgNPs may be a feature of strains, which is independent of the morphological type and bacterial species [80]. The data presented in **Table 3** confirm that some strains belonging to the same species were characterized by different sensitivity to silver nanoparticles. The introduction of new technologies, for example, the selective laser melting technology, in the production of the new generation of implants, requires their enrichment with a coating which

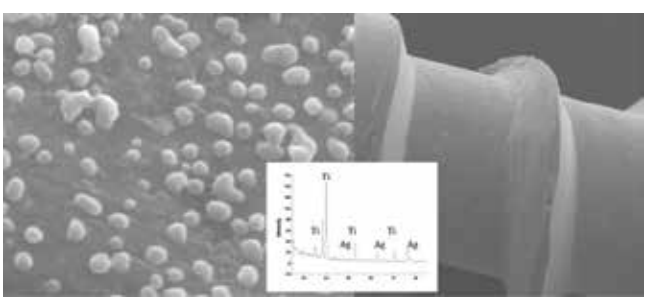

Figure 5. SEM images of silver nanoparticles deposited on the surface of the titanium screw, fixing the implant with the bone.

Bacterial strains	Bacterial count (CFU) after incubation on the surface of the silicon substrate (control sample)	Bacterial count (CFU) after incubation on the surface of the nanosilver coating (sample)	AE (%) percentage estimation of the antibacterial activity of nanosilver layers
Deinococcus radiopugnans	4.20×10^3	0	100
Burkholderia cepacia	1.70×10^4	0	100
Escherichia coli	1.24×10^3	1.46×10^2	88.2
Bacillus licheniformis	1.45×10^4	1.50×10^1	99.9
Staphylococcus lentus	3.15×10^3	2.80×10^3	11.1
Staphylococcus epidermidis C2	2.65×10^3	7.45×10^2	71.9
Tatumella ptyseos	7.30×10^1	0	100
Staphylococcus xylosus	6.20×10^2	0	100
Leuconostoc spp.	8.30×10^2	1.25×10^2	84.9
Staphylococcus epidermidis	8.16×10^2	0	100
Acinetobacter lwoffii	2.52×10^3	2.19×10^3	13.1
Pasteurella spp.	8.45×10^4	0	100
Pseudomonas luteola	4.20×10^3	0	100
Deinococcus grandis	9.30×10^4	0	100
Brevundimonas vesicularis	1.20×10^1	1.10×10^1	8.3
Gemella haemolysans C26	8.50×10^1	0	100
Streptococcus mitis	6.53×10^2	4.01×10^2	38.6
Bacteroides ovatus/thetaiotaomicron A23	1.45×10^3	1.53×10^3	0
Bifidobacterium spp.	5.30×10^3	0	100
Propionibacterium acnes	4.35×10^4	0	100
*Bacteroides ovatus/thetaiotaomicron NC*35	1.50×10^1	0	100
Gemella haemolysans C36	1.30×10^4	0	100
Fusobacterium necrophorum/ nucleatum D3	1.80×10^2	1.20×10^2	33.3
Fusobacterium necrophorum/ nucleatum D14	1.42×10^2	0	100

Table 3. Influence of silver nanoparticles on the selected aerobic, anaerobic, and relatively anaerobic bacteria, which have been isolated from the oral cavity and sites after the teeth extraction (the presented data are based on Ref. [80]).

will provide the appropriate bio-integration properties and antimicrobial activity. Studies of Devilin-Mullin et al. [81] on the deposition of silver nanolayers using ALD method on the surface of orthopedic implants produced by SLM technology are a good example.

Silver nanoparticles (size 40–90 nm) contribute to the clear growth reduction of a major osteolytic pathogen by *Staphylococcus epidermidis* on the implant surface, as well as to support the growth and differentiation of human cell lines important for bone regeneration. The interest in silver as an agent of countering bacterial infections dangerous to humans has greatly expanded the possibilities of its use. The application of the CVD technique to functionalize the wound dressings by their enrichment with silver particles has allowed obtaining a product with good antibacterial properties. A strong antibacterial effect against *Staphylococcus aureus* and *Klebsiella pneumoniae* strains even for low concentration of silver with coated wound dressing was reported by Spange et al. [69]. The risk of nosocomial infections has led to the development of research on the preparation of antimicrobial surface coatings on glass and ceramic tiles. Varghese et al. [39] revealed the promising properties of silver-silica coatings on the surface of above mentioned substrates produced by CVD technology. Results of these investigations showed that the standard test strains gave a $\log_{10} = 5$ reduction factor after 1-4 h, while more resistant methicicllin resistant *Staphylococcus aureus* (MRSA) was reduced by a $\log_{10} > 5$ after 24 h. This activity was maintained after simulated aging and washing cycles. Besides the aforementioned surface modifications of substrates (metallic, ceramic, or glasses) by metallic silver particles, nanocomposite coatings in which metallic or ceramic matrixes are enriched with AgNPs are also popular. The presence of silver particles in the structure of such materials can give them new properties or strengthen their anti-infection activity. The formation of the Ti/Ag composite on the surface of titanium substrates clearly inhibits adhesion of *Staphylococcus epidermidis* strains (ca. 42–55%) versus titanium as a reference sample, independently of the amount of incorporated silver (0.7–9%) [82]. Simultaneously, this type of composite significantly inhibits adhesion of *Klebsiella pneumoniae* strains (ca. 38–42%) for samples containing only 3–4% of silver. It suggests that bacterial sensitivity to silver depends not only on the type of strains but also on the amount of silver grains introduced to the composite. High antimicrobial activity of TiO_2/Ag layers produced by CVD method on the surface of glass substrates is another example worthy of highlighting [36, 50]. In this case, hospital-related pathogens were more resistant on AgNPs activity in comparison to usually tested bacteria strains, however their reduction to the 95–99.9% level was observed.

According to Mungkalasiri et al. [51], titania/silver nanocomposite coatings exhibit good antibacterial activity in the dark (*Staphylococcus aureus* strains, without the earlier UV activation), when they contain less then 1 at.% of silver.

Results of our works on TiO_2/Ag systems (**Figure 6**) show that besides the amount of incorporated AgNPs (ca. 1–4 wt.%), the polymorphic structure of the titania matrix may also significantly influences their antimicrobial properties [52]. The best activity against the *E. coli* strain was observed for TiO_2 anatase/rutile coatings (94–100% mortality of *E. coli*). The pure anatase layer exhibited weaker biocide properties (only 47% mortality). However, the enrichment of the TiO_2 anatase layer with ca. 4 wt% of silver caused significant increase in its activity up to 99.9% (mortality).

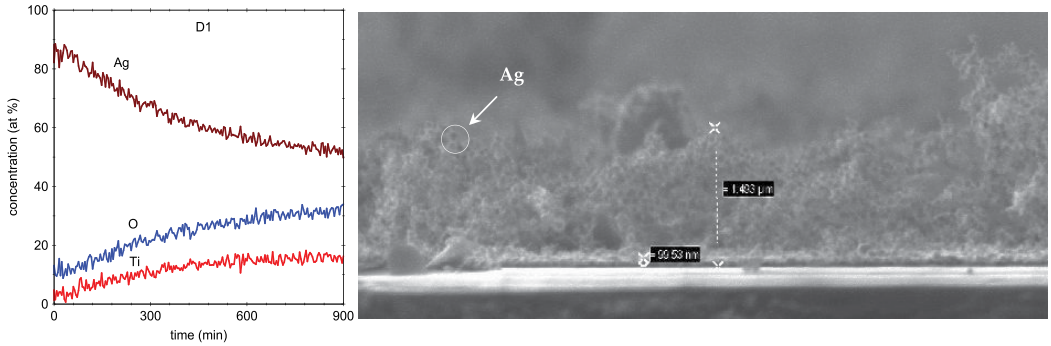

Figure 6. SEM images and XPS depth profile of the TiO_2/Ag composite coating deposited on the surface of titanium implant (CVD, titania matrix were obtained using $[Ti_6O_6(H_2O)_2(O^iBu)_6(OOC^tBu)_6]$ as the precursor, T_D = 713 K, p = 3 hPa, t =60 min, Ar, and silver nanoparticles were deposited using $[Ag(OOCCH_2{}^tBu)(PEt_3)]$ as the precursor, T_D = 433 K, p = 1.5 hPa, t = 60 min, Ar) [52].

Also Li et al. [83] who investigated the biocide activity of titania nanotubes (TNT) and TNT/Ag, have taken into account the above mentioned dependency. The antibacterial efficiency of TNT coatings was observed to change in the order of anatase > rutile > amorphous. In all the studied cases, TNT/Ag system yielded the best antimicrobial activity. Studies on TNT and TNT/Ag materials both in the dark and under the UV light revealed that beside the incorporation of ca. 10 nm silver particles into titania tubes, the tube diameter is also an important factor which significantly influences the antibacterial properties of these systems [30]. Obtained results showed that antimicrobial activity of coatings composed of d_{TNT} = 100 nm tubes was better than that for layers composed of d_{TNT} = 75 and 50 nm ones. In our investigations, we have focused on bioactivity studies on TNT/Ag nanocomposites produced by the enrichment of TNT coatings with AgNPs using CVD and ALD methods [46, 58]. Independently of the applied method, the best antibacterial activity was noticed for systems composed of TNT tubes of diameter lower than 25 nm and decorated by silver particles localized on the top edges of tubes. This can be explained in terms of the synergy of two effects: (a) properties of TiO_2 layers composed of small diameter tubes, which support inhibition of the bacterial biofilm development [84, 85] and (b) the presence of Ag particles deposited on the TNT layer surface. The latter factor is associated with the strong antimicrobial activity of silver particles resulting in the direct interaction AgNPs-bacteria and the release of silver ions in the water environment. Brennan et al. [86] reported that silver-containing hydroxyapatite coatings (Ag-HA) give better efficiency as biocidal agents (against MRSA) in comparison to uncoated HA coatings. The studies of titanium plates covered by Ag-HA and HA coatings and implanted subcutaneously in the backs of rats confirm it.

In concluding this section, it is important to note that despite extensive research into the biocidal activity of silver, both as nanolayers and as nano-particles, the exact mechanism of this process is not yet completely understood. This is due to several factors (e.g. particle

size and shape, stability, crystallinity, and reactivity) that can affect this activity at the same time. Among the mechanisms of these processes, which are proposed in literature [87–89], the most comprehensive is the one proposed by Marambio-Jones and Hoek [90]. The postulated mechanism assumes that silver antimicrobial activity can result from: (a) up-taking of free silver ions followed by distribution of ATP production and DNA replication; (b) generation of reactive oxygen species (ROS) by Ag nanoparticle and Ag + ion; and (c) penetration of Ag nanoparticles through damaged cell membranes. A more detailed mechanism has been proposed by Naidu et al. [91] containing several steps: (a) the attachment of silver nanoparticles to the cell membrane and also penetration inside the bacteria; (b) the interaction of silver ions with bacterial membranes, which contain sulfur-containing proteins as well as with phosphorus-containing compounds like DNA; (c) attack on the respiratory chain in bacterial mitochondria leading to the cell death; and (d) the release of Ag ions inside the bacterial cells (in an environment with lower pH), leading to the formation of free radicals and inducing the oxidative stress.

Our analysis of literature data suggests that silver materials (nanoparticles, nanolayers, and nanocomposites) give good bactericidal activity even at very low concentrations. According to postulated mechanisms, this activity is due to the ability of bacterial cells to absorb and concentrate Ag ions. The antibacterial efficiency of silver particles depends both on the morphological differences that exist between the bacteria, as well as on the particles size, their location on the substrate surface and the reactivity.

6. Bio-integration properties and toxicity of silver-based materials

Capabilities of CVD and ALD techniques enable the fabrication of materials containing silver nanoparticles of different size, shape, and reactivity, which can be designed to make them suitable for specific biomedical applications. Despite extensive studies, investigations of problems such as materials bio-integration, their anti-inflammatory properties, and toxicity are still being carried out. According to Dobrovolskaia and McNel [92], these studies can be separated into two following categories: (1) response of nanoparticles which are specifically modified to stimulate the immune system and (2) undesirable side-effects of other nanoparticles. Zhang et al. [93] observed the formation of fibroblasts on the surfaces of studied samples investigating cytotoxicity of Ti-MAO-Ag layers (MAO—microarc oxidation, the 3 T3 cell colony formation). The slight differences in fibroblasts morphology on the surface of layers with and without silver indicated the similar bio-compatibility of Ti-MAO-Ag and Ti-MAO systems. Moreover, no cytotoxicity of these materials has been found. Studies of bactericidal activity and biocompatibility (*in vitro* and *in vivo* investigations) of TNT/Ag coatings (silver was implanted into TNT layers by plasma immersion ion implantation (PIII) method) revealed that despite excellent antimicrobial efficiency of systems in which silver particles were localized on the TNT layer surface, their biocompatibility was impaired [73]. On the other hand, the deposition of most silver particles on the walls (inside of nanotubes) resulted in an improvement of the biocompatibility of TNT/Ag systems. However, it was comparable to TNT coatings not enriched with Ag nanoparticles. The results of cyto-compatibility

studies of rat calvaria osteoblasts on the surface of TiN/Ag films confirmed also their good biocompatibility [94]. The lack of significant differences between biocompatibility of TiO_2/Ag layers and uncoated titanium surface was noticed by Chang et al. [95] (MTT assay of human gingival fibroblast (HGF)). Studies on the L929 murine fibroblast adhesion (measured after 24 h) and proliferation (assessed after 72 h) on the surface of Ti/Ag and TNT/Ag coatings (containing AgNPs deposited by CVD technique) revealed clear influence of silver particles presence on the biocompatibility of these materials [46]. In all cases of TNT/Ag layers, the adhesion of cells and proliferation were significantly better than that in the case of uncoated titanium surface. The size, amount, and location of AgNPs on the surface of TNT substrates seem to decide the biocompatibility of studied coatings. In the case of TNT/Ag materials incorporated by ALD silver particles (produced on the surface of Ti6Al4V samples), the better adhesion and proliferation of fibroblast cells in comparison to uncoated sample of Ti6Al4V were also noticed [58]. Analysis of presented data showed that the results concerning biocompatibility properties of silver nanolayers and nanocomposites containing AgNPs were not clear and required further work on this topic. This fact makes necessary studies on the adhesion and proliferation of various cells, with the use of multifarious deposition/incorporation AgNPs methods and with the use of nanoparticles of different size, stability, and structure.

The strong antimicrobial properties of materials based on silver nanoparticles or layers, which have been reported by many investigators, have led to interest in their applications in different medical fields, especially in implantology. Research on their toxicity is therefore essential. According to literature data, AgNPs are cytotoxic for several types of cells; for example, human peripheral blood mononuclear cells, human alveolar macrophage cell line, neuroendocrine cells, rat liver cell line, and mouse germline cells [86, 91]. The mechanism of toxicity has not been clearly explained. However considering the earlier reports it may be associated with the ionization of silver ions in the cells, which can lead to changes in the permeability of the cell membrane to both potassium and sodium, interaction with mitochondria, and induction of the apoptosis path via the production of ROS which leads to cell death [91]. Based on previous research, we can assume that the concentration and size of silver nanoparticles are the main factors affecting their cytotoxicity. Milić et al. demonstrated that in spite of a significant uptake into the cells, AgNPs had only insignificant toxicity at concentration lower than 25 mg/l, whereas Ag^+ exhibited a significant decrease in cell viability at 1/5 of this concentration [96]. The results of Comet assay, according to Brennan et al. [86], the concentration of AgNPs higher than 10 μg/g revealed the cytotoxicity effect on primary human mesenchymal stem cells and osteoblasts. Low toxicity or lack of toxicity for silver nanoparticles of diameter c.a. 20 nm was noticed both for colloidal nanoparticles (negative zeta potential), Ag-montmorillonite nanocomposite, and also Ag-DOPA-Ti (DOPA-Ti = titanium substrate coated with poly(dopamine) [75, 97, 98]. However, AgNPs of diameters ca. 24 nm showed cytotoxic activity to macrophages, causing a pro-inflammatory response and apoptosis [86]. Based on previous reports, the lack of clear results concerning silver nanoparticles toxicity to human should be emphasized. It may be associated with the relatively short-time of experiments and also with the fact that most of them are based on *in vitro* cellular studies [91].

7. Concluding remarks

Despite relatively small amounts of literature reports concerning the use of chemical vapor deposition (CVD), and atomic layer deposition (ALD) techniques in the production of biomedical materials, both methods reveal large possibilities in this regards. The most important advantage of these methods is the possibility of controlling the production of different materials based on silver on substrates of different shape, surface morphology, and structure. According to the type of used precursor and the deposition conditions (deposition temperature, time, and deposition rate), it is possible to produce the uniform silver nanolayers, dispersed silver nanoparticles (AgNPs) or their aggregates, and nanocomposite coatings enriched with silver nanoparticles. Through the control of the nucleation and growth conditions of nanoparticles, it becomes possible to direct the size of deposited AgNPs, their structure, stability, purity, and their location on the substrate surface. Thus, it becomes possible to optimize physicochemical properties and bioactivity of the produced materials. From the biomedical point of view, the ability of silver nanoparticles to ions release is the important topic. It may happen that the material containing even the low amount of silver nanoparticles reveals high biocide activity because of large amount of released Ag^{+}. The use of CVD and ALD techniques creates opportunities to the incorporation of AgNPs to substrates of a complex shape and also to the formation of ceramic or polymeric composites enriched with silver nanoparticles. The placement of AgNPs inside the matrix may lead to the process of releasing of silver ions over longer periods of time. Such procedure results in the material of optimal microbicidal activity (spread over the time) and simultaneously reduces the cytotoxicity of this material by decreasing of the amount of silver ions released. It is likely that silver-based materials obtained using above-mentioned techniques may be widely and safely used as a biocide agent not only in biomedical and cosmetic technologies but also in the food and textile industry.

Silver nanoparticles and silver-based materials are one of the most attractive materials for variety of applications. In this chapter, we have provided comprehensive review of synthesis methods, antimicrobial properties, and cytotoxity of Ag-based nanomaterials. Releasing of silver ions (mainly responsible for the toxicity of silver) from AgNPs and silver-based products has been especially emphasized. It was felt necessary to put together detailed data about both the positive as well as negative aspects of silver-based nanomaterials in order to outline their potential safe applications, especially in biomedical technologies and in advanced environmental treatments (air, water, and surface disinfection). AgNPs and AgNPs-based nanomaterials can be used as safe antimicrobial products only if their toxicity will be on the optimally low level. Using the techniques, which provide the strict control on the size, shape, concentration, and location of AgNPs on the surface (like CVD and ALD), it might be possible to produce wide group of innovative Ag-based nanomaterials with tremendous antibacterial properties without noticeable risk to humans or the environment.

Author details

Piotr Piszczek* and Aleksandra Radtke

*Address all correspondence to: piszczek@chem.umk.pl

Faculty of Chemistry, Nicolaus Copernicus University in Toruń, Poland

References

[1] Santiago AS, Peláez-Vargas A, García C. Coating and surface treatments on orthodontic metallic materials. Coatings. 2013;**3**:1-15. DOI: 10.3390/coatings3010001

[2] Ahmad MZ, Akhter S, Jain GK, Rahman M, Pathan SA, Ahmad FJ, Khar RK. Metallic nanoparticles: Technology overview & drug delivery applications in oncology. Expert Opinion on Drug Delivery. 2010;**7**:927-942. DOI: 10.1517/17425247.2010.498473

[3] Rivero PJ, Urrutia A, Goicoechea J, Arregui FJ. Nanomaterials for functional textiles and fibers. Nanoscale Research Letters. 2015;**10**:501. DOI: 10.1186/s11671-015-1195-6

[4] Mihov D, Katerska B. Some biocompatible materials used in medical practice. Trakia Journal of Sciences. 2010;**8**:119-125

[5] Paschoal AL, Vanâncio EC, Canale Lde C, da Silva L, Huerta-Vilca D, Motheo Ade J. Metallic biomaterials TiN-coated: Corrosion analysis and biocompatibility, Artificial Organs. 2003;**27**:461-464

[6] Rebollar E, Sanz M, Esteves C, Martínez NF, Ahumada Ó, Castillejo M. Gold coating of micromechanical DNA biosensors by pulsed laser deposition. Journal of Applied Physics. 2012;**112**:1-6. DOI: 10.1063/1.4761986

[7] Palve BM. Review on nanomaterial: Chemical synthesis, properties and its applications. Explorer. 2016;**1**:43-55

[8] Sanyal MK, Datta A, Hazra S. Morphology of nanostructured materials. Pure and Applied Chemistry. 2002;**74**:1553-1570

[9] Tran QH, Nguyen VQ, Le A-T. Silver nanoparticles: Synthesis, properties, toxicology, applications and perspectives. Advances in Natural Sciences: Nanoscience and Nanotechnology. 2013;**4**:1-20. DOI: 10.1088/2043-6262/4/3/033001

[10] Zhang H, Wu M, Sen A. Silver nanoparticle antimicrobials and related materials, chapter 1. In: Cioffi N, Rai M, editors. Nano-Antimicrobials. Berlin Heidelbrg: Springer-Verlag; 2012. DOI: 10.1007/978-3-642-24428-5_1

[11] Barwick S. Silver: Nature's Purifier Used on the Space Shuttle and in Swimming Pools, http://colloidalsilversecrets.blogspot.com/2009/04/silver-natures-purifier-used-on-space.html

[12] Banach M, Szczygłowska R, Bryk M. Chemical sciences journal building materials with antifungal efficacy enriched with silver nanoparticles. Chemical Sciences Journal. 2014;**5**:1-5. DOI: 10.4172/2150-3494.1000085

[13] Mishra M, Chauhan P. Nanosilver and its medical implications. Journal of Nanomedicine Research. 2015;**2**. DOI: 10.15406/jnmr.2015.02.00039

[14] Abeer SA, Sanad SH, Bahlool SO. Nanotechnology application on cotton fibers, yarn and fabric and its impact on their qualities and antimicrobial resistance, Egypt. Journal of Agricultural Research. 2014;**92**:153-167

[15] Zhang X-F, Liu A-G, Shen W, Gurunathan S. Silver nanoparticles: Synthesis, characterization, properties, applications, and therapeutic approaches. International Journal of Molecular Sciences. 2016;**17**:1-34. DOI: 10.3390/ijms17091534

[16] Gajbhiye S, Sakharwade S. Silver nanoparticles in cosmetics. Journal of Cosmetics, Dermatological Sciences and Applications. 2016;**6**:48-53

[17] Morones JR, Elechiguerra JL, Camacho A, Holt K, Kouri JB, Ramírez JT, Yacaman MJ. The bactericidal effect of silver nanoparticles. Nanotechnology. 2005;**16**:2346-2353

[18] Malalila NG, Swai HS, Hilonga A, Kadam DM. Antimicrobial dependence of silver nanoparticles on surface plasmon resonance bands against *Escherichia coli*. Nanotechnology, Science and Applications. 2017;**10**:1-9. DOI: 10.2147/NSA.S 123681

[19] Jiang XC, Chen CY, Chen WM, Yu AB. Role of citric acid in the formation of silver Nanoplates through a synergistic reduction approach. Langmuir. 2010;**26**:4400-4408

[20] Guzman M, Dille J, Godet S. Synthesis and antibacterial activity of silver nanoparticles against gram-positive and gram-negative bacteria. Nanomedicine: Nanotecnology, Biology, Medicine. 2012;**8**:37-45

[21] Martínez-Castañón GA, Niño-Martínez N, Martínez-Gutierrez F, Martínez-Mendoza JR, Ruiz F. Synthesis and antibacterial activity of silver nanoparticles with different sizes. Journal of Nanoparticle Research. 2008;**10**:1343-1348

[22] Sulaiman GM, Ali EH, Jabbar II, Saleem AH. Synthesis, characterization, antibakterial and cytotoxic effects of silver nanoparticles. Digest Journal of Nanomaterials and Biostructures. 2014;**9**:787-796

[23] Zielinska A, Skwarek E, Zaleska A, Gazda M, Hupka J. Preparation of silver nanoparticles with controlled particle size. Procedia Chemistry. 2009;**1**:1560-1566

[24] Chen J, Li S, Luo J, Wang R, Ding W. Enhancement of the antibacterial activity of silver nanoparticles against Phytopathogenic bacterium Ralstonia solanacearum by stabilization. Journal of Nanomaterials. 2016:1-15. ID 7135852. DOI: 10.1155/2016/7135852

[25] Jyoti K, Baunthiyal M, Singh A. Characterization of silver nanoparticles synthesized using Urtica Dioica Linn. Leaves and their synergistic effects with antibiotics. Journal of Radiation Research and Applied Science. 2016;**9**:217-227

[26] He Y, Du Z, Ma S, Liu Y, Li D, Huang H, Jiang S, Cheng S, Wu W, Zhang K, Zheng X. Effects of green-synthesized silver nanoparticles on lung cancer cells in vitro and grown as xenograft tumors in vivo. Internanational Journal Nanomedicine. 2016;**11**:1879-1887. DOI: 10.2147/IJN.S103695

[27] Xue B, He D, Gao S, Wang D, Yokoyama K, Wang L. Biosynthesis of silver nanoparticles ny the fungus *Arthroderma fulvum* and its antifungal activity against of Candida, Aspergillus and Fusarium. International Journal of Nanomedicine. 2016;**11**:1899-1906. DOI: 10.2147/IJN.S98339

[28] Ajitha B, Reddy YA, Reedy PS. Biosynthesis of silver nanoparticles using momordica charantia leaf broth: Evaluation of their innate antimicrobial and catalytic activities. Journal of Photochemistry and Photobiology B: Biology. 2015;**146**:1-9

[29] Arabatzis IM, Stergiopoulos T, Bernard MC, Labou D, Neophytides SG, Falaras P. Silver-modified titanium dioxide thin films for efficient photodegradation of methyl orange. Applied Catalysis B: Environmental. 2003;**42**:187-201

[30] Zhao C, Feng B, Li Y, Tan J, Lu X, Weng J. Preparation and antibacterial activity of titanium nanotubes loaded with Ag nanoparticles in the dark and under the UV light. Applied Surface Science. 2013;**280**:8-14

[31] Guo Z, Chen C, Gao Q, Li Y, Zhang L. Fabrication of silver-incorporated TiO_2 nanotubes and evaluation on its antibacterial activity. Materials Letters. 2014;**137**:464-467

[32] Liu X, Liu Z, Lu J, Wu X, Xu B, Chu W. Electrodeposition preparation of Ag nanoparticles loaded TiO_2 nanotube arrays with enhanced photocatalytic performance. Applied Surface Science. 2014;**288**:513-517

[33] Hou X, Ma H, Liu F, Deng J, Ai Y, Zhao X, Mao D, Li D, Liao B. Synthesis of Ag ion-implanted TiO_2 thin films for antibacterial application and photocatalytic performance. Journal of Hazardous Materials. 2015;**299**:59-66

[34] Lv X, Gao F, Yang Y, Wang T. A facile electrochemical approach to form TiO_2/Ag Heterostructure films with enhanced Photocatalytic activity. Industrial and Engineering Chemistry Research. 2016;**55**:107-115

[35] Kodas TT, Hampden-Smith MJ. The Chemistry of Metal CVD. Weinheim: VCH Verlagsgesellschft mbH; 1994

[36] Brook LA, Evans P, Foster HA, Pemble ME, Steele A, Sheel DW, Yates HM. Highly bioactive silver and silver/titania composite films grown by chemical vapour deposition. Journal of Photochemistry and Photobiology A: Chemistry. 2007;**187**:53-63

[37] Yates HM, Brook LA, Sheel DW. Photoactive thin silver films by atmospheric pressure CVD. International Journal of Photoenergy. 2008:1-8. ID 870392. DOI: 10.1155/2008/870392

[38] Spange S, Pfuch A, Wiegand C, Beier O, Hipler UC, Grünler B. Atmospheric pressure plasma CVD as a tool of fubtionalise would dressings. Journal of Materials Science: Materials in Medicine. 2015;**26**:76. DOI: 10.1007/s10856-015-5417-3

[39] Varghese S, Elfakhri S, Sheel DW, Sheel P, Bolton FJ, Foster HA. Novel antibacterial silver-silica surface coatings prepared by chemical vapour deposition for infection control. Journal of Applied Microbiology. 2015;**115**:1107-1116

[40] Grodzicki A, Łakomska I, Piszczek P, Szymańska I, Szłyk E. Copper(I), silver(I) and gold(I) carboxylate complexes as precursors in chemical vapour deposition of thin metallic films. Coordination Chemistry Reviews. 2005;**241**:2232-2258

[41] Gao L, Härter P, Linsmeier C, Wiltner A, Emling R, Schmitt-Landsieded D. Silver metal organic chemical vapor deposition for advanced silver metallization. Microelectronic Engeneering. 2005;**82**:296-300

[42] Lu YF, Takai M, Shiokawa T, Aoyagi Y. Growth of ultra-thin silver films by Excimer-laser-induced decomposition of silver acetate in air. Japanese Journal of Applied Physics, Part 2. 1994;**33**:L1313-L1315

[43] Edwards DA, Harker RM, Mahon MF, Molloy KC. Aerosol-assisted chemical vapour deposition (AACVD) of silver films from triorganophosphine adducts of silver carboxylates, including the structure of $[Ag(O_2CC_3F_7)(PPh_3)_2]$. Inorganica Chimica Acta. 2002;**328**:134-146

[44] Szłyk E, Piszczek P, Grodzicki A, Chaberski M, Goliński A, Szatkowski J, Błaszczyk T. CVD of Ag(I) complexes with tertiary phosphines and perfluorinated carboxylanes – A new class of silver precursors. Chemical Vapor Deposition. 2001;**7**:1-6

[45] Szłyk E, Piszczek P, Chaberski M, Goliński A. Studies of thermal decomposition process of Ag(I) perfluorinated carboxylates with temperature variable IR and MS. Polyhedron. 2001;**20**:2853-2861

[46] Piszczek P, Lewandowska Ż, Radtke A, Jędrzejewski T, Kozak W, Sadowska B, Szubka M, Talik E, Fiori F. The study of immunological activity of titania nanotube coatings loaded with CVD of silver grains. Nanomaterials. 2017;**7**:(274):1-9. DOI: 10.3390/nano7090274

[47] Piszczek P, Szłyk E, Chaberski M, Taeschner C, Leonhard A, Bała W, Bartkiewicz K. Characterization of silver trimethylacetate complexes with tertiary phosphines as a chemical vapor deposition precursors of silver films. Chemical Vapor Deposition. 2005; **11**:53-59

[48] Szymańska I, Piszczek P, Szczęsny R, Szłyk E. Thermal and MS studies of silver(I) 2,2-dimethylbutyrate complexes with tertiary phosphines and their application for CVD of silver films. Polyhedron. 2007;**26**:2440-2448

[49] Paramonov SE, Kuzmina NP, Troyanov SI. Synthesis and crystal structure of silver(I) carboxylate complexes, $Ag(P^nBu_3)[C(CH_3COO)]$ and $Ag(Phen)_2[CF_3COO]\cdot H_2O$. Polyhed ron. 2003;**22**:837-841

[50] Foster HA, Sheel DW, Sheel P, Evans P, Varghese S, Rutschke N, Yates HM. Antimicrobial activity of titania/silver and titania.Copper films prepared by CVD. Journal of Photochemistry and Photobiology A: Chemistry. 2010;**216**:283-289

[51] Mungkalasiri J, Bedel L, Emieux F, Dorė J, Renaud FNR, Sarantopoulos C, Maury F. CVD elaboration of nanostructured TiO_2-Ag thin films with efficient Antibakterial properties. Chemical Vapor Deposition. 2016;**16**:35-41

[52] Piszczek P, Muchewicz Ż, Radtke A, Gryglas M, Dahm H, Różycki H. CVD of TiO_2 and TiO_2/Ag antimicrobials layers: Deposition from the hexanuclear μ-oxo Ti(IV) complex as a precursor, and the characterization. Surface and Coatings Technology. 2013;**222**:38-43

[53] Lim BS, Rahtu A, Gordon RG. Atomic layer deposition of transition metals. Nature Materials. 2003;**2**:749-754

[54] Hämäläinen J, Ritala M, Leskelä M. Atomic layer deposition of Noble metals and their oxides. Chemistry of Materials. 2014;**26**:786-801

[55] Thomas JM, Thomas WJ. Principles and Practice of Heterogeneous Catalysis. Weinheim: VCH Verlagsgesellschft mbH; 1997

[56] Mäkelä M, Hatanpää T, Mizohata K, Meinander K, Niinistö J, Räisänen J, Ritala M, Leskelä M. Studies on thermal atomic deposition of silver thin films. Chemistry of Materials. 2017;**29**:2040-2045

[57] Niskanen A, Hatanpää T, Arstula K, Leskelä M, Ritala M. Radical-enhanced atomic layer deposition of silver thin films using phosphine-adducted silver carboxylates. Chemical Vapor Deposition. 2007;**13**:408-413

[58] Radtke A, Jędrzejewski T, Kozak W, Sadowska B, Wieckowska-Szczakiel M, Talik E, Mäkelä M, Leskelä M, Piszczek P. Optimization of the silver clusters PEALD process on the surface of 1-D titania coatings. Nanomaterials. 2017;**7**:(193):1-19. DOI: 10.3390/nano7070193.

[59] van den Bruele FJ, Smets M, Illiberi A, Creyghton Y, Buskens P, Roozeboom F, Poodt P. Atmospheric pressure plasma enhanced spatial ALD of silver. Journal of Vacuum Science and Technology A. 2015;**33**:01A131-1-01A131-6

[60] Kariniemi M, Niinistö J, Hatanpää T, Kemell M, Sajavaara T, Ritala M, Leskelä M. Plasma-enhanced atomic layer deposition of silver thin films. Chemistry of Materials. 2011;**23**:2901-2907

[61] Chalker PR, Romani S, Marshall PA, Rosseinsky MJ, Rushworth S, Williams PA. Liquid injection atomic layer deposition of silver nanoparticles. Nanotechnology. 2010;**21**:(40):1-12. DOI: 10.1088/0957-4484/21/40/405602

[62] Devin-Mullin A, Todd NM, Golrokhi Z, Geng H, Konerding MA, Ternan NG, Hunt JA, Potter PJ, Sutcliffe C, Jones E, Lee PD, Mitchell CA. Atomic layer deposition of a silver nanolayer on advanced titanium orthopecic implants inhibits bacterial colonization and supports vascularized de novo bone ingrowth. Advanced Healthcare Materials. 2017:1700033. DOI: 10.1002/adhm.201700033

[63] Golrokhi Z, Chalker S, Sutcliffe J, Potter J. Self-limiting atomic layer deposition of conformal nanostructured silver films. Applied Surface Science. 2016;**364**:789-797

[64] Mackus AJM, Verheijen MA, Leick N, Bol AA, Kessels MM. Influence of oxygen exposure on the nucleation of platinium atomic layer deposition: Consequences for film growth, nanopatterning, and nanoparticle synthesis. Chemistry of Materials. 2013;**25**: 1905-1911

[65] Masango SS, Peng L, Marks LD, Van Duyne RP, Stair PC. Nucleation and growth of silver nanoparticles by AB and ABC-type atomic layer deposition. Journal of Physical Chemistry C. 2014;**118**:17655-17661

[66] Campbell CT. Ultrathin metal films and paricles on oxide surfaces: Structural, electronic and chemisorptive properties. Surface Science Reports. 1997;**27**:1-111

[67] Kumar R, Műnstedt H. Silver release from antimicribial polyamide/silver composites. Biomaterials. 2005;**26**:2081-2088

[68] Zhao L, Wang H, Huo K, Cui L, Zhang W, Ni H, Zhang Y, Wu Z, Chi PK. Antibakterial nano-structured titania coating incorporated with silver nanoparticles. Biomaterials. 2011;**32**:5706-5716

[69] Zhang L, Zhang L, Yang Y, Zhang W, Lv H, Yang F, Lin C, Tang P. Inhibitory effect of super-hydrophobicity on silver release and antibacterial properties of super-hydropobic Ag/TiO_2 nanotubes. Journal of Biomedical Materials Research Part B: Applied Biomaterials. 2015;**00B**:1-9

[70] Spange S, Pfuch A, Wiegand C, Beier O, Hipler UC, Grünler B. Atmospheric pressure plasma CVD as a tool to functionalise wound dressings. Journal of Materials Science: Materials in Medicine. 2015;**26**:76. DOI: 10.1007/s10856-015-5417-3

[71] Wu X, Li J, Wang L, Huang D, Zuo Y, Li Y. The release properties of silver ions from Ag-nHA/TiO_2/PA66 antimicrobial composite scaffolds. Biomedical Materials. 2010;**5**:1-7. DOI: 10.1088/1748-6041/5/4/044105

[72] Akhavan O, Ghaderi E. Self-accumulated Ag nanoparticles on mesoporous TiO_2 thin film with high bactericidal activities. Surface and Coating Technology. 2010;**204**:3676-3683

[73] Mei S, Wang H, Wang W, Tong L, Pan H, Ruan C, Ma Q, Liu M, Yang H, Zhang L, Cheng Y, Zhang Y, Zhao L, Chu PK. Antibacterial effects and biocompatibility of titanium surfaces with graded silver incorporation in titania nanotubes. Biomaterials. 2014;**35**: 4255-4265

[74] Holdrook RD, Rykaczewski K, Stayments ME. Dynamics of silver nanoparticle release from wound dressings revealed via in situ nanoscale imaging. Journal of Materials Science: Materials in Medicine. 2014;**25**:2481-2489. DOI: 10.1007/s10856-014-5265-6

[75] Wang J, Li Z, Liang Y, Zhu S, Cui Z, Bao H, Liu Y, Yang X. Cytotoxity and antibacterial efficiency of silver nanoparticles deposited onto depamine-functionalised titanium. Materials Express. 2015;**5**:191-200. DOI: 10.1166/mex.2015.1231

[76] Rogulska A, Pisarek M, Andrzejczuk M, Lewandowska M, Kurzydłowski KJ, Janik-Czachor M. Surface characterization of Ca-P/Ag/TiO2 nanotube compositelayers on Ti intendent for biomedical applications. Journal of Biomedical Materials Research. Part A. 2012;**100**:1954-1962

[77] Khalipour P, Lampe K, Wagner M, Stigler B, Heiss C, Ullrich MS, Domann E, Schnettler R, Alt V. Ag/SiO_xC_y plasma polymer coating for antimicrobial protection of fracture fixation devices. Journal of Biomedical Materials Research Part B: Applied Biomaterials. 2010;**94B**:196-202

[78] Wan YZ, Raman S, He F, Huang Y. Surface modification of medical metals by ion implantation of silver and copper. Vacuum. 2007;**81**:1114-1118

[79] Yoon K-Y, Byeon JH, Park J-H, Hwang J. Susceptibility constants of *Escherichia Coli* and Bacillus Subtilis to silver and copper nanoparticles. Science of the Total Environment. 2007;**373**:572-575

[80] Grodzicki A, Jakubiak J, Jędrzejczyk W, Piszczek P, Różycki H, Wrótniak-Drzewiecka W. Effect of silver nanoparticles on survival of oral cavity ontocenosis bacteria; part I. Tests using Koch's plate dilution method. Acta Medica. 2010;**2**:26-37

[81] Devlin-Mullin A, Todd NM, Golrokhi Z, Geng H, Konerding MA, Ternan NG, Hunt JA, Potter RJ, Sutcliffe C, Jones E, Lee PD, Mitchell CA. Atomic layer deposition of a silver Nanolayer on advanced titanium Orthopedic implants inhibits bacterial colonization and supports vascularized de novo bone ingrowth. Advanced Healthcare Materials. 2017;**1700033**:1-14. DOI: 10.1002/adhm.201700033

[82] Ewald A, Glückermann SK, Thull R, Gbureck U. Antimicrobial titanium/silver PVD coatings on titanium. Biomedical Engineering Online. 2006;**5**(22)1-10. DOI: 10.1186/1475-925X-5-22

[83] Li H, Cui Q, Feng B, Wang J, Lu X, Weng J. Antibacterial activity of TiO_2 nanotubes: Influence of crystal phase morphology and Ag deposition. Applied Surface Science. 2013;**284**:179-183

[84] Lewandowska Ż, Piszczek P, Radtke A, Jędrzejewski T, Kozak W, Sadowska B. The evaluation of the impact of titania nanotube covers morphology and crystal phase on their biological properties. Journal of Materials Science: Materials in Medicine. 2015;**26**(163):1-12. DOI: 10.1007/s10856-015-5495-2

[85] Radtke A, Topolski A, Jędrzejewski T, Kozak W, Sadowska B, Wieckowska-Szczakiel M, Szubka M, Talik E, Nielsen L, Piszczek P. Studies on the bioactivity and photocatalytic properties of titania nanotube coatings produced with the use of the low potential anodization of Ti6Al4V alloy surface. Nanomaterials. 2017;**7**(197):1-15. DOI: 10.3390/nano7080197

[86] Brennan SA, Fhoghlú CN, Devitt BM, Mahony FJO', Brabazon D, Walsh A. Silver nanoparticles and their orthopaedic applications. The Bone & Joint Journal. 2015;**97-B**:1-8

[87] Jung WK, Koo HC, Kim KW, Shin S, So Hyun Kim SH, Park YH. Antibacterial activity and mechanism of action of the silver ion in *Staphylococcus aureus* and *Escherichia coli*. Applied and Environmental Microbiology. 2008;**74**:2171-2178

[88] Rabeah Rawashdeh R, Haik Y. Antibacterial mechanisms of metallic nanoparticles: A review, dynamic biochemistry, process biotechnology and molecular biology. Global Science Books. 2009;**3**(Special Issue 2):12-20

[89] Li W-R, Xie X-B, Shi Q-S, Zeng H-Z, OU-Yang Y-S, Chen Y-B. Antibacterial activity and mechanism of silver nanoparticles on Escherichia Coli. Applied Microbiology and Biotechnology. 2010;**85**:1115-1122

[90] Marambio-Jones C, Hoek EMV. A review of the antibacterial effects of silver nanomaterials and potential implications for human health and the environment. Journal of Nanoparticle Research. 2010;**12**:1531-1551

[91] Naidu KSB, Govender P, Adam JK. Biomedical applications and toxicity of nanosilver: A review. Medical Technology S.A. 2015;**29**:13-19

[92] Dobrovolsaia MA, McNeil SE. Immunological properties of engineered nanomaterials. Nature Nanotechnology. 2007;**2**:469-477

[93] Zhang P, Zhang Z, Li W. Antibacterial TiO_2 coating incorporating silver nanoparticles by microarc oxidation and ion implantation. Journal of Nanomaterials. 2013:1-8. ID 542878, DOI: 10.1155/2013/542878

[94] Xu R, Yang X, Jiangb J, Li P, Zhang X, Wu G, Chub PK. Effects of silver plasma immersion ion implantation on the surface characteristics and cytocompatibility of titanium nitride films. Surface and Coating Technology. 2015;**279**:166-170

[95] Chang Y-Y, Lai C-H, Hsu J-T, Tang C-H, Liao W-C, Huang H-L. Antibacterial propetries and human gingival fibroblast cell compatibility of TiO_2/Ag compound and ZnO films on titanium based material. Clinical Oral Investigations. 2012;**16**:95-100

[96] Milić M, Leitinger G, Pavičić I, Advdičević MZ, Dobrović S, Goessler W, Vrček IV. Cellular uptake and toxicity effects od silver nanoparticles in mammalian kidney cells. Journal of Applied Toxicology. 2014:1-12. DOI: 10.1002/jat.3081

[97] Salvioni L, Galbiati E, Collico V, Alessio G, Avvakumova S, Corsi F, Tortora P, Prosperi D, Colombo M. Negative;y charged silver nanoparticles with potent antibacterial activity and reducted toxity for pharmaceutical preparations, international j. Nanomedicine. 2017;**12**:2017-2530. DOI: 10.2147/IJN.S127799

[98] Kiruba Daniel SCG, Tharmaraj V, Sironmani TA, Pitchumani K. Toxicity and immunological activity of silver nanoparticles. Applied Clay Science. 2010;**48**:547-551

Chapter 10

Copper Metal for Semiconductor Interconnects

Yi-Lung Cheng, Chih-Yen Lee and Yao-Liang Huang

Additional information is available at the end of the chapter

http://dx.doi.org/10.5772/intechopen.72396

Abstract

Resistance-capacitance (*RC*) delay produced by the interconnects limits the speed of the integrated circuits from 0.25 mm technology node. Copper (Cu) had been used to replace aluminum (Al) as an interconnecting conductor in order to reduce the resistance. In this chapter, the deposition method of Cu films and the interconnect fabrication with Cu metallization are introduced. The resulting integration and reliability challenges are addressed as well.

Keywords: Cu interconnects, BEOL, damascene, resistivity, reliability

1. Introduction

During the last about 50 years, Si-based integrated circuits (ICs) have been developed with numerous applications in the computer, communication, and consumer electronics industries. There has also been tremendous progress in the manufacturing of ICs over the past 60 years. The minimum feature size has advanced from 10 μm down to 10 nm, the cost per transistor has decreased by seven orders of magnitude, and the maximum number of transistors per chip has increased by at least 10 orders of magnitude [1]. Generally, technology node advances every 2 years with the shrinkage of the feature size by 0.7 times. Hence, the area of IC chip can be approximately reduced by 50%, resulting in doubling of the IC chips produced in a fixed area.

The main purpose of continuous scaling of the device dimensions is to improve the performance of the semiconductor microprocessors and to pack more devices in the same area. However, as the technology node is advanced to 0.25 μm, the back-end-of-line (BEOL) interconnect of ICs becomes the bottleneck in the improvement of IC performance [2]. In other words, as the feature size of ICs is continuously scaling down, the speed of the device increases due to a shorter channel length, although, resistance-capacitance (*RC*) delay produced by the interconnects

limits the chip speed. This *RC* delay is the product of the dielectric capacitance (*C*) and the conductor resistance (*R*), which can be calculated according to Eqs. (1) and (2), respectively.

$$C = k\frac{LT}{S} \tag{1}$$

$$R = \rho\frac{L}{WT} \tag{2}$$

where k is dielectric constant and ρ is metal resistivity. L, W, and T are the length, width, and thickness of metal line, respectively. S is the spacing between metal lines.

Table 1 provides the estimated critical dimensions of the BEOL interconnect from 90 to 7 nm technology nodes. As shown, with the advance of the technology node, the smaller line width and pitch result in the increased resistance of the metal lines and the increased capacitance between the neighboring metal lines. This leads to a larger *RC* delay in the advanced technology nodes, which surpasses the gate delay and becomes a limiting factor in ICs performance [3–6].

In order to slow down the increase of *RC* delay, the possible solution is to change the materials used in the BEOL interconnects. A dielectric film with the relative dielectric constant (k) lower than 4.0 (called low-k) had replaced a conventional chemical vapor deposition (CVD)-SiO_2 film with a k value of 4.0 as an interconnect insulator because it can provide lower capacitance between the neighboring metal lines. The low-k materials currently used in the BEOL interconnects are SiOF (k = 3.5–3.8), SiCOH (k = 2.2–3.2), or air gap (k~1.0) [7–11]. On the other hand, to reduce the resistance of BEOL interconnects, a metal material with a lower resistivity (ρ) than that of aluminum (Al), which is the traditional conductor used in 3.0–0.25 μm technology nodes, is considered to be a candidate to replace Al conductor. **Table 2** lists the electrical resistivity for different metals. Among all metals in the world, three kinds of metal have lower resistivity than Al with a resistivity of 2.65 Ωμ-cm: Gold (Au; 2.214 Ωμ cm), copper (Cu; 1.678 Ωμ cm), and silver (Ag: 1.587 Ωμ cm). Compared with these three metals, Cu has been recognized to be a candidate as a conductor in the BEOL interconnects for integration consideration. Additionally, higher electromigration reliability than Al by at least 10 times is another advantage for Cu as a conductor because Cu has a lower diffusivity than Al. Based on these reasons, semiconductor industries are fully transitioning toward using Cu instead of Al in future IC applications [12–15].

In this connection, this chapter is an attempt to provide an overview of Cu conductor used in the BEOL interconnects of ICs in the past, present, and future. This chapter is organized as

Technology node		Critical dimension (nm)								
		130	90	65	45	32	22	14	10	7
Interconnect	Pitch	400	280	200	126	104	88	56	40	28
	Width	200	140	100	63	52	44	28	20	14

Table 1. Interconnect dimensions with technology nodes.

Metal	Melting point (°C)	Resistivity (ρ) at 298K (μΩ-cm)
Silver (Ag)	961	1.587
Copper (Cu)	1084	1.678
Gold (Au)	1064	2.214
Aluminum (Al)	660	2.650
Tungston (W)	3422	5.280

Table 2. Melting point and resistivity of different metals.

follows: in Section 2, we describe the process flow of Cu damascene metallization. Then, in Section 3, the deposition methods of Cu metal are introduced and compared. Next, the integration and reliability issues of Cu metallization are discussed in Sections 4 and 5, respectively. Finally, short conclusion and future trend for conductors used in the BEOL interconnects are provided in Section 6.

2. Copper damascene metallization

Unlike Al metallization, Cu cannot be easily patterned by reactive ion etching (RIE) due to the low volatility of Cu etching by-products, such as Cu chlorides and Cu fluorides [16, 17]. Hence, to fabricate Cu interconnects, a different process flow which is called "damascene" process has been developed, including "single damascene" and "dual damascene" processes [18–23]. In the "single damascene" process, only trench or via is fabricated after completing the process. While in the dual damascene process, both via and trench can be fabricated simultaneously, in which both via and trench can be performed with the same metallization step. Thus, Cu interconnects are usually fabricated by cost-effective dual damascene technology.

In order to fabricate Cu dual damascene interconnects, various process flows were developed. "Via first" and "Trench first" dual damascene processes are commonly used, as plotted in **Figure 1**.

The process flow of Cu dual damascene metallization is described as below: After processing of Metal-1 (M-1), the etching stop layer (Cu barrier dielectric layer) and the Via-1 (V-1)/Metal-2 (M-2) dielectric layer (e.g., SiCOH low-*k*) are subsequently deposited. For the etching stop layer, also called Cu barrier dielectric layer, SiN or SiCN can be used, providing functions to protect Cu from oxidation and protect Cu from diffusion into the low-*k* dielectric during processing or device operation. These materials have much higher dielectric constants than that of the low-*k* dielectric. The dielectric constant of SiN film ranges from 6.8 to 7.3 and that of SiCN layer from 4.0 to 5.0, depending on the process conditions [24–26]. Sometimes, a sandwich dielectric stack film (SiCOH/Si(C)N/SiCOH) is used in order to control the depths of the

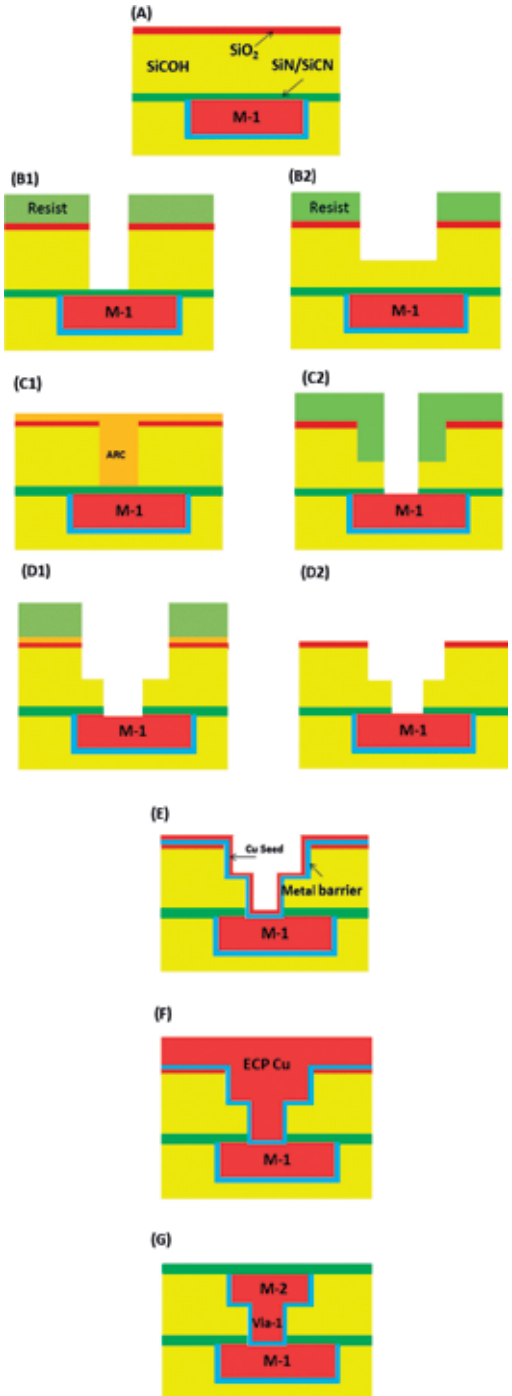

Figure 1. Via first (B1–D1) and Trench first (B2–D2) approaches for dual damascene patterning. (A) Dielectrics (SiN/SiCN, SiCOH, SiO_2) deposition; (B1) Via-1 lithography and RIE; (B2) M-2 trench lithography and RIE; (C1) ARC plug; (C2) Via-1 lithography; (D1) M-2 trench lithography and RIE and etching stop layer opening; (D2) Via-1 RIE; (E) metal barrier and Cu seed deposition; (F) electroplating Cu deposition; and (G) Cu CMP and dielectric barrier deposition.

via and metal precisely. These steps will increase the effective dielectric constant, raising the capacitance. The dense SiO_2 layer can be capped onto the SiCOH low-*k* dielectric to mitigate damage on the low-*k* dielectric caused by the subsequent process steps, such as photoresist, and Cu chemical mechanical polishing (CMP). This layer will not appear in the final structure of the fabricated Cu interconnects because it can be removed by Cu CMP process.

For "Via first" process, Via-1 is patterned first, stopping on the SiN (or SiCN) layer that protects Cu from oxidation. Then, the Metal-2 trench is patterned and the final step is the removal of the SiN (or SiCN) etch stop from the bottom of the via. For the "Trench first" process, the "via patterning" and "trench pattering" steps are reversed.

The metal deposition in the dual damascene structure consists of three steps: Cu barrier layer, Cu seed layer, and bulk Cu layer. Currently, the first two steps are performed by sputtering and the last step uses Cu electroplating (ECP) method. The used material for Cu barrier layer is a TaN/Ta barrier layer, which prevents Cu from diffusing into the dielectric, A Cu seed layer helps to the growth of electroplated Cu film. Cu electroplating provides to fill in the via and trench. After completing the metal deposition, Cu chemical mechanical polishing (CMP) process is used to remove the excess metal over the field regions. Thus, a layer of Cu dual damascene structure (via and trench) is finished. To construct multiple metal levels, these steps are repeated for each metal level. After the last metal layer is fabricated, thick dielectric passivation layer (e.g., SiO_2/SiN bi-layer) is deposited and via is opened to the bond pads.

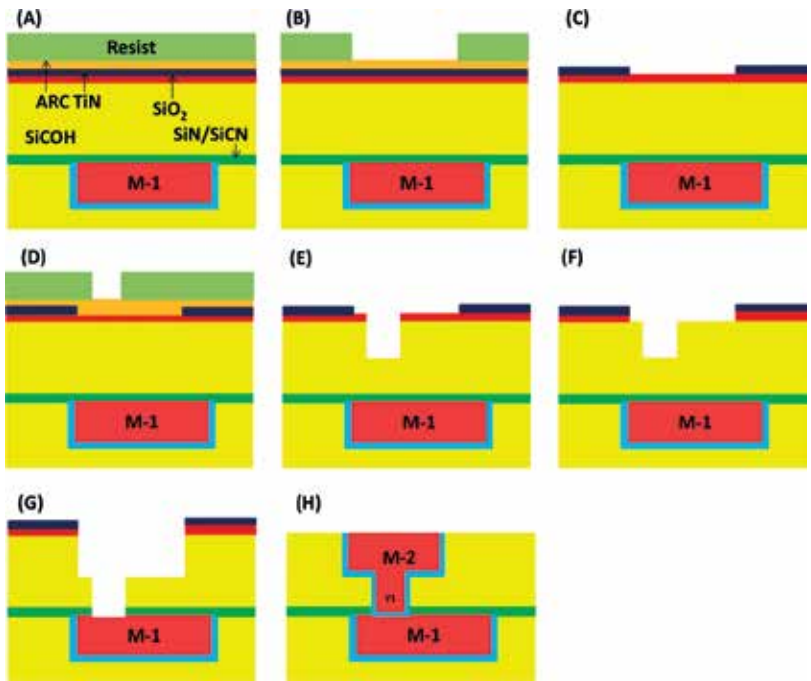

Figure 2. Metal hardmask approach for dual damascene patterning. (A) TiN, ARC, and resist deposition; (B) M-2 metal hardmask RIE; (C) M-2 trench lithography; (D) Via-1 lithography; (E) Via-1 RIE; (F) M-2 oxide hardmask RIE; (G) M-2/Via-1 RIE and M-1 capping layer RIE; and (H) M-2/Via-1 Cu metallization.

Further reduction of the capacitance between the meal conductors is required as the device dimensions are continuously scaled down. The porous low-*k* material with a dielectric constant as low as 2.2 is adopted as an interconnect insulator [9]. The porous low-*k* material can be produced by adding pores (<2 nm diameter) to the SiCOH film. The obtained dielectric constant depends on the porosity. A higher porosity results in a lower dielectric constant; however, open pore are formed (high pore connectivity). The open pore in the porous low-*k* film allows water and other contaminations to diffuse into the dielectric. Moreover, during the interconnect fabrication, the porous low-*k* material is exposed to oxygen plasma environments in the conventional resist strip step. Ions and radicals produced from oxygen plasmas can severely damage the porous low-*k* material. These issues result in an increased dielectric constant and degraded dielectric breakdown reliability for the porous low-*k* material. To minimize the damage on the porous low-*k* material, low-*k* material optimization and resist strip condition are chosen, and the process integration modification has been provided. The integration approach for dual damascene patterning is transformed to "metal hardmask" method from 32 nm technology node as shown in **Figure 2** [27]. In the metal hardmask method, the resist strip damage on the porous low-*k* material can be minimized because the resist is stripped prior to the trench and via etching. However, this method requires the extra steps and good process control to avoid the integration issues.

3. Copper deposition method

In addition to the need of lower resistivity, the other requirement for Cu film is to fill the high aspect ratio vias and trenches without voids in the dual damascene structure. After continuous research and development for many years, Cu film can now be deposited by various technologies, such as physical vapor deposition (PVD), chemical vapor deposition (CVD), laser reflow, atomic layer deposition (ALD), and plating (electrolytic and electroless) [28–33]. **Table 3** lists the properties of Cu films obtained by different deposition technologies. Evaporation and

Deposition method	CVD	PVD (Evaporation)	PVD (Sputtering)	Laser reflow	ALD	Electroplating (ECP)	Electroless plating
Resistivity (μΩ-cm at RT)	> 2	1.80~2.2	1.75~2.0	~2.5	> 2	~2	~ 2
Impurities	C, O	O	Ar	—	C, O	—	—
Deposition rate (nm/min)	100~150	> 200	>100	—	<10	~200	~ 100
Deposition temperature (°C)	150~250	melt	RT	melt	100~200	RT	50~80
Step coverage	Good	Fair~Poor	Fair	—	Excellent	Good	Good
Via-filling capbility	Good	Poor	Poor	Goog	Excellent	Fair	Fair
Enviromental impact	Good	Good	Good	Good	Good	Poor	Poor
Cost	High	Low	High	High	High	Fair	Fair
RT: Room temperature (25°C)							

Table 3. Comparison of various Cu deposition technologies.

sputtering methods belong to PVD technology, which can provide a lower resistivity as compared to other technologies. The latter method is widely used in the semiconductor industry.

In current Cu metallization, electroplating method is used to fill the high aspect ratio via and trench in the dual damascene structure. However, in order to successfully deposit Cu film during ECP process, a Cu seed layer is needed. Sputtering deposition is the preferred method to deposit the Cu seed layer because it can produce high-purity films. In the sputtering process to deposit Cu film, Ar plasma is used to sputter Cu target and then the sputtering Cu material is deposition on the wafer. The biggest challenge for Cu sputtering process is to achieve good step coverage in the high aspect ratio via and trench. With the reduction of interconnect dimensions in the advanced technology nodes, this problem is becoming thrilling. To achieve adequate conformity in high aspect ratio via and trench in the dual damascene structure for advanced technology nodes, ionized PVD [34] or atomic layer deposition (ALD) [35] technologies have been developed for Cu seed layer deposition with demonstrated good step-coverage.

After depositing a Cu seed layer, ECP process is used to fill-in via and trench dual damascene structure. ECP process is performed by immersing the wafers in a solution containing cupric ions, sulfuric acid, and trace organic additives [36]. By applying an electric current, Cu ion (Cu^{+2}) is reduced to Cu, which deposit onto the seed layer. To achieve void-free filling in the high aspect ratio feature for ECP process, the "bottom-up" or "super-filling" strategy is adopted. By means of the bottom-up (or super-filling) method, the deposition of Cu film is growing from the bottom to the top, so no void is formed in the via and trench. To meet this goal, the additives in the ECP solution play an important role. The additives must consist of both suppressors and accelerators. The former is polymers, such as polyethylene glycol, which reduce the plating rate at the top of features by blocking of growth sites on the Cu surface. While the latter is dimercaptopropane sulfonic acid (SPS) with sulfide and thiol-like functional groups, which enhance the plating rate at the bottom of features because the functional groups strongly absorb on Cu surfaces [36, 37]. Consequently, ECP process can provide a void-free filling process for via and trench dual damascene structure under an adequate combination of suppressor and accelerator additives.

4. Integration issues of copper metal

In the advance technology nodes, the critical dimensions of BEOL interconnects are continuously scaled down. Additionally, new materials (Cu and low-*k*) and a dual damascene process have been introduced. Furthermore, new technologies, such as electroplating and Cu CMP, have been used in the semiconductor fabrication line. Thus, more integration challenges are raised, as described below:

4.1. Width effect on resistivity of Cu

As the dimensions of Cu interconnects are reduced, the resistivity increases dramatically due to grain boundary scattering, surface scattering, and an increasing fraction of refractory metal liner in the trench (**Figure 3**) [38, 39].

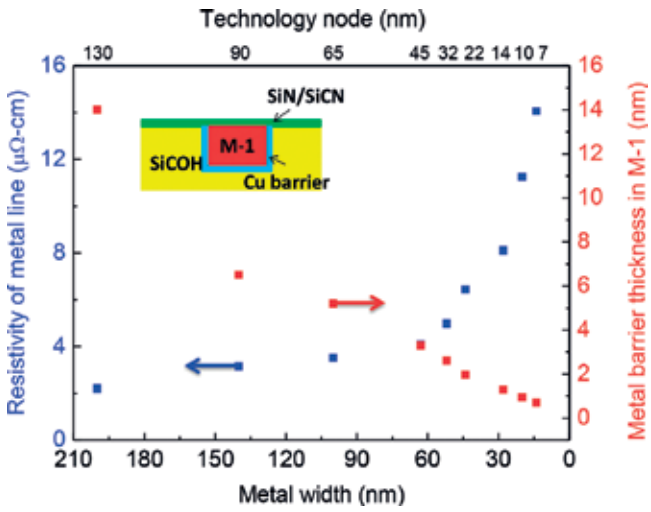

Figure 3. Resistivity of metal line and thickness of Cu barrier layer with technology nodes [40].

The first factor that increases the resistivity of the metal line is grain boundary scattering. The smaller gain size in Cu lines results in more grain boundaries, leading to an increased resistivity. Unfortunately, Cu gain size scales as the critical dimensions of the Cu line in dual damascene interconnect. It is difficult to achieve large grain size in narrow lines because grain growth of Cu in trenches is inhibited at small dimensions. Therefore, subtractive Cu method is the possible solution to increase the Cu grain size [41]. That is, Cu film is patterned by etching process. In such a case, Cu grain size would be much larger because Cu deposition is not restricted in the narrow lines. However, there remain many challenges to solve for etching of Cu including etching chemistry, hardmask, and hardware. Moreover, encapsulation of Cu line with barrier/liner materials is another issue to solve.

Surface scattering increases as the critical dimensions of the Cu line becomes smaller than the bulk mean free path of the electrons. To solve this issue, new material such as tungsten (W), silicides, carbon nanotube, or collective excitations could be an alternative to Cu as interconnects [42, 43]. Even though the bulk resistivity of W and silicide films is much larger than that of Cu film, the shorter mean free path of the electrons will lower the surface scattering effect. Another advantage of W interconnects is no-barrier process because the diffusivity of W metal is very low. The latter two materials (carbon nanotube and collective excitations) can provide a different conductance mechanism, but they are still in the research and development phase. Therefore, for these new conductor materials to successfully integrate into the semiconductor industry is a long way off.

As the dimensions of Cu interconnects are continuously scaled down for the advanced technology nodes, a larger fraction of the metal line cross-section is occupied by the refractory metal barrier film. The resistivity of the refractory metal barrier film is far larger than that of Cu metal. Therefore, the overall resistivity of the metal line is significantly increased. The direct strategy to reduce the resistance rise is to decrease the thickness of the metal barrier film. However, the accompanied problems are poor step coverage and Cu diffusion into the dielectric. The improved

sputtering method or atomic layer deposition method can be used to deposit a thinner liner layer [44–46]. The most promising method is to adopt a self-forming barrier process by depositing Mn-based film. The deposited Mn film can react with silicon-based dielectrics to form a self-forming dielectric barrier by annealing. A smooth MnO_x layer can be formed at Cu/dielectric film interface. This layer also provides a good adhesion for Cu film deposition. Furthermore, if this self-forming barrier process is controlled precisely, there is no barrier at the via bottom connecting the underlying metal line because of high diffusivity of Mn in Cu [47, 48]. This results in a lower via resistance and a better reliability for Cu interconnects.

4.2. Cu diffusion into the dielectric

Cu is easily diffused into the dielectric under a thermal and/or electric stress, causing a dielectric failure. For this reason, Cu film must be surrounded by a good diffusion barrier layer. Generally, the barrier layer in the sides and bottom of the Cu line is metal barrier film and is typically a TaN/Ta bilayer [49], while that on the top is dielectric barrier film, such as silicon nitride (SiN), silicon carbide (SiC), silicon carbonitride (SiCN), and silicon oxynitride (SiON) [24–26, 50, 51].

Both Ta and TaN are good Cu diffusion barrier layers. Besides, TaN can provide good adhesion to the dielectric, and Ta can provide a surface with good wettability of the Cu seed layer. Based on these characteristics, a TaN/Ta bilayer instead of a Ta/TaN bilayer is the best choice for a Cu diffusion barrier layer. Moreover, Ti-based and Ru-based barrier layers are alternatives to act as a Cu barrier layer for cost and resistivity consideration [52, 53]. However, the Cu barrier efficiency of Ti and Ru is not as good as that of Ta-based films. Therefore, a multilayer film of Ti/TiN/Ti is used as a Cu diffusion barrier layer; TiN can prevent excessive reaction between Ti and Cu, which can increase the resistivity of the wire. The top Ti layer can provide good wetting of Cu film because Cu wetting on TiN is very poor. Ru-based layer can provide a lower resistivity and a better Cu wettability than Ta layer; however, its Cu diffusion barrier is very poor. So, a TaN/Ru or Ti/Ru bilayer is used for Cu diffusion barrier [54–56].

The diffusion barrier layer on the top of Cu wires is typically a dielectric barrier film. However, its Cu barrier efficiency and adhesion ability with Cu film are poorer than those of a metal barrier layer. To address these issues, an extra metal layer (Ta/TaN or CoWP) is capped on the top surface of Cu wires before a dielectric barrier film deposition [57]. This extra process to deposit a metal layer is very challenging because of selectivity deposition on the Cu lines. However, control of this process can make a significant improvement on reliability for Cu interconnects if it is controlled precisely.

4.3. Cu oxidation

The other disadvantage for Cu interconnects is that Cu film can be oxidized during the water rinse and exposure to air. In addition to increasing the resistance of Cu wires, the formed Cu oxides cause reliability degradation due to the weakened adhesion at the Cu interfaces. During the fabrication of Cu dual damascene structure, there are two stages in which Cu film could be exposed to air. One stage is via-opening before Cu metallization deposition. The other stage is the completion of Cu CMP before a dielectric barrier layer deposition. Hence, to remove Cu

oxides and avoid Cu re-oxidation, an *in situ* clean is required. The mechanism to remove Cu oxides in clean process can be achieved by either physical removal or chemical reaction [58].

Ar sputtering clean to physically remove Cu oxides is a typical physical method. However, during Ar sputtering process, the corners of vias and trenches are chamfered and re-sputtering Cu atoms are trapped onto the sidewalls of the via [58]. The former phenomenon leads to an increased leakage current between the neighboring wires. The latter phenomenon results in strong degradation in dielectric reliability. Hence, the energy and time in the Ar sputtering clean process must be carefully controlled in order to alleviate these two phenomena. Moreover, a "barrier-first" process was provided to minimize the detrimental effects caused by Ar sputtering clean [59]. In this barrier-first process, a TaN layer is deposited first and Ar sputtering clean is then performed to etch through the TaN layer and the contamination at the bottom of the via. Finally, a Ta layer is deposited. Due to the presence of the TaN layer, the chamfering at the top corner of vias and trenches and the re-sputtered Cu atoms and contaminations into the dielectric can be effectively reduced during Ar sputtering clean process.

The chemical clean to remove Cu oxides can also minimize the detrimental effects caused by the Ar sputtering clean. The mechanism of chemical clean is based on the oxidation-reduction reaction. Hydrogen (H) atom is typically the reducing agent. Hence, H_2 or NH_3 is widely used reduction gas [60–62]. The chemical clean is processed under a plasma process, which increases the activity of the reaction. During chemical plasma clean process, Cu oxides can be reduced; however, the dielectric (e.g. low-*k*) is also exposure to a plasma environment. The dielectric is damaged by plasma irradiation. This leads to an increased dielectric constant and a reduced dielectric breakdown filed. Therefore, the drawback of using chemical plasma cleaning to remove Cu oxides is the plasma-induced damage on the dielectric (e.g. low-*k* damage). To minimize the damage on the dielectric and keep Cu oxide removal efficiency, a remote plasma technology has been proposed [63].

4.4. Cu chemical mechanical polishing

The chemical mechanical polishing (CMP) process has been used to polish oxide dielectric film and W plug in Al metallization since 0.35 μm technology node. As the BEOL interconnect was transferred to Cu metallization, due to the adoption of damascene structure, dielectrics do not needed to be polished by the CMP process. Instead, the excess Cu films in the damascene structure are necessary to be removed by CMP process. Cu CMP process can be regarded as a new technology and has a different consideration from oxide CMP process, hence, it is very challenging. During CMP process, the wafers are placed face-down on a rotating pad on which the slurry is dispensed, resulting in the removal of the film by chemical reaction and mechanical force. In Cu CMP process, the excess Cu film and metal barrier layer must be removed to fabricate Cu metallization. Typically, there are three main steps in Cu CMP process [64]. The first step is Cu film removal, stopping on the barrier layer. In this step, removal selectivity is not considered because only Cu film is polished. The second step is the barrier layer removal, stopping on the dielectric. During this step, both barrier layer and Cu film are polished. The last step is over-polishing to ensure that all metals are removed from the field regions in all parts of the wafer. Cu film, barrier layer, and the dielectric are polished simultaneously. In the

http://dx.doi.org/10.5772/intechopen.72396

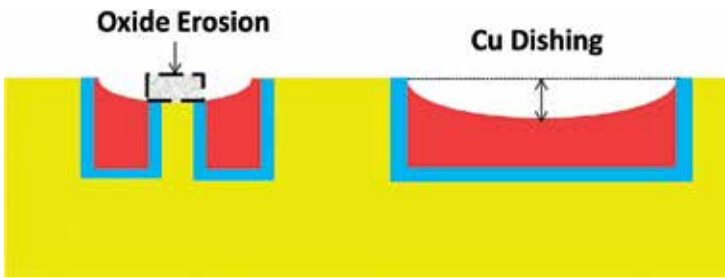

Figure 4. Side view schematic of Cu dishing and oxide erosion induced by the Cu CMP process.

last two steps, the selectivity should be considered because it is of importance to reach high-degreed planarization.

Cu dishing and oxide erosion as shown in **Figure 4** are the main problems associated with Cu CMP process [65–67]. As porous low-*k* dielectric films are used as the BEOL insulators to further reduce the capacitance between the metal lines, these two issues also become more severe. Therefore, the Cu CMP process is needed to be optimized. Since the formation mechanism of these two problems is due to the faster polish rate and lower selectivity in the slurry, reducing the down-force during Cu CMP process and/or optimizing the used slurry are feasible methods to minimize these effects.

Additionally, the pattern density of the Cu line also influences the performance of Cu CMP process. Generally, in the region of high Cu pattern density, the polishing rate is high and the thinning of the Cu line is observed due to a high polishing rate, resulting in a large variation in the resistance of the metal line. Thus, design rules to restrict the local Cu pattern density are provided for IC designers based on Cu CMP process [68]. Therefore, to reach high IC performance, inserting the dummy Cu lines to increase Cu pattern density is a general method to minimize the pattern effect of the Cu CMP process. Moreover, low downforce during the over-polish step in Cu CMP process is required to minimize this effect from the perspective of the process [69].

Moreover, cracks, delamination, scratching and contamination are the problems accompanied with Cu CMP process because the Cu CMP process is basically a frictional process. These problems can be solved through: (i) reducing the down-force during Cu CMP process; (ii) improving the adhesion between layers in the interconnect; (iii) optimizing the used slurry; (iv) depositing a relatively dense material, such as SiO_2 or nonporous SiCOH films on the top of the porous low-*k* dielectric film; and (v) performing an optimized wetting clean after the CMP process [70–72].

5. Reliability of copper metal

In the Cu interconnects, there are three main reliability items: electromigration (EM), stress-induced voiding (SIV), and time-dependent dielectric breakdown (TDDB) [18]. The first two items are used to assess metal reliability, while the last item is to evaluate dielectric reliability. However, all reliability items are related to each component of Cu interconnects.

5.1. Electromigration (EM)

The failure of interconnects through electromigration (EM) has been a long-standing concern for the development of highly reliable ICs. The first EM-related failure of Al-interconnect based circuit was observed in 1966 [73]. For the past 60 years, intense efforts have been made on either Al interconnects or the newly introduced Cu interconnects to enhance the resistance against EM.

The phenomenon of EM involves metal atoms migration in a metal conductor due to a stress with a high electrical current density (~10^5 A/cm) [74]. As an electric current is applied on a metal lead, the momentum transfer is occurred from the electrons to the metallic atoms, resulting in the migration of the metallic atoms. Therefore, the depletion and accumulation of the metallic atoms in a metal lead would be observed, which occur in the cathode and anode sides of a metal lead, respectively. As a lead is depleted at the cathode side, voids will form and the resistance will increase. If the voids grow large enough to spans the whole line, open line will be observed. At the anode end of the wire, metal atoms will accumulate, resulting in a hydrostatic stress. If the stress is high enough and the dielectrics are weak, metal extrusions may form, causing leakage between the neighboring metal lines [18, 75]. In Cu interconnects, the Ta/TaN barrier layers at the bottom of the via can act as blocking boundaries, which provide a higher EM resistance than Cu. Hence, during an EM stress, the depletion and accumulation phenomenon occur in the Cu line.

This stress produces a back flux of atoms that is opposite in the direction to the flux from electromigration, which is called the "Blech effect" or Short-length effect" [76–79]. This buildup stress causes a reverse migration process, which reduces or compensates for the effective metal material flow toward the anode side during EM. Thus, the EM failure time can be effectively improved. Moreover, this back-stress force becomes obvious as the length of the wire decreases. Therefore, the short wires that have a length below a critical threshold length (typically on the order of 5–50 μm), the back flux of atoms prevents killer voids from forming, and the wires are immortal.

To accelerate the fails and save the test time, the EM test is performed under a high-current density and a high-temperature condition. The failure time (t) of Cu line is widely described by using Black's equation [80, 81]:

$$t = Aj^{-n}\exp\left(\frac{E_a}{kT}\right) \tag{3}$$

where j is the current density, E_a is the activation energy for diffusion, k is the Boltzmann constant, T is the temperature, A is a constant, and n is the current exponent, which value is typically between 1 and 2. If n value is close to 1, the EM kinetics is dominated by void growth, whereas $n = 2$ corresponds to kinetics limited by void nucleation [82].

The activation energy for diffusion is varied by the different diffusional mechanisms as listed in **Table 4** [83]. Diffusion process caused by EM can be divided into bulk diffusion, grain boundary diffusion, surface diffusion, and interface diffusion. In Al and Cu interconnects, the

Metal	Activation Energy for different diffusion paths (eV)			
	Bulk	Grain boundary	Surface	Interface
Al	1.4	0.4~0.5	NA	---
Al/Cu (alloy)	1.2	0.6~0.7	NA	0.9~1.1
Cu	2.1	1.1~1.2	0.6~0.7	0.8~1.3

Table 4. Activation energy for different diffusion paths for Al, Al/Cu, and Cu metal.

activation energies for diffusion in different diffusion paths are different. In Cu interconnects, interface diffusion has the lowest activation energy, presenting the major path for EM. Whereas in Al interconnects, grain boundary diffusion is a fast EM path due to a lower activation energy [83–86].

In Cu metallization, the "line-via" structure is widely used for EM characterization. Two typical EM test structures: "downstream stressing" and "upstreaming stressing," as shown in **Figure 5**. In order to minimize the Blech effect on EM results, the length of the tested Cu line must be sufficiently long. Generally, the length is about 200–250 μm. During an EM test, the resistance is monitored with the stressing time. As the monitored resistance is increased by a certain value or a certain percentage, this time is defined as the EM failure time. Generally, 20–30 samples are tested for an EM test. The measured failure times are usually plotted using a log-normal distribution and analyzed [23].

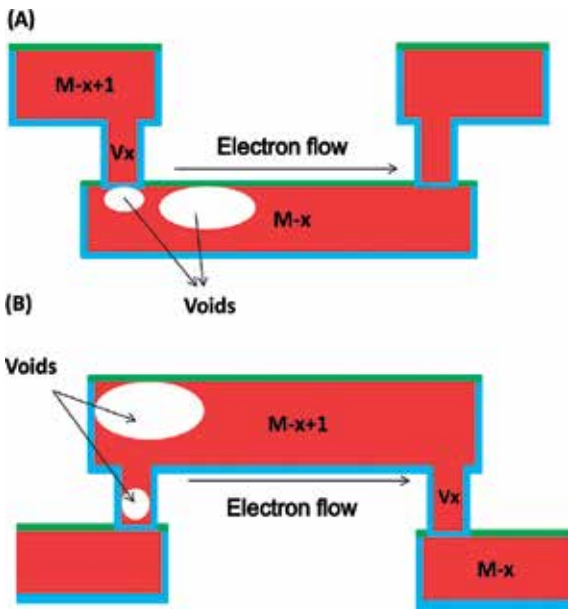

Figure 5. Side view schematic of electromigration test structures and void formation locations. (A) Downstream stressing structure and (B) upstream stressing structure.

In a "downstream stressing" test structure, electron flow is from metal-2 to metal-1 through Via-1. The EM-induced void will form under the via (early failure) and in the wire far from the via (late failure). In an "upstream stressing" test structure, electron flow is from metal-1 to metal-2 through Via-1. The EM-induced void will form inside the via (early failure) and in the wire (late failure). The early failure occurred in both test structures is related to via process or metal barrier deposition. The late failure is directly linked to Cu/dielectric interface or Cu line property. Therefore, to mitigate Cu EM phenomenon, these related processes are needed to be optimized.

Many factors, such as design related, process related, and environmental related factors, can significantly affect Cu EM reliability, as summarized below:

5.1.1. Scaling effect

As device and wire dimensions are reduced in the advanced technology nodes, it is desirable to increase the maximum required current density in Cu lines, thus a longer EM lifetime of Cu lines should be achieved [40]. **Figure 6** plots the maximum required current density at 105°C for Cu lines. The reason for this increase is that the drive current in the devices increases and the switching speed increases as the dimension of the device is scaling. Simultaneously, the dimension of the metal line is minimized. Hence, the metal line should sustain a higher current density.

The EM performance, however, could not be improved as the dimensions of Cu lines decrease. Actually, the EM lifetime decreases as shown in **Figure 7**. Two reasons can explain this result. First, as the dimensions of via and trench decreases, the void size required to cause a EM fail decreases accordingly [86]. This leads to a short time to form a "killer" void. The other reason is due to the grain size in Cu lines. Experimental results indicated that the grain size decreases with line width as the width of Cu lines is less than 0.2 μm. In Cu lines with the smaller grain

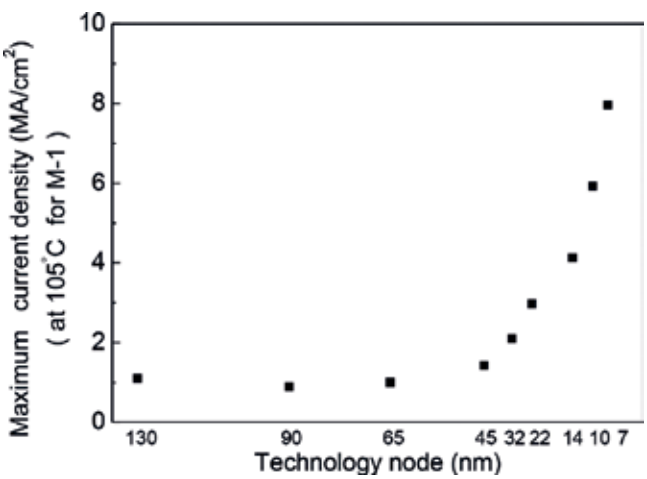

Figure 6. Maximum required current density at 105°C for M-1 Cu lines with technology nodes [40].

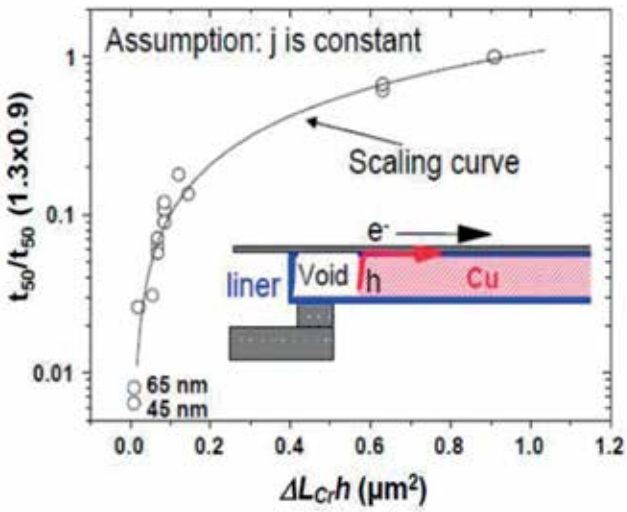

Figure 7. Experiment and model results of electromigration lifetime scaling with the reduction of interconnect dimension. Reproduced with permission from Ref. [86].

size, grain boundary diffusion can be significant during an EM stress, resulting in a lower EM lifetime [87].

For the advanced technology nodes, EM reliability is becoming a critical challenge due to a high EM requirement and a low EM performance. Therefore, a number of Cu interconnect fabrication technologies or ways to improve the EM performance for narrow Cu lines are necessary. Moreover, from the perspective of stressing method, alternative current (AC) stressing can enlarge EM lifetime of Cu lines as compared to the conventional direct current stressing [88, 89]. The improvement in EM lifetime is attributed to the effect of damage healing. Under AC conditions, the partial Cu atoms migrating in one direction at one polarity stress would migrate back to its original location at the reversing polarity stress. Consequently, the Cu line suffers less damage from EM for a given time, resulting in a long EM lifetime. Additionally, the effect of damage healing from AC stress depends on the operation frequency. As the operation frequency is above 10 Hz, the effect of self-healing becomes significant and increases with the operation frequency. When the operation frequency is up to about 10 kHz, this effect is saturated. Thus, no further EM lifetime improvement is observed at the operation frequencies above this point [88].

5.1.2. Cu interface effect

The interface between Cu line and the capping layer is the dominating EM transport path for Cu damascene interconnects due to the lowest activation energy for diffusion [83]. Therefore, to obtain a long EM lifetime, the improvement of Cu interface is the most effective method by increasing the adhesion between these layers [90]. A typical dielectric capping process consists of two main steps: plasma clean to remove Cu oxides and a Cu barrier dielectric deposition (either SiN or SiCN) [91, 92].

A plasma clean has a pronounced effect on the EM improvement as compared to a barrier dielectric deposition. This is attributed to the enhanced adhesion between Cu line and barrier dielectric layer. H_2 or NH_3 plasma clean is typically used, which can remove the Cu oxide from the top surface of Cu metallization through chemical reaction. The obtained results were contradictory [93–95] since some authors reported H_2-based plasma clean is better. These apparent contradictions may result from the wide variety of plasma chambers and the plasma conditions. Nevertheless, it is clear that both the H_2 and NH_3 plasma clean can enhance EM lifetime. Additionally, in order to strengthen adhesion, a SiH_4 exposure process is inserted between a plasma clean and a dielectric deposition processes to form a thin Cu silicide layer. This way, the EM lifetime was enhanced due to the improved adhesion [96, 97].

The effect of Cu dielectric capping layer on EM is not as obvious as compared to that of a plasma clean although it is concluded that the improvement in the adhesion between Cu line and dielectric capping layer can enhance EM. SiN and SiCN capping layers have similar EM lifetime, but have longer EM lifetime as compared to SiC capping layer [98]. The formation of Cu compound (Cu_3N) at the interface for providing a better interface is a possible mechanism.

Based on these results, an alternative to improve Cu interface is through the use of a metal capping layer in replace of a dielectric capping layer. Due to the reduction in interface diffusion, EM lifetime was found to have a huge improvement. The used metal capping layer can be Ta/TaN or CoWP [57], the latter capping layer reported to provide a larger EM improvement than the former. Moreover, in Cu damascene lines with bamboo-like grain structure (i.e., no grain boundary diffusion), the activation energies for diffusion were 1.0 eV for an SiN or SiCN capping layer, 1.4 eV for an Ta/TaN capping layer, and 2.4 eV for a CoWP capping layer [99]. This suggests that the diffusion mechanism is changed from interface diffusion to bulk diffusion for CoWP capping layer. In the cast of Ta/TaN capping layer, although the interface diffusion mechanism is still dominating, the interface bonding between the Cu and the capping layer is enhanced.

Figure 8 compares various technologies for EM improvement in terms of EM improvement efficiency (EM lifetime improvement ratio and the resistance increase ratio). CoWP capping layer is shown to be the best approach with a higher EM life-time improvement and a lower resistance increase.

5.1.3. Microstructure effect

The microstructure of Cu interconnects also plays an important role in EM performance. The important microstructure parameters include grain size (with respect to line width), grain distribution, and grain orientation. Each of these parameters influences EM performance and is impacted by Cu metallization steps. Generally, large grain size or bamboo grain structure, tight grain distribution, and (111) grain orientation are helpful for EM improvement. Experimental results indicated that electroplated Cu line has relatively large grain size and tight grain distribution as compared to CVD Cu line, resulting in longer EM lifetime [100]. Furthermore, an annealing (<400°C) step after electroplating and before Cu CMP step can increase the grain size of Cu lines due to gain growth and recrystallization, resulting in increased EM lifetime [101].

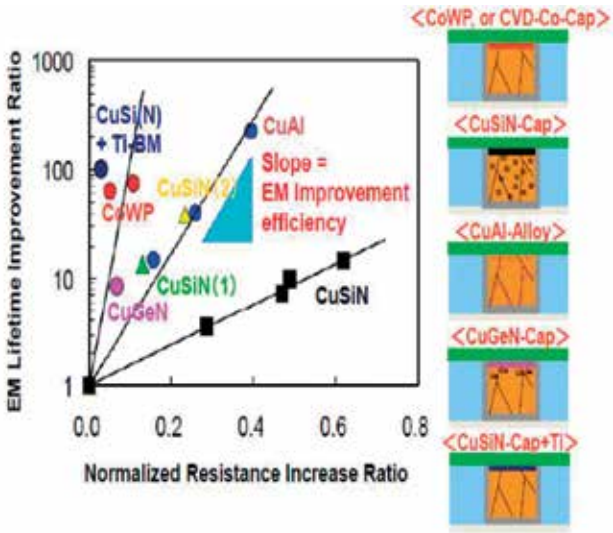

Figure 8. Comparison of electromigration lifetime improvement versus the resistance increase for various electromigration improvement technologies [40].

5.1.4. Dielectric effect

A lower EM lifetime was found when a low-*k* dielectric is used as an insulator in Cu interconnects [102, 103]. This reduction is amplified with decreasing the dielectric constant of low-*k* dielectrics. There are several reasons to explain the lower EM life-time for low-*k* dielectrics. First, the modulus of the low-*k* dielectrics is lower than that of SiO_2 film and decreases with the reduction of the dielectric constant. Because of the lower modulus, the Blech effect and the critical length for line immortality will be reduced [103]. Second, the barrier layers often have weak adhesion to low-*k* materials; the weak adhesion can result in extrusion fails during an EM stress [104]. Finally, low-*k* materials have lower thermal conductivity than does SiO_2. Hence, more joule heating is generated for a given current density [105], resulting in a higher temperature in the Cu wire, and therefore a faster diffusion rate of EM.

5.1.5. Cu seed layer doping effect

Doping impurities such as Al [106, 107], Ag [108], Mn [109–111], Magnesium (Mg) [112, 113], Zirconium (Zr) [114], and Tin (Sn) [115] into the Cu layer is an effective method to improve the EM lifetime. The main disadvantage of this approach is that the impurities increase the resistivity of Cu line. To avoid a huge increase in the resistivity, the dopant concentration is kept relatively low and the dopant is usually introduced in the Cu seed layer deposition process. Additionally, an extra annealing process is needed after completing Cu metallization. The purpose is that the dopant impurities segregate at grain boundaries and interfaces between the Cu line and the capping layer by an annealing. Thus, Cu migration rate of EM is retarded due to the reduction in the grain boundary and interface diffusions [106, 110]. The measured EM lifetime was found to be enhanced by at least one order of magnitude and is positively proportional to the doping concentration.

Among the dopants used, Al and Mn have received more attention because they have shown to increase EM lifetime significantly. Furthermore, Mn is the promising candidate for providing some advantages. Its low solubility in Cu lines allows minimum increase in resistivity by optimizing the post-metal annealing [109]. Moreover, Mn has high affinity for oxygen, resulting in the formation of MnO_x layer with the dielectric film by annealing. The formed MnO_x layer can act as a Cu barrier layer, thus avoiding depositing a metal barrier layer [47, 48].

5.2. Stress-induced voiding (SIV)

Like EM, voids will form in the metal line for stress-induced voiding. But these two reliability terms have different mechanisms. Whereas EM is induced by electron wind force under an electric field, stress-induced voiding (SIV) is due to stress migration. As a passivated Cu interconnect is annealed at moderate temperatures (200–250°C), tensile stress in the metal is established. If this built-up tensile stress is above the critical stress, voids will form in the Cu line, leading to a resistance increase or an open line. The built-up stress in the metal line is caused by two mechanisms: One is thermal stress due to thermal expansion mismatch between the metal line and the dielectric insulator; and the other is growth stress due to grain growth in the metal line [116–118].

The unique characteristic of stress-induced void is that the maximum rate of void growth in Cu line does not occur at a high temperature, as shown in **Figure 9**. To achieve large enough voids to fail the circuit, the stress built-up (void nucleation) and Cu atom migration (void accumulation) must occur in sequence. However, the temperature-dependence effect of these two mechanisms is totally different. If stress-induced void is originated from thermal expansion mismatch during the dielectric capping layer deposition, a "stress-free" temperature can be obtained. This stress-free temperature is related to the deposition temperature of the dielectric capping layer and subsequent processes. The stress-free temperature is close to the inter-level dielectric deposition temperature, generally being 300–450°C. As the stress temperatures is

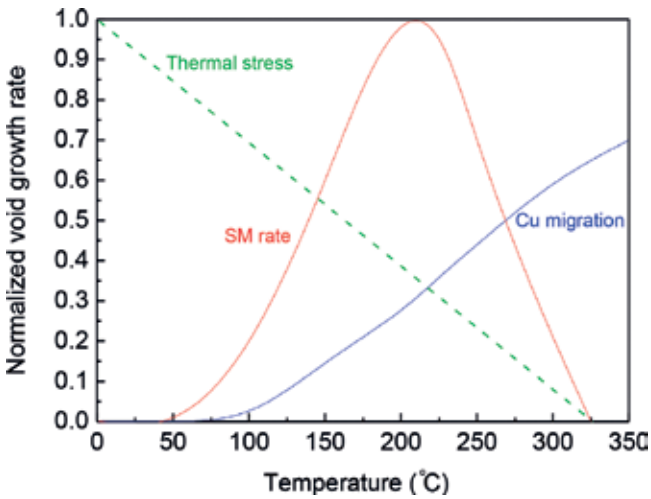

Figure 9. Void growth rate of stress-induced void as a function of temperature [116].

close to the stress-free temperature, the tensile stress (σ) in the metal line is low, so that the void growth rate is low. On the other hand, the Cu diffusivity is increased with increasing the temperature, leading to a high void growth rate at high temperatures. These two different mechanisms result in a significant void growth at intermediate temperatures (150–250°C) [116, 119, 120]. Therefore, for a newly developed process for Cu interconnects, the stress temperature for the maximum rate of void growth in Cu line should be characterized in advance.

The test structure of stress-induced void is simple via-chain structures. The resistance is monitored as a function of time at the stress temperature [121]. As the resistance is increased by a certain value (5–10%), this time is defined as the lifetime for stress-induced void.

The main affecting factors for stress-induced voids in Cu lines can be categorized as follows.

5.2.1. Scaling effect

The main failure mode of stress-induced void is void formation under vias due to the stress gradient in the underlying Cu line and the presence of the via-metal interface [116]. As the formation void is spanned the whole via, which is called "killer void," the electric current is stopped, leading to a failure of circuits. Therefore, the failure rate for stress-induced void in Cu line increases with decreasing via size (**Figure 10**).

On the other hand, the failure rate for stress-induced void in Cu line increases with increasing line width (**Figure 10**) opposite to what is observed with Al line [116, 117, 122]. Two mechanisms can explain this unique behavior. One is that the hydrostatic stress increases with increasing the width of Cu lines based on the result of stress simulation [123]. Hence, a stronger driving force for void formation is produced in wide Cu lines than in narrow Cu lines. The other mechanism can be explained by the theory of "active diffusion volume" [124]. In this theory, the formation void is related to the number of vacancies, which are available within a diffusion length of the via. The wider Cu lines can provide a greater number of

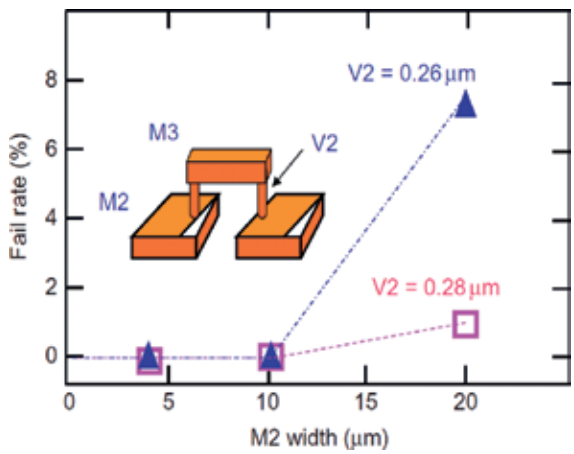

Figure 10. Failure rate of stress-induced void versus M2 line width and V2 via size after annealing stress at 225°C for 1000 h. Reproduced with permission from Ref. [122].

vacancies to form void under the bottom of the via. Thus, the wider Cu lines take less time to form a "killer void" and have a weak resistance against stress-induced void. To solve stress-induced void reliability issue on the narrow via and wide line, a design solution is provided by inserting redundant vias in the wide Cu line [125, 126]. By this approach, the stress gradient is reduced and the volume of the killer void is increased, thus enhancing stress-induced void.

5.2.2. Cu surface effect

Stress-induced void in Cu lines are mostly observed under vias [116]. A high tensile stress in the metal at the edge of the via and a weak adhesion between the barrier metal and the underlying Cu at the bottom of the via are responsible for this failure mode. A high tensile stress in the metal at the edge of the via was detected through stress simulation modeling [127, 128]. At this point, if the tensile stress exceeds the critical stress, a void will nucleate and then grow along the interface between the barrier metal and the underlying Cu at the bottom of the via. Once a void forms, the critical stress will be reduced, making the stress field surrounding the void becomes less tensile. The resulting stress gradient favors vacancy diffusion toward the void resulting in further growth.

To solve this failure mode of stress-induced void, providing a better Cu interface is the main strategy. Therefore, the approaches to optimize Cu interfaces applied for EM improvement also provide great help for stress-induced void [129–131].

5.2.3. Cu grain boundary effect

Stress-induced void can also be observed at grain boundaries in Cu lines [132]. Thus, grain boundary is another diffusion path. Decreasing the grain boundaries in Cu lines (i.e. maximizing Cu grain size) can minimize the fail rate of stress-induced void, similar to the improvement in EM reliability. The most effective method to maximize Cu grain size is by the use of an annealing process. The operation timing is after Cu plating and before Cu CMP step. It is noted that the maximum annealing temperature must be limited after dielectric capping layer deposition because high-temperature annealing after dielectric capping layer deposition can lead to high rates of stress-induced void formation due to either confined grain growth or due to increased stress in the Cu line [122, 132]. Additionally, the use of metal capping layers [133] and/or Cu alloying lines [106, 107], which are used to improve EM has also shown to reduce the failure rate of stress-induced void.

5.2.4. Via barrier effect

The early failure of stress-induced void occurs inside the via due to a defect in the via with a lower tensile stress [124]. Since Cu atoms will migrate to the regions of higher tensile stress, the vacancies will diffuse to the regions of lower tensile stress. If there is a defect in the via, then void nucleation will be further enhanced in the via. Poor coverage of seed layer and undesirable gap filling of electroplating are the precursors for void formation. As the dimensions of Cu interconnects shrink, these two processes are becoming more challenging. To ensure low resistance of the metal line in the advanced technology nodes, the thickness of Cu barrier layer is required to thin down as much as possible. However, the issues of Cu diffusion into the

dielectric, metal barrier layer coverage on the bottom and sidewalls of trenches and vias and Cu plating gap filling are important.

This failure mode of stress-induced voids can be eliminated with good metal barrier layer coverage on the bottom and sidewalls of trenches and vias and void-free Cu-filling process. To achieve these goals, pore sealing on porous low-*k* dielectrics [134], good control of the via and trench profiles [135], use of ALD barrier technology [136], and optimization of the additives in the Cu plating process [37] have been demonstrated.

5.3. Time-dependent dielectric breakdown (TDDB)

During a prolonged stress at high electric fields, electric damage can occur in dielectric materials. This induces the loss of the insulating properties for a dielectric material for which the resistance state is converted from high to low. Finally, an electrical breakdown occurs as a conducting path is formed. This loss of reliability is called "time-dependent-dielectric breakdown" (TDDB) [137–141].

The time-dependent dielectric breakdown can occur in gate dielectrics and BEOL dielectrics [142, 143]. The former has been an important reliability issue because the thickness of gate dielectrics is continuously decreased with the advance of technology node although the latter is not a key issue in Al interconnects because the applied electric field across the BEOL dielectric is low due to the relatively large spacing between the metal lines. However, as the technology node of ICs is continuously advancing, the lateral electric field across the BEOL dielectric significantly increases due to the reduction of interconnect dimension. Simultaneously, the used BEOL dielectric is transforming to low-*k* dielectrics with a lower dielectric constant than 4.0. The breakdown strength of low-*k* dielectrics is lower than that of SiO_2 film and typically decreases with the reduction of the dielectric constant. These combined effects result in a critical challenge in time-dependent dielectric breakdown for BEOL dielectrics in the advanced technology nodes [144, 145].

The test structure for the TDDB reliability evaluation has two typical configurations: comb-comb or comb-serpentine layout [146–149], as shown in **Figure 11**. Typically, metal-1 is the most commonly used metal level because it has the smallest pitch. During a test, one electrode (e.g., serpentine) is grounded and a constant positive voltage is applied to the other electrode (e.g., comb). The leakage current is measured with the stress time. The typical leakage current versus the stress time is the initial decrease in leakage current due to trapping of charge, followed by stress-induced leakage current, and finally breakdown [150]. The stress time with a sharp increase in the monitored leakage current, is corresponding to the breakdown time.

Since the time-dependent dielectric breakdown is used to assess the dielectric reliability, its performance is strongly dependent on the property of a dielectric. Additional investigations have indicated that a high density of defect sites in the as-deposited dielectric (especially for low-*k* materials) [151], damage or contamination of the dielectric from processes such as plasma and CMP processes [152–154], and patterning problems such as line edge roughness or via misalignment [155, 156] resulted in the low breakdown strength of BEOL dielectrics.

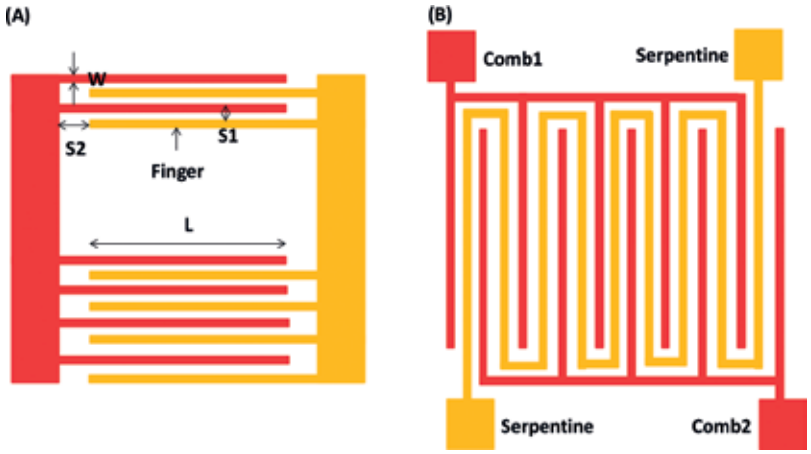

Figure 11. Top view schematic of time-dependent dielectric breakdown test structures. (A) Comb-comb structure. (B) Comb-serpentine structure.

Consequently, the optimization of the BEOL interconnect process can effectively improve time-dependent dielectric breakdown reliability.

Additionally, Cu metallization also influences the TDDB performance. Cu diffusion into the dielectric leads to serious degradation in BEOL dielectrics reliability [157–159]. Cu diffusion into the dielectric can be through the dielectric and metal barrier layers, which are interfacial diffusion and bulk diffusion, respectively. The interfacial diffusion is considered to be the dominant Cu diffusion path. This can be demonstrated by the fact that dielectric breakdown between neighboring Cu wires generally occurs at the interface between the capping layer and the dielectric [150, 160]. The interface is expected to have a higher trap density than the bulk dielectrics due to the bond mismatch between the different materials or due to contaminants from the Cu CMP process [153, 161]. Hence, the interface between the capping layer and the dielectric is the preferred diffusion and leakage path for Cu atoms. Moreover, the fabricated Cu lines are generally tapered shape (wider at the top than at the bottom), so the space is smallest at the top of the Cu line, leading to the highest electric field at this location. Due to the combination of high electric field and high-defect density, the interface is the dominant path for Cu diffusion.

Moreover, "Cu-diffusion-catalyzed breakdown" theory has been proposed to explain lower dielectric breakdown strength for Cu diffusion into the dielectric [162]. In this theory, Cu could act as a precursor for an ultimate dielectric breakdown. As the concentration of Cu in the dielectric reaches a critical value, the dielectric breakdown event occurs. Two possible mechanisms can account for Cu-induced dielectric breakdown. First, the diffused Cu atoms can catalyze the bond breakage reaction by inducing permanent bond displacement in the dielectric. The other mechanism is that the accumulated Cu atoms in the dielectric form clusters of nanoparticles. As these clusters are connected, a metallic shorting bridge or a local dielectric thinning is established, triggering a dielectric breakdown.

In addition to the reduced dielectric breakdown strength and failure time, Cu diffusion into the dielectric alters the TDDB electric field acceleration model, which is used to determine the fail rate or lifetime at the use conditions (the high-field stress data must be extrapolated to the lower fields at the use conditions). The "E-model" [163–165], which is a field-driven model and chemical bond breakage mechanism, fails to describe the low-*k* TDDB behavior with Cu diffusion. Instead, "$E^{1/2}$-model" [146, 166] is the most appropriate model. It is postulated that the accelerated electrons, injected from the cathode, transport inside low-*k* dielectric by means of Schottky-Emission or Poole-Frenkel conduction. Some electrons undergo thermalization under high field and high temperature and impact the Cu atoms at the anode. This produces the positive Cu ions, which in turn inject into the dielectric under the field along a fast diffusion path. Since the current in the Schottky-Emission or Poole-Frenkel conduction is proportional to $E^{1/2}$, the "$E^{1/2}$-model" is the possible model to describe low-*k* time-dependent dielectric breakdown with Cu diffusion. However, the TDBD model is not yet fully accepted and so it remains an open issue.

To minimize Cu diffusion into the dielectric to avoid reliability degradation in TDDB, several process strategies have been proposed including using adequate metal barrier layers [167, 168], minimizing residues after post-CMP cleaning [169], and minimizing air exposure prior to capping of the Cu [150, 153]. Additionally, alternating polarity operation method instead of direct current stress could increase dielectric breakdown lifetime, resulting from recovery effect due to the backward migration of Cu ions during the reverse-bias stress [170, 171].

6. Conclusions

To improve the performance of ICs by reducing *RC* delay, the conductor with a lower resistivity in interconnects should be rechosen. In the past two decades, better performance of ICs was achieved by using Cu conductor in place of Al conductor. Currently, although Cu metallization has been successfully integrated into ICs, a different and complex process to fabricate Cu interconnects has many remaining issues, resulting in integration and reliability challenges.

In future, the interconnect process returning to subtractive metal process from dual damascene process is one possible solution. Furthermore, looking for an alternative to replace Cu is an ongoing important topic for research and development. Silver, carbon nanotube, graphene, or photonic interconnects are possible candidates.

Author details

Yi-Lung Cheng*, Chih-Yen Lee and Yao-Liang Huang

*Address all correspondence to: yjcheng@ncnu.edu.tw

Department of Electrical Engineering, National Chi-Nan University, Nan-Tou, Taiwan, ROC

References

[1] Thompson SE, Parthasarathy S. Moore's law: The future of Si microelectronics. Materials Today. 2006;**9**:20-25

[2] Grill A, Gates SM, Ryan TE, Nguyen SV, Priyadarshini D. Progress in the development and understanding of advanced low *k* and ultralow *k* dielectrics for very large-scale integrated interconnects – State of the art. Applied Physics Reviews. 2014;**1**:011306-011312

[3] Bohr M. MOS transistors: Scaling and performance trends. Semiconductor International. 1995;**18**(6):75-80

[4] Grill A. Porous pSiCOH ultralow-*k* dielectrics for chip interconnects prepared by PECVD. Annual Review of Materials Research. 2009;**39**:49-69

[5] Kim CY, Navamathavan R, Lee HS, Woo JK, Hyun MT, Lee KM, Jeung WY, Choi CK. Ultraviolet irradiation effect on the properties of leakage current current and dielectric breakdown of low-dielectric-constant SiOC(H) films using comb capacitor structure. Thin Solid Films. 2011;**519**:6732-6736

[6] Broussous L, Berthout G, Rebiscoul D, Rouessac V, Ayral A. Mechanical properties of a plasma-modified porous low-*k* material. Microelectronic Engineering. 2010;**87**:466-469

[7] Cheng YL, Wang YL, Liu CW, Wu YL, Lo KY, Liu CP, Lan JK. Characterization and reliability of low dielectric constant fluorosilicate glass and silicon rich oxide process for deep sub-micro device application. Thin Solid Films. 2001;**398–399**:544-548

[8] Cheng YL, Wang YL, Lan JK, Chen HC, Lin JH, Wu YL, Liu PT, Wu YC, Feng MS. Effect of carrier gas on the structure and electrical properties of low dielectric constant SiCOH film using trimethylsilane prepared by plasma enhanced chemical vapor deposition. Thin Solid Films. 2004;**469**:178-183

[9] Grill A. Plasma enhanced chemical vapor deposited SiCOH dielectrics: From low-*k* to extreme low-*k* interconnect materials. Journal of Applied Physics. 2003;**93**:1785-1790

[10] Chang YM, Chang WY, Leu J, Cheng YL. Effect of thermal treatment on physical, electrical properties and reliability of porogen-containing and porogen-free ultralow-*k* dielectrics. Thin Solid Films. 2013;**528**:67-71

[11] Noguchi J, Sato K, Konishi N, Uno S, Oshima T, Ishikawa K, et al. Process and reliability of air-gap Cu interconnect using 90-nm node technology. IEEE Transactions on Electron Devices. 2005;**52**:352-359

[12] Dixit GA, Havemann RH. Overview of interconnect – Copper and low-*k* integration. In: Handbook of Semiconductor Manufacturing Technology. 2nd ed. NY: CRC Press; 2008 (Chapter 2)

[13] Isaac RD. The future of CMOS technology. IBM Journal of Research and Development. 2000;**44**:369-378

[14] Huang HY, Hsieh CH, Jeng SM, Tao HJ, Cao M, Mii YJ. A new enhancement layer to improve copper performance. In: IEEE Interconnect Technology Conference Proceedings. 2010. paper 4.2

[15] Havemann RH, Hutchby JA. High-performance interconnects: An integration overview. Proceedings of the IEEE. 2001;**89**(5):586-601

[16] Plummer JD, Deal MD, Griffin PB. Silicon VLSI Technology. Upper Saddle River, NJ: Prentice Hall; 2000

[17] Havemann RH, Antonelli GA, Arendt GK, Danek M, McKerrow AJ, Weinberg RS. Copper BEOL solutions for advanced memory. Solid State Technology. 2009;**31**:10-13

[18] Jeffery G. Process technology for copper interconnects. In: Handbook of Thin Film Deposition. 2012. pp. 221-269

[19] Quirk M, Serda J. Semiconductor Manufacturing Technology. Upper Saddle River, NJ: Prentice-Hall; 2001

[20] Gambino J, Chen F, He J. Copper interconnect technology for the 32 Nm node and beyond. In: IEEE Custom Integrated Circuits Conference Proceedings. PA: Warrebdale; 2009. pp. 141-148

[21] Shapiro MJ, Nguyen SV, Matsuda T, Dobuzinsky D. CVD of fluorosilicate glass for ULSI applications. Thin Solid Films. 1995;**270**:503-507

[22] Kriz J, Angelkort C, Czekalla M, Huth S, Meinhold D, Pohl A, et al. Overview of dual damascene integration schemes in Cu BEOL integration. Microelectronic Engineering. 2008;**85**:2128-2132

[23] Takei S. Resist poisoning studies of gap fill materials for patterning metal trenches in via-first dual damascene process. Japanese Journal of Applied Physics. 2008;**47**:8766-8770

[24] Matz LM, Tsui T, Engbrecht ER, Taylor K, Haase G, Ajmera S, et al. Structural characterization of silicon carbide dielectric barrier materials. In: Brongersma SH, Taylor TC, Tsujimura M, Masu K, editors. Advanced Metallization Conference Proceedings 2005. Warrendale, PA: MRS; 2006. pp. 437-443

[25] Cheng YL, Chen SA, Chiu TJ, Wei BJ, Wu J, Chang HJ. Electrical and reliability performance of nitrogen-doped silicon carbide dielectric by chemical vapor deposition. Journal of Vacuum Science and Technology B. 2010;**28**(3):573-576

[26] Cheng YL, Chiu TJ, Wei BJ, Wang HJ, Wu J, Wang YL. Effect of copper barrier dielectric deposition process on characterization of copper interconnects. Journal of Vacuum Science & Technology B. 2010;**28**(3):567-572

[27] Travaly V, Van Aelst J, Truffert V, Verdonck P, Dupont T, Camerotto E, et al. Key factors to sustain the extension of a MHM-based integration scheme to medium and high porosity PECVD low-*k* materials. In: IEEE International Interconnect Technology Conference Proceedings. 2008. pp. 52-54

[28] Hinsinger O, Fox R, Sabouret E, Goldberg C, Verove C, Besling W, et al. Demonstration of an extendable and industrial 300 mm BEOL integration for the 65-nm technology node. In: IEEE International Electron Devices Meeting Proceedings. 2004. pp. 317-320

[29] Cooney EC, Strippe DC, Korejwa JW, Simon AH, Uzoh C. Effects of collimator aspect ratio and deposition temperature on copper sputtered seed layers. Journal of Vacuum Science and Technology A. 1999;**17**:1898-1903

[30] Reid J, Mayer S, Broadbent E, Klawuhn E, Ashtiani K. Factors influencing damascene feature fill using copper PVD and electroplating. Solid State Technology. 2000;**43**:86-94

[31] Kodas TT, Shin H-K, Chi K-M, Hampden-Smith MJ, Farr JD, Paffett M. Selective low-temperature chemical vapor deposition of copper from (hexafluoroacetylacetonato)copper(I)trimethylphosphine, (hfa)CuP(me)$_3^+$. Advanced Materials. 1991;**3** (5):246-248

[32] Chen ST, Chung YC, Fang JS, Cheng YL, Chen GS. Enhancement of seeding for electroless Cu plating of metallic barrier layers by using alkyl self-assembled monolayers. Applied Surface Science. 2017;**405**:350-358

[33] Fang JS, Chen GS, Cheng YL, Chin TS. Direct, sequential growth of copper film on TaN/ta barrier substrates by alternation of Pb-UPD and Cu-SLRR. Electrochimica Acta. 2016; **206**:45-51

[34] Hopwood JA. The role of ionized physical vapor deposition in integrated circuit fabrication. Thin Solid Films. 2000;**27**:1-7

[35] Li Z, Rahtu A, Gordon RG. Atomic layer deposition of ultrathin copper metal films from a liquid copper(I) amidinate precursor. Journal of the Electrochemical Society. 2006; **153**(11):C787-C794

[36] Reid J, McKerrow A, Varadarajan S, Kozlowski G. Copper electroplating approaches for 16 nm technology. Solid State Technology. 2010;**53**:14-17

[37] Huang Y-C, Lin X, Zheng B, Ngai CS, Paneccasio V, Behnke J, et al. High performance copper plating process for 65 nm and 45 nm technology nodes. In: Brongersma SH, Taylor TC, Tsujimura M, Masu K, editors. Advanced Metallization Conference Proceeding, 2006. Warrendale, PA: MRS. 2005. pp. 507-511

[38] Lee HB, Hong JW, Seong GJ, Lee JM, Park H, Baek JM, et al. A highly reliable Cu interconnect technology for memory devices. In: IEEE International Interconnect Technology Conference Proceedings. 2007. pp. 64-66

[39] Steinhogl W, Schindler G, Steinlesberger G, Traving M, Engelhardt M. Comprehensive study of the resistivity of copper wires with lateral dimensions of 100 nm and smaller. Journal of Applied Physics. 2005;**97**:0237061-0237067

[40] The International Technology Roadmap for Semiconductor, ITRS 2015. https://www.semiconductors.org/main/2015_international_technology_roadmap_for_semiconductors_itrs/

[41] Schuegraf K, Abraham MC, Brand A, Naik M, Thakur R. Semiconductor logic technology innovation to achieve sub-10 nm manufacturing. IEEE Journal of the Electron Devices Society. 2013;**1**(3):66-75

[42] Ward JW, Nichols J, Stachowiak TB, Ngo Q, Egerton EJ. Reduction of CNT interconnect resistance for the replacement of Cu for future technology nodes. IEEE Transactions on Nanotechnology. 2012;**11**(1):56-62

[43] Li B, Luo Z, Shi L, Zhou JP, Rabenberg L, Ho PS, Allen RA, Cresswell MW. Controlled formation and resistivity scalling of nickel silicide nanolines. Nanotechnology. 2009; **20**:085304

[44] Forster J, Gopalraja P, Gung TJ, Sundarrajan A, Fu X, Hammond N, et al. A PVD based barrier technology for the 45 nm node. Microelectronic Engineering. 2005;**82**:594-599

[45] Simon AH, Bolom T, Tang TJ, Baker B, Peters C, Rhoads B, et al. Extendability study of a PVD Cu seed process with Ar Rf-plasma enhanced coverage for 45 nm interconnects. Materials Research Society Proceedings. 2008;**1079**:N03-N04

[46] Rossnagel SM. Physical vapor deposition. In: Doering R, Nishi Y, editors. Handbook of Semiconductor Manufacturing Technology. 2nd ed. NY: CRC Press; 2008 (Chapter 15)

[47] Au Y, Lin Y, Kim H, Beh E, Liu Y, Gordon RG. Selectivity CVD of manganese self-aligned capping layer for Cu interconnects in microelectronics. Journal of the Electrochemical Society. 2010;**157**(6):D341-D345

[48] Usui T, Tsumura K, Nasu H, Hayashi Y, Minamihaba G, Toyoda H, et al. High performance ultra low-*k* (*k* = 2.0/keff = 2.4)/Cu dual-damascene interconnect technology with self-formed $MnSi_xO_y$ barrier layer for 32 nm-node. In: IEEE International Interconnect Technology Conference Proceedings. 2006. pp. 216-218

[49] Edelstein D, Uzoh C, Cabral C Jr, DeHaven P, Buchwalter P, Simon A, et al. An optimal liner for copper damascene interconnects. In: McKerrow AJ, Shacham-Diamond Y, Zaima S, Ohba T, editors. Proceedings of the Advanced Metallization Conference 2001. 2002. pp. 541-547

[50] Cheng YL, Wu J, Chiu TJ, Chen SA, Wang YL. Comprehensive comparison of electrical and reliability characteristics of various copper barrier films. Journal of Vacuum Science & Technology B. 2011;**29**(3):031207-1-031207-7

[51] Kim SW. Dielectric barrier, etch stop, and metal capping materials for state of the art and beyond metal interconnects. Journal of Solid State Science and Technology. 2015;**4**(1): N3029-N3047

[52] Kumar N, Moraes K, Narasimhan M, Gopalraja P. Advanced metallization needs copper. Semiconductor International. 2008;**31**(5):26-33

[53] Wu W, Wu HJ, Dixit G, Shaviv R, Gao M, Mountsier T, et al. Ti-based barrier for Cu interconnect applications. In: Proceedings of the IEEE International Interconnect Technology Conference. 2008. pp. 202-204

[54] Yang C-C, Cohen S, Shaw T, Wang P-C, Nogami T, Edelstein D. Characterization of ultrathin-Cu/Ru(Ta)/TaN liner stack for copper interconnects. IEEE Electron Device Letters. 2010;**31**:722-724

[55] Rullan J, Ishizaka T, Cerio F, Mizuno S, Mizusawa Y, Ponnuswamy T, et al. Low resistance wiring and 2Xnm void free fill with CVD ruthenium liner and direct seed copper. In: IEEE Interconnect Technology Conference Proceedings. 2010. paper 8.5

[56] Tagami M, Furutake N, Saito S, Hayashi Y. Highly-reliable low-resistance Cu interconnects with PVD-Ru/Ti barrier metal toward automotive LSIs. In: IEEE Interconnect Technology Conference Proceedings. 2008. pp. 205-207

[57] Hu CK, Gignac L, Rosenberg R, Liniger E, Rubino J, Sambucetti C, et al. Reduced Cu interface diffusion by CoWP surface coating. Microelectronics and Reliability. 2003;**70**:406-411

[58] Tokei Z, Lanckmans F, Van den bosch G, Van Hove M, Maex K, Bender H, et al. Reliability of copper dual damascene influenced by pre-clean. In: IEEE International Symposium on the Physical and Failure Analysis of Integrated Circuits. 2002. pp. 118-123

[59] Alers GB, Rozbicki RT, Harm GJ, Kailasam SK, Ray GW, Danek M. Barrier-first integration for improved reliability in copper dual damascene interconnects. In: IEEE International Interconnect Technical Conference Proceedings. 2003. pp. 27-29

[60] Fu X, Forster J, Yu J, Gopalraja P, Bhatnagar A, Ahn S, et al. Advanced preclean for integration of PECVD SiCOH ($k < 2.5$) dielectrics with copper metallization beyond 45 nm technology. In: IEEE International Interconnect Technology Conference Proceedings. 2006. pp. 51-53

[61] Chang YM, Leu J, Lin BH, Wang YL, Cheng YL. Comparison of H_2 and NH_3 treatments for copper interconnects. Advances in Materials Science and Engineering. 2013;**2013**:7. Article ID: 825195

[62] Baklanov MR, Shamiryan DG, Tokei Z, Beyer GP, Conard T, Vanhaelemeersch S, et al. Characterization of Cu surface cleaning by hydrogen plasma, Journal of Vacuum Science & Technology B. 2001;**19**:1201-1211

[63] Cheng YL, Huang JF, Chang YM, Leu J. Impact of plasma treatment on structure and electrical properties of porous low dielectric constant SiCOH material. Thin Solid Films. 2013;**544**:537-540

[64] Kamigata Y, Kurata Y, Masuda K, Amanokura J, Yoshida M, Hanazono M. Why abrasive free Cu slurry is promising? Materials Research Society Proceedings. 2001;**671**:M1.3

[65] Kondo S, Yoon BU, Tokitoh S, Misawa K, Sone S, Shin HJ, et al. Low-pressure CMP for 300-mm ultra low-k (k = 1.6–1.8)/Cu integration. In: IEEE International Electron Devices Meeting Proceedings. 2004. pp. 151-154

[66] Chapelon LL, Chaabouni H, Imbert G, Brun P, Mellier M, Hamioud K, et al. Dense SiOC cap for damage-less ultra low k integration with direct CMP in C45 architecture and beyond. Microelectronic Engineering. 2008;**85**:2098-2101

[67] Heylen N, Camerotto E, Volders H, Travaly Y, Vereecke G, Beyer GP, et al. CMP process optimization for improved compatibility with advanced metal liners. In: IEEE International Interconnect Technology Conference Proceedings. 2010. pp. 17-19

[68] Landis HS, Sucharitaves J-T. Changing density requirements for semiconductor manufacturing. In: McKerrow AJ, Sacham-Diamand Y, Shingubara S, Shimogaki Y, editors. Advanced Metallization Conference Proceedings. Warrendale, PA: MRS; 2007. pp. 535-542

[69] Oshida D, Takewaki T, Iguchi M, Taiji T, Morita T, Tsuchiya Y, et al., Quantitative analysis of correlation between insulator surface copper contamination and TDDB lifetime based on actual measurement. In: IEEE International Interconnect Technology Conference Proceedings. 2008. pp. 222-224

[70] Ueki M, Onodera T, Ishikawa A, Hoshino S, Hayashi Y. Defectless monolithic low-*k*/Cu interconnects produced by chemically controlled chemical mechanical polishing process with in situ end-point-detection technique. Japanese Journal of Applied Physics. 2010;**49**: 04C029-1-04C029-6

[71] Kanki T, Shirasu T, Takesako S, Sakamoto M, Asneil AA, Idani N, et al. On the elements of high throughput Cu-CMP slurries compatible with low step heights. In: Proceedings of the IEEE International Interconnect Technology Conference. 2008. pp. 79-81

[72] Chen SW, Kung TM, Liu CP, Chang SC, Cheng YL, Wang YL. Effect of electric potential and mechanical force on copper electro-chemical mechanical planarization. Japanese Journal of Applied Physics. 2012;**51**:036504-1-036504-7

[73] Black JR. Electromigration – A brief survey and some recent results. IEEE Transactions on Electron Devices. 1969;**16**:338-347

[74] Blech IA, Herring C. Stress generation by electromigration. Applied Physics Letters. 1976;**29**:131-133

[75] Lin MH, Lin YL, Chen JM, Yeh M-S, Chang KP, Su KC, Wang T. Electromigration lifetime improvement of copper interconnect by cap/dielectric interface treatment and geometrical design. IEEE Transactions on Electron Devices. 2005;**52**(12):2602-2608

[76] Christiansen C, Li B, Gill J. Blech effect and lifetime projection for Cu/low-*k* interconnects. In: IEEE International Interconnect Technology Conference Proceedings. 2008. pp. 114-116

[77] Cheng YL, Lee SY, Chiu CC, Wu K. Back stress model on electromigration lifetime prediction in short length copper interconnects. In: 46th IEEE Annual International Reliability Physical Symposium Proceedings Conference (IRPS). 2008. pp. 685-686

[78] Thompson CV. Using line-length effects to optimize circuit-level reliability. In: 15th IEEE Annual Int. Symp. on the Physical and Failure Analysis of Integrated Circuits (IPFA). 2008. pp. 63-66

[79] Cheng YL, Chang WY, Wang YL. Line width dependence on electromigration performance for short and long Cu interconnects. Journal of Vacuum Science and Technology B. 2010;**28**(3):973-977

[80] Black JR. Electromigration failure modes in aluminum metallization for semiconductor devices. Proceedings of the IEEE. 1969;**57**:1587-1594

[81] Lloyd JR. Black's law revisited—Nucleation and growth in electromigration failure. Microelectronics and Reliability. 2007;**47**:1468-1472

[82] Blair JC, Ghate PB, Haywood CT. Concerning electromigration in thin films. Proceedings of the IEEE. 1971;**59**:1023-1024

[83] Tan CM, Roy A. Electromigration in ULSI interconnects. Materials Science and Engineering. 2007;**58**:1-75

[84] Scorzoni A, Neri B, Caprile C, Fantini F. Electromigration in Thin-film Inter-connection Lines: Models, Methods and Results, Material Science Reports. Vol. 7. New York: Elservier; 1991. pp. 143-219

[85] Hau-Riege CS. An introduction to Cu electromigration. Microelectronics and Reliability. 2004;**44**:195-205

[86] Hu C-K, Gignac L, Rosenberg R. Electromigration of Cu/low dielectric constant interconnects. Microelectronics and Reliability. 2006;**46**:213-231

[87] Rru C, Kwon K-W, Loke ALS, Lee H, Nogami T, Dubin VM, Kavan RA, Ray GW, Wang SS. Microstructure and reliability of Cu interconnects. IEEE Transactions on Electron Devices. 1999;**46**:1113-1120

[88] Tao J, Cheung NW, Hu C. Metal electromigration damage healing under bidirectional current stress. IEEE Electron Device Letters. 1993;**14**:554-556

[89] Tao J, Chen JF, Cheung NW, Hu C. Modeling and characterization of electromigration failures under bidirectional current stress. IEEE Transactions on Electron Devices. 1996; **43**(5):800

[90] Lane MW, Liniger EG, Lloyd JR. Relationship between interfacial adhesion and electromigration in Cu metallization. Journal of Applied Physics. 2003;**93**:1417-1421

[91] Gosset LG, Chhun S, Guillan J, Gras R, Flake J, Daamen R, et al. Self aligned barrier approach: overview on process, module integration, and interconnect performance improvement challenges. In: IEEE International Interconnect Technology Conference Proceedings. 2006. pp. 84-86

[92] Stamper AK, Baks H, Cooney E, Gignac L, Gill J, Hu C-K, et al. Damascene copper integration impact on electomigration and stress migration. In: Brongersma SH, Taylor TC, Tsujimura M, Masu K, editors. Proceedings of the Advanced Metallization Conference 2005. Pittsburgh, PA: MRS; 2006. pp. 727-733

[93] Mandal RP, Cheung D, Yau W-F, Cohen B, Rengarajan S, Chou E. Comparison of $\kappa = 3$ silicon oxide-based dielectric pre-copper metallization preclean processes using black diamond. In: IEEE/SEMI Advanced Semiconductor Manufacturing Conference Proceedings. 1999, pp. 299-303

[94] Chhun S, Gosset LG, Casanova N, Guillaumond JF, Dumont-Girard P, Federspiel X, Pantel R, Arnal V, Arnaud L, Torres J. Microelectronic Engineering. 2004;**76**:106-112

[95] Vairagar AV, Mhaisalkar SG, Krishnamoothy A. Effect of surface treatment on electromigration in sub-micro Cu damascene interconnects. Thin Solid Films. 2004;**462-463**: 325-330

[96] Li B, Christiansen C, Gill J, Sullivan T, Yashchin E, Filippi R. Threshold electromigration failure time and its statistics for Cu interconnects. Journal of Applied Physics. 2006; **100**:114516

[97] Wei FL, Gan CL, Tan TL, Hau-Riege CS, Marathe AP, Vlassak JJ, et al. Electromigration-induced extrusion failures in Cu/low-*k* interconnects. Journal of Applied Physics. 2008;**104**:023529-1-023529-10

[98] Ogawa ET, Lee K-D, Blaschke VA, Ho PS. Electromigration reliability issues in dual-damascene Cu interconnections. IEEE Transactions on Reliability. 2002;**51**:403-419

[99] Vairagar AV, Mhaisalkar SG, Tu KN, Gusak AM, Meyer MA, Zschech E. In situ observation of electromigration-induced void migration in dual-damascene Cu interconnect structures. Applied Physics Letters. 2004;**85**:2502-2504

[100] Hu C-K, Gignac L, Baker B, Liniger E, Yu R. Impact of Cu microstructure on electromigration reliability. In: IEEE International Interconnect Technology Conference Proceedings. 2007. pp. 93-95

[101] Choi Z-S, Monig R, Thompson CV. Effects of microstructure on the formation, shape, and motion of voids during electromigration in passivated copper interconnects. Journal of Materials Research. 2008;**23**:383-391

[102] Cheng YL, Wang YL, Chen HC, Lin JH. Effect of inter-level dielectrics on electromigration in damascene copper interconnect. Thin Solid Films. 2006;**494**:315-319

[103] Hau-Riege SP, Thompson C. The effects of the mechanical properties of the confinement material on electromigration in metallic interconnects. Journal of Materials Research. 2000;**15**:1797-1802

[104] Lee K-D, Lu X, Ogawa ET, Matsuhashi H, Ho PS. Electromigration study of Cu/low-*k* dual-damascene interconnects. In: IRPS Proceedings. 2002. pp. 322-326

[105] Mosig K, Blaschke V. Electromigration reliability of Cu/spin-on porous ultra low-*k* interconnects. In: McKerrow AJ, Shacham-Diamond Y, Zaima S, Ohba T, editors. AMC Proceedings, 2002. Pittsburgh, PA: MRS; 2001. pp. 427-432

[106] Maekawa K, Mori K, Kobayashi K, Kumar N, Chu S, Chen S, et al. Improvement in reliability of Cu dual-damascene interconnects using Cu-Al alloy seed. In: Erb D, Ramm P, Masu K, Osaki A, editors. AMC Proceedings. Warrendale, PA: MRS; 2004. pp. 221-226

[107] Yokogawa S, Tsuchiya H. Effects of Al doping on the electromigration performance of damascene Cu interconnects. Journal of Applied Physics. 2007;**101**:013513

[108] Isobayashi A, Enomoto Y, Yamada H, Takahashi S, Kadomura S. Thermally robust Cu interconnects with Cu-Ag alloy for sub 45 nm node. In: IEEE International Electron Device Meeting Proceedings. 2004. pp. 953-956

[109] Koike J, Haneda M, Iijima J, Wada M, Cu alloy metallization for self-forming barrier process. In: IEEE International Interconnect Technology Conference Proceedings. 2006. pp. 161-163

[110] Ohoka Y, Ohba Y, Isobayashi A, Hayashi T, Komai N, Arakawa S, et al. Integration of high performance and low cost Cu/ultra low-*k* SiOC (*k* = 2.0) interconnects with self-formed barrier technology for 32 nm-node and beyond. In: IEEE International Interconnect Technology Conference Proceedings. 2007. pp. 67-69

[111] Takewaki T, Kaihara R, Ohmi T, Nitta T. Excellent electro/stress-migration-resistance surface-silicide passivated giant-grain Cu-Mg alloy interconnect technology for gig scale integration (GSI). IEDM Technical Digest. IEEE International Electron Devices Meeting. 1995:253-256

[112] Braeckelmann G, Venkatraman R, Capasso C, Herrick M. Integration and reliability of copper magnesium alloys for multilevel interconnects, In: Interconnect Technology, IEEE International Conference. 2000. pp. 236-238

[113] Igarashi Y, Ito T. Electromigration properties of copper-zirconium alloy interconnect. Journal of Vacuum Science and Technology B. 1998;**16**:2745-2750

[114] Tonegawa T, Hiroi M, Motoyama K, Fujii K, Miyamoto H. Suppression of bimodal stress-induced voiding using high-diffusive dopant Cu-alloy seed layer. In: Interconnect Technology, IEEE International Conference. 2003. pp. 216-218

[115] Lee KL, Hu CK, Tu KN. In situ scanning electron microscope comparison studies on electromigration of Cu and Cu(Sn) alloys for advanced chip interconnects. Journal of Applied Physics. 1995;**78**:4428-4437

[116] Ogawa ET, McPherson JW, Rosal JA, Dickerson KJ, Chiu T-C, Tsung LY, et al. Stress-induced voiding under vias connected to wide Cu metal leads. In: IEEE International Reliability Physics Symposium Proceedings. 2002. pp. 312-321

[117] Paik J-M, Park I-M, Joo Y-C, Park K-C. Linewidth dependence of grain structure and stress in damascene Cu lines. Journal of Applied Physics. 2006;**99**:024509

[118] Sullivan TD. Stress-induced voiding in microelectronic metallization: Void growth models and refinements. Annual Review of Materials Science. 1996;**26**:333-364

[119] Gan D, Li B, Ho PS. Stress-induced void formation in passivated Cu films, materials, technology and reliability of advanced interconnects. MRS Proceedings. 2005;**863**:259-264

[120] Oshima T, Hinode K, Yamaguchi H, Aoki H, Torii K, Saito T, et al. Suppression of stress-induced voiding in copper interconnects. In: IEEE International Electron Device Meeting Proceedings. 2002. pp. 757-760

[121] Ohring M. Reliability and Failure Analysis of Electronic Materials and Devices. NY: Academic Press; 1998

[122] Gambino JP, Lee TC, Chen F, Sullivan TD. Reliability of copper interconnects: Stress-induced voids. Electrochemical Society Transactions. 2009;**18**:205-211

[123] Li Y-L, Tokei Z, Roussel P, Groeseneken G, Maex K. Layout dependency induced deviation from poisson area scaling in BEOL dielectric reliability. Microelectronics and Reliability. 2005;**45**:1299-1304

[124] Doong KYY, Wang RCJ, Lin SC, Hung LJ, Lee SY, Chiu CC, et al. Stress-induced voiding and its geometry dependency characterization. In: IEEE International Reliability Physics Symposium Proceedings. 2003. pp. 156-160

[125] McCullen K. Redundant via insertion in restricted topology layouts, proceedings of the eighth international symposium on quality. Electronic Design. 2007:821-828

[126] Yoshida K, Fujimaki T, Miyamoto K, Honma T, Kaneko H, Nakazawa H, et al. Stress-induced voiding phenomena for an actual CMOS LSI interconnects. In: IEEE International Electron Device Meeting Proceedings. 2002. pp. 753-756

[127] Zhai CJ, Yao HW, Besser PR, Marathe A, Blish II RC, Erb D, et al. Stress modelling of Cu/low-k BEOL-applications to stress migration. International Reliability Physics Symposium Proceedings. 2004. pp. 234-239

[128] Hau-Riege CS, Hau-Riege SP, Marathe AP. The effect of interlevel dielectric on the critical tensile stress to void nucleation for the reliability of Cu interconnects. Journal of Applied Physics. 2004;**96**:5792-5796

[129] Vairagar AV, Gan Z, Shao W, Mhaisalkar SG, Li H, Tu KN, Chen Z, Zschech E, Engelmann HJ, Zhang S. Improvement of electromigration lifetime of submicrometer dual-damascene Cu interconnects through surface engineering. Journal of the Electrochemical Society. 2006;**153**(9):G840-G845

[130] Fischer AH, Glasow AV, Penka S, Ungar F. Process optimization-the key to obtain highly reliable Cu interconnects. In: Proceedings of the IEEE International Interconnect Technology Conference. 2003. pp. 253-255

[131] Yi S-M, Shim C, Lee H-C, Han J-W, Kim K-H, Joo Y-C. Effect of capping layer and post-CMP surface treatments on adhesion between damascene Cu and capping layer for ULSI interconnects. Microelectronic Engineering. 2008;**85**(3):621-624

[132] Shaw TM, Gignac L, Liu X-H, Rosenberg RR, Levine E, McLaughlin P, et al. Stress voiding in wide copper lines. In: Baker SP, Korhonen MA, Arzt E, Ho PS, editors. Stress-Induced Phenomena in Metallization. New York: AIP; 2002. pp. 177-183

[133] Ishigami T, Kurokawa T, Kakuhara Y, Withers B, Jacobs J, Kolics A, et al. High reliability Cu interconnection utilizing a low contamination CoWP capping layer. IEEE International Interconnect Technology Conference Proceedings. 2004. pp. 75-77

[134] Armini S, Prado JL, Krishtab M,. Swerts J, Verdonck P, Meersschaut J, Conard T, Blauw M, Struyf H, Baklanov MR. Pore sealing of k 2.0 dielectricsassisted by self-assembled monolayers deposited from vapor phase. Microelectronic Engineering. 2014;**120**:240-245

[135] Chen F, Li B, Lee T, Christiansen C, Gill J, Angyal M, et al. Technology reliability qualification of a 65 nm CMOS Cu/low-*k* BEOL interconnect. IEEE International Symposium on the Physical and Failure Analysis of Integrated Circuits. 2006. pp. 97-105

[136] Lee HJ, Hong TE, Kim SH. Atomic layer deposited self-forming Ru-Mn diffusion barrier for seedless Cu interconnects. Journal of Alloys and Compounds. 2016;**686**:1025-1031

[137] Kimura M. Oxide breakdown mechanism and quantum physical chemistry for time-dependent dielectric breakdown. In: IEEE International Reliability Physics Symposium Proceedings. 1997. pp. 190-200

[138] Ogawa ET, Kim J, Haase GS, Mogul HC, McPherson IW. Leakage, breakdown, and TDDB characteristics of porous low-*k* silica-based interconnect dielectrics. In: IEEE International Reliability Physics Symposium Proceedings. 2003. pp. 166-172

[139] Chen F, McLaughlin P, Gambino J, Wu E, Demarest J, Meatyard D, et al. The effect of metal area and line spacing on TDDB characteristics of 45 nm low-*k* SiCOH dielectrics. In: IEEE International Reliability Physics Symposium Proceedings. 2007. pp. 382-389

[140] Kim J, Ogawa ET, McPherson JW. Time dependent dielectric breakdown characteristics of low-*k* dielectric (SiOC) over a wide range of test areas and electric fields. In: IEEE International Reliability Physics Symposium Proceedings. 2007. pp. 399-404

[141] Gambino J, Lee TC, Chen F, Sullivan TD. Reliability challenges for advanced copper interconnects: electromigration and time-dependent dielectric breakdown (TDDB). In: Proceedings of the IEEE International Symposium on the Physical and Failure Analysis of Integrated Circuits. 2009. pp. 677-684

[142] Hunter WR. The analysis of oxide reliability data. International Reliability Workshop Final Report. 1998. pp. 114-134

[143] Alers GB, Jow K, Shaviv R, Kooi G, Ray GW. Interlevel dielectric failures in copper/low-*k* structures. IEEE Transactions on Device and Materials Reliability. 2004;**4**(2):148-152

[144] Noguchi J. Dominant factors in TDDB degradation of Cu interconnects. IEEE Transactions on Electron Devices. 2005;**52**(8):1743-1750

[145] Chen F, Shinosky M. Addressing Cu/low-*k* dielectric TDDB-reliability challenges for advanced CMOS technologies. IEEE Transactions on Electron Devices. 2009;**56**(1):2-12

[146] Chen F, Bravo O, Harmon D, Shinosky M, Aitken J. Cu/low-*k* dielectric TDDB reliability issues for advanced CMOS technologies. Microelectronics and Reliability. 2008;**48**:1375-1383

[147] Ueno K, Kameyama A, Matsumoto A, Iguchi M, Takewaki T, Oshida D, et al. Time-dependent dielectric breakdown characterization of 90-and 65-nm-node Cu/SiOC interconnects with via plugs. Japanese Journal of Applied Physics. 2007;**46**:1444-1451

[148] Haase GS, Ogawa ET, McPherson JW. Reliability analysis method for low-*k* interconnect dielectrics breakdown in integrated circuits. Journal of Applied Physics. 2005;**98**:034503

[149] Chen F, Bravo O, Chanda K, McLaughlin P, Sullivan T, Gill J, et al. A comprehensive study of low-*k* SiCOH TDDB phenomena and its reliability lifetime model development. In: IEEE International Reliability Physics Symposium Proceedings. 2006. pp. 46-53

[150] Chen F, Chanda K, Gill J, Angyal M, Demarest J, Sullivan T, et al. Investigation of CVD SiCOH low-*k* time-dependent dielectric breakdown at 65 nm node technology. In: IEEE International Reliability Physics Symposium Proceedings. 2005. pp. 501-507

[151] Baklanov MR, Zhao L, Besien EV, Pntouvaki M. Effect of porogen residue onelectrical characteristics of ultra low-*k* materials. Microelectronic Engineering. 2011;**88**:990-993

[152] Noguchi J, Ohashi N, Jimbo T, Yamaguchi H, Takeda K, Hinode K. Effect of NH_3-plasma treatment and CMP modification on TDDB improvement in Cu metallization. IEEE Transactions on Electron Devices. 2001;**48**:1340-1345

[153] Cheng YL, Lin BH, Huang SW. Effect of O_2 plasma treatment on physical, electrical, and reliability characteristics of low dielectric constant materials. Thin Solid Films. 2014;**572**: 44-50

[154] Liv J, Gan D, Hu C, Kiene M, Hu PS, Volksen W, Miller RD. Porosity effect on the dielectric constant and thermomechanical properties of organosilicate films. Applied Physics Letters. 2002;**81**:4180-4182

[155] Tőkei Z, Croes K, Beyer GP. Reliability of copper low-*k* interconnects. Microelectronic Engineering. 2010;**87**(3):348-354

[156] Chen F, Lloyd JR, Chanda K, Achanta R, Bravo O, Strong A, et al. Line edge roughness and spacing effect on low-*k* TDDB characteristics. In: IEEE International Reliability Physics Symposium Proceedings. 2008. pp. 132-137

[157] Noguchi J, Miura N, Kubo M, Tamaru T, Yamaguchi H, Hamada N, et al. Cu-ion-migration phenomena and its influence on TDDB lifetime in Cu metallization. In: IEEE International Reliability Physics Symposium Proceedings. 2003. pp. 287-292

[158] Raghavan G, Chiang C, Anders PB, Tzeng S, Villasol R, Bai G, Bohr M, Fraser DB. Diffusion of copper through dielectric films under bias temperature stress. Thin Solid Films. 1995;**262**:168-176

[159] Lloyd JR, Murray CE, Ponoth S, Cohen S, Liniger E. The effect of Cu diffusion on the TDDB behavior in a low-*k* interlevel dielectrics. Microelectronics and Reliability. 2006; **46**:1643-1647

[160] Suzumura N, Yamamoto S, Kodama D, Makabe K, Komori J, Murakami E, et al. A new TDDB degradation model based on Cu ion drift in Cu interconnect dielectrics. In: IEEE International Reliability Physics Symposium Proceedings. 2006. pp. 484-489

[161] Oshida D, Takewaki T, Iguchi M, Taiji T, Morita T, Tsuchiya Y, et al. Quantitative analysis of correlation between insulator surface copper contamination and TDDB

lifetime based on actual measurement. In: IEEE Interconnect Technology Conference Proceedings. 2008. pp. 222-224

[162] Chen F, Shinosky MA. Electron fluence driven, Cu catalyzed, interface breakdown mechanism for BEOL low-*k* time dependent dielectric breakdown. Microelectronics and Reliability. 2014;**54**(3):529-540

[163] McPherson JW, Mogul HC. Underlying physics of the thermochemical E model in describing low-field time-dependent dielectric breakdown in SiO_2 thin films. Journal of Applied Physics. 1998;**84**:1513-1523

[164] Haase GS, McPherson JW. Modeling of interconnect dielectric lifetime under stress conditions and new extrapolation methodologies for time-dependent dielectric breakdown. In: IEEE International Reliability Physics Symposium Proceedings. 2007. pp. 390-398

[165] Lloyd JR, Liniger E, Shaw TM. Simple model for time-dependent dielectric breakdown in inter- and intralevel low-*k* dielectrics. Journal of Applied Physics. 2005;**98**:084109

[166] McPherson JW. Time dependent dielectric breakdown physics–models revisited. Microelectronics and Reliability. 2012;**52**:1753-1760

[167] Tokei Z, Sutcliffe V, Demuynck S, Iacopi F, Roussel P, Beyer GP, et al. Impact of the barrier/dielectric interface quality on reliability of Cu porous-low-*k* interconnects. In: IEEE International Reliability Physics Symposium Proceedings. 2004. pp. 326-332

[168] Li Y, Tokei Z, Mandrekar T, Mebarki B, Groeseneken G, Maex K. Barrier integrity effect on leakage mechanism and dielectric reliability of copper/OSG interconnects, materials, technology and reliability of advanced interconnects. MRS Proceedings. 2005;**863**:265-270

[169] Yamada Y, Konishi N, Noguchi J, Jimbo T. Influence of CMP slurries and post-CMP cleaning solutions on Cu interconnects and TDDB reliability. Journal of the Electrochemical Society. 2008;**155**(7):H485-H490

[170] Jung S-Y, Kim B-J, Lee NY, Kim B-M, Yeom SJ, Kwak NJ, Joo Y-C. Bias polarity and frequency effects of Cu-induced dielectric breakdown in damascene Cu interconnects. Microelectronic Engineering. 2011;**89**:58-61

[171] Cheng YL, Lee CY, Huang YL, Sun CR, Lee WH, Chen GS, Fang JS, Phan BT. Cu-induced dielectric breakdown of porous low dielectric constant film. Journal of Electronic Materials. 2017;**46**(6):3627-3633

Chapter 11

Preparation of Highly Dispersed Pd-Supported Catalysts for Hydrogenation Processes by Microemulsion Method

Jan Patera, Iva Paterová, Jiří Krupka and Květa Jirátová

Additional information is available at the end of the chapter

http://dx.doi.org/10.5772/intechopen.72986

Abstract

Preparation of nano-dispersed palladium particles on alumina support is described here using reverse microemulsion (water-in-oil) method. This synthesis protocol leads to a narrow Pd particle size distribution with particles of average size, which were significantly smaller compared to those prepared by classical impregnation method. It is shown that the particle size could be effectively controlled both by the microemulsion chemical composition such as concentration of $PdCl_2$ and the water/surfactant molar ratio and by the catalyst reduction process. Under the optimal reaction conditions, a Pd/Al_2O_3 catalyst with a homogeneous distribution of Pd particles of average size ~2.2 nm was obtained.

Keywords: Pd catalyst, particle size, reverse microemulsion, impregnation, particle size distribution

1. Introduction

Powder Pd-supported catalysts are indispensable in chemical processes to produce fine chemicals and intermediates in the pharmaceutical industry. These Pd-based catalysts are particularly used as universal catalysts for hydrogenation under mild conditions, which avoid the destruction of the reaction components. They are used, e.g. in reductive amination, carbonyl reduction, nitro compound reduction and reduction of imines and Schiff bases.

Pd-supported catalysts are also highly selective hydrogenation or hydrotreating catalysts widely used in important industrial processes, e.g. in selective hydrogenation of acetylene to ethylene of C2 cracking fraction and selective hydrogenation of triple and diene bonds to

the corresponding olefins in C3 fraction or selective hydrogenation of phenols to ketones, e.g. cyclohexanone from phenol. Palladium is also very active in the hydrogenation of nitro compounds and it is used in the production of aniline by DuPont and the Bayer process.

The activity of supported catalysts containing noble metals is influenced by the type of catalyst support, the type of noble metal, the amount of an active component in the catalyst, the way of catalyst preparation, etc. The preparation of the supported catalysts in most cases requires the highest metal dispersion and thus the largest surface area of an active component. For these reasons, the particle size of Pd in supported catalysts can have a significant effect on catalytic activity and selectivity of these catalysts. For some types of reactions, it is necessary to optimize the size of metal crystallites at a certain critical value. If the average particle size of Pt is higher or lower than its optimal value, the activity of such a catalyst for toluene combustion in the gas phase decreases [1].

The distribution of the active component in the catalyst pellet along with the diameter and shape of the active component particles is closely connected with the method of the preparation [2]. That is why it is important to choose a suitable method for the preparation of the catalyst to provide an optimal dispersion of the active component in the catalyst and also its optimal location in the catalyst. There are various methods for catalyst preparation. The most commonly practiced techniques are incipient wetness impregnation with a metal salt solution, ion exchange with a metal-containing cation or anion and the use of organometallic complexes as precursors [3]. Using incipient wetness impregnation, the nanoparticles in solution can be stabilized by capping agents such as sugars (glucose, starch, carboxymethyl cellulose) to avoid aggregation and widening of the particle size distribution [4]. The use of microemulsion could be another preparation method promising the formation of small metal nanoparticles of a narrow size distribution, located on the external surface of the support. This method is described in this chapter.

The term microemulsion was first defined by Schulman and Friend in the 1940s [5]. Microemulsion (a reverse micellar system) is defined as a thermodynamically stable dispersion of two immiscible liquids stabilized by a surface film of emulsifier. It is a three-component system consisting of organic phases: oil, an aqueous phase and a surfactant. The surfactant is a substance which stabilizes the emulsion by reducing the interfacial tension between the dispersed particles of water in oil to a minimum, thus preventing the formation of large aggregates. For the preparation of heterogeneous catalysts, microemulsions of type W/O (water-in-oil) are important since highly dispersed particles of the metal salts or the metal particles can be prepared.

Synthesis of the metal nanoparticles from the microemulsion was first reported by Boutonnet et al. in 1982 [6], who synthesized the metal nanoparticles of Pt, Pd, Rh and Ir by the reduction of the salt dissolved in the aqueous phase of W/O microemulsion using hydrazine or hydrogen. Nanoparticles were used for the preparation of the supported catalysts. Kishida et al. [7, 8] described a new method of preparation of Rh catalysts with the very narrow metal dispersion. Isolated metal crystallites were first synthesized by hydrazine reduction of a metal precursor in the microemulsion. Subsequently the catalyst support was precipitated by the hydrolysis of metal alkoxide (tetraethyl orthosilicate, aluminium triisopropoxide, zirconium or titanium tetrabutoxide) in the microemulsion and the metal nanoparticles were

immobilized on the catalyst support. However, under such conditions, a part of the active metal particles is closed in pores of the support and therefore is catalytically inactive. By this phenomenon, the authors explained the differences between the values obtained from chemisorption measurements and TEM (transmission electron microscopy). Some of the metal particles buried in the support were not exposed on the surface for CO chemisorption [8]. Nevertheless, the catalysts prepared in this way showed higher activity than similar ones prepared by conventional incipient wetness impregnation method. These authors studied the effect of the surfactant selection and its molar ratio to water in the preparation of catalysts using the microemulsion. The dependence of the effect of the molar ratio of water and surfactant on the resulting particle size went through a minimum, but for each microemulsion system was specific. Kosydar et al. [9] used two microemulsion systems with anionic bis(2-ethylhexyl)sulfosuccinate (AOT) and non-ionic polyoxyethylene(7–8)octylphenyl ether (Triton-X 114) surfactants. Pd nanoparticles with sizes in a narrow range but various average sizes (8–9 and 4 nm) were obtained using hydrazine hydrate or NaH_2PO_2 as a reducing agent. Semagina et al. [10], Heshmatpour et al. [11] and Noh et al. [12] also reported on the application of water/AOT/isooctane microemulsion system for the preparation of Pd nanoparticles. Different nanoparticle size and size distributions were obtained depending on the reducing agent or precursor salt. Using N_2H_4 as a reducing agent, larger nanoparticles and a broader size ranges (6–13 nm) were obtained compared to $NaBH_4$ (3.9–5 nm). Although reducing agent plays an important role in the size of the metal nanoparticles formed, Chen et al. [13] reported on the formation of similar Pd nanoparticle size when N_2H_4 or $NaBH_4$ was used as a reducing agent, thus indicating the contribution of other factors. Thus Perez-Coronado et al. [14] synthetized Pd nanoparticles by a water-in-oil (w/o) microemulsion method using the water/AOT/isooctane system. N_2H_4 and $NaBH_4$ were used as reducing agents and water-to-surfactant ratios between 3 and 7 were considered. Results [14] showed that Pd nanoparticles with higher size were obtained when the water-to-surfactant molar ratio was increased. Lower reaction time and higher evaporation temperature led to the formation of smaller Pd nanoparticles. Higher values of mean size Pd nanoparticles were obtained with N_2H_4 compared to $NaBH_4$. Wojcieszak et al. [15] investigated the size of palladium nanoparticles (1.6 wt.%) synthesized by the modified water-in-oil microemulsion method using hydrazine as the reducing agent by varying the nature of the organic surfactant and solvent. The results confirmed the dependence of the particle size on the nature of organic surfactants. Smaller particles were obtained with organic solvents and anionic surfactants. Kim et al. [16] compared the catalytic performance of Pd/ZrO_2 catalysts prepared from microemulsion with the ones prepared by the conventional impregnation method. The catalysts prepared by the microemulsion method exhibited a much higher activity for the hydrogenation of CO, the size distribution of Pd particles of the catalysts was remarkably narrow, and the average particle size was much smaller than that of the catalysts prepared by the impregnation method. It was found that the Pd particle size of the catalyst prepared by the microemulsion method could be controlled by the concentration of palladium salts in water pools. Kim et al. [16] also found that some of Pd particles of the catalyst were partly or wholly buried in zirconia support. Significantly higher activity of Pt catalysts for the combustion of toluene prepared from the microemulsion compared to those prepared by the impregnation with the aqueous solution of H_2PtCl_6 was observed by Rymeš et al. [1] as well. Pt particle size was up to ten times smaller. Pocoroba

et al. [17] prepared 2.5 wt.% Pd/Al_2O_3 exhaust gas catalysts by incipient wetness impregnation technique and from microemulsion as well. Contrary to other authors, the catalysts prepared by incipient wetness impregnation technique consisted of smaller crystallite size than 2 nm and Pd was found to be well dispersed in comparison to microemulsion when the particle size was in the 20–40 nm range and the distribution of noble metal was irregular.

Eriksson et al. [18] published an extensive review focused on the preparation of catalysts from microemulsion and their applications in heterogeneous catalysis. This review covered most of the applications concerning heterogeneous catalysts, not only Pd supported but other noble metals were mentioned as well. It was concluded that the majority of the catalysts obtained from microemulsion showed high catalytic activity and the main advantages of using microemulsion technique were related to the possibility of controlling properties such as particle size, morphology and size distribution.

The aim of the study described here was to prepare highly dispersed Pd hydrogenation catalyst by the microemulsion method since the microemulsion method is more suitable for metal catalysts preparation [7, 8, 16] in comparison with conventional incipient wetness impregnation method. In this research, the focus was on optimizing the microemulsion preparation conditions, investigating the influence of reduction conditions, evaluating the physical properties and comparing them with the properties of the catalysts prepared by incipient wetness impregnation method. Details of these procedures and results are presented in the following pages. It is noted that the results presented in the figures and tables are original and not published anywhere before.

2. Experimental

2.1. Catalyst preparation

The reverse micellar system W/O was prepared from a commercial surfactant IGEPAL CO-520 dissolved in cyclohexane. The reason for choosing non-ionogenic surfactant was to reduce the influence of impurities such as Na^+, K^+ and SO_4^{2-} (which are contained in ionogenic surfactants) on the properties of the resulting catalyst. The concentration of the surfactant in cyclohexane was 0.5 mol/dm^3. The aqueous solution of palladium chloride (0.85 g of $PdCl_2$ solution of concentration 1.0 mol/dm^3) was added to the microemulsion prepared in such amounts that the catalyst (B [ME]) with demanded amount 3 wt.% of Pd was obtained. The exact amount of commercial support (2.49 g of γ-Al_2O_3, S_{BET} = 313 m^2/g) calcined at 623 K was inserted in the microemulsion. The commercial surfactant IGEPAL CO-520 in the amount of 4.23 and 15.0 g of cyclohexane was used. This suspension was stirred under reflux and tempered at 298 K for 24 h. Precipitates were decanted, filtered, washed with ethanol and then dried at 393 K overnight. The samples were calcined in air at 623 K for 2 h. The catalyst prepared by this method will be denoted by [ME].

Catalysts I [IMP] and J [IMP] were prepared by incipient wetness impregnation. Impregnation of the commercial support (2.25 g of γ-Al_2O_3, S_{BET} = 313 m^2/g) with aqueous solution of palladium chloride (0.99 g of $PdCl_2$ solution of concentration 1.5 mol/dm^3) stabilized with hydrochloric

acid in such amount to obtain the catalyst (J [IMP]) with 3 wt.% of Pd. 20.0 g H_2O was used. The mixture was stirred for 24 h at room temperature. After filtration, the catalyst was first dried at 393 K for 2 h, then calcined in air at 623 K for 2 h.

The active component of the catalyst in the form of palladium oxide prepared by both methods was subsequently reduced to metallic palladium.

2.2. Catalyst reduction

Reduction of Pd precursors was carried out either in gas phase using hydrogen or in liquid phase using hydrazine monohydrate. The catalysts reduced in the gas phase by a mixture of hydrogen and helium (10:90) were placed in a quartz tube. Reduction was performed at 723 K with a heating rate 15 K/min for 2 h and was followed by desorption of hydrogen in inert gas at the same temperature for 1 h.

Reduction in the liquid phase was done using hydrazine monohydrate in the stoichiometric excess of 3:1 at 363 K for 2 h. After reduction, the sample had to be washed with ethanol to remove excess reducing agent and was dried at 393 K in an inert atmosphere.

2.3. Characterization of the catalysts

2.3.1. Surface area

BET surface areas of the catalysts were determined using Pulse Chemisorb 2700, Micromeritics, USA.

2.3.2. Size and distribution of palladium particles

Morphology, particle size and particle size distribution of metal were determined by transmission electron microscopy (HRTEM) on JEOL JEM 3010 operating at 300 kV and equipped with an energy-dispersive spectroscopy (EDS) detector (INCA/Oxford) and CCD Gatan (Digital Micrograph software). The transmission electron analysis was carried out on samples that were subsequently dispersed in propan-2-ol, followed by the application of a drop of a diluted suspension on Cu grid.

Pd particle size was determined using CO chemisorption as well. For the measurements, a custom-made apparatus was used [19]. The catalyst was dried prior to measurement in the air at 393 K for 2 h. The sample treatment was performed first in the inert and then in the reducing atmosphere. The treatment in the reducing H_2 atmosphere was carried out for the reduction of PdO contained in the catalyst. Since hydrogen is not only very strongly absorbed on the surface of Pd, but also dissolved in the subsurface layers of the metal it is necessary to include hydrogen desorption step at 523 K after reduction of the catalyst. Hydrogen desorption provided decomposition of the resulting β-hydride of Pd, which is very easily formed even at room temperature and, according to literature, is unstable at high temperatures and low pressure [20]. CO chemisorption measurements were carried out with CO (5 vol.% in He) at 298 K using pulse technique. To calculate average Pd particle size (d_{AV}) and specific surface area of Pd (S_{Pd}) from chemisorption data, the following parameters were used: constant depending

on the shape of metal particles and contact with the support (k = 6); surface density of metal atoms (C_{Pd} = 1.26 × 10^{19} atom/m^2) and stoichiometry of adsorption Pd:CO (S_{AV} = 2) [21].

2.3.3. Reducibility of active centres of catalyst

Temperature-programmed reduction (TPR) was used to describe the reducibility of different active centres and their concentrations. The samples were first dried in air at 393 K for 2 h to constant weight. TPR analysis of the samples was performed using a commercial device Autochem II 2920 Micromeritics, USA, with H_2/Ar mixture 5/95. During the analysis, the temperature was increased linearly with time to a temperature of 923 K with a heating rate of 5 K/min.

2.3.4. Metal content determination

The metal content was determined directly by X-ray fluorescence (XRF) analysis and indirectly by atomic absorption spectrometry (AAS). The indirect determination of Pd content in the catalyst consisted of a liquid sample analysis, which was prepared by multiple leaching of a defined amount of Pd catalyst using aqua regia. Quantitative transfer of Pd in the solution was indicated by the support discoloration and the last extract from the catalyst was colourless as well. Quantitative dissolution of Pd gave $PdCl_4^{2-}$ solution which was analysed by atomic absorption spectroscopy.

3. Results and discussion

3.1. Effect of preparation conditions of microemulsions on the physical properties of catalysts

When the effect of preparation conditions of microemulsions was monitored, attention was paid to two parameters namely the concentration of metal salts in the aqueous solution and the molar ratio of water and surfactant.

3.1.1. Effect of $PdCl_2$ concentration

According to literature [7, 8, 16], the concentration of metal component precursor in the form of soluble salts in the aqueous solution has a significant impact on the final size of metal particles. Therefore, the effect of $PdCl_2$ concentration in the aqueous solution was studied. Palladium catalysts were prepared from $PdCl_2$ solutions of different concentrations in the range from 0.25 to 1.5 mol/dm^3. Other preparation conditions of microemulsions such as surfactant type, its concentration in the solvent and the molar ratio of water to surfactant remained constant. The molar ratio of water to surfactant was 4 to evaluate the influence of $PdCl_2$ concentration on Pd crystallite size in the final catalyst.

The observed Pd crystallite size dependence on the concentration of $PdCl_2$ goes through a minimum as is shown in **Table 1**. When using 1 M solution of $PdCl_2$ for the preparation of the

Catalyst	c($PdCl_2$) [mol/dm^3]	w_{Pd} [%]	d_{AV} (Pd)[a] [nm]	S_{Pd} [m^2/g$_{Pd}$]
A [ME]	1.50	2.9	3.0	131.4
B [ME]	1.00	2.9	2.2	180.9
C [ME]	0.50	2.5	2.3	172.8
D [ME]	0.25	2.1	2.6	152.2

[a]Determined from chemisorption measurements.

Table 1. Effect of $PdCl_2$ concentration on Pd crystallite size in the resulting catalyst.

microemulsion, the resulting average Pd particle size determined by CO chemisorption was 2.2 nm. When the effect of $PdCl_2$ concentration on the final particle size of Pd in the prepared catalyst was evaluated, an efficiency of Pd loading on the support was studied as well. When using both 1 and 0.5 M solutions, highly dispersed catalysts with Pd particle size of approximately 2.3 nm were obtained. However, when using $PdCl_2$ solution of 1 M concentration, the catalyst with desired Pd content of 3 wt.% was obtained, while at the concentration of 0.5 M, the Pd content was only 2.5 wt.%.

3.1.2. Effect of molar ratio of water to surfactant

Another parameter influencing the final metal particles is the molar ratio of water and surfactants, the so-called R factor. The amount of surfactant in the microemulsion affects the size and shape of water drops dispersed in an oil phase. Too high a value of R factor can lead to the formation of unstable microemulsion and its breaking. To evaluate the influence of the R factor values, $PdCl_2$ concentration of 1 mol/dm^3 was used based on the results shown in **Table 1**.

The values reported in **Table 2** show that the molar ratio of water and the surfactant does not affect the final Pd content loading on the support since the Pd content was close to the desired value of 3 wt.% for all catalysts.

When increasing the surfactant content in microemulsion, Pd dispersion increased. When R factor was equal to 8, the final Pd particle size determined from chemisorption data was 2.3 nm.

Catalyst	R factor	w_{Pd} [%]	d_{AV} (Pd)[a] [nm]	S_{Pd} [m^2/g$_{Pd}$]
E [ME]	4	2.9	2.2	180.9
F [ME]	8	2.9	2.3	172.4
G [ME]	12	2.9	2.8	142.7
H [ME]	16	2.8	4.1	96.9

[a]Determined from chemisorption measurements.

Table 2. Effect of molar ratio of water to surfactant on Pd crystallite size in the resulting catalyst.

On further lowering the R factor, the particle size remained almost unchanged. Therefore, for the further preparation of catalyst, the value of R = 4 was used. This result is in compliance with the conclusions mentioned by Perez-Coronado [14] and Kim et al. [16], who minimized the Pd particle size in a similar system (Pd/ZrO_2) using R factor equal to 4.4.

3.2. Controlled sintering of metal component

The process of calcination is necessary for removing the surfactant after catalyst preparation using the microemulsion technique. Calcination is also responsible for the decomposition of metal precursors to the formation of oxides; therefore, calcination is carried out in air atmosphere at high temperatures. Calcination at various high temperatures can affect the resulting metal particle size in the prepared catalyst because of the sintering of the particles. Recently it has been reported by Forman et al. [22] that silica-encapsulated Pd nanoparticles prepared from microemulsion showed more sintering-resistant behaviour compared to the particles prepared by the impregnation method.

Pd catalyst prepared from microemulsion and subsequently calcined at 723 K showed high dispersion with a narrow size distribution of Pd crystallites since almost 80% of Pd particles were in the range 1–3 nm based on HRTEM measurements (**Figures 1** and **2**).

P0 [ME] catalyst was divided into five parts (**Table 3**), which were treated in the range from 773 to 1223 K in an inert atmosphere for 2 h. In this temperature range, no irreversible changes of the catalyst support were observed. BET surface areas of 3% Pd/Al_2O_3 catalysts calcined at 723 and 1223 K were 274 and 264 m^2/g, respectively.

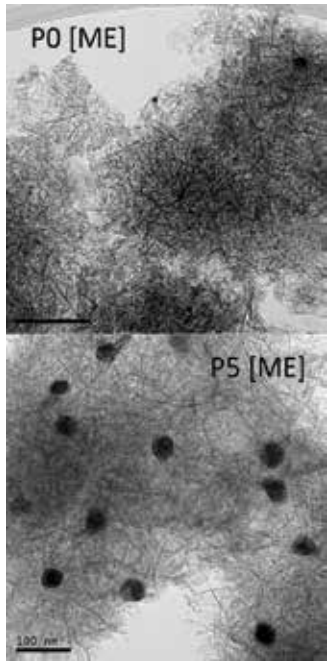

Figure 1. HRTEM micrographs of highly dispersed catalysts P0 [ME] and P5 [ME] (bar length = 100 nm).

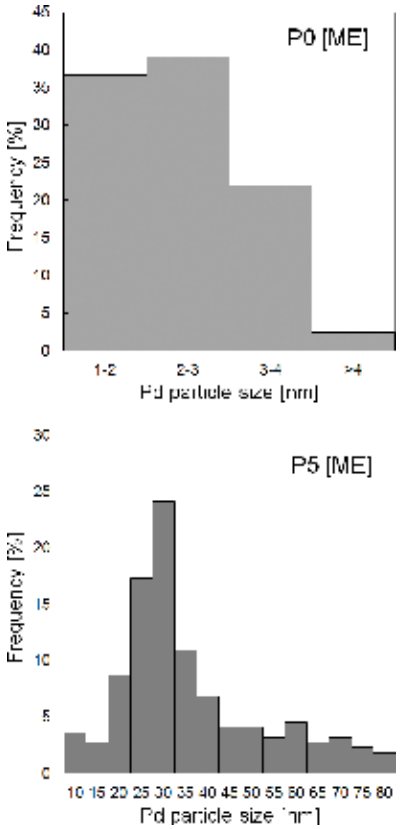

Figure 2. Histograms of Pd particle sizes determined by HRTEM in catalysts (P0 [ME] and P5 [ME]) prepared by the microemulsion technique.

Results obtained from both chemisorption measurements (**Table 3**) and HRTEM analyses (**Figure 2**) for very small metal particles (in units of nm) showed high degree of sintering at a temperature of 923 K. However, when using temperatures higher than 1023 K, further significant decrease of Pd specific surface area (S_{Pd}) did not occur. S_{Pd} values of the catalysts treated at temperatures 1023, 1123 and 1223 K were almost constant (**Table 3**).

Catalyst	$T_{calcination}$ [K]	d_{AV} (Pd)[a] [nm]	S_{Pd} [m^2/g_{Pd}]
P0 [ME]	723	2.2	169.6
P1 [ME]	773	5.7	70.1
P2 [ME]	923	16.3	25.6
P3 [ME]	1023	27.6	14.4
P4 [ME]	1123	31.3	12.7
P5 [ME]	1223	32.0	12.4

[a]Determined from chemisorption measurements.

Table 3. Effect of calcination temperature on Pd crystallite size in the resulting catalyst.

Pd catalyst prepared from microemulsion and subsequently calcined at 723 K showed high dispersion with a narrow size distribution of Pd crystallites since almost 80% of Pd particles were in the range 1–3 nm based on HRTEM measurements (**Figures 1** and **2**).

The results obtained from HRTEM analyses confirmed that Pd particle size after reaching a certain size did not increase. The largest Pd crystallites found in the HRTEM micrographs had the size of approximately 80 nm. At the Pd content of 3 wt.%, these crystallites were large enough to be separated from each other on the support. The further sintering of Pd particles could occur only with difficulty.

Catalysts treated at higher temperatures compared to P0 [ME] catalyst showed a wider size distribution (**Figure 2**). For example, the catalyst sintered at 1223 K contained 70% of Pd particles in the range 15–40 nm. The average particle size determined by CO chemisorption was 32 nm. Controlled sintering at high temperatures does not lead to a catalyst with a narrow particle size distribution. Sintering is very fast probably due to the high metal content in the catalyst. To prepare a series of the catalysts with different Pd dispersion, but with the narrow particle size distribution, it is necessary to choose a different method than controlled sintering, e.g. to control the particle size with microemulsion preparation conditions. It would be necessary to optimize several parameters so that the catalysts prepared under different conditions showed, besides the Pd dispersion, the same parameters such as content of metal and impurities.

3.3. Effect of catalysts' reduction on Pd particle size

Reduction of metal precursors of the catalysts can be performed in several ways. The most common is reduction in the gas phase using hydrogen or its mixture with an inert gas as a reducing agent. Another way is reduction in the liquid phase using hydrazine or formaldehyde.

To determine the temperature needed to reduce PdO, produced during calcination of the metal precursors in air atmosphere at high temperatures, TPR was used. On the TPR record of the catalyst, two reduction maxima were observed in the temperature range from 578 to 663 K. Therefore for the reduction of Pd/Al_2O_3 catalyst in the gas phase, the temperature of 723 K was chosen. At the temperature of approximately 363 K, a negative peak was clearly visible. It represented a decomposition of β-hydride of Pd described in literature [20] which is formed due to contact of Pd with hydrogen.

The dispersion of Pd in the catalysts reduced in the gas and the liquid phase was determined from the CO chemisorption measurements of Pd specific surface area. It was found that the catalyst reduced in the liquid phase showed lower S_{Pd} value determined by CO chemisorption. It was assumed that this difference can be caused by the blocking of active sites for CO adsorption by unreacted hydrazine. This was denied by experiment (*b* in **Table 4**) using the higher drying temperature for desorption of impurities in an inert atmosphere (623 K). S_{Pd} value of that catalyst was close to the previous experiment (*a* in **Table 4**). Since hydrazine reduction was performed at 363 K, no sintering of Pd crystallites can occur. Also, desorption at 623 K should not cause the sintering of Pd crystallites because reduction in the gas phase was carried out at 723 K and this phenomenon was not observed. The lower values of S_{Pd} can be

Reducing agent	S_{Pd} [m^2/g_{Pd}]	d_{AV} (Pd)[c] [nm]
H_2 (g)	169.6	2.2
N_2H_4 (l)[a]	65.8	—
N_2H_4 (l)[b]	70.6	5.8

[a]Drying of the catalyst sample at 393 K after reduction in the liquid phase.
[b]Drying of the catalyst sample at 623 K after reduction in the liquid phase.
[c]Determined by HRTEM.

Table 4. Effect of reducing agent on Pd specific surface area and on Pd crystallite size.

explained by recrystallization of Pd particles, their diffusion on the support and a formation of larger clusters. The formation of larger Pd crystallites during reduction in the liquid phase was confirmed by d_{AV} (Pd) determination from HRTEM measurements (**Table 4**).

This observation is inconsistent with the commonly known theory, according to which the reduction performed in the liquid phase should be the more efficient way to keep high dispersion of the metal on the support.

3.4. Preparation of catalysts by incipient wetness impregnation

Method of incipient wetness impregnation of the support with aqueous solutions of salts and acids is a basic procedure for the preparation of heterogeneous catalysts. This procedure was used to compare such prepared catalyst with that prepared from the microemulsion. The amount of impregnation solution was chosen to keep the same Pd content and concentration in the resulting suspension with the support as in the preparation of A [ME] catalyst using the microemulsion. The other preparation conditions namely impregnation time, calcination temperature and reduction in the gas phase have been retained as well. The Pd particle size in the resulting catalyst was determined by CO chemisorption.

The determined Pd content in such prepared catalyst (I [IMP]) was only 1.5 wt.% (**Table 5**). Therefore, for further comparison, the catalyst with two-times higher Pd content (J [IMP]) in the impregnation solution was prepared. Increasing Pd content on the support led to the increase of Pd crystallite size and the decrease in the specific surface area of Pd in the catalyst. J [IMP] catalyst of comparable Pd content, prepared by incipient wetness impregnation, contained Pd particles of average size 5.6 nm. Obtained results therefore indicate that the microemulsion preparation technique leads to higher dispersion of Pd than wet impregnation method.

Catalyst	w_{Pd} [%]	S_{Pd} [m^2/g_{Pd}]	d_{AV} (Pd)[a] [nm]
I [IMP]	1.5	79.2	4.7
J [IMP]	2.7	66.8	5.6

[a]Determined by HRTEM.

Table 5. Properties of catalysts prepared by incipient wetness impregnation of support.

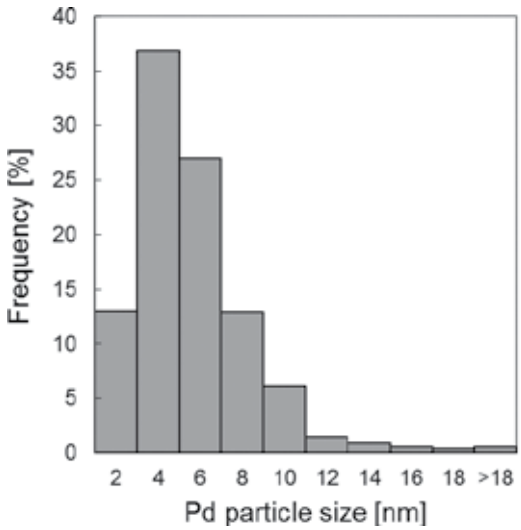

Figure 3. Histogram of Pd particle sizes determined by HRTEM in I [IMP] catalyst.

Based on HRTEM measurements it was found that the Pd particle size distribution of I [IMP] catalyst was broader in comparison with P0 [ME] catalyst (**Figures 2** and **3**). The highest frequency of particles was in the range 2–6 nm. However, I [IMP] catalyst contained particles larger than 10 nm unlike P0 [ME] catalyst.

4. Conclusions

Experimental results presented here show that the Pd/Al_2O_3 catalysts prepared from the microemulsions contained much smaller Pd particles and had narrower distribution of Pd particle size than the catalysts prepared by classical incipient wetness impregnation of the supports with water solutions of palladium chloride.

Study of the effect of the preparation conditions of the microemulsions was focused on the concentration of $PdCl_2$ in an aqueous solution and the molar ratio of water and surfactant. It was found that the optimal $PdCl_2$ concentration was equal to 1 mol/dm^3. Using this concentration, catalysts with the highest Pd content and high Pd dispersion were obtained. The average particle size in such catalysts was 2.2 nm. Another condition of the microemulsion preparation technique influencing the final size of metal particles was the molar ratio of water and surfactant. It was found that with decreasing ratio of water and surfactant, Pd dispersion on the support increased. The optimal value of R factor equal to 4 for the microemulsion system with used surfactants was found. Thus, the prepared catalyst showed a narrow particle size distribution, containing 80% Pd crystallites in the range 1–3 nm.

Using controlled sintering at high temperatures the catalyst with the narrow particle size distribution could not be obtained. Pd particle sintering proceeded very fast at temperatures

above 773 K. Catalysts calcined at higher temperatures in the range from 1023 to 1223 K showed almost the constant value of the d_{AV} (Pd) ~ 30 nm. Pd particle size after reaching a certain value did not further increase. The largest particles were up to 80 nm.

Furthermore, it was found that the method of reduction has a significant effect on the resulting Pd dispersion. The average particle size of palladium in catalysts reduced in the gas phase using hydrogen was lower than the one reduced in the liquid phase using hydrazine monohydrate. These results were confirmed by HRTEM measurements.

Acknowledgements

This work was realized within the Operational Programme Prague—Competitiveness (CZ.2.16/3.1.00/24501) and "National Program of Sustainability" (NPU I LO1613) MSMT-43 760/2015.

Author details

Jan Patera[1], Iva Paterová[1]*, Jiří Krupka[1] and Květa Jirátová[2]

*Address all correspondence to: iva.paterova@vscht.cz

1 Department of Organic Technology, UCT Prague, Prague, Czech Republic

2 Institute of Chemical Process Fundamentals of the CAS, v. v. i., Prague, Czech Republic

References

[1] Rymeš J, Ehret G, Hilaire L, Boutonnet M, Jirátová K. Microemulsions in the preparation of highly active combustion catalysts. Catalysis Today. 2002;**75**:297-303. DOI: 10.1016/S0920-5861(02)00082-2

[2] Radic N, Grbic B, Jovanovič Ž, Terlecki-Baričevič A, Arsinjevič Z. Microemulsions in the preparation of highly active combustion catalysts. In: Proceedings of the Seventh Congress on Catalysis; Varna; 1996. p. 377

[3] Hegedus LS, editor. Catalyst Design: Progress and Perspectives. New York: Wiley; 1987. 288 p

[4] Bacik DB, Zhang M, Zhao D, Roberts CB, Seehra MS, Singh V, Shah N. Synthesis and characterization of supported polysugar-stabilized Pd nanoparticle catalysts for enhanced hydro-dechlorination of trichloroethylene. Nanotechnology. 2012;**23**:294004. DOI: 10.1088/0957-4484/23/29/294004

[5] Schulman JH, Friend JA. Light scattering investigation of the structure of transparent oil-water disperse systems. II. Journal of Colloid Science. 1949;**4**:497-509. DOI: 10.1016/0095-8522(49)90046-X

[6] Boutonnet M, Kizling J, Stenius P, Maire G. The preparation of monodisperse colloidal metal particles from microemulsions. Colloids and Surfaces. 1982;**5**:209-225. DOI: 10.1016/0166-6622(82)80079-6

[7] Kishida M, Fujita T, Umakoshi K, Ishiyama J, Nagata H. Novel preparation of metal-supported catalysts by colloidal microparticles in a water-in-oil microemulsion; catalytic hydrogenation of carbon dioxide. Journal of the Chemical Society, Chemical Communications. 1995;**7**:763-764. DOI: 10.1039/c39950000763

[8] Kishida M, Umakoshi K, Ishiyama J, Nagata H, Wakabayashi K. Hydrogenation of carbon dioxide over metal catalysts prepared using microemulsion. Catalysis Today. 1996;**29**:355-359. DOI: 10.1016/0920-5861(95)00304-5

[9] Kosydar R, Góral M, Gurgul J, Drelinkiewicz A. The effect of support properties in the preparation of Pd size-controlled catalysts by "water-in-oil" microemulsion method. Catalysis Communications. 2012;**22**:58-67. DOI: 10.1016/j.catcom.2012.02.018

[10] Semagina N, Renken A, Laub D, Kiwi-Minsker L. Synthesis of monodispersed palladium nanoparticles to study structure sensitivity of solvent-free selective hydrogenation of 2-methyl-3-butyn-2-ol. Journal of Catalysis. 2007;**246**:308-314. DOI: 10.1016/j.jcat.2006.12.011

[11] Heshmatpour F, Abazari R, Balalaie S. Preparation of monometallic (Pd, Ag) and bimetallic (Pd/Ag, Pd/Ni, Pd/Cu) nanoparticles via reversed micelles and their use in the Heck reaction. Tetrahedron. 2012;**68**:3001-3011. DOI: 10.1016/j.tet.2012.02.028

[12] Noh J, Meijboom R. Dendrimer-templated Pd nanoparticles and Pd nanoparticles synthesized by reverse microemulsions as efficient nanocatalysts for the Heck reaction: A comparative study. Journal of Colloid and Interface Science. 2014;**415**:57-69. DOI: 10.1016/j.jcis.2013.10.004

[13] Chen M, Feng Y, Wang L, Zhang L, Zhang J. Study of palladium nanoparticles prepared from water-in-oil microemulsion. Colloids and surfaces A: Physicochemical and Engineering Aspects. 2006;**281**:119-124. DOI: 10.1016/j.colsurfa.2006.02.024

[14] Perez-Coronado AM, Calvo L, Alonso-Morales N, Heras F, Rodriguez JJ, Gilarranz MA. Multiple approaches to control and assess the size of Pd nanoparticles synthesized via water-in-oil microemulsion. Colloids and Surfaces A: Physicochemical and Engineering Aspects. 2016;**497**:28-34. DOI: 10.1016/j.colsurfa.2016.02.012

[15] Wojcieszaka R, Genetb MJ, Eloya P, Gaigneauxa EM, Ruiza P. Supported Pd nanoparticles prepared by a modified water-in-oil microemulsion method. Studies in Surface Science and Catalysis. 2010;**175**:789-792

[16] Kim W, Hayashi H, Kishida M, Nagata H, Wakabayashi K. Methanol synthesis from syngas over supported palladium catalysts prepared using water-in-oil microemulsion. Applied Catalysis, A: General. 1998;**169**:157-164. DOI: 10.1016/S0926-860X(98)00007-6

[17] Pocoroba E, Pettersson LJ, Agrell J, Boutonnet M, Jansson K. Exhaust gas catalysts for heavy-duty applications: Influence of the Pd particle size and particle size distribution on the combustion of natural gas and biogas. Topics in Catalysis. 2001;**16**:407-412

[18] Eriksson S, Nylén U, Rojas S, Boutonnet M. Preparation of catalysts from microemulsions and their applications in heterogeneous catalysis. Applied Catalysis A: General. 2004;**265**:207-219. DOI: 10.1016/j.apcata.2004.01.014

[19] Patera J, Krupka J, Pašek J, Paterová I, Jirátová K, Murafa N. Determination of specific surface area of palladium in hydrogenation catalysts by carbon monoxide chemisorption. Chemicke Listy. 2012;**106**:1122-1128

[20] Lewis FA. The Palladium-Hydrogen System. New York: Academic Press; 1967. p. 178. DOI: 10.1002/bbpc.19670710933

[21] Dudková I, Dvořák B. Carbon monoxide chemisorption on palladium surface. Chemicke Listy. 2008;**103**:1092-1099

[22] Forman AJ, Park J-N, Tang W, Y-S H, Stocky GD, McFarland EW. Silica-encapsulated Pd nanoparticles as a regenerable and sintering-resistant catalyst. ChemCatChem. 2010;**2**:1318-1324. DOI: 10.1002/cctc.201000015

Chapter 12

Symbiosis in Plasmonic Nanoparticles

Abhinav Malasi and Ritesh Sachan

Additional information is available at the end of the chapter

http://dx.doi.org/10.5772/intechopen.71730

Abstract

The focus of this chapter is on how the symbiotic relationship existing in nature can easily be translated to the nanoscale systems, particularly in plasmonic nanoparticles. Here, we discuss the synthesis and properties of bimetallic nanoparticles, consisting of plasmonic silver (Ag) with ferromagnetic cobalt (Co). The symbiotic properties in the Co-Ag bimetallic plasmonic nanoparticles are discussed in the chapter where Ag and Co are the beneficiary elements due to the presence of each other. These bimetallic plasmonic nanomaterials demonstrate multi-functionalities which are not just limited to well-known bio-sensing or magneto-optical effects but also expand to highly unexpected and exotic properties such as extreme oxidation resistance, ferroplasmons, improved quality factor, and tunable radiative quantum efficiency.

Keywords: plasmonics, ferromagnetic, bimetallic nanoparticles, symbiosis, ferroplasmon, quantum efficiency, quality factor, EELS, galvanic coupling, nanosphere lithography, dewetting

1. Introduction

Symbiosis is a natural phenomenon where the co-existence of two entities mutually benefits their survival. Symbiosis is the key ingredient for the existence of life on this planet whether on the surface or under the water. Some of the most common and sought out symbiotic pairs on land are honey bee and flower, birds/mammals and fruit of plants, and in the oceans are corals and algae or clown fish and sea anemones [1]. Even the plants coexist with the natural environment in which the ecosystem and its evolution are symbiotic [2].

This behavior, when observed at the nanoscale, is expected to lead to many interesting phenomena in the field of nanomaterials. For symbiosis to occur at the nanoscale, multi-metallic nanoparticle systems are required where individual components can mutually benefit

and introduce multi-functionalities. In the field of nanomaterials, there is a deliberate drive towards synthesizing materials with multiple functionalities in a single nanostructure and the most simplistic system is bimetallic nanoparticles. The studies on bimetallic nanoparticle systems have shown improved magneto-plasmonic response, enhanced catalytic activities, efficient energy conversion, tunable plasmonic properties, leading to phenomenon like plasmon hybridization and Fano resonances (the interference between narrow bandwidth plasmons and the broader plasmons/continuum) to name a few [3–7]. These properties exhibited by multi-metallic nanomaterial system and has led to the seminal research on the symbiosis in bimetallic particles at the nanoscale. The focus of this book chapter is on the symbiotic properties of bimetallic nanoparticles, particularly those of silver (Ag), an excellent plasmonic material, and cobalt (Co), a ferromagnetic material. These material systems find applications in sensing of biological and chemical agents, catalysis, energy harvesting, data storage, and nanoelectronics.

The contents of the book chapter are organized as follows: Section 2 covers the synthesis techniques involved in the fabrication of bimetallic Co-Ag nanoparticle arrays; Section 3 focuses on the basic characterization techniques that were involved in various studies discussed in Section 4. In Section 4, a detailed discussion on the various symbiotic properties is presented followed by a discussion on other existing symbiotic systems in Section 5 and concluding remarks in Section 6.

2. Synthesis of bimetallic nanoparticles

The synthesis of bimetallic nanoparticles has been reported by both physical and chemical routes using the top-down as well as bottom-up approaches. In the view of this focused chapter, the techniques using physical vapor deposition of metal thin films are specifically emphasized. The two discussed techniques viz. (i) pulsed laser induced dewetting (PLiD) and (ii) colloidal lithography, are adopted due to their merits of being robust, time efficient and comparatively cost efficient as compared to other methods incorporating vapor deposition systems.

2.1. Pulsed laser induced dewetting (PLiD)

The nanoparticles synthesized by PLiD fall in the category of self-organization. Self-organization is a phenomenon in which the intrinsic force plays a prominent role in arranging the patterns with definite length scale and shape, thus stabilizing the system. Some of the common examples of self-organization are skin pigmentation in animals and solar system. At the nanoscale, examples of self-organization can be seen in protein folding self-assembly, the formation of micelles and droplet formation from the breakage of thin polymer and metal films. The phenomenon of breaking of thin metal or polymer films into droplets is called spinodal dewetting which leads to characteristic size and spacing [8–10]. Spinodal dewetting works on the principle of thermodynamic instabilities occurring due to the mismatch in the surface energy of a thin liquid metal film on the non-wetting substrate surface, which leads

http://dx.doi.org/10.5772/intechopen.71730

to the breakage of the film to more stable state in the form of droplets. Some of the most common examples of spinodal dewetting are the hydrophobic leaf surfaces, oil droplet formation on the water surface, the windshield of vehicles after rain etc. This technique has been used to synthesize a wide variety of nanoparticles of different sizes, shapes, and materials.

The SEM in **Figure 1(a)** shows the typical Co-Ag nanoparticle arrays of dewetted metal film. The inset of the figure depicts the mono-modal size distribution. The average nanoparticle size and spacing of the dewetted nanoparticles depends on the initial film thickness. This gives the control to precisely synthesize the desired size of the nanoparticles. The nanoparticle spacing and size cannot be varied independently and are dependent on each other because of material volume conservation [11, 12]. This suggests that by independently controlling the film thickness of individual metals in a bilayer system, a wide size range can be achieved. Using the theoretical relation between the film thickness and the nanoparticle size, a parameter space of nanoparticle size as a function of Ag volume percentage is plotted for total thickness varying in the range 2–20 nm for Co/Ag/SiO_2 and Ag/Co/SiO_2 regions as shown in **Figure 1(b)**. It is interesting to note here that a wide array of nanoparticles of different sizes and composition can be synthesized using this technique. This technique also gives the flexibility to vary the nanoparticle size by keeping the Ag volume fixed or varying the Ag volume amount by keeping the size fixed.

The drawback of dewetting is the lack of independent control of either of the nanoparticle size or spacing which restricts its use for synthesizing nanoparticles within the interacting regime (interparticle spacing ≤ nanoparticle size). If this barrier could be broken, this technique would be highly useful for making large 2D nanoparticles arrays beneficial for plasmonic

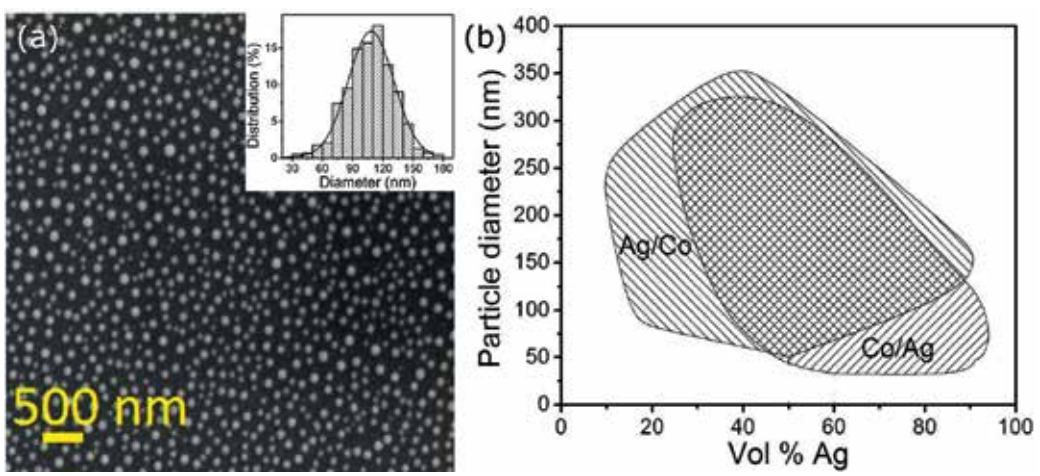

Figure 1. (a) SEM image of Co-Ag nanoparticle with a monomodal size distribution of 113 ± 30 nm. The inset shows the size distribution of the nanoparticles. (b) Theoretically generated nanoparticle size parameter space as a function of Ag amount for the configurations Co/Ag/SiO_2 and Ag/Co/SiO_2 with the total film thickness of the system varied between 2 and 20 nm. (a) from [13] is used in accordance with the Creative Commons Attribution (CC BY) license (https://creativecommons.org/licenses/by/4.0/). (b) is reproduced from Ref. [12]. © IOP Publishing. Reproduced with permission. All rights reserved.

related research requiring energy hotspots. Recently, Yadavali and Kalyanaraman reported that the particle spacing of the nanoparticles can be independent of the initial film thickness which is not the case in classical spinodal dewetting by creating Rayleigh-Taylor instabilities at the metal film surface in contact with liquid creating large pressure gradients due to evaporation [14].

2.2. Colloidal lithography

Lithographic techniques are well suited towards making large area 2D periodic ordered structures. The formation of these periodic structures involves the three basic steps, i.e. mask formation, material deposition, and mask etching. It gives the flexibility to print complex geometries of ordered 2D arrays of nanostructures on large areas. The drawback to most of the lithographic techniques are the cumbersome steps to achieve the final product which is time and resource consuming, and also requiring the use of expensive instruments. Van Duyne and co-workers came out with a fast and inexpensive technique to pattern large area 2D periodic nanostructures by forming masks of self-assembled colloidal nanoparticles called the nanospheres lithography (NSL) [15]. The self-assembly of a monolayer of hexagonally packed colloidal nanoparticles can be either done on hydrophilic substrates or at the air-water interface [15, 16]. Once the mask is ready, the metal is deposited through the gaps between the colloidal beads arrangement. The template is then etched, leaving the hexagonally arranged patterns of metal nano-triangles on the substrate. The in-plane dimensions of the features formed by NSL depend solely on the size of the colloidal nanoparticles [15].

The biggest challenge using this technique is to avoid the formation of a large number of vacancy and dislocation defects [17]. To tackle the control of defect formation is to control the evaporation rate of the fluid containing the beads [18, 19]. The evaporating fluid forces the beads to move towards the crystallized area due to the internal flow of the fluid. Other ways are to confine the solution and apply mechanical or physical force by gas flow to form ordered arrangement [16, 20, 21].

NSL requires the direction of metal flux being deposited to be perpendicular to the substrate plane. This restricts the control to vary the nanoparticle geometry and is limited to nano-triangles, which are truncated pyramids and can be further tuned to semi-spherical shape [22, 23]. Many variations of colloidal lithography in the form of angle-resolved NSL, shadow-sphere lithography, hole mask colloidal lithography, and shrinkable hole mask lithography exists which can create complex geometries like crescents, dimers, pillars, chiral structures etc. [24–27].

3. Characterization

The as-prepared samples were characterized for their morphology by SEM and optical properties by UV-vis spectroscopy. The statistical information on the average nanoparticle size and distribution were calculated by analyzing the SEM images using image analysis software (ImageJ by NIH) [28]. EDX mapping study on bimetallic Co-Ag nanoparticles revealed the

http://dx.doi.org/10.5772/intechopen.71730

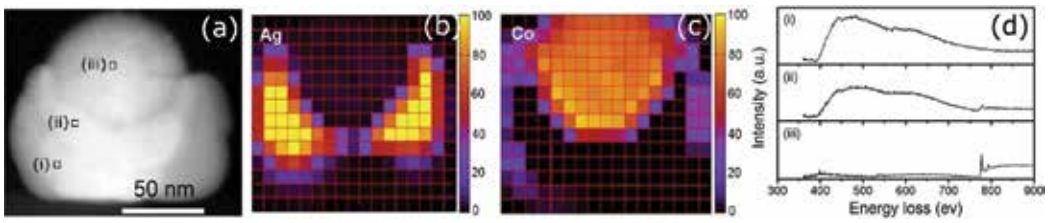

Figure 2. (a) Cross-sectional HAADF image of Ag-Co hemispherical nanoparticle synthesized by PLiD. Core-loss EELS mapping of (b) Ag and (c) Co for the hemispherical nanoparticle. (d) The EELS spectra measured for the nanoparticle measured at three different regions marked in (a). Reproduced from Ref. [12].

volume ratio of the two metals remained intact after the nanoparticle synthesis. EDX analysis revealed the average Co:Ag X-ray count of the synthesized nanoparticles followed a linear relationship with the Co:Ag film thickness ratio [12].

In the present case of characterizing symbiotic bimetallic nanoscale systems, core-loss EELS (electron energy loss spectroscopy) is employed to understand the elemental distribution, inter-mixing or alloying, chemical reactivity and electronic structure in a single nanoparticle. An example is shown in **Figure 2** where the elemental distribution of Ag and Co is mapped using Ag-M_{45} and Co-L_{23} edges in bimetallic nanoparticles. A high-angle annular dark field (HAADF) image of Ag-Co bimetallic nanoparticle is shown in **Figure 2(a)**, along with the Ag (**Figure 2(b)**) and Co (**Figure 2(c)**) elemental maps. The representative core-loss EELS edges of Ag and Co obtained from the region (i), (ii) and (iii) regions are shown in **Figure 2(d)** [12]. This method is also used to quantify the surface oxidation in the Ag-Co nanoparticles and to study the oxidation state of formed metal oxides [29]. The information about the optical behavior is also obtained using low-loss EELS and will be discussed in Section 4.3.

4. Symbiotic properties

In this section, we discuss the tuning and improvement or enhancement in four different properties caused by the mutual sharing or transfer of free electrons between Ag and Co, leading to symbiosis at the nanoscale.

4.1. Tuning the plasmon resonance and its sensitivity

The materials displaying optical properties at the nanoscale are termed as plasmonic materials. Plasmonics can be defined as when the metal nanoparticles interact with light of sizes less than or equivalent to the wavelength, the free electrons start to resonate at a certain frequency called the plasmon resonance frequency. The plasmon resonance is a material property and depends on the shape, size, composition, and environment of the nanoparticle. The other viable option to vary the plasmon resonance is by synthesizing multi-metallic nanoparticle composites. Multi-metallic nanoparticles open the door to incorporate multiple functionalities in a single nanoparticle. Depending on the synthesis approach and the reaction conditions,

amount of mixing of metals within a nanoparticle can vary from being immiscible like core-shell, to partially miscible, or to completely miscible and also gives advantage on tuning the nanoparticle morphology from spheres to rods and from discs to crescents [30, 31].

Kalyanaraman and co-workers extensively studied the Ag-Co bimetallic system synthesized by PLiD [11, 12, 29, 32–35]. Two separate studies were conducted on these bimetallic nanoparticles, one in which the bimetal composition was fixed while the nanoparticle size was varied. In the other case, the Ag amount was fixed and the Co amount was varied. In the first study, three different compositions of Ag (71.5%, 83.3%, and 100%) in the nanoparticles were studied which were achieved by keeping the starting volume ratio of the metals fixed. It was observed that for fixed composition and increasing nanoparticle size, the plasmon resonance red shifted as shown in **Figure 3(a)**. This observation is explained by using Maxwell-Garnett (MG) approach. The MG approach calculates the effective complex dielectric of a system in which small grains of metal 1 are embedded in metal 2, and is only dependent on the volume fraction and complex dielectric functions of the metals, suggesting for fixed composition, the effective complex dielectric should be the same [36]. Hence an increase in size shifts the plasmon to higher wavelength, consistent with the plasmonic theory. For the

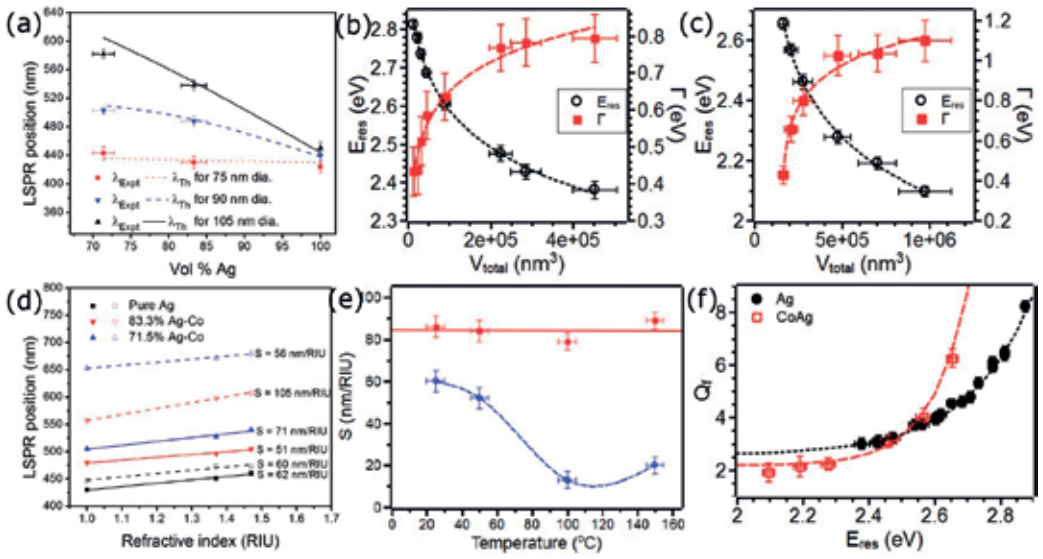

Figure 3. (a) Comparison of the localized surface plasmon resonance (LSPR) wavelength for different composition of Ag in a single nanoparticle as a function of three different nanoparticle sizes. (b) and (c) Comparison of the plasmon resonance energy and bandwidth of pure Ag and Co-Ag nanoparticles as a function of total nanoparticle volume, respectively. (d) LSPR positions of three different compositions of Ag measured at three different refractive index liquids. The slopes of the straight-line fits give the refractive index sensitivity of the nanoparticles denoted by *S*. (e) Refractive index sensitivity comparison of Co-Ag and Ag nanoparticles synthesized from 1 nm Co on 5 nm Ag and 5 nm Ag as a function of annealing temperature (modified color scheme). (f) Experimentally measured quality factor comparison of different compositions of Co-Ag nanoparticles and different sizes of Ag nanoparticles as a function of their plasmon resonance energy. (a) and (d) from Ref. [12]. (b), (c) and (f) from Ref. [13], (e) reproduced with permission from Ref. [29].

http://dx.doi.org/10.5772/intechopen.71730

second study, nanoparticles were synthesized by dewetting of stacked Co/Ag/SiO_2 system. The optical properties of different sized nanoparticles were studied by varying the thickness of Co film from 1 to 5 nm while keeping the thickness of Ag film fixed at 5 nm. Similarly, pure Ag nanoparticles were synthesized by varying the initial film thickness from 1 to 10 nm. The plasmon resonance energy and plasmon bandwidth for Ag and Co-Ag nanoparticles as a function of nanoparticle volume are plotted in **Figure 3(b)** and **(c)**, respectively. Similarly, on increasing the nanoparticle volume, the plasmon resonance energy decreases or red-shifts and the nanoparticle bandwidth increases.

After tuning the plasmon resonance energy, the sensitivity and stability of these nanoparticles are tested. On conducting the refractive index (RI) sensing of the bimetallic nanoparticles, it is observed that for some composition and sizes of Co-Ag nanoparticles, they showed improved RI sensitivity over pure Ag nanoparticles, shown in **Figure 3(d)**. In another study, bimetals of Co-Ag nanoparticles (83.3% Ag) heated to 150°C, showed stable RI sensitivity while Ag nanoparticles for the same starting film thickness are highly unstable as evident from **Figure 3(e)**. The reason for this ultra-stability is discussed in Section 4.2. A general idea about the sensor's performance can also be acquired by calculating its quality factor. The quality factor is a direct measure of the sensitivity of a system to detect, higher the quality factor means more sensitive the system. For a plasmonic sensor, the experimental quality factor can be calculated as $Q = E_{res}/\Gamma$, E_{res} being the plasmon resonance energy and Γ the bandwidth of the plasmon resonance. The quality factor comparison of the samples discussed in second study is plotted as a function of resonance energy in **Figure 3(f)**. The crossover of the quality factor in **Figure 3(f)** is explained by comparing the bandwidths (**Figure 3(b)** and **(c)**) of the two systems for plasmon resonance energies greater than 2.5 eV. At the same plasmon resonance energy, the nanoparticle with higher quality factor means that it has a narrow bandwidth. This leads to the question: what are the different factors contributing to the broadening of plasmon bandwidth?

To explain the broadening of the bandwidth, we use the two-level model to explain the results, which is analogous to molecular spectroscopy in which the plasmon decays by dephasing of coherent oscillations (remember the definition of plasmon, which is a coherent oscillation of electrons) [37]. The dephasing occurs as a result of many interactions occurring due to electron-electron, electron-phonon, electron-defect and electron-surface interactions [37, 38]. These events follow Matthiessen's rule as these scattering events are statistically independent channels and thus can be added up [37, 38]. So, the total bandwidth of Co-Ag bimetallic nanoparticles should be the sum of the contributions from individual metals, which clearly is not the case as seen in **Figure 3(f)**. This leads to the possibility of some sort of electronic interaction taking place at the nanoscale between Ag and Co. It also suggests that the sensitivity is highly dependent on nanoparticle size and composition, as evident from **Figure 3(d)**.

4.2. Oxidation stability

Metal structures at the nanoscale have high reactivity and so are susceptible to oxidation. Because of this reason, Ag which has the best optical properties is not favored over Au [39]. The inertness of Au makes it a more plausible material than Ag which scums to its chemical

and structural instabilities [40, 41]. Shortage of stable plasmonic materials creates the demand for research on alternate or new stable plasmonic materials required for various applications at the nanoscale [42, 43]. A lot of different solutions or alternative routes have been presented to stabilize metal nanoparticles but they either are short-term solutions or undermine the pure metal properties. The brighter side of these solutions has resulted in finding new and improved properties in some cases. By synthesizing core-shell of Au-Ag, the Ag could be stabilized via electron transfer from Au core, but the nanoparticle properties degrade over time due to the alloying between Au and Ag at the interface [44]. These synthesized core-shell structures at a critical thickness of Ag shell are resilient to harsh chloride ion environment without any visible degradation under transmission electron microscope.

In another study, the Ag nanostructures were stabilized by processing them with low-temperature single hydrogen atoms. The idea was to stabilize nanostructures by filling the interstitial sites with a hydrogen atom to prevent Ag atom diffusion [41]. Covering Ag nanostructures with a monolayer of graphene could protect them from oxidation for almost a period of a month [45]. The other possibility is by surface passivation of Ag nanostructures with organic molecules. The choice of an organic molecule can preferentially control the optical or the electrical properties [46].

Sachan et al. stabilized the Ag nanoparticles by synthesizing bimetals of Ag and Co having segregated regions within a single nanoparticle using PLiD. The oxidation behavior was studied using optical spectroscopy and core-loss EELS mapping and showed prolong optical stability of Ag nanoparticles [12, 29, 34]. This ultra-stability was due to the galvanic coupling between Co and Ag at the nanoscale where Co was acting as a sacrificial anode, thus protecting Ag surface by providing electrons as shown in **Figure 4(a)**. The study was further extended by Malasi et al. to understand the role of Co composition in these bimetals and how the Co-Ag nanoparticle life could be extended [34]. On studying the extended optical bandwidth decay of these nanoparticles, two observations were made. Firstly, the decay behavior of Co and Ag of the bimetals followed two different trends displaying a sharp boundary demarcating the change in trends from inverse logarithmic to exponential decay shown in **Figure 4(b)**. Second observation suggested that the decay trends observed in pure metal oxidation were consistent with the decay of the individual metals of the bimetallic nanoparticle and overlapped perfectly. The change in decay behavior suggested that the two metals have segregated regions, the results of which are consistent with the EELS observation. The only question that remained here to answer was whether the Co oxidized completely or not before the change in the optical bandwidth decay trends. To answer this, a theoretical model is used to quantify the oxidation of Co in the bimetallic nanoparticle system, details of which are available in Ref. [34]. Co-Ag bimetals showed almost 12 times better shelf life than pure Ag nanoparticles for 50% degradation in the optical bandwidth and depending on Co amount, the Ag could be oxide free for almost a year. The lifetimes were established using effective medium theory, which is a versatile way to study nanoparticles in embedded media [47, 48].

To explore the other possibilities of stability studies in Co-Ag bimetal system, Kalyanaraman and co-workers studied the extraordinary optical transmission (EOT) of perforated holes of triangular shapes in Ag and Ag/Co films [49]. The findings suggested that Ag films deposited

http://dx.doi.org/10.5772/intechopen.71730

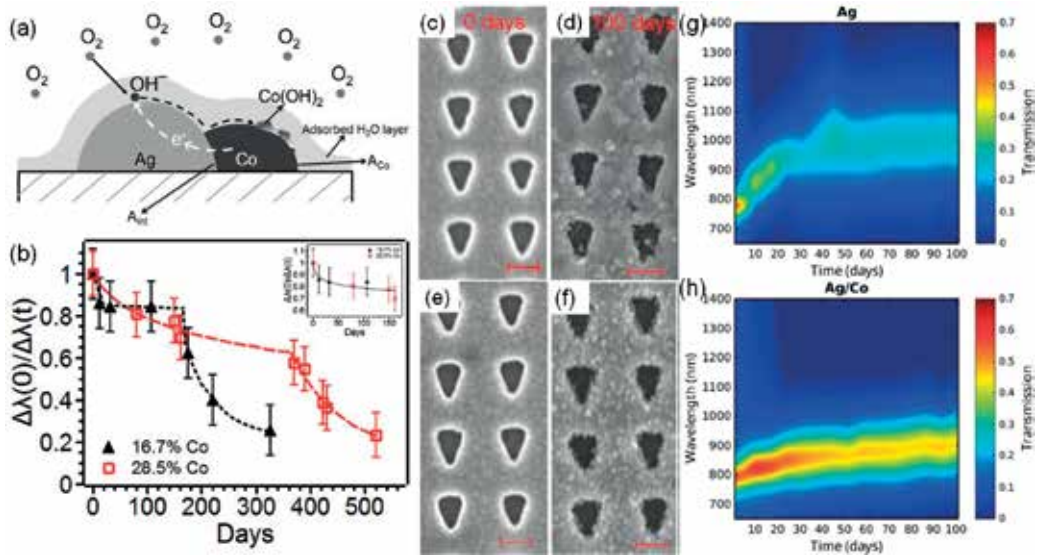

Figure 4. (a) Schematic showing the galvanic coupling in a single bimetallic Co-Ag nanoparticle. (b) Optical bandwidth decay of two different concentrations of Co (solid triangles and hollow squares) in the bimetallic Co-Ag nanoparticles plotted as a function of days. Each curve follows two different trends, inverse logarithmic and exponential decay corresponding to that of pure Co and pure Ag, respectively. The inset shows the overlap of Co oxidation in Co-Ag nanoparticles, where the dashed line is an inverse logarithmic function as a guide to the eye. SEM images depicting the morphology of triangular shaped EOTs of pure Ag captured on (c) 0 days and (d) after 100 days. Similarly, SEM images for the morphology of Ag/Co EOT captured on (e) day 0 and (f) after 100 days. (g) and (h) are the contour maps for the resonance decay of Ag and Ag/Co EOT devices, respectively. (a) reproduced with permission from Ref. [29]. (b) reproduced from Ref. [34]. © IOP Publishing. Reproduced with permission. All rights reserved. (c)–(h) from Ref. [49], used in accordance with the Creative Commons Attribution (CC BY) license (https://creativecommons.org/licenses/by/4.0/).

on top of Co films showed much improved EOT stability in ambient air as can be visualized from the SEM images shown in **Figure 4(c)–(f)**. The study was carried out for 100 days which showed 1.9 times better plasmon peak stability and 1.7 times better bandwidth stability over pure Ag EOT. The contour maps in **Figure 4(g)** and **(h)** shows the plasmon resonance decay as a function of days. The map shows the change in the behavior of Ag EOT, initially the plasmon significantly red-shifts leading up to day 40 after that the plasmon resonance intensity starts decaying very rapidly in comparison to Ag/Co EOT showing slower red-shift and stable plasmon resonance intensity. The stabilization of bimetal EOT is attributed to the underlying Co layer, which prevents Ag to dewet on the glass substrate. This is evident from the SEM images where material build-up is present for pure Ag EOTs due to dewetting on glass substrate but absent in Ag/Co EOTs.

4.3. Ferro-plasmons

As discussed in the preceding sections, due to the scarcity of plasmonic materials or rather stable plasmonic materials at room temperature, a lot of attention has been diverted on the study of bimetallic nanoparticle systems. The interaction between the bimetallic nanoparticles

has led to interesting optical phenomena such as plasmon hybridization and Fano interference resonance. These optical phenomena occur due to the interactions between various plasmon modes, dark and bright modes, or sub-radiant and super-radiant modes. Hybridization of two plasmonic resonances leads to a lower energy resonance, i.e. the sub-radiant mode with narrow bandwidth and the higher energy resonance acting as a continuum, i.e. the super-radiant mode, in asymmetric nanoparticle systems [50, 51]. The above mentioned optical phenomena are observed in a wide variety of plasmonic nanostructures such as multishells, cavities, and heterodimers [52–54].

One such optical phenomenon observed in the bimetallic Ag-CoFe and Ag-Co nanoparticles is the ferroplasmon (FP), intense LSPR (localized surface plasmon resonance) excited in the visible spectrum of light on the surface of ferromagnetic CoFe and Co when in contact with plasmonic Ag [32]. FP is an intense LSPR with long plasmon decay length scales in the visible spectrum of light. As mentioned earlier, the exhibition of a strong LSPR in the visible spectrum is the characteristic property of the noble metals (Ag, Au, and Cu). Other metals, including the ferromagnetic metals (e.g. Co, Ni, Fe) have non-existent or highly damped visible plasmons. Recent studies of Ni nanostructures have demonstrated the sustenance of surface plasmon in the visible spectrum of light [55]. The discovery of FP is possible due to the advances in transmission electron microscopy equipped with a monochromated electron probe in STEM with energy resolutions of ~150 meV, enabling the quantitative study of well-resolved plasmon peaks at the nanoscale using low-loss EELS with high energy and spatial resolution. **Figure 5** shows the comparative study of plasmon excitations on the surface of bimetal Ag-CoFe, pure Ag and pure CoFe nanoparticles, resolved by low-loss EELS. The EELS spectra are shown in **Figure 5(a)** from Ag region of Ag-CoFe nanoparticle and the isolated Ag nanoparticle, taken from the square area marked in the HAADF images in **Figure 5(b)** and **(c)**. Both the spectra exhibit peaks in the visible range corresponding to the well-known surface plasmon in Ag. In contrast, the EELS spectrum shown in **Figure 5(e)** obtained from CoFe in Ag-CoFe show a strong and distinct plasmon peak, referred to as FP, at 2.7 eV, unlike the featureless spectrum for the isolated CoFe nanoparticle. The EELS spectra for CoFe corresponds to the red square marked on the CoFe side of the bimetal nanoparticle and the isolated nanoparticle marked on the HAADF images in **Figure 5(b)** and **(d)**, respectively. The evolution of FP in the Ag-CoFe bimetallic system is thoroughly studied as a function of nanoparticle size and found to be consistently present [32]. The presence of FP is an intricate play between the nanoparticle morphology and the interface shared between them, which was demonstrated by the absence of FP in dimers of Ag-Co nano-triangles placed in close proximity [56].

The physical origin of FP is explained by qualitative theoretical models such as dipole-dipole interaction, hybridization model, and Fano interference as these all arise due to the coupling between different plasmon modes [50, 51, 57]. A simple dipole-dipole interaction approach considers the coupling between same (dipole-dipole) or different (dipole-quadrupole) modes and successfully describes the electromagnetic energy transfer between two nanoparticles. However, it lacks the complete explanation due to inherently neglecting the interaction of other modes of plasmon oscillation. Alternatively, another model based on the plasmon hybridization effectively explain the existence of FP peak evolved at 2.7 eV, but also predict

http://dx.doi.org/10.5772/intechopen.71730

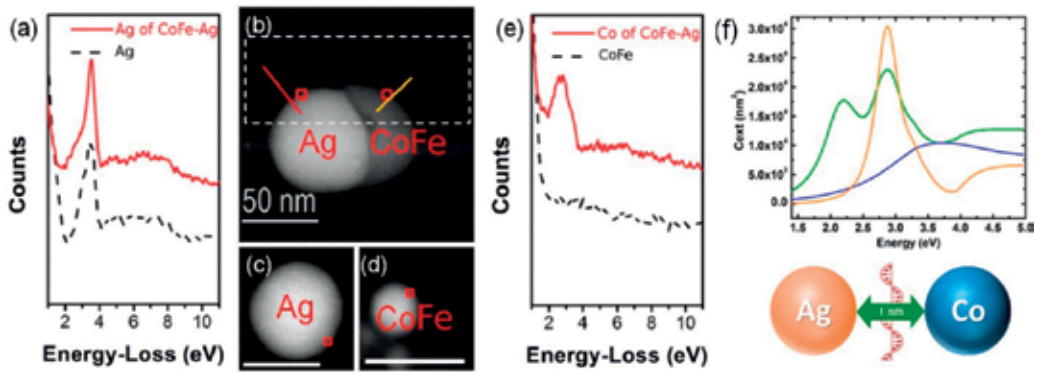

Figure 5. (a) EELS spectra from the surface of Ag side of Ag-CoFe (solid line) and isolated Ag nanoparticle. (b), (c) and (d) are the HAADF images of bimetallic Ag-CoFe, isolated Ag, and isolated CoFe nanoparticles, respectively. (e) EELS spectra from the surface of CoFe side of Ag-CoFe (solid line) and isolated CoFe nanoparticle. The EELS spectra are measured from the small red boxes marked on the HAADF images. (f) Comparison of extinction spectra simulated for pure Ag (orange line), pure Co (blue line) and dimer of Ag-Co (green line) nano-spheres. The schematic represents the Ag-Co dimer system separated by 1 nm. Reprinted (adapted) with permission from [32, 58]. Copyright (2014) American Chemical Society.

additional high-order peak, which is not observed experimentally in EELS. In the hybridization model, the coupling can be assumed as an instantaneous Coulomb interaction between the surface charge density of various components. In another approach, electrodynamic simulations were performed showing the interaction between spherical Ag and Co nanoparticles with their surfaces separated by a nanometer gap [58]. This gives rise to new plasmon mode at higher energy due to the interaction between Ag and Co nanospheres, as shown in **Figure 5(f)** where the optical spectrum of pure Co and pure Ag nanospheres are plotted in blue and orange, respectively. The green color corresponds to the spectrum obtained from the interaction between the Ag-Co nanospheres shown in the schematic. This analytical approach depends on the interaction of two spherical nanoparticles and the use of non-contacting geometry, assuming the contact between Ag and Co will not influence the interaction process. FP nanoparticle system still lacks a detailed theoretical study which is only possible by finite difference time domain or discrete dipole approximation simulations by taking account the hemispherical shaped nanoparticle.

4.4. Radiative quantum efficiency

Plasmonic nanoparticles are an efficient medium for transferring the coupled electromagnetic waves in and out of the system. How well the nanoparticles will couple to the electromagnetic waves depends on their shape, size, material, and ambient dielectric environment and is measured by the radiative quantum efficiency. The dependence of radiative quantum efficiency on the Au nanoparticle shape and size was first demonstrated by Sonnichsen et al. [59]. As the volume of nanostructure increased, the radiative contributions in the bandwidth increased, leading to increased quantum efficiencies. The other interesting observation regarding Co-Ag bimetal system is the tuning of radiative quantum efficiency in a much wider energy range by controlling the Co amount and keeping the Ag volume fixed [13]. This is achieved by

experimentally calculating the radiative and non-radiative contributions in the bandwidth, which are then used to calculate the radiative quantum efficiency calculated as: $\eta = \frac{\Gamma_{1,R}}{\Gamma_{1,R} + \Gamma_{1,NR}}$, where Γ is the bandwidth and subscripts *R* and *NR* stand for radiative and non-radiative respectively.

Continuing the discussion in Section 4.1 on bandwidth broadening, another assumption to consider is to neglect the contributions from electron scattering on the broadening of the bandwidth as discussed in Ref. [13]. The only contributions worth mentioning are the radiative losses and non-radiative absorption. As mentioned earlier, the bandwidth depends on the nanoparticle volume and dielectric function, hence the simplified expression can be written as, $\Gamma_2^{exp}(E_{res}, V) = \frac{1}{2}\Gamma_{1,R}(E_{res}, V) + \frac{1}{2}\Gamma_{1,NR}(E_{res}, V)$, here E_{res} is the plasmon resonance energy and V is the nanoparticle volume. Since, Γ_2^{exp} is experimentally measured, and if either one of the radiative or non-radiative contributions could be measured independently, this will lead to calculating the radiative quantum efficiency.

Working under the limit of dipolar approximation, the radiative losses at the plasmon resonance energy are only dependent on the nanoparticle volume and thus can be written as $\Gamma_{1,R}(E_{res}, V) \propto V$ [60]. The proportionality constant *K* is a material parameter of metal understudy and is independent of the nanoparticle volume, shape, size and the dielectric environment. To work under the dipolar approximation, the nanoparticle should follow $V/\lambda^3 \ll 1$, where λ is the wavelength of light. Under this condition, the nanoparticle polarizability is dominated by the dipolar components and higher order multipoles can be ignored. The samples under study followed this approximation and for the size and resonance energy range followed the above condition ($V/\lambda^3 \leq 10^{-2}$). Once it is established that we are working under the dipolar approximation, the proportionality constant *K* is calculated by taking two different geometries having the same plasmon resonance energy as described in Ref. [59]. For our study, we synthesized Ag nano-triangles by NSL technique and used the data of Ag hemispherical nanoparticles to calculate *K*. As, we are working on Ag and at the same plasmon resonance energy, the non-radiative losses (radiative contributions are due to the dielectric of the material) of the two shapes will cancel out. Hence, *K* is calculated, $K = \frac{\Delta\Gamma_{1,R}}{\Delta V} = 2\frac{\Delta\Gamma_2^{exp}}{\Delta V}$. **Figure 6(a)** compares the bandwidth of Ag nano-triangles and hemispheres as a function of plasmon resonance energy. Inset of **Figure 6(a)** shows *K* as a function of plasmon resonance energy with the average $K = 8.1 \pm 2.3 \times 10^{-7}$ eV/nm^3 plotted as a dashed line. The value of *K* is further used to calculate the contributions of radiative and non-radiative components and finally the radiative quantum efficiency.

After establishing the contributions of the radiative and non-radiative components to the broadening of Ag nanoparticle (**Figure 6(b)**), a similar analysis was done for Co-Ag nanoparticles. Consider the two previously established facts: (i) Ag and Co have segregated regions within a single nanoparticle and the average nanoparticle spacing is much greater than the average diameter, hence near-field coupling is non-existent for this case; and (ii) the bimetallic nanoparticle does not follow the Matthiessen's rule as evident from the quality factor calculations discussed previously. So, we proposed the possibility of the modification of the radiative bandwidth of Ag due to the presence of Co. This assumption is made based on the ferroplasmon discovery, since the segregated Ag and Co had plasmons at almost the same resonance

http://dx.doi.org/10.5772/intechopen.71730

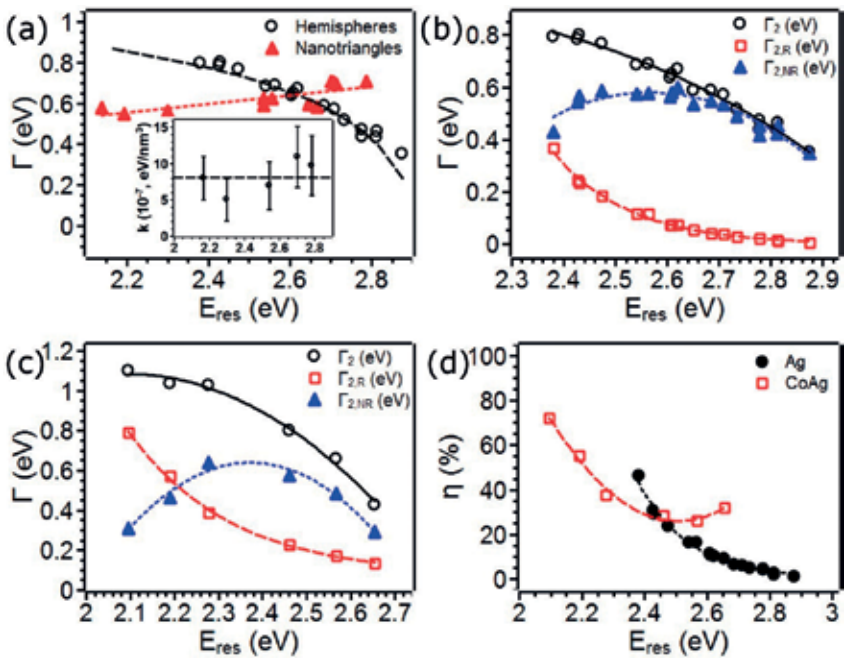

Figure 6. (a) Compares the bandwidth of hemispherical Ag nanoparticles with Ag nano-triangles plotted against plasmon resonance energy. The inset depicts the *K* values calculated at different plasmon resonance energy with the dashed horizontal line depicting the average *K* value. (b) and (c) Plots the total bandwidth with its radiative and non-radiative components against plasmon resonance energy for Ag and Co-Ag nanoparticles, respectively. (d) Radiative quantum efficiency comparison for Ag and Co-Ag nanoparticles as a function of plasmon resonance energy. Ref. [13] is used in accordance with the Creative Commons Attribution (CC BY) license (https://creativecommons.org/licenses/by/4.0/).

energy, further encouraging to assume Co-Ag nanoparticle equivalent to one big Ag nanoparticle of similar volume. Keeping this assumption, we calculated the bandwidth contributions for the bimetallic nanoparticle as previously discussed. The radiative, non-radiative and total experimental bandwidth values for different Co-Ag nanoparticles is plotted as a function of plasmon resonance energy in **Figure 6(c)**.

To support the above assumption, we used an analytical model describing the interaction between two non-bianisotropic systems placed adjacent to each other and within the interaction regime [61]. This metamaterial system of a good (Ag in our case) and poor (Co in our case) conductor is analogous to RLC circuit. The active power of the individual components and the RLC system is calculated to explain the results. It is demonstrated that by increasing the surface to volume ratio, the active power changes sign from negative to positive for Co. An opposite change is observed in the active power for Ag, in the same frequency interval. The cross-over from positive to negative is also observed for the total active power of the system [13]. When surface to volume ratio is small (weak coupling), the total active power remains positive, but as the surface to volume ratio increases, the power switches sign in the frequency interval of study. For the total active power to be zero at a certain frequency, if the active power of Co is zero, then the active power of Ag will also be zero. This suggests that

the presence of Co modifies the power of Ag, which is also our experimental observation. Similar observations can be deduced from the quality factor results depicted in **Figure 3(f)**, as the Co amount is increased the quality factor decrease, suggesting weak coupling due to the decrease in surface to volume ratio.

Hence, we can seamlessly assume that the presence of Co is modifying the radiative bandwidth of Co-Ag nanoparticles and working under the assumptions highlighted above, it is safe to calculate the radiative bandwidth of Co-Ag by considering the whole nanoparticle equivalent to a single Ag nanoparticle of the same volume. This way the radiative quantum efficiency for the Ag and Co-Ag nanoparticles is calculated and plotted in **Figure 6(d)** as a function of plasmon resonance energy. So, by controlling the Co amount, the radiative quantum efficiency of Ag is tuned in a much wider energy range.

5. Other symbiotic systems

The above examples suggest that the synthesis of bimetallic or multi-metallic nanoparticles offers a wide variety of possibilities to tune/enhance or even discover new phenomenon occurring at the nanoscale. Symbiosis is not just limited to metals but is possible in other material systems as well. Few examples of widely studied combination of materials showing symbiosis are Au with Ag/Pd/Co or ZnO/SnO_2 systems. By synthesizing core-shell nanoparticles of Au-Ag, the optical properties of Au could be tuned below its inter-band transition [6]. The other interesting feature of core-shell nanoparticle is that by tuning the thickness of Ag shell, the bimetallic nanoparticle can sustain Fano resonance and Ag outer shell can provide chemical stability in harsh chloride ion environment due to the electron transfer from the Au core to the Ag shell [6, 44]. Au nanostructures also show a symbiotic relationship with Pd, by demonstrating better plasmonic refractive index sensing in Au-Pd core-shell nanoparticles over pure Au nanostructures [62]. On the other hand, the presence of plasmonic property of Au enhances the H_2 detection limit of Au-Pd bimetal system over pure Pd nanostructures [63]. In addition to looking at individual metal pairs, magneto-plasmonic (MP) field itself shows symbiosis at the nanoscale. The study of magneto-optics or active plasmonics is a mix of plasmonic and magnetic properties. Enhancement in magneto-optical (MO) activity occurs due to the presence of plasmonic resonance excitation causing electromagnetic field enhancement in the MO material. On the other hand, in active plasmonics, the plasmonic properties are tuned by the application of the external magnetic field. Co-Au system best describes the MP system, in which thin films of Co/Au tends to show active plasmonic while Au/Co/Au disks tend to show enhanced MO activity [4, 64]. Metal oxide system of ZnO/SnO_2 which forms a heterojunction also tends to show symbiosis at the nanoscale. Synthesizing core-shell nanowires of SnO_2-ZnO tends to demonstrate better NO_2 gas sensing under UV radiation over pure ZnO or SnO_2 nanowires [65]. The enhancement is due to the increased resistance caused by the photogeneration of electron-hole pairs under UV light. On the other hand, SnO_2 nanostructures stabilize ZnO in an aqueous environment, improves its biocompatibility and help tailor the excitonic luminescence properties [66].

6. Conclusions

In this chapter, we have provided a glimpse of the endless possible symbiotic properties observed at the nanoscale due to the interaction between nanomaterials demonstrating different properties. By selecting the right combination of materials, we demonstrated that their properties can be uniquely tailored as well as new characteristics can evolve. We highlight that there are a number of possible ways for material selection to synthesize multi-functional nanomaterials. The choice can be made per their position in the periodic table, their position in the chemical potential series, according to their properties or by their metallurgical interactions. The properties are not limited to the choice of material but can be tuned by controlling the shape, size and the dielectric environment of the nanomaterial. The research at the nanoscale has opened up a number of possibilities, which were not feasible a few decades ago. By controlling the nanoparticle morphology, Ni nanopillars have shown plasmon resonance in the visible spectrum of light while Au being diamagnetic has shown MO activity in pure Au nanodisks [55, 67]. These few discoveries point to the fact that nanotechnology is a vast pool of unknowns.

This book chapter focused on the symbiosis observed in bimetallic Co-Ag nanoparticles synthesized by PLiD. This was achieved by the synthesis route followed and the parameters considered while selecting the materials. Synthesis of bimetallic Co-Ag nanoparticles by PLiD helped in achieving segregated regions of Co and Ag within a single nanoparticle. This was confirmed by core-loss EELS mapping of the bimetallic nanoparticle. These nanoparticles were characterized for their optical properties by UV-vis spectroscopy and low-loss EELS. These bimetals showed improved or wider tuning of properties of their individual metal components which could be explained by the mutual sharing of free electrons between them, which had an uncanny resemblance to the symbiosis, observed in nature. The symbiotic properties can be broken down into two sections: (1) Co being the beneficiary and (2) Ag being the beneficiary. The examples for the former case can be summarized as the existence of a new surface plasmon resonance on Co surface, which was called as Ferroplasmon, whose discovery was facilitated by low-loss EELS study, and the enhancement in MO activity observed in these bimetallic Co-Ag nanoparticles (not discussed here) [22]. Similar observations for the latter case are the galvanic coupling, plasmon resonance tuning, enhancement in the plasmon quality factor and tuning of radiative quantum efficiencies. These few examples suggest the choice of materials and their properties can open new research fields which are not just limited to plasmonic and magnetic materials.

Acknowledgements

Ritesh Sachan acknowledges the National Academy of Sciences (NAS), USA, for awarding the NRC research fellowship. Ritesh Sachan also acknowledges ARO Grant No. W911NF-16-2-0038. Authors are also thankful for the useful discussions with John Prater and Ramki Kalyanaraman during the preparation of this chapter.

Author details

Abhinav Malasi[1]* and Ritesh Sachan[2,3]*

*Address all correspondence to: amalasi@utk.edu and rsachan@ncsu.edu

1 StudyFox, Leudelange, Luxembourg

2 Materials Science Division, Army Research Office, Research Triangle Park, North Carolina, USA

3 Department of Materials Science and Engineering, North Carolina State University, Raleigh, North Carolina, USA

References

[1] LaJeunesse TC, Thornhill DJ, Cox EF, Stanton FG, Fitt WK, Schmidt GW. High diversity and host specificity observed among symbiotic dinoflagellates in reef coral communities from Hawaii. Coral Reefs. 2004;**23**:596-603. DOI: 10.1007/s00338-004-0428-4

[2] Tilman D, Snell-Rood EC. Diversity breeds complementarity. Nature. 2014;**515**:44-45. DOI: 10.1038/nature13929

[3] Armelles G, Cebollada A, Garcia-Martin A, Gonzalez MU. Magnetoplasmonics: Combining magnetic and plasmonic functionalities. Advanced Optical Materials. 2013; **1**:10-35. DOI: 10.1002/adom.201200011

[4] Temnov VV, Armelles G, Woggon U, Guzatov D, Cebollada A, Garcia-Martin A, et al. Active magneto-plasmonics in hybrid metal-ferromagnet structures. Nature Photonics. 2010;**4**:107-111. DOI: 10.1038/nphoton.2009.265

[5] Linic S, Christopher P, Ingram DB. Plasmonic-metal nanostructures for efficient conversion of solar to chemical energy. Nature Materials. 2011;**10**:911-921. DOI: 10.1038/nmat3151

[6] Pena-Rodriguez O, Pal U. Au@Ag core-shell nanoparticles: Efficient all-plasmonic Fano-resonance generators. Nanoscale. 2011;**3**:3609. DOI: 10.1039/C1NR10625B

[7] Guo S, Dong S, Wang E. Three-dimensional Pt-on-Pd bimetallic nanodendrites supported on graphene nanosheet: Facile synthesis and used as an advanced nanoelectrocatalyst for methanol oxidation. ACS Nano. 2010;**4**:547-555. DOI: 10.1021/nn9014483

[8] Favazza C, Kalyanaraman R, Sureshkumar R. Robust nanopatterning by laser-induced dewetting of metal nanofilms. Nanotechnology. 2006;**17**:4229-4234. DOI: 10.1088/0957-4484/17/16/038

[9] Trice J, Thomas D, Favazza C, Sureshkumar R, Kalyanaraman R. Pulsed-laser-induced dewetting in nanoscopic metal films: Theory and experiments. Physical Review B. 2007;**75**:235439. DOI: 10.1103/PhysRevB.75.235439

[10] Sharma A, Jameel AT. Nonlinear stability, rupture and morphological phase separation in thin fluids on apolar and polar substrates. Journal of Colloid and Interface Science. 1993;**161**:190-208. DOI: 10.1006/jcis.1993.1458

[11] Krishna H, Shirato N, Yadavali S, Sachan R, Strader J, Kalyanaraman R. Self-organization of nanoscale multilayer liquid metal films: Experiment and theory. ACS Nano. 2011;**5**:470-476. DOI: 10.1021/nn1022632

[12] Sachan R, Yadavali S, Shirato N, Krishna H, Ramos V, Duscher G, et al. Self-organized bimetallic Ag-Co nanoparticles with tunable localized surface plasmons showing high environmental stability and sensitivity. Nanotechnology. 2012;**23**:275604 (1-8). DOI: 10.1088/0957-4484/23/27/275604

[13] Malasi A, Taz H, Ehrsam M, Goodwin J, Garcia H, Kalyanaraman R. Enhanced and tunable optical quantum efficiencies from plasmon bandwidth engineering in bimetallic CoAg nanoparticles. APL Photonics. 2016;**1**:76101. DOI: 10.1063/1.4954698

[14] Yadavali S, Kalaynaraman R. Nanomaterials synthesis by a novel phenomenon: The nanoscale Rayleigh-Taylor instability. AIP Advances. 2014;**4**:47116. DOI: 10.1063/1.4871482

[15] Hulteen JC, Van Duyne RP. Nanosphere lithography: A materials general fabrication process for periodic particle array surfaces. Journal of Vacuum Science and Technology A. 1995;**13**:1553-1558. DOI: 10.1116/1.579726

[16] Meng X, Qiu D. Gas-flow-induced reorientation to centimeter-sized two-dimensional colloidal single crystal of polystyrene particle. Langmuir. 2014;**30**:3019-3023. DOI: 10.1021/la404944w

[17] Jensen TR, Schatz GC, Van Duyne RP. Nanosphere lithography: Surface plasmon resonance spectrum of a periodic array of silver nanoparticles by ultraviolet-visible extinction spectroscopy and electrodynamic modeling. The Journal of Physical Chemistry B. 1999;**103**:2394-2401. DOI: 10.1021/jp984406y

[18] Denkov ND, Velev OD, Kralchevsky PA, Ivanov IB, Yoshimura H, Nagayama K. Two-dimensional crystallization. Nature. 1993;**361**:26. DOI: 10.1038/361026a0

[19] Rakers S, Chi LF, Fuchs H. Influence of the evaporation rate on the packing order of polydisper latex monofilms. Langmuir. 1997;**13**:7121-7124. DOI: 10.1021/la970757c

[20] Amos RM, Rarity JG, Tapster PR, Shepherd TJ, Kitson SC. Fabrication of large-area face-centered-cubic hard-sphere colloidal crystals by shear alignment. Physical Review E. 2000;**61**:2929. DOI: 10.1103/PhysRevE.61.2929

[21] Kuai SL, Hu XF, Hache A, Truong VV. High-quality colloidal photonic crystals obtained by optimizing growth parameters in a vertical deposition technique. Journal of Crystal Growth. 2004;**267**:317-324. DOI: 10.1016/j.jcrysgro.2004.03.015

[22] Malasi A. Symbiotic plasmonic nanomaterials: Synthesis and properties [thesis]. Knoxville: University of Tennessee; 2016

[23] Malasi A, Ge J, Carr C, Garcia H, Duscher G, Kalyanaraman R. Two-dimensionally ordered plasmonic and magnetic nanostructures on transferable electron transparent

substrates. Particle and Particle Systems Characterization. 2015;**32**:970-978. DOI: 10.1002/ppsc.201500048

[24] Nemiroski A, Gonidec M, Fox JM, Jean-Remy P, Turnage E, Whitesides GM. Engineering shadows to fabricate optical metasurfaces. ACS Nano. 2014;**8**:11061-11070. DOI: 10.1021/nn504214b

[25] Fredriksson H, Alaverdyan Y, Dmitriev A, Langhammer C, Sutherland DS, Zach M, et al. Hole-mask colloidal lithography. Advanced Materials. 2007;**19**:4297-4302. DOI: 10.1002/adma.200700680

[26] Kosiorek A, Kandulski W, Glaczynska H, Giersig M. Fabrication of nanoscale rings, dots, and rods by combining shadow nanosphere lithography and annealed polystyrene nanosphere masks. Small. 2005;**1**:439-444. DOI: 10.1002/smll.200400099

[27] Haynes CL, McFarland AD, Smith MT, Hulteen JC, Van Duyne RP. Angle-resolved nanosphere lithography: Manipulation of nanoparticle size, shape, and interparticle spacing. The Journal of Physical Chemistry B. 2002;**106**:1898-1902. DOI: 10.1021/jp013570+

[28] Schneider CA, Rasband WS, Eliceiri KW. NIH Image to ImageJ: 25 years of image analysis. Nature Methods. 2012;**9**:671-675. DOI: 10.1038/nmeth.2089

[29] Sachan R, Ramos V, Malasi A, Yadavali S, Bartley B, Garcia H, et al. Oxidation-resistant silver nanostructures for ultrastable plasmonic applications. Advanced Materials. 2013; **25**:2045-2050. DOI: 10.1002/adma.201204920

[30] Gilroy KD, Ruditskiy A, Peng H-C, Qin D, Xia Y. Bimetallic nanocrystals: Syntheses, properties, and applications. Chemical Reviews. 2016;**116**:10414-10472. DOI: 10.1021/acs.chemrev.6b00211

[31] Mayer KM, Hafner JH. Localized surface plasmon resonance sensors. Chemical Reviews. 2011;**111**:3828-3857. DOI: 10.1021/cr100313v

[32] Sachan R, Malasi A, Ge J, Yadavali S, Krishna H, Gangopadhyay A, et al. Ferroplasmons: Intense localized surface plasmons in metal-ferromagnetic nanoparticles. ACS Nano. 2014;**8**:9790-9798. DOI: 10.1021/nn5031719

[33] Khenner M, Yadavali S, Kalyanaraman R. Controlling nanoparticles formation in molten metallic bilayers by pulsed-laser interference heating. Mathematical Modelling of Natural Phenomena. 2012;**7**:20-38. DOI: 10.1051/mmnp/20127403

[34] Malasi A, Sachan R, Ramos V, Garcia H, Duscher G, Kalaynaraman R. Localized surface plasmon sensing based investigation of nanoscale metal oxidation kinetics. Nanotechnology. 2015;**26**:205701. DOI: 10.1088/0957-4484/26/20/205701

[35] Sachan R, Malasi A, Yadavali S, Griffey B, Dunlap J, Duscher G, et al. Laser induced self-assembled nanostructures on electron transparent substrates. Particle and Particle Systems Characterization. 2015;**32**:476-482. DOI: 10.1002/ppsc.201400183

[36] Garcia H, Kalyanaraman R, Sureshkumar R. Nonlinear optical properties of multi-metal nanocomposites in a glass matrix. Journal of Physics B: Atomic, Molecular and Optical Physics. 2009;**42**:175401. DOI: 10.1088/0953-4075/42/17/175401

[37] Link S, El-Sayed MA. Shape and size dependence of radiative, non-radiative and photothermal properties of gold nanocrystals. International Reviews in Physical Chemistry. 2000;**19**:409-453. DOI: 10.1080/01442350050034180

[38] Link S, El-Sayed MA. Spectral properties and relaxation dynamics of surface plasmon electronic oscillations in gold and silver nanodots and nanorods. The Journal of Physical Chemistry B. 1999;**103**:8410-8426. DOI: 10.1021/jp9917648

[39] West PR, Ishii S, Naik GV, Emani NK, Shalaev VM, Boltasseva A. Searching for better plasmonic materials. Laser & Photonics Reviews. 2010;**4**:795-808. DOI: 10.1002/lpor.200900055

[40] Han Y, Lupitskyy R, Chou T-M, Stafford CM, Du H, Sukhishvili S. Effect of oxidation on surface-enhanced Raman scattering activity of silver nanoparticles: A quantitative correlation. Analytical Chemistry. 2011;**83**:5873-5880. DOI: 10.1021/ac2005839

[41] Losurdo M, Bergmair I, Giangregorio MM, Dastmalchi B, Bianco GV, Helgert C, et al. Enhancing chemical and optical stability of silver nanostructures by low-temperature hydrogen atoms processing. The Journal of Physical Chemistry C. 2012;**115**:23004-23012. DOI: 10.1021/jp307936k

[42] Naik GV, Kim J, Boltasseva A. Oxides and nitrides as alternative plasmonic materials in the optical range. Optical Materials Express. 2011;**1**:1090-1099. DOI: 10.1364/OME.1.001090

[43] Naik GV, Shalaev VM, Boltasseva A. Alternative plasmonic materials: Beyond gold and silver. Advanced Materials. 2013;**25**:3264-3294. DOI: 10.1002/adma.201205076

[44] Shankar C, Dao ATN, Singh P, Higashimine K, Mott DM, Maenosono S. Chemical stabilization of gold coated by silver core-shell nanoparticles via electron transfer. Nanotechnology. 2012;**23**:1-10. DOI: 10.1088/0957-4484/23/24/245704

[45] Li X, Li J, Zhou X, Ma Y, Zheng Z, Duan X, et al. Silver nanoparticles protected by monolayer graphene as a stabilized substrate for surface enhanced Raman spectroscopy. Carbon. 2014;**66**:713-719. DOI: 10.1016/j.carbon.2013.09.076

[46] Fafarman AT, Hong SH, Oh SJ, Caglayan H, Ye X, Diroll BT, et al. Air-stable, nanostructured electronic and plasmonic materials from solution-processable, silver nanocrystal building block. ACS Nano. 2014;**8**:2746-2754. DOI: 10.1021/nn406461p

[47] Garcia H, Sachan R, Kalyanaraman R. Optical plasmon properties of Co-Ag nanocomposites within the mean-field approximation. Plasmonics. 2012;**7**:137-141. DOI: 10.1007/s11468-011-9286-4

[48] Malasi A, Kalyanaraman R, Garcia H. From Mie to Fresnel through effective medium approximation with multipole contributions. Journal of Optics. 2014;**16**:65001. DOI: 10.1088/2040-8978/16/6/065001

[49] Farah AE, Davidson R, Malasi A, Pooser RC, Lawrie B, Kalyanaraman R. Cobalt stabilization of silver extraordinary optical transmission sensing platforms. Applied Physics Letters. 2016;**108**:43101. DOI: 10.1063/1.4940389

[50] Prodan E, Radloff C, Halas NJ, Nordlander P. A hybridization model for the plasmon response of complex nanostructures. Science. 2003;**302**:419-422. DOI: 10.1126/science.1089171

[51] Miroshnichenko AE, Flach S, Kivshar YS. Fano resonances in nanoscale structures. Reviews of Modern Physics. 2010;**82**:2257-2298. DOI: 10.1103/RevModPhys.82.2257

[52] Mukherjee S, Sobhani H, Lassiter JB, Bardhan R, Nordlander P, Halas NJ. Fanoshells: Nanoparticles with built-in Fano resonances. Nano Letters. 2010;**10**:2694-2701. DOI: 10.1021/nl1016392

[53] Cetin AE, Altug H. Fano resonant ring/disk plasmonic nanocavities on conducting substrates for advanced biosensing. ACS Nano. 2012;**6**:9989-9995. DOI: 10.1021/nn303643w

[54] Chen F, Alemu N, Johnston RL. Collective plasmon modes in a compositionally asymmetric nanoparticle dimer. AIP Advances. 2011;**1**:032134 (1-16). DOI: 10.1063/1.3628346

[55] Chen J, Albella P, Pirzadeh Z, Alonso-Gonzalez P, Huth F, Bonetti S, et al. Plasmonic nickel nanoantennas. Small. 2011;**7**:2341-2347. DOI: 10.1002/smll.201100640

[56] Ge J, Malasi A, Passarelli N, Pérez LA, Coronado EA, Sachan R, et al. Ferroplasmons: Novel plasmons in metal-ferromagnetic bimetallic nanostructures. Microscopy and Microanalysis. 2015;**21**(S3):2381-2382. DOI: 10.1017/S1431927615012684

[57] Brongersma ML, Hartman JW, Atwater HA. Electromagnetic energy transfer and switching in nanoparticle chain arrays below the diffraction limit. Physical Review B. 2000;**62**:R16356-R16359. DOI: 10.1103/PhysRevB.62.R16356

[58] Passarelli N, Pérez LA, Coronado EA. Plasmonic interactions: From molecular plasmonics and Fano resonances to ferroplasmons. ACS Nano. 2014;**8**:9723-9728. DOI: 10.1021/nn505145v

[59] Sonnichsen C, Franzl T, Wilk T, von Plessen G, Feldmann J, Wilson O, et al. Drastic reduction of plasmon damping in gold nanorods. Physical Review Letters. 2002;**88**:77402. DOI: 10.1103/PhysRevLett.88.077402

[60] Wokaun A, Gordon JP, Liao PF. Radiation damping in surface-enhanced Raman-scattering. Physical Review Letters. 1982;**48**:957-960. DOI: 10.1103/PhysRevLett.48.957

[61] Tsakmakidis KL, Wartak MS, Cook JJH, Hamm JM, Hess O. Negative-permeability electromagnetically induced transparent and magnetically active metamaterials. Physical Review B. 2010;**81**:195128. DOI: 10.1103/PhysRevB.81.195128

[62] Sugawa K, Tahara H, Yamashita A, Otsuki J, Sagara T, Harumoto T, et al. Refractive index susceptibility of the plasmonic palladium nanoparticle: Potential as the third plasmonic sensing material. ACS Nano. 2015;**9**:1895-1904. DOI: 10.1021/nn506800a

[63] Jiang R, Qin F, Ruan Q, Wang J, Jin C. Ultrasensitive plasmonic response of bimetallic Au/Pd nanostructures to hydrogen. Advanced Functional Materials. 2014;**24**:7328-7337. DOI: 10.1002/adfm.201402091

[64] Meneses-Rodriguez D, Ferreiro-Vila E, Prieto P, Anguita J, Gonzalez MU, Garcia-Martin JM, et al. Probing the electromagnetic field distribution within a metallic nanodisk. Small. 2011;**7**(23):3317. DOI: 10.1002/smll.201101060

[65] Park S, An S, Mun Y, Lee C. UV-enhanced NO_2 gas sensing properties of SnO_2-core/ZnO-shell nanowires at room temperature. ACS Applied Materials & Interfaces. 2013;**5**:4285-4292. DOI: 10.1021/am400500a

[66] Roge V, Georgantzopoulou A, Mehennaoui K, Fechete I, Garin F, Dinia A, et al. Tailoring the optical properties of ZnO nano-layers and their effect on in vitro biocompatibility. RSC Advances. 2015;**5**:97635-97647. DOI: 10.1039/C5RA16156H

[67] Sepúlveda B, González-Díaz JB, García-Martín A, Lechuga LM, Armelles G. Plasmon-induced magneto-optical activity in nanosized gold disks. Physical Review Letters. 2010;**104**:147401. DOI: 10.1103/PhysRevLett.104.147401

Section 4

Biomedical and Other Applications

Chapter 13

Applications of Gold Nanoparticles in Cancer Imaging and Treatment

Shouju Wang and Guangming Lu

Additional information is available at the end of the chapter

http://dx.doi.org/10.5772/intechopen.70901

Abstract

Cancer is one of the leading causes of death worldwide. In the last two decades, the development of nanotechnology has facilitated our ability to design new nanoparticles for the diagnosis and treatment of cancer. In this chapter, we reviewed the applications of gold nanoparticles as contrast agents for cancer imaging, including optical imaging, photoacoustic imaging, and X-ray–based imaging. We also reviewed their applications as delivery carriers for small molecule drugs, therapeutic genes, vaccines, and adjuvants and as therapeutic agents by themselves in cancer treatment, including photothermal therapy, photodynamic therapy, and radiation therapy.

Keywords: gold nanoparticles, cancer, cancer imaging, cancer treatment, localized surface plasmon resonance

1. Introduction

With over 7 million new deaths per year, cancer remains one of the leading causes of death worldwide. The mortality of cancer is estimated to reach 13.1 million in the next two decades. Surgery, radiation therapy, and chemotherapy are key players in treatment of cancer. These treatments slow the progression of disease and prolong the survival of patients. Nonetheless, new treatments are in urgent need due to the greater understanding of the complexity of genetic and environmental factors. Recently, the development of nanotechnology has facilitated our ability to design new nanoparticles for the diagnosis and treatment of cancer [1].

Due to their unique physical and chemical properties, gold nanoparticles (ranging from 1 to 100 nm in one dimension at least) have attracted remarkable attention in recent years [2]. The gold nanoparticles are suitable for drug delivery given their large surface area to

volume ratio. Owing to localized surface plasmon resonance (LSPR), gold nanoparticles, such as gold nanorods, nanocages, nanoshells, and nanostars, have strong light scattering and/or absorbance and have been extensively explored for bioimaging, cancer treatment, and both. In addition, given the strong binding affinity of gold to thiol and amine groups, the surface of gold nanoparticles can be easily functionalized with biomolecules such as DNA, siRNA, peptides, antibodies, and receptors. Gold nanoparticles also have a long history for clinical applications (for the treatment of rheumatoid arthritis) [3].

2. Gold nanoparticles in cancer imaging

2.1. Light scattering–based imaging

The scattering cross section of gold nanoparticles increases with the growth of their size. In general, gold nanoparticles can scatter light with the cross section more than 1 million times stronger than that of the emission from a fluorescent dye. Gold nanoparticles with a diameter greater than 10 nm can be visualized by dark-field scattering microscopy. Compared to a fluorescent dye, the gold nanoparticles are photostable and the scattering light does not blink. These features make gold nanoparticles attractive imaging probes for optical imaging.

Different shapes of gold nanoparticles, such as gold nanorods, nanocages, and nanostars, have been tested by dark-field scattering microscopy. In 2003, Sokolov *et al.* [4] conjugated antibodies against epidermal growth factor receptor (EGFR), a glycoprotein that is overexpressed in epithelial malignant cells, for molecular-specific optical imaging. The gold nanoparticles they used were ~12 nm in diameter, which is approximately the same size as that of antibodies. The EGFR-overexpressed cells can be visualized individually by the strong scattering light reflected from a laser pointer with power output less than 5 mW. Later, El-Sayed *et al.* [5] demonstrated that the anti-EGFR antibodies–conjugated gold nanoparticles can differentiate EGFR-overexpressed malignant cells from healthy cells by simple dark-field optical microscopy. Other gold nanoparticles with different size and shapes were also explored. As demonstrated by Huang *et al.* [6], gold nanorods could scatter light in near-infrared (NIR) region and thus enable detection of head and neck cancer cells in biological tissues. In this work, they found that the extinction spectra of the gold nanorods on the cell surface were greatly red-shifted compared with that of free nanorods of the same size. This red shift is believed to rise from the change in the local refractive index after binding between gold nanoparticles and cells or the interparticle interaction between the gold nanorods on the cell surface. By conjugation, gold nanostars with hyaluronic acid, our group [7] demonstrated that CD44-overexpressed malignant cells could be observed under dark-field optical microscopy through the binding between cell surface receptor and functionalized gold nanostars.

Another imaging modality based on light scattering is optical coherence tomography (OCT). OCT captures the changes in phase and intensity from the scattered light to provide optical cross-sectional images of tissues. It employs NIR light to produce a three-dimensional image of tissues with micrometer resolution. Gobin *et al*. [8] demonstrated dramatic contrast

enhancement of tumors on OCT images after systematically injected gold nanoshells. The quantification of OCT images showed a 56% increase in tumor intensity 20 h after the injection of gold nanoshells. In contrast, conventional optimal contrast agents for OCT, such as microbubbles and microspheres, typically enhance contrast less than 5% *in vivo*. Cang *et al.* [9] described that gold nanocages with a 35 nm edge length can provide enhanced contrast for OCT in tissue phantoms. Similarly, gold nanorods with LSPR wavelengths overlapping the OCT light source have been demonstrated for OCT contrast enhancement [10]. One interesting observation in that report is that the gold nanorods generate little signal when the wavelength of OCT source is outside their spectral bandwidth. This result indicates the possibility of spectral multiplexing for contrast-enhanced OCT.

2.2. Photoacoustic imaging

The photoacoustic imaging (PAI) is based on the acoustic waves generated by the thermal expansion of materials induced by optical excitation. When a pulsed laser irradiates materials, the temperature rise of the materials produces ultrasonic waves by periodic thermal expansion. The images of PAI are then constructed by detection of the ultrasonic waves. Since the ultrasonic wave penetrates deeper than light in tissues, the imaging volume and depth of PAI are significantly higher than those of optical imaging.

Gold nanoparticles have been highly attractive for PAI due to their excellent photothermal conversion ability and tunable optical properties. Jokerst *et al*. [11] visualized photoacoustic signal from gold nanorods accumulated in ovarian cancer tumors *in vivo* by PAI. The increase fold of photoacoustic signal was in good linear relationship with the concentration of intravenously injected gold nanorods ($R^2 = 0.97$). *Song et al*. demonstrated the use of gold nanocages as lymph node tracers for PAI. They identified gold nanocages labeled sentinel lymph nodes as deep as 33 mm below the skin surface in an animal model. Our group worked with Lin and coworkers [12] demonstrated that gold vesicles composed of assembled gold nanoparticles have strong photoacoustic signal due to the plasmonic coupling between the adjacent gold nanoparticles in the vesicular membranes. To specifically target tumor neovasculature, our group worked with Nie and coworkers [13] to functionalize gold nanostars with cyclic arginine-glycine-aspartic acid (cRGD) peptides, which possess high affinity to integrin $\alpha_v\beta_3$ overexpressed by neovessels of tumors. As shown in **Figure 1**, benefited from targeting ability of cRGD-conjugated gold nanostars, three-dimensional photoacoustic images of tumor neovessels could be obtained with high spatial resolution and deep imaging depth (up to centimeters under skin) using a laser fluence of 6 mJ/cm^2, which is far less than the safety limit for laser skin exposure (20 mJ/cm^2). Another work from our group designed pH (low) insertion peptides (pHLIPs)-conjugated gold nanostars for tumor targeting PAI [14]. pHLIPs are 35 amino acid peptides with pH-dependent transmembrane activity. After conjugation, the functionalized gold nanostars could be activated in the mild acidic microenvironment of tumors and internalized by cells rapidly. The photoacoustic images showed that at 24 h after systematic injection, the pHLIPs-conjugated nanostars had a 50% higher tumor signal than the gold nanostars without functionalization.

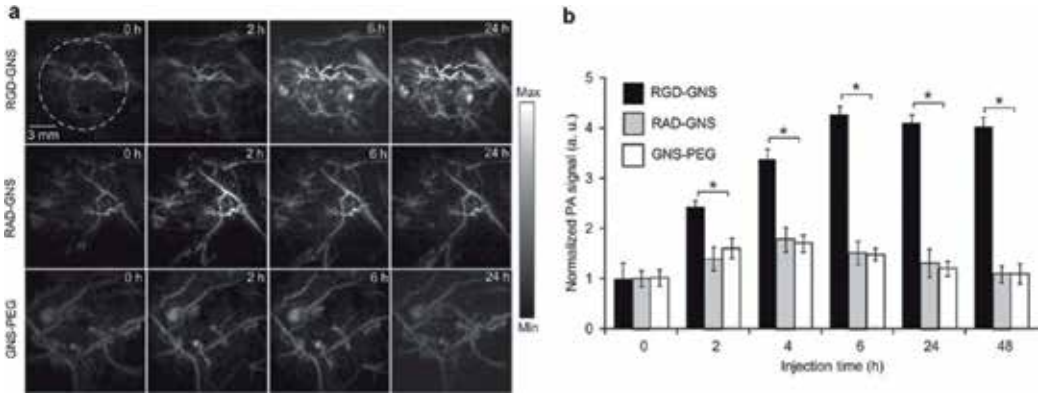

Figure 1. cRGD-conjugated gold nanostars for PAI. (a) Sequential photoacoustic images captured before, 2, 6, and 24 h post injection of RGD-GNS, control peptide–conjugated gold nanostars (RAD-GNS), and PEGylated gold nanostars (GNS-PEG). (b) Quantification of the signal intensity in region of interest. Reproduced from Ref. [13].

2.3. X-ray–based imaging

Computed tomography (CT) is one of the most widely used diagnostic imaging modalities for cancer. It can obtain whole volume 3D anatomical images with high spatial resolution in a cost-effective fashion. However, the contrast between different types of soft tissues is poor on CT images; thus, contrast agents, like iodine-based compounds, need to be injected to differentiate tumors from healthy tissues.

Since the attenuation of X-rays depends greatly on the atomic numbers of elements, gold has a stronger X-ray attenuation coefficient than other elements naturally existed in human bodies. Therefore, the accumulation of gold nanoparticles in tumors can significantly increase X-ray attenuation, resulting in high contrast between tumor and healthy tissues on CT images. Deoxyglucose-labeled gold nanoparticles are described as potential CT contrast agents [15]. The cancer cell samples showed significant contrast enhancement after incubation with these gold nanoparticles on multiple CT slices. The use of acetylated dendrimer-entrapped gold nanoparticles to image cancer *in vivo* is also reported [16]. The gold nanoparticles with a mean diameter of 2.6 nm were able to increase the attenuation of tumors after intratumoral and intraperitoneal administration in a mice model of human lung adenocarcinoma. Our group demonstrated that PEGylated gold nanostars have higher CT values when compared to iodixanol at equivalent concentration. The CT images of tumor-bearing mice exhibited 10-fold enhancement in tumors after injection of PEGylated gold nanostars (**Figure 2**) [17]. We also reported the use of Gd chelates–conjugated gold nanoprisms as a new class of contrast agents for CT/MRI dual-modality imaging [18]. The CT values of Gd chelates–conjugated gold nanoprisms had a linear relationship with the concentration of gold at an attenuation coefficient calculated to be 959.3 HU L g^{-1}. The conjugated Gd chelates exhibited high T1 relaxivity for MR imaging.

The surface of gold nanoparticles can be easily functionalized with tumor-targeting moieties, such as ligands, antibodies, and aptamers, to selectively image tumors via active targeting strategy. For example, Hainfeld *et al.* [19] conjugated gold nanoparticles with polyethylene

http://dx.doi.org/10.5772/intechopen.70901

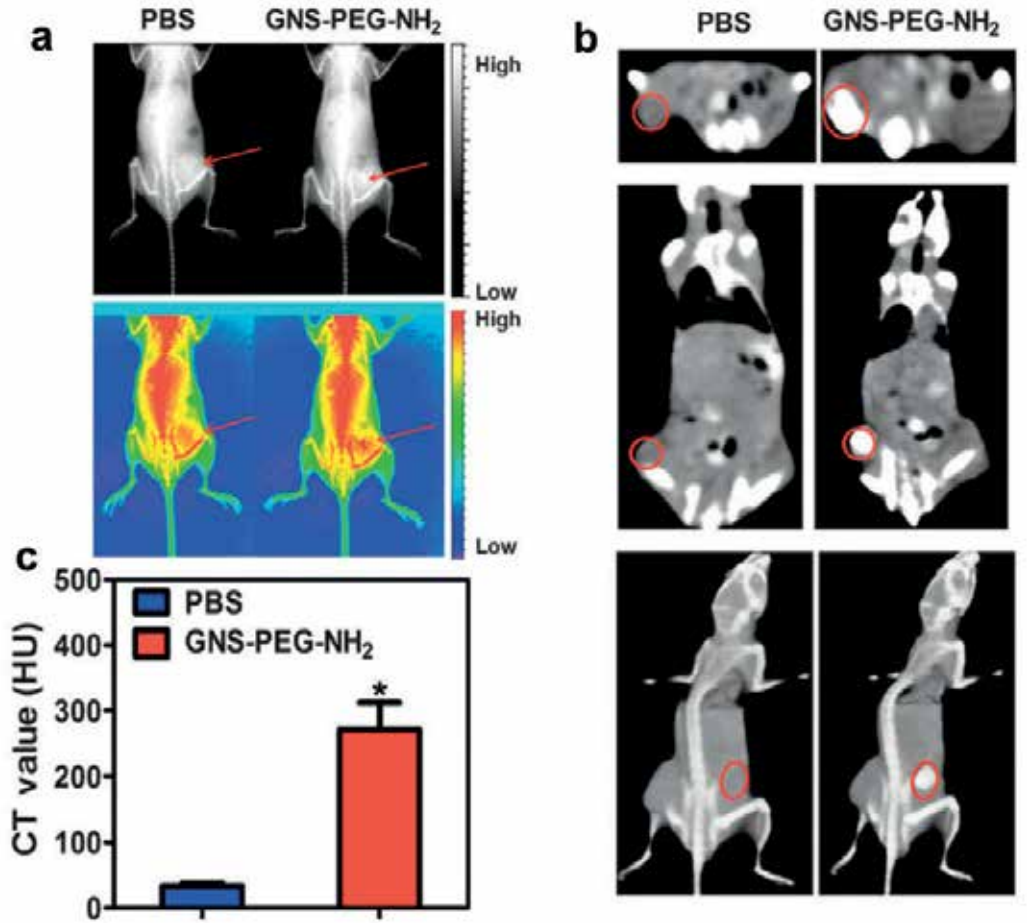

Figure 2. Amino-PEG functionalized gold nanostars (GNS-PEG-NH_2) for X-ray and CT imaging. (a) and (b) X-ray and CT images of MCF-7 tumor-bearing mice after intratumoral of PBS and GNS-PEG-NH_2. (c) Corresponding CT values of tumors in (b). Reproduced from Ref. [17].

glycol (PEG) and anti-Her2 antibodies (Herceptin) as Her2-targeting diagnostic tools. An *in vitro* study showed the nanoconjugates specifically targeting Her2-positive breast cancer BT-474 cells *vs.* Her2-negative breast cancer MCF7 cells with a gold mass ratio of 39.4 ± 2.7:1. In the *in vivo* studies, the BT-474 tumors showed 1.6 times higher CT attenuation than MCF7 tumors after intravenous injection of anti-HER2–conjugated gold nanoparticles. The Housefield Unit (HU) of BT-474 tumors was 22-fold higher than that of surrounding muscles, enabling the detection of small tumors on micro-CT. In another report, Kim *et al.* [20] functionalized gold nanoparticles with a prostate-specific membrane antigen (PSMA) RNA aptamer to establish prostate cancer targeting CT probes. The aptamer-conjugated gold nanoparticles exhibited fourfold higher CT values in PSMA-overexpressed LNCaP cells than that in PSMA negative PC3 cells. Furthermore, the aptamers on gold nanoparticles could be used to load doxorubicin to kill targeted cells more efficiently.

3. Gold nanoparticles in drug delivery

3.1. Small molecule drug delivery

Gold nanoparticles have been explored as drug carriers due to the following advantages: (1) the large surface area provides high loading capacity for drug loading and improves the hydrophilicity and stability of drugs; (2) the ability to modify surface with targeting ligands to enhance the tumor selective accumulation compared to free drugs; (3) the passive targeting ability to tumor site due to their leaky neovessels, which is called enhanced permeability and retention(EPR) effect; and (4) the controlled release of loaded drugs in response to internal or external stimulus.

The enhanced tumor accumulation of gold nanoparticles can be utilized for drug delivery to increase therapeutic potent and reduce side effects. Xiao *et al.* [21] demonstrated that cRGD-conjugated gold nanorods selectively delivered doxorubicin to tumors with a tumor/muscle ratio as high as 16.6 ± 1.2 at 5 h post injection. Given that the nanorods were labeled with radioactive 64Cu, the biodistribution of nanorods could be easily observed and quantified by microPET/CT *in vivo*. In another work, You *et al.* [22] connected TNYL-RAW, a 14-mer peptide with high binding affinity to EphB4, with doxorubicin-loaded gold nanoshells. Since EphB4 is a receptor overexpressed by numerous types of tumor, such nanoshells selectively delivered doxorubicin to Hey tumors in nude mice model at 24 h after intravenous injection.

Gold nanoparticles can release loaded drugs in response to external stimulus like light. You *et al.* [23] reported successful loading of doxorubicin on gold nanoparticles and nanoshells after 24 h of mixing at room temperature. Interestingly, they found that the payload of doxorubicin is exceptionally high (up to 70%) in gold nanoshells than that in gold nanoparticles (~20%). They believed the hollow interior of the nanoparticles increased the effective surface area for the high payload loading of doxorubicin. Furthermore, the release of doxorubicin can be triggered by NIR laser irradiation to selectively increase the drug amount in tumors. Similarly, Yavuz *et al.* [24] used the hollow interiors of gold cages to load doxorubicin and covered the surface of gold nanocages with thermoresponsive polymers to prevent the preloading doxorubicin leaked from the porous walls. Such design enables the gold nanoparticles to release drugs in an NIR laser controlled fashion.

Some gold nanoparticles are designed to behave dramatically to various internal stimuli in the microenvironment of tumors. For instance, Wang *et al.* [25] tethered doxorubicin onto gold nanoparticles with a PEG spacer *via* an acid-labile linkage. They found that this smart drug carrier could release doxorubicin in response to the low pH of endosome and enhance therapeutic efficacy by overcoming the drug resistance of MCF-7/ADR cancer cells.

3.2. Gene delivery

Gene therapy attempts to treat cancer by altering the dysregulated gene expression of tumor cells. The successful regulation of gene expression requires compaction of DNA/RNA, rapid cellular uptake and endosomal escape, protection from degradation in blood stream and cytoplasm, and effective delivery of DNA/RNA to the nucleus. Therefore, carriers for efficient and safe DNA/RNA delivery are critical for the development of gene therapy.

Gold nanoparticles provide a potent platform for therapeutic gene delivery. Braun *et al.* [26] coated 40 nm gold nanoshells with siRNA and Tat peptide-lipid cell internalizing agents to silence gene expression in a particular subset of cells. They showed that the gene silencing can be temporally and spatially controlled using a pulsed NIR laser *via* light-induced siRNA release. Jensen *et al.* [27] complexed a high-density monolayer of siRNA on the surface of gold nanoparticles, a nanostructure so-called spherical nucleic acid (SNA), to knockdown the expression of oncoprotein Bcl2Like12 (Bcl2L12) of glioma cells. The *in vitro* studies showed SNAs accumulated in human glioma U87MG cells efficiently and neutralized Bcl2L12, a potent caspase and p53 inhibitor specifically overexpressed by the majority of human primary gliomas, without any chemical modifications and auxiliary transfection methods. After intravenous injection, the SNAs penetrated the blood-brain barrier, disseminated throughout glioma explants, inhibited Bcl2L12 expression in glioma and reduced tumor volume in mice model, without adverse side effects. To specifically deliver siRNA to tumors, our group constructed a CD44-targeting heat shock protein 72 (Hsp72) depletion nanosystem by assembling gold nanostars with siRNA against Hsp72 and hyaluronic acid, a targeting moiety binds to CD44, in a layer-by-layer manner [7]. We showed that the obtained nanosystem could selectively inhibit the expression of Hsp72 in triple negative breast cancer (TNBC) cells, sensitize TNBC cells to hyperthermia and enhance the therapeutic efficacy of photothermal therapy with minimal side effect both *in vitro* and *in vivo*.

3.3. Adjuvant and vaccine delivery

Immunotherapy is a burgeoning therapeutic modality for cancer treatment. The goal of immunotherapy is to harness the host immune system to attack and eradicate cancer cells [28]. There are several ways to enhance the innate power of immune system to fight cancer. Using cancer vaccine is one of the most extensively studied approaches to boost the immune system's response [29].

Gold nanoparticles are promising for delivery of cancer vaccine, because they preferentially accumulate within tissues and cells of the immune system, and have a large surface area for vaccine loading. Lin *et al.* [30] conjugated large quantities of self-assembled tumor-associated peptides on the surface of gold nanoparticles as a cancer vaccine platform. The so-called gold nanovaccines were able to effectively deliver antigens to dendritic cells (DCs) and stimulated cytotoxic T lymphocytes (CTL) better than free peptides.

Since the tumor cells can secrete immunosuppressive cytokines and/or attract immune suppressive cells to evade the attack from immune system, co-delivery of adjuvants with vaccine has been explored to elicit a stronger CTL response to existing tumors. In one study, Lee *et al.* connected red fluorescent protein (RFP, as a model cancer antigen) and CpG oligodeoxynucleotide (CpG ODN, a short single-stranded synthetic DNA used as vaccine adjuvant) on 7 nm gold nanoparticles [31]. The nanoparticles were injected *via* footpad to RFP-expressing B16F10 melanoma tumor-bearing mice. After interacted with DCs, remarkable antitumor activity was induced through a Th1-mediated cell response. In another report, gold nanoparticles were conjugated with both tumor-associated glycopeptides antigens and a peptide from

complement derived protein C3d to act as an adjuvant to activate B-cells [32]. The immunized mice represented robust immune response with production of immunoglobulins, containing both IgM and IgG isotypes.

4. Gold nanoparticles in cancer treatment

4.1. Photothermal therapy

Photothermal therapy (PTT) is a central application of gold nanoparticles in cancer treatment. Gold nanoparticles absorb incident photons and convert them to heat to destroy cancer cells. Due to their unique optical properties as a result of LSPR, gold nanoparticles absorb light with extremely high efficiency (cross section at ~10^{9} M^{-1} cm^{-1}), which ensures effective PTT at relatively low radiation energy. The abnormal vascular structure of tumor is inefficient in dissipating heat, thus the tumors are more sensitive to hyperthermia than healthy tissues. When irradiated by light, the heat generated by gold nanoparticles causes biomolecule denaturation and cellular membrane disruption and kills tumor cells [33].

The wavelength of incident light is important for PTT. The NIR light has maximal penetration in tissues because most components of biotissues, including water, hemoglobin, skin, and other pigments, show minimal absorption and scattering of light in this region. Typically, the NIR light can reach ~1 cm deep in human body. Various nanoparticles that can absorb NIR light have been synthesized and tested for PPT, including nanorods, nanoshells, nanocages, nanostars, nanovesicles, and so on. Hirsch *et al.* [34] demonstrated that PEGylated silica@Au gold nanoshells induced irreversible thermal damage to tumor under exposure to low dose of NIR light (4 W/cm^2) for 4–6 min after systematic injection. Without nanoshells, the exposure of NIR light increased temperature less than 10°C. In the *in vivo* studies, the temperature of tumor was monitored by MRI in real time, and the maximal depths of thermal damage spanning were about 4–6 mm after 6 min of irradiation.

Selective PTT has been demonstrated by using tumor-targeting gold nanoparticles. One strategy for selective PTT is to design immune-targeted gold nanoparticles against receptors overexpressed by cancer cells. For instance, in an experiment designed by Huang *et al.*, [6] gold nanorods were conjugated to anti-EGFR antibodies, incubated with malignant oral epithelial cells (HOC 313 clone 8 and HSC 3) and normal epithelial cells (HaCat), followed by exposure to NIR laser at 800 nm. It is found that HOC 313 clone 8 and HSC 3 destroyed at about half the laser energy required to destroy HaCat cells. Another strategy is using engineered gold nanoparticles responsible to the microenvironment of tumors. Nam *et al.* [35] synthesized a hydrolysis-susceptible citraconic amide moiety and introduced to the surface of 10-nm sized gold nanoparticles. After internalization by cancer cells, the obtained "smart" gold nanoparticles exhibited both positive and negative charges in response to the low pH of endosomes. Then, the electrostatic between the nanoparticles induced rapid aggregation and shifted the absorption to NIR region. In this way, the gold nanoparticles can selectively destroy cancer upon NIR laser irradiation. In another report from our group [36], gold nanostars were decorated

with long-chain amine/carboxyl-terminated PEG. Such gold nanostars were designed to change cell affinity reversibly in response to the change of extracellular pH by utilizing the reversible protonation of amine and carboxyl groups. After intravenous injection, these gold nanostars showed enhanced tumor accumulation and photothermal therapeutic efficacy than that of pH-insensitive PEGylated gold nanostars.

One strategy to increase the therapeutic index of PTT is to increase the photothermal conversion efficacy of gold nanoparticles. Higher photothermal conversion efficacy means lower laser power density required for tumor ablation and less damage to skin and other healthy tissues. Chen *et al.* [37] found that the photothermal conversion efficacy decreases as the effective radius of gold nanorods increases. The highest conversion efficacy (~95%) was determined in gold nanorods with size of 10 × 38 nm. In another report [38], the conversion efficacy is 21% for gold nanorods with size of 7 × 23 nm. Therefore, the conversion efficacy of gold nanoparticles is highly dependent on their size and shape. Huang *et al.* [39] reported the synthesis of gold bellflowers by a liquid-liquid-gas triphase interface system. The gold bellflowers showed photothermal conversion efficiency at 74%, which is higher than most reported gold nanoparticles. Ma and coworkers working with our group [40] demonstrated similar photothermal conversion efficiency (~70%) in triangular gold nanoprisms (**Figure 3**).

Reversing the thermoresistance of malignant cells is another pathway to enhance the therapeutic effect of PTT. Recently, Wang *et al.* [41] complexed gold nanorods with siRNA against BAG3, a cytoprotective protein preventing cell death from hyperthermia, to sensitize cancer cells to PTT treatment. They demonstrated that the gold nanorods-siRNA complex enhanced apoptosis and antitumor effect of PTT both *in vitro* and *in vivo* by knocking down the expression of BAG3 in tumor cells. Our group entrapped siRNA against Hsp72, a key chaperone for the thermoresistance of cells, onto the surface of gold nanostars [7]. We showed that the siRNA functionalized gold nanostars sensitized breast cancer cells to hyperthermia and significantly enhanced the therapeutic efficacy. Similarly, Chen *et al.* [42] loaded a small molecule Glut1 inhibitor of diclofenac (DC) on the surface of gold nanorods. The DC depleted the Glut1 level in tumor cells, blocked glycolysis, decreased ATP level, and finally inhibited the expression of heat shock proteins (Hsp). Without the protection from Hsp, the tumor cells were more easily to be destroyed by PTT.

Due to the effect of surface melting, gold nanoparticles may undergo laser-induced shape transformation far below the bulk melting point and lose the photothermal conversion ability. Gold nanoparticles are easier to reshape under irradiation of a pulse laser than under that of a continuous wave laser because the light energy is harder to release from the lattice of gold nanoparticles to surrounding tissues upon pulse laser irradiation [43]. Takahashi et al. [44] demonstrated that gold nanorods were reshaped into spherical nanoparticles under pulsed NIR laser irradiation and did not kill cells upon successive laser irradiation. Wang et al. compared the photothermal stability of gold nanorods, nanohexapods, and nanocages under pulsed laser irradiation. They showed that gold nanorods started to melt at 15 mW/cm^2, whereas nanohexapods and nanocages started to melt at 25 mW/cm^2. Chen *et al.* [45] found that gold nanocages were stable under continuous wave laser but melt to nanoparticles under

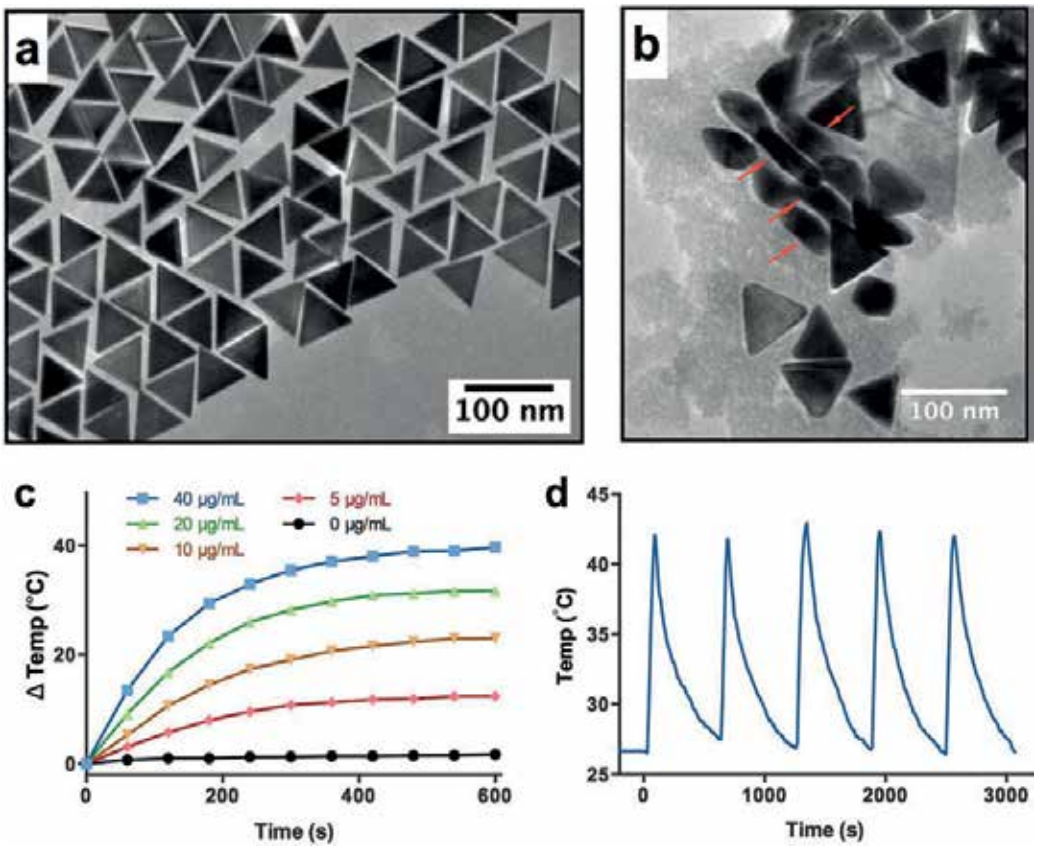

Figure 3. PEGylated gold nanoprism for PTT. (a) and (b) Representative TEM images of PEGylated gold nanoprism. (c) Heating curves of various concentration of PEGylated gold nanoprism under laser irradiation. (d) Photostability of gold nanoprism under five cycles of laser irradiation. Reproduced from Ref. [40].

pulse laser. Thus, the type of laser and the photothermal stability of gold nanoparticles should be considered in practical applications of PTT.

4.2. Photodynamic therapy

The principle of photodynamic therapy (PDT) has been known for over 100 years. PDT involves three nontoxic components, photosensitizer, light, and oxygen, that are needed to generate singlet oxygen ($^1O_2$) or/and reactive oxygen species (ROS) to kill cells. Generally, the photosensitizer is administrated to localize in tumor first, activated by light of a specific wavelength to transfer energy from light to molecular oxygen, and damage cells by the generated $^1O_2$ and ROS. Since $^1O_2$ and ROS quench after a very short time, PDT is a localized treatment similar to PTT. However, due to the poor solubility of most photosensitizers, it is challenging to deliver them to tumor with high specificity for treatment.

To address this challenge, gold nanoparticles are engineered as carriers of photosensitizer. Camerin et al. [46] bound Zn(II)-phthalocyanine disulfide (C11Pc), a photosensitizer bearing

hexyl chains and a sulfur terminated C11 chain, with gold nanoparticles and investigated the photodynamic therapeutic effect in a melanoma mice model. Compared with free C11Pc, the ratio between the amount of photosensitizer recovered from melanoma and skin increased from 2.3 to 5.5 for gold nanoparticles bound C11Pc at 24 h after injection. The nanoparticle-bound C11Pc also showed a better antitumor effect than that of free C11Pc at the same concentration.

With rational design, the PDT and PTT effect of photosensitizer-loaded gold nanoparticles can be combined to further enhance the therapeutic efficacy via synergistic effect. Jang *et al.* [47] developed a gold nanorods-photosensitizer complex (GNR-AlPcS4) for PDT/PTT dual-modality treatment. In *in vitro* studies, GNR-AlPcS4–treated cells showed fourfold greater intracellular uptake and enhanced therapeutic efficacy than that of free AlPcS4-treated cells. After intravenous injection of GNR-AlPcS4, PDT and PTT effect can be induced by irradiation of 670 and 810 nm laser separately. Compared with PDT alone, the tumor growth inhibition increased from 79 to 95% for PDT/PTT treatment. Our group covalently conjugated Chlorin e6, a commonly used photosensitizer, with gold nanostars [48]. The peak of LSPR of gold nanostars was tuned to match the absorbance of Chlorin e6. Such design enables the simultaneous activation of PDT and PTT effect upon irradiation of single wavelength NIR laser (**Figure 4**). Our results demonstrated that the photostability of photosensitizers and gold nanostars is different, and thus the ratio between PDT and PTT effect can be modulated by adjusting irradiation time. The synergistic PDT/PTT effect significantly enhanced the therapeutic efficacy and inhibited the growth of breast cancer in animal models.

Certain gold nanoparticles have the ability to generate $^1O_2$ and ROS upon light irradiation, allowing them to act as photosensitizers by themselves rather than as delivery vehicles. Krpetić *et al.* [49] showed endosomal gold nanoparticles disrupted endosome and distributed into cytosol of cancer cells upon low-intensity laser irradiation. They ruled out the possibility of photothermal effect as the underlying mechanism due to the low intensity of laser used in their experiments and observed higher concentration of ROS in the cells incubated with gold nanoparticles than in the control cells incubated without nanoparticles after laser irradiation. Pasparakis [50] found that the gold nanoparticles, with a mean diameter of 40 nm, could generate $^1O_2$ upon either pulse or continuous wave laser irradiation. Cancer cell death was observed after incubation with gold nanoparticles, followed by laser irradiation. Although these reports demonstrated the potential of using gold nanoparticles as photosensitizers in the future, the wavelengths of light used in these experiments are 514 and 532 nm. The poor penetration ability of light in this wavelength region limits their potential for *in vivo* applications.

4.3. Photon-based radiation therapy

Radiation therapy (RT) is a major component of the modern therapeutic modalities of cancer. Photon-based radiation therapy uses high-energy gamma rays, typically 8–18 MeV for deep tumors, to control the growth of tumor by causing DNA damage *via* direct ionization or through production of free radicals and secondary electrons [51]. Since gamma rays have a low linear energy transfer (LET, energy deposited per unit distance traversed), a large fraction of radiation dose deposits in healthy tissue before and behind the planned target volume [52].

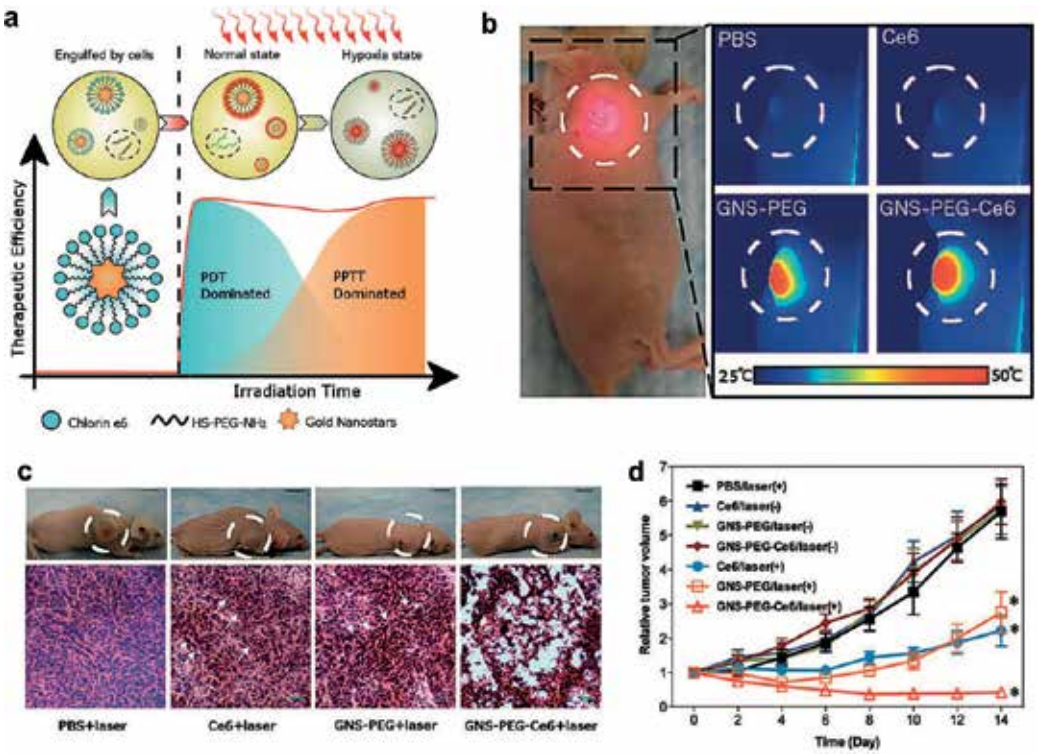

Figure 4. Chlorin e6-conjugated gold nanostars (GNS-PEG-Ce6) for PDT/PTT. (a) Schematic representation of PDT/PTT upon single laser irradiation. (b) Thermal images of MDA-MB-435 tumor-bearing mice under laser irradiation. (c) Digital photos and H&E stained tumor sections collected from each group of mice at the 8th day post treatment. (d) Tumor growth curves of each group after treatment. Reproduced from Ref. [48].

When gamma rays excited core electrons near the atomic nucleus of elements, low energy electrons may be released by a so-called Auger de-excitation processes. Gold nanoparticles have high atomic number and are more likely to generate Auger electrons when compared to light elements of biological tissues. The Auger electrons are effective in breaking DNA and only damage cells in a short distance less than the size of a single cell. This short-range therapeutic effect makes gold nanoparticles potent to selectively sensitize tumor cells to photon-based radiation therapy. Hainfeld *et al.* [53] demonstrated the use of gold nanoparticles with a mean diameter of 1.9 nm for enhancement of radiation therapy. After a single intravenous injection of gold nanoparticles, the tumor-to-normal tissue gold concentration ratios reached about 8:1. The 1-year survival of mice bearing EMT-6 breast cancer increased from 20% (with X-rays alone) to 86% (sensitized by gold nanoparticles) after several minutes of 250 kV gamma ray irradiation. The nanoparticles treated mice presented no overt clinical signs for more than 1 year.

One problem of using ultrasmall nanoparticles is the relatively short half-life due to the rapid excretion from kidney. To reduce the dosage of gold, larger nanoparticles with tumor-targeting moieties have been exploited. In one study, thio-glucose bound gold nanoparticles were synthesized as a sensitizer to enhance radiation therapy for ovarian cancer cells [54]. Since

malignant cells metabolize faster than healthy cells, the glucose coating of gold nanoparticles resulted in an ~31% increase of cell uptake compared to that of naked nanoparticles. As a result, the inhibition of cell proliferation increased 30.48% for 90 kV and 26.88% for 6 MV gamma ray irradiation. In another report, 30 nm gold nanoparticles were conjugated to Herceptin, a monoclonal antibody against Her2, to target MDA-MB-361 in a subcutaneous mice model [55]. After gamma ray irradiation, the tumors treated with gold nanoparticles resulted in 46% tumor regression, whereas the tumors treated by gamma ray alone increased 16% in tumor volume.

Although larger gold nanoparticles achieve improved accumulation in specific tumors due to the EPR (enhanced penetration and retention) effect, some authors argue that as gold nanoparticles become larger, more of the secondary electrons occur in the core of the nanoparticles, thus reducing the dose delivered to the cytoplasm around the nanoparticles. Therefore, the best size range of gold nanoparticles for photon-based radiation therapy is still under debate.

4.4. Ion-based radiation therapy

Ion-based radiation therapy is another type of RT. Instead of utilizing high-energy gamma rays, ion-based radiation therapy uses ion beams as the radiation source, such as the ions of hydrogen (protons), helium, carbon, or oxygen. The ion radiation is attractive because it has a strong LET near the end of the track, which is called the Bragg peak. The location of Bragg peak can be extended by increasing the energy of the ion so that the volume of irradiation can be better defined in ion irradiation than in photon irradiation.

One of the proposed mechanisms for radiosensitization of gold nanoparticles is that the ion beams excite surface plasmons and thus increase the yield of secondary electrons. Li *et al*. [56] demonstrated the radiosensitization effect of gold nanoparticles for proton therapy *in vitro*. They compared the difference between effect of gold nanoparticles with different size (5 and 10 nm) and proton beams with different LET (10 and 25 keV μm^{-1}). A pronounced radiosensitization effect of gold nanoparticles was observed after irradiation of proton beam with high LET, but not with low LET. The effect was more remarkable for large gold nanoparticles than for small gold nanoparticles. Recently, Lin *et al.* established a biological model of gold nanoparticles–enhanced proton therapy [57]. They suggested that the radiosensitization effect would only exist when the gold nanoparticles were internalized into cells, especially into cell nucleus. Kim *et al.* [58] intravenously injected 14 nm gold nanoparticles into CT26 tumor bearing mice and utilized proton beam to irradiate CT26 tumor at 24 h post injection. They observed 100% complete tumor regression (CTR) in mice treated with a proton dose of 31 Gy and tumoral gold concentration of 41 Au/g tissues. In contrast, the CTR was 37–62% for mice treated by proton alone.

5. Future perspectives

As discussed above, the extensive research on gold nanoparticles over the past decade has indicated their potential for a rich variety of applications in cancer imaging and treatment.

Many advances were enabled by the understanding of the chemical synthesis and biobehavior of gold nanoparticles. These understandings will certainly lead to more practical clinical applications. The use of gold nanoparticles for drug delivery and photothermal therapy was proved for phase I and phase II clinical trials [59].

Although gold nanoparticles offer an attractive platform for new novel modalities for cancer imaging and treatment, it is very important to carefully and precisely study their toxicity in potential applications for human. Although the gold is relatively inert for biotissues, these nanoparticles tend to remain in the body, especially in liver and spleen for a long time. Thus, the long-term toxicity of nanoparticles is an issue for their use in humans. Since the reported biodistribution and toxicity vary greatly with the size, shape, and coating of gold nanoparticles, it seems that the safety of gold nanoparticles is dependent on many factors, and so, this needs to be examined for every single synthetic formula and application [60].

One unique property of gold nanoparticles is their LSPR effect, which enables a variety of imaging and treatment modalities, such as light scattering imaging, photothermal therapy, photodynamic therapy, and so on. However, the penetration depth of light in biotissues is no more than several centimeters and cannot reach most tumors in human body. Combining other imaging and therapeutic modalities may provide a strategy to overcome this limitation [61].

Acknowledgements

This project is financially supported by the National Key Basic Research Program of the P.R. China (program no. 2014CB744504), the National Natural Science Foundation of China (program no. 81501588), and the Natural Science Foundation of Jiangsu Province (program no. BK20140734).

Author details

Shouju Wang* and Guangming Lu

*Address all correspondence to: shoujuwang@gmail.com

Jinling Hospital, Nanjing University, Nanjing, China

References

[1] Zhang X. Gold nanoparticles: Recent advances in the biomedical applications. Cell Biochemistry and Biophysics. 2015;**72**(3):771-775

[2] Yang X, Yang M, Pang B, Vara M, Xia Y. Gold nanomaterials at work in biomedicine. Chemical Reviews. 2015;**115**(19):10410-104088

[3] Muddineti OS, Ghosh B, Biswas S. Current trends in using polymer coated gold nanoparticles for cancer therapy. International Journal of Pharmaceutics. 2015;**484**(1-2):252-267

[4] Sokolov K, Follen M, Aaron J, Pavlova I, Malpica A, Lotan R, et al. Real-time vital optical imaging of precancer using anti-epidermal growth factor receptor antibodies conjugated to gold nanoparticles. Cancer Research. 2003;**63**(9):1999-2004

[5] El-Sayed IH, Huang X, El-Sayed MA. Surface plasmon resonance scattering and absorption of anti-EGFR antibody conjugated gold nanoparticles in cancer diagnostics: applications in oral cancer. Nano Letters. 2005;**5**(5):829-834

[6] Huang X, El-Sayed IH, Qian W, El-Sayed MA. Cancer cell imaging and photothermal therapy in the near-infrared region by using gold nanorods. Journal of the American Chemical Society. 2006;**128**(6):2115-2120

[7] Wang S, Tian Y, Tian W, Sun J, Zhao S, Liu Y, et al. Selectively sensitizing malignant cells to photothermal therapy using a CD44-targeting heat shock protein 72 depletion nanosystem. ACS Nano. 2016;**10**(9):8578-8590

[8] Gobin AM, Lee MH, Halas NJ, James WD, Drezek RA, West JL. Near-infrared resonant nanoshells for combined optical imaging and photothermal cancer therapy. Nano Letters. 2007;**7**(7):1929-1934

[9] Cang H, Sun T, Li Z-Y, Chen J, Wiley BJ, Xia Y, et al. Gold nanocages as contrast agents for spectroscopic optical coherence tomography. Optics Letters. 2005;**30**(22):3048-3050

[10] Troutman TS, Barton JK, Romanowski M. Optical coherence tomography with plasmon resonant nanorods of gold. Optics Letters. 2007;**32**(11):1438-1440

[11] Jokerst JV, Cole AJ, Van de Sompel D, Gambhir SS. Gold nanorods for ovarian cancer detection with photoacoustic imaging and resection guidance via Raman imaging in living mice. ACS Nano. 2012;**6**(11):10366-10377

[12] Lin J, Wang S, Huang P, Wang Z, Chen S, Niu G, et al. Photosensitizer-loaded gold vesicles with strong plasmonic coupling effect for imaging-guided photothermal/photodynamic therapy. ACS Nano. 2013;**7**(6):5320-5329

[13] Nie L, Wang S, Wang X, Rong P, Ma Y, Liu G, et al. In vivo volumetric photoacoustic molecular angiography and therapeutic monitoring with targeted plasmonic nanostars. Small. 2014;**10**(8):1585-1593

[14] Tian Y, Zhang Y, Teng Z, Tian W, Luo S, Kong X, et al. pH-dependent transmembrane activity of peptide-functionalized gold nanostars for computed tomography/photoacoustic imaging and photothermal therapy. ACS Applied Materials & Interfaces. 2017;**9**(3):2114-2122

[15] Aydogan B, Li J, Rajh T, Chaudhary A, Chmura SJ, Pelizzari C, et al. AuNP-DG: Deoxyglucose-labeled gold nanoparticles as X-ray computed tomography contrast agents for cancer imaging. Molecular Imaging and Biology. 2010;**12**(5):463-467

[16] Wang H, Zheng L, Peng C, Guo R, Shen M, Shi X, et al. Computed tomography imaging of cancer cells using acetylated dendrimer-entrapped gold nanoparticles. Biomaterials. 2011;**32**(11):2979-2988

[17] Tian Y, Luo S, Yan H, Teng Z, Pan Y, Zeng L, et al. Gold nanostars functionalized with amine-terminated PEG for X-ray/CT imaging and photothermal therapy. Journal of Materials Chemistry B. 2015;**3**:4330-4337

[18] Liu W, Liu K, Zhao Y, Zhao S, Luo S, Tian Y, et al. T1-weighted MR/CT dual-modality imaging-guided photothermal therapy using gadolinium-functionalized triangular gold nanoprism. RSC Advances. 2017;**7**(26):15702-15708

[19] Hainfeld JF, O'Connor MJ, Dilmanian FA, Slatkin DN, Adams DJ, Smilowitz HM. Micro-CT enables microlocalisation and quantification of Her2-targeted gold nanoparticles within tumour regions. The British Journal of Radiology. 2011;**84**(1002):526-533

[20] Kim D, Jeong YY, Jon S. A drug-loaded aptamer-gold nanoparticle bioconjugate for combined CT imaging and therapy of prostate cancer. ACS Nano. 2010;**4**(7):3689-3696

[21] Xiao Y, Hong H, Matson VZ, Javadi A, Xu W, Yang Y, et al. Gold nanorods conjugated with doxorubicin and cRGD for combined anticancer drug delivery and PET imaging. Theranostics. 2012;**2**(8):757-768

[22] You J, Zhang R, Xiong C, Zhong M, Melancon M, Gupta S, et al. Effective photothermal chemotherapy using doxorubicin-loaded gold nanospheres that target EphB4 receptors in tumors. Cancer Research. 2012;**72**(18):4777-4786

[23] You J, Zhang G, Li C. Exceptionally high payload of doxorubicin in hollow gold nanospheres for near-infrared light-triggered drug release. ACS Nano. 2010;**4**(2):1033-1041

[24] Yavuz MS, Cheng Y, Chen J, Cobley CM, Zhang Q, Rycenga M, et al. Gold nanocages covered by smart polymers for controlled release with near-infrared light. Nature Materials. 2009;**8**(12):935-939

[25] Wang F, Wang Y-C, Dou S, Xiong M-H, Sun T-M, Wang J. Doxorubicin-tethered responsive gold nanoparticles facilitate intracellular drug delivery for overcoming multidrug resistance in cancer cells. ACS Nano. 2011;**5**(5):3679-3692

[26] Braun GB, Pallaoro A, Wu G, Missirlis D, Zasadzinski JA, Tirrell M, et al. Laser-activated gene silencing via gold nanoshell-siRNA conjugates. ACS Nano. 2009;**3**(7):2007-2015

[27] Jensen SA, Day ES, Ko CH, Hurley LA, Luciano JP, Kouri FM, et al. Spherical nucleic acid nanoparticle conjugates as an RNAi-based therapy for glioblastoma. Science Translational Medicine. 2013;**5**(209):209ra152-209ra152

[28] Meir R, Shamalov K, Betzer O, Motiei M, Horovitz-Fried M, Yehuda R, et al. Nanomedicine for cancer immunotherapy: Tracking cancer-specific T-cells in vivo with gold nanoparticles and CT imaging. ACS Nano. 2015;**9**(6):6363-6372

[29] Toy R, Roy K. Engineering nanoparticles to overcome barriers to immunotherapy. Bioengineering & Translational Medicine. 2016;**1**(1):47-62

[30] Lin AY, Lunsford J, Bear AS, Young JK, Eckels P, Luo L, et al. High-density sub-100-nm peptide-gold nanoparticle complexes improve vaccine presentation by dendritic cells in vitro. Nanoscale Research Letters. 2013;**8**(1):72

[31] Lee I-H, Kwon H-K, An S, Kim D, Kim S, MK Y, et al. Imageable antigen-presenting gold nanoparticle vaccines for effective cancer immunotherapy in vivo. Angewandte Chemie, International Edition. 2012;**51**(35):8800-8805

[32] Brinãs RP, Sundgren A, Sahoo P, Morey S, Rittenhouse-Olson K, Wilding GE, et al. Design and synthesis of multifunctional gold nanoparticles bearing tumor-associated glycopeptide antigens as potential cancer vaccines. Bioconjugate Chemistry. 2012;**23**(8):1513-1523

[33] Riley RS, Day ES. Gold nanoparticle-mediated photothermal therapy: applications and opportunities for multimodal cancer treatment. Wiley Interdisciplinary Reviews. Nanomedicine and Nanobiotechnology. 2017;**9**(4)

[34] Hirsch LR, Stafford RJ, Bankson JA, Sershen SR, Rivera B, Price RE, et al. Nanoshell-mediated near-infrared thermal therapy of tumors under magnetic resonance guidance. Proceedings of the National Academy of Sciences of the United States of America. 2003;**100**(23):13549-13554

[35] Nam J, La W-G, Hwang S, Ha YS, Park N, Won N, et al. pH-responsive assembly of gold nanoparticles and "spatiotemporally concerted" drug release for synergistic cancer therapy. ACS Nano. 2013;**7**(4):3388-3402

[36] Wang S, Teng Z, Huang P, Liu D, Liu Y, Tian Y, et al. Reversibly extracellular pH controlled cellular uptake and photothermal therapy by PEGylated mixed-charge gold nanostars. Small. 2015;**11**(15):1801-1810

[37] Chen H, Shao L, Ming T, Sun Z, Zhao C, Yang B, et al. Understanding the photothermal conversion efficiency of gold nanocrystals. Small. 2010;**6**(20):2272-2280

[38] Hessel CM, P Pattani V, Rasch M, Panthani MG, Koo B, Tunnell JW, et al. Copper selenide nanocrystals for photothermal therapy. Nano Letters. 2011;**11**(6):2560-2566

[39] Huang P, Rong P, Lin J, Li W, Yan X, Zhang MG, et al. Triphase interface synthesis of plasmonic gold bellflowers as near-infrared light mediated acoustic and thermal theranostics. Journal of the American Chemical Society. 2014;**136**(23):8307-8313

[40] Ma X, Cheng Y, Huang Y, Tian Y, Wang S, Chen Y. PEGylated gold nanoprisms for photothermal therapy at low laser power density. RSC Advances. 2015;**5**(99):81682-81688

[41] Wang B-K, X-F Y, Wang J-H, Li Z-B, Li P-H, Wang H, et al. Gold-nanorods-siRNA nanoplex for improved photothermal therapy by gene silencing. Biomaterials. 2016;**78**:27-39

[42] Chen W-H, Luo G-F, Lei Q, Hong S, Qiu W-X, Liu L-H, et al. Overcoming the heat endurance of tumor cells by interfering with the anaerobic glycolysis metabolism for improved photothermal therapy. ACS Nano. 2017;**11**(2):1419-1431

[43] Link S, Burda C, Nikoobakht B, El-Sayed MA. How long does it take to melt a gold nanorod?: A femtosecond pump–probe absorption spectroscopic study. Chemical Physics Letters. 1999;**315**(1-2):12-18

[44] Takahashi H, Niidome T, Nariai A, Niidome Y, Yamada S. Photothermal reshaping of gold nanorods prevents further cell death. Nanotechnology. 2006;**17**(17):4431-4435

[45] Chen J, Glaus C, Laforest R, Zhang Q, Yang M, Gidding M, et al. Gold nanocages as photothermal transducers for cancer treatment. Small. 2010;**6**(7):811-817

[46] Camerin M, Magaraggia M, Soncin M, Jori G, Moreno M, Chambrier I, et al. The in vivo efficacy of phthalocyanine-nanoparticle conjugates for the photodynamic therapy of amelanotic melanoma. European Journal of Cancer. 2010;**46**(10):1910-1918

[47] Jang B, Park J-Y, Tung C-H, Kim I-H, Choi Y. Gold nanorod-photosensitizer complex for near-infrared fluorescence imaging and photodynamic/photothermal therapy in vivo. ACS Nano. 2011;**5**(2):1086-1094

[48] Wang S, Huang P, Nie L, Xing R, Liu D, Wang Z, et al. Single continuous wave laser induced photodynamic/plasmonic photothermal therapy using photosensitizer-functionalized gold nanostars. Advanced Materials. 2013;**25**(22):3055-3061

[49] Krpetić Z, Nativo P, Sée V, Prior IA, Brust M, Volk M. Inflicting controlled nonthermal damage to subcellular structures by laser-activated gold nanoparticles. Nano Letters. 2010;**10**(11):4549-4554

[50] Pasparakis G. Light-induced generation of singlet oxygen by naked gold nanoparticles and its implications to cancer cell phototherapy. Small. 2013;**9**(24):4130-4134

[51] Haume K, Rosa S, Grellet S, Śmiałek MA, Butterworth KT, Solov'yov AV, et al. Gold nanoparticles for cancer radiotherapy: a review. Cancer Nanotechnology. 2016;**7**(1):8

[52] Cooper DR, Bekah D, Nadeau JL. Gold nanoparticles and their alternatives for radiation therapy enhancement. Frontiers in Chemistry. 2014;**2**:86

[53] Hainfeld JF, Slatkin DN, Smilowitz HM. The use of gold nanoparticles to enhance radiotherapy in mice. Physics in Medicine & Biology. 2004;**49**(18):N309-N315

[54] Geng F, Song K, Xing JZ, Yuan C, Yan S, Yang Q, et al. Thio-glucose bound gold nanoparticles enhance radio-cytotoxic targeting of ovarian cancer. Nanotechnology. 2011;**22**(28):285101

[55] Chattopadhyay N, Cai Z, Kwon YL, Lechtman E, Pignol J-P, Reilly RM. Molecularly targeted gold nanoparticles enhance the radiation response of breast cancer cells and tumor xenografts to X-radiation. Breast Cancer Research and Treatment. 2013;**137**(1):81-91

[56] Li S, Penninckx S, Karmani L, Heuskin A-C, Watillon K, Marega R, et al. LET-dependent radiosensitization effects of gold nanoparticles for proton irradiation. Nanotechnology. 2016;**27**(45):455101

[57] Lin Y, McMahon SJ, Paganetti H, Schuemann J. Biological modeling of gold nanoparticle enhanced radiotherapy for proton therapy. Physics in Medicine & Biology. 2015; **60**(10):4149-4168

[58] Kim J-K, Seo S-J, Kim H-T, Kim K-H, Chung M-H, Kim K-R, et al. Enhanced proton treatment in mouse tumors through proton irradiated nanoradiator effects on metallic nanoparticles. Physics in Medicine & Biology. 2012;**57**(24):8309-8323

[59] Shah M, Badwaik VD, Dakshinamurthy R. Biological applications of gold nanoparticles. Journal of Nanoscience and Nanotechnology. 2014;**14**(1):344-362

[60] Boisselier E, Astruc D. Gold nanoparticles in nanomedicine: Preparations, imaging, diagnostics, therapies and toxicity. Chemical Society Reviews. 2009;**38**(6):1759-1782

[61] Hwang S, Nam J, Jung S, Song J, Doh H, Kim S. Gold nanoparticle-mediated photothermal therapy: Current status and future perspective. Nanomedicine. 2014;**9**(13):2003-2022

Chapter 14

Structure-Dependent Biological Response of Noble Metals: From Nanoparticles, Through Nanowires to Nanolayers

Jakub Siegel, Marek Staszek, Markéta Polívková, Michaela Valová, Pavla Šuláková and Václav Švorčík

Additional information is available at the end of the chapter

http://dx.doi.org/10.5772/intechopen.71440

Abstract

Noble metals in their diverse nanoforms bring revolution to many fields of science and technology, as they provide unique properties over their bulk counterparts. Thanks to these completely unprecedented properties, commercial sphere pressure is growing to use them in everyday life. Unfortunately, one of the issues that are subject to dramatic changes is the reactivity of these structures. This may have often fatal consequences to the living organisms. Due to the fact that the mechanism of action of metal nanostructures on living organisms is not yet fully elucidated even in the case of the most studied noble metals such as gold and silver, it is necessary to continue intensively in their research, characterization and categorization. The main prerequisite for the undistorted study of interactions of nanostructures with living organisms is the use of suitable methods of their preparation. Within this context, this chapter attempts to summarize current knowledge form the field of synthesis of metal nanoparticles, layers, wires, and other nanostructures, especially regarding novel techniques of their preparation and extend them by our own results in this area, in the context of their biological properties. More specifically, antibacterial efficacy and potential cytotoxicity of those structures are thoroughly addressed.

Keywords: nanoparticles, nanowires, nanolayers, antibacterials, cytotoxicity, sputtering, noble metals

1. Introduction

This chapter is devoted to the very contemporary themes of polymer nano-metallization, the process giving the polymers exceptional properties in biological applications, namely the bactericidal

action while preserving sufficiently low cytotoxicity level [1–8], as well as to novel techniques for metal nanoparticle (NP) synthesis providing antibacterial, cell-conform entities [9, 10]. So far many efforts has been spent to synthesize the next generation antimicrobial materials applicable in the health-care industry in response to increasing resistance of the pathogens to conventional antibiotics [9–12]. A lot of strategies have been developed to produce those sophisticated man-made materials which hinders their single-key classification. Here, we chose a categorization based on the way of metal incorporation into/on polymer matrix. From this point of view, one can primarily consider the form in which the both components enter the preparation process to form metal-polymer composite. Therefore the composites may be classified into (i) *in-situ* synthesized [13–17]; both polymer and metal are present in reaction chamber in which both components form from their precursors in chemical reaction. Within this protocol, silver nanoparticles have been synthesized in starch-based hydrogels consisting of dissolved N-vinyl pyrrolidone, acrylamide, or acrylic acid dispersed in water. Final polymerization was accomplished by gamma irradiation [13]. Vimala et al. [15] also utilized hydrogels prepared by polymerizing acrylamide with starch and cross-linking agent in the controlled reduction of trapped silver ions by $NaBH_4$. To eliminate toxic borohydrate, which is accompanied by hydrogen evolution, glucose and chitosan have also been used as reducing agents for Ag ions [17]. Reducing mechanism of sugars has been described in detail in Ref. [16]. Another group of composites form (ii) semi *in-situ* synthesized materials; only one component is present in the form of precursor (metals usually precipitate in/on the matrix polymer under the chemical reaction or physical deposition [1–6, 8, 12], whereas polymers are usually heat-treated while the finalized metal nanoparticles are mixed in Ref. [18]). Last group forms (iii) *ex-situ* synthesized composites; both components enter the preparation process until their complete synthesis [4, 19, 20]. The latter mentioned approach generally covers the processes such as grafting, embedding, chemisorption, physisorption, and non-reactive implantation.

In the following text, we attempt to summarize current knowledge form the field of metal nanoparticles, layers, wires, and other nanostructures, especially regarding to novel techniques of their synthesis and extend them by our own results in this area in the context of their biological properties. More specifically, antibacterial efficacy and potential cytotoxicity of those structures are thoroughly addressed.

2. Metal nanoparticles in liquids: preparation fundamentals

Cathode sputtering is a well-established method for the preparation of thin films. It involves bombardment of the target of required composition with energy particles that causes the atoms to be ejected from the target material. These atoms gradually settle on the substrate, where they form a thin layer. Since the whole process takes place under reduced pressure, only solid substrates have been used for a long time. It was not until 1996, when Gao-xiang. et al. [21] tried to prepare a thin layer on a liquid medium by sputtering process. Silicone oil has been chosen as a substrate and it was found that to produce a thin film on this oil is needed to use a power of more than 30 watts. At lower power levels, the layer did not develop and a nanoparticles (NPs) solution was formed instead. Unfortunately, these NPs were not characterized because

the research focused solely on the preparation of the layers [21]. Since then, the research in this area has divided on two streams. The first focuses on the preparation of metallic layers on liquid substrates with their potential use in lunar telescopes [22]. The second one is dealing with the preparation of NPs. The advantage of this method is the ability to prepare NPs without the use of reducing agents and other surfactants. The resulting system typically consists of only two components (1) the liquid substrate used and the (2) nanoparticles formed. As a liquid substrate, any liquid with a sufficiently low vapor pressure can be selected. However, especially for the preparation of NPs, it is desirable that such liquids have the ability to stabilize forming NPs sufficiently. For this reason, ionic [23] or macromolecular [24] fluids are most often chosen. Even a low-molecular glycerol [10] has been documented.

Ionic liquids meet these requirements very well. These liquids consist of an organic cation and an inorganic or organic anion, typically with the melting point below 100°C. The main advantages of ionic liquids is almost zero vapor pressure (e.g. [Bmim]PF6 at room temperature having the vapor pressure of 0.1 nPa [25]), high thermostability, large electrochemical window (range of the voltage at which the substance may be reduced as well as oxidized), fire resistance and in particular solvation properties [26]. For the preparation of NPs, it is also advantageous that ionic liquids generally have a low surface tension which results in a higher nucleation rate and thus NPs of nanometer sizes up to atomic clusters can be prepared [23]. On the other hand, liquid electrolytes are often toxic [27], which is a limiting factor for the subsequent use of produced NPs.

For this reason, toxicologically acceptable macromolecular fluids are used, such as vegetable oils [28], polyethylene glycols (PEG) [29] of different molecular weights and its derivatives [4, 30]. Compared to ionic liquids, macromolecular liquids are characterized by higher vapor pressure (e.g. 0.26 and 0.45 kPa at room temperature for castor oil and soybean oil, respectively [31]) and a worse ability to stabilize NPs [24]. For PEG (and its derivatives), it is highly advantageous to use a PEG of a specific molecular weight, since it directly determines PEG properties, including vapor pressure, stabilization capabilities and also viscosity [32].

An exceptional position between liquid substrates used to prepare NPs by sputtering has glycerol [10]. Compared to previously described substrates, glycerol is naturally biocompatible because it is a fat component in the form of its esters. Another undisputed advantage of glycerol is its frequent use in the cosmetics and soap industries, resulting in both its low production cost and available and well-measured values of all important physicochemical parameters. On the contrary, its disadvantage is substantially higher vapor pressure (22 mPa at room temperature) [33].

Independently on the liquid substrate selection, NPs of different sizes were prepared by sputtering [24]. However, it is apparent from the present results that the resulting NP size is determined primarily by the choice of liquid media. The question, however, remains where the NP is growing in the liquid and how the fluid is involved in this growth. In essence, only three scenarios can occur: (i) NPs nucleation and their growth occur exclusively on the surface of the liquid, (ii) nucleation takes place on the surface of the liquid; whereas the growth itself is already in its volume, and (iii) the sputtered atoms have sufficient energy to penetrate into the volume of the liquid, where both processes (nucleation and growth) take place [34]. In

this case, the penetration depth of the sputtered atoms is the function of their kinetic energy, which may explain the dependence of the final NP size on the deposition parameters. For processes (i) and (ii), the parameters such as working current, voltage, pressure, etc. have only the significance regarding liquid surface saturation velocity. Which of the above-mentioned scenarios will occur depends, according to one part of the scientific community, on the surface and volume composition of the liquid [28], according to others, on the viscosity of the liquid and the vapor tension [35]. Supporters of the first theory assume that after the formation of the nucleus at the liquid/vacuum interface, nanostructures on the surface of the liquid develop, which then diffuse into the volume of the liquid. Here, the nanostructures are self-assembled to the most energy-efficient structure [36]. The second theory is based on the so-called diffusion length, being the maximum length in which the sputtered atoms or the formed nucleus can move. At higher viscosities (lower diffusion lengths), these entities have smaller ability to migrate and the resultant colloidal solution thus contains particles of smaller size and narrower distribution [37].

A more detailed view into the formation mechanism of NPs was provided by Anantha et al. [38]. They describe the process of preparing uniform NPs using a so-called *shared coarsening* model. This model is based on the classical nucleation theory and crystal growth. After the impact of the sputtered atoms on the liquid-vacuum interface (or at a short distance below the liquid surface level), a saturated concentration is quickly reached. Atoms are homogeneously distributed throughout the volume and spontaneous nucleation occurs once the critical concentration is exceeded. In the neighborhood of these nuclei, so-called exclusion zones[1] are created. All sputtered atoms that hit this zone are involved in the growth of the nucleus. Since these zones have a hemispherical shape, secondary nuclei are formed in free space between primary exclusion zones. Subsequently, the primary nucleus grows at the expense of the secondary ones- the *shared coarsening* occurs. When sputtering is terminated at the time of formation of secondary nuclei, the resulting colloidal solution contains uniform NPs. With longer sputtering periods, the particles grow further until they begin to touch each other. This results in change of NPs shape, their agglomeration and the undesirable phenomenon of so-called Oswald ripening takes a place.

Thus, this model considers the sputtering time as one of the most important parameters for the preparation of uniform NPs. This is, however, in direct contradiction with a number of studies that have found the sputtering time not essentially important with respect to size and distribution [39]. This can be explained by the fact that the model published by Anantha et al. [38] does not reflect changes in concentration throughout the whole volume of the liquid. During deposition, the deposited material accumulates at the liquid-vacuum interface (or at a small depth below the surface). Therefore it is clear, that from the very beginning of the deposition the diffusion flow of the emerging NPs will increase, which can be characterized by the first Fick's law for unidirectional diffusion.

$$J_i = -D_i \frac{\partial c_i}{\partial x}, \tag{1}$$

[1]In some literature the term denuded zone instead of the exclusion zone is used.

where J_i means diffusion flux, D_i diffusion coefficient, c_i concentration of sputtered material, and x direction of the flux (in this case the depth of the liquid). Diffusion coefficient in this equation is temperature dependent variable, which can be described for spherical particles by the Stokes-Einstein equation.

$$D = \frac{k_B T}{6\pi\eta r}, \tag{2}$$

where k_B is Boltzman constant, η viscosity of liquid medium, T temperature, and r NP radius. Theoretically, there may be case in which the formed NPs are driven away with diffusion flux J, leave space in the liquid-vacuum interface, where new nuclei and NPs can be formed. In this case, the size distribution of the prepared NPs may not have been deteriorated.

Since the diffusion coefficient is a parameter which dependents also on the viscosity of the medium and the diffusion length, it is obvious that the most important variable in the preparation of NPs by sputtering is the choice of the liquid itself and the temperature during deposition process. Several groups focused on the examination of the dependence of NP size on viscosity of used medium. From **Table 1**, it is apparent, that our research group [40] achieved remarkable results. We successfully controlled the NP size in temperature range 0–20°C with average size change 0.5 nm/°C (see **Figure 1**) [40]. On the other hand, above this range we observed significant evaporation of glycerol. This evaporation influenced the mechanism of formed NPs, resulting in the production of smaller ones. From **Table 1**, it is also apparent, that most pronounced changes were observed on those substrates having a higher viscosity dependence on the temperature. The knowledge gained from this work can be used to study the physicochemical properties of NPs, as they declare the possibility of preparing NPs of the

Temperature	Nanoparticles size [nm]		
	PEG600	C_4mim^+/BF_4^-	PVP-Glycerine
5°C			12.8
10°C			13.1
15°C			15.6
20°C	2.73	0.75	7.2
30°C	3.70	0.70	7.8
40°C	4.67	1.34	
50°C	5.55	2.30	
60°C	7.40	2.76	
70°C		3.24	
80°C		3.61	

Table 1. Dependence of nanoparticle size on temperature in different liquid media: PEG600 ionic liquid [37] C_4mim^+/BF_4^- [35] and PVP-glycerine system [40].

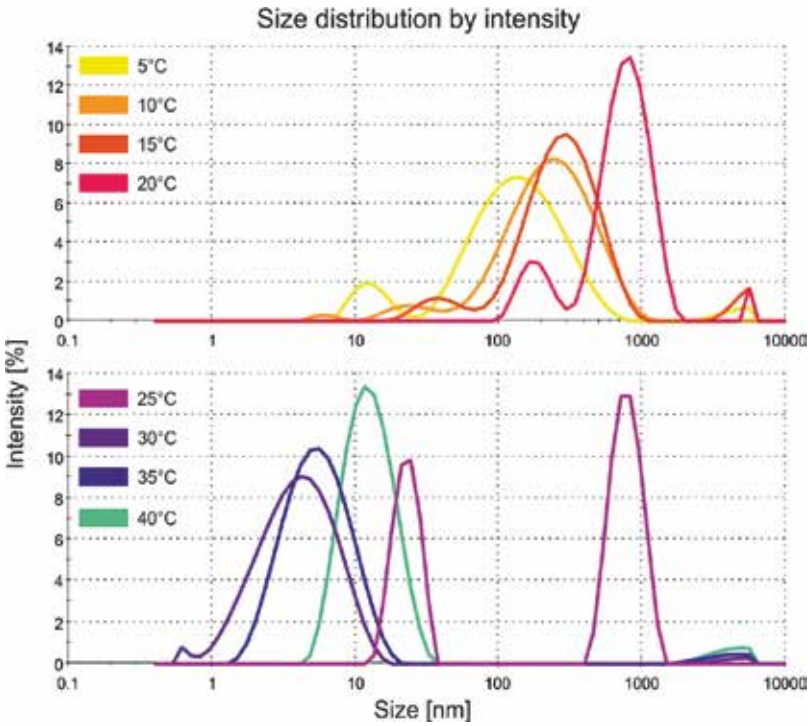

Figure 1. Dynamic light scattering analysis of aqueous solutions of silver NPs prepared at different temperatures of the liquid substrate [40].

desired size, while maintaining a constant environment containing minimal number of components. The whole process of evaluating NPs physicochemical properties is thus simplified, in particular, to the consideration of different environment influence. This is very advantageous, for example, in the detection of potential toxicological properties of these structures. These NP properties must be known very precisely owing to the boom of their use in broad commercial applications and products [41].

3. Nanoparticles cytotoxicity

Currently, there can be found enormous number of scientific papers dealing with NPs toxicity. Unfortunately, despite of the amount of information available, the NP toxicological properties cannot be clearly interpreted, especially the toxic doses. This applies even for the most studied types of NPs – gold and silver ones (see reviews [42, 43]). This fact was considered in our related study [9], addressing NPs biological properties. We used cathode sputtering method to prepare NPs of gold (6.1 ± 1.0 nm), silver (4.2 ± 0.9 nm), palladium (2.5 ± 0.6 nm), and platinum (1.8 ± 0.6 nm). Prepared NP suspensions were further diluted with water for ion chromatography in a weight ratio of 1:3 (glycerol:water). This step is necessary as the isotonicity of the solution is achieved (see **Figure 2**) and the bioassay distortion is avoided. For

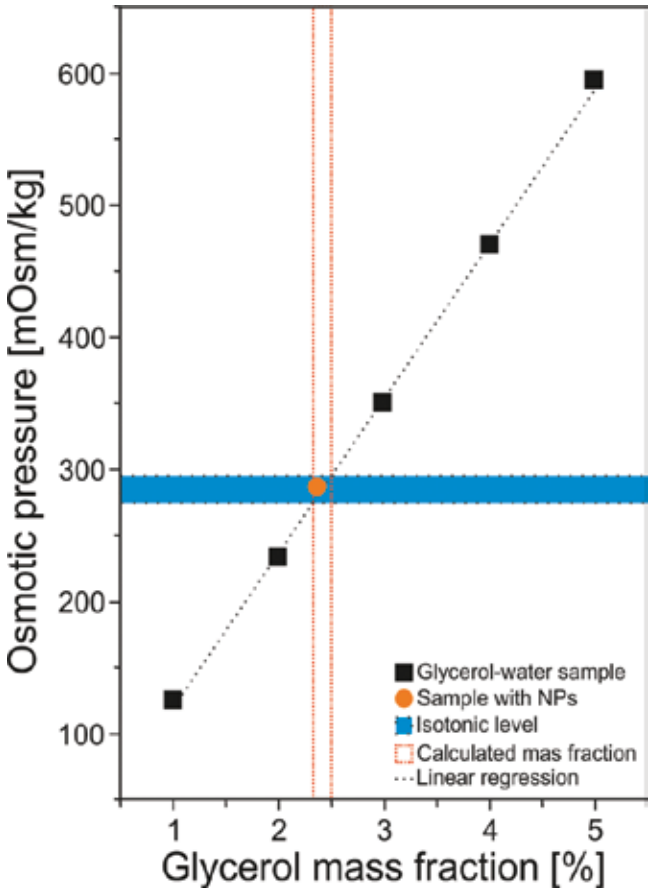

Figure 2. Dependence of tonicity on the composition of solution glycerol:water. The blue band indicates the isotonic environment from which the glycerol:water ratio was calculated by linear regression. The orange dot indicates thus solution enriched with silver nanoparticles.

bioassay purposes, it is also important that our NPs were stabilized electrostatically and not sterically, in contrary to most published results of other scientific groups [44, 45], thus avoiding further bioassay distortion caused by surfactants side-effects. Prepared colloidal solutions were then subjected to various cell lines via WST-1 assay. More specifically, the NPs were tested against A549 (human lung carcinoma cells), HaCaT (human keratinocytes), RAW 264.7 (mouse macrophages), CHO-K1 (Chinese hamster ovary), NIH 3 T3 and L929 (both mouse embryonic fibroblasts), the cell lines commonly used to evaluate the cytotoxic potential of pollutants [24]. The cytotoxic potential was investigated for 24, 48 and 72 h over the NPs concentration range of 0–6.150 mg/ml [9].

Figure 3 illustrates the results obtained for L929 cell line. The differences in absorbance values on y-axis directly correlate with the formation of formazan, which is metabolized by viable cells. In **Table 2**, all results are summarized in the form of the half maximal inhibitory concentration (IC50). It obvious, that the highest toxicity was observed in case of Pt and Pd

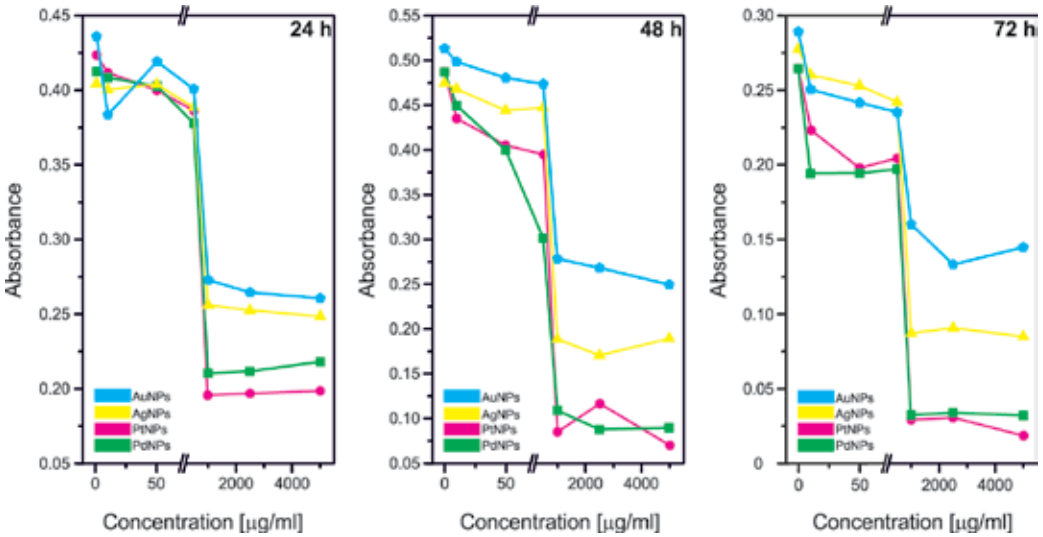

Figure 3. Cytotoxicity of Ag, Au, Pd, and Pt nanoparticles on L929 cells after 24, 48 , and 72 h of treatment.

nanoparticles, less for Ag and almost no toxicity for Au NPs. These results are partially consistent with the findings of Asharani et al. [46], who examined the cytotoxic potential of Ag NPs (5–25 nm), Au NPs (15–35 nm), and Pt NPs (3–10 nm) on the zebra fish embryos. In their work, the cytotoxicity of the gold nanoparticles was not observed, and the mortality rates for Ag NPs and Pt NPs (at concentrations of 100 mg/ml) were determined to 30 ± 12.8% and 50 ± 9.9%, respectively. It is interesting that Ag [46] and Pt NPs [47] are generally reported as highly cytotoxic, while Au NPs [46, 48] are usually considered as biocompatible. This inconsistency with the above-mentioned works can be due to both, different sizes of prepared NPs and the preparation process itself. In referred study [46], authors used a reduction synthesis for preparation of NPs, so the resulting colloids might contain toxic entities such as chlorine

Cell line	IC_{50} [μg·ml^{-1}] for 72 h			
	AgNPs	AuNPs	PdNPs	PtNPs
HaCaT	2,250	1,970	1,060	1,010
Hep G2	2,075	3,900	1,425	908
CHO-K1	1,840	2,300	920	855
L929	1,710	1,900	900	770
NIH 3T3	820	1,190	425	550
RAW 267.7	1,580	1,370	880	960

Table 2. The IC_{50} values for individual cell lines after 72 h of treatment with the tested nanoparticles. IC_{50} represents concentration, which causes 50% reduction of cell viability measured by WST-1.

anions, PVA, etc. Authors, despite of their attempt to transfer NPs to the aqueous solution by centrifugation, do not declare the purity of colloid solution before the evaluation of the biological properties. Therefore, the comparison of our results with the above-mentioned work (but also others, e.g. [42]) is rather difficult. In addition, the NP surfactants can cause a dramatic change in their potential toxicological behavior, which remains a challenge to most of works dealing with such type of NPs.

4. Metal-based treatment of polymers

Nowadays, an investigation of non-conventional antibiotic treatment of polymeric medical devices consists from various ways. One of the effective approaches is antibacterial-active biocompatible polymers, where their applications are gentle and safe. One can distinguish two types of antibacterial polymers: (i) polymers which exhibit antibacterial efficacy by themselves and/or (ii) their antibacterial properties are acquired by their controlled modification [49].

In the first case, one can converse natural or synthetic polymers and co-polymers with charged active groups, for example, biguanides, quaternary ammonium, pyridinium, or phosphonium salts [50–52]. The second group represents antibacterial-treated polymers, which achieved their antibacterial activity by adding of organic and/or inorganic antibacterial agents in various manners, such as (i) by incorporation into polymeric matrix or (ii) formation of antibacterial coatings on polymeric surface. Their efficacy is then two-step; their presence on the polymeric surface ensure the reduction of initial bacterial adhesion and thereafter deactivation of already adherent bacterial colonies [53].

In recent days, all of above-mentioned ways of treatment are still developing areas, which produce materials with excellent antimicrobial capability. However, one of the most promising areas in this regard is nanotechnology. Nanostructured noble metals, either incorporated or forming coatings, exhibit strong antibacterial activity against broad spectrum of microorganisms, where bacterial resistance is missing [5, 54–56]. Therefore, in the further text we are focusing our interest on a group of nanostructured noble metals, especially coating-forming ones. This type of surface modifications of biocompatible polymers might not only provide significant antibacterial protection, but also enhance biocompatibility of the resulting composites.

The enhancements of material biocompatibility and antibacterial efficacy by the modification of surface morphology have been referred in several studies [1, 5, 8, 57–59]. Generally, to enhance the functionality of polymeric materials, the formation of nanostructured thin films on its surface might be an effective way. Moreover, one can prepare nanostructured coatings with increased surface area using nanolayers (thin films) as default structures, by their thermally induced transformation into island-like structures. Such increase of surface area often leads to the enhancement of resulting antibacterial response. The formation of island-like structures by low temperature annealing of thin films has been described for silver [5], palladium [8], and gold [57]. Another way to increase the specific surface area and roughness of antibacterial coating is laser patterning of polymeric surface prior to metal deposition, which

leads to the formation of ordered nanowire arrays [1]. This method usually provides better adhesion and proliferation of human cells; at least at those which prefer rougher substrates [58]. Thus, the surface modification enables a direct control over the material biocompatibility, which might be significantly enhanced [59].

In this subsection, we present three types of metal (Ag and Pd) nanostructures; nanolayers (NLs), islands (NIs), and wires (NWs), supported on biocompatible polymer polyethylene naphthalate (PEN), and discus the influence of surface morphology/roughness change (unlike pristine PEN) on their resulting biological response. Surfaces of all used materials were thoroughly characterized by X-ray photoelectron spectroscopy (XPS), focused ion beam cut - scanning electron microscopy (FIB-SEM), and atomic force microscopy (AFM). Thereafter, the biological testing of the samples was accomplished. Antibacterial properties were examined using Gram-negative bacteria *Escherichia coli* (*E. coli*) and Gram-positive *Staphylococcus epidermidis* (*S. epidermidis*), which commonly cause hospital-acquired infections related to biofilm formation due to long-term applications of catheters and other medical devices. Finally, cell-conformity study of all types of composites was carried out using mouse embryonic fibroblasts (L929) as a routinely used cell line for this purpose.

4.1. Preparation of metal nanostructures

Metal (Ag and Pd) coatings on polyethylene naphthalate were prepared by DC sputtering. For a calibration of sputtering device, sputtering times on a glass substrate, simultaneously coated with PEN samples, varied from 10 to 200 s. Effective thicknesses of metal layers were determined by AFM scratch method. To produce island-like structures with increased antibacterial-active surface area, prepared samples were annealed in air atmosphere at 250°C for 1 h, then cooled down in air and stored under laboratory conditions. In this work, we present samples with 20 nm thick Ag and Pd layers (sputtering time 200 s, 20°C, current of 15 mA, total argon pressure of 5 Pa, and electrode distance of 50 mm) and corresponding annealed ones as representatives.

The combination of polymer laser pre-treatment and metal vacuum evaporation was used for the preparation of self-organized, fully separated Ag and Pd NW arrays of the thickness of 20 nm. To prepare periodic nanostructures (ripples) on PEN surface, PEN samples were treated by KrF excimer laser (6000 laser pulses, laser fluence of 10 $mJ \cdot cm^{-2}$). Then, laser-patterned (rippled) PEN was used as a template for Ag and Pd NW arrays (thickness of 20 nm) prepared by vacuum evaporation under the glancing angle of $\phi = 70°$. The thickness of metal NWs was monitored *in-situ* by quartz crystal microbalance during the vacuum evaporation process, and verified by FIB-SEM analysis and AFM scratch test of metal simultaneously deposited on a glass substrate.

Due to the experimental set-up of vacuum evaporation process [the glancing angle (ϕ) of 70°] the formation of metal NWs took place preferably from one side of rippled PEN (for graphical representation see [1]). Mild ripples´ structure is in a correlation with the glancing angle of incidence (so-called shadow effect). The shadow effect modulates the spatial distribution of metal flux and induces the nucleation of metal mainly near to the tops of the illuminated ridges and NWs are formed from one side of the ripples (the highest metal flux) [60]. As the

thickness of the metal coating of polymer increases, the agglomeration and coarsening of the metal clusters increases until a polycrystalline array of metal NWs is formed [61]. This phenomenon was verified by FIB-SEM (see **Figure 4**) and has already been observed also for Au NWs arrays supported on PET [62, 63].

4.2. X-ray photoelectron spectroscopy (XPS)

For the determination of atomic concentrations of elements in metal NLs and NIs, X-ray photoelectron spectroscopy (XPS) analysis was performed under the electron take-off angle of 0° (**Table 3**). In case of metal NWs, the electron take-off angle was 0 and 81°, from which samples were analyzed from both sides; left and right (**Table 4**, for graphical representation see [1]). The analytical information about the chemical composition from the perpendicular direction to the surface (0°) originates from greater depth (8–10 atomic layers), compared to the electron take-off angle of 81°, which provides information just from 1 to 2 atomic layers [1, 64]. The presence of C and O is given by the stoichiometry of polyethylene naphthalate, and might be extended by the hydrocarbon impurities, which are often adsorbed on the surfaces of the polar polymeric materials from air [65]. Detected Ag, in case of Ag-coated samples, and Pd, in case of Pd-coated ones, comes from the process of DC sputtering (NLs, NIs) and vacuum evaporation (NWs).

The results for metal NLs and NIs (**Table 3**) indicated that annealing of pristine PEN caused no significant changes in chemical composition of polymer. Due to diffusion and aggregation of metal during annealing, detected concentrations of metal for annealed Ag (Ag NIs/PEN) and Pd (Pd NIs/PEN) samples were lower, compared to as-sputtered ones (both, Ag and Pd NLs/PEN). However, observed decrease was at the expense of the concentrations of elements originating from the underlying polymer, where underlying polymer become partially uncovered. In the light of the results of surface ablation (XPS) and metal release (ICP-MS) [1], however, we attribute these compositional changes not only to the coalescence of metal into separate NIs, but also to embedding of these clusters into the polymer interior. This ultrathin (ones of nm) surface incorporation was probably caused by polymer overlay reaching almost the tops of individual metal islands (so-called "curtain" effect, for graphical representation

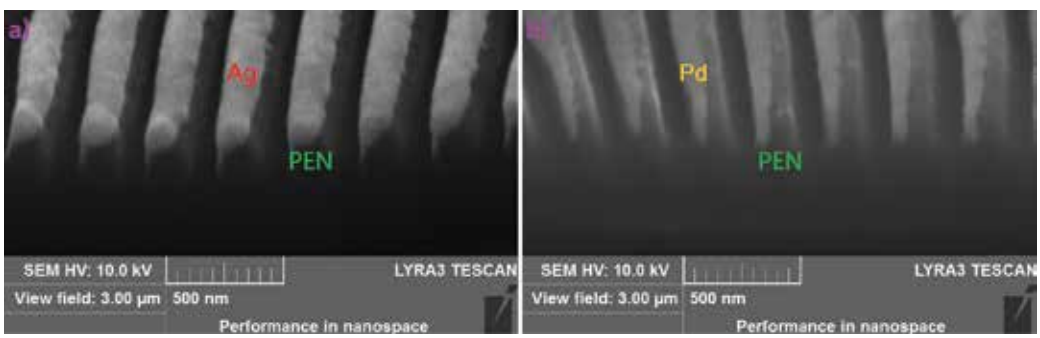

Figure 4. FIB-SEM images of (a) silver and (b) palladium NW arrays supported on laser-patterned PEN.

Sample	Atomic concentrations of elements (at. %)			
	C	O	A g	Pd
pristine PEN	72.2	27.8	-	-
annealed PEN	73.1	26.9	-	-
Ag NLs/PEN	58.4	12.0	29.6	-
Ag NIs/PEN	61.5	30.1	8.4	-
Pd NLs/PEN	73.5	1.2	-	25.3
Pd NIs/PEN	65.6	18.3	-	16.1

Table 3. Atomic concentrations of C(1s), O(1s), Ag(3d), and Pd (3d) for both, pristine and rippled PEN, Ag and Pd/PEN composites measured by XPS, electron take-off angle of 0°.

see [8]). The relatively high value of the atomic concentration of O for the annealed sample coated by Ag (Ag NIs/PEN) could be explained by higher propensity of this sample to oxidation during annealing.

The results for metal NWs are shown in **Table 4**. Unlike the work of Tuma et al. [66], in which a two-step deposition of silver was performed and a dramatic increase of at.% of Ag from the

Angle (°)	Sample	Atomic concentrations of elements (at. %)			
		C	O	Ag	Pd
0	pristine PEN	72.2	27.8	-	-
	rippled PEN	74.4	25.6	-	-
	Ag NWs/PEN	67.7	12.9	19.4	-
	Pd NWs/PEN	80.2	13.4	-	6.4
81 left	pristine PEN	73.0	27.0	-	-
	rippled PEN	79.3	20.7	-	-
	Ag NWs/PEN	63.1	12.1	24.8	-
	Pd NWs/PEN	62.1	12.0	-	25.9
81 right	pristine PEN	73.1	26.9	-	-
	rippled PEN	79.5	20.5	-	-
	Ag NWs/PEN	75.9	15.5	8.6	-
	Pd NWs/PEN	74.4	16.6	-	9.0

Table 4. Atomic concentrations of C(1s), O(1s), Ag(3d), and Pd(3d) for both, pristine and rippled PEN, Ag and Pd NWs/PEN samples measured by XPS; electron take-off angle of 0 and 81° from left and right side of samples.

right side after the second deposition for Ag nanostructures on laser-patterned poly(methyl) methacrylate was observed (18.7% from the right, left 8%), in this work, one-step deposition of metal (Ag or Pd) was used. The results revealed higher values of the atomic concentrations of both, Ag and Pd, from the left side (24.8% from the left, right 8.6% in case of Ag, 25.9 and 9.0% for Pd, respectively). The difference between our and Tumas' results, however, originates only from the rotation of samples during the analysis. The results for the electron take-off angle of 81° from the left and right side for the individual samples of pristine and laser-patterned PEN, showed undistinguishable differences in the atomic concentrations of elements. However, the measurements of metal/polymer composites under the same electron take-off angle revealed above-mentioned significant differences in the concentrations of metal, in case of both, Ag and Pd samples, which verified well the formation of NWs only from the one side of the ripples, which is in well accordance with above-mentioned shadow effect. The different results observed between the samples of pristine and laser-patterned PEN, particularly evident for the electron take-off angle of 81° (both left and right arrangement), were given by the change in the chemical-compositional arrangement caused by the exposure of a laser beam, which is associated with the change of the samples´ surface morphology, evident from atomic force microscopy (AFM) images (see **Figure 6**).

4.3. Atomic force microscopy (AFM)

Because the surface morphology of material has a great impact to its biocompatibility, AFM analysis was employed, too (see **Figures 5** and **6**). The surface morphology of the samples was characterized by surface roughness (R_a) measurements and three-dimensional AFM scans. **Figure 5** shows metal NLs and NIs/PEN composites, **Figure 6** metal NWs/PEN composites.

In **Figure 5**, one can see that the surfaces of pristine PEN and as-sputtered samples (both Ag and Pd NLs) were mildly corrugated with practically the same value of surface roughness. No significant morphology changes were observed after annealing of pristine polymer. However, one can see a remarkable change of the surface morphology of metal-coated samples after annealing (see differences between Ag and Pd NLs/PEN and Ag and Pd NIs/PEN); the annealing caused a complete rearrangement of the surface. Thermal accumulation in metal coating resulted in changes in the amorphous phase of PEN (T_g^{PEN} = 120°C). As the metal coating become rough, noticeable increase of R_a appears; cca two orders of magnitude higher compared to as-sputtered ones (NLs). After the annealing, one can observe the transformation of continuous metal coatings into isolated nanoislands homogeneously distributed over the PEN surface in case of both, Ag and Pd NIs samples. This phenomenon is in accordance with the results of XPS measurements (see **Table 3**); the values of atomic concentrations of metal (both, Ag and Pd) after annealing were decreased at the expense of C and O originating from PEN. Moreover, size and shape of metal NIs might be effectively controlled by the thickness of coating preceding the annealing process [8]. As mentioned above, the formation of island-like structures should lead to the increase of antibacterial-active surface area, resulting in enhanced antibacterial efficacy [5, 8, 57]. However, in this case, annealing resulted in above described "curtain" effect; partial covering of metal nanoislands by thin PEN layer (see Section 4.2. XPS). Based on these results, one can expect rather lower antibacterial efficacy than in case of NLs.

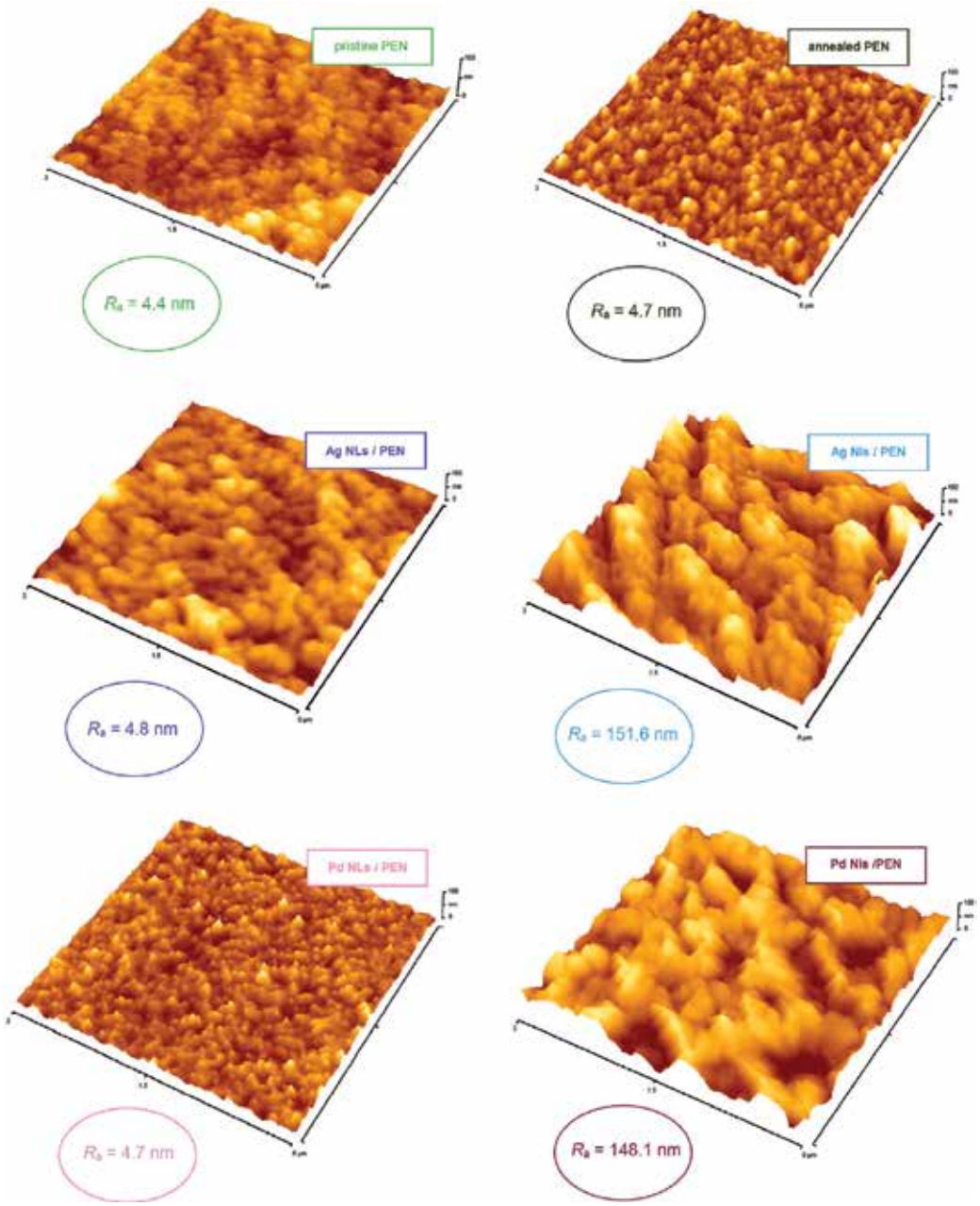

Figure 5. AFM images of PEN, both before (pristine) and after (annealed) annealing, Ag and Pd/PEN composites, together with their surface roughness (R_a).

The results of AFM analysis of metal NWs samples, both Ag and Pd (**Figure 6**) corresponds to FIB-SEM ones (see **Figure 4**), however, FIB-SEM analysis, by which, for example, the distribution and shape of nanowires might be evaluated, is more informative; AFM scans cannot provide the

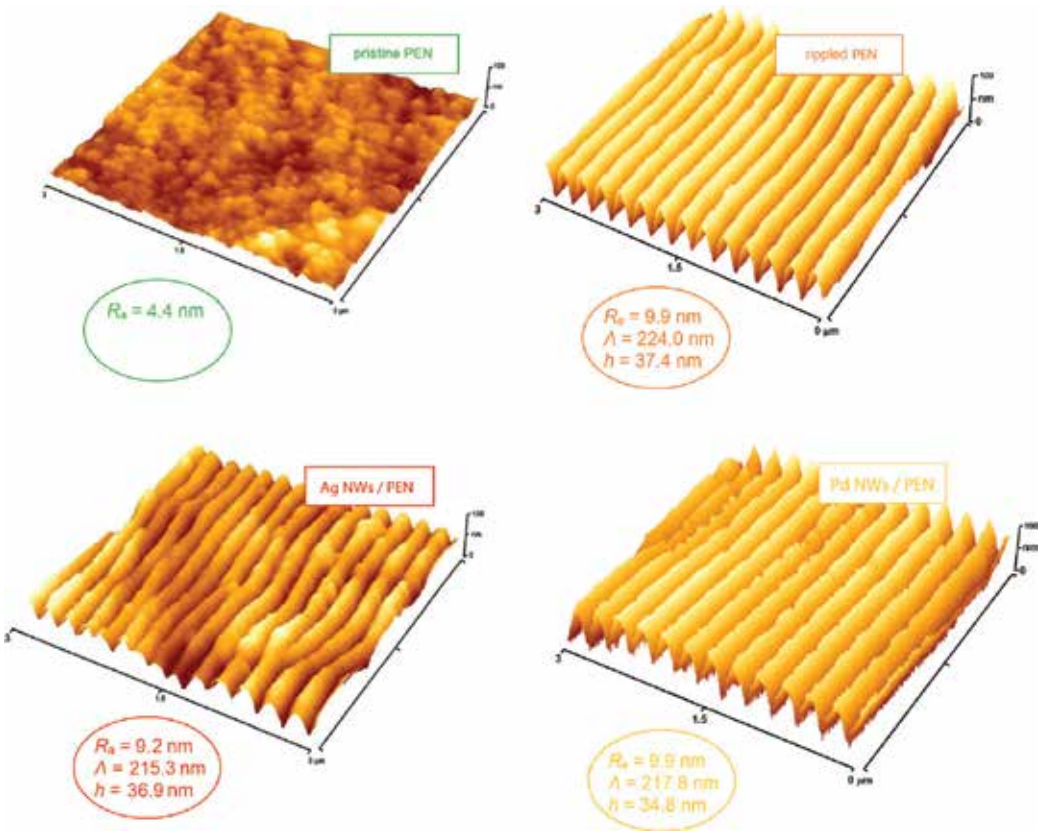

Figure 6. AFM images of PEN, both before (pristine) and after (rippled) laser patterning, Ag and Pd/PEN composites, together with their surface roughnesses (R_a), periodicities (Λ), and heights (h).

imaging of fully separated metal NWs. Using FIB cuts, one can observe the interface between a polymeric substrate (PEN) and metal (see **Figure 4(a)** and **(b)** for Ag and Pd NWs, respectively) and, in case of the analysis of the samples having various thicknesses of NWs, as in the work of Siegel et al. [62], it is also possible to distinguish significant differences between the prepared structures. Surface modification of polymer, such as laser patterning discussed in this paragraph, enables a direct control over the material biocompatibility; significantly increases the adhesion and proliferation of human cells on artificial substrates, and the resulting biocompatibility of material might be effectively enhanced [59]. One of the most important parameter of surface morphology, which has a great impact on the biocompatibility of material, is its surface roughness, which also plays an important role in its resulting antibacterial effects. For example, nanoscale surface roughness was effective to reduce plaque colonization on titanium implants [67]. Thus, the increase of biocompatibility and antibacterial effects of nanometal/polymer composites by laser patterning gives a convenient combination of materials′ properties for their applications in medicine and health-care industry. Regarding to this, we summarized surface morphology and roughness (R_a) of all prepared samples, including the parameters such as periodicity (Λ) and height (h) of nanostructures in case of ripples and wires. **Figure 6** shows self-organized and

well-separated periodic ripples homogenously distributed over the PEN surface. The value of R_a was considerably increased after laser patterning (4.4 nm for PEN and 9.9 nm for PEN ripples). There were no significant differences observed after metal deposition (9.2 nm for Ag and 9.9 nm for Pd, respectively). The values of periodicity and height of Ag NWs/PEN (Λ = 215.3 nm, h = 36.9 nm) and Pd NWs/PEN samples (Λ = 217.8 nm, h = 34.8 nm) were mildly decreased compared to patterned PEN (PEN ripples) sample (Λ = 224.0 nm, h = 37.4 nm), which was probably caused by a partial filling of the ripples by metal during vacuum evaporation process.

4.4. Antibacterial properties

Antibacterial effects of the samples related to control ones (physiological solution) are shown in **Figure 7** for metal NLs and NIs/PEN composites and in **Figure 8** for NWs/PEN composites, both Ag and Pd, in which two environmental bacterial strains (a) Gram-negative *E. coli* and (b) Gram-positive *S. epidermidis* were studied. The samples were examined in both, static and dynamic (shaking at 130 rpm) mode at 24°C (*E. coli*) and 37°C (*S. epidermidis*) for 3 and 24 h of incubation by the drop plate method [68]. After overnight incubation on agar plates, the number of colony forming units (CFU) of each strain was counted. The experiments were accomplished under sterile conditions.

In **Figure 7**, generally, one can see no antibacterial effects of pristine and annealed PEN, except insignificant effect in case of annealed sample cultivated for 3 h in dynamic mode with *E. coli* (**Figure 7(a)**). This phenomenon which might due to rougher surface morphology of this sample (see **Figure 5** AFM), which, together with shaking in dynamic mode, might cause this mild inconformity for bacterial colonies in short period of time (3 h) during which they accustom to surrounding environment [69]. Thereafter, one can observe generally increasing antibacterial effects with incubation time for all composites and treatment conditions, which is in correlation with (i) increasing concentration of released metals into physiological solution with time and (ii) longer contact of bacterial strains with the surface of antibacterial-active-coated samples, both Ag and Pd. For details, see ICP-MS results [8]. When comparing the results of NLs and NIs coatings in case of both metals, one can reveal that metal NLs/PEN samples exhibited similar or higher antibacterial response than NIs ones, which is in accordance with XPS results (see **Table 3**) and data published elsewhere [8], which attributed this behavior to so-called "curtain" effect; metal islands partially covered by thin polymer film. Thus, in the case of PEN, the change of surface morphology induced by annealing did not lead to increased antibacterial activity. When compared to the results for Ag and Pd samples, more significant antibacterial efficacy was observed for Pd ones, in case of both, NLs and NIs/PEN composites. It outlines that Pd nanostructures might be used as more effective alternative of the most commonly used Ag [70–72] for antibacterial coating of medical devices. The differences between the results in **Figure 7(a) and (b)** showed that *S. epidermidis* (**Figure 7(b)**) was more sensitive to both metals compared to *E. coli* (**Figure 7(a)**); the most striking is a total inhibition (no countable amount of CFU) in both modes and incubation times for Pd samples, both NLs and NIs. These different results for different bacterial strains might be explained by generally accepted phenomenon about different composition of their cell walls; positively charged particles of noble metals then more facile penetrate through the cell walls of Gram-positive bacteria (*S. epidermidis*) [73].

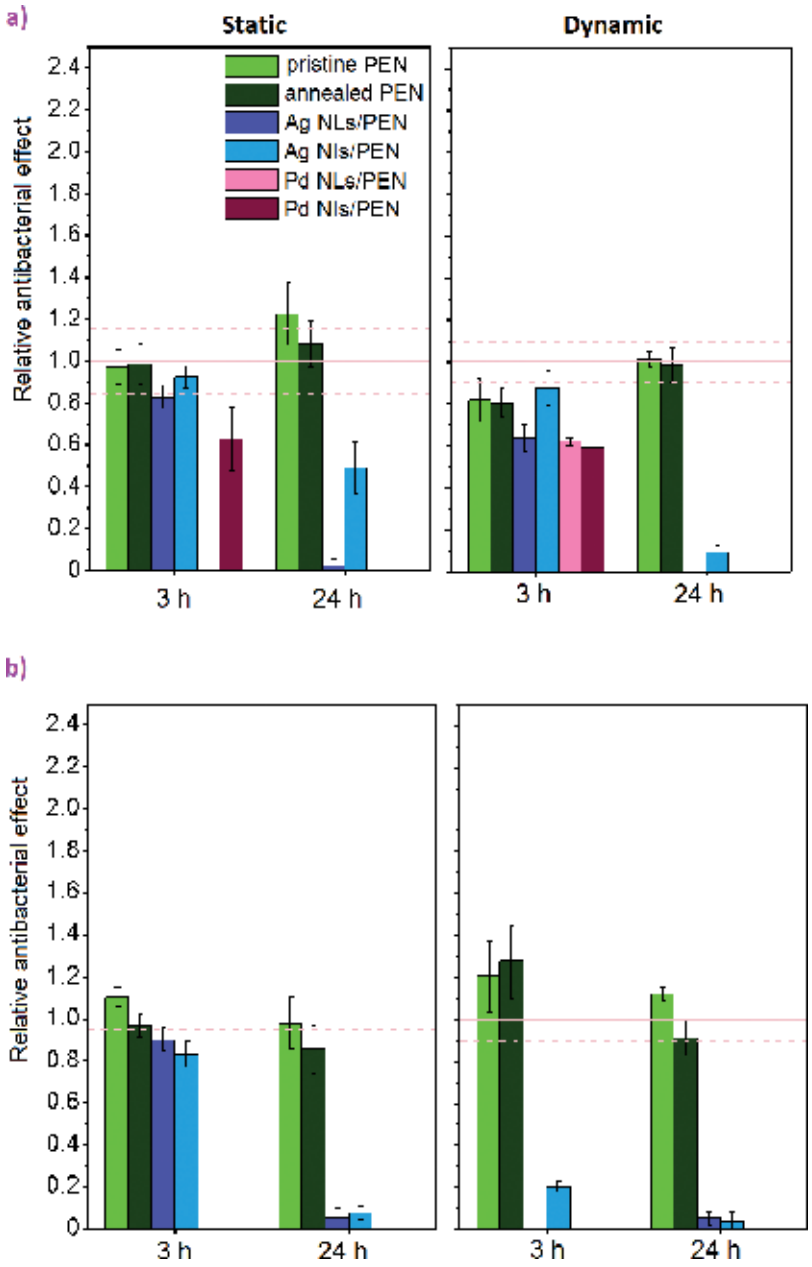

Figure 7. Relative antibacterial effect; number of CFU for examined sample divided by number of CFU for control sample (physiological solution) of the bacterial colonies of (a) *E. coli* and (b) *S. epidermidis* for both, pristine and annealed PEN, Ag and Pd/PEN composites measured in static and dynamic mode. Pink line represents a reference level (number of CFU in physiological solution) for corresponding bacterial strains together with its uncertainty (dash line).

The results for pristine and rippled PEN, Ag NWs/PEN and Pd equivalents are in **Figure 8**. One can see that pristine and rippled PEN were not antibacterial-active in all conditions. The exception is rippled PEN in dynamic mode after 24 h of cultivation of *S. epidermidis*

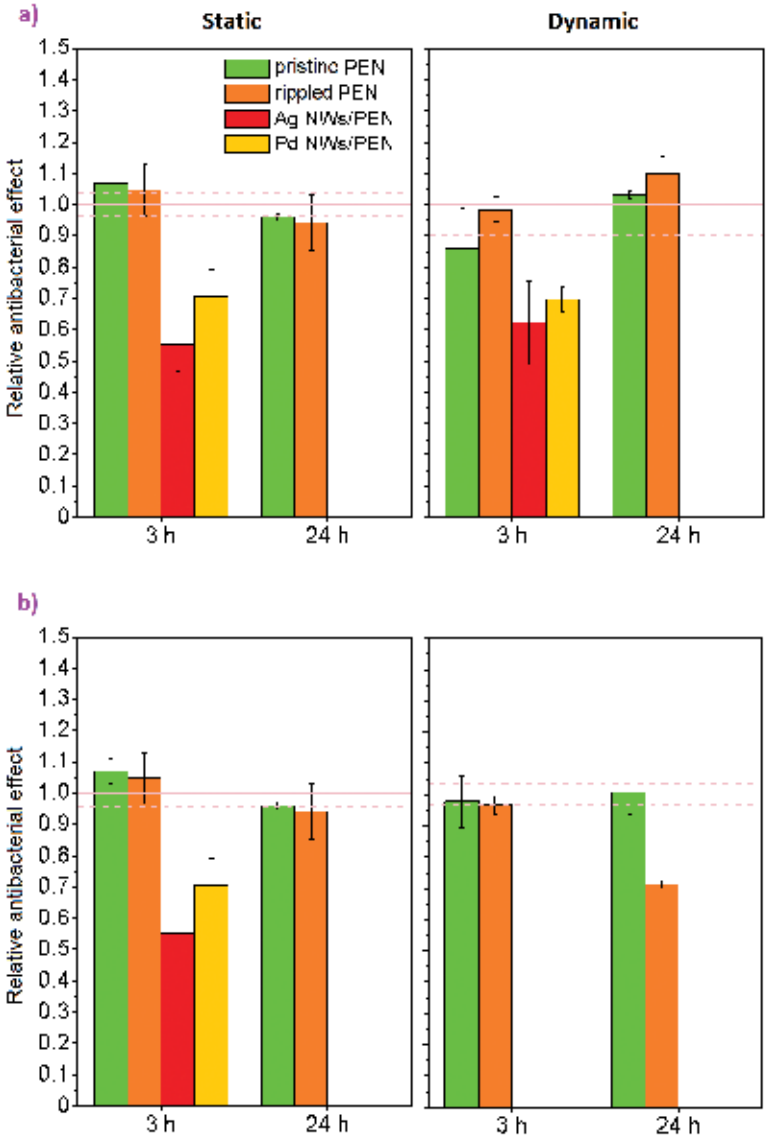

Figure 8. Relative antibacterial effect; number of CFU for examined sample divided by number of CFU for control sample (physiological solution) of the bacterial colonies of (a) *E. coli* and (b) *S. epidermidis* for both, pristine and rippled PEN, Ag and Pd NWs/PEN samples measured in static and dynamic mode. Pink line represents a reference level (number of CFU in physiological solution) for corresponding bacterial strains together with its uncertainty (dash line).

(**Figure 8(b)**). Mild antibacterial effect (ca. 30% of control sample) might be a consequence of higher sensitivity of Gram-positive bacteria to physicochemical and surface properties of a materials, with which they are in a contact, such as hydrophilicity/hydrophobicity, surface charge, presence of some functional groups, and, as in this case, surface morphology and

roughness (see **Figure 6**, AFM) [74, 75]. Antibacterial effect of Ag NWs/PEN and Pd ones samples increase with incubation time in both bacterial strains and both modes. Unlike *E. coli* (**Figure 8(a)**), these samples even exhibited total inhibition (no countable CFUs) after both, 3 and 24 h of incubation of *S. epidermidis* in dynamic conditions (**Figure 8(b)**). The difference between the results of *E. coli* and *S. epidermidis* might be explained by above-mentioned different composition of their cell walls; positively charged particles of noble metals then more facile penetrate through the cell walls of Gram-positive bacteria (*S. epidermidis*) [73]. The samples of Ag and Pd NWs showed comparable antibacterial effects between themselves in case of both bacterial strains, incubation times and modes, which well corresponds with presumed use of Pd NWs as an alternative of the most commonly used Ag in its medical applications as a strongly effective antibacterial agent (antibacterial coatings of catheters and other medical devices) [70–72].

4.5. Cell viability tests

Because the increase of the surface roughness of material (see **Figures 5** and **6** AFM) can, in some cases, lead to its enhanced biocompatibility (adhesion and proliferation of human cells [58, 59]), this paragraph is dedicated to cell viability testing of prepared Ag and Pd composites. Cell viability results for NLs and NIs structures are shown in **Figure 9**, for NWs in **Figure 10**.

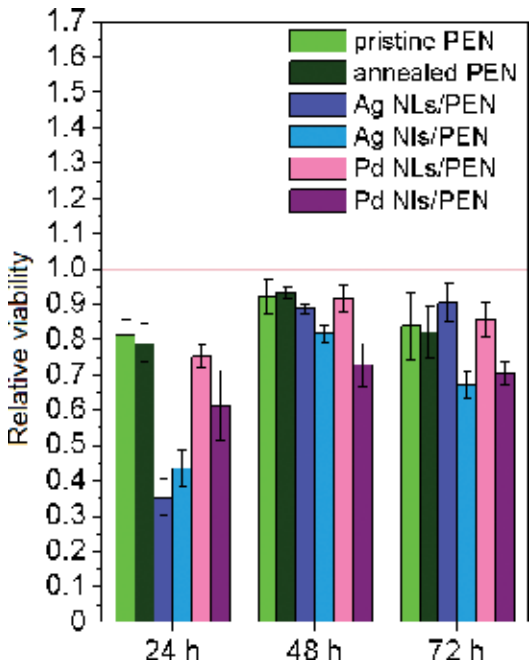

Figure 9. Relative viability; absorbance of examined sample divided by absorbance of control sample (TCPS) of the L929 model cell line for both, pristine and annealed PEN, Ag and Pd/PEN composites. Pink line represents a reference level (absorbance of TCPS) together with its uncertainty (dash line).

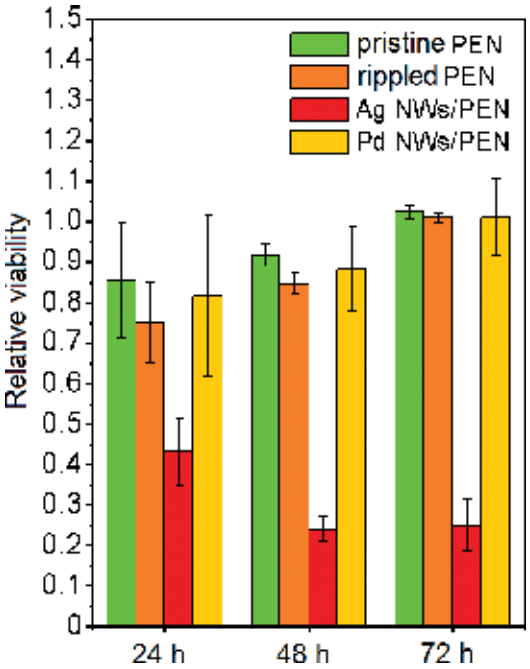

Figure 10. Relative viability; absorbance of examined sample divided by absorbance of control sample (TCPS) of the L929 model cell line for rippled PEN, and Ag and Pd NWs/PEN samples. Pink line represents a reference level (absorbance of TCPS) together with its uncertainty (dash line).

In recent studies, one can observe the references about cytotoxicity of nanostructured metal-based coatings of medical devices to human cells, from which Ag NWs seems to be the most cytotoxic ones [76–78]. Therefore, data from these assays serve as well for safer applications of nanometal/polymer composites in medicine and health-care industry in terms of their cytotoxicity. In following, relative viability of mouse embryonic fibroblasts (L929) was studied by WST-1 cytotoxicity assay [79, 80]. This assay is based on a reduction of tetrazolium salt, which yields water-soluble formazan by oxidoreductases of metabolically active (viable) cells. Formazan is then spectrophotometrically measured at 450 nm. The measured absorbance is directly proportional to the amount of the arisen formazan, which corresponds to the oxidoreductase activity, and thus, to the number of viable cells. Model cell line was cultivated for 24, 48 and 72 h, and acquired absorbance value for examined samples was divided by absorbance value for control sample (standard tissue culture polystyrene, TCPS).

Figure 9 shows the results for pristine and annealed PEN, NLs and NIs/PEN composites, both Ag and Pd. One can see that cell viability on PEN substrate was not changed by annealing and was comparable with control sample (TCPS) after longer cultivation times (48 and 72 h) in case of both, pristine and annealed equivalent. Insignificant decrease of relative cell viability of these samples, as well as the samples of NLs and NIs, both Ag and Pd, after 24 h, is connected with worse adaptation of cell culture after its deployment on the surfaces of the samples; TCPS is a material with optimized properties for *in vitro* cultivation of eukaryotic cells, and therefore, is frequently used as a "gold" cultivation standard [81]. Generally, one can

observe low cytotoxicity of all samples (NLs and NIs ones), where the cell viability on NLs samples (Ag and Pd) was superior. Interestingly, cell viability after longer cultivation times (48 and 72 h) on NLs samples was comparable regardless of the metal used. The same results were observed on NIs; both metals were comparably safe for cells. More significant cytotoxicity of annealed samples (Ag and Pd NIs/PEN) compared to as-sputtered ones (NLs/PEN) was presumably caused by high sensitivity of L929 cell line to rougher surfaces [69], rather than by cytotoxic action of metals; the results of XPS analysis (see **Table 3**) and other results published elsewhere [8] revealed partial covering of metal NIs by thin polymer layer, which decreased the amount of the metals available for cytotoxic action. To sum up, the increase of surface area and roughness in our case (see **Figure 5** AFM) did not led to the enhanced biocompatibility of the samples.

Cell viability results as obtained for pristine and rippled PEN, Ag and Pd NWs/PEN samples are shown in **Figure 10**. After all cultivation times, pristine PEN was not find to be cytotoxic. However, rippled one showed mild cytotoxicity after 24 and 48 h of cultivation of L929 cell line (ca. 15% of TCPS), which disappeared after 72 h. Since L929 cell line is characterized by high sensitivity to rougher surfaces [69], accordingly to previous case of NIs samples, it indicates that the cytotoxic effects were caused by more difficult adaptation and fixation of L929 onto rippled surface of PEN. Cytotoxicity testing confirms significant cytotoxic effects of Ag NWs, reported in a literature [76–78], which was, in the case of ours, determined to more than 50% of TCPS and increased with cultivation time. On the other hand, no cytotoxicity was detected for Pd NWs, in case of all cultivation times. Therefore, these samples could be a safer alternative to Ag NWs ones. Alike in previous case, increased surface area and roughness; induced now by laser patterning and subsequent metal deposition, did not resulted in improved biocompatibility.

5. Conclusions

We have shown that cathode sputtering can be used to prepare NPs of the desired size, which are suitable for subsequent study of their physicochemical properties, since the resulting system is usually composed of only two components; the NPs and the liquid medium used. In particular, sputtering into glycerol is advantageous for detecting of NPs biological properties without the need to consider the surfactant interaction. Results obtained in those systems can be used not only for qualitative research, for example, whether the NPs cytotoxicity is due to ROS induction or dissolution, but also for quantitative determination of toxic dose values.

This chapter also attempted to give comprehensive overview on various kinds of antibacterial-active nanostructured metal coatings of biocompatible PEN potentially applicable in medical devices. Various nanostructures such as NLs, NIs, and NWs were considered and their biological, antibacterial properties and cytotoxic efficacy were broadly discussed. The most commonly used metal in medical and health-care applications (nanostructured Ag) was confronted with Pd. It was found that the increase of surface roughness led to decrease of antibacterial effects of all nanostructured metal/PEN composites; particularly due to so-called "curtain " effect in case of NIs ones and biocompatibility, due to relatively high sensitivity

of used L929 cell line to rougher surfaces. The metal-coated samples forming NLs and NIs structures exhibited insignificant cytotoxic effects; taking into account the extent of action, which were presumably caused by increased surface roughness of the samples, rather than by cytotoxic action of nanostructured metal. Generally, the lowest cytotoxicity was found for metal NLs/PEN composites, both Ag and Pd at the same level. The higher antibacterial efficacy of Pd ones, however, predetermines them as a more suitable alternative in medical and health-care applications. Regarding to results of antibacterial and cytotoxicity tests, in case of laser-patterned samples, it turned out that both Ag and Pd NWs/PEN composites have the appropriate antibacterial properties. However, only Pd ones fulfill the condition of cells´ safety, which makes them suitable candidates for the use as antibacterial coatings of medical devices instead of Ag. The potential applications of Ag NWs in medicine and health-care industry are found to be limited and their contact with living tissues, for example, the treatment of medical devices, should be minimized.

Acknowledgements

Financial support of this work from the GACR projects Nos. 17-10907S and P108/12/G108 is gratefully acknowledged.

Author details

Jakub Siegel*, Marek Staszek, Markéta Polívková, Michaela Valová, Pavla Šuláková and Václav Švorčík

*Address all correspondence to: jakub.siegel@vscht.cz

Department of Solid State Engineering, University of Chemistry and Technology Prague, Prague, Czech Republic

References

[1] Polivkova M, Strublova V, Hubacek T, Rimpelova S, Svorcik V, Siegel J. Surface characterization and antibacterial response of silver nanowire arrays supported on laser-treated polyethylene naphthalate. Materials Science and Engineering C: Materials for Biological Applications. 2017;**72**:512-518. DOI: 10.1016/j.msec.2016.11.072

[2] Polivkova M, Siegel J, Rimpelova S, Hubacek T, Kolska Z, Svorcik V. Cytotoxicity of Pd nanostructures supported on PEN: Influence of sterilization on Pd/PEN interface. Materials Science and Engineering C: Materials for Biological Applications. 2017;**70**:479-486. DOI: 10.1016/j.msec.2016.09.032

[3] Polivkova M, Hubacek T, Staszek M, Svorcik V, Siegel J. Antimicrobial treatment of polymeric medical devices by silver nanomaterials and related technology. International Journal of Molecular Sciences. 2017;**18**:1-24. DOI: 10.3390/ijms18020419

[4] Reznickova A, Siegel J, Slavikova N, Kolska Z, Staszek M, Svorcik V. Metal nanoparticles designed PET: Preparation, characterization and biological response. Reactive and Functional Polymers. 2016;**105**:1-8. DOI: 10.1016/j.reactfunctpolym.2016.05.012

[5] Siegel J, Polivkova M, Staszek M, Kolarova K, Rimpelova S, Svorcik V. Nanostructured silver coatings on polyimide and their antibacterial response. Materials Letters. 2015; **145**:87-90. DOI: 10.1016/j.matlet.2015.01.050

[6] Slepicka P, Kasalkova NS, Siegel J, Kolska Z, Bacakova L, Svorcik V. Nano-structured and functionalized surfaces for cytocompatibility improvement and bactericidal action. Biotechnology Advances. 2015;**33**:1120-1129. DOI: 10.1016/j.biotechadv.2015.01.001

[7] Siegel J, Polivkova M, Kasalkova NS, Kolska Z, Svorcik V. Properties of silver nanostructure-coated PTFE and its biocompatibility. Nanoscale Research Letters. 2013;**8**:1-10. DOI: 10.1186/1556-276x-8-388

[8] Polivkova M, Valova M, Siegel J, Rimpelova S, Hubacek T, Lyutakov O, Svorcik V. Antibacterial properties of palladium nanostructures sputtered on polyethylene naphthalate. RSC Advances. 2015;**5**:73767-73774. DOI: 10.1039/c5ra09297c

[9] Staszek M, Siegel J, Rimpelova S, Lyutakov O, Svorcik V. Cytotoxicity of noble metal nanoparticles sputtered into glycerol. Materials Letters. 2015;**158**:351-354. DOI: 10.1016/j.matlet.2015.06.021

[10] Staszek M, Siegel J, Kolarova K, Rimpelova S, Svorcik V. Formation and antibacterial action of Pt and Pd nanoparticles sputtered into liquid. Micro & Nano Letters. 2014;**9**:778-781. DOI: 10.1049/mnl.2014.0345

[11] Siegel J, Kolarova K, Vosmanska V, Rimpelova S, Leitner J, Svorcik V. Antibacterial properties of green-synthesized noble metal nanoparticles. Materials Letters. 2013;**113**:59-62. DOI: 10.1016/j.matlet.2013.09.047

[12] Lyutakov O, Kalachyova Y, Solovyev A, Vytykacova S, Svanda J, Siegel J, Ulbrich P, Svorcik V. One-step preparation of antimicrobial silver nanoparticles in polymer matrix. Journal of Nanoparticle Research. 2015;**17**:1-11. DOI: 10.1007/s11051-015-2935-3

[13] Eid M. Gamma radiation synthesis and characterization of starch based polyelectrolyte hydrogels loaded silver nanoparticles. Journal of Inorganic and Organometallic Polymers and Materials 2011;**21**:297-305. DOI: 10.1007/s10904-010-9448-4

[14] Shervani Z, Yamamoto Y. Carbohydrate-directed synthesis of silver and gold nanoparticles: Effect of the structure of carbohydrates and reducing agents on the size and morphology of the composites. Carbohydrate Research. 2011;**346**:651-658. DOI: 10.1016/j.carres.2011.01.020

[15] Vimala K, Sivudu KS, Mohan YM, Sreedhar B, Raju KM. Controlled silver nanoparticles synthesis in semi-hydrogel networks of poly(acrylamide) and carbohydrates: A rational methodology for antibacterial application. Carbohydrate Polymers. 2009;**75**:463-471. DOI: 10.1016/j.carbpol.2008.08.009

[16] Batabyal SK, Basu C, Das AR, Sanyal GS. Green chemical synthesis of silver nanowires and microfibers using starch. Journal of Biobased Materials and Bioenergy. 2007;**1**:143-147. DOI: 10.1166/jbmb.2007.016

[17] Vosmanska V, Kolarova K, Rimpelova S, Kolska Z, Svorcik V. Antibacterial wound dressing: Plasma treatment effect on chitosan impregnation and in situ synthesis of silver chloride on cellulose surface. RSC Advances. 2015;**5**:17690-17699. DOI: 10.1039/c4ra16296j

[18] Han J, Wang M, Hu Y, Zhou C, Guo R. Conducting polymer-noble metal nanoparticle hybrids: Synthesis mechanism application. Progress in Polymer Science. 2017;**70**:52-91. DOI: 10.1016/j.progpolymsci.2017.04.002

[19] Svorcik V, Kolska Z, Siegel J, Slepicka P. "Short" dithiol and Au nanoparticles grafting on plasma treated polyethyleneterephthalate. Journal of Nano Research. 2013;**25**:40-48. DOI: 10.4028/www.scientific.net/JNanoR.25.40

[20] Siegel J, Lyutakov O, Polívková M, Staszek M, Hubáček T, Švorčík V. Laser-assisted immobilization of colloid silver nanoparticles on polyethyleneterephthalate. Applied Surface Science. 2017;**420**:661-668. DOI: 10.1016/j.apsusc.2017.05.151

[21] Gao-xiang Y, Chun-mu F, Qi-rui Z, Hong-liang G, Xuan-jia Z. Structural and critical behaviors of Ag rough films deposited on liquid substrates. Chinese Physics Letters. 1996;**13**:772. DOI: 10.1088/0256-307X/13/10/016

[22] Borra EF, Seddiki O, Angel R, Eisenstein D, Hickson P, Seddon KR, Worden SP. Deposition of metal films on an ionic liquid as a basis for a lunar telescope. Nature. 2007;**447**:979. DOI: 10.1038/nature05909

[23] Antonietti M, Kuang D, Smarsly B, Zhou Y. Ionic liquids for the convenient synthesis of functional nanoparticles and other inorganic nanostructures. Angewandte Chemie International Edition. 2004;**43**:4988-4992. DOI: 10.1002/anie.200460091

[24] Wender H, Migowski P, Feil AF, Teixeira SR, Dupont J. Sputtering deposition of nanoparticles onto liquid substrates: Recent advances and future trends. Coordination Chemistry Reviews. 2013;**257**:2468-2483. DOI: 10.1016/j.ccr.2013.01.013

[25] Paulechka YU, Kabo GJ, Blokhin AV, Vydrov OA, Magee JW, Frenkel M. Thermodynamic properties of 1-butyl-3-methylimidazolium hexafluorophosphate in the ideal gas state. Journal of Chemical & Engineering Data. 2003;**48**:457-462. DOI: 10.1021/je025591i

[26] Hanusek J. Iontove kapaliny—nový směr v "zelene" chemii. Chemicke Listy. 2005;**99**:265-267

[27] Thuy Pham TP, Cho C-W, Yun Y-S. Environmental fate and toxicity of ionic liquids: A review. Water Research. 2010;**44**:352-372. DOI: 10.1016/j.watres.2009.09.030

[28] Wender H, de Oliveira LF, Feil AF, Lissner E, Migowski P, Meneghetti MR, Teixeira SR, Dupont J. Synthesis of gold nanoparticles in a biocompatible fluid from sputtering deposition onto castor oil. Chemical Communications 2010;**46**:7019-7021. DOI: 10.1039/c0cc01353f

[29] Slepicka P, Elashnikov R, Ulbrich P, Staszek M, Kolska Z, Svorcik V. Stabilization of sputtered gold and silver nanoparticles in PEG colloid solutions. Journal of Nanoparticle Research. 2015;**17**:1-15. DOI: 10.1007/s11051-014-2850-z

[30] Reznickova A, Slepicka P, Slavikova N, Staszek M, Svorcik V. Preparation, aging and temperature stability of PEGylated gold nanoparticles. Colloids and Surfaces A: Physicochemical and Engineering Aspects. 2017;**523**:91-97. DOI: 10.1016/j.colsurfa.2017.04.005

[31] Ndiaye PM, Tavares FW, Dalmolin I, Dariva C, Oliveira D, Oliveira JV. Vapor pressure data of soybean oil, castor oil, and their fatty acid ethyl ester derivatives. Journal of Chemical & Engineering Data. 2005;**50**:330-333. DOI: 10.1021/je049898o

[32] Gref R, Lück M, Quellec P, Marchand M, Dellacherie E, Harnisch S, Blunk T, Müller RH. 'Stealth' corona-core nanoparticles surface modified by polyethylene glycol (PEG): Influences of the corona (PEG chain length and surface density) and of the core composition on phagocytic uptake and plasma protein adsorption. Colloids and Surfaces B: Biointerfaces. 2000;**18**:301-313. DOI: 10.1016/S0927-7765(99)00156-3

[33] Association GP. Physical Properties of Glycerine and its Solutions. Glycerine Producers' Association. New York; 1963

[34] Wender H, de Oliveira LF, Migowski P, Feil AF, Lissner E, Prechtl MH, Teixeira SR, Dupont J. Ionic liquid surface composition controls the size of gold nanoparticles prepared by sputtering deposition. Journal of Physical Chemistry C 2010;**114**:11764-11768. DOI: 10.1021/jp102231x

[35] Hatakeyama Y, Takahashi S, Nishikawa K. Can temperature control the size of Au nanoparticles prepared in ionic liquids by the sputter deposition technique? Journal of Physical Chemistry C. 2010;**114**:11098-11102. DOI: 10.1021/jp102763n

[36] Richter K, Birkner A, Mudring A-V. Stabilizer-free metal nanoparticles and metal–metal oxide Nanocomposites with long-term stability prepared by physical vapor deposition into ionic liquids. Angewandte Chemie International Edition. 2010;**49**:2431-2435. DOI: 10.1002/anie.200901562

[37] Hatakeyama Y, Morita T, Takahashi S, Onishi K, Nishikawa K. Synthesis of gold nanoparticles in liquid polyethylene glycol by sputter deposition and temperature effects on their size and shape. Journal of Physical Chemistry C. 2011;**115**:3279-3285. DOI: 10.1021/jp110455k

[38] Anantha P, Cheng T, Tay YY, Wong CC, Ramanujan RV. Facile production of monodisperse nanoparticles on a liquid surface. Nanoscale. 2015;**7**:16812-16822. DOI: 10.1039/C5NR05904F

[39] Ali M, Abarca G, Eberhardt D, Gual A, Bernardi F, Teixeira SR, Dupont J. "Save money" during hydrogenation reactions by exploiting the superior performance of Pd-NPs deposited on carbon black by magnetron sputtering. Tetrahedron. 2017;**73**:5593-5598. DOI: 10.1016/j.tet.2016.11.043

[40] Staszek M, Siegel J, Polivkova M, Svorcik V. Influence of temperature on silver nanoparticle size prepared by sputtering into PVP-glycerol system. Materials Letters. 2017;**186**:341-344. DOI: 10.1016/j.matlet.2016.10.036

[41] Tsuzuki T. Commercial scale production of inorganic nanoparticles. International Journal of Nanotechnology. 2009;**6**:567-578. DOI: 10.1504/IJNT.2009.024647

[42] Park E-J, Bae E, Yi J, Kim Y, Choi K, Lee SH, Yoon J, Lee BC, Park K. Repeated-dose toxicity and inflammatory responses in mice by oral administration of silver nanoparticles. Environmental Toxicology and Pharmacology. 2010;**30**:162-168. DOI: 10.1016/j.etap.2010.05.004

[43] Lima R, Seabra AB, Durán N. Silver nanoparticles: A brief review of cytotoxicity and genotoxicity of chemically and biogenically synthesized nanoparticles. Journal of Applied Toxicology. 2012;**32**:867-879. DOI: 10.1002/jat.2780

[44] Shukla R, Bansal V, Chaudhary M, Basu A, Bhonde RR, Sastry M. Biocompatibility of gold nanoparticles and their Endocytotic fate inside the cellular compartment: A microscopic overview. Langmuir. 2005;**21**:10644-10654. DOI: 10.1021/la0513712

[45] Pernodet N, Fang X, Sun Y, Bakhtina A, Ramakrishnan A, Sokolov J, Ulman A, Rafailovich M. Adverse effects of citrate/gold nanoparticles on human dermal fibroblasts. Small. 2006; **2**:766-773. DOI: 10.1002/smll.200500492

[46] Asharani PV, Lianwu Y, Gong Z, Valiyaveettil S. Comparison of the toxicity of silver, gold and platinum nanoparticles in developing zebrafish embryos. Nanotoxicology. 2011;**5**:43-54. DOI: 10.3109/17435390.2010.489207

[47] Gao J, Liang G, Zhang B, Kuang Y, Zhang X, Xu B. FePt@CoS_2 Core-Shell Nanocrystals as a potent agent to kill HeLa cells. Journal of the American Chemical Society. 2007;**129**:1428-1433. DOI: 10.1021/ja067785e

[48] Bakri SJ, Pulido JS, Mukherjee P, Marler RJ, Mukhopadhyay D. Absence of histologic retinal toxicity of intravitreal nanogold in a rabbit model. Retina. 2008;**28**:147-149. DOI: 10.1097/IAE.0b013e3180dc9360

[49] Muñoz-Bonilla A, Fernández-García M. Polymeric materials with antimicrobial activity. Progress in Polymer Science. 2012;**37**:281-339. DOI: 10.1016/j.progpolymsci.2011.08.005

[50] Timofeeva L, Kleshcheva N. Antimicrobial polymers: Mechanism of action, factors of activity, and applications. Applied Microbiology and Biotechnology. 2011;**89**:475-492. DOI: 10.1007/s00253-010-2920-9

[51] Tashiro T. Antibacterial and bacterium adsorbing macromolecules. Macromolecular Materials and Engineering. 2001;**286**:63-87. DOI: 10.1002/1439-2054(20010201)286:2<63: AID-MAME63>3.0.CO;2-H

[52] Gabriel GJ, Som A, Madkour AE, Eren T, Tew GN. Infectious disease: Connecting innate immunity to biocidal polymers. Materials Science and Engineering: R: Reports. 2007;**57**:28-64. DOI: 10.1016/j.mser.2007.03.002

[53] Page K, Wilson M, Parkin IP. Antimicrobial surfaces and their potential in reducing the role of the inanimate environment in the incidence of hospital-acquired infections. Journal of Materials Chemistry. 2009;**19**:3819-3831. DOI: 10.1039/b818698g

[54] Roe D, Karandikar B, Bonn-Savage N, Gibbins B, Roullet J-B. Antimicrobial surface functionalization of plastic catheters by silver nanoparticles. The Journal of Antimicrobial Chemotherapy. 2008;**61**:869-876. DOI: 10.1093/jac/dkn034

[55] Yao Y, Ohko Y, Sekiguchi Y, Fujishima A, Kubota Y. Self-sterilization using silicone catheters coated with Ag and TiO2 nanocomposite thin film. Journal of Biomedial Materials Research Part B Applied Biomaterials. 2008;**85**:453-460. DOI: 10.1002/jbm.b.30965

[56] Siegel J, Polívková M, Kasálková NS, Kolská Z, Švorčík V. Properties of silver nanostructure-coated PTFE and its biocompatibility. Nanoscale Research Letters. 2013;**8**:388. DOI: 10.1186/1556-276X-8-388

[57] Siegel J, Krajcar R, Kolská Z, Hnatowicz V, Švorčík V. Annealing of gold nanostructures sputtered on polytetrafluoroethylene. Nanoscale Research Letters. 2011;**6**:588. DOI: 10.1186/1556-276X-6-588

[58] Yeung T, Georges PC, Flanagan LA, Marg B, Ortiz M, Funaki M, Zahir N, Ming W, Weaver V, Janmey PA. Effects of substrate stiffness on cell morphology, cytoskeletal structure, and adhesion. Cytoskeleton. 2005;**60**:24-34. DOI: 10.1002/cm.20041

[59] Rebollar E, Frischauf I, Olbrich M, Peterbauer T, Hering S, Preiner J, Hinterdorfer P, Romanin C, Heitz J. Proliferation of aligned mammalian cells on laser-nanostructured polystyrene. Biomaterials. 2008;**29**:1796-1806. DOI: 10.1016/j.biomaterials.2007.12.039

[60] Belardini A, Larciprete MC, Centini M, Fazio E, Sibilia C, Bertolotti M, Toma A, Chiappe D, de Mongeot FB. Tailored second harmonic generation from self-organized metal nano-wires arrays. Optics Express 2009;**17**:3603-3609. DOI: 10.1364/oe.17.003603

[61] Toma A, Chiappe D, Massabo D, Boragno C, Buatier de Mongeot F. Self-organized metal nanowire arrays with tunable optical anisotropy. Applied Physics Letters. 2008;**93**:163104. DOI: 10.1063/1.3002319

[62] Siegel J, Heitz J, Reznickova A, Svorcik V. Preparation and characterization of fully separated gold nanowire arrays. Applied Surface Science. 2013;**264**:443-447. DOI: 10.1016/j.apsusc.2012.10.041

[63] Siegel J, Heitz J, Švorčík V. Self-organized gold nanostructures on laser patterned PET. Surface and Coating Technology. 2011;**206**:517-521. DOI: 10.1016/j.surfcoat.2011.07.080

[64] Tyler B, Castner D, Ratner B. Regularization: A stable and accurate method for generating depth profiles from angle-dependent XPS data. Surface and Interface Analysis. 1989;**14**:443-450. DOI: 10.1002/sia.740140804

[65] Lewis KB, Ratner BD. Observation of surface rearrangement of polymers using ESCA. Journal of Colloid and Interface Science. 1993;**159**:77-85. DOI: 10.1006/jcis.1993.1299

[66] Tůma J, Lyutakov O, Huttel I, Siegel J, Heitz J, Kalachyova Y, Švorčík V. Silver nanostructures prepared by oriented evaporation on laser-patterned poly (methyl methacrylate). Journal of Materials Science. 2013;**48**:900-905. DOI: 10.1007/s10853-012-6812-5

[67] Rimondini L, Farè S, Brambilla E, Felloni A, Consonni C, Brossa F, Carrassi A. The effect of surface roughness on early in vivo plaque colonization on titanium. Journal of Periodontology. 1997;**68**:556-562. DOI: 10.1902/jop.1997.68.6.556

[68] Herigstad B, Hamilton M, Heersink J. How to optimize the drop plate method for enumerating bacteria. Journal of Microbiological Methods. 2001;**44**:121-129. DOI: 10.1016/S0167-7012(00)00241-4

[69] Taylor RL, Verran J, Lees GC, Ward AP. The influence of substratum topography on bacterial adhesion to polymethyl methacrylate. Journal of Materials Science: Materials in Medicine. 1998;**9**:17-22. DOI: 10.1023/A:1008820313720

[70] Knetsch ML, Koole LH. New strategies in the development of antimicrobial coatings: The example of increasing usage of silver and silver nanoparticles. Polymer. 2011;**3**:340-366. DOI: 10.3390/polym3010340

[71] Leaper DJ. Silver dressings: Their role in wound management. International Wound Journal. 2006;**3**:282-294. DOI: 10.1111/j.1742-481X.2006.00265.x

[72] Tran N, Tran PA. Nanomaterial-based treatments for medical device-associated infections. Chemphyschem. 2012;**13**:2481-2494. DOI: 10.1002/cphc.201200091

[73] Jung WK, Koo HC, Kim KW, Shin S, Kim SH, Park YH. Antibacterial activity and mechanism of action of the silver ion in Staphylococcus Aureus and *Escherichia coli*. Applied and Environmental Microbiology. 2008;**74**:2171-2178. DOI: 10.1128/AEM.02001-07

[74] Gao J, Niklason L, Langer R. Surface hydrolysis of poly (glycolic acid) meshes increases the seeding density of vascular smooth muscle cells. Journal of Biomedical Materials Research. 1998;**42**:417-424. DOI: 10.1002/(SICI)1097-4636(19981205)42:3<417:AID-JBM11>3.0.CO;2-D

[75] Kim SR. Surface modification of poly (tetrafluoroethylene) film by chemical etching, plasma, and ion beam treatments. Journal of Applied Polymer Science. 2000;**77**:1913-1920. DOI: 10.1002/1097-4628(20000829)77:9<1913:Aid-App7>3.0.Co;2-#

[76] Stoehr LC, Gonzalez E, Stampfl A, Casals E, Duschl A, Puntes V, Oostingh GJ. Shape matters: Effects of silver nanospheres and wires on human alveolar epithelial cells. Particle and Fibre Toxicology. 2011;**8**:36. DOI: 10.1186/1743-8977-8-36

[77] Zhang T, Wang L, Chen Q, Chen C. Cytotoxic potential of silver nanoparticles. Yonsei Medical Journal. 2014;**55**:283-291. DOI: 10.3349/ymj.2014.55.2.283

[78] Kim MJ, Shin S. Toxic effects of silver nanoparticles and nanowires on erythrocyte rheology. Food and Chemical Toxicology. 2014;**67**:80-86. DOI: 10.1016/j.fct.2014.02.006

[79] Mosmann T. Rapid colorimetric assay for cellular growth and survival: Application to proliferation and cytotoxicity assays. Journal of Immunological Methods. 1983;**65**:55-63. DOI: 10.1016/0022-1759(83)90303-4

[80] Ishiyama M, Tominaga H, Shiga M, Sasamoto K, Ohkura Y, Ueno K. A combined assay of cell vability and in vitro cytotoxicity with a highly water-soluble tetrazolium salt, neutral red and crystal violet. Biological & Pharmaceutical Bulletin. 1996;**19**:1518-1520. DOI: 10.1248/bpb.19.1518

[81] Peskova V, Kubies D, Hulejova H, Himmlova L. The influence of implant surface properties on cell adhesion and proliferation. Journal of Materials Science: Materials in Medicine. 2007;**18**:465-473. DOI: 10.1007/s10856-007-2006-0

Chapter 15

Structure and Applications of Gold in Nanoporous Form

Jay K. Bhattarai, Dharmendra Neupane,
Bishal Nepal, Vasilii Mikhaylov,
Alexei V. Demchenko and Keith J. Stine

Additional information is available at the end of the chapter

http://dx.doi.org/10.5772/intechopen.71439

Abstract

Nanoporous gold (np-Au) has many interesting and useful properties that make it a material of interest for use in many technological applications. Its biocompatible nature and ability to serve as a support for self-assembled monolayers of alkanethiols and their derivative make it a suitable support for the immobilization of carbohydrates, enzymes, proteins, and DNA. Its chemically inert, physically robust and conductive high-surface area makes it useful for the design of electrochemistry-based chemical/bio-sensors and reactors. Furthermore, it is also used as solid support for organic molecular synthesis and biomolecules separation. Its enhanced optical property has application in design of plasmonics-based sensitive biosensors. In fact, np-Au is one of the few materials that can be used as a transducer for both optical and electrochemical biosensing. Due to the presence of low-coordination surface sites, np-Au shows remarkable catalytic activity for oxidation of molecules like carbon monoxide and methanol. Owing to the importance of np-Au, in this chapter we will highlight different strategies of fabrication of np-Au and its emerging applications based on its unique properties.

Keywords: nanoporous gold (np-Au), dealloying, catalysis, biosensor, actuator, plasmonics

1. Introduction

The importance of the nanoporous materials has been well established historically by the extensive use of zeolite and activated carbon in separation and purification for industrial and clinical applications [1, 2]. Research on nanoporous materials for gas storage, drug delivery, catalysis, sensing, and optoelectronic applications are ongoing with the focus of using the

properties of nanoporous materials to their fullest to improve nanotechnology to the state-of-the-art. In recent years, nanostructures of gold have gained great attention because of their broad range of potential applications in the fields of medicine and energy. Gold nanoparticles (AuNPs) have already been used in a clinical trial for the thermal ablation of solid tumors as a photothermal agent due to its unique optical properties [3]. It has also shown promising results in drug delivery and as a contrast agent for imaging to advance cancer therapy [4]. Gold nanorods (GNs) have also shown promising results in biosensing, drug delivery, photothermal therapy, and imaging.

Gold in the nanoporous form, so-called nanoporous gold (np-Au), has gathered considerable attention recently, as it is a robust 3-dimensional nanostructured form of gold with a very high surface area-to-volume ratio and still maintains the properties of AuNPs and GN [5]. The size of the pores and ligament of np-Au can be easily tuned and are in the range from few nanometers to few hundreds of nanometers [6]. The AuNPs and GNs easily aggregate if suitable conditions were not provided making them less useful for some nanotechnology applications. The np-Au not only circumvents this problem but is simple to prepare and easy to handle for wide varieties of applications.

Through this survey and discussion, we will demonstrate that there is a growing interest in this material, which is justified by its many emerging applications. As a support for enzyme immobilization, the material has accommodated a range of enzymes and is suitable for the development of enzyme reactors. Numerous biosensors for metabolites and for biomarkers have been introduced using np-Au as a support. The applications to catalysis have included many of the oxidation reactions suitable for gold nanoparticles, but with the advantage of possible use in a free-standing intact format. The support of surface plasmons by the material opens up possibilities for use in the development of optical biosensors.

This chapter will cover different synthetic strategies for the preparation of np-Au in different forms. We will also discuss the methods commonly used to characterize np-Au, including scanning electron microscopy, transmission electron microscopy, tomography, and gas adsorption isotherm measurements. Finally, we will focus on the broad range of applications of np-Au, including chemical sensing, electrochemical and optical biosensing, catalysis, and mechanical actuation.

2. Methods of preparation

2.1. Dealloying

The most common method of preparing np-Au is by dealloying [7]. It is a top-down approach where the alloy of gold containing other less noble metals is treated in a corrosive environment with or without applying a potential. The dealloying process selectively removes the less noble metal from Au-M alloy (M═Ag, Cu, Sn, Al, etc.) creating the nanoporous structure having interconnected ligaments [7, 8]. The shape and size of the alloy is important as the np-Au formed after the dealloying process maintains the shape and size of

the alloy. The np-Au can be fabricated as a supported thin film or a free-standing structure. The supported np-Au is physically stable and easy to handle compared to the free-standing np-Au and is most commonly prepared for use as a working electrode in electrochemical experiments. Using supported np-Au, it is convenient to separate the interfacial boundary between np-Au and the clip holding the electrode. **Figure 1A** shows SEM images of the cross-section of np-Au supported on gold wire prepared by first forming the Au-Ag alloy using electrochemical deposition followed by dealloying in HNO_3 for 24 h to selectively remove Ag [9]. **Figure 1A′** is a low magnification SEM image of surface morphology of the as-prepared np-Au and the inset is the high magnification image [9]. Low magnification image shows crack formation throughout the surface due to the volume shrinkage during dealloying whereas high magnification image shows a porous structure having inter-ligament gap (pore size) of 27 ± 7 nm and ligament width of 26 ± 5 nm.

On the other hand, if the electrochemical connection is not desired, the free-standing np-Au is the material of choice for different applications, such as optical biosensing, solid-support organic synthesis, and protein separation. Free-standing np-Au plates, leaves and wires can be easily fabricated by simply dealloying the commercially available 10–12 Karat gold alloys in the desired form. The thicker the alloy, the longer should be the dealloying time for the effective removal of the sacrificial metals. Dealloying time is also important in determining

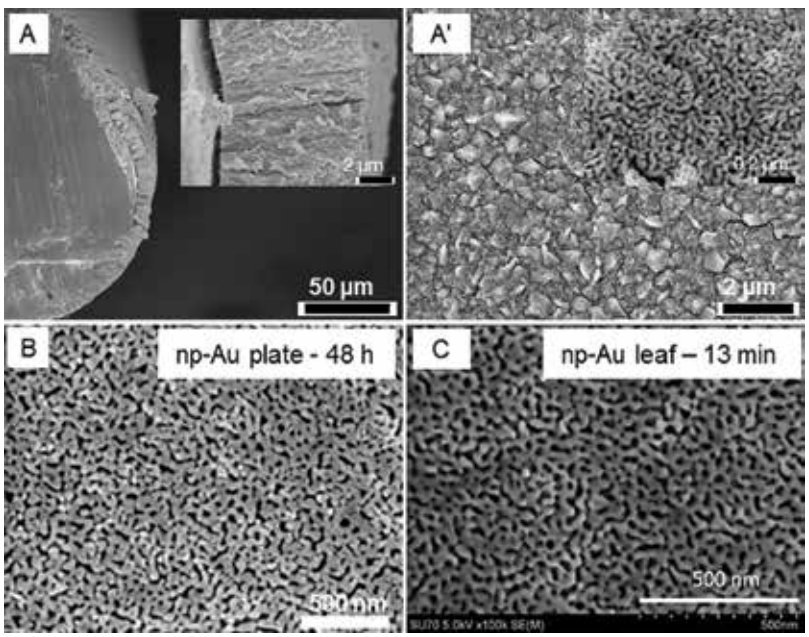

Figure 1. SEM images of np-Au in different form prepared by dealloying in concentrated HNO_3. (A) Cross-section of Au supported np-Au obtained by 24 h selective dissolution of Ag from Au-Ag alloy, where the alloy was prepared by providing potential of −1.0 V (vs. Ag/AgCl) for 10 min on the gold wire. (A′) Top view of the as-prepared np-Au at low magnification. Insets are the corresponding high magnification images. Reproduced and slightly modified with permission from ref. [9], Copyright 2016, Elsevier. (B) np-Au plate dealloyed for 48 h. Reproduced from ref. [10]. (C) np-Au leaf (~110 nm) dealloyed for 13 min. Reproduced with permission from ref. [11], Copyright 2011, Elsevier.

the sizes of pores and ligaments. **Figure 1B** and **C** show the np-Au plate (~250 μm thick) dealloyed for 48 h and np-Au leaf (~110 nm thick) dealloyed for 13 min in HNO_3, respectively [10, 12]. It was found that the structure and the composition of np-Au leaf after dealloying for 2 h in nitric acid are comparable to that of np-Au plate dealloyed for 48 h with the pores size nearly 30 nm and nearly 2 atomic percentage of residual silver [11, 13].

When desired, np-Au can also be created in wide varieties of free or surface bound micro and nanostructures. The micro and nanostructures of np-Au can be created using three strategies: (1) template (2) dewetting, and (3) solvent coarsening. The template-based strategy is the most common as wide varieties of desired structures can be created. Silver chloride (AgCl) can be used as a sacrificial template to prepare different types of zero-dimensional np-Au nanostructures, such as nanoframes, bowls and shells [14, 15, 22], **Figure 2A** and **B**. This solution phase synthetic strategy of np-Au can be performed by depositing Au nanoparticles from $HAuCl_4$ precursor on to AgCl template using hydroquinone as a reducing agent and polyvinyl pyrrolidone (PVP) as a stabilizing agent. The sacrificial AgCl template can then be removed using concentrated NH_4OH, and PVP can be removed by treating the np-Au with piranha solution. The adsorption of PVP on growing Au nanoparticle highly influences the growth of np-Au nanostructure.

Polystyrene (PS) beads are frequently used as a template for np-Au preparation as they are readily available and can be easily removed using heat or chloroform. Nyce and co-workers used PS-bead to synthesize monoliths containing hollow np-Au of nearly 10 μm in diameter [17]. First, they created monolithic hollow Au/Ag alloy particle by subsequent electroless deposition of Au and Ag on PS-bead followed by casting and heat removal of the template.

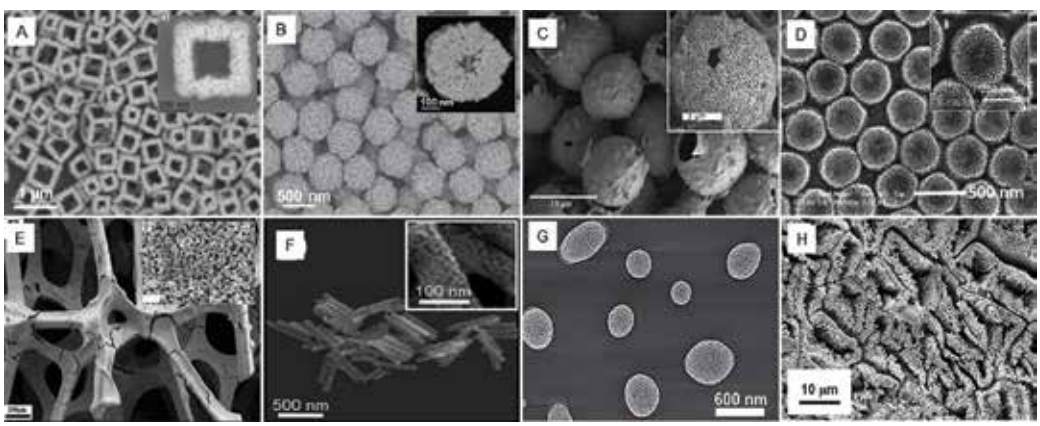

Figure 2. SEM images of np-Au nano- and micro-structures prepared using different methods. (A) and (B) np-Au nanoframes and nanoshells prepared using AgCl as a template. The template used for C, D, E, and F are polystyrene beads, anodized Al_2O_3 films, and Ni macroporous foam, respectively. (G) Nanoparticles formed using dewetting technique on SiO_2/Si surface from 20 nm thick Ag and 10 nm thick Au layer. (H) np-Au coarsened by immersion into concentrated HCl solution for 24 h. Top surface divided into "plots" by coarsened nanoporous walls. The typical side length of the "plots" was approximately from several micrometers to 20 μm. Reproduced with permission from Refs. [14–21], respectively. (A) Copyright 2015, American Chemical Society, (B) Copyright 2014, Macmillan Publishers Limited, (C) Copyright 2007, American Chemical Society, (D) Copyright 2016, American Chemical Society, (E) Copyright 2014, The Royal Society of Chemistry, (F) Copyright 2008, American Chemical Society, (G) Copyright 2012, The Royal Society of Chemistry, and (H) Copyright 2006, American Chemical Society.

Finally, the hollow Au/Ag alloy was dealloyed in HNO_3 to create monolithic hierarchical np-Au, **Figure 2C**. PS-bead can also be used as a mask to generate a semi-random array of np-Au disk on silicon or glass surface [16, 19]. For this, silicon or glass support is sputter deposited with gold and silver alloy on top of which the monolayer of PS-beads is prepared. Oxygen plasma treatment is then employed to shrink the immobilized PS-bead and separate it from the neighboring beads followed by sputter-etching in argon plasma to transfer the pattern of the bead to the alloy film. Finally, PS-beads were dissolved in chloroform to obtain the alloy disk and dealloyed in concentrated nitric acid to obtain the np-Au disk, **Figure 2D**.

Three-dimensional (3D) structures of metals and metal oxides can be used as a template for preparation of np-Au of different shapes and sizes. 3D-macroporous Ni foam was used as a template to prepare the three-dimensional np-Au film supported on Ni surface [19, 23]. In this method, Au-Sn alloy film was first electrodeposited onto the surface of Ni foam followed by removal of Sn in NaOH and H_2O_2 solution by treating for 3 days at room temperature, resulting in three-dimensional np-Au, **Figure 2E**. Significant advances in preparing monodisperse np-Au nanorods and nanowires of desired size have been made by using porous anodic aluminum oxide (AAO) as a template. The AAO having pore sizes of around 100–200 nm and wide varieties of thickness can be used as a template for preparing np-Au nanorods [18], nanowires [24], and nanotubes [25], **Figure 2F**. In this method, one side of the alumina template is closed by sputtering or evaporating a conducting copper film, followed by electrochemical cathodic deposition of gold and silver alloy through the template. The alloy nanostructures can be stripped as a free structure when Al_2O_3 and deposited Cu film is dissolved in suitable solutions. KOH can be used to dissolve Al_2O_3, and a mixture of $CuCl_2$ and HCl can be used to dissolve the Cu film. Finally, removing Ag from Au-Ag alloy gives the nanoporous nanostructures. By decreasing or alternating gold/silver composition ratios to prepare the alloy on Al_2O_3 template followed by dealloying, step-like np-Au nanowires such as nano-cones and nano-barbells can be prepared [26].

Dewetting bilayers of gold and sacrificial less noble metal on SiO_2 or TiO_2 surface at elevated temperature leads to the inter-diffusion between bilayered metals to form an alloy while shrinking the volume to generate the isolated particles or droplets [20, 27, 28], **Figure 2G**. Removal of the sacrificial less noble metal using dealloying or etching creates the np-Au nanoparticle similar in shape and size to the alloy particle [29, 30]. Using this technique, ordered array of np-Au nanoparticles can be created on nanoimprint lithography prepatterned SiO_2/Si substrates, where the size of the np-Au particles can be easily controlled by varying the metal layer thickness [31].

The np-Au ligaments and pores can be easily modified by keeping it in corrosive solvent for different period of time. It has been found that keeping np-Au in HNO_3 for longer time creates the stress to the ligaments, which start merging at some locations decreasing the size of pores or completely closing the pore while at the other locations ligaments keeps separating further generating large pores. This process results into larger but fewer numbers of pores and ligaments [10]. We have found that after 42 days of dealloying in nitric acid, the average interligament gaps and ligaments width increases to 115 ± 32 and 160 ± 47 nm, respectively from 27 ± 7 and 38 ± 8 nm obtained after 24 h dealloying. Interestingly, when np-Au is immersed

in concentrated hydrochloric acid for 24 h, the ligaments of np-Au gets coarsened by several hundred nanometers and divides into regions of few micrometers to 20 μm in size, generating np-Au prism [21], **Figure 2H**.

2.2. Electrochemical etching of gold electrode

Thin layer np-Au films can be created on the surface of gold electrodes by applying a potential with or without the use of sacrificial metals from electrolyte solution. Different strategies have been utilized to prepare np-Au using this method, including holding a high anodic potential for different times [32], ramping up the potential from 0 V to very high potential (>20 V) in few seconds [33, 34], cycling the potential between two points at a specific rate in suitable electrolyte [35], and using the combination of these methods. Chloride-containing electrolytes are commonly used for this technique, which create np-Au through electro-dissolution of Au into $AuCl_2^-$ and $AuCl_4^-$, disproportion of $AuCl_2^-$ to Au atom and $AuCl_4^-$, and deposition of Au atom back on gold electrode to form np-Au [32]. Deng and co-workers demonstrated that by simply holding the potential at 0.9 V (vs. Hg/Hg_2SO_4, sat.) in 2 M HCl, np-Au film can be created on the gold surface within a minute [32]. Later, the same group proved the effectiveness of the chloride ions for np-Au formation by taking 1 M KCl as an electrolyte. By providing 1.29 V versus saturated calomel electrode for 300 s the authors were able to create np-Au in neutral KCl solution [36]. The work has been further elaborated using 0.5 M NH_4Cl as an electrolyte to prepare np-Au structure by providing the anodic potential of 1.32 V (vs. SCE) [37]. It has been found that the roughness factor, the ratio of the electrochemical active surface area to the geometric area, of np-Au depends on potential step time, which can be enhanced when hydroxylamine hydrochloride ($NH_2OH{\cdot}HCl$) solution is mixed with NH_4Cl to prevent bubble formation during the np-Au formation step. Non-chloride-containing electrolytes like citric acid have also been used to prepare np-Au on gold rod by providing the anodic potential of 4.0 V for 3 h to create the ultra-high surface area with the roughness factor higher than 1000 [38].

Instead of simply sweeping the anodic potential linearly, multi-cycle potential scans can be used to prepare np-Au on the polished gold electrode using suitable electrolytes. In the cathodic potential scan, the sacrificial metal ions from the solution can be electrodeposited to create gold alloy in situ which on the subsequent anodic potential scan is removed from the surface of the gold electrode [39]. After the multiple cathodic/anodic cycles, np-Au with a high surface area can be generated, **Figure 3**. Hu and co-workers prepared a thin layer of np-Au on the gold electrode surface by etching the electrode by providing multiple electrochemical cycles in the potential range −0.72 to 1.88 V at 10 mV s^{-1} in benzyl alcohol electrolyte containing 1.5 M $ZnCl_2$ at 120°C [35]. In this study, Zn plate and a Zn wire were used as the counter and reference electrodes, respectively.

Nanoporous gold can also be formed by first polarizing the pure gold electrode, holding it at a certain potential for specific time, and finally reversing the potential to clean the gold surface. By polarizing the gold electrode from 0.0 to 2.0 V at the scan rate of 0.02 V s^{-1} in 0.5 M H_2SO_4, holding the potential at 2.0 V for 60 min to form a gold oxide (orange-yellowish surface) followed by reverse potential scan to reduce the oxide layer on the gold surface (black surface), Sukeri et al. succeeded in preparing np-Au film on pure gold surface [40]. Similarly, Nishio

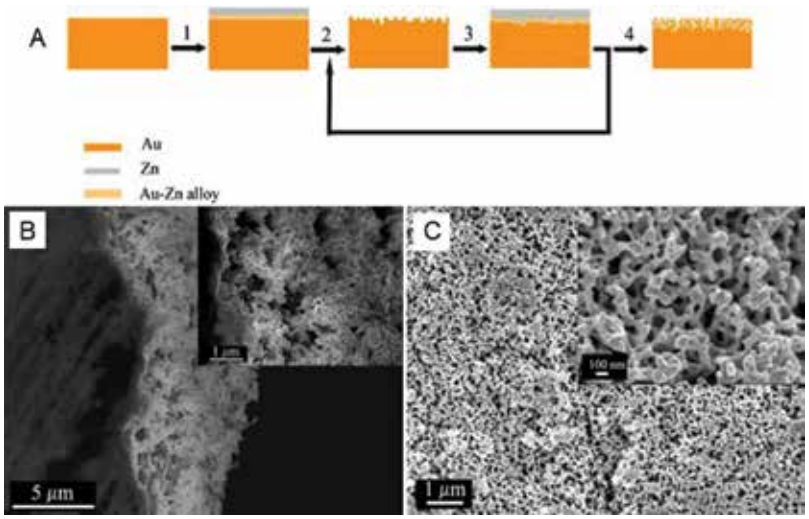

Figure 3. (A) Schematic illustration of the formation of np-Au film electrode by a multicyclic electrochemical alloying/dealloying method. Step 1, electrodeposition of Zn and formation of Au-Zn alloy; step 2, electrochemical dealloying; step 3, electrodeposition of Zn and formation of Au-Zn alloy again; step 4, formation of np-Au film after multicyclic alloying/dealloying. (B) and (C) SEM images of np-Au electrodes after 30 cycles of alloying/dealloying in ZnCl2/BA electrolyte at 120°C, where (B) is cross-sectional view and (C) is planar view. The inset in (B) and (C) are the corresponding images with higher magnification. Reproduced with permission from Ref. [39], Copyright 2007, American Chemical Society.

and Masuda used oxalic acid to create the carbonaceous passivation film on gold surface by holding the potential at 1.8 V versus Hg/Hg_2SO_4 reference electrode, which on the reverse scan breaks down to form np-Au film with a uniform hole size of 20 nm [41]. The study has also shown that acidity is not the key factor for the np-Au formation by anodizing the sample in neutral sodium oxalate solution. Fang et al. used 1:1 (v/v) mixture of hydrofluoric acid and dimethylformamide as an etching electrolyte while suddenly ramping up the potential from 0 V to 40 V over 12 s or from 0 to 20 V over 24 s [33]. The latter slower voltage ramp was found to create the larger pores. On the other hand, the pore size created by directly holding the potential for 20 V or 40 V in the same electrolyte solution for similar time was found to create the smaller pore sizes. Xu and co-workers anodized the cleaned gold wire using potential of 5 V for 180 s in 0.15 M phosphate buffer to form oxides on electrode surface (evident by salmon pink color of the electrode surface) followed by reduction of gold oxide by 1 M ascorbic acid solution at room temperature to prepare np-Au (evident by change in color of the electrode surface to black) [42].

3. Characterization

The shape and size of nano-and micro-structured np-Au along with their pores and ligaments size is characterized by scanning electron microscopy (SEM). SEM images are also important to determine the cracks on the surface of np-Au. For the very thin np-Au samples and for distinguishing the foreign elements incorporated within np-Au at high resolution, transmission

electron microscopy (TEM) images are useful [43]. Filled nanoporous spaces by foreign elements appear dark on TEM images, which can be distinguished from the control np-Au appearing light. High-resolution transmission electron microscope (HRTEM) can further reveal the lattice spacing of the foreign element which may either vary significantly from that of the np-Au or show the epitaxial relationship with the continuous lattice fringes [44]. It can also reveal different kinds of lattice defects present within np-Au [7]. Transmission electron tomography can be used to generate bicontinuous 3D-structure of np-Au showing the internal structure of the np-Au [45].

Energy dispersive X-ray spectroscopy (EDS) can be used to confirm the removal of less noble metal from np-Au through which the time needed for the complete removal of sacrificial metals can be estimated. Change in grain size and crystal structures of alloy or np-Au are studied using X-ray/electron diffraction. Based on the appearance of the characteristic X-ray diffraction peaks, the np-Au hybrid electrode with wide varieties of metals can be prepared [23].

When sufficient mass of np-Au is available, the surface area and pore size of np-Au can be determined using nitrogen adsorption/desorption isotherms. BET surface area analysis and BJH pore size distribution analysis provide the information about surface area and pores, respectively [46]. These methods are mainly useful for characterizing unsupported np-Au monoliths. For the supported np-Au electrode, a simpler and easier method to determine the surface area is through the cyclic voltammetry (CV) using oxide stripping method. In this method, charge under the cathodic peak generated due to the stripping of oxide from the gold surface is used to calculate the actual surface area of np-Au. However, electrochemically active or accessible surface area of np-Au can be determined using CV of redox probes or mediators.

4. Modification of np-Au surface

4.1. Self-assembled monolayers

Self-assembled monolayers (SAMs) of thioalkyl derivatives on the planar gold surface are a well-studied field [47]. Different types of biomolecules, such as protein, DNA and carbohydrates can be strongly bound and presented on the surface of gold as a SAM mimicking the cell surface or their natural form [48]. Biomolecules can be either modified with the thiolated linker first and allowed to form a SAM or immobilized on the previously formed SAM by reacting with the terminal functional group. Np-Au surface can be modified with different types of SAM in the same way as done in a planar gold surface by immersing the np-Au on the ethanolic solution of desired SAM-forming molecules for few hours to overnight [9]. SAM formation on np-Au surface is of higher interest because high surface area of np-Au allows large number of desired molecules on the surface. However, SAM on np-Au is not as well organized as that on planar gold surface and chances of intermolecular interactions between the terminal functional group are higher [49]. The nature and size of the terminal group and length of the linker determine how deep the monolayers are formed and are functionally active in the interior of np-Au. When np-Au-based glucose sensor was constructed by immobilizing glucose oxidase (GOD) onto the SAMs of carboxylic acid terminated alkanethiol having different

chain lengths, it was found that the sensitivity of the biosensor decreases with the increase in chain length [50]. This phenomenon has been explained by the better SAM formation of the longer chain length molecules on the np-Au surface, helping to immobilize higher number of enzymes and hence creating more difficulty for the electron transfer to occur. However, increase in thickness due to the longer chain length may also be the reason behind the difficulty for electron transfer to occur. The type of terminal functional group and chain length of SAM play vital roles in loading and releasing of drugs in np-Au. A negatively charged fluorescein (a small-molecule drug surrogate) shows lower loaded inside np-Au when np-Au surface was functionalized with carboxy-terminated SAM compared to when modified with amine-terminated SAM [51]. This is due to the repulsive interaction of negatively charged fluorescein with the carboxylic group and attractive interaction with the amine group. It was also found that increasing the chain length (11 carbons) of SAMs changed the pore area decreasing the access of fluorescein to the interior of np-Au and hence reducing loading capacity [51].

4.2. Metal and metal oxides

Modification or decoration of the np-Au surface with other metal or metal oxide can build up functionalities to the already versatile np-Au structures. Modifying the np-Au with a tiny amount of platinum, palladium and TiO_2 nanoparticles not only greatly increase the effective surface area but also enhance the electrocatalytic performance toward methanol oxidation [52–54]. Modifying the np-Au with platinum and palladium also significantly improves the structural stability of np-Au whereas TiO_2 suppresses the coarsening of the nanoporous structure after multiple uses. Modifying np-Au surface with metals and metal oxides, such as Pt, Pd, Cu, Ni, Ru, CuO, TiO_2, and CoO have shown significantly enhanced sensitivity toward the nonenzymatic detection of glucose with very good selectivity in the biological matrix [55–62]. When np-Au is modified with Ru to form np-Au/Ru nanocomposite and immobilized further into GCE with chitosan as a capping agent to create an electrode, it can act as a better non-enzymatic glucose sensor with good sensitivity and selectivity compared to bare np-Au [58]. The modified GC/np-Au-Ru/CHIT electrode shows six-fold higher amperometric sensitivity of 240 $\mu A\ mM^{-1}\ cm^{-2}$. Modifying the np-Au with ultrathin nickel (Ni) film enables detection of glucose with the sensitivity as high as 5070.9 $mA\ mM^{-1}\ cm^{-2}$, which is nearly 340 times higher compared to that on the polished gold electrode [63].

The immersion-electrodeposition method is one of the simplest methods to modify the np-Au surface with metals and metal oxides [52]. In this method, np-Au is immersed in a suitable salt solution, allowed to soak for certain time and electrodeposited by applying a suitable potential. Platinum was decorated on np-Au by first immersing np-Au in H_2PtCl_6 solution for 10 min followed by electrodeposition by sweeping the potential at 50 $mV\ s^{-1}$ between 0 and 1.1 V (vs. RHE) for 3 cycles in 0.1 M $HClO_4$ solution [52]. Similarly, iridium oxide was electrodeposited on np-Au using multiple cyclic voltammetry scans [64]. This method is suitable for modifying the external surface or thin films of np-Au with metal and metal oxides, but modifying the interior part of the thicker np-Au structure is challenging mainly because of the mass transport limitation leading to the closing of external pores before completely modifying the interior surface. There are different alternatives to overcome this situation. Underpotential deposition of the reactive metal to form a monolayer followed by galvanic displacement of the reactive metal by the atoms of

desired metal can modify the np-Au surface while conserving the original structure of np-Au. Np-Au surface can be modified with Ni using galvanic displacement reaction of underpotential deposited zinc [63]. Similarly, Cu can be underpotential deposited on the np-Au surface to decorate it with Pt using a galvanic displacement reaction [43]. However, the residual metal such as silver, which is left while dealloying np-Au, can also be used in galvanic replacement reaction to decorate Pt using H_2PtCl_6 solution [65]. Water dispersed TiO_2 nanoparticles were loaded inside np-Au followed by annealing to embed the TiO_2 particles on the np-Au surface [53]. The desired noble metal can also be included as one of the constituents of the alloy, which remains on the np-Au surface after the dealloying process removing less noble metal/s [54].

5. Applications

5.1. Chemical sensor

Nanoporous gold without any further modification with other metals or biological molecules can act as a chemical sensor owing to its high surface area, ability to catalyze certain analytes at low potentials, resistance against surface fouling and pH, and fast mass transportation [66]. It has been successfully used to detect arsenic [As(III)], a toxic metal ion whose exposure can lead to many health issues including cancer, using square wave anodic stripping voltammetric technique to the concentration as low as 0.0315 ppb with the sensitivity of 44.64 $\mu A\ cm^{-2}\ mM^{-1}$ [67]. World Health Organization's recommended limit of arsenic in the drinking water is 10 ppb. Phenolic compounds, such as phenol and catechol have been considered as priority toxic pollutants by US-EPA but still extensively used by many chemical companies for various applications. A suitable detection method for these compounds is a need for monitoring its concentration in environment and food products. By applying a suitable detection potential, np-Au electrode can not only detect the phenolic compounds down to few micromolar range [68] but also selectively distinguish one from another [69]. However, np-Au can also be easily modified with biomolecules and different types of other metals for its use in bio/chemical sensing.

5.2. Enzyme immobilization

Nanoporous gold is a suitable solid support for the immobilization of enzymes because of its biocompatible nature, ability to form self-assembled monolayers on the surface, and high surface area-to-volume ratio [5]. Once the enzyme is immobilized on the electrode surface, it is very important that it maintains its enzymatic activity for further usage. Np-Au increases the stability and functionality of the immobilized or entrapped enzymes by decreasing their tendency to unfold due to its constrained environment [70, 71]. Lignin peroxidase (LiP) immobilized on np-Au was found to retain 55% of its initial activity after 2 h at 45°C whereas free LiP was completely deactivated under similar conditions [71]. Another study reported that alcohol dehydrogenase (ADH) or glucose oxidase (GOD) immobilized on np-Au lost only 5.0 and 4.2% of the original current response, respectively, after storage for 1 month at 4°C [70]. By creating the appropriate pore size of the np-Au, the leaching can also be drastically reduced from the electrode [70]. The larger the pore size of np-Au, the higher will be the leaching. On the other hand,

smaller pores may block the enzymes from entering the np-Au interior portion. Fortunately, due to the ability of np-Au to form SAMs, enzymes can be strongly and covalently bound on np-Au surface increasing the loading and activity of the enzyme while decreasing the leaching [72, 73]. Nevertheless, physical adsorption of enzyme on np-Au is widely used to prepare the enzyme-based biosensor, because of comparative stability, the ease of preparation and few steps required [74]. The leakage of the physically immobilized enzymes can be reduced by using polymers like chitosan [75] and Nafion [70]. The high surface area of np-Au helps to amplify the response signal of the analyte during biosensing due to the large numbers of immobilized enzymes.

5.3. Electrochemical biosensor

Supported np-Au is a suitable solid support for immobilization of different types of protein (e.g., antibodies, enzymes, and lectins), carbohydrates, and RNA/DNA molecules because of its clean surface, robust structure, high surface area and biocompatible nature [76]. These immobilized biomolecules on np-Au, called receptors, can be used as biosensors for the detection of various analytes, such as poisonous metal ions, small organic molecules, and other biomolecules. Because of the highly conductive nature of np-Au electrode, it can be used as a transducer for the detection of analytes using different electrochemical techniques. The commonly used electrochemical techniques for np-Au-based biosensing are cyclic voltammetry (CV), chronoamperometry (CA), chronocoulometry (CC), electrochemical impedance spectroscopy (EIS), differential pulse voltammetry (DPV) and square wave voltammetry (SWV). Except EIS which is based on the resistance of the electrode, all the other techniques are based on the measurement of current or charge whose signal is directly proportional to the concentration of the analyte. DPV and SWV are pulse-based techniques, which have the ability to discriminate against the charging current by only sampling the Faradaic current at the end of the pulse. As a result, a very small concentration of a sample can be detected precisely. Electrochemical biosensors can be classified as DNA aptasensor, enzymatic biosensor, and immunosensor based on the type of receptor molecule used. Recently, Zeng et al. prepared regenerable DPV-based aptasensor on the np-Au surface for the detection of Hg^{2+} with the limit of detection as low as 0.0036 nM [77]. The non-enzymatic amperometric glucose sensor is possible using np-Au electrode [11] or by modifying the np-Au surface with other metals or metal oxides [78]. However, np-Au surface can be modified with glucose oxidase to use the synergistic catalytic properties of both np-Au and glucose oxidase for the detection of glucose. In one such study, high sensitivity of 12.1 μA mM^{-1} cm^{-2} with the linear responses ranging from 50 μM to 10 mM was obtained with a low detection limit of 1.02 μM [79]. The prepared structure possesses strong anti-interference capability against many molecules present in human serum. Np-Au surface was used for detecting various cancer biomarkers based on sandwich-type immunosensing. Np-Au electrode immobilized on graphene surface was combined with horseradish peroxidase-encapsulated liposomes as labels and thionine as electron mediator for the detection of cancer antigen 15-3 using DPV [80]. The linear range of the immunoassay was found to be 2×10^{-5}–40 U mL^{-1} with a limit of detection of 5×10^{-6} U mL^{-1}. Similarly, DPV was used to detect carcinoembryonic antigen (CEA) by immobilizing anti-CEA on np-Au [81] and CV was used to detect prostate specific antigen (PSA) by immobilizing anti-PSA [82].

5.4. Actuator

The phenomenon of change in surface stress and strain of np-Au due to the adsorption or desorption of gas or water can be used to convert chemical energy into a mechanical response [83, 84]. One way to prepare such surface driven actuator is by alternate exposure to ozone and carbon monoxide on np-Au surface [85]. Exposure of ozone on np-Au surface leads to adsorption of oxygen on clean Au, whereas CO exposure cleans the Au surface by reacting with adsorbed oxygen to release carbon dioxide, **Figure 4A** and **B**. Another way to generate such stress on np-Au surface is by volumetric changes of np-Au by physical adsorption and desorption of polar water molecules [84]. This method can create reversible strain amplitudes up to 0.02% in response to a 15% change in relative humidity. The ligaments of np-Au actuator coarsen with time leading to a substantial loss in performance. In such case, np-Au can be modified with platinum or polyaniline to prepare a composite porous structure [83, 86]. Np-Au/Pt alloys prepared by dealloying ternary alloy of Ag-Au-Pt to create very small structure size and large specific surface area can significantly enhance the stress and strain in the bulk of the material reaching linear strain ~1.3% [83].

5.5. Plasmonic response

Propagating surface plasmon resonance (SPR) is the evanescent electromagnetic waves found in the interface of thin metal (e.g., Au and Ag)-dielectric interface, which propagates at the distance on the order of tens to hundreds of microns along *x*- and *y*-axis, but decays on the order of 200 nm along the *z*-axis [87]. However, if the oscillation of surface plasmons is confined within the surface of the nanostructures of the metal (e.g., Au and Ag), it is called LSPR [88].

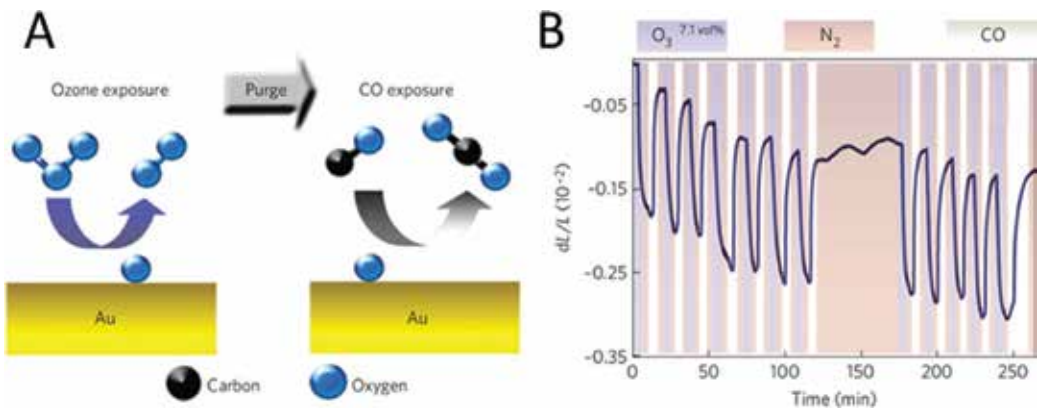

Figure 4. (A) Illustration of surface-chemistry-driven actuation in np-Au. Au surfaces can be switched back and forth between an oxygen-covered and clean state by alternating exposure to ozone (O_3) and carbon monoxide (CO). (B) Performance of a surface-chemistry-driven np-Au actuator. Strain versus time as the np-Au actuator is alternately exposed to a mixture of ~7% O_3 in O_2 and pure CO. Between exposures, the sample compartment was purged for 3 min with ultrahigh-purity N_2. Ozone exposure causes contraction, whereas CO exposure restores the original sample dimension. The response is mostly elastic, with only a small irreversible component. The system is very stable, and interrupting the exposure sequence for 1 h causes only a small drift of the signal. Reproduced with permission from Ref. [85], Copyright 2009, Macmillan Publishers Limited.

Both the SPR and LSPR are sensitive to change in refractive index around the metal-dielectric interface. This property can be used to design a label-free, sensitive and high-throughput biosensor to study the interaction of biomolecules.

Thin films (~100 nm) of np-Au can generate both the SPR and LSPR simultaneously [89]. Kim et al. studied biotin-streptavidin interaction on the surface of np-Au film fabricated by oblique angle deposition using SPR [90]. They found that there is an enhancement in SPR response due to np-Au compared to when studied on conventional bare gold film. The reason for enhancement in SPR response is attributed to excitation of local plasmon field and an increased surface area for the reaction. In the absorption spectra, two characteristic LSPR peaks can be observed for np-Au, one near 490 nm and other around 550–650 nm [91, 92]. The LSPR peak of np-Au at 490 nm is nearly independent of change in refractive index [92] and the peak at 550–650 nm is relatively wider compared to that obtained from Au nanoparticles and nanorods. The wide peak decreases the sensitivity of the biosensor limiting the use of np-Au in biosensing experiments. However, preparing np-Au nanostructures, such as np-Au disks can greatly enhance the plasmonic response due to high-density internal plasmonic "hot-spots" [19, 93]. By using these structures, the plasmonic bands can be tuned from 900 to 1850 nm by changing the diameter of the disk from 300 to 700 nm. The disk with a diameter of 300 nm shows the LSPR peak in relatively lower wavelength region and is sharper compared to the disk with higher diameter.

5.6. Heterogeneous catalysis

With the discovery of nanoparticles and nanoporous structures of gold, studies and understanding of the gold as a heterogeneous catalyst have been emerging. Heterogeneous catalysis is vital for (1) environmental waste management, as green chemistry reactions are possible and (2) synthesizing desired products, which is either not possible with homogeneous catalysis or requires poisonous chemicals if done without a catalyst. Gold nanoparticles, because of their high surface area and other unique properties, have shown promising results in heterogeneous catalysis. However, for the nanoparticles to be used in liquid phase catalysis, they should be functionalized with a suitable stabilizing agent or else they may undergo undesired aggregation decreasing the surface area and hence the catalytic activity. The functionalized stabilizing agent can also decrease the effective surface area and may passivate the surface faster. Unsupported np-Au, a bulk 3D-structure of gold having nanometer-sized pores and ligaments, can overcome these shortcomings. Besides having high surface area, it is easy to prepare, stable at harsh reaction conditions, and has less possibility of contamination. Furthermore, the structure can be easily reused and recycled, making it an ideal green catalyst for many reactions. Np-Au has already shown significant catalytic activity in many important gas-phase and liquid-phase reactions, such as oxidation of CO, alcohols, and carbohydrates. We will briefly discuss some of the reactions below.

5.6.1. CO-oxidation

CO-oxidation is one of the important reactions necessary in controlling air pollution, such as through automotive or industrial emission and in hydrogen purification in fuel cells [94]. One of the early experiments to show the use of unsupported np-Au in CO-oxidation was conducted

independently by Xu et al. [95] and Zielasek et al. [96]. Their experiment not only presented some of the important information on CO-oxidation but also became a crucial step toward the use of unsupported np-Au for gas-phase heterogeneous catalysis. Unlike palladium and platinum-based catalysts, np-Au shows important catalytic activity for CO-oxidation even at very low temperature down to −30°C and are tolerant to CO poisoning [97], **Figure 5**. It was found that unlike in supported gold catalysts, preactivation steps by passing O_2 at high temperature is not the necessary step for unsupported np-Au [95]. CO conversion rate of 99.5% and >85% could be achieved for nearly 20 h when reaction performed at room temperature and −30°C, respectively. However, catalytic efficiency was found to decrease faster at room temperature due to coarsening of the porous structure [95]. Residual silver [96] or Cu [98] in the np-Au have been linked to strongly influence the catalysis of CO, however, there is no evidence to support the ability of residual silver or copper alone on catalysis below 100°C. There is no consensus among the scientists over the exact mechanism of CO-oxidation over np-Au catalyst. Some suggest that

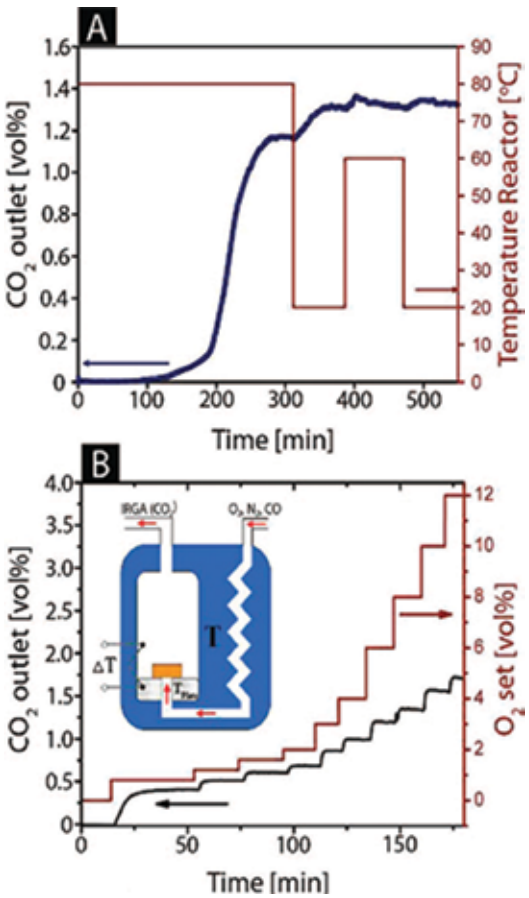

Figure 5. Catalysis: (A) CO_2 signal typically detected at the reactor out during activation of a np-Au disk; (B) CO_2 signal (outlet) for increasing O_2 concentration at the reactor inlet (CO as carrier gas, reactor temperature 20°C). Reproduced with permission from Ref. [97], copyright 2009, American Chemical Society.

the residual metal helps to activate the molecular oxygen and hence np-Au should be considered a bimetallic catalyst [97] while others think low coordinated gold atoms present on the ligaments surface due to various steps and kinks are responsible for activating molecular oxygen [6]. Long-term stability of the np-Au catalysts for CO-oxidation at room temperature is still a challenge.

5.6.2. Methanol oxidation

Methyl formate is an important precursor for the manufacture of formic acid, formamide, and dimethyl formamide, which is prepared in the industry at thousands of tons each year by combining poisonous carbon monoxide gas with methanol for the better selectivity [99]. However, it is possible to synthesize methyl formate from partial oxidation of methanol using suitable catalyst without using CO [100]. Monolithic unsupported np-Au has shown promising potential to be used in a gas-phase catalysis for selective conversion of methanol to methyl formate [101]. This is due to its high surface area, presence of considerable number of low-coordinated surface Au atoms, and availability of small percentage of Ag as a residual atom [101, 102]. Unlike nanoparticles, nanoporous structures are highly resistance to sintering and are successful in circumventing the limitation of bulk structure for dissociating the bound oxygen on its surface [103]. Strongly bound oxygen on the surface decreases the catalytic efficiency of the gold. Wittstock et al. used unsupported monolithic np-Au disc for the selective gas-phase oxidative coupling of methanol to methyl formate at low temperature with selectivity above 97% and high turnover frequencies [103]. Thin film of supported np-Au prepared on aluminum microfiber to form a composite structure was found to be cost effective, highly active, selective, and stable for oxidative coupling of methanol to methyl formate [104]. The composite structure is capable of achieving ~100% methyl formate selectivity with ~25% methanol conversion at 100°C and stable for more than 300 h without any sign of sintering.

On the other hand, the electrocatalytic oxidation of methanol using precious metal catalysts is of great interest for its use in direct methanol fuel cells. Pt-based catalyst strongly chemisorbs the intermediate species generated during electrooxidation of methanol poising the catalyst. However, these intermediate species have weak interactions with gold surface. Np-Au has high surface area and can transfer electrons better than the bulk and Au nanoparticle-supported electrode, making it a suitable catalyst for electrochemical oxidation of methanol [105]. Unfortunately, it was observed that the np-Au structures are coarsened quickly with the multi-cycling of the potential [52]. However, decorating the surface of np-Au by small amount of Pt to form nanoporous bimetallic Au-Pt alloy nanocomposites can greatly enhance the structural stability and the electrocatalytic activity toward methanol oxidation [106]. The nanoporous bimetallic Au-Pt alloy nanocomposites can also be prepared by dealloying the ternary alloy of gold, platinum, and other less noble metal [107]. This type of modified np-Au can work as a suitable catalyst for electrooxidation of other small organic molecules, such as formic acid, formaldehyde, and ethanol [108].

5.6.3. Liquid-phase catalysis

Recent works have proved that np-Au has remarkable catalytic activity in liquid-phase catalytic reactions. This type of reactions are not only selective but also work without any

additives or stabilizing agents while avoiding cumbersome work-up procedures like filtration or centrifugation. Yin et al. used unsupported np-Au for the aerobic oxidation of D-glucose to D-gluconic acid with the high selectivity of 99% under the mild reaction conditions [109]. At pH = 7.0 the conversion to gluconic acid was ~33% which reached 78% at pH = 9.0. Interestingly, the catalytic activity was found to link with the size of the ligaments with that of 6 nm showing highest catalytic activity and resistant to deactivation. It was also observed that low-coordinated Au surfaces are the active reaction site whereas the presence of residual Ag does not favor the glucose oxidation. However, the np-Au-catalyzed reaction for the direct preparation of formamide from the reaction of alcohols and amines under aerobic conditions shows that the presence of small percentages of Ag in np-Au enhances the oxidation process [110]. Yamamoto group have extensively studied the use of unsupported np-Au in liquid-phase catalysis for wide varieties of organic reactions [111]. They catalyze aerobic oxidation reaction of alcohols in batch and flow systems while monitoring the adsorptions of O_2 and alcohol onto np-Au surface using thermal desorption spectroscopy analysis [112]. The aerobic oxidation of 1-phenylbutanol with flow system using np-Au as the catalyst and methanol as solvent at 60°C for 20 min yields 99% of the corresponding ketone with the 100% conversion. Similarly, np-Au catalyst is used for the activation of bis(pinacolato)diboron that allows the direct diboration of alkynes [113]. It was observed that np-Au can cleave the B-B bond of bis(pinacolato)diboron without the use of any additives. Np-Au catalyst is also used to reduce aldimines ($R^1HC{=}NR^2$) in the presence of aldehydes (R^1CHO) giving corresponding amines ($R^1H_2C\text{-}NHR^2$) with high yields and 100% selectivity [111]. Unsupported np-Au also helps to obtain excellent chemical yields with remarkable chemo-selectivity in the hydrogenation of aldehydes and semi-hydrogenation of alkynes [114, 115].

6. Summary

A substantial progress has been made during the last two decades in the synthesis, modification and functionalization of np-Au due to their many important and unique properties. Chemical dealloying is a quick and easy means of creating np-Au whether it is a self-supported bulk or solid-supported thin film; however, electrochemical dealloying is useful for control tuning of pores and ligament size of the thin films and might not be as useful for dealloying bulk structures. Recent knowledge on techniques to control the shape and size of np-Au and size of its pores and ligament has increased its importance in wide range of disciplines, including catalysis, optical and electrochemical chemical and biomolecules sensing, actuator, bioreactors, biomedicine, and energy.

In summary, np-Au is a versatile nanostructured framework that has diverse application not only as a pure material but also by functionalizing it with diverse types of organic molecules and metal or metal oxide nanostructures to convert it into multifunctional composite material. Converting np-Au into the multifunctional nanostructures can greatly increase its potential applications in different other fields of nanotechnology that were not previously envisioned.

Acknowledgements

The authors acknowledge recent support of their work in this area by University of Missouri – St. Louis and by the NIGMS awards R01-GM090254 and R01-GM111835.

Author details

Jay K. Bhattarai, Dharmendra Neupane, Bishal Nepal, Vasilii Mikhaylov, Alexei V. Demchenko and Keith J. Stine*

*Address all correspondence to: kstine@umsl.edu

Department of Chemistry and Biochemistry, University of Missouri – St. Louis, Saint Louis, MO, USA

References

[1] Kadirvelu K, Thamaraiselvi K, Namasivayam C. Removal of heavy metals from industrial wastewaters by adsorption onto activated carbon prepared from an agricultural solid waste. Bioresource Technology. 2001;**76**(1):63-65

[2] Kornberg AE, Dolgin J. Pediatric ingestions: Charcoal alone versus ipecac and charcoal. Annals of Emergency Medicine. 1991;**20**(6):648-651

[3] Anselmo AC, Mitragotri S. Nanoparticles in the clinic. Bioengineering & Translational Medicine. 2016;**1**(1):10-29

[4] Jain S, Hirst DG, O'Sullivan JM. Gold nanoparticles as novel agents for cancer therapy. The British Journal of Radiology. 2012;**85**(1010):101-113

[5] Stine KJ, Jefferson K, Shulga OV. Nanoporous gold for enzyme immobilization. In: Minteer SD, editor. Enzyme Stabilization and Immobilization: Methods and Protocols. New York, NY: Springer; 2017. p. 37-60

[6] Wittstock A, Biener J, Bäumer M. Nanoporous gold: A new material for catalytic and sensor applications. Physical Chemistry Chemical Physics. 2010;**12**(40):12919-12930

[7] Zhang Z, Wang Y, Qi Z, Lin J, Bian X. Nanoporous gold ribbons with bimodal channel size distributions by chemical dealloying of Al−Au alloys. The Journal of Physical Chemistry C. 2009;**113**(4):1308-1314

[8] Xiao X, Si P, Magner E. An overview of dealloyed nanoporous gold in bioelectrochemistry. Bioelectrochemistry. 2016;**109**:117-126

[9] Sharma A, Bhattarai JK, Nigudkar SS, Pistorio SG, Demchenko AV, Stine KJ. Electrochemical impedance spectroscopy study of carbohydrate-terminated alkanethiol

monolayers on nanoporous gold: Implications for pore wetting. Journal of Electroanalytical Chemistry. 2016;**782**:174-181

[10] Bhattarai JK. Electrochemical Synthesis of Nanostructured Noble Metal Films for Biosensing. University of Missouri; St. Louis, MO, USA, 2014

[11] Chen LY, Lang XY, Fujita T, Chen MW. Nanoporous gold for enzyme-free electrochemical glucose sensors. Scripta Materialia. 2011;**65**(1):17-20

[12] Farghaly AA, Lam M, Freeman CJ, Uppalapati B, Collinson MM. Potentiometric measurements in biofouling solutions: Comparison of nanoporous gold to planar gold. Journal of the Electrochemical Society. 2015;**163**(4):H3083-H3087

[13] Ding Y, Kim YJ, Erlebacher J. Nanoporous gold leaf: "Ancient technology"/advanced material. Advanced Materials. 2004;**16**(21):1897-1900

[14] Chew WS, Pedireddy S, Lee YH, Tjiu WW, Liu Y, Yang Z, Ling XY. Nanoporous gold nanoframes with minimalistic architectures: Lower porosity generates stronger surface-enhanced raman scattering capabilities. Chemistry of Materials. 2015;**27**(22):7827-7834

[15] Pedireddy S, Lee HK, Tjiu WW, Phang IY, Tan HR, Chua SQ, Troadec C, Ling XY. One-step synthesis of zero-dimensional hollow nanoporous gold nanoparticles with enhanced methanol electrooxidation performance. Nature Communications. 2014;**5**:4947

[16] Qiu S, Zhao F, Zenasni O, Li J, Shih WC. Nanoporous gold disks functionalized with stabilized G-quadruplex moieties for sensing small molecules. ACS Applied Materials & Interfaces. 2016;**8**(44):29968-29976

[17] Nyce GW, Hayes JR, Hamza AV, Satcher JH. Synthesis and characterization of hierarchical porous gold materials. Chemistry of Materials. 2007;**19**(3):344-346

[18] Bok H-M, Shuford KL, Kim S, Kim SK, Park S. Multiple surface plasmon modes for a colloidal solution of nanoporous gold nanorods and their comparison to smooth gold nanorods. Nano Letters. 2008;**8**(8):2265-2270

[19] Ke X, Xu Y, Yu C, Zhao J, Cui G, Higgins D, Chen Z, Li Q, Xu H, Wu G. Pd-decorated three-dimensional nanoporous Au/Ni foam composite electrodes for H_2O_2 reduction. Journal of Materials Chemistry A. 2014;**2**(39):16474-16479

[20] Wang D, Schaaf P. Nanoporous gold nanoparticles. Journal of Materials Chemistry. 2012;**22**(12):5344-5348

[21] Hakamada M, Mabuchi M. Nanoporous gold prism microassembly through a self-organizing route. Nano Letters. 2006;**6**(4):882-885

[22] Pedireddy S, Lee HK, Koh CSL, Tan JMR, Tjiu WW, Ling XY. Nanoporous gold bowls: A kinetic approach to control open shell structures and size-tunable lattice strain for electrocatalytic applications. Small. 2016;**12**(33):4531-4540

[23] Ke X, Xu Y, Yu C, Zhao J, Cui G, Higgins D, Li Q, Wu G. Nanoporous gold on three-dimensional nickel foam: An efficient hybrid electrode for hydrogen peroxide electroreduction in acid media. Journal of Power Sources. 2014;**269**:461-465

[24] Hsieh Y-T, Sun IW. One-step electrochemical fabrication of nanoporous gold wire arrays from ionic liquid. Chemical Communications. 2014;**50**(2):246-248

[25] Shin T-Y, Yoo S-H, Park S. Gold nanotubes with a nanoporous wall: Their ultrathin platinum coating and superior electrocatalytic activity toward methanol oxidation. Chemistry of Materials. 2008;**20**(17):5682-5686

[26] Laocharoensuk R, Sattayasamitsathit S, Burdick J, Kanatharana P, Thavarungkul P, Wang J. Shape-tailored porous gold nanowires: From nano barbells to nano step-cones. ACS Nano. 2007;**1**(5):403-408

[27] Khristosov MK, Bloch L, Burghammer M, Kauffmann Y, Katsman A, Pokroy B. Sponge-like nanoporous single crystals of gold. Nature Communications. 2015;**6**(8841):1-7

[28] Nguyen NT, Altomare M, Yoo JE, Schmuki P. Efficient photocatalytic H2 evolution: Controlled dewetting-dealloying to fabricate site-selective high-activity nanoporous Au particles on highly ordered TiO_2 nanotube arrays. Advanced Materials. 2015;**27**(20):3208-3215

[29] Wang D, Schaaf P. Silicon/silicide grown out of nanoporous gold nanoparticles. Physica Status Solidi A. 2013;**210**(8):1512-1515

[30] Kosinova A, Wang D, Schaaf P, Kovalenko O, Klinger L, Rabkin E. Fabrication of hollow gold nanoparticles by dewetting, dealloying and coarsening. Acta Materialia. 2016;**102**:108-115

[31] Wang D, Ji R, Albrecht A, Schaaf P. Ordered arrays of nanoporous gold nanoparticles. Beilstein Journal of Nanotechnology. 2012;**3**:651-657, 7 pp

[32] Deng Y, Huang W, Chen X, Li Z. Facile fabrication of nanoporous gold film electrodes. Electrochemistry Communications. 2008;**10**(5):810-813

[33] Fang C, Bandaru NM, Ellis AV, Voelcker NH. Electrochemical fabrication of nanoporous gold. Journal of Materials Chemistry. 2012;**22**(7):2952-2957

[34] Fang C, Shapter JG, Voelcker NH, Ellis AV. Electrochemically prepared nanoporous gold as a SERS substrate with high enhancement. RSC Advances. 2014;**4**(37):19502-19506

[35] X-B H, Liu Y-L, Zhang H-W, Xiao C, Qin Y, Duo H-H, J-Q X, Guo S, Pang D-W, Huang W-H. Electrochemical monitoring of hydrogen sulfide release from single cells. ChemElectroChem. 2016;**3**(12):1998-2002

[36] Xia Y, Huang W, Zheng J, Niu Z, Li Z. Nonenzymatic amperometric response of glucose on a nanoporous gold film electrode fabricated by a rapid and simple electrochemical method. Biosensors and Bioelectronics. 2011;**26**(8):3555-3561

[37] Zhou C, Xia Y, Huang W, Li Z. A rapid anodic fabrication of nanoporous gold in NH4Cl solution for nonenzymatic glucose detection. Journal of the Electrochemical Society. 2014;**161**(12):H802-H808, 7 pp

[38] Jeong H, Kim J. Fabrication of nanoporous Au films with ultra-high surface area for sensitive electrochemical detection of glucose in the presence of Cl. Applied Surface Science. 2014;**297**:84-88

[39] Jia F, Yu C, Ai Z, Zhang L. Fabrication of nanoporous gold film electrodes with ultrahigh surface area and electrochemical activity. Chemistry of Materials. 2007;**19**(15):3648-3653

[40] Sukeri A, Saravia LPH, Bertotti M. A facile electrochemical approach to fabricate a nanoporous gold film electrode and its electrocatalytic activity towards dissolved oxygen reduction. Physical Chemistry Chemical Physics. 2015;**17**(43):28510-28514

[41] Nishio K, Masuda H, et al. Angewandte Chemie International Edition. 2011;**50**(7):1603-1607 S1603/1-S1603/5

[42] Xu H, Zheng QL, Yang P, Liu JS, Xing SJ, Jin LT. Electrochemical synthesis of silver nanoparticles-coated gold nanoporous film electrode and its application to amperometric detection for trace Cr(VI). Science China Chemistry. 2011;**54**(6):1004-1010

[43] Liu P, Ge X, Wang R, Ma H, Ding Y. Facile fabrication of ultrathin Pt overlayers onto nanoporous metal membranes via repeated Cu UPD and in situ redox replacement reaction. Langmuir. 2009;**25**(1):561-567

[44] Ge X, Yan X, Wang R, Tian F, Ding Y. Tailoring the structure and property of Pt-decorated nanoporous gold by thermal annealing. The Journal of Physical Chemistry C. 2009;**113**(17):7379-7384

[45] Fujita T, Qian L-H, Inoke K, Erlebacher J, Chen M-W. Three-dimensional morphology of nanoporous gold. Applied Physics Letters. 2008;**92**(25):251902

[46] Tan YH, Davis JA, Fujikawa K, Ganesh NV, Demchenko AV, Stine KJ. Surface area and pore size characteristics of nanoporous gold subjected to thermal, mechanical, or surface modification studied using gas adsorption isotherms, cyclic voltammetry, thermogravimetric analysis, and scanning electron microscopy. Journal of Materials Chemistry. 2012;**22**(14):6733-6745

[47] Bhattarai JK, Neupane D, Mikhaylov V, Demchenko AV, Stine KJ. Self-assembled monolayers of carbohydrate derivatives on gold surfaces. In: Caliskan M, Kavakli IH, Oz GC, editors. Carbohydrate. Rijeka: InTech; 2017 p Ch. 04

[48] Bhattarai JK, Tan YH, Pandey B, Fujikawa K, Demchenko AV, Stine KJ. Electrochemical impedance spectroscopy study of Concanavalin A binding to self-assembled monolayers of mannosides on gold wire electrodes. Journal of Electroanalytical Chemistry. 2016;**780**:311-320

[49] Patel DA, Weller AM, Chevalier RB, Karos CA, Landis EC. Ordering and defects in self-assembled monolayers on nanoporous gold. Applied Surface Science. 2016;**387**:503-512

[50] Xiao X, Li H, Wang M, Zhang K, Si P. Examining the effects of self-assembled monolayers on nanoporous gold based amperometric glucose biosensors. Analyst. 2014; **139**(2):488-494

[51] Polat O, Seker E. Effect of surface-molecule interactions on molecular loading capacity of nanoporous gold thin films. The Journal of Physical Chemistry C. 2016;**120**(34):19189-19194

[52] Zhang J, Liu P, Ma H, Ding Y. Nanostructured porous gold for methanol electro-oxidation. The Journal of Physical Chemistry C. 2007;**111**(28):10382-10388

[53] Kudo A, Fujita T, Lang X, Chen L, Chen M. Enhanced electrochemical performances of nanoporous gold by surface modification of titanium dioxide nanoparticles. Materials Transactions. 2010;**51**(9):1566-1569

[54] Lang XY, Guo H, Chen LY, Kudo A, JS Y, Zhang W, Inoue A, Chen MW. Novel nanoporous Au-Pd alloy with high catalytic activity and excellent electrochemical stability. The Journal of Physical Chemistry C. 2010;**114**(6):2600-2603

[55] Yi Q, Yu W. Electrocatalytic activity of a novel titanium-supported nanoporous gold catalyst for glucose oxidation. Microchimica Acta. 2009;**165**(3-4):381-386

[56] Qiu H, Huang X. Effects of Pt decoration on the electrocatalytic activity of nanoporous gold electrode toward glucose and its potential application for constructing a nonenzymatic glucose sensor. Journal of Electroanalytical Chemistry. 2010;**643**(1-2):39-45

[57] Toghill KE, Xiao L, Phillips MA, Compton RG. The non-enzymatic determination of glucose using an electrolytically fabricated nickel microparticle modified boron-doped diamond electrode or nickel foil electrode. Sensors and Actuators B: Chemical. 2010;**147**(2):642-652

[58] Shim JH, Cha A, Lee Y, Lee C. Nonenzymatic amperometric glucose sensor based on nanoporous gold/ruthenium electrode. Electroanalysis. 2011;**23**(9):2057-2062

[59] Tavakkoli N, Nasrollahi S. Non-enzymatic glucose sensor based on palladium coated nanoporous gold film electrode. Australian Journal of Chemistry. 2013;**66**(9):1097-1104

[60] Guo M-M, Wang P-S, Zhou C-H, Xia Y, Huang W, Li Z. An ultrasensitive non-enzymatic amperometric glucose sensor based on a cu-coated nanoporous gold film involving co-mediating. Sensors and Actuators B: Chemical. 2014;**203**:388-395

[61] Xiao X, Wang M, Li H, Pan Y, Si P. Non-enzymatic glucose sensors based on controllable nanoporous gold/copper oxide nanohybrids. Talanta. 2014;**125**:366-371

[62] Zhang C, Huang B, Qian L, Yuan S, Wang S, Chen R. Electrochemical biosensor based on nanoporous Au/CoO core-shell material with synergistic catalysis. Chemphyschem. 2016;**17**(1):98-104

[63] Huang JF. Facile preparation of an ultrathin nickel film coated nanoporous gold electrode with the unique catalytic activity to oxidation of glucose. Chemical Communications. 2009;(10):1270-1272

[64] Kim YH, Kim GH, Kim MS, Jung SD. Iridium oxide-electrodeposited nanoporous gold multielectrode array with enhanced stimulus efficacy. Nano Letters. 2016;**16**(11):7163-7168

[65] Gu X, Cong X, Ding Y. Platinum-decorated Au porous nanotubes as highly efficient catalysts for formic acid electro-oxidation. Chemphyschem. 2010;**11**(4):841-846

[66] Jiang J, Holm N, O'Brien K. Improved anodic stripping voltammetric detection of arsenic (III) using nanoporous gold microelectrode. ECS Journal of Solid State Science and Technology. 2015;**4**(10):S3024-S3029

[67] Yang M, Chen X, Liu J-H, Huang X-J. Enhanced anti-interference on electrochemical detection of arsenite with nanoporous gold in mild condition. Sensors and Actuators B: Chemical. 2016;**234**:404-411

[68] Lu L, Huang X, Dong Y, Huang Y, Pan X, Wang X, Feng M, Luo Y, Fang D. Facile method for fabrication of self-supporting nanoporous gold electrodes via cyclic voltammetry in ethylene glycol, and their application to the electrooxidative determination of catechol. Microchimica Acta. 2015;**182**(7-8):1509-1517

[69] Quynh BTP, Byun JY, Kim SH. Non-enzymatic amperometric detection of phenol and catechol using nanoporous gold. Sensors and Actuators B: Chemical. 2015;**221**:191-200

[70] Qiu H, Xue L, Ji G, Zhou G, Huang X, Qu Y, Gao P. Enzyme-modified nanoporous gold-based electrochemical biosensors. Biosensors and Bioelectronics. 2009;**24**(10):3014-3018

[71] Qiu H, Li Y, Ji G, Zhou G, Huang X, Qu Y, Gao P. Immobilization of lignin peroxidase on nanoporous gold: Enzymatic properties and in situ release of H_2O_2 by co-immobilized glucose oxidase. Bioresource Technology. 2009;**100**(17):3837-3842

[72] Chen L, Fujita T, Chen M. Biofunctionalized nanoporous gold for electrochemical biosensors. Electrochimica Acta. 2012;**67**:1-5

[73] Yang XN, Huang XB, Hang RQ, Zhang XY, Qin L, Tang B. Improved catalytic performance of porcine pancreas lipase immobilized onto nanoporous gold via covalent coupling. Journal of Materials Science. 2016;**51**(13):6428-6435

[74] Qiu H, Xu C, Huang X, Ding Y, Qu Y, Gao P. Immobilization of laccase on nanoporous gold: Comparative studies on the immobilization strategies and the particle size effects. The Journal of Physical Chemistry C. 2009;**113**(6):2521-2525

[75] Ahmadalinezhad A, Chen A. High-performance electrochemical biosensor for the detection of total cholesterol. Biosensors and Bioelectronics. 2011;**26**(11):4508-4513

[76] Pandey B, Bhattarai JK, Pornsuriyasak P, Fujikawa K, Catania R, Demchenko AV, Stine KJ. Square-wave voltammetry assays for glycoproteins on nanoporous gold. Journal of Electroanalytical Chemistry. 2014;**717-718**:47-60

[77] Zeng G, Zhang C, Huang D, Lai C, Tang L, Zhou Y, Xu P, Wang H, Qin L, Cheng M. Practical and regenerable electrochemical aptasensor based on nanoporous gold and thymine-Hg^{2+}-thymine base pairs for Hg^{2+} detection. Biosensors and Bioelectronics. 2017;**90**:542-548

[78] Zhou C, Tang X, Xia Y, Li Z. Electrochemical fabrication of cobalt oxides/nanoporous gold composite electrode and its nonenzymatic glucose sensing performance. Electroanalysis. 2016;**28**(9):2149-2157

[79] Wu C, Sun H, Li Y, Liu X, Du X, Wang X, Xu P. Biosensor based on glucose oxidase-nanoporous gold Co-catalysis for glucose detection. Biosensors and Bioelectronics. 2015;**66**:350-355

[80] Ge S, Jiao X, Chen D. Ultrasensitive electrochemical immunosensor for CA 15-3 using thionine-nanoporous gold-graphene as a platform and horseradish peroxidase-encapsulated liposomes as signal amplification. Analyst. 2012;**137**(19):4440-4447

[81] Sun X, Ma Z. Electrochemical immunosensor based on nanoporpus gold loading thionine for carcinoembryonic antigen. Analytica Chimica Acta. 2013;**780**:95-100

[82] Wei Q, Zhao Y, Xu C, Wu D, Cai Y, He J, Li H, Du B, Yang M. Nanoporous gold film based immunosensor for label-free detection of cancer biomarker. Biosensors and Bioelectronics. 2011;**26**(8):3714-3718

[83] Jin H-J, Weissmueller J. Bulk nanoporous metal for actuation. Advanced Engineering Materials. 2010;**12**(8):714-723

[84] Detsi E, Chen ZG, Vellinga WP, Onck PR, De Hosson JTM. Actuating and sensing properties of nanoporous gold. Journal of Nanoscience and Nanotechnology. 2012;**12**(6):4951-4955

[85] Biener J, Wittstock A, Zepeda-Ruiz LA, Biener MM, Zielasek V, Kramer D, Viswanath RN, Weissmuller J, Baumer M, Hamza AV. Surface-chemistry-driven actuation in nanoporous gold. Nature Materials. 2009;**8**(1):47-51

[86] Detsi E, Onck P, De Hosson JTM. Metallic muscles at work: High rate actuation in nanoporous gold/polyaniline composites. ACS Nano. 2013;**7**(5):4299-4306

[87] Willets KA, Van Duyne RP. Localized surface plasmon resonance spectroscopy and sensing. Annual Review of Physical Chemistry. 2007;**58**:267-297

[88] Bhattarai JK, Sharma A, Fujikawa K, Demchenko AV, Stine KJ. Electrochemical synthesis of nanostructured gold film for the study of carbohydrate–lectin interactions using localized surface plasmon resonance spectroscopy. Carbohydrate Research. 2015;**405**:55-65

[89] Yu F, Ahl S, Caminade A-M, Majoral J-P, Knoll W, Erlebacher J. Simultaneous excitation of propagating and localized surface plasmon resonance in nanoporous gold membranes. Analytical Chemistry. 2006;**78**(20):7346-7350

[90] Kim N-H, Choi M, Leem JW, JS Y, Kim TW, Kim T-S, Byun KM. Improved biomolecular detection based on a plasmonic nanoporous gold film fabricated by oblique angle deposition. Optics Express. 2015;**23**(14):18777-18785

[91] Jalas D, Shao LH, Canchi R, Okuma T, Lang S, Petrov A, Weissmüller J, Eich M. Electrochemical tuning of the optical properties of nanoporous gold. Scientific Reports. 2017;**7**:44139

[92] Lang X, Qian L, Guan P, Zi J, Chen M. Localized surface plasmon resonance of nanoporous gold. Applied Physics Letters. 2011;**98**(9):093701

[93] Zeng J, Zhao F, Li M, Li C-H, Lee TR, Shih W-C. Morphological control and plasmonic tuning of nanoporous gold disks by surface modifications. Journal of Materials Chemistry C. 2015;**3**(2):247-252

[94] Haruta M. New generation of gold catalysts: Nanoporous foams and tubes-is unsupported gold catalytically active? Chemphyschem. 2007;**8**(13):1911-1913

[95] Xu C, Xu X, Su J, Ding Y. Research on unsupported nanoporous gold catalyst for Co oxidation. Journal of Catalysis. 2007;**252**(2):243-248

[96] Zielasek V, Jurgens B, Schulz C, Biener J, Biener MM, Hamza AV, Baumer M. Gold catalysts: Nanoporous gold foams. Angewandte Chemie International Edition. 2006; **45**(48):8241-8244

[97] Wittstock A, Br N, Schaefer A, Dumbuya K, Kübel C, Biener MM, Zielasek V, Steinrück H-P, Gottfried JM, Jr B. Nanoporous Au: An unsupported pure gold catalyst? The Journal of Physical Chemistry C. 2009;**113**(14):5593-5600

[98] Kameoka S, Tsai AP. CO oxidation over a fine porous gold catalyst fabricated by selective leaching from an ordered $AuCu_3$ intermetallic compound. Catalysis Letters. 2007;**121**(3-4):337-341

[99] Reutemann W, Kieczka H. Formic Acid. In: Ullmann's Encyclopedia of Industrial Chemistry. Wiley-VCH Verlag GmbH & Co. KGaA; Weinheim, Germany; 2000

[100] Yang Z, Li J, Yang X, Wu Y. Catalytic oxidation of methanol to methyl formate over silver – A new purpose of a traditional catalysis system. Catalysis Letters. 2005;**100**(3):205-211

[101] Wang L-C, Personick ML, Karakalos S, Fushimi R, Friend CM, Madix RJ. Active sites for methanol partial oxidation on nanoporous gold catalysts. Journal of Catalysis. 2016;**344**:778-783

[102] Xu B, Siler CGF, Madix RJ, Friend CM. Ag/Au mixed sites promote oxidative coupling of methanol on the alloy surface. Chemistry – A European Journal. 2014;**20**(16):4646-4652

[103] Wittstock A, Zielasek V, Biener J, Friend CM, Baeumer M. Nanoporous gold catalysts for selective gas-phase oxidative coupling of methanol at low temperature. Science. 2010;**327**(5963):319-322

[104] Zhang QF, Li YK, Zhang L, Chen L, Liu Y, Lu Y. Structured nanoporous-gold/Al-fiber: Galvanic deposition preparation and reactivity for the oxidative coupling of methanol to methyl formate. Green Chemistry. 2014;**16**(6):2992-2996

[105] CF Y, Jia FL, Ai ZH, Zhang LZ. Direct oxidation of methanol on self-supported nanoporous gold film electrodes with high catalytic activity and stability. Chemistry of Materials. 2007;**19**(25):6065-6067

[106] Jia J, Cao L, Wang Z. Platinum-coated gold nanoporous film surface: Electrodeposition and enhanced electrocatalytic activity for methanol oxidation. Langmuir. 2008;**24** (11):5932-5936

[107] Zhang Z, Wang Y, Wang X. Nanoporous bimetallic Pt-Au alloy nanocomposites with superior catalytic activity towards electro-oxidation of methanol and formic acid. Nanoscale. 2011;**3**(4):1663-1674

[108] Ge X, Wang R, Cui S, Tian F, Xu L, Ding Y. Structure dependent electrooxidation of small organic molecules on Pt-decorated nanoporous gold membrane catalysts. Electrochemistry Communications. 2008;**10**(10):1494-1497

[109] Yin H, Zhou C, Xu C, Liu P, Xu X, Ding Y. Aerobic oxidation of D-glucose on support-free nanoporous gold. The Journal of Physical Chemistry C. 2008;**112**(26):9673-9678

[110] Tanaka S, Minato T, Ito E, Hara M, Kim Y, Yamamoto Y, Asao N. Selective aerobic oxidation of methanol in the coexistence of amines by nanoporous gold catalysts: Highly efficient synthesis of formamides. Chemistry – A European Journal. 2013;**19**(36):11832-11836

[111] Takale BS, Bao M, Yamamoto Y. Gold nanoparticle (AuNPs) and gold nanopore (AuNPore) catalysts in organic synthesis. Organic & Biomolecular Chemistry. 2014;**12**(13):2005-2027

[112] Asao N, Hatakeyama N, Menggenbateer MT, Ito E, Hara M, Kim Y, Yamamoto Y, Chen M, Zhang W, Inoue A. Aerobic oxidation of alcohols in the liquid phase with nanoporous gold catalysts. Chemical Communications. 2012;**48**(38):4540-4542

[113] Chen Q, Zhao J, Ishikawa Y, Asao N, Yamamoto Y, Jin T. Remarkable catalytic property of nanoporous gold on activation of diborons for direct diboration of alkynes. Organic Letters. 2013;**15**(22):5766-5769

[114] Takale BS, Wang S, Zhang X, Feng X, Yu X, Jin T, Bao M, Yamamoto Y. Chemoselective reduction of α,β-unsaturated aldehydes using an unsupported nanoporous gold catalyst. Chemical Communications (Cambridge, United Kingdom). 2014;**50**(92):14401-14404

[115] Wagh YS, Asao N. Selective transfer semihydrogenation of alkynes with nanoporous gold catalysts. Journal of Organic Chemistry. 2015;**80**(2):847-851

Chapter 16

Colorimetric Detection of Copper Ion Based on Click Chemistry

Lingwen Zeng, Zhiyuan Fang and Yunbo Wang

Additional information is available at the end of the chapter

http://dx.doi.org/10.5772/intechopen.76024

Abstract

Two colorimetric assays, lateral flow biosensor (LFB) and hemin/G-Quadruplex DNAzyme-based colorimetric assay, were developed for the detection of copper ion based on click chemistry. Two single-strand DNA (ssDNA) with azide- and alkyne-modified at 3′ and 5′ separately can be linked by the Cu^{+}-catalyzed click chemistry. For hemin/G-Quadruplex DNAzyme-based assay, the two ssDNA fragments linked by Cu^{+}-catalyzed click chemistry could form a complete G-rich sequence that severed as a horseradish peroxidase. In the presence of hemin and K^{+}, the colorless substrate tetramethyl benzidine (TMB) is catalyzed into a colored product by the G-rich sequence. The concentration of Cu^{2+} can then be quantitatively analyzed by measuring the color density. For the LFB assay, the two ligated ssDNA fragments could form a sandwich complex between an ssDNA fragment immobilized on gold nanoparticles and another ssDNA fragment on test zone of a biosensor, respectively. The biosensor enables visual detection of copper ion with excellent specificity. In comparison with conventional methods, the present assays are simpler to operate and more cost-effective to use, and so have great potential in point-of-care diagnosis and environmental monitoring.

Keywords: colorimetric detection, lateral flow biosensor, click chemistry, copper ion detection

1. Introduction

Cu^{2+} is one of the important cofactors or structural components for numerous enzymes needed in metabolic processes, and therefore, an essential micronutrient for human life. However, high intracellular concentration of Cu^{2+} can cause adverse health effects, such as liver damage, gastrointestinal disturbance, and neurodegenerative diseases including

Alzheimer, Menkes, and Wilson diseases [1, 2]. The maximum contamination concentration for Cu^{2+} in drinking water set by the U.S. Environmental Protection Agency (EPA) is 20 mM [3]. Therefore, sensitive and specific analytical methods for the monitoring and detection of Cu^{2+} pollution in environment and food are imperative.

The standard methods for Cu^{2+} determination include graphite furnace atomic absorption spectrometry (AAS) [4, 5] and inductively coupled plasma atomic emission spectroscopy (ICPAES) [6]. These methods have advantages of high sensitivity and repeatability, which enable the analysis of a variety of samples. However, the shortcomings of these techniques are that they require expensive instruments and experienced operators. Recently, a variety of methods based on Cu^{2+}-specific DNAzyme have been developed for Cu^{2+} detection [7–11]. Although these methods are effective, the reaction of Cu^{2+}-dependent DNA-cleaving DNAzyme needs strict conditions, these methods are not suitable for real sample analysis. Furthermore, the use of fluorophore-labeled oligonucleotides is not only expensive but also increases the complexity of the operation.

Cu^{+}-catalyzed click chemistry refers to the [3 + 2] cycloaddition reaction between an azide group and an alkyne group at room temperature in aqueous solution, which finally results in the formation of a five-membered triazole ring [12]. The reactivity of in situ-generated copper(I) acetylides renders this reaction with high efficiency and selectivity. The applications of click chemistry allow the modification of a wide range of biomolecules. Since click reaction acts in a quick, irreversible, and water uninterruptible manner, it has widely been used in biomedical fields, such as drug discovery [13, 14], bioconjugations [15], and imaging [16]. Due to the ability of adding probes into target molecules, extensive research was carried out for the detection of biomolecules and disease diagnosis based on click chemistry, including viral infection [17], carbohydrate detection [18], enzyme [19], single nucleotide polymorphism [20] and ions [21].

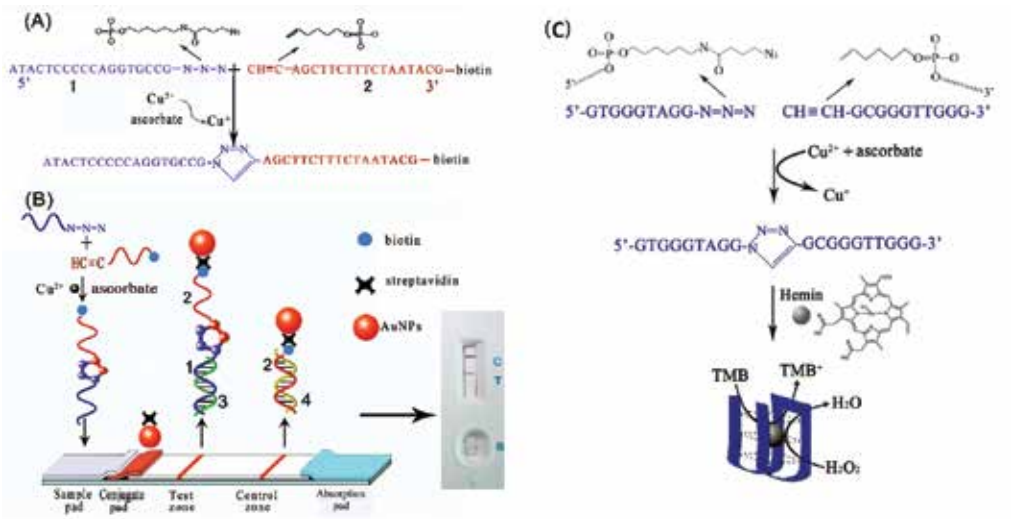

Figure 1. Principle of the biosensor for Cu^{2+} detection. (A) The formation of the ligation product of azide-DNA and alkyne/biotin-DNA based on Cu^{+}-promoted click chemistry. (B) The product is analyzed by a lateral flow biosensor. (C) Hemin/G-quadruplex HRP-mimicking DNAzyme formed by the catalyzation of click chemistry. The self-assembly of hemin/G-quadruplex catalyzed its colorless substrate TMB into a colored product (adapted from [22, 23]).

In this chapter, two simple methods for Cu^{2+} detection based on Cu^{+}-catalyzed click chemistry by the reduction of Cu^{2+} in the presence of sodium ascorbate were proposed. **Figure 1** shows a lateral flow biosensor based on Cu^{+}-catalyzed click chemistry [22, 23]. The two biosensors have the following features: (1) easy to use and operate; (2) no requirement for bulky and costly apparatus; (3) high sensitivity; and (4) excellent selectivity to other metal ions. Details of the methods, procedures, and results are presented below. A section on Summary and Future Directions is given at the end of the chapter.

2. Materials

The materials used in this project and their suppliers are listed below:

- Sodium ascorbate: Shanghai Aladdin Reagent Co., Ltd. (Shanghai, China).
- Ammonium peroxodisulfate (AP), urea, copper(II) chloride dihydrate, potassium chloride, and other metal ions: Guangzhou Chemical Reagent Factory (Guangzhou, China).
- SYBR Green II, hemin, dimethylsulfoxide (DMSO), bovine serum albumin (BSA), and human serum: Sigma-Aldrich (St. Louis, USA).
- 3, 3′, 5, 5′-tetramethyl benzidine hydrochloride dihydrate (TMB-2HCl): Cellway-Lab (Luoyang, China).
- Phosphate buffer solution (PBS): Genetimes Technology, Inc. (Shanghai, China).
- Tris-base, boric acid, ethylene diamine tetraacetic acid (EDTA), Triton X-100, and hydrogen peroxide (H_2O_2): Guangzhou WhiGa Technology Ltd. (Guangzhou, China).
- Oligonucleotides purified by HPLC: Shanghai Sangon Biotechnology Co., Ltd. (Shanghai, China).
- Rinsing buffer: 1% BSA and 8% sucrose containing 0.05% NaN_3. Rinsing buffer was stored at 4°C until use.
- Sample pad buffer: 0.01 M PBS pH 7.8 containing 0.5% BSA, 5% Triton X-100, and 0.05% NaN_3. Sample pad buffer was stored at 4°C.
- Loading buffer: 4× SSC containing 0.1% Triton X-100.
- Adhesive plate: PVC plate, obtained from Vinostech, Shanghai, China.
- Nitrocellulose membrane: AE99, 25 mm × 30 cm, capillary rate: 140 ± 40 s, thickness: 145 ± 20 μm, obtained from GE Healthcare, Shanghai, China.
- Fiberglass, absorbent paper: Shanghai Jie Ning Biotechnology, Shanghai, China.
- Dispenser: XYZ dispenser HM3030, obtained from Shanghai Kinbio, Shanghai, China.
- Cutter: Automatic Strip Cutter ZQ2000, obtained from Shanghai Kinbio, Shanghai, China.
- Strip reader: Test Strip Reader DT2032, obtained from Shanghai Kinbio, Shanghai, China.

Probe name	Sequence (5′ → 3′)
Azide-DNA	ATACTCCCCCAGGTGCCG
Alkyne/biotin-DNA	AGCTTCTTTCTAATACG
Control zone-DNA	CGTATTAGAAAGAAGCTCGTATTAGAAAGAAGCT
Test zone-DNA	CGGCACCTGGGGGAGTATCGGCACCTGGGGGAGTAT

Table 1. DNA probes used in this assay.

All buffer solutions used in this study were prepared in our lab. Other chemicals were purchased from standard commercial sources and the sequences of the oligonucleotides are listed in **Table 1**.

3. Lateral flow biosensor detection of Cu^{2+}

3.1. Preparation of streptavidin-modified gold nanoparticle (AuNP-SA) conjugates

AuNPs with 15 nm were prepared as follows: heat 100 mL of 0.01% $HAuCl_4$ to boil and add 4 mL of 1% trisodium citrate immediately in a 500-mL round-bottom flask with rapid stirring. The solution was boiled for additional 10 min after its color turned red. After then, it was cooled to room temperature with gentle stirring.

AuNP–SA conjugates were prepared as follows: pH of 1 mL AuNP solution was adjusted by adding 4 μL of 0.1 M K_2CO_3, followed by adding 10 mg (46 μL) SA. The mixture was incubated at room temperature for 1 h with gentle shaking. AuNP was blocked with 1% BSA. The mixture was incubated at room temperature for another 1 h with gentle shaking. After blocking, AuNP was collected and rinsed three times with rinsing buffer (12,103 rpm, 20 min). The red pellet was resuspended in 50 mL of rinsing buffer and then stored at 4°C until use.

3.2. Construction of lateral flow biosensor

The biosensor was constructed as follows:

- The sample pad (17 mm × 30 cm) was prepared by soaking a glass fiber pad in sample pad buffer. The pad was then dried and stored in a low-humidity chamber at room temperature;
- The conjugate pad (8 mm × 30 cm) was prepared by dispensing AuNP-SA solution (10 μL cm^{-1}) onto the fiberglass using a dispenser. The pad was dried at room temperature for 12 h and stored at room temperature in low humidity until use;
- Test zone and control zone were prepared by dispensing 30 μL control zone DNA (100 μM) and 30 μL of test zone DNA (100 μM) onto the nitrocellulose membrane simultaneously by a lateral flow dispenser. There should be 5 mm distance between the test zone and the control zone. The nitrocellulose membrane was exposed to ultraviolet light for 15 min to

immobilize DNA. The membrane was then dried in low humidity at room temperature. It was stored in ziplock bag with desiccant at room temperature.

- Lateral flow biosensor was assembled by adhesion of the four components onto a plastic adhesive backing (60 mm × 30 cm). Each component had a part of 2 mm overlapped. The backing along with four components was then cut into 0.4-cm wide strips using a paper cutter.

3.3. Detection of Cu^{2+} using the lateral flow biosensor

- Azide-DNA and alkyne/biotin-DNA were mixed at the same mole ratio (10 μM, 2 μL) in 14 μL of PBS buffer, followed by adding 2 μL of Cu^{2+} solution.
- Test without Cu^{2+} was used as control.

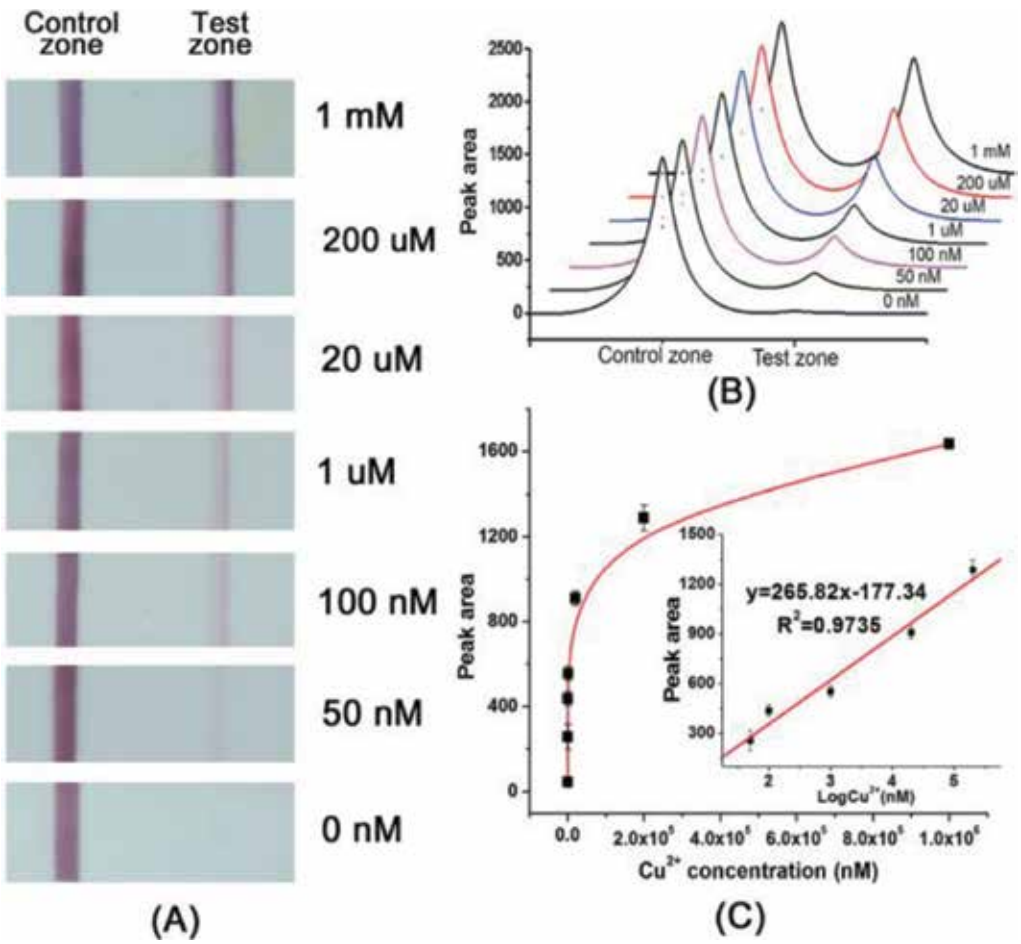

Figure 2. Sensitivity of the assay. (A) Typical photo images of the strip. (B) Recorded corresponding optical intensities of the strip. (C) Plots of the optical intensities of red bands on the test zone vs. different concentrations of Cu^{2+}. Inset: calibration curve of the optical intensities of red bands on the test zone vs. the log value of Cu^{2+} concentration. The error bars represent the standard deviation of three independent measurements (reproduced with permission from [22]).

- Sodium ascorbate (2 μL) was added to a final concentration of 600 mM to accelerate the reaction between azide and alkyne group.
- Shake gently at room temperature for 45 min.
- After the reaction, 4 μL of loading buffer was added and mixed with the above mixture. It was then loaded onto the sample pad. Results could be observed visually in 15 min, and the optical intensities of test zone and control zone were recorded using the strip reader.

3.4. Results of biosensor for Cu^{2+} detection

As shown in **Figure 2**, visible test zone could be observed in the presence of 100 nM Cu^{2+}, which was determined as the limit of detection (LOD) for visual detection. The linear range between optical intensities and logarithm of Cu^{2+} concentration was 50 nM to 200 mM with a linear equation of optical intensity = 265.82x − 177.3 (R^2 = 0.9735).

4. Colorimetric detection of Cu^{2+}

The detection was based on the hemin/G-quadruplex HRP-mimicking DNAzyme produced by Cu(+)-catalyzed click chemistry between azide- and alkyne-modified short G-rich sequences. The intact G-quadruplex can catalyze its colorless substrate TMB into a colored product, indicating the content of copper ion.

4.1. Preparation of chemicals

- Azide-modified G1 and alkyne-modified G2 were mixed at a mole ratio of 1:1 in reaction buffer at a final concentration of 1 μM.
- Cu^{2+} with various concentrations was added. Control experiment (in the absence of Cu^{2+}) was conducted under the same condition.
- Sodium ascorbate (2 μL) was added to a final concentration of 100 μM to accelerate the reaction between azide and alkyne group.
- Shake the mixture gently for 2 h at RT.
- After the reaction, add 1 μM hemin and 100 mM KCl, continued to shake for 20 min in order to form the hemin/G-quadruplex HRP-mimicking DNAzyme in aqueous solution.
- Equal volume (30 μL) of 0.5% (w/v) H_2O_2 and 0.05% (w/v) TMB were added to DNA-hemin mixture.
- 40 μL of 2 M H_2SO_4 was added to stop the reaction in 15 min, transferred solution into a 96-well microtiter plate. Record the OD values at 450 nm in each well using the microplate reader.

4.2. Results of colorimetric Cu^{2+} detection

The color intensity of the solution in each well increased with increasing Cu^{2+} concentration from 100 nM to 200 μM. In the absence of Cu^{2+}, the color of the solution had almost no change and

http://dx.doi.org/10.5772/intechopen.76024

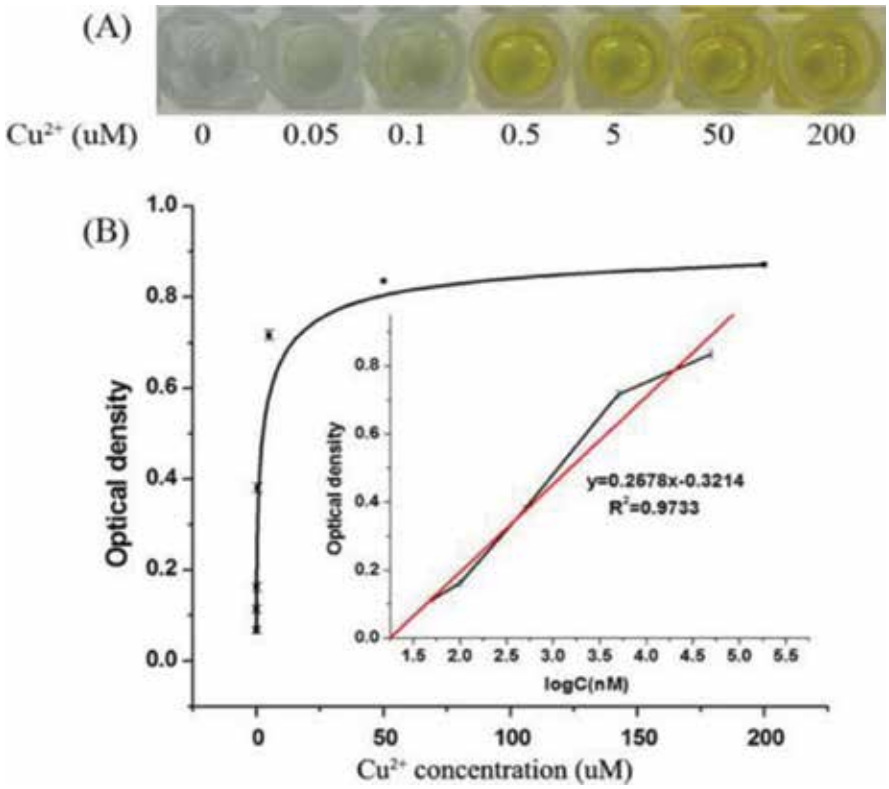

Figure 3. The sensitivity for Cu^{2+} detection based on click chemistry and hemin/G-quadruplex DNAzyme. (A) Photo images of the color intensity with different concentrations of Cu^{2+} (0, 100 nM, 200 nM, 500 nM, 1 μM, 10 μM, 100 μM, and 200 μM). (B) Plots of the OD value at 450 nm vs. Cu^{2+} concentration. Insert: calibration curve of OD value at 450 nm vs. the logarithm of Cu^{2+} concentration. The error bars represent the standard deviation of three independent measurements (reproduced with permission from [23]).

was still colorless. Calibration curve shows that the OD value is proportional to the logarithm of Cu^{2+} concentration in the range of 0.05–50 μM with a linear equation of OD value = 0.2578 ($logCu^{2+}$) − 0.3214 (R^2 = 0.9733). Using this equation, the limit of detection (LOD) of 5.9 nM was calculated based on triple standard deviation plus the mean of blanks [23] (**Figure 3**).

5. Summary and future directions

In summary, we have successfully constructed two sensors for rapid detection of copper ion based on click chemistry. Separated elements of probes were constructed at the presence of copper ion, which mediated the following color detection. The present methods are independent of complex operations and costly apparatus, while high sensitivity is achieved. The LOD of visual and colorimetric assay are 100 nM and 5.9 nM, respectively, which are much lower than 20 mM defined by EPA limit of Cu^{2+} in drinking water. In the future, the development of one-step process of microfluidic devices that integrate click chemistry and color development would provide even more convenient and more sensitive assays.

Author details

Lingwen Zeng[1,3]*, Zhiyuan Fang[2] and Yunbo Wang[3]

*Address all correspondence to: zeng6@yahoo.com

1 Institute of Environment and Safety, Wuhan Academy of Agricultural Sciences, Wuhan, China

2 The Fifth Affiliated Hospital of Guangzhou Medical University, Guangzhou, China

3 School of Food Science and Engineering, Foshan University, Foshan, Guangdong, China

References

[1] Si W, Liu J, Cai L, Jiang H, Zheng C, He X, Wang J, Zhang X. Health risks of metals in contaminated farmland soils and spring wheat irrigated with Yellow River water in Baotou, China. Bulletin of Environmental Contamination and Toxicology. 2015;**94**(2):214

[2] Pal A. Copper toxicity induced hepatocerebral and neurodegenerative diseases: An urgent need for prognostic biomarkers. Neurotoxicology. 2014;**40**:97

[3] Nath B, Chaudhuri P, Birch G. Assessment of biotic response to heavy metal contamination in *Avicennia marina* mangrove ecosystems in Sydney Estuary, Australia. Ecotoxicology and Environmental Safety. 2014;**107**:284

[4] Sacmaci S, Sahan S, Sahin U, Kartal S, Ulgen A. On-line solid-phase separation/preconcentration for the determination of copper in urine by flame atomic absorption spectrometry. Materials Science & Engineering. C, Materials for Biological Applications. 2014;**44**:240

[5] Stecka H, Jedryczko D, Welna M, Pohl P. Determination of traces of copper and zinc in honeys by the solid phase extraction pre-concentration followed by the flame atomic absorption spectrometry detection. Environmental Monitoring and Assessment. 2014;**186**(10):6145

[6] Li W, Simmons P, Shrader D, Herrman TJ, Dai SY. Microwave plasma-atomic emission spectroscopy as a tool for the determination of copper, iron, manganese and zinc in animal feed and fertilizer. Talanta. 2013;**112**:43

[7] Li H, Huang XX, Cai Y, Xiao HJ, Zhang QF, Kong DM. Label-free detection of Cu(2+) and Hg(2+) ions using reconstructed Cu(2+)-specific DNAzyme and G-quadruplex DNAzyme. PLoS One. 2013;**8**(9):e73012

[8] He JL, Zhu SL, Wu P, Li PP, Li T, Cao Z. Enzymatic cascade based fluorescent DNAzyme machines for the ultrasensitive detection of Cu(II) ions. Biosensors & Bioelectronics. 2014;**60**:112

[9] Yin H, Kuang H, Liu L, Xu L, Ma W, Wang L, Xu C. A ligation DNAzyme-induced magnetic nanoparticles assembly for ultrasensitive detection of copper ions. ACS Applied Materials & Interfaces. 2014;**6**(7):4752

[10] He Y, Tian J, Zhang J, Chen S, Jiang Y, Hu K, Zhao Y, Zhao S. DNAzyme self-assembled gold nanorods-based FRET or polarization assay for ultrasensitive and selective detection of copper(II) ion. Biosensors & Bioelectronics. 2014;**55**:285

[11] Wang F, Orbach R, Willner I. Detection of metal ions (Cu^{2+}, Hg^{2+}) and cocaine by using ligation DNAzyme machinery. Chemistry. 2012;**18**(50):16030

[12] Rostovtsev VV, Green LG, Fokin VV, Sharpless KB. A stepwise Huisgen cycloaddition process: Copper(I)-catalyzed regioselective "ligation" of azides and terminal alkynes. Angewandte Chemie (International Ed. in English). 2002;**41**(14):2596

[13] Kolb HC, Sharpless KB. The growing impact of click chemistry on drug discovery. Drug Discovery Today. 2003;**8**(24):1128

[14] Whiting M, Muldoon J, Lin YC, Silverman SM, Lindstrom W, Olson AJ, Kolb HC, Finn MG, Sharpless KB, Elder JH, et al. Inhibitors of HIV-1 protease by using in situ click chemistry. Angewandte Chemie (International Ed. in English). 2006;**45**(9):1435

[15] Wang Q, Chan TR, Hilgraf R, Fokin VV, Sharpless KB, Finn MG. Bioconjugation by copper(I)-catalyzed azide-alkyne [3 + 2] cycloaddition. Journal of the American Chemical Society. 2003;**125**(11):3192

[16] Cai Z, Li BT, Wong EH, Weisman GR, Anderson CJ. Cu(I)-assisted click chemistry strategy for conjugation of non-protected cross-bridged macrocyclic chelators to tumour-targeting peptides. Dalton Transactions. 2015;**44**(9):3945

[17] Kalveram B, Lihoradova O, Indran SV, Head JA, Ikegami T. Using click chemistry to measure the effect of viral infection on host-cell RNA synthesis. Journal of Visualized Experiments. 2013;**78**:e50809

[18] Wu ZL, Huang X, Burton AJ, Swift KA. Glycoprotein labeling with click chemistry (GLCC) and carbohydrate detection. Carbohydrate Research. 2015;**412**:1

[19] van Geel R, Debets MF, Lowik DW, Pruijn GJ, Boelens WC. Detection of transglutaminase activity using click chemistry. Amino Acids. 2012;**43**(3):1251

[20] Sun H, Peng X. Template-directed fluorogenic oligonucleotide ligation using "click" chemistry: Detection of single nucleotide polymorphism in the human p53 tumor suppressor gene. Bioconjugate Chemistry. 2013;**24**(7):1226

[21] Hua C, Zhang WH, De Almeida SR, Ciampi S, Gloria D, Liu G, Harper JB, Gooding JJ. A novel route to copper(II) detection using 'click' chemistry-induced aggregation of gold nanoparticles. Analyst. 2012;**137**(1):82

[22] Wang D, Ge C, Wang L, Xing X, Zeng L. A simple lateral flow biosensor for the rapid detection of copper(ii) ions based on click chemistry. RSC Advances. 2015;**5**(92):75722

[23] Ge C, Luo Q, Wang D, Zhao S, Liang X, Yu L, Xing X, Zeng L. Colorimetric detection of copper(II) ion using click chemistry and hemin/G-quadruplex horseradish peroxidase-mimicking DNAzyme. Analytical Chemistry. 2014;**86**(13):6387

Chapter 17

Properties and Applications of Ruthenium

Anil K. Sahu, Deepak K. Dash, Koushlesh Mishra, Saraswati P. Mishra, Rajni Yadav and Pankaj Kashyap

Additional information is available at the end of the chapter

http://dx.doi.org/10.5772/intechopen.76393

Abstract

Ruthenium (Ru) with atomic number of 44 is one of the platinum group metals, the others being Rh, Pd, Os, Ir and Pt. In earth's crust, it is quite rare, found in parts per billion quantities, in ores containing some of the other platinum group metals. Ruthenium is silvery whitish, lustrous hard metal with a shiny surface. It has seven stable isotopes. Recently, coordination and organometallic chemistry of Ru has shown remarkable growth. In this chapter, we review the application of Ru in diverse fields along with its physical and chemical properties. In the applications part of Ru we have primarily focused on the biomedical applications. The biomedical applications are broadly divided into diagnostic and treatment aspects. Ru and their complexes are mainly used in determination of ferritin, calcitonin and cyclosporine and folate level in human body for diagnosis of diseases. Treatment aspects focuses on immunosuppressant, antimicrobial and anticancer activity.

Keywords: ruthenium, platinum group, biomedical application, rare element, cancer, isotopes

1. Discovery of ruthenium

Ruthenium is one of the 118 chemical elements given in the periodic table. Out of these 118 elements, 92 elements originated from natural sources and remaining 26 elements have been synthesized in laboratories [1, 2]. The last naturally occurring element to be discovered was Uranium in 1789 [1, 3]. Technetium was the first man-made element to be synthesized in the year 1937 [2]. Recently in the year 2016, four of the man-made elements were included in periodic table. The four newly added elements goes by the name nihonium (Nh), moscovium (Mc), tennessine (Ts), and oganesson (Og), respectively for element 113, 115, 117 and 118 [4].

Discovery of Ruthenium had many twist and turns. A polish Chemist Jedrzej Sniadecki (1768–1838) in 1808 was first to announce the discovery of an element which he named Vestium after an asteroid called Vesta [3]. However, none of the contemporary Chemists were able to confirm his discovery. Later he again reported discovery of element 44 while working on the platinum ores from South America and published his results but again none of the fellow chemist were able to confirm the element 44 [4]. Due to repeated failures of his claim, Sniadecki got depressed and dropped the idea of further research on this element [1, 5]. After 20 years, a Russian chemist, Gottfried W. Osann, claimed the discovery of element 44. His discovery had the same fate as that of Sniadecki as none of his fellow chemist could repeat his results [5].

At last in the year 1844, another Russian chemist Carl Ernst Claus [also known in Russian as Karl Karlovich Klaus (1796–1864)] tried his luck on discovery of element 44. He succeeded in it as he gave positive proof about the new element extracted from platinum ores obtained from the Ural Mountains in Russia [6]. Claus had suggested the name of newly discovered element as Ruthenium after the name Ruthenia which was the ancient name of Russia. Earlier Osann had also suggested the same name for the element 44 [2, 5]. Ruthenium with atomic number 44 was given the symbol Ru. It is included in group 8, period 5 and block d in modern periodic table and it is a member of the platinum group metals [5].

2. Occurrence in nature

Like other platinum group metals, Ruthenium is also one of the rare metals in the earth's crust. It is quite rare in that it is found as about 0.0004 parts per million of earth crust [6]. This fraction of abundance makes it sixth rarest metal in earth crust. As other platinum group metals, it is obtained from platinum ores [7]. For instance, it is also obtained by purification process of a mineral called osmiridium [5].

3. Electronic configuration of Ru

In the modern periodic table, group 8 consists of four chemical elements. These elements are Iron (Fe), Ruthenium (Ru), Osmium (Os) and Hassium (Hs) [7]. Ruthenium has atomic number of 44, that is, it contains 44 electrons distributed in atomic orbitals and its nucleus has 44 protons and 57 neutrons (**Figure 1**). Electron distribution in atomic or molecular orbitals is called electron configuration which for Ru and the other group 8 chemical elements is shown in **Table 1**. Except for Ru, the electron configuration of group 8 elements shows two electrons in their outer most shell; Ruthenium has only one electron in its outermost shell. This tendency is quite similar to its neighboring metals such as niobium (Nb), molybdenum (Mo) and rhodium (Rh) [8].

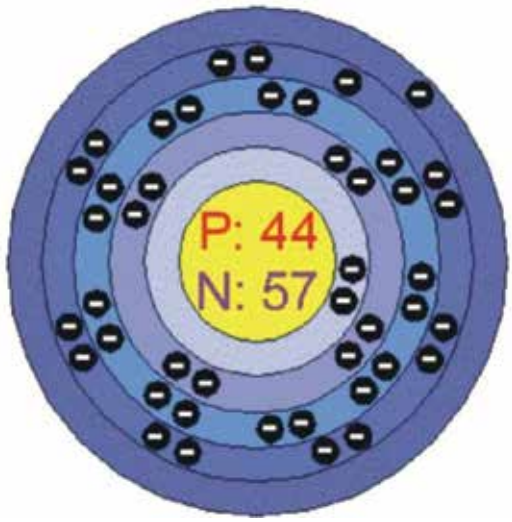

Figure 1. Schematic of the electron configuration and nucleus of an atom of Ruthenium.

Atomic number	Element	Electron configuration	Number of electrons per shell
26	Iron (Fe)	$1s^2\ 2s^2\ 2p^6\ 3s^2\ 3p^6\ 4s^2\ 3d^6$	2,8,14,2
44	Ruthenium (Ru)	$1s^2\ 2s^2\ 2p^6\ 3s^2\ 3p^6\ 4s^2\ 3d^{10}\ 4p^6\ 5s^1\ 4d^7$	2,8,18,15,1
76	Osmium (Os)	$1s^2\ 2s^2\ 2p^6\ 3s^2\ 3p^6\ 4s^2\ 3d^{10}\ 4p^6\ 5s^2\ 4d^{10}\ 5p^6\ 6s^2\ 4f^{14}\ 5d^6$	2,8,18,32,14,2
108	Hassium (Hs)	$1s^2\ 2s^2\ 2p^6\ 3s^2\ 3p^6\ 4s^2\ 3d^{10}\ 4p^6\ 5s^2\ 4d^{10}\ 5p^6\ 6s^2\ 4f^{14}\ 5d^{10}\ 6p^6\ 7s^2\ 5f^{14}\ 6d^6$	2,8,18,32,32,14,2

Table 1. Electron configuration of group 8 chemical elements.

4. Isotopes of Ru

Any atom having same number of protons, but different number of neutrons is termed as an Isotope. Isotopes can be differentiated on the basis of mass number as each isotope consists of different mass number which is being written on the right of the element name [1, 7]. Mass number indicates sum total of proton and neutron present in the nucleus of atom [9]. Ruthenium has many isotopes although only seven of them are stable. Apart from seven stable isotopes, 34 radioactive isotopes of Ruthenium are also found [8]. The most stable radioactive isotopes are ^{106}Ru, ^{103}Ru, ^{97}Ru having a half-life of 373.59, 39.26, 2.9 days, respectively. Other characteristics of the main isotopes are listed in **Table 2** [8].

Main isotopes of Ruthenium			
S. No.	**Isotopes**	**Abundance**	**Half-life**
1	^{96}Ru	5.54%	Stable with 52 neutrons
2	^{97}Ru	Synthetic	2.9 days
3	^{98}Ru	1.87%	Stable with 54 neutrons
4	^{99}Ru	12.76%	Stable with 55 neutrons
5	^{100}Ru	12.60%	Stable with 56 neutrons
6	^{101}Ru	17.06%	Stable with 57 neutrons
7	^{102}Ru	31.55%	Stable with 58 neutrons
8	^{103}Ru	Synthetic	39.26 days
9	^{104}Ru	18.62%	Stable with 60 neutrons
10	^{106}Ru	Synthetic	373.59 days

Table 2. Physical properties of platinum group elements.

5. Physical and chemical properties of Ru

Ruthenium (Ru), Rhodium (Rh), Palladium (Pd), Osmium (Os), Iridium (Ir) and Platinum (Pt) form the Platinum group metals. Some of the fundamental properties of platinum group metals are summarized in **Table 3** [8]. Ruthenium is silvery whitish, lustrous hard metal with a shiny surface. At room temperature, Ru does not lose its luster because it is unreactive in that condition but shows paramagnetic behavior [7]. At the higher temperature of around 800°C, Ru reacts with oxygen and gets oxidized [11]. It also reacts with halogens at higher temperature. As far as dissolution is concerned, Ruthenium does not dissolve in most of the acid or mixture of acids such as aqua regia which is a mixture of hydrochloric acid and nitric acid [7, 10]. When it is reacted with alkali it forms ruthenate ion which leads to dissolution of Ruthenium in alkalies (Eq. 1) [6].

	Ru	**Rh**	**Pd**	**Os**	**Ir**	**Pt**
Atomic number	44	45	46	76	77	78
Atomic weight	101.07 u ± 0.02 u	102.9055 u ± 0.00002 u	106.42 u ± 0.01 u	190.23 u ± 0.03 u	192.217 u ± 0.003 u	195.084 u
Electronic configuration	Kr 4d7 5 s1	Kr 4d8 5 s1	Kr 4d10	Xe 4f14 5d6 6 s2	Xe 4f14 5d7 6 s2	Xe 4f14 5d9 6 s1
Density(g/cc)	12.2	12.41	11.9	22.59	22.56	21.45
Melting point(°C)	2334	1963	1555	3033	2447	1768
Boiling point(°C)	4150	3697	2963	5027	4130	3825
Electronegativity	2.2	2.28	2.2	2.2	2.2	2.28

Table 3. Characteristics of main isotopes of ruthenium.

$$\underset{\text{Ruthenium}}{[Ru]} \xrightarrow{\text{Alkali}} \underset{\text{Ruthenate ion}}{[RuO_4^{2-}]} \quad (1)$$

6. Chemical reactivity of ruthenium

6.1. Oxidation reaction of ruthenium

As noted above, Ruthenium undergoes oxidation reaction to form Ruthenium oxide [11]. When Ruthenium oxide undergoes further oxidation in the presence of sodium metaperiodate, Ruthenium tetraoxide (RuO_4) is formed (Eq. 2), with properties somewhat similar to those of OsO_4, in that both are strong oxidizing agents. However, RuO_4 differs from OsO_4 since it can easily oxidize diluted form of hydrochloric acid as well as ethanol at normal room temperature [12]. At temperatures above 100°C, RuO_4 get reduced to its dioxide. RuO_4 also has specific stain property which is utilized in electron microscopy to investigate organic polymer samples [11, 13].

$$\underset{\text{Ruthenium}}{[Ru]} \longrightarrow \underset{\text{Ruthenium Oxide}}{[RuO_2]} \xrightarrow{[NaIO_4]} \underset{\text{Ruthenium Tetraoxide}}{[RuO_4]} \quad (2)$$

At lower oxidation states such as +2 or +3, Ru does not undergo oxidation reaction. Ruthenium reacts with hydroxide ions to attain higher coordination number [13]. Ruthenium does not form oxoanion readily as seen with iron. Ruthenium attains +7 oxidation states when it reacts with cold and diluted potassium hydroxide to form potassium perruthenate [14]. Ruthenium can also attain same oxidation state when potassium ruthenate gets oxidize in the presence of chlorine gas [9].

6.2. Coordination complexes of ruthenium

Coordination complex is the process where a center molecule makes bond with surrounding atoms or ions which are also known as ligands. Ruthenium readily forms coordinate complexes with different derivatives. It reacts with pentaamines to form different coordination complex. Ruthenium reacts with pyridine derivatives to form tris (bipyridine) ruthenium (II) chloride (Eq. 3) [15]. Ruthenium also reacts with carbon containing compounds. Ruthenium forms Roper's complex when trichloride form of Ruthenium reacts with carbon monoxide [10, 15]. Ruthenium makes hydride complex when Ruthenium trichloride is heated in presence of alcohol which then reacts with triphenylphosphine to form chlorohydridotris (triphenylphosphine) ruthenium (II) (Eq. 4) [10].

$$\underset{\text{Ruthenium}}{[Ru]} + \underset{\text{Pyridine}}{C_5H_5N} \longrightarrow \underset{\text{tris (bipyridine) ruthenium (II) chloride}}{C_{30}H_{24}N_6Cl_2Ru.6H_2O} \quad (3)$$

$$RuCl_3.XH_2O + C_{18}H_{15}P \xrightarrow{\text{Heat, Alcohol}} C_{54}H_{45}Cl_2P_3Ru \text{ ---------}$$

Ruthenium Trichloride — Triphenylphosphine — Chlorohydridotris(triphenylphosphine)Ru(II)

(4)

6.3. Catalytic activity of ruthenium

Ruthenium acts as a catalyst in many reactions. In the olefin metathesis, the carbene and alkylidene complex of Ruthenium act as a catalyst. In Fischer Tropsch reaction (Eq. 5), Ruthenium also acts as a catalyst [16]. Fischer Tropsch reaction is a reaction in which liquid hydrocarbons are formed as a product of reaction between hydrogen and carbon monoxide. Decomposition process of ammonia also employs Ru as catalyst [17]. Ru also catalyzes group of reactions called "borrowing hydrogen reactions". Borrowing hydrogen reaction is a reaction where two atoms of hydrogen are transferred to the catalyst to covert alcohol to carbonyl. The same reaction occurs in the conversion of alcohol to alkenes [5, 17].

Ruthenium carbonyl complex catalyzes the conversion of primary alcohol to aldehydes and secondary alcohol to aldehydes and ketones in the presence of a co-oxidant N-methylmorpholine-N-oxide (NMO) [8]. Ruthenium acts as a unique catalyst in oxidation reaction because of its varying oxidation state that ranges from −2 to +8 [6].

$$(2n+1)\,H_2 + n\,CO \xrightarrow{\text{Ru(Catalyst)}} C_nH_{2n+2} + n\,H_2O \quad (5)$$

7. Ruthenium complexes

In recent years, there has been remarkable growth and evaluation in the field of coordination and organometallic chemistry of Ru. Many publications have appeared recently on the formation of Ru-based complexes and their applications in such areas as medicine, catalysis, biology, nanoscience, redox and photoactive materials. These developments can be related to the fact that Ru has the unique ability to exist in multiple oxidation states. Examples of these complexes and various applications of Ru are reviewed in the following sections.

7.1. Development of half-sandwich para-cymene ruthenium (II) naphthylazophenolato complexes

Ruthenium (II)-arene complex has a structure of three-legged piano stool with a metal at the center in a quasi-octahedral geometry which is occupied by byan arene complex. 2-(naphthylazo)phenolate ligands reacts with chloro-bridged (g6-p-cymene) ruthenium complex [{(g6-pcymene)RuCl}2(l-Cl)2] in methanol having molar ratio 1:1 at room temperature leads to formation of monomeric ruthenium(II) complexes. The formed complexes (**Figure 2**)

http://dx.doi.org/10.5772/intechopen.76393

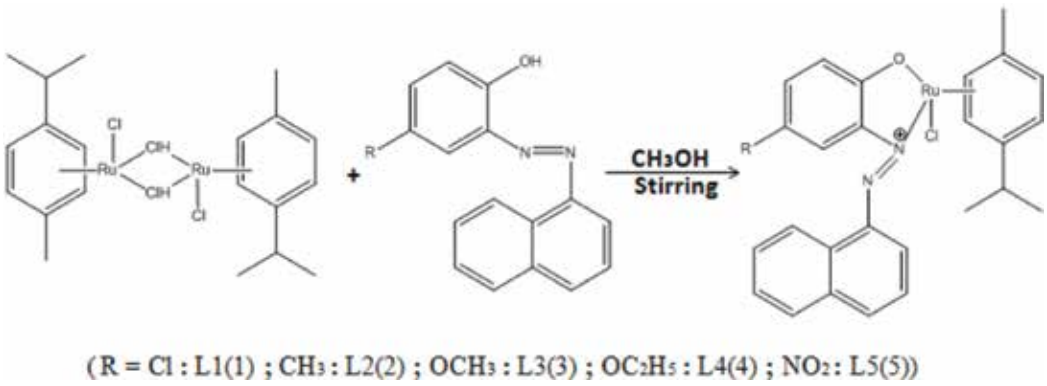

Figure 2. Structure of (p-cymene) ruthenium (II) 2-(naphthylazo)phenolate complexes.

show the solubility in polar solvents (dichloromethane and acetone) and are insoluble in non-polar solvents (aspentane and hexane). It is stable in air and shows diamagnetic nature with the +2 oxidation state [6, 10].

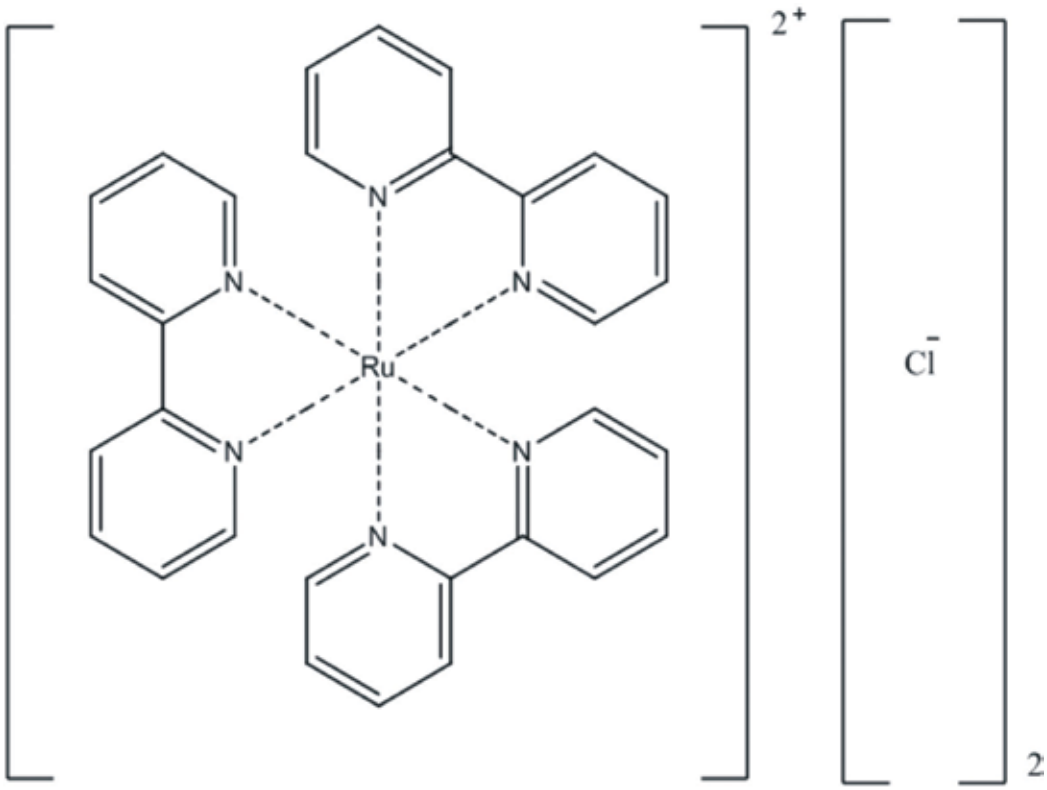

Figure 3. Structure of Tris (bipyridine) ruthenium (II) chloride.

7.2. Development of functionalized polypyridine ligands for ruthenium complexes

Polypyridine are coordination complexes containing polypyridine ligands such as 2,2′-bipyridine, 1,10-phenanthroline and 2,2′,6′2″-terpyridine. Polypyridines are multi-denated ligands which are responsible for characteristics property of metal complex they formed. Some of complexes show the characteristics of absorption of light by a process called metal-to-ligands charge transfer (MLCT). This said property of metal complex is due to the change in substituent to the polypyridine moiety. Among the polypyridine ligands for ruthenium complexes the mostly studied complex is Tris (bipyridine) ruthenium (II) chloride (**Figure 3**). It is a red crystalline salt having a hexahydrate form. Tris (bipyridine) ruthenium (II) chloride salt is prepared when aqueous solution of ruthenium trichloride reacts with 2,2′-bipyridine in the presence of reducing agent hypo-phosphorus acid. In this reaction Ru(III) gets reduced to Ru(II) [18].

8. Applications of ruthenium

Ruthenium has a wide variety of application in diverse fields. Few of the applications of Ruthenium are listed below.

8.1. General applications

Ruthenium finds application both in electronic industry and chemical industry. In electrical industry it is used in manufacturing of electronic chips [19]. Chemically it is used in the form of anodes for chlorine production in electrochemical cells [20]. Ruthenium is used as a hardener when it is mixed with other metals to form alloy. This characteristic of ruthenium is used in the preparation of jewelry of palladium [18, 20]. When Ruthenium forms alloy with titanium it improves its corrosion resistant property. Ruthenium alloys also find application in manufacturing of turbines of jet engines [17]. Fountain pen nibs also contain Ru tips. Ruthenium has also application in therapy. For instance 106 isotope of Ru has application in radiotherapy of malignant cells of eye [11]. RuO_4 is used in criminal investigations as it reacts with any fat or fatty substance having sebaceous pigments to give black or brown coloration due to formation of ruthenium dioxide pigments [12].

Ruthenium complexes tend to absorb light rays of visible spectrum. This property of ruthenium finds application in manufacturing solar cells for production of solar energy. [16] Ruthenium vapor get deposited on the surface of substrate and has magneto-resistive property. This property of Ru is used in making a layer or film on hard disk drives [12].

8.2. Biomedical applications

8.2.1. Applications in diagnosis

- Ruthenium is used for determination of calcitonin level in blood. This determination is helpful in diagnosis and treatment of diseases related to thyroid and parathyroid

glands. In treatment of medullary thyroid carcinoma (MTC), determination of calcitonin level plays an important role. The process of determination of calcitonin level involves one step sandwich assay method. This method is carried out in two incubation steps. Each incubation process takes 9 min each. In first incubation, 50 microliters of sample of biotinylated monoclonal human calcitonin specific antibody and monoclonal human calcitonin specific antibody labeled with ruthenium complex are incubated. This incubation leads to formation of sandwich like complex where human calcitonin is carrying both biotinylated and ruthenylated complex. After the first step, second incubation step is done where streptavidin-coated microparticles is added. Streptavidin-coated microparticle makes complex with biotin. After the incubation step, measurement is done. For measurement, the mixture of incubation is aspirated into measuring cells and micro particles of mixture are magnetically attracted to the surface of electrode. After that the unbound particles are removed. Voltage is applied on to the electrode and induction of chemi-lumiscent emission is done and after that the response is studied with photomultiplier [12].

- Folate is the main constituent of synthesis of DNA. It is also essential for formation of red blood cells. Deficiency of folate leads to megalobalstic anemia. Deficiency of folate is estimated by determination of folate level in erythrocytes as well as serum. Ruthenium plays an important role in Elecys folate RBC assay in estimating folate deficiency in RBC. The process involved in folate determination is competition principle. This process involves three steps incubation method. In first incubation step folate pretreatment reagent is added which leads to release of folate from its binding sites (erythrocytes). In the second incubation step, Ru-labeled folate binding protein is added which makes complex with the sample. In the third incubation step streptavidin bounded microparticles are added which get attached to unbound sites of ruthenium-labeled folate binding protein. The whole complex is bound to solid phase via streptavidin and biotin. For measurement, the mixture of incubation is aspirated into measuring cells and microparticles of mixture are magnetically attracted to the surface of electrode. After that the unbound particles are removed. Voltage is applied on to the electrode and induction of chemi-lumiscent emission is done and after that the response is studied with photomultiplier [12].

- Ruthenium is also employed in detection of cyclosporine by Elecsys cyclosporine assay. Determination of cyclosporine is an important aspect for management of liver, kidney, heart lungs and bone marrow transplant patients receiving cyclosporine therapy [12].

8.2.2. Applications in treatment

History of medical science shows metals like gold has always been used for medicinal purpose. Though it is known that metals may have beneficial effect for health, but the exact mode of activity remains unknown. Ruthenium also has been applied in treatment [21].

- **Immunosuppressant:** Immunosuppressant is drug used to suppress hyperactivity of body's immune system. An immunosuppressant Cyclosporin A which has wide application in treatment of disease like anemia and psoriasis eczema has shown side effects such as nausea, renal diseases, and hypertension. To modify the action of Cyclosporin A,

complex is made with Ru(III). Ruthenium cyclosporin complex gives a stable compound which results in an inhibitory effect on T lymphocyte proliferation [22].

- **Antimicrobial action:** antimicrobial drugs are drugs that inhibit microbial growth in human body. Ruthenium complex has its effectiveness against wide range of parasitic diseases. Microbial strains which are exposed to a certain kind of antimicrobial therapy become resistant to that drug. The resistance develops because the microbes mutate themselves against the organic compound of the drug. But with the formation of complex with certain metals the effectiveness of the drug increases as the microbes are unable to deal with the metal part of the organometallic complex of drug. In case of Chloroquine, Plasmodium species develops résistance against it, whereas when Chloroquine is complexed with ruthenium, resistance does not develop [23].
- **Antibiotic action:** antibiotics are drugs which are made from one particular microorganism and act on the other microorganism. Synthetic antibiotics are also nowadays made in laboratory. Antibiotic exhibit their action by entering the cell of microbes and targeting any vital biosynthetic pathway. Ruthenium has upper edge if it gets complexes with synthetic antibiotics. Ruthenium being a metal has better tendency to bind to the cellular component similar to Iron. When an organic moiety gets bind to a metal ion, at that time sharing or delocalization of cations between the two moieties occurs. The change in charges among the component of drug increases the permeability of cellular component in favor of drug. For example, Thiosemicarbazone shows a remarkable increase in its activity due to formation of complex of Ru [24].
- **Inhibitory effect on nitric oxides:** nitric oxide is a cellular component which is produced by many cells. The main physiological role of nitric oxide is to produce vasodilation. Nitric oxide does this action my increasing cellular level of cyclic-guanosine 3′,5′-monophosphate (CGMP) which is a secondary messenger in the physiological system. Over production of nitric acid can cause many disorders associated with respiratory system such as tumor of respiratory system. It also causes severe hypotension on over production. It also causes gastric inflammatory disorders. Ruthenium has beneficial effect in treatment of over production of nitric oxides. When ruthenium is administered in complex form such as ruthenium poly amino carboxylates, excess nitric oxide present in blood binds to this complex readily and reduces ruthenium to form an unabsorbable complex there by inhibiting its unwanted effects [25].

8.2.3. Applications of Ruthenium in cancer research

- **Anti-carcinogenic activity:** cancer or carcinoma is a stage where body cells undergo uncontrolled proliferation and having invasiveness and metastatic property. To treat carcinoma, drug therapy aims at inhibiting synthesis of cancerous protein as well as inhibiting DNA replication. In market there are drugs such as Cisplatin which uses platinum as anticancer agent. Though platinum has shown better results in treatment of cancer but in some cancers, platinum is unable to show positive results. This shortcoming of Platinum made way for use of Ruthenium as a new entrant in treatment of cancer. Ruthenium shows

the ability to bind to the DNA and inhibits its replication as well as protein synthesis. Ruthenium has low aqueous solubility which was the only drawback of it. This drawback was countered by using dialkyl sulfoxide derivative of ruthenium. The mechanism of action of ruthenium as an anticancer agent is that it causes apoptosis of tumor cells by acting at DNA level. Apoptosis is a controlled destruction of cells [17, 18].

- **Radiation therapy:** in cancer treatment radiotherapy has also been used. Radiation therapy becomes beneficial only when it is proximal to the cancerous cell. The agents used in radiation therapy are called radio sensitizers. To increase the proximity to cancerous cells radio sensitizers' complexes with ruthenium are used as Ru has the affinity to bind to DNA easily [18, 19].
- **Photodynamic therapy:** it is a therapy where chemicals and electromagnetic radiations are used. In this therapy chemicals are targeted on the cancerous cell, these chemicals become cytotoxic when they interact with electromagnetic radiation. In this therapy Ruthenium find its application as it increases the access of these chemicals to the cancerous cells [20, 21].
- **Action on cancerous mitochondria:** mitochondria are the power house of any cell. This makes it a potential target for anticancer therapy. Ruthenium red is a type of ruthenium which is used to stain mitochondria. Mitochondrial surface has some calcium entity on it. When ruthenium red is added, it reacts with this calcium and stains the mitochondria. Ruthenium red also has tumor inhibiting activity. However, ruthenium red is not preferably used clinically as it has major side effects [20, 22].
- **Effect on metastasis:** metastasis is the ability of cancerous cell to spread in the body by lymphatic or circulatory system. A tumor cell more than 1 mm in size requires additional blood supply to spread in the body. Formations of new blood vessels are called angiogenesis. Drugs which act as anti-metastasis many inhibit this action. Ruthenium complexes anti-metastatsis drug namely NAMI-A does the same action by binding to the mRNA and production of denatured protein which gets accumulated on the surface of tumor making a hard film and prevents any blood supply to the tumor cell. This action inhibits the metastasis. Ruthenium has additional benefit that it easily crosses any cell so the reach of the drug increases [23, 26].

9. Summary and conclusions

Ruthenium with atomic number of 44 and symbol Ru was discovered by Russian chemist Karl Klaus (1796–1864). In earth's crust, it is quite rare, found in parts per billion quantities, in ores containing some of the other platinum group metals. It is silvery whitish, lustrous hard metal with a shiny surface. The ability of Ru to exist in many oxidation states is an important property of this rare element which plays an important part in its applications. Ruthenium readily forms coordinate complexes and these complexes have their applications in diverse fields such as medicine, catalysis, biology, nanoscience, redox and photoactive

materials. In biomedical fields Ru is used for diagnosis and treatment purpose. For example, Ru is used for determination of calcitonin level in blood which is helpful in diagnosis and treatment of diseases related to thyroid and parathyroid glands. Also, Ru plays an important role in Elecys folate RBC assay in estimating folate deficiency in RBC. Ruthenium cyclosporin complex gives a stable compound which results in an inhibitory effect on T lymphocyte proliferation which shows its immune-suppressant action. Ruthenium complex has its effectiveness against wide range of parasitic diseases. Ruthenium shows the ability to bind to the DNA and inhibits its replication as well as protein synthesis. This property helps in the treatment of cancer. This chapter gives a brief account of the various properties of Ru which are exploited for applications in the medical field. It is likely that in the coming years, further research will lead to even more useful applications of this miraculous element.

Author details

Anil K. Sahu[1], Deepak K. Dash[1], Koushlesh Mishra[1], Saraswati P. Mishra[1], Rajni Yadav[2] and Pankaj Kashyap[1]*

*Address all correspondence to: pankajkashyap333@gmail.com

1 Royal College of Pharmacy, Chhattisgarh Swami Vivekanand Technical University, Raipur, Chhattisgarh, India

2 Columbia Institute of Pharmacy, Raipur, Chhattisgarh, India

References

[1] Medici S, Peana M, Nurchi VM. Noble metals in medicine: Latest advances. Coordination Chemistry Reviews. 2015;**284**:329-350. DOI: 10.1186/s13065-015-0126-z

[2] Matthew G, Vander H. Targeting Cancer metabolism. A therapeutic window opens. Nature Reviews Drug Discovery. 2011;**10**:671-684. DOI: 10.1038/nrd3504

[3] Blunden BM, Rawal A, Stenzel MH. Superior chemotherapeutic benefits from the ruthenium-based anti-metastatic drug NAMI-A through conjugation to polymeric micelles. Macromolecules. 2014;**47**:1646-1655. DOI: 10.1021/ma402078d

[4] Pastuszko A, Niewinna K, Czyz M. Synthesis, X-ray structure, electrochemical properties and cytotoxic effects of new arene ruthenium(II) complexes. Organometallic Chemistry. 2013;**14**:745-746. DOI: 10.1016/j.jorganchem.2013.07.020

[5] Ivry E, Ben-Asuly A, Goldberg I, Lemcoff NG. Amino acids as chiral anionic ligands for ruthenium based asymmetric olefin metathesis. Chemical Communications. 2015;**51**:3870-3873. DOI: 10.1039/C5CC00052A

[6] Ablialimov O, Kędziorek M, Malinska M, Wozniak K. Synthesis, structure, and catalytic activity of new ruthenium(II) indenylidene complexes bearing unsymmetrical *N*-heterocyclic carbenes. Organometallics. 2014;**33**:2160-2171. DOI: 10.1021/om4009197

[7] Valente A, Garcia MH. Synthesis of macromolecular ruthenium compounds: A new approach for the search of anticancer drugs. Inorganics. 2014;**2**:96-114. DOI: 10.3390/inorganics2010096

[8] Meija J. Atomic weights of the elements 2013 (IUPAC technical report). Pure and Applied Chemistry. 2016;**88**(3):265-291. DOI: 10.1515/pac-2015-0305

[9] Motswainyana WM, Ajibade PA. Anticancer activities of mononuclear ruthenium(II) coordination complexes. Advances in Chemistry. 2015:1-21. DOI: 10.1155/2015/859730

[10] Marx VM, Sullivan AH, Melaimi M. Cyclic alkyl amino carbene (CAAC) ruthenium complexes as remarkably active catalysts for ethenolysis. Angewandte Chemie, International Edition. 2015;**54**:1919-1923. DOI: 10.1002/anie.201410797

[11] Singh SK, Pandey DS. Multifaceted half-sandwich arene-ruthenium complexes: Interactions with biomolecules, photoactivation, and multinuclearity approach. RSC Advances. 2014;**4**:1819-1840. DOI: 10.1039/C3RA44131H

[12] Rezayee NM, Huff CA, Sanford MS. Tandem amine and ruthenium-catalyzed hydrogenation of CO2 to methanol. Journal of the American Chemical Society. 2015;**137**:1028-1031. DOI: 10.1021/ja511329m

[13] Miyada T, Kwan EH, Yamashita M. Synthesis, structure, and bonding properties of ruthenium complexes possessing a boron-based PBP pincer ligand and their application for catalytic hydrogenation. Organometallics. 2014;**33**:6760-6770. DOI: 10.1021/om500585j

[14] Xian-Lan H, Liang Z-H, Zeng M-H. Ruthenium(II) complexes: Structure, DNA-binding, photocleavage, antioxidant activity, and theoretical studies. Journal of Coordination Chemistry. 2011;**64**:3792-3807. DOI: 10.1089/dna.2009.0979

[15] Corral E, Hotze CG, Den D. Ruthenium polypridyl complexes and their modes of interaction with DNA: Is there a correlation between these interactions and the antitumor activity of the compounds. Journal of Biological Inorganic Chemistry. 2009;**14**:439-448. DOI: 10.1007/s00775-008-0460-x

[16] Shoba C, Satyanarayana S. Synthesis, characterization, and DNA-binding properties of Ru (II) molecular "light switch" complexes. Journal of Coordination Chemistry. 2012;**65**(3): 474-486. DOI: 10.1080/00958972.2011.649736

[17] Sava G, Bergamo A. Ruthenium drugs for cancer chemotherapy: An ongoing challenge to treat solid tumours. Cancer Drug Discovery and Development. 2009;**1**:57-66. DOI: 10.1007/978-1-60327-459-3_8

[18] Ang WH, Dyson PJ. Classical and non-classical ruthenium-based anticancer drugs: Towards targeted chemotherapy. European Journal of Inorganic Chemistry. 2006;**20**:4003-4018. DOI: 10.1002/ejic.200600723

[19] Daxiong H, Haiyan W, Nailin R. Molecular modelling of B-DNA site recognition by Ru intercalators: Molecular shape selection. Journal of Molecular Modeling. 2004;**10**:216-222. DOI: 10.1016/S0006-3495(96)79587-5

[20] Gunanathan C, Milstein D. Bond activation and catalysis by ruthenium pincer complexes. Chemical Reviews. 2014;**114**:12024-12087. DOI: 10.1039/c3nj00315a

[21] Tönnemann J, Scopelliti R, Severin K. (Arene) ruthenium complexes with imidazolin-2-imine and imidazolidin-2-imine ligands. European Journal of Inorganic Chemistry. 2014; **14**:4287-4293. DOI: 18.5586/Inorg.Chem.9172442001

[22] Mukherjee T, Ganzmann C, Bhuvanesh N, Gladysz JA. Syntheses of enantiopure bifunctional 2-guanidinobenzimidazole cyclopentadienyl ruthenium complexes: Highly enantioselective organometallic hydrogen bond donor catalysts for carbon-carbon bond forming reactions. Organometallics. 2014;**33**:6723-6737. DOI: 10.3490/molecules200917274

[23] Saez R, Lorenzo J, Prieto MJ, Font-Bardia M. Influence of PPh3 moiety in the anticancer activity of new organometallic ruthenium complexes. Journal of Inorganic Biochemistry. 2014;**136**:1-12. DOI: 10.3390/molecules23010159

[24] Clavel CM, Păunescu E, Nowak-Sliwinska P, Dyson PJ. Thermoresponsive organometallic arene ruthenium complexes for tumour targeting. Chemical Science. 2014;**5**:1097-1101. DOI: 10.3390/molecules200917244

[25] Adeniyi AA, Ajibade PA. An insight into the anticancer activities of Ru(II)-based metallocompounds using docking methods. Molecules. 2013;**18**:10829-10856. DOI: 10.3390/molecules180910829

[26] Zhang S, Ding Y, Wei H. Ruthenium polypyridine complexes combined with oligonucleotides for bioanalysis: A review. Molecules. 2014;**19**:11933-11987. DOI: 10.3390/molecules190811933

Section 5

Metallurgy and Recovery

Chapter 18

Extraction of Platinum Group Metals

Bongephiwe Mpilonhle Thethwayo

Additional information is available at the end of the chapter

http://dx.doi.org/10.5772/intechopen.73214

Abstract

About 80% of the worlds' reserves for platinum group metals (PGMs) are in South Africa's Bushveld Igneous Complex. Processing of PGM involves comminution, flotation, smelting, converting, base metals refinery and precious metals refinery. Due to increasing chrome content in the feed and the challenges associated with operating high chrome feed, alternative routes to smelting of PGM are being investigated. Some hydrometallurgical routes have been proposed. However, none of the reported potential routes have yet been commercialised.

Keywords: platinum group metals, chrome, smelting, UG2, Merensky

1. Introduction

Platinum group metals (PGMs) are a group of six elements, namely iridium (Ir), osmium (Os), platinum (Pt), palladium (Pd), rhodium (Rh) and ruthenium (Ru) [1, 2]. PGMs together with gold and silver are classified as noble or precious metals because of their high corrosion and oxidation resistance [1–3]. The world's reserves of platinum group metals/elements are estimated at 100 million kilogrammes, of which over 80% is contained in South Africa's Bushveld Igneous Complex [4]. Summary of the PGM reserves by country is shown in **Table 1** [5]. PGMs are used in a number of industrial processes and commercial applications including automotive, jewellery, electronics, dentistry, catalysts, needles, pivots, temperature measurements, special crucibles and investments amongst others [5–7].

Country	PGM reserves (kg)
United States	900 000
Canada	310 000
Russia	1 100 000
South Africa	63 000 000
Other countries	800 000
World total (rounded)	66 000 000

Table 1. World's reserves of PGM [5].

2. Geology

In South Africa, the PGM ore is mined in the western and eastern limb of the Bushveld Igneous Complex [8]. Within the Bushveld Igneous Complex, the Merensky reef, the Platreef and Upper Group 2 (UG2) reef are exploited for platinum production [1, 4, 9]. Merensky and Platreef have similar chemical and mineral composition [6, 10]. These reefs typically have fairly low contents of sulphides. UG2 differs from the two reefs in that it has low nickel and copper content [3]; compared to UG2, Merensky reef has higher amounts of chalcopyrite, pentlandite and pyrrhotite [8]. Chromite spinel can be up to 4% by mass in a UG2 concentrate, while a Merensky concentrate can have <1% by mass chromite spinel [8, 10].

Mineral	Formula
Sulphide minerals	
Chalcopyrite	$CuFeS_2$
Pentlandite	$(Fe, Ni, Co)_9S_8$
Pyrite	FeS_2
Pyrrhotite	$Fe_{1-x}S_x$
Gangue minerals	
Alteration silicates	Hydrated minerals
Chromite spinel	$FeCr_2O_4$
Pyroxenes	$(Mg, Fe)SiO_3 – Ca(Mg, Fe)Si_2O_6$
Olivine	$(Mg, Fe)_2SiO_4$
Plagioclase/feldspar	$NaAlSi_3O_8 – CaAl_2Si_2O_8$
Quartz	SiO_2
Haematite	Fe_2O_3

Table 2. Sulphide and gangue mineralogy of a typical PGM concentrate [11].

A typical mineralogy of the flotation concentrate blend is shown in **Table 2** [11]. Eksteen (2011) [8] has given the fractions of typical minerals in the UG2 and Merensky concentrates. The abundant gangue minerals in a typical PGM concentrate are orthopyroxene, talc, clinopyroxene and plagioclase [8]; other gangue minerals are <5% by mass [8].

3. Sources of PGM

The principal sources of PGM are sulphide and arsenide minerals such as $PtAs_2$, PtS, $Pt(AsS)_2$, (Pt,Pd)S, (Pt,Pd,Ni)S, RuS_2 and Pd_3Sb and elemental ruthenium [3, 7]. Noble metals together with cobalt (Co), copper (Cu), iron (Fe) and nickel (Ni) belong to the class of transition metals in the periodic table [6]. Geologically, PGM associates with base metal sulphides such as chalcopyrite ($CuFeS_2$), millerite (NiS), pentlandite $(Fe,Ni)_9S_8$, pyrite (FeS_2) and pyrrhotite ($Fe_{1-x}S$) [3, 12, 13]. Troilite carries trace amounts of iridium, while chalcopyrite has trace amounts of Ru, Pd, Ir and Pt [13]. Gangue minerals associated with PGM-containing minerals are feldspar, biotite, plagioclase and pyroxene [12].

4. PGM ore processing: an overview

Typical process route for treating PGM ore with the approximate PGM grade in each process is shown in **Figure 1** [1, 7, 9].

4.1. Comminution

The PGM ore is initially treated in primary and secondary crushers after which it is sent to rod and ball milling circuits. The milled PGM ore is treated using gravity separators and flotation cells; xanthate and dithiophosphate collectors are typical reagents used for flotation at a pH of 7.5–9 [1]. A sulphide-rich PGM concentrate is produced in the flotation cells [6].

Typical composition of UG2 and Merensky flotation concentrate is shown in **Table 3** [14]. A typical PGM content in the flotation concentrate is in **Table 4** [9]. The UG2 concentrate has higher chrome content when compared to the Merensky as seen in **Tables 3** and **4**. UG2 also has higher PGM content than the Merensky concentrate. The concentrate from the flotation cells is dried and smelted to separate the sulphides from the silicates [9].

4.2. PGM ore smelting

To separate the PGM-rich sulphides from the gangue minerals, smelting is used. Rectangular six-in-line or circular three-electrode electric furnaces are typical in the PGM industry [12]. Smelting is a high-temperature process step where the sulphides (valuable minerals) are separated from the silicates (gangue minerals). Energy required for melting the concentrate is provided by Joule heating when an electric current is passed through the resistive bath [15]. The electrodes are used for electrical connections between the power supply and the bath. Graphite electrodes are inserted into the resistive bath such that when a current is applied through the electrodes, thermal energy is generated [6, 15].

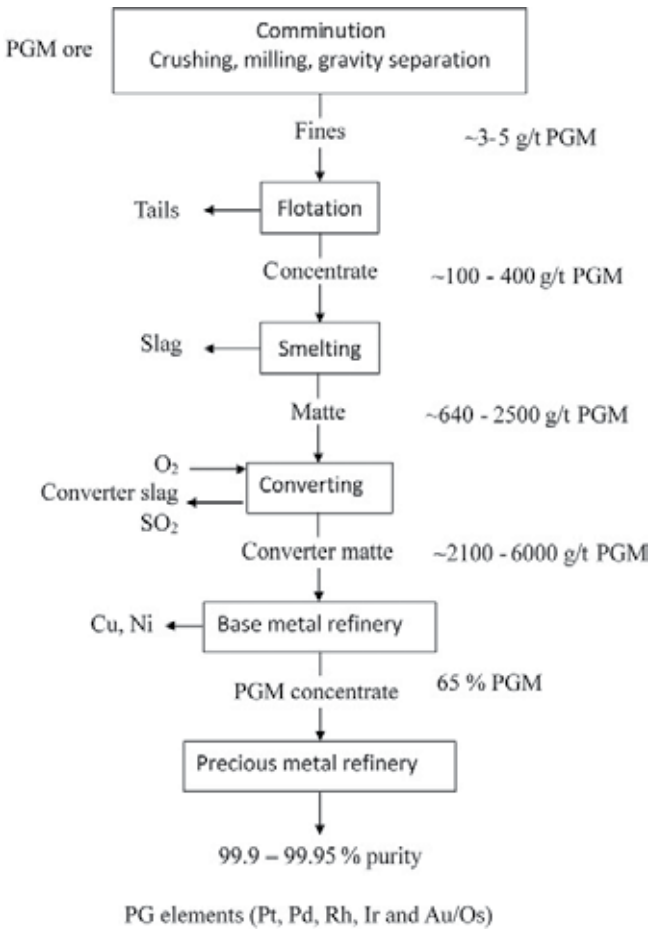

Figure 1. Typical process flow diagram for PGM ore processing [9, 12].

	Al_2O_3	CaO	Cr_2O_3	Cu	FeO	MgO	Ni	S	SiO_2	PGM (g/t)
Merensky	1.6	2.2	0.3	2.1	22.3	18.2	3.2	9	41.4	100 - 250
UG2	5.0	2.4	2.9	0.8	12.6	21.0	1.7	3.6	44.0	300 - 600

Table 3. Typical composition of Merensky and UG2 concentrate [14].

The PGM concentrate is introduced into the smelter through the feed ports situated on the furnace roof. The concentrate forms a thick bed (~400 mm) on top of the molten bath. The heat generated in the resistive bath causes the concentrate bed to melt gradually [8].

The operating temperature of the smelter at the concentrate zone can range from 600 to 900°C [16]. The liquidus temperature of base metal sulphides associated with PGMs is 850–875°C, whereas the liquidus temperature of the corresponding silicates is approximately 1350°C [16]. The sulphides in a PGM concentrate start melting at the concentrate bed since temperature at

Assay	Merensky	UG2	Platreef
PGM-4E	200	200	120
Pt-% of 4E	63.5	56.7	45.1
Pd	28.1	29.4	45.7
Rh	4.4	13.0	3.2
Au	4.0	0.9	6.0
Ir	0.6	1.6	1.0
Ru	6.8	9.6	3.5
Ni %	6.0	1.4	4.9
Cu	3.4	0.7	2.5
Co	0.15	0.05	0.2
Cr_2O_3	0.6	3.0	0.3
Sulphur	15-20	4-6	10-15
USD value/tonne	14009	16526	7397

Table 4. Typical content of a PGM flotation concentrate [9].

the concentrate zone can exceed the liquidus temperature of the sulphides. The silicate minerals melt when they reach the molten bath (concentrate-slag interface) [16]. The silicates and sulphides are immiscible; upon melting they form two separate layers.

The molten silicates and oxides form a fayalitic-forsteric slag layer, while the PGM-containing sulphides form a matte layer [16]. The specific gravity of matte ranges from 4.8 to 5.6, and that of slag ranges from 2.8 to 3.8 [6, 15]. Owing to the difference in specific gravities of matte and slag, the slag forms a top layer. Matte being denser than slag falls through the slag layer and settles underneath the slag. Matte consists of base metal sulphides (cobalt, copper, iron and nickel). Matte serves as a collector for the PGMs [6, 7, 14].

Operating temperature of matte and slag varies with the composition of the concentrate [8]. Typical smelter operating temperature for matte varies from 1380 to 1600°C, and that of slag varies from 1500 to 1680°C [8].

The molten slag and matte are tapped out of the smelter through the tap holes situated at the sidewall of the furnace. After tapping, the matte either can be fed directly to the converters as tapped or can be granulated before the conversion step; matte treatment varies with the producers.

4.2.1. Industrial PGM-furnace matte

Anglo American Platinum (Amplats), Impala Platinum (Implats) and Lonmin are three major producers of PGM in South Africa [9]. Typical compositions of matte from selected smelters are shown in **Table 5**. Matte from different smelters seems to have comparable amounts of major components (Cu, Fe, Ni and S). The slight difference is that the amount of iron in Amplats matte is slightly higher than the iron in a Lonmin matte (**Table 5**).

	Co	Cr	Cu	Fe	Ni	S
Amplats-Waterval	0.5	0.5	9.0	41.0	17.0	27.0
Lonmin-Merensky/UG2	0.5	0.2	9.7	37.0	17.0	28.0
Lonmin-UG2	0.5	0.3	9.8	35.0	17.0	28.0

Table 5. Typical chemical composition of industrial matte from selected smelters (% by mass) [12].

	Al_2O_3	CaO	Co	Cr_2O_3	Cu	FeO	MgO	Ni	S	SiO_2
Amplats-Waterval	3.3	6.4	0.1	0.8	0.1	31.0	15.0	0.2	0.5	46.0
Lonmin-Merensky	2.0	9.8	0.1	1.2	0.1	28.0	19.0	0.2	0.0	44.0
Lonmin-UG2	3.9	13.0	0.0	2.4	0.1	9.2	22.0	0.1	0.0	47.0

Table 6. Typical chemical composition of industrial slag from different smelters (% by mass) [12].

4.2.2. Industrial PGM-furnace slag

Gangue minerals associated with PGM-containing minerals are feldspar, biotite, plagioclase and pyroxene ($[Ca,Na]Al_{1-2}Si_{3-2}O_8$) [12]. During smelting these gangue minerals form a slag that is a silicate rich phase. Typical composition of a PGM-furnace slag from different smelters is shown in **Table 6** [12]. The oxide compounds in Amplats and Lonmin-Merensky slag are comparable; Lonmin-UG2 slag has higher Cr_2O_3, CaO and MgO; and its FeO content is significantly lower when compared to that of the slag from Amplats and Lonmin-Merensky ore.

4.3. Converting

After smelting, the furnace matte is treated in Pierce-Smith converters or Ausmelt process where iron sulphide is oxidised to ferrous oxide and sulphur is oxidised to sulphur dioxide [9]. Sulphur dioxide is removed as an off-gas, and iron oxide is removed as a fayalitic slag. The slag phase of the converter contains significant amounts of entrained PGM and is recycled to the smelting furnace to recover the entrained PGM. The converter matte is cooled, milled and treated in base metals refinery (BMR) [1, 9].

4.4. Purification

Typical hydrometallurgical processes used for PGM purification are as follows: dissolution-precipitation (pressure oxidation leach), solvent extraction and ion exchange and molecular recognition technology [17]. Pressure oxidation leach is a typical hydrometallurgical process used to separate base metals from the PGM residue. The base metals are leached, while the PGMs remain in the residue. The PGM residue is sent to a precious metal refinery where various solution extraction and precipitation methods are used to separate individual metals [1]. Solvent extraction is another method by which PGMs can be separated from the base metals [7].

5. Operational challenges facing PGM industry

South Africa is faced with increasing cost of electricity which has direct impact on the energy-intensive processes such as smelting [1, 18]. South African PGM producers generally process a Merensky concentrate where available; otherwise, the Merensky and UG2 concentrates are blended together to achieve the required feed composition for the smelter. In recent years, the depletion of the Merensky reef has forced the PGM producers to mine the UG2 reef that has up to 60% chromite. As a consequence, the concentrate from the floatation cells has high chrome content than the amount that the smelters are designed to handle. In reducing conditions, the operating temperature limits the solubility of Cr_2O_3 in a typical slag. At 1450–1650°C the solubility of Cr_2O_3 in slag is limited to 1.8% by mass. As such the smelters have battled with numerous challenges owing to the treatment of a high chrome concentrate [9, 19].

5.1. Challenges associated with smelting high chromite concentrate

The challenges associated with high chrome feed to the smelter are the following [19]:

- Formation of chromite spinels which are insoluble in slag.
- Chromite spinels have high melting points as such they increase the liquidus temperature of the slag and they lower the fluidity of the slag [19].
- Chromite spinels increase the overall temperature of the constituents (slag and matte) [8].
- When the matte temperature is above the liquidus temperature of the slag freeze-lining, the matte dissolves the freeze-lining; this leads to corrosion of the refractories by corrosive PGM melt [8].
- There are FeO- and CrO-based spinels; the proportion of Fe and Cr in the spinel may vary, as such there are spinels that are heavier than the matte, while other spinels are slightly lighter than matte. Spinels which are denser than matte settle on the hearth; the accumulation of spinels on the hearth reduces the volume of the furnace [8].
- Spinels with intermediate density form a 'mushy' layer at the slag-matte interface; this leads to the entrainment of matte in slag [8].
- High chrome decreases electrical conductivity of the bath leading to electrical control problems in the furnace [19].
- Higher chrome levels affect the matte temperatures during conversion step (matte temperatures above 1355°C have been observed); this causes damage to the refractory lining. Cold dope (revert) is normally used to lower the temperature of the matte during conversion [16, 19].

A number of approaches have been investigated to deal with the chrome problem. The following actions have eased chromite problem in the smelters:

- Deep electrode immersion operating at high power densities causes sufficient mixing which keeps the solids in suspension [8, 21], but high power densities adversely affect the refractory life. To minimise the effect of high power input on the refractory life of the sidewall lining, the phase voltage is increased without increasing the current levels [19].
- Some producers stopped recycling the converter slag to the furnaces since the converter slag has high chrome content [19, 20].
- The flux addition in the furnace was discontinued since lower CaO levels increased the solubility of the chromite in the slag [19, 20].
- The control of furnace inputs and control of furnace parameters (power, furnace availability) are essential in controlling chrome content [19].
- Selective reduction improves the solubility of chromium in the slag [20].
- Tapping out the intermediate layer intentionally [22].
- Decreasing the chromium input to the smelters [20].
- Another innovation able to manage chrome-rich ores is the ConRoast process. This process involves removing and capturing sulphur from the concentrate prior to smelting in a DC arc furnace. Roasting a concentrate makes smelting more environmentally friendly; it also enables furnaces to accept any proportion of chromite, resulting in more efficient and cost-effective platinum production [9, 23].

5.2. Premature failure of refractory lining

Due to high operating temperatures (1350 to >1600°C) [8] associated with PGM smelting, the smelter has to be lined with refractories at the hot face. To prolong the service life of the refractories, sufficient cooling of the refractories is required at the cold face of the refractory wall. Copper waffle coolers are typically used in the cold face of the refractories to extract heat away from the refractories [24]. Due to high operating temperature and corrosiveness of the PGM melt, premature failure of the waffle copper coolers has been experienced in PGM smelters [24] in the upper sidewall region. Failure of waffle copper coolers causes explosions, loss of production and costs associated with furnace rebuild. The failure of waffle copper coolers was preceded by the consumption of conventional refractory bricks (MgO_x-CrO_x) which were used to form the furnace lining. The refractory brick (MgO_x-CrO_x) had low resistance to chemical attack by liquid PGM melt. To prevent the occurrences of copper cooler failures, conventional bricks have been replaced by the graphite blocks in recent designs of PGM smelter refractory walls [25]. Graphite blocks are only applied at the hot face of the upper sidewall (against the concentrate and the slag zone).

With the graphite block lining, a frozen protective skull forms at the hot face of the refractory. The formation of the protective skull is attributed to the efficient cooling of the refractory wall by waffle coolers. The frozen skull is the melt that solidified due to the surface temperature of the graphite that was lower than the liquidus temperature of the melt [25].

Graphite blocks have increased the service life of the waffle copper coolers through the formation of a protective layer. However, high infiltration of melt is still observed at the matte-slag tidal zone. This is a challenge that still needs to be addressed; currently, conventional bricks or monolithics are used at lower sidewall of the PGM smelter refractory. It is desired to extend the graphite blocks to the lower sidewall of the PGM smelter refractory wall against the matte zone [25]. It is envisaged that using carbon-based refractory at the hot face of the matte zone (lower sidewall) will improve the service life of the furnace lining in PGM smelters [25].

6. Opportunities in PGM processing

The PGM industry faces challenges with increasing chrome content in the feed and premature failure of refractory lining in the smelter. Alternative ways to process the PGM have become attractive due to the challenges associated with the conventional smelting process [1, 18]. A hydrometallurgy (Kell) process has been probed as an alternative to smelting PGM. The Kell process has three stages: stage 1 is the leaching of base metal sulphides in an acidic sulphate medium (pressure oxidation); stage 2 is roasting of the residue from stage 1; and stage 3 is atmospheric leaching of PGMs in a chloride media. The leached precious metals are further treated in refineries to recover metals [18]. Other hydrometallurgical routes have been discussed in Ref. [1]. These hydrometallurgical processes have advantages over the smelting process since they reduce the operating costs drastically [1]. However, the alternative hydrometallurgical routes of processing PGMs have not yet been commercialised [1].

7. Conclusions

In this chapter, an overview of PGM processing has been presented. The conventional smelting process has challenges with high chromium feed, premature failure of refractory lining and increased operating cost associated with increasing cost of electricity in South Africa. The Kell process is an alternative way to process a PGM concentrate, and it has a number of advantages such as less energy consumption, less energy cost, less electricity consumption, less CO_2 emissions and no restriction on chrome content of feed. Other hydrometallurgical routes have been investigated, but none has been commercialised yet.

Author details

Bongephiwe Mpilonhle Thethwayo

Address all correspondence to: 77mpilot@gmail.com

University of Johannesburg, Johannesburg, South Africa

References

[1] Safarzadeh MS, Horton M, Van Rythoven AD. Review of recovery of platinum group metals from copper leach residues and other resources. Mineral Processing and Extractive Metallurgy Review. 2018;**39**(1):1-17

[2] Glaister BJ, Mudd GM. The environmental costs of platinum–PGM mining and sustainability: Is the glass half-full or half-empty? Minerals Engineering. 2010;**23**(5):438-450

[3] Xiao Z, Laplante AR. Characterizing and recovering the platinum group minerals – A review. Minerals Engineering. 2004;**17**(9):961-979

[4] Junge M, Wirth R, Oberthür T, Melcher F, Schreiber A. Mineralogical siting of platinum-group elements in Pentlandite from the Bushveld complex, South Africa. Mineralium Deposita. 2015;**50**(1):41-54

[5] Jewell S, Kimball SM. Mineral Commodity Summaries 2015. U.S. Geological Survey. Reston, Virginia: CreateSpace Independent Publishing Platform; 2015;**196**:120-121

[6] Jones RT. An overview of Southern African PGM smelting, nickel and cobalt 2005: Challenges in extraction and production. In: 44th Annual Conference of Metallurgists, Calgary, Alberta, Canada: Canadian Institute of Mining, Metallurgy and Petroleum. 21-24 August 2005. pp. 147-178

[7] Hayes PC. Process Principles in Minerals & Materials Production. 3rd ed. Australia: Hayes Publishing CO; 2003. pp. 278-279

[8] Eksteen JJ. A mechanistic model to predict matte temperatures during the smelting of UG2-rich blends of platinum group metal concentrates. Minerals Engineering. 2011; **24**(7):676-687

[9] Cramer LA. What is your PGM concentrate worth? In: Third International Platinum Conference, 'Platinum in Transformation', Johannesburg, South Africa: South African Institute of Mining and Metallurgy; 2008. pp. 5-9

[10] Nell J. Melting of platinum group metal concentrates in South Africa. Journal of the South African Institute of Mining and Metallurgy. 2004;**104**(7):423-428

[11] Andrew NJ, van Beek B, Lexmond A, Zietsman JH. Effect of Feed Composition Fluctuations on a Platinum Furnace Energy Balance and Slag Temperature. The Southern African Institute of Minng and Metallurgy, Pyrometallurgical Modelling-Principles and Practices, Kempton Park, South Africa, 4-5 August 2014. pp. 117-126

[12] Jones RT. Platinum smelting in South Africa. South African Journal of Science. 1999;**95**: 525-534

[13] Cabri LJ, Rudashevsky NS, Rudashevsky VN. Current approaches for the process mineralogy of platinum-group element ores and tailings. In: Ninth International Congress for Applied Mineralogy ICAM. Geological Society of India. 2009. pp. 9-17

[14] Liddell KS, McRae LB, Dunne RC. Process routes for beneficiation of noble metals from Merensky and UG-2 ores. Mintek Review. 1986;**4**:33-44

[15] Habashi F. Textbook of Pyrometallurgy. Canada: Métallurgie Extractive Québec; 2002. pp. 237-242

[16] Eksteen JJ, Van Beek B, Bezuidenhout GA. Cracking a hard nut: An overview of Lonmin's operations directed at smelting of UG2-rich concentrate blends. Journal of the Southern African Institute of Mining and Metallurgy. 2011;**111**(10):681-690

[17] Bezuidenhout GA, Eksteen JJ, Akdogan G, Bradshaw SM, De Villiers JPR. Pyrometallurgical upgrading of PGM-rich leach residues from the western platinum base metals refinery through roasting. Minerals Engineering. 2013;**53**:228-240

[18] Liddell K, Newton T, Adams M, Muller B. Energy consumptions for Kell hydrometallurgical refining versus conventional pyrometallurgical smelting and refining of PGM concentrates. In: The 4th International Platinum Conference, Platinum in Transition 'Boom or Bust'. Johannesburg, South Africa: The Southern African Institute of Mining and Metallurgy; 2010. pp. 181-186

[19] Coetzee V. Common-sense improvements to electric smelting at impala platinum. Journal of the Southern African Institute of Mining and Metallurgy. 2006;**106**(3):155-164

[20] Hundermark RJ, Mncwango SB, de Villiers LPS, Nelson LR. The Smelting Operations of Anglo American's Platinum Business: An Update, Southern African Pyrometallurgy 2011. Johannesburg: Southern African Institute of Mining and Metallurgy; 6-9 March 2011. pp. 295-307

[21] Liddell KS, Adams MD. Kell hydrometallurgical process for extraction of platinum group metals and base metals from flotation concentrates. Journal of the Southern African Institute of Mining and Metallurgy. 2012;**112**(1):31-36

[22] Barnes AR, Newall AF. Spinel Removal from PGM Smelting Furnaces. Southern African Pyrometallurgy, 5-6 March 2006. Johannesburg, South Africa: Southern African Institute of Mining & Metallurgy; 2006. pp. 77-88

[23] Jones RT, Geldenhuys IJ. The pros and cons of reductive matte smelting for PGMs. Minerals Engineering. 2011;**24**(6):495-498

[24] McDougall I, Eksteen JJ. Sidewall design to improve lining life in a platinum smelting furnace. In: International Smelting Technology Symposium (Incorporating the 6th Advances in Sulphide Smelting Symposium). Warrendale, PA: TMS (The Minerals, Metals & Materials Society); 2012. pp. 47-54

[25] Thethwayo BM. Sulphidation of copper coolers in PGM smelters. [MSc thesis]. South Africa: University of Pretoria; 2010

Chapter 19

Rare Earth Extraction from NdFeB Magnets

Jiro Kitagawa and Masami Tsubota

Additional information is available at the end of the chapter

http://dx.doi.org/10.5772/intechopen.70881

Abstract

There is a considerable interest in the extraction of rare earths (RE) from NdFeB magnets in order to recycle rare earth elements. Although the wet process using acid is in practical use in the in-plant recycle of sludge, higher selectivity between rare earths and Fe at room temperature is desired. We have recently proposed a pretreatment of corrosion before the hydrochloric acid (HCl) leaching and the oxalic acid precipitation. Almost full recovery of rare earths can be achieved even at room temperature process. In practical extraction methods, employing wet processes, the discharge of waste acid solution is a problem that needs to be solved to reduce the environmental impact. We further present an encouraging demonstration of rare earth extraction from NdFeB magnet using a closed-loop HCl-based process. Triple extraction has been conducted, and the recovery ratio of rare earths is approximately 50% in each extraction, which is reduced from almost 100% recovery in a one-shot extraction. Despite the reduced extraction efficiency, our method with a rather small number of procedures at almost room temperature is still highly advantageous in terms of cost and environmental friendliness. This study represents the initial step toward the realization of a closed-loop acid process in the recycling of rare earth elements.

Keywords: recycle, corrosion, closed-loop acid process

1. Introduction

Rare earths (RE) are widely consumed in polish, catalysts, rare earth magnets, and so on [1]. Due to the skewed distribution of production countries for RE, many countries depend on the imports from other countries. For example, in Japan, the amount of import of RE metals reached 6479 tons in 2014. The import price, severely depending on international markets, fluctuates widely. Japan is promoting the provisions such as development of alternative materials and the recycle of rare earths. Because the demand of NdFeB magnets has been growing rapidly in recent years because of their use in motors of electric vehicles, wind

turbines, etc., the recycling of RE elements extracted from used magnets has become an important research area [2–5].

There are two main classes of recycling of RE: dry and wet processes. As for the dry process, the recovery of Nd metal has been demonstrated [6] by employing Mg acting as an extraction medium, which forms a low-viscosity liquid alloy with Nd. It has been reported that RE can be separated by a selective reduction and a distillation [7]. The large difference of vapor pressure between $RECl_2$ and $RECl_3$ is skillfully utilized, and the selection efficiency is highly improved. Recently, the difference of oxygen affinity between RE and transition metals has also received attention in that this difference is used as a RE separation. For example, the mixture with flux $FeO{\cdot}B_2O_3$ is a promising method for high purity and high extraction ratio of RE oxide [8]. Thermal isolation of RE oxides from NdFeB magnets using carbon as a reducing agent has been reported [9]. However, many attempts based on the dry process proposed so far are still at the initial laboratory stage.

Development of ore dressing technologies has promoted wet process methods [10, 11], which have already been applied to recycling the sludge of in-plant scrap. After the acid leaching of scrap using HCl, HNO_3, and H_2SO_4, and the filtration of insoluble material mainly containing Fe, acid solution is reacted with oxalic or carbonic acid to form a precipitate containing RE elements. The calcined precipitate becomes RE oxides, which can be returned to the initial manufacturing process of NdFeB magnet. The roasting of NdFeB magnet [12–14] as a pretreatment improves the selectivity between rare earths and Fe, but the recovery ratio of RE is usually rather low with acid (especially HCl) leaching at room temperature. Nearly 100% recovery is achieved [12, 13] when HCl solution is heated to 80–180°C. In the acid leaching method for sludge [15], it is also necessary to heat the acid solution up to 80°C. We have recently proposed a pretreatment of corrosion [16] before the HCl leaching and the oxalic acid precipitation. In this method, the recovery ratio of Nd reaches 97% even when a room temperature process is used.

From the standpoint of sustainability and ecology, the main issue of the wet process is the discharge of waste acid solution. The recyclability of waste acid crucially depends on the efficient extraction of the constituent elements of the magnet from the used acid. One of the promising methods for Fe extraction involves a reaction with an ionic liquid [12, 17–20], which often possesses a high selectivity between rare earths and Fe. Trihexyl(tetradecyl)phosphonium chloride (Cyphos® IL101) is a well-characterized ionic liquid that can extract Fe^{3+} ions in HCl solution with no extraction of trivalent rare earth ions [12, 18]. A possible closed-loop acid process for roasted NdFeB magnet has also been proposed, and the elemental technologies are well investigated [12]. However, an actual demonstration with reuse of waste acid solution has not been performed.

In this study, we introduce the full recovery of rare earth from NdFeB magnet using a wet process with the pretreatment of corrosion but without a closed-loop acid process. After that we describe the detailed experimental results of multiple rare earth extraction in a closed-loop acid process [21].

http://dx.doi.org/10.5772/intechopen.70881

2. Materials and methods

We used two kinds of commercial NdFeB magnets (Niroku seisakusyo). The elemental component of one magnet (denoted as magnet (1)) according to the manufacturer is Nd:Fe:B:the other elements (Dy et al.) = 28:66:1:5 in wt%. The composition of the other magnet (denoted as magnet (2)) was checked by an energy-dispersive X-ray spectrometer equipped in a field emission scanning electron microscope (JEOL, JSM-7100F) and determined to be $Nd_{1.6}Pr_{0.6}Fe_{14}B$. **Figure 1(a)** shows the process flow without a closed-loop acid process. A demagnetized and pulverized NdFeB magnet (1), weighing approximately 0.5 g, was immersed in 3% NaCl solution (300 mL) for 1 week. An air pump provided constant air flow to the solution to accelerate the corrosion.

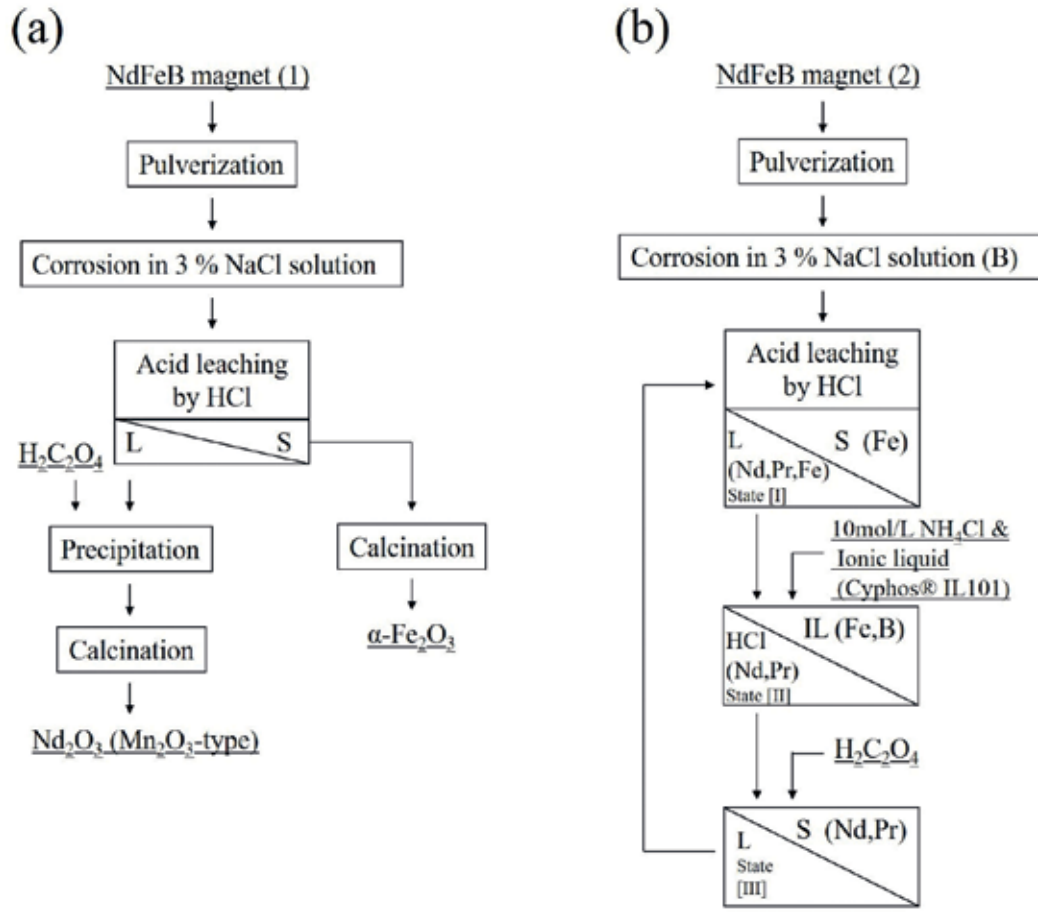

Figure 1. (a) Procedures for rare earth recovery from NdFeB magnet (1) without closed-loop acid process. (b) Procedures for rare earth recovery from NdFeB magnet (2) with closed-loop acid process. S, L, and IL denote the solid, liquid, and ionic liquid, respectively. In procedure (b), elements expected to be present in the solid or solution are denoted.

The corroded sample was leached into HCl solution (100 mL) ranging from 0.1 to 0.3 mol/L, at room temperature. The insoluble material was calcined at 800°C for 5 h to obtain α-Fe_2O_3. The solution after removal of the insoluble was reacted with 0.26 g oxalic acid. The precipitate after the reaction was also calcined at 800°C for 5 h to obtain cubic Mn_2O_3-type Nd_2O_3 (c-Nd_2O_3).

To examine the feasibility of closed-loop acid process, the process flow was modified as shown in **Figure 1(b)**. In this case, the corroded sample was leached in HCl solution (100 mL) with 0.2 mol/L or 0.5 mol/L for 1–2 h. After removal of the insoluble material, the solution was reacted with ionic liquid Cyphos® IL101 (HCl:ionic liquid = 4:1 in volume ratio), purchased from Sigma-Aldrich. The salting-out agent 10 mol/L NH_4Cl was added to the solution. The mixture underwent magnetic stirring at 750 rpm and 60°C for 10 min. Then, it was centrifuged at 2500 rpm for 10 min and split into each component. The HCl solution was reacted with oxalic acid.

Several samples, calcined at 800°C for 5 h in the air, were evaluated using a powder X-ray diffractometer (Shimadzu, XRD-7000 L) with Cu-Kα radiation. We employed an inductively coupled plasma atomic emission spectrometer (Shimadzu, ICPE-9000) to analyze the concentrations of Nd, Pr, Fe, and B dissolved in HCl or NaCl solution. The concentrations were determined by the working curves of standard Nd, Pr, Fe, and B liquids.

3. Results and discussion

The XRD pattern of corroded magnet (1) is shown in **Figure 2**, in which the XRD pattern of magnet (1) itself is also displayed. The main phase of magnet (1) is $Nd_2Fe_{14}B$ with additional minor phase of $NdFe_4B_4$. The XRD pattern of $Nd_2Fe_{14}B$ completely disappears in the corroded magnet, partially containing the XRD pattern of γ-FeOOH denoted by the filled triangles. In order to investigate the origin of the rest of the diffraction peaks (open circles) in the corroded sample, we have corroded NdFeB magnet (1) by hydrogenating it at 600°C for 12 h under a high pressure of hydrogen. The hydrogenated sample [22], as shown in the bottom pattern of **Figure 2**, shows the decomposition into Nd hydride (NdH_{2+x}) and α-Fe. Therefore, in each compound, the corrosion process would independently occur. The XRD pattern of corroded sample after the hydrogenation almost coincides with that of directly corroded magnet (1). Considering that α-Fe corroded into the Fe hydroxide (γ-FeOOH), a Nd hydroxide is probably responsible for the rest of the diffraction peaks (open circles) in the corroded sample. We note here that the NaCl concentration is not optimized. We simply suppose the sea water which is an abundant resource. The preliminary result using more concentrated NaCl solution (10%) also leads to the same results.

We checked the XRD pattern of insoluble material after HCl leaching of the corroded sample as shown in **Figure 3(a)**. The diffraction peaks match well with those of the XRD pattern of γ-FeOOH, which transforms into α-Fe_2O_3 through the calcination (see **Figure 3(b)**). **Figure 3(a)** supports that the Nd hydroxide would be selectively dissolved into HCl solution, in which Nd ions are generated. The oxalic acid precipitation was performed to recover Nd. The precipitate has been calcined and evaluated by XRD pattern, which is displayed in **Figure 3(b)** with the simulated pattern of c-Nd_2O_3. The XRD patterns are well matched between the calcined precipitate and c-Nd_2O_3, suggesting the successful recovery of Nd in the form of Nd oxide.

http://dx.doi.org/10.5772/intechopen.70881

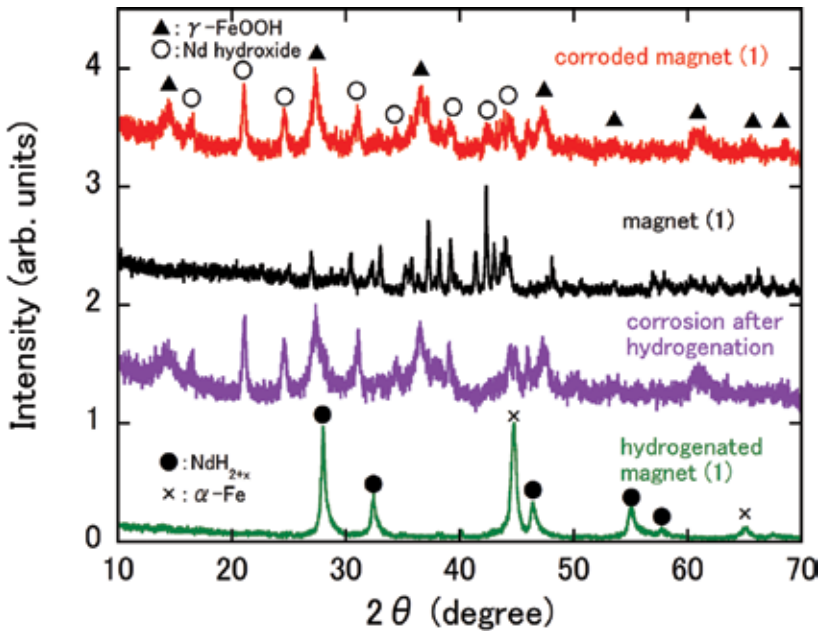

Figure 2. XRD patterns of corroded magnet, corroded sample after hydrogenation, and hydrogenated magnet. The employed magnet is magnet (1). The origin of each pattern is shifted by an integer value for clarity. Based partly on Ref. [16].

Figure 4 shows the leaching time dependences of effective recovery ratio R of Nd through 0.1, 0.2, and 0.3 mol/L HCl leaching. R was obtained by the equation.

$$R = (\text{Mass of Nd in } Nd_2O_3)/(\text{Mass of Nd in magnet}) \times 100 \quad (1)$$

For each HCl concentration, R increases with increasing leaching time, and approximately saturates, however exceeds 100% at some conditions. The excess above 100% would be due to the existence of impurity phases in c-Nd_2O_3 and/or incomplete filtration technique.

Next, we show the experimental results of rare earth extraction using the closed-loop acid process. The starting magnet is magnet (2) with the mass of approximately 0.5 g. The distribution of constituent elements in our method mentioned above is partially unknown. Thus, a one-shot extraction with 0.2 mol/L HCl and 0.26 g oxalic acid but with no use of ionic liquid was performed. **Table 1** shows the distribution of each ion in the NaCl solution after removal of the corroded sample and in the HCl solution after removal of precipitates produced by the reaction with oxalic acid. In the NaCl solution, only B is detected. A sufficient amount of oxalic acid can efficiently separate rare earths. A large amount of Fe stays in the HCl solution. The expected ion concentrations of the completely dissolved 0.5 g magnet are 1041 mg/L for Nd, 381 mg/L for Pr, 3527 mg/L for Fe, and 49 mg/L for B, respectively. The summation of the B concentrations in the two states listed in **Table 1** is not far from 49 mg/L. Then, approximately 30% of B can be separated by the NaCl solution, and the remaining B stays in the HCl solution. Approximately 60% of the Fe ions are contained in the insoluble material obtained after HCl leaching. The recovery ratio of Nd (Pr) is 99% (97%).

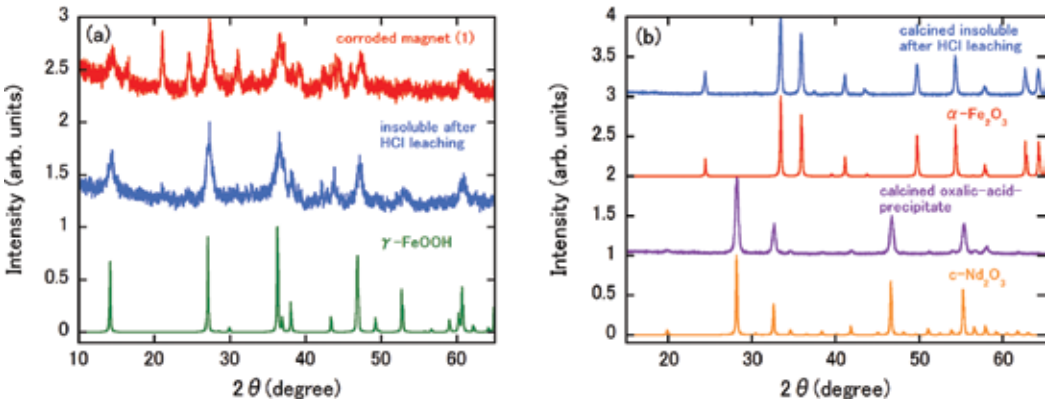

Figure 3. (a) XRD patterns of corroded magnet (1) and insoluble material after HCl (0.1 mol/L, 30 min) leaching and γ-FeOOH. (b) XRD patterns of insoluble material and oxalic acid precipitate in HCl solution. They were calcined in the air. The simulation patterns of α-Fe_2O_3 and c-Nd_2O_3 are also shown. The HCl concentration is 0.2 mol/L, and the leaching time is 2 h. The origin of each pattern in (a) and (b) is shifted by an integer value for clarity. Based partly on Ref. [16].

Following the results of Ref. [12] which reported that salting-out agent NH_4Cl plays an essential role in full extraction of Fe by an ionic liquid, the dependence of extraction efficiency on NH_4Cl concentration was determined. Without NH_4Cl, the extraction efficiency of Fe is only 40%, increasing to 75% with 5 mol/L NH_4Cl and 95% for 10 mol/L NH_4Cl. In this experiment, we also found that B is fully extracted by the ionic liquid. We speculate that Cyphos® IL101 represented by $C_{38}H_{68}ClP$ transforms into $C_{38}H_{68}FeCl_4$, after the incorporation of Fe^{3+} ions. Thus, the extraction efficiency of Fe severely depends on the Cl concentration, and the salting-out agent NH_4Cl is necessary to provide enough Cl ions.

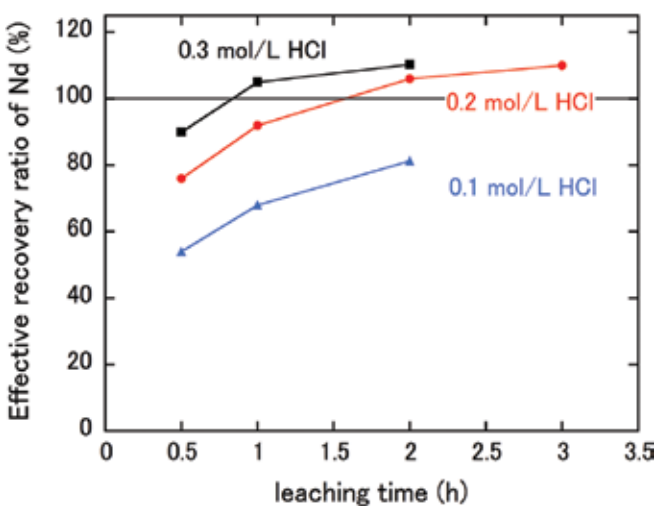

Figure 4. Leaching time dependences of effective recovery ratio of Nd. The examined HCl solutions are 0.1, 0.2, and 0.3 mol/L. Based partly on Ref. [16].

Solution	Nd (mg/L)	Pr (mg/L)	Fe (mg/L)	B (mg/L)
NaCl after removal of corroded magnet	ND	ND	ND	12.3
HCl after removal of oxalic acid precipitates	10.6	13.0	1480	28.6

ND means not detected. Based on Ref. [21].

Table 1. Distribution of Nd, Pr, Fe, and B in the one-shot recovery process.

The preliminary experiment for a closed-loop process of HCl solution was performed using 0.5 mol/L HCl to reduce the experimental time. The oxalic acid mass was maintained at 0.26 g. Hereafter, the HCl solutions after removal of insoluble material in the acid leaching, after Fe extraction by the ionic liquid, and after removal of rare earths by oxalic acid precipitation are denoted state [I], [II], and [III], respectively (see also **Figure 1(b)**). **Table 2** shows the Nd, Pr, and Fe concentrations of these states during each cycle. In the first cycle, approximately 24% of rare earths are extracted together with Fe by the ionic liquid. Only Nd and Pr are separated by the reaction with the oxalic acid. In state [I] during the second cycle, the concentrations of Nd and Pr are approximately one-quarter of those during the first cycle, which means an immediate precipitation due to excess oxalic acid in the previous cycle.

The preliminary experiment suggested that the weight of oxalic acid needs to be adjusted. The weight of oxalic acid for a 0.5 g magnet, reproducing the initial concentrations of Nd and Pr in state [I] in the second cycle, has been searched as shown in **Figure 5**. The vertical axis shows the difference in Nd (Pr) ion concentration in state [I] between the first and second cycles, which is denoted as $\triangle c$. A positive value for $\triangle c$ indicates a poor precipitation efficiency, and a negative value indicates an excess oxalic acid. For each element, $\triangle c$ linearly decreases with increasing weight of oxalic acid. A weight of 0.1675 g oxalic acid can reproduce the initial Nd (Pr) ion concentration of state [I] in the second cycle. The chemical equation for oxalic acid precipitation is.

$$1.46\,Nd^{3+} + 0.54\,Pr^{3+} + 3H_2C_2O_4 \rightarrow \left(Nd_{0.73}Pr_{0.27}\right)_2\left(C_2O_4\right)_3 + 3H_2\uparrow \quad (2)$$

If the starting magnet weight is 0.5 g, the ideal amount of oxalic acid is 0.1335 g. However, as shown in **Figure 5**, Nd and Pr would not fully precipitate for 0.1335 g of oxalic acid. To achieve sufficient precipitation, the amount of oxalic acid that is consumed must be 1.3 times larger.

Cycle	State of solution	Nd (mg/L)	Pr (mg/L)	Fe (mg/L)
First	[I]	929	346	2320
	[II]	707	264	105
	[III]	16.9	17.4	109
Second	[I]	218	94	2770
	[II]	231	99	132
	[III]	ND	ND	134

The notations of solutions are defined in **Figure 1(b)**. ND means not detected. Based partly on Ref. [21].

Table 2. Distribution of Nd, Pr, and Fe in the preliminary experiment of a closed loop for HCl solution.

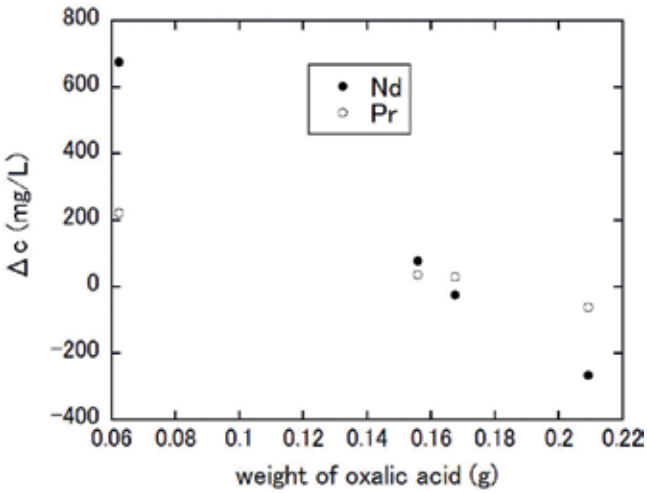

Figure 5. A plot of Δc vs. the weight of oxalic acid. Δc represents the difference in Nd (Pr) ion concentration after HCl leaching of corroded magnet between the first and second cycles. Based partly on Ref. [21].

From the preliminary experiments for the closed-loop process of HCl solution, we have obtained the conditions of 10 mol/L NH_4Cl and 0.1675 g oxalic acid for the recycling of 0.5 g magnet. **Table 3** shows the results of a demonstration of triple rare earth extraction from 0.5 g magnet with the closed loop of HCl solution. The HCl concentration was 0.5 mol/L to expedite the experiment. The concentrations of Nd and Pr ions are measured in states [I], [II], and [III]. In each cycle, 10–15% of Nd and Pr ions are extracted together with Fe ions by the ionic liquid, as in the preliminary experiment (see **Table 2**). Contrary to our expectation, 30–35% of Nd and Pr ions remain in solution after the oxalic acid precipitation. However, these ions apparently do not contribute to the rare earth concentrations of state [I] in the next cycle; the

Cycle	State of solution	Nd (mg/L)	Pr (mg/L)	Recovery ratio of Nd (%)	Recovery ratio of Pr (%)
First	[I]	971	370	50	47
	[II]	818	311		
	[III]	328	136		
Second	[I]	980	406	49	50
	[II]	836	357		
	[III]	352	156		
Third	[I]	919	410	61	56
	[II]	842	360		
	[III]	280	130		

The notations of the solutions are defined in **Figure 1(b)**. Based partly on Ref. [21].

Table 3. The distribution of Nd and Pr and the recovery ratio of each element in a triple rare earth extraction.

concentrations of Nd and Pr ions in state [I] are the same as those during the previous cycle. The recovery ratio of each element, calculated by eliminating the amount of element extracted by the ionic liquid, is approximately 50% in all cycles. **Figure 6** shows the XRD pattern of calcined insoluble material after HCl leaching in the second cycle. The simulated patterns of $Nd_{0.73}Pr_{0.27}FeO_3$ and α-Fe_2O_3 are also exhibited. Elemental Nd (Pr) is partially recovered together with Fe. The XRD pattern in **Figure 6** supports the idea that the Nd and Pr elements, which are present in the same concentration as the ions in state [III], would enter insoluble material in state [I] in the next cycle.

In our method, Cyphos® IL101 is rather expensive, and the regeneration of the ionic liquid by stripping Fe^{3+} is required to reduce the cost. We examined two stripping methods. The first one is the stripping using NaOH solution. After the reaction of the ionic liquid containing Fe^{3+} ions with NaOH solution, $Fe(OH)_3$ is expected to be precipitated, and Fe_2O_3 would be obtained after the calcination. The ionic liquid was reacted with NaOH solution (1 mol/L) with a volume ratio of Cyphos® IL101:NaOH solution = 1:2.The calcined precipitate was checked by the XRD pattern, and it is shown in **Figure 7(a)**. The obtained pattern is in good agreement with the XRD pattern of $NaFeO_2$. The recovery ratio of Fe is estimated to be 17%. The second method is the employment of ammonia solution, for which 100% stripping of Fe^{3+} has been already reported [23]. We roughly followed the reported recipe [23]. The yellow-colored ionic liquid containing Fe^{3+}, which was obtained in the actual process flow, was reacted with the ammonia solution (approximately 3 wt.%) with a volume ratio of Cyphos® IL101:ammonia solution = 1:10.

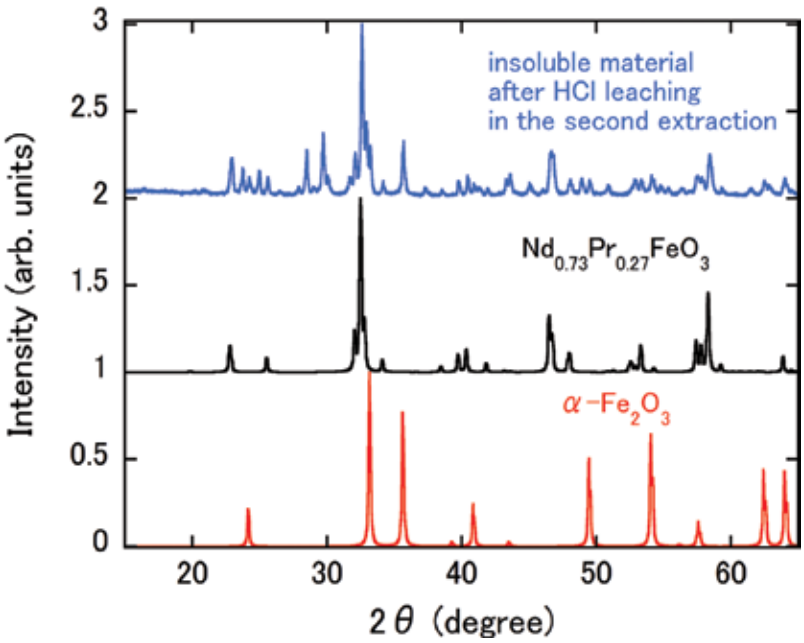

Figure 6. XRD pattern of calcined insoluble material after HCl leaching in the second extraction. The simulated $Nd_{0.73}Pr_{0.27}FeO_3$ and α-Fe_2O_3 patterns are also shown. The origin of each pattern is shifted by an integer value for clarity. Based partly on Ref. [21].

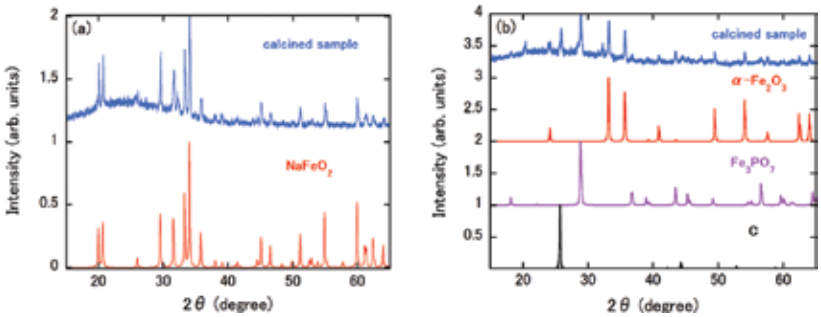

Figure 7. (a) XRD pattern of the calcined sample recovered from used Cyphos® IL101 reacted with NaOH solution. The simulated $NaFeO_2$ pattern is also presented. The origin of each pattern is shifted by an integer value for clarity. (b) XRD pattern of calcined sample recovered from used Cyphos® IL101 reacted with ammonia solution. The simulated α-Fe_2O_3, Fe_3PO_7, and C patterns are also presented. The origin of each pattern is shifted by an integer value for clarity. (Based partly on Ref. [21]).

The precipitate at the interface between the liquids was collected using a cellulose filter and calcined together with the filter in the air. **Figure 7(b)** shows the XRD pattern of the calcined sample recovered from used Cyphos® IL101. The figure also displays the simulated patterns of α-Fe_2O_3, Fe_3PO_7, and C. The experimental XRD pattern closely matches the superposition of simulated patterns. The sources of P and C atom contamination would be Cyphos® IL101 containing P and the cellulose filter, respectively. Despite the contamination due to our insufficient filtration technique, Fe can be stripped. Furthermore, the yellow-colored ionic liquid once again became transparent after Fe^{3+} stripping, which means the ionic liquid is regenerated.

Focusing on the one-shot recovery processes, a comparison between our method and other methods [12–15] based on the acid leaching mentioned in Introduction is shown in **Table 4**. The number of steps in the recovery processes and the rare earth recovery ratio of each method are similar. The roasting used in Refs. [12–14] would have a cost disadvantage. Although Ref. [15] does not employ roasting, HNO_3 has a disadvantage because waste discharge containing nitrate salt is severely controlled by law for environmental reasons. The acid leaching process in our method and in Ref. [14] is performed at room temperature, which means that these are

Items	Our method [16]	[12]	[13]	[14]	[15]
Pretreatment	Corrosion at RT	Roast at 950°C	Roast at 500–1000°C	Roast at 750°C	Sludge
Acid	HCl	HCl	HCl	H_2SO_4	HNO_3
Acid leaching temperature	RT	80°C	180°C	RT	80°C
B separation	30%	Not separated	Not separated	Not separated	Not separated
Recovery ratio of rare earths (%)	97	100	100	100	94

RT means room temperature. Based partly on Ref. [21].

Table 4. Comparison between our method and other methods based on acid leaching in a one-shot recovery process.

safe processes. Since B is harmful, its separation is highly desired. Our method has achieved 30% B separation, whereas the other methods do not report a clear B separation. If a closed-loop acid process with a high recovery ratio of rare earths is realized, our method is promising because each step except Fe extraction by ionic liquid is performed at room temperature. This condition and the rather simple procedures lead to a safe and low-cost recovery process. In addition, the peculiar feature of B separation in our method is environmentally friendly.

4. Summary

Rare earth extraction methods based on acid leaching are entering the stage of practical use. To address the issue of rather low selectivity between rare earths and Fe at the room temperature acid-process, we have proposed the pretreatment of corrosion. Our method has improved the selectivity, and rare earth recovery ratio, in one-shot extraction, reaches to almost 100% even at room temperature. For sustainability and environmental considerations, the recyclability of waste acid solution is one of the central issues in rare earth recycling, and this has not been well investigated. In this work, we have experimentally determined the recovery ratio of rare earth elements in our method with the closed-loop acid process. This ratio is approximately 50%, reduced from almost full recovery in a one-shot extraction. Although the recovery ratio is rather low at the present stage, our encouraging result should lead to rapid advancement of the study of recycling using a closed-loop acid process.

5. Future directions

The demonstration of closed-loop process for HCl solution indicates that the precipitation by oxalic acid is not sufficient, although the amount of oxalic acid is larger than the ideal amount calculated using the chemical formula of precipitation. To increase the recovery ratios of rare earth elements, if the amount of oxalic acid is increased, it will result in a reduced recovery ratio in the second cycle, as deduced from **Table 2**. Thus, a trade-off between the number of rare earth extractions and the recovery ratio of rare earths might exist for the present precipitation condition. The main cause of the reduced recovery ratio is the insufficient ionization of oxalic acid. The degree of ionization of oxalic acid strongly depends on the pH of the solution. The ionization concentration generally increases with increasing pH, and the full ionization of oxalic acid with an ideal weight of 0.1335 g would be realized. Another issue to be considered is the partial rare earth extraction by the ionic liquid. If the oxalic acid precipitation process is performed before the process of Fe^{3+} extraction by the ionic liquid, only rare earth elements would be separated due to the high selectivity between rare earths and Fe under oxalic acid precipitation. Thus, the issue would be resolved by reversing the sequence of the two processes. As shown in **Figure 6**, unassigned peaks of material other than α-Fe_2O_3 and $Nd_{0.73}Pr_{0.27}FeO_3$ are present in the XRD spectrum. In our study, complete separation of the ionic liquid from the HCl solution is difficult, which results in contamination of the calcined sample. Further improvement of the separation technique is needed to obtain a pure calcined sample.

Acknowledgements

This research was supported by the Matching Planner Program of the Japan Science and Technology Agency (JST). J.K. is grateful for the support provided by the Comprehensive Research Organization of Fukuoka Institute of Technology.

Author details

Jiro Kitagawa[1]* and Masami Tsubota[2]

*Address all correspondence to: j-kitagawa@fit.ac.jp

1 Department of Electrical Engineering, Faculty of Engineering, Fukuoka Institute of Technology, Fukuoka, Japan

2 Physonit Inc., Hiroshima, Japan

References

[1] Goonan TG. Rare earth elements—End use and recyclability. U.S. Geological Survey Scientific Investigations Report. 2011;**2011-5094**:1-15

[2] Tanaka M, Oki T, Koyama K, Narita H, Oishi T. Recycling of rare earths from scrap. Handbook on the Physics and Chemistry of Rare Earths. 2013;**43**:159-211

[3] Binnemans K, Jones PT, Blanpain B, Gerven TV, Yang Y, Walton A, Buchert M. Recycling of rare earths: A critical review. Journal of Cleaner Production. 2013;**51**:1-22

[4] Darcy JW, Bandara D, Mishra B, Emmert MH. Challenges in recycling end-of-life rare earth magnets. JOM. 2013;**65**:1381-1382

[5] Rademaker JH, Kleijn R, Yang Y. Recycling as a strategy against rare earth element criticality: A systemic evaluation of the potential yield of NdFeB magnet recycling. Environmental Science & Technology. 2013;**47**:10129-10136

[6] Takeda O, Okabe TH, Umetsu Y. Recovery of neodymium from a mixture of magnet scrap and other scrap. Journal of Alloys and Compounds. 2006;**408-412**:387-390

[7] Uda T, Jacob KT, Hirasawa M. Technique for enhanced rare earth separation. Science. 2000;**289**:2326-2329

[8] Bian Y, Guo S, Jiang L, Tang K, Ding W. Extraction of rare earth elements from permanent magnet scraps by FeO-B_2O_3 flux treatment. Journal of Sustainable Metallurgy. 2015;**1**:151-160

[9] Maroufi S, Khayyam R, Sahajwalla V. Thermal isolation of rare earth oxides from Nd-Fe-B magnets using carbon from waste tyres. ACS Sustainable Chemistry & Engineering. 2017;**5**:6201-6208

[10] Xie F, Zhang TA, Dreisinger D, Doyle F. A critical review on solvent extraction of rare earths from aqueous solutions. Minerals Engineering. 2014;**56**:10-28

[11] Yang Y, Walton A, Sheridan R, Güth K, Gauß R, Gutfleisch O, Buchert M, Steenari B-M, Gerven TV, Jones PT, Binnemans K. REE recovery from end-of-life NdFeB permanent magnet scrap: A critical review. Journal of Sustainable Metallurgy. 2017;**3**:122-149

[12] Hoogerstraete TV, Blanpain B, Gerven TV, Binnemans K. From NdFeB magnets towards the rare-earth oxides: A recycling process consuming only oxalic acid. RSC Advances. 2014;**4**:64099-64111

[13] Japan Oil, Gas and Metals National Co., National Institute of Advanced Industrial Science and Technology, Tohoku Univ. Method of rare-earth extraction by acid leaching. Japanese Unexamined Patent Application Publication 2011; No. 2011-184735

[14] Önal MAR, Borra CR, Guo M, Blanpain B, Gerven TV. Recycling of NdFeB magnets using sulfation, selective roasting, and water leaching. Journal of Sustainable Metallurgy. 2015;**1**:199-215

[15] Rabatho JP, Tongamp W, Takasaki Y, Haga K, Shibayama A. Recovery of Nd and Dy from rare earth magnetic waste sludge by hydrometallurgical process. Journal of Material Cycles and Waste Management. 2013;**15**:171-178

[16] Kataoka Y, Ono T, Tsubota M, Kitagawa J. Improved room-temperature-selectivity between Nd and Fe in Nd recovery from Nd-Fe-B magnet. AIP Advances. 2015;**5**:117212

[17] Billard I. Ionic liquids: New hopes for efficient lanthanide/actinide extraction and separation? Handbook on the Physics and Chemistry of Rare Earths. 2013;**43**:213-273

[18] Hoogerstraete TV, Wellens S, Verachtert K, Binnemans K. Removal of transition metals from rare earths by solvent extraction with an undiluted phosphonium ionic liquid: Separations relevant to rare-earth magnet recycling. Green Chemistry. 2013;**15**:919-927

[19] Dupont D, Binnemans K. Recycling of rare earths from NdFeB magnets using a combined leaching/extraction system based on the acidity and thermomorphism of the ionic liquid [Hbet][Tf2N]. Green Chemistry. 2015;**17**:2150-2163

[20] Parmentier D, Hoogerstraete TV, Metz SJ, Binnemans K, Kroon MC. Selective extraction of metals from chloride solutions with the tetraoctylphosphonium oleate ionic liquid. Industrial and Engineering Chemistry Research. 2015;**54**:5149-5158

[21] Kitagawa J, Uemura R. Rare earth extraction from NdFeB magnet using a closed-loop acid process. Scientific Reports. 2017;**7**:8039

[22] Kataoka Y, Kawamoto Y, Ono T, Tsubota M, Kitagawa J. Hydrogenation of Nd-Fe-B magnet powder under a high pressure of hydrogen. Results in Physics. 2015;**5**:99-100

[23] Wellens S, Hoogerstrete TV, Möller C, Thijs B, Luyten J, Binnemans K. Dissolution of metal oxides in an acid-saturated ionic liquid solution and investigation of the back-extraction behaviour to the aqueous phase. Hydrometallurgy. 2014;**144-145**:27-33

Edited by Mohindar Singh Seehra and Alan D. Bristow

The use of copper, silver, gold and platinum in jewelry as a measure of wealth is well known. This book contains 19 chapters written by international authors on other uses and applications of noble and precious metals (copper, silver, gold, platinum, palladium, iridium, osmium, rhodium, ruthenium, and rhenium). The topics covered include surface-enhanced Raman scattering, quantum dots, synthesis and properties of nanostructures, and its applications in the diverse fields such as high-tech engineering, nanotechnology, catalysis, and biomedical applications. The basis for these applications is their high-free electron concentrations combined with high-temperature stability and corrosion resistance and methods developed for synthesizing nanostructures. Recent developments in all these areas with up-to-date references are emphasized.

Published in London, UK

IntechOpen

ISBN 978-1-83881-377-2